Over the Resonance

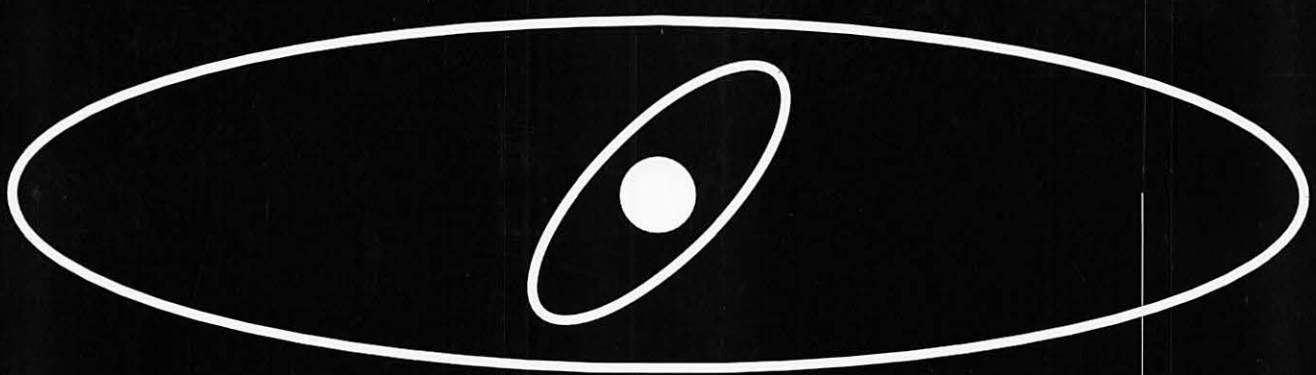

Proceedings of the 35th Symposium on Celestial Mechanics
March 6-8, 2003 at Izu-Nagaoka-Onsen, Shizuoka, Japan
Eiichiro Kokubo, Hideyoshi Arakida, & Tadato Yamamoto (eds.)

天体力学Ｎ体力学研究会　2003年3月6日～3月8日　KKR伊豆長岡保養所「千歳荘」にて

伊豆長岡天体力学Ｎ体力学研究会集録

平成15年3月6日(木)–8日(土)

静岡県田方郡伊豆長岡町 伊豆長岡保養所千歳荘

Over the Resonance
-共鳴の後で-

Proceedings of the 35th Symposium on Celestial Mechanics

March 6–8, 2003 at Izu-Nagaoka-Onsen, Shizuoka, Japan

Editors: E. Kokubo, H. Arakida, and T. Yamamoto

Preface/序文

2002 年度の天体力学 N体力学研究会 (通称伊豆長岡 N体) は、2003 年 3 月 6 日から 8 日にかけてまだ温泉の温かさがうれしい早春の伊豆長岡温泉千歳荘にて滞在型研究会の形で開催されました。口頭発表が 18 件、ポスター発表が 21 件あり、参加者は大学生からシニア研究者までの 55 名を数えました。

伊豆長岡 N体のメインテーマは、Over the Resonance –共鳴のあとで–ということで、天体力学の真髄である「共鳴 (resonance)」でした。軌道共鳴現象は銀河円盤から惑星リングまでさまざまなスケールでの円盤系のダイナミクスで重要な役割を果たしています。例えば、銀河円盤での構造形成、惑星系の構造形成、惑星リングの構造形成などをあげることができます。今回は軌道共鳴の基本である平均運動共鳴と永年共鳴についての 2 つの招待講演を企画しました。平均運動共鳴については吉川真氏 (宇宙科学研究所) に、永年共鳴については木下宙氏 (国立天文台) にレビューしていただきました。興味深くわかりやすいレビューをしていただいた両氏にはこの場を借りて感謝したいと思います。また、関連する 3 つの共鳴現象についての寄与講演もお願いしました。Lindblad 共鳴については武田隆顕氏 (国立天文台) が、自転-軌道共鳴については跡部恵子氏 (東京工業大学) が、そして古在共鳴については小久保英一郎 (国立天文台) が講演しました。

共鳴のおもしろさ奥の深さを感じてもらえましたでしょうか。これらの共鳴現象の基礎物理、相互関係、そして結果として何が起きるのかを理解していただけたなら世話人としてうれいし限りです。

研究会運営にあたっては千歳荘の職員の方々に大変お世話になりました。厚くお礼申し上げます。また、国立天文台の福島登志夫氏には集録の出版費用を提供していただきました。厚くお礼申し上げます。

平成 16 年初春 世話人代表 小久保英一郎

Editors/世話人

小久保英一郎 (Kokubo, Eiichiro) 国立天文台理論天文学研究系
kokubo@th.nao.ac.jp
荒木田英禎 (Arakida, Hideyoshi) 国立天文台天文情報公開センター
h.arakida@nao.ac.jp
山本一登 (Yamamoto, Tadato) 総合研究大学院大学
tadato.yamamoto@nao.ac.jp

Table of Contents/目次

"Over the Resonance" Feature Articles

Dynamical resonances in planetary formation and evolution
Shigeru Ida 1
Obliquity variations of terrestrial planets in habitable zones
Keiko Atobe, Shigeru Ida, and Takashi Ito 2
Mean motion resonances in the solar system
Makoto Yoshikawa 21
Visualization of Lindblad and corotation resonances
Takaaki Takeda 33
A note on secular resonances
Hiroshi Kinoshita 39
Kozai Mechanism ("Resonance")
Eiichiro Kokubo 52

Stellar Dynamics

Long-term evolution of stellar self-gravitating system away from the thermal equilibrium : connection with non-extensive statistics
Atsushi Taruya and Masa-aki Sakagami 60
On the "stellar dynamical" evidences for massive black holes
Junichiro Makino 70
Formation of non-Gaussian velocity distribution after the collapse in self-gravitating system
Naoko Kanaeda, Osamu Iguchi, and Yasuhide Sota 77
Fractal structure in one-dimensional sheet model and expansion law
Takayuki Tatekawa and Kei-ichi Maeda 88
Formation and evolution of a globular cluster system
Tsuyoshi Sakamoto and Masashi Chiba 95

Kinematics of tidal debris from omega Centauri's progenitor galaxy
Arihiro Mizutani, Masashi Chiba, and Tsuyoshi Sakamoto 115

Formation of Planetary Systems

Formation of terrestrial planets in a dissipating gas disk with Jupiter and Saturn
Junko Kominami and Shigeru Ida 128
Migration mechanism of proto-Neptune
Keisuke Takahashi and Sei-ichiro Watanabe 144
The evidence of an early stellar encounter and orbital evolution due to gas drag in Edgeworth-Kuiper belt objects
Hiroshi Kobayashi 149
Three-body affairs in the outer solar system
Yoko Funato, Junichiro Makino, Piet Hut, Eiichiro Kokubo, and Daisuke Kinoshita 190
Gravitational interaction between a planet and an optically thin protoplanetary disk
Masafumi Ito and Hidekazu Tanaka 198
Disk-planet gravitational interaction
Kei Sakai and Hidekazu Tanaka 205

Solar System Dynamics

Direct calculation method of the Poisson parentheses for the Keplerian elements
Takeshi Inoue 208
Return of shepherding satellites
Hiroshi Daisaka and Junichiro Makino 216
Final answer to the problem of the excess secular variation in the longitude of the perihelion of Mercury
Takeshi Inoue 230
Subgroups of the Kreutz sungrazers
Hideo Sumitani 235

Resonance structure in Kuiper belt
Hiroshi Nakai and Hiroshi Kinoshita 243
Candidate Centaurs trapped in mean motion resonances with a giant planet
Yoshimitsu Masaki and Hiroshi Kinoshita 255

Earth Rotation

Examination of the eclipse records of Japanese medieval times and the Earth's rotation
Mitsuru Sôma, Kiyotaka Tanikawa, Kin-aki Kawabata, and Hiromichi Imae 267
Time variation of the moment of inertia of the Earth derived from Chinese and Japanese records of ancient solar eclipses
Kin-aki Kawabata, Kiyotaka Tanikawa, and Mitsuru Sôma 282

Dynamics of Artificial Satellites

Problems in the orbital determination for NOZOMI spacecraft 2
Makoto Yoshikawa 299
Development of solar radiation pressure computation software
Toshihiro Kubo-oka 307

Theory of Dynamical Systems

Homoclinic structure of a reduced nonlinear symplectic map chain
Shin-itiro Goto and Kazuhiro Nozaki 313
Collinear three-body problem with non-equal masses by symbol dynamics
Masaya Masayoshi Saito and Kiyotaka Tanikawa 324
Low-dimensional subsystems in anharmonic lattices
Susumu Shinohara 332
A classification of subproblems in the Newtonian N-body problem
Masayoshi Sekiguchi 340

A complete list of integrable two-dimensional homogeneous polynomial potentials with a polynomial first integral up to quartic in the momenta
Katsuya Nakagawa and Haruo Yoshida 345
Is Arnold diffusion relevant to global diffusion?
Seiichiro Honjo and Kunihiko Kaneko 367
Non-Birkhoff periodic orbits in a zone of instability
Kiyotaka Tanikawa and Yoshihiro Yamaguchi 377
A zone void of monotone points in the standard map
Yoshihiro Yamaguchi and Kiyotaka Tanikawa 385

Numerical Techniques

Efficient orbit integration by scaling for Kepler energy consistency
Toshio Fukushima 396
Explicit symmetric multistep methods for first-order differential equations
Tadato Yamamoto and Toshio Fukushima 411
Comment on Cowell's method
Noriaki Watanabe 427

Appendix

Symbols and Names often used in Celestial Mechanics 442

Symposium program 446
Author index and participant list 449

惑星形成・進化における力学的共鳴

Dynamical resonances in planetary formation & evolution

井田 茂（東工大・地惑）
Shigeru Ida (Tokyo Institute of Technology)

	その場相互作用	平均場相互作用
軌道共鳴	平均運動共鳴	永年共鳴
自転・軌道共鳴	自転・公転共鳴	歳差・軌道面変動共鳴

共鳴に捕まえる

一方的な
角運動量輸送

軌道共鳴：その場相互作用

その場相互作用

軌道共鳴	平均運動共鳴
自転・軌道共鳴	自転・公転共鳴

ガリレオ衛星
海王星とEKBOs
GL876, HD82943

共鳴に捕まえる

円盤・惑星共鳴：Lindblad 共鳴
⇔平均運動共鳴

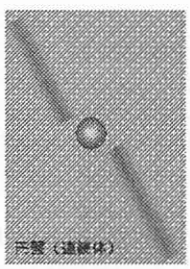

フーリエ展開

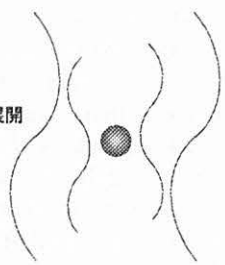

自転・軌道共鳴：その場相互作用

その場相互作用

軌道共鳴	平均運動共鳴
自転・軌道共鳴	自転・公転共鳴

locking
月、ガリレオ衛星
水星
Hot Jupiters

共鳴に捕まえる

軌道共鳴：平均場相互作用

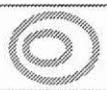

平均場相互作用

軌道共鳴	永年共鳴
自転・軌道共鳴	歳差・軌道面変動共鳴

小天体群の構造形成
Sweeping
小惑星帯、EKBOsの力学加熱
eccentric planets の e 交換

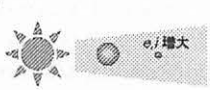

一方的な
角運動量輸送

自転・軌道共鳴：平均場相互作用

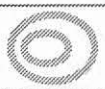

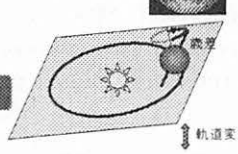

平均場相互作用

軌道共鳴	永年共鳴
自転・軌道共鳴	歳差・軌道面変動共鳴

自転軸傾度の変動
陸上生命発生の条件

一方的な
角運動量輸送

Obliquity Variations of Terrestrial Planets in Habitable Zones

Keiko Atobe[1], Shigeru Ida[1], and Takashi Ito[2]
1 Department of Earth and Planetary Sciences, Tokyo Institute of Technology,
2-12-1 Ookayama, Meguro-ku, Tokyo 152-8551, Japan
Email: atobe@geo.titech.ac.jp
2 Astronomical Data Analysis Computer Center, National Astronomical Observatory,
Mitaka, Tokyo 181-8588, Japan

Submitted to Icarus

ABSTRACT

We have derived analytical formulae of obliquity variations of terrestrial planets in spin-orbit resonant regions as well as in non-resonant regions. With our formulae, we have investigated obliquity variations of possible terrestrial planets in habitable zones (HZs) perturbed by a giant planet(s) in extrasolar planetary systems. All the extrasolar planets so far discovered are inferred to be Jovian-type gas giants, however, terrestrial planets could also exist in the extrasolar planetary systems. In order for life, in particular for land-based life, to evolve and survive on a possible terrestrial planet in a HZ, small obliquity variations of the planet is required in addition to its orbital stability, because large obliquity variations may cause significant climate change. In general, large obliquity variations are caused by spin-orbit resonances where the precession frequency of a planet's spin nearly coincides with one of the precession frequencies of the ascending node of the planet's orbit. Considering a system that consists of a host star, a hypothetical giant planet(s), and a hypothetical mass-less terrestrial planet, we derived the analytical formulae of obliquity variation amplitude of the terrestrial planet. In some cases, we compared the analytical formulae with numerical integration of the precession equation and found excellent agreement. Using our analytical expressions, we evaluated the obliquity variations of terrestrial planets with prograde spins in HZs. We found that the obliquity of a terrestrial planet in a HZ is most largely affected by the giant planet when the giant planet is so far from the HZ that the orbit of the terrestrial planet is hardly perturbed. The obliquity variations of terrestrial planets are rather small when the giant planet is so close to largely affect the orbit of the terrestrial planet. We investigated the obliquity variations of possible terrestrial planets in the HZs in the known extrasolar planetary systems. We found about half of the known extrasolar planetary systems show small obliquity variations (smaller than 10 degrees) over the entire HZs. However, the systems with both small obliquity variations and stable orbits in their HZs are only 1/5 of the known systems. Most of such systems are comprise with short-period giant planets. If additional planets are found in the known planetary systems, they generally tend to enhance obliquity variations of possible terrestrial planets. On the other hand, a large and/or close satellite that significantly enhances precession rate of the spin axis of the terrestrial planet is likely to reduce obliquity variations of the planet on a stable orbit near 1AU. Moreover, if a terrestrial planet is in retrograde spin state, the spin-orbit resonance does not occur. Retrograde spin, or a large and/or close satellite might be essential for land-based life to survive on a terrestrial planet in a HZ.

1. INTRODUCTION

More than 100 extrasolar planets around nearly 90 Sun-like stars are now known (see e.g., http://cfa-www.harvard.edu/planets/). The main technique used to detect these planets is to observe reflex motion of host stars due to planetary motion through the Doppler shift of stellar spectral lines (e.g., Marcy et al. 2000). The planets so far found are as massive as Jupiter, so all the known extrasolar planets are considered to be Jupiter-like giant planets. However, it is reasonable to expect that terrestrial planets (relatively small rocky planets) could be present in some of the extrasolar planetary systems where a giant planet(s) has been detected. Are there terrestrial planets which could harbor life like the Earth does in the extrasolar planetary systems?

All organisms which we are familiar with on the Earth require liquid water during at least part of their life cycle. In order for life to emerge on a terrestrial planet, it is also necessary that their orbits remain confined in the habitable zone (HZ) of its host star over the length of time required for biological evolution. A stel-

lar HZ is the range of distances from a star allowing the existence of liquid water at the surface of a terrestrial planet (Abe 1993; Kasting et al. 1993). The orbital stability of hypothetical Earth-like planets inside the HZs of extrasolar planetary systems have already been investigated through numerical simulations by many authors (Gehman et al. 1996; Jones et al. 2001; Jones and Sleep 2002; Noble et al. 2002; Menou and Tabachnik 2003). Here, orbital stability means that the orbits of the hypothetical terrestrial planets remain confined in stellar HZs over the time required for the evolution of life. In general, if the orbits of giant planets are located in the vicinity of the HZs, terrestrial planets cannot exist on stable orbits long enough inside the HZs because of the strong perturbing influence of the giant planets. Menou and Tabachnik (2003) studied the orbital stability of 85 known extrasolar planetary systems. Their results indicate that more than half of the 85 systems are unlikely to harbor habitable terrestrial planets, however, about a quarter of the known extrasolar systems could have terrestrial planets on stable orbits in the HZs as our own Solar System.

Not long-term orbital stability of terrestrial planets in stellar HZs but also moderate climate on these planets may be necessary for the evolution of life. Planetary climate is greatly influenced by the insolation distribution and intensity, which depends on the orbital parameters and spin motion of a planet, especially eccentricity, obliquity, and the precession motion of the planet (Milankovitch 1941; Berger 1984, 1989). Because of their equatorial bulge, planets are subject to the torque arising from the gravitational force of a host star (and possibly of their satellites and of other planets). This torque causes precessional motion of the spin axis of the planet about its orbit normal. On the other hand, gravitational interactions with other planets cause the orbit normals to precess and nutate about the normal to the invariable plane of the system. So the obliquity of a planet generally changes periodically. In particular, for a land-based life like human beings to evolve and survive, small obliquity variations of those planets are required to keep moderate climate. Then, we treat the change of obliquity of terrestrial planets especially in this paper.

Obliquity, the angle of a spin axis of a planet relative to its orbital plane, changes the latitudinal distribution of yearly insolation on the planet. Changes in obliquity, inducing insolation distribution change, could be an important driver of climate variations. The Earth's obliquity varies by $\pm$ 1.3° around its mean value of 23.3° in a period about 4×10^4 years (Ward 1974, 1992). The glacial cycle of the Earth has been triggered by the periodic change of obliquity to some extent, through the variation of insolation at the edge of glacier in northern hemisphere. Even such small variation of the obliquity has produced significant variations in the Earth's climate at least during the Quaternary.

Mars' obliquity is believed to have suffered from a large-scale oscillation with an amplitude as much as $\sim$ 20° around its average of $\sim$ 25° on a time scale $\sim 10^5$–10^6 years (Ward 1973, 1974; Ward and Rudy 1991). Such a large variation is a result of a coupling between the precession rate of Mars' spin axis and one of the frequencies of its orbital precession. This is called the spin-orbit resonance. Laskar and Robutel (1993) and Touma and Wisdom (1993) showed that the obliquity of terrestrial planets except the Earth could have experienced large and chaotic variations throughout their histories. As a result of the chaotic variations on a long timescale, the range of Mars' obliquity change can be as large as 0° to 60°. Furthermore, obliquity of a moon-less Earth would vary radically in the range from 0° to 85° (Laskar and Robutel 1993; Laskar et al. 1993; Laskar 1996). If the Earth's obliquity had such a large variation, its climate would drastically change, providing a significant obstacle to the development of complex life on the Earth.

The analysis on the behavior of the planetary obliquity performed so far, however, has been concerned mostly with the orbital configuration of the planets in our Solar System through numerical calculations. In order to investigate the spin-orbit resonance in extrasolar planetary systems and discuss obliquity variations of possible terrestrial planets in HZs in the systems, it is useful to derive the generalized analytical formulae which express variations of the obliquity.

The oscillation amplitude of obliquity in non-resonant regions was derived by Ward (1974) through a linear analysis of the secular precession equation. Ward et al. (2002) showed the amplitude for a mass-less body in the place of Mars as a function of the rotational period and the semimajor axis of the particle with the analytical formulae. However, the non-resonant formulae cannot describe the oscillation amplitude of obliquity in the regions near spin-orbit resonances where the oscillation amplitude is not small. As we show later, the regions affected by the spin-orbit resonance are sometimes wide, and the non-resonant formulae significantly underestimate the amplitude near the edge of the resonant regions while they overestimate the amplitude near the center. Therefore, it is important to evaluate the amplitude also in spin-orbit resonant regions.

In the present paper, we investigate how the oscillation amplitude of the obliquity of terrestrial planets in a HZ depends on the masses and the orbits of giant planets, in resonant regions as well as in non-resonant ones. Through analytical arguments and numerical calculations of secular precession equations, we derive the resonance width and amplitude of obliquity near spin-orbit resonances. We also derive obliquity amplitude in non-resonant regions through a different approach form Ward (1974), which completely agrees with the results by Ward (1974). With our formulae, we can predict the amplitude of obliquity of a terrestrial planet in spin-orbit resonant regions as well as in an non-resonant regions.

Applying our results to the known extrasolar planetary systems, we investigate how strongly possible terrestrial planets are affected by the spin-orbit resonances. We find that the possible terrestrial planets in only 1/5 of the known extrasolar planetary systems exhibit both small obliquity variations ($\Delta\epsilon \leq 10°$, where $\Delta\epsilon$ is the variation amplitude of obliquity) and the possibility of the orbital stability over the entire HZs. Our results show that terrestrial planets often suffer large obliquity variations by the spin-orbit resonances even if they have stable orbits.

In the next section, we explain our model and basic equations. In Section 3, we derive the analytical formulae, which are confirmed by numerical calculations. Using the analytical formulae, we discuss what kind of giant planet causes large obliquity variation of terrestrial planets in a HZ, in Section 4. In Section 5, we show the results of applications of our results to the known extrasolar planetary systems. Sections 6 and 7 are devoted to discussion and conclusion.

2. MODEL AND BASIC EQUATIONS

We investigate obliquity variations of a hypothetical terrestrial planet in a planetary system with a given giant planet(s). Here we consider the terrestrial planet with oblate figure and neglect its gravitational effects on the host star and the giant planet.

Spin axis of a terrestrial planet precesses around the orbit normal because of the gravitational torque raised by other objects in the system exerted on the oblate figure of the terrestrial planet. The secular precession equation of the spin axis $\hat{s}$ of the planet is given by (e.g., Ward 1974)

$$\frac{d\hat{s}}{dt} = \alpha(\hat{s}\cdot\hat{n})(\hat{s}\times\hat{n}), \tag{1}$$

where $\hat{s}$ is a unit vector in the direction of spin axis and $\hat{n}$ is that of the normal to the orbital plane of the terrestrial planet. The precession constant α is

$$\begin{aligned}\alpha &= \frac{3Gm_c ED}{4\pi a^3} \\ &\simeq 8.6\times10^{-5}\left(\frac{m_c}{1M_\odot}\right) \\ &\quad\times\left(\frac{a}{1\mathrm{AU}}\right)^{-3}\left(\frac{D}{24\mathrm{hour}}\right)^{-1}[\mathrm{rad.\ yr^{-1}}],\end{aligned} \tag{2}$$

where G is the gravitational constant, m_c is the mass of the central star, D and a are the spin rotation period and the semi-major axis of the terrestrial planet, and E is its dynamical ellipticity, assuming $E \propto D^{-2}$ (e.g., Laskar and Robutel 1993). Here we only consider the torque by a central star. The torque by the giant planet can be neglected compared with that by the central star unless the orbits of the terrestrial and giant planets are so close that the terrestrial planet is orbitally unstable. The torque by satellites of the terrestrial planet (if they exist) can be effective. Actually, the precession of the Earth's spin axis is increased by a factor 3 by the torque by the Moon, although no other satellites in the Solar System raise such large torque. The torque by satellites can be taken into account by appropriately increasing α (Ito et al. 1995).

Obliquity ϵ of the terrestrial planet, the angle between $\hat{s}$ and $\hat{n}$, is obtained by

$$\hat{s}\cdot\hat{n} = \cos\epsilon. \tag{3}$$

The relationship among the reference plane (which is the invariant plane in this paper), orbital plane, and the equator of the terrestrial planet is schematically shown in Figure 1. Note that $\hat{s}$ is perpendicular to the equatorial plane. Since we assume that the planet's rotation period is sufficiently shorter than the period of precession and obliquity variation, its spin axis coincides with its principal axis.

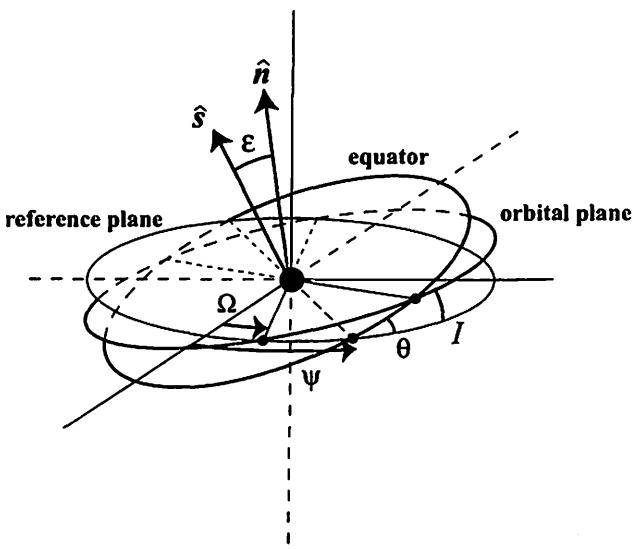

Fig. 1.— Relationship between the reference plane, orbital plane and equator.$\hat{s}$ is the unit vector in the direction of the spin axis, $\hat{n}$ is that normal to the orbital plane, ϵ is the obliquity, θ is the angle of the equator relative to the reference plane, ψ is the longitude of the equator, I is the orbital inclination, and Ω is the longitude of the ascending node.

If $\hat{n}$ is constant with time, Eq. (1) shows that ϵ is also constant. However, $\hat{n}$ generally varies by the gravitational perturbations exerted by other planets, which are the giant planets in the systems we consider here. Because we are interested in orbitally stable cases, we use the secular perturbation theories (e.g., Brouwer and Clemence 1961) to describe orbital change of the terrestrial planet. Let I and Ω be the orbital inclination and the longitude of the ascending node of the terrestrial planet. Then, $\hat{n} = (\sin I\sin\Omega, -\sin I\cos\Omega, \cos I)$ in the Cartesian frame with the x-y plane being the reference plane. Assuming that $I \ll 1$, secular variations of I and Ω are written as

$$I\sin\Omega = I_0\sin(Bt+\gamma) + \sum_{i=1}^{N_s} I_i\sin(f_i t+\gamma_i), \tag{4}$$

$$I\cos\Omega = I_0\cos(Bt+\gamma) + \sum_{i=1}^{N_e} I_i\cos(f_i t+\gamma_i), \quad (5)$$

where f_i are the eigenfrequrncies of this system and N_e is number of eigenfrequencies. Free oscillation frequency B and forced inclinations I_i are given by

$$B = -2n\sum_{j=1}^{N_g}\mu_j a F_j, \quad (6)$$

$$I_i = \frac{2n\sum_{j=1}^{N_g}\mu_j a F_j I_{ji}}{B-f_i}, \quad (7)$$

where n is the mean motion of the terrestrial planet,

$$F_j = \frac{1}{8a^*}\alpha_j b_{3/2}^{(1)}(\alpha_j), \quad (8)$$

$a^* \equiv \max(a,a_j)$, $\alpha_j \equiv \min(a,a_j)/\max(a,a_j)$, a and a_j are the semi-major axis of the terrestrial planet and the giant planet j, $b_s^{(m)}(\alpha_j)$ are Laplace coefficients (e.g., Brouwer and Clemence 1961), N_g is number of giant planets, and μ_j is the mass of giant planet j normalized by the host star mass, m_j/m_c. I_{ji} are eigenvectors for f_i. Since we here adopt the invariant plane as the reference plane, $I_i = I_{ji} = 0$ when $N_g = 1$; $I_{11} = I_{21} = 0$ and I_{j2} are orbital inclinations of giant planet j when $N_g = 2$. Free inclination I_0, and phase parameters γ and γ_i are determined by initial conditions. Since we only consider the lowest order terms of eccentricity and inclination, the evolution of inclination is independent of eccentricity. We investigate the oscillation amplitude of ϵ, using Eqs. (1), (4) and (5).

3. FORMULAE OF OBLIQUITY VARIATIONS

3.1. ANALYTICAL DERIVATION

We derive analytical formulae of amplitude of obliquity oscillation, $\Delta\epsilon$, in the region near spin-orbit resonances as well as in non-resonant region. Ward (1974) derived the expression for $\Delta\epsilon$ in the non-resonant regions when I (in radian) $\ll 1$, through analytical method different from ours. We mainly focus on resonant regions, which have not been studied in detail.

We assume that $I \ll 1$ as Ward (1974). With this assumption, substitution of Eqs. (4) and (5) into (1) yields (see Appendix)

$$\frac{d\psi}{dt} \simeq -\alpha\cos\epsilon + \alpha\cos\epsilon\cot\theta\,[I_0\cos(\psi-\Omega_0) + \sum_{i=1}^{N_e} I_i\cos(\psi-\Omega_i)] + \mathcal{O}(I^2), \quad (9)$$

$$\frac{d(\cos\epsilon)}{dt} \simeq I_0 B\sin\theta\sin(\psi-\Omega_0) + \sum_{i=1}^{N_e} I_i f_i\sin\theta\sin(\psi-\Omega_i) + \mathcal{O}(I^2), \quad (10)$$

where ψ is the longitude of the equator of the terrestrial planet in the reference frame, and θ is the angle between the equator of the terrestrial planet and the reference plane. We denote $Bt+\gamma$ by Ω_0 and $f_i t+\gamma_i$ by Ω_i.

If a precession frequency of spin axis approaches one of the orbital precession frequencies, $\dot\psi - \dot\Omega_0 \simeq 0$ or $\dot\psi - \dot\Omega_i \simeq 0$, the first or second term of the right hand side of Eqs. (9) and (10) does not change a sign ($\sin\theta$ has a definite sign), so that ϵ tends to secularly increase or decrease to have a large amplitude. This is the spin-orbit resonance. On the other hand, in non-resonance case, since the terms in the right hand side of Eqs. (9) and (10) oscillates around zero with time, ϵ oscillates with a small amplitude, $\sim \mathcal{O}(I)$ (see section 3.1.2.).

Since $I \ll 1$, the precession frequency ($\dot\psi$) is approximately given by $-\alpha\cos\epsilon$. It should be noted that $\dot\psi \simeq -\alpha\cos\epsilon$ is negative for prograde spin rotation ($\epsilon < 90°$) and positive for retrograde one ($\epsilon > 90°$) while $\dot\Omega_0$ and $\dot\Omega_i$ are always negative. So spin-orbit resonance occurs only for the planets with prograde spin. We will discuss planetary spin later.

First we consider the system with a giant planet and a terrestrial planet. We address systems with multiple giant planets later. In the one giant planet system, I_0 is the inclination angle between the orbital planes of the giant and the terrestrial planet. Since $I_i = 0$, $I = I_0$ and I_0 does not change with t, and Ω is a linear function of t given by $Bt+\gamma$ ($=\Omega_0$) (Eqs. 4 and 5).

In this case, Equation (9) is reduced to

$$\frac{d}{dt}(\psi-\Omega_0) \simeq (-B-\alpha\cos\epsilon) + \alpha\cos\epsilon\cot\theta I_0\cos(\psi-\Omega_0) + \mathcal{O}(I^2). \quad (11)$$

Spin-orbit resonance occurs when $\dot\psi - \dot\Omega_0 \simeq 0$. Scaling time t by $1/\sqrt{\alpha I_0|B|\sin\epsilon_*}$, where ϵ_* is a particular obliquity, Equation (11) is

$$\frac{dx}{d\tilde t} \simeq \frac{-B-\alpha\cos\epsilon}{\sqrt{\alpha I_0|B|\sin\epsilon_*}} + \frac{\cos\epsilon\cot\theta}{\sqrt{|B|\sin\epsilon_*}}\sqrt{\alpha I_0}\cos x + \mathcal{O}(I^{3/2}), \quad (12)$$

where $x = \psi - \Omega_0$ and $\tilde t = \sqrt{\alpha I_0|B|\sin\epsilon_*}\,t$. We will take a resonant obliquity as ϵ_* to analyze resonant regions, while a time averaged one is taken as ϵ_* to analyze in non-resonant regions. Since we are interested in the terrestrial planet in a prograde spin state, $0 \le \epsilon_* < 90°$.

3.1.1. RESONANT REGIONS

Because we assume that $I \ll 1$, the second term in the right-hand side of Eq. (12) is much smaller than the first term. To investigate time variation of ϵ near a resonance, we adopt resonant obliquity ϵ_r that satisfies $\cos\epsilon_r = |B|/\alpha$ as ϵ_*. Then, Eq. (12) is reduced to

$$\frac{dx}{d\tilde t} = y, \quad (13)$$

where

$$y = -\frac{|B|+\alpha\cos\epsilon}{\sqrt{\alpha I_0|B|\sin\epsilon_r}}. \quad (14)$$

Since $\theta \simeq \epsilon$ for $I \ll 1$, Eq. (10) is reduced to $d(\cos\epsilon)/dt = I_0 B \sin\epsilon \sin x$, so that time derivative of Eq. (13) is

$$\frac{d^2x}{dt^2} = \frac{\sin\epsilon}{\sin\epsilon_r}\sin x \simeq \sin x, \tag{15}$$

where we neglect the displacements in ϵ from the exact resonant obliquity ϵ_r, compared with the change in x. Integrating Eq. (15) with Eq. (13), we obtain

$$H = \cos x + \frac{1}{2}y^2, \tag{16}$$

where H is an integration constant. Equation (12) including the second term yields a similar integration constant,

$$H = \cos x + \frac{1}{2}y', \tag{17}$$

where $y' = y + \sqrt{I_0 \cot^3\epsilon_r}\cos x$. The modified resonant obliquity ϵ_r' is given from $y' = 0$ by

$$\cos\epsilon_r' = \cos\epsilon_r(1 + I_0 \cot\epsilon_r \cos x). \tag{18}$$

If $\cos x < 0$ (> 0), ϵ_r' is slightly larger (smaller) than ϵ_r.

Curves of constant H obtained by Eq. (17) are plotted on the x-y plane in Figure 2a. We show the curves in the case of $m_c = 1M_\odot$, $m_1 = 1M_J$ (M_J is the mass of Jupiter), $a_1 = 5.2$AU, $a = 1.1$AU, $D = 24$hour and $I_0 = 1.3°$. The results obtained by numerically integrating Eq. (1) are plotted in Fig. 2b. Integrations start at $x = \pi$ with different y such that H calculated by the x and y correspond to those plotted in Fig. 2a. The integrated trajectories are in excellent agreement with corresponding analytical contours in Fig. 2a. If $H > 1$, the angle x circulates with oscillation in y on the same period; the oscillation amplitude decreases with increase in H. If $-1 < H < 1$ (H cannot take values < -1), the angle x librates in the limited range, accompanied by oscillation in y with relatively large amplitude around $y = 0$, which corresponds to $\epsilon = \epsilon_r$. $H = 1$ is the separatrix, which divides the libration region from the circulation region.

For each trajectory with $-1 < H < 1$, $y = \pm\sqrt{2(H - \cos x)}$. The maximum deviation $|\Delta y|$ from $y = 0$ (the resonant center) is

$$|\Delta y|_{\max} = 2, \tag{19}$$

which occurs when $x = \pi$ and $H \to 1$. When initial y ($y_{\rm ini}$) satisfies $-|\Delta y|_{\max} < y_{\rm ini} < |\Delta y|_{\max}$, initial x ($x_{\rm ini}$) such that the initial point $(x_{\rm ini}, y_{\rm ini})$ lies on the libration trajectory with $H \to 1$ exists. In this case, y on the trajectory varies in the range of $-|\Delta y|_{\max} < y < |\Delta y|_{\max}$. We call the region of $-|\Delta y|_{\max} < y < |\Delta y|_{\max}$ as "resonant region". $|\Delta y|_{\max}$ is the resonant (half) width to lowest-order accuracy. However, all trajectories with y in this region do not necessarily belong to the libration region. It depends on $x_{\rm ini}$ whether a trajectory with $y_{\rm ini}$ in resonant region belong to the libration region or not. According to the definition of y (Eq. 14), when α, B and I_0 are given, ϵ uniquely corresponds to some particular value of y. The variation of y corresponds to that of ϵ. The maximum change in obliquity is

$$\begin{aligned} |\Delta\cos\epsilon|_{\max} &= 2\sqrt{I_0|B|\sin\epsilon_r/\alpha} \\ &= 2\sqrt{I_0\cos\epsilon_r\sin\epsilon_r}, \end{aligned} \tag{20}$$

where we use $|B| = \alpha\cos\epsilon_r$ in the last equation. The range of ϵ in the resonant region is specified by

$$\cos\epsilon_r - |\Delta\cos\epsilon|_{\max} \le \cos\epsilon \le \cos\epsilon_r + |\Delta\cos\epsilon|_{\max}. \tag{21}$$

We present a schematic illustration of the resonant region as a function of initial obliquity $\epsilon_{\rm ini}$ and the variation range of ϵ in Figure 3a. In Fig. 3a, we denote $\cos^{-1}(\cos\epsilon_r \mp |\Delta\cos\epsilon|_{\max})$ by $\epsilon_\pm$. When $\epsilon_{\rm ini}$ is in the range of $\epsilon_- \le \epsilon_{\rm ini} \le \epsilon_+$, ϵ can evolve following the curve of $H \to 1$ with a particular $x_{\rm ini}$ as shown in Fig. 2a, and so the maximum variation range of ϵ is $\epsilon_- \le \epsilon \le \epsilon_+$. For all $\epsilon_{\rm ini}$ in the resonant region, the maximum variation is the same as the range of the resonant region.

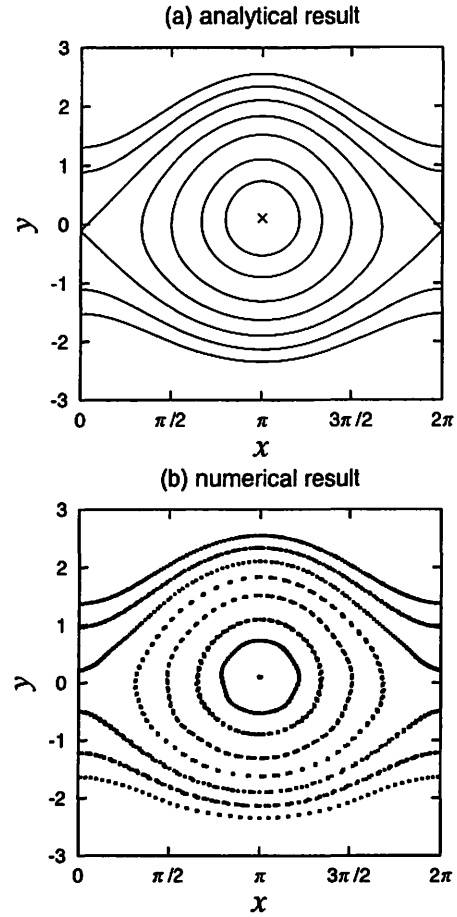

Fig. 2.— The curves of constant H are plotted on the x-y plane, in the case of $m_c = 1M_\odot$, $m_1 = 1M_J$ (M_J is the mass of Jupiter), $a_1 = 5.2$AU, $a = 1.1$AU, $D = 24$hour and $I_0 = 1.3°$; the curves of $H = -1.0, -0.8, -0.5, 0, 0.5, 1.0, 1.5, 2.0$ from the inner one to the outer respectively. (a) The curves of constant H analytically calculated according to Eq. (17). (b) The trajectories obtained by numerical integration of Eq. (1).

Then, we can illustrate the resonant region as a square area in Fig. 3a. When the variation is small enough, $|\Delta \cos\epsilon|_{\max} \simeq \sin\epsilon_{\rm r}|\Delta\epsilon|_{\max}$. Then Eq. (20) is reduced to

$$|\Delta\epsilon|_{\max} = 2\sqrt{I_0/\tan\epsilon_{\rm r}}. \tag{22}$$

Since $\cos\epsilon_{\rm r} \pm |\Delta\cos\epsilon|_{\max} \simeq \cos(\epsilon_{\rm r} \mp |\Delta\epsilon|_{\max})$, Eq. (21) is

$$\epsilon_{\rm r} - |\Delta\epsilon|_{\max} \le \epsilon \le \epsilon_{\rm r} + |\Delta\epsilon|_{\max}. \tag{23}$$

Note that $|\Delta\epsilon|_{\max}$ only depends directly on I_0 and $\epsilon_{\rm r}$. The other parameters, the semi-major axis a, the rotation period D of the terrestrial planet, the semi-major axis a_j, and mass m_j of the giant planet, determine $\epsilon_{\rm r}$. $|\Delta\epsilon|_{\max}$ depends on these parameters only through $\epsilon_{\rm r}$. Ward (1982) showed through higher order expansion of Eq. (1) that $|\Delta\epsilon|_{\max} \sim \sqrt{I_0/\tan\epsilon_{\rm r}}$ at $\epsilon_{\rm ini} = \epsilon_{\rm r}$, although the derivation was not presented. His result is consistent with our formulae at $\epsilon_{\rm ini} = \epsilon_{\rm r}$ in the limit of $\Delta\epsilon \to 0$ expect for a factor 2.

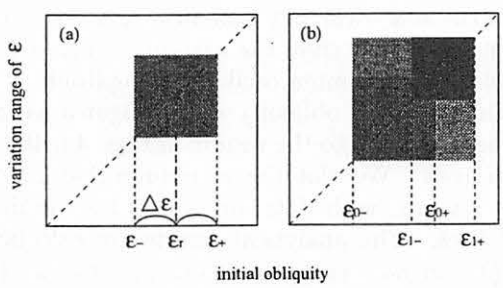

Fig. 3.— Schematic illustrations of the resonant regions. (a) An example of the resonant region in a single giant planet system. (b) An example of the overlapped resonant region resulting from two resonant regions in two giant planets system. We denote $\cos^{-1}(\cos\epsilon_{\rm r} \mp |\Delta\cos\epsilon|_{\max})$ by $\epsilon_\pm$. The maximum variation range of ϵ in resonant region is the same as $\epsilon_- \le \epsilon \le \epsilon_+$.

Figures 2 show that there are two fixed points at $y = 0$: the point $x = \pi$, the center of an ellipse, is a stable fixed point while $x = 0$ and $x = 2\pi$, saddle points, are unstable fixed points. The scaling factor for t^{-1}, $\sqrt{\alpha I_0|B|\sin\epsilon_{\rm r}} = \alpha\sqrt{I_0\cos\epsilon_{\rm r}\sin\epsilon_{\rm r}}$, in Eqs. (14) and (15) is no other than a frequency of the libration around the stable fixed point.

If other giant planets exist, there are other resonant regions associated with orbital variations with frequencies f_i. In the same way as Eq. (20), the resonant widths of the individual spin-orbit resonances are given by

$$|\Delta\cos\epsilon|_{\max,i} = 2\sqrt{I_i\cos\epsilon_{{\rm r},i}\sin\epsilon_{{\rm r},i}}, \tag{24}$$

where $\cos\epsilon_{{\rm r},i} = |f_i|/\alpha$ $(i = 1, 2, \cdots, N_e)$. Defining $f_0 \equiv B$, we hereafter use Eq. (24) for $i = 0, 1, 2, \cdots, N_e$. Frequencies of libration of individual resonances are $\alpha\sqrt{I_i\cos\epsilon_{{\rm r},i}\sin\epsilon_{{\rm r},i}}$. If resonant widths of two resonant regions overlap, an expanded resonant region appears as schematically illustrated in Figure 3b. In a two giant planets system, the orbital precession of the terrestrial has two frequencies, f_0 and f_1. We consider the case with $f_0 > f_1$ (the case with $f_0 < f_1$ is similar). We denote the resonant region associated with f_0 by $\epsilon_{0-} \le \epsilon \le \epsilon_{0+}$, and one with f_1 by $\epsilon_{1-} \le \epsilon \le \epsilon_{1+}$. Suppose that two resonant regions overlap: $\epsilon_{1-} \le \epsilon_{0+}$ (see Fig. 3b). When $\epsilon_{0-} \le \epsilon_{\rm ini} \le \epsilon_{0+}$, ϵ can vary in the range $\epsilon_{0-} \le \epsilon \le \epsilon_{0+}$. When ϵ enters the range of $\epsilon_{1-} \le \epsilon$ $(\le \epsilon_{0+})$, ϵ is in the resonant region associated with f_1 as well, $\epsilon_{1-} \le \epsilon \le \epsilon_{1+}$. As a result, the variation range of ϵ is extended to $\epsilon_{0-} \le \epsilon \le \epsilon_{1+}$ as shown in Fig. 3b. When $\epsilon_{\rm ini}$ is in $\epsilon_{1-} \le \epsilon_{\rm ini} \le \epsilon_{1+}$, the variation range is extended in the same way. In general, if the individual resonant regions $(\epsilon_{i-} \le \epsilon \le \epsilon_{i+})$ overlap, the merged resonant region is given by $\min_i(\epsilon_{i-}) \le \epsilon \le \max_i(\epsilon_{i+})$. In the overlapped resonant region, multiple libration frequencies exist, so that variations of ϵ seems to be chaotic (e.g., Laskar and Robutel 1993). When resonances overlap, the analysis assuming an isolated resonance is, in principle, no longer valid. However, as shown in section 3.2, the simple prescription for merging of resonances into an extended resonance region stated here well reproduces numerical results.

3.1.2. NON-RESONANT REGIONS

In non-resonant regions (trajectories with $H > 1$), the angle x circulates with relatively small oscillation in y, which implies oscillation of ϵ with small amplitude. In the cases with ϵ far from $\epsilon_{\rm r}$, the approximation $\sin\epsilon \simeq \sin\epsilon_{\rm r}$ in Eq. (15) is not appropriate; instead, $\sin\epsilon \simeq \sin\epsilon_{\rm av}$ is more appropriate, where $\epsilon_{\rm av}$ is time averaged obliquity. Here, we adopt the time averaged obliquity $\epsilon_{\rm av}$ as ϵ_* and scale time t by $1/\sqrt{\alpha I_0|B|\sin\epsilon_{\rm av}}$. Integrating the scaled Eq. (11), the integration constant to the lowest order accuracy is given by a similar form in resonant regions (Eq. 16) as

$$H = \cos x + \frac{1}{2}Y^2, \tag{25}$$

where $Y = -(B+\alpha\cos\epsilon)/\sqrt{\alpha I_0|B|\sin\epsilon_{\rm av}}$. Let $\langle Y\rangle$ and ΔY be the time averaged value of Y and $\Delta Y \equiv Y - \langle Y\rangle$ along a trajectory. Assuming $|\Delta Y| \ll |\langle Y\rangle|$, Eq. (25) reads as

$$\Delta Y \cdot \langle Y\rangle \simeq -\cos x + H - \frac{1}{2}\langle Y\rangle^2. \tag{26}$$

Since H and $\langle Y\rangle^2/2$ are constant along a given trajectory, ΔY takes the maximum value when $x = \pi$,

$$|\Delta Y|_{\max} \simeq \frac{1}{\langle Y\rangle} = \frac{\sqrt{\alpha I_0|B|\sin\epsilon_{\rm av}}}{|B+\alpha\cos\epsilon_{\rm av}|}. \tag{27}$$

According to the definition of Y, the equivalent oscillation amplitude of ϵ is

$$|\Delta\epsilon|_{\max} \simeq \frac{\sqrt{\alpha I_0|B|\sin\epsilon_{\rm av}}}{\alpha\sin\epsilon_{\rm av}}|\Delta Y|_{\max}. \tag{28}$$

Substituting Eq. (27) into (28), oscillation amplitude of ϵ in non-resonant regions is given by

$$|\Delta\epsilon|_{\max} = \left| \frac{BI_0}{B + \alpha \cos \epsilon_{\rm av}} \right|. \qquad (29)$$

This expression is in complete agreement with one derived by Ward (1974).

In the cases with multiple giant planets, total maximum oscillation amplitude of ϵ is linear superposition of the amplitude due to individual frequencies,

$$|\Delta\epsilon|_{\max} = \sum_{i=0}^{N_c} \left| \frac{f_i I_i}{f_i + \alpha \cos \epsilon_{\rm av}} \right|. \qquad (30)$$

3.2. NUMERICAL RESULTS

To verify the analytical formulae we derived in Section 3.1, we numerically integrate Eq. (1) with Eqs. (3) to (5) with a forth order Runge-Kutta scheme and compare the results with the analytical formulae. We will show that our numerical results are in excellent agreement with our analytical results, Eqs. (24) and (30). We calculated time evolution in ϵ of a hypothetical terrestrial planet with various initial obliquity from 0° to 90° at every 1° in various systems over 3×10^6 years, which is as long as at least a few times the typical timescale of spin-orbit resonance. The maximum value (ϵ_+) and the minimum value (ϵ_-) of ϵ during the numerical integration are plotted in Figures 4 as a function of initial obliquity $\epsilon_{\rm ini}$, in one giant planet system with $m_c = 1M_\odot, m_1 = 1M_{\rm J}$, where $M_{\rm J}$ is the mass of Jupiter, $a_1 = 5.2$AU, and $I_0 = 1.3°$ (Fig. 4a), and in two giant planet system with $m_1 = 1M_{\rm J}$, $a_1 = 5.2$AU, $m_2 = 1M_{\rm S}$, where $M_{\rm S}$ is the mass of Saturn, $a_2 = 9.5$AU, $I_{11} = I_{21} = 0, I_{12} = 0.36°$ and $I_{22} = 0.89°$ (Figs. 4b and 4c). I_{12} and I_{22} coincide with the inclination of Jupiter and Saturn measured from the invariant plane. In Figs. 4a, 4b, and 4c, (a, D) = (1.1AU, 24hour), (0.8AU, 24hour) and (1.4AU, 2.4hour) respectively. Corresponding resonant obliquity $\epsilon_{\rm r}$ calculated by $\cos\epsilon_{{\rm r},i} = |f_i|/\alpha$ are 51.7° (Fig. 4a), 81.5°, 43.1° (Fig. 4b), and 78.4°, 67.0° (Fig. 4c). The amplitude and oscillation range of ϵ depend on initial $\psi - \Omega_0$ even if the spin axis has the same initial obliquity as shown in Section 3.1. For each initial obliquity, we calculate the cases with initial $\psi - \Omega_0$ at every 10° from 0° to 360°.

Figure 4a shows that obliquity has large amplitude if initial obliquity $\epsilon_{\rm ini}$ is in 36° to 66° around 51.7°. As stated in Section 3.1, the range of $\epsilon_{\rm ini}$ in resonant region coincides with the maximum variation range of ϵ. Figure 4b shows two resonant regions, one is due to the resonance of free orbital precession frequency, extending from 79° to 84° around 81.5°, and the other is due to the resonance of an eigenfrequency of the system extending from 36° to 49° around 43.1°. In Figure 4c, two resonant regions overlap, resulting in one large resonant region extending from 59° to 85°.

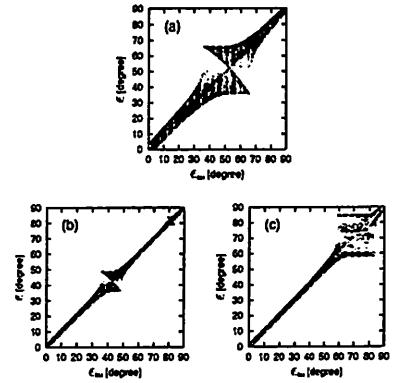

Fig. 4.— The maximum and minimum values reached by obliquity ϵ during the integration on 3×10^6 years as a function of initial obliquity $\epsilon_{\rm ini}$. One giant planet system with (a) $m_1 = 1M_{\rm J}, a_1 = 5.2$AU, $a = 1.1$AU, $D = 24$hours and $I = 1.3°$, and two giant planet system with $m_1 = 1M_{\rm J}, a_1 = 5.2$AU, $m_2 = 1M_{\rm S}, a_2 = 9.5$AU, (b) $a = 0.8$AU, and $D = 24$hours and (c) $a = 1.4$AU, and $D = 2.4$hours.

Although Figs. 2 already showed the agreement between the analytical and numerical results in one giant planet system, we show the agreement more explicitly. We plot the maximum oscillation amplitude of ϵ as a function of initial obliquity $\epsilon_{\rm ini}$ in Figures 5a, 5b and 5c, corresponding to the results in Figs. 4a, 4b and 4c, respectively. We plot the amplitude that is numerically obtained with dots, and analytical results with solid lines. The analytical results are calculated by Eq. (30) in non-resonant regions and by Eq. (24) in resonant regions. The analytical results (Eqs. 24 and 30) show excellent agreement with the numerical results in both resonant and non-resonant regions except for slight deviations at the boundaries between resonant and non-resonant regions. We also plot the amplitude calculated by Eq. (30) in resonant regions with dashed lines. Figures 5 show that the analytical formula for the non-resonant region (Eq. 30) underestimates the amplitude of ϵ near the edge of resonant region, while it overestimates near $\epsilon_{\rm ini} \simeq \epsilon_{\rm r}$. In Fig. 5c, we also plot the oscillation amplitudes of individual resonances with dashed-dot lines. The amplitude of ϵ is well reproduced even in the overlapped resonant regions.

4. OBLIQUITY VARIATION IN A HABITABLE ZONE IN EXTRASOLAR PLANETARY SYSTEMS

We have derived analytical expressions for the amplitude of obliquity variation ($|\Delta\epsilon|_{\max}$), which show excellent agreement with numerical calculations. Hereafter, we denote $|\Delta\epsilon|_{\max}$ by $\Delta\epsilon$. Using our analytical expressions, we study what kind of giant planet causes large obliquity variations of terrestrial planets in a habitable zone (HZ). As mentioned in Section 1, for land-based life to evolve and survive on a terrestrial planet in a HZ, small obliquity variation of the planet may be required, in addition to the planet's orbital stability. Because we do not know specific locations of terrestrial planets,

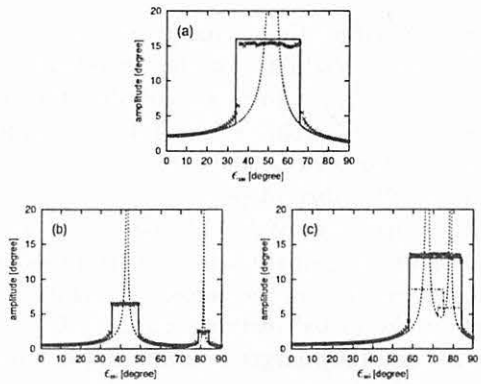

Fig. 5.— The maximum oscillation amplitude of obliquity of a terrestrial planet ϵ as a function of initial obliquity $\epsilon_{\rm ini}$. Dots show numerical results. Solid lines show the analytical expression given by Eqs. (24) and (30) in Section 3.1. Dashed lines show the amplitude given by Eq. (30) in resonant region. Dashed-dot lines in (c) show the individual amplitude of the resonance of free orbital precession frequency and of eigenfrequency.

their spin periods, and critical $\Delta\epsilon$ for land-based life in extrasolar planetary systems, we calculate the probability that a terrestrial planet has $\Delta\epsilon$ larger than some given values, averaged over an entire HZ and likely spin periods.

Locations of the spin-orbit resonance are predicted by

$$\dot{\psi} - \dot{\Omega}_i \simeq -(f_i + \alpha\cos\epsilon) \simeq 0, \qquad (31)$$

where f_i $(i = 0, 1, 2, \cdots, N_e)$ are the frequencies of the orbital variation of a terrestrial planet and α is the precession constant. f_0 represents the free orbital precession frequency and f_i for $i = 1, 2, \cdots, N_e$ represent the eigenfrequencies of the system (see Section 3.1). Corresponding obliquity variation amplitude $\Delta\epsilon$ is estimated by Eqs. (24) and (30). Given the initial orbital elements and masses of the host star and the giant planet(s) in the system, f_0 depends only on the semi-major axis a of a terrestrial planet (Eq. 6) and α depends on a and its spin period D (Eq. 2). Figures 6 show the examples of obliquity variation amplitudes for a terrestrial planet, as a function of a and D:

- system1:
  $m_1 = 1M_{\rm J}, a_1 = 0.1{\rm AU}, I_0 = 0.05$ (Fig. 6a)
- system2:
  $m_1 = 1M_{\rm J}, a_1 = 1.0{\rm AU}, I_0 = 0.05$ (Fig. 6b)
- system3:
  $m_1 = 1M_{\rm J}, a_1 = 0.1{\rm AU}, I_{12} = 0.05$
  $m_2 = 1M_{\rm J}, a_2 = 1.0{\rm AU}, I_{22} = 0.05$ (Fig. 6c)

In Figs. 6, we adopt the mass of the host star $m_{\rm c} = 1M_\odot$ and initial obliquity $\epsilon_{\rm ini} = 25°$. Figs. 6 show that the variation amplitude of ϵ depends on a and D.

The regions where obliquity has a large amplitude can be classified into 3 types:

I : The regions of spin-orbit resonances with f_0

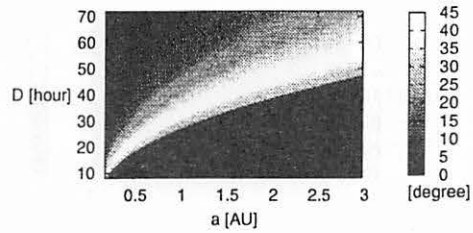

Fig. 6a.— Obliquity variation amplitude ($\Delta\epsilon$) for a terrestrial planet as a function of a and D, in the case of $m_1 = 1M_{\rm J}, a_1 = 0.1{\rm AU}$ and $I_0 = 0.05$ (system 1). The color bar indicates $\Delta\epsilon$ in degree.

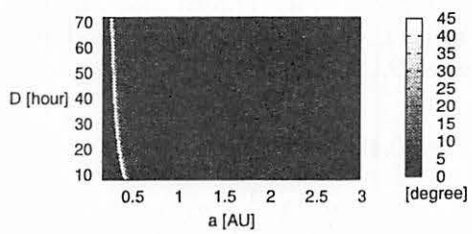

Fig. 6b.— Obliquity variation amplitude for a terrestrial planet as a function of a and D, in the case of $m_1 = 1M_{\rm J}, a_1 = 1.0{\rm AU}$ and $I_0 = 0.05$ (system 2).

II : The regions of spin-orbit resonances with f_i $(i = 1, 2, \cdots, N_e)$

III : The regions of secular resonances (at the location satisfying $f_0 = f_i$)

It is noted that the regions II and III do not appear in the systems with a single giant planet.

In the case of a single giant planet system, f_0 can be expressed in a simple form. We derive a simple approximate expression of the resonant region as follows. The dependence of f_0 on a comes from the a-dependence of the Laplace coefficients $b^{(1)}_{3/2}(\alpha_1)$, where $\alpha_1 = \min(a, a_1)/\max(a, a_1)$ (see Eqs. 6 and 8). In general, $b^{(1)}_{3/2}(\alpha_1)$ cannot be expressed with a simple function of a and a_1. However, when the orbits of terrestrial and giant planets are sufficiently separated, $b^{(1)}_{3/2}(\alpha_1) \simeq 3(a_1/a)$ at $a > a_1$ and $b^{(1)}_{3/2}(\alpha_1) \simeq 3(a/a_1)$ at $a < a_1$, according to our numerical calculations. Substituting these expressions into Eq. (6), f_0 can be written as

$$f_0 \simeq -4.5\times10^{-3}\left(\frac{m_{\rm c}}{1M_\odot}\right)^{-1/2}\left(\frac{m_1}{1M_{\rm J}}\right) \times\left(\frac{a_1}{1{\rm AU}}\right)^p\left(\frac{a}{1{\rm AU}}\right)^q [{\rm rad.\ yr}^{-1}], \qquad (32)$$

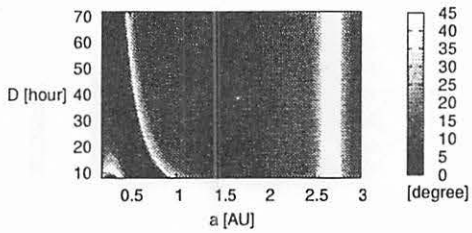

Fig. 6c.— Obliquity variation amplitude for a terrestrial planet as a function of a and D, in the case of $m_1 = 1M_J, a_1 = 0.1\mathrm{AU}, I_{12} = 0.05, m_2 = 1M_J, a_1 = 1.0\mathrm{AU}$, and $I_{22} = 0.05$ (system 3).

where $p = 2$ and $q = -7/2$ for $a > a_1$ and $p = -3$ and $q = 3/2$ for $a < a_1$. Substituting Eqs. (2) and (32) into Eq. (31), we obtain the spin period at spin-orbit resonance, D_r, as

$$D_\mathrm{r} \simeq 0.42 \left(\frac{\cos\epsilon_\mathrm{ini}}{\cos 25^\circ}\right) \left(\frac{m_\mathrm{c}}{1M_\odot}\right)^{3/2} \times \left(\frac{m_1}{1M_J}\right)^{-1} \left(\frac{a_1}{1\mathrm{AU}}\right)^{p'} \left(\frac{a}{1\mathrm{AU}}\right)^{q'} [\mathrm{hour}] \quad (33)$$

where $p' = -2$ and $q' = 1/2$ for $a > a_1$ and $p' = 3$ and $q' = -9/2$ for $a < a_1$. Although this formula is valid only when the orbits of the giant and the terrestrial planets are well separated, it provides a good account for the characteristics of resonant regions on the a-D plane in Figs. 6a and 6b.

When a system contains multiple giant planets, f_0 and D_r cannot be expressed analytically. However, type I resonant regions on the a-D plane in such a system is approximately given by the superposition of resonant regions in a single giant planet systems with a cut-off over a crossing point of the individual type I resonant regions, because f_0 in this systems is given by the sum of f_0 in the individual single giant planet systems. The resonant region at $\lesssim 0.5\mathrm{AU}$ in Fig. 6c is the result of such superposition of individual type I resonant regions in Figs. 6a and 6b.

Type II resonant region is found in the region at 0.5–1AU in Fig. 6c. Since the eigenfrequencies f_i ($i = 1, 2, \cdots, N_e$) are constant on a, D_r has a dependence on a like $D_\mathrm{r} \propto a^{-3}$ (see Eq. 2). When $f_0 = f_i$, obliquity has large amplitude whether the spin-orbit resonance exists or not because I_i given in Eq. (7) is large (type III resonant region). Type III region appears at $\sim 2.7\mathrm{AU}$ in Fig. 6c. Since f_0 and f_i ($i = 1, 2, \cdots, N_e$) do not depend on D, this region is perpendicular to the x-axis on the a-D plane.

In order to quantify the effects of the spin-orbit resonances on the terrestrial planets in a HZ, we consider the restricted area on the a-D plane by appropriate D and a in a HZ and calculate the fraction of the area where $\Delta\epsilon$ is larger than some given values ($\Delta\epsilon_\mathrm{cirt}$) to evaluate the probability for the terrestrial planets to have $\Delta\epsilon > \Delta\epsilon_\mathrm{crit}$. Since we consider the terrestrial planets like the Earth, we here take 8–72hours as the appropriate range of D, and a=0.7–1.3AU as a HZ, for simplicity. We also adopt $\epsilon_\mathrm{ini} = 25^\circ$. The different choices of the range of D, HZ, and ϵ_ini do not significantly affect the global features of the probability distributions we show in the below. The choice of I does not affect the global features either, but as shown in Eqs. (24) and (30), larger I results in the larger variation of ϵ and enhances area fractions below. We discuss the choice of I in the known extrasolar systems in the next section.

Table I shows area fractions with $\Delta\epsilon \geq 10^\circ$, $\geq 20^\circ$ and $\geq 40^\circ$ in the system 1, 2, and 3 in Figs. 6. The area fractions in this table indicate the degree of overlapping of resonant regions with HZ. In system 1, type I resonant region overlaps with the HZ, while there is no overlapping in system 2. In system 3, type III resonant region overlaps with the HZ. Figure 7 shows the results of similar procedures for single giant planet systems with different semi-major axis of the giant planet, a_1, in the case of $m_1 = 1M_J, I = 0.05$ and initial obliquity $\epsilon_\mathrm{ini} = 25^\circ$. Spin-orbit resonance is most effective at $a_1 \sim 0.1\mathrm{AU}$ and 5AU, and it is hardly effective at $a_1 \sim 1\mathrm{AU}$.

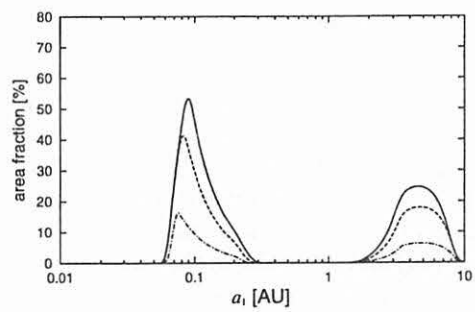

Fig. 7.— The area fraction with $\Delta\epsilon \geq 10^\circ$ (solid line), $\geq 20^\circ$ (dashed line), and $\geq 30^\circ$ (dot-dashed line) as a function of the semi-major axis of a giant planet a_1, in the case of $m_\mathrm{c} = 1M_\odot$, $m_1 = 1M_J$ and $I_0 = 0.05$.

We explain this dependence on a_1, using Eq. (33). The spin period in the spin-orbit resonance given by Eq. (33) increases with decreasing a_1 for $a > a_1$ or with increasing a_1 for $a < a_1$. Equation (33) is equivalent to

$$a_{1r} \simeq \begin{cases} 0.13 \left(\frac{\cos\epsilon_\mathrm{ini}}{\cos 25^\circ}\right)^{1/2} \left(\frac{m_\mathrm{c}}{1M_\odot}\right)^{3/4} \left(\frac{m_1}{1M_J}\right)^{-1/2} \\ \quad \times \left(\frac{a}{1\mathrm{AU}}\right)^{1/4} \left(\frac{D}{24\mathrm{hour}}\right)^{-1/2} \quad [\mathrm{AU}] \text{ for } a > a_1 \\ 3.9 \left(\frac{\cos\epsilon_\mathrm{ini}}{\cos 25^\circ}\right)^{-1/3} \left(\frac{m_\mathrm{c}}{1M_\odot}\right)^{-1/2} \left(\frac{m_1}{1M_J}\right)^{1/3} \\ \quad \times \left(\frac{a}{1\mathrm{AU}}\right)^{3/2} \left(\frac{D}{24\mathrm{hour}}\right)^{1/3} \quad [\mathrm{AU}] \text{ for } a < a_1, \end{cases} \quad (34)$$

where a_{1r} is the semi-major axis of the giant planet that

TABLE I
EXAMPLES OF AREA FRACTIONS.

system	$\Delta\epsilon \geq 10°$*1 (%)	$\Delta\epsilon \geq 20°$*2 (%)	$\Delta\epsilon \geq 40°$*3 (%)
system 1	45.86	31.39	6.15
system 2	0.00	0.00	0.00
system 3	16.38	7.50	0.12

NOTE.—(*)The percentages indicate the fraction of the area where $\Delta\epsilon$ is larger than (1) 10°, (2) 20°, and (3) 40° in the area with D=8–72hours and a=0.7–1.3AU(HZ).

causes spin-orbit resonance at a. This equation implies that the most effective a_1 for the obliquity variation of the terrestrial planet with $a \simeq 1$AU and $D \simeq 24$ hour are ~ 0.13AU and ~ 3.9AU in the cases with $\epsilon_{\rm ini} = 25°, m_{\rm c} = 1M_\odot$, and $m_1 = 1M_{\rm J}$, which is consistent with Fig. 7. When the terrestrial planet is too close to the giant planet, $a \sim a_1$, f_0 is much larger than $\alpha \cos\epsilon_{\rm r}$ with D =8–72 hours. In this case, very small D (rapid rotation) is necessary for the terrestrial planet to be in resonance. However, such a rapid rotation rate breaks up the planet (e.g., Lissauer et al. 2000, and references therein). On the other hand, when the giant planet is too far from the terrestrial planet ($a_1 \gtrsim 10$AU or $a_1 \lesssim 0.05$AU), f_0 is too small for the spin-orbit resonance. For spin-orbit resonance to occur in this case, spin rate must be smaller by order of magnitude than 24 hours, which is unrealistic except when tidal force exerted by a host star or thick atmosphere damps the spin. Thus, Eq. (34) explains the dependence on a_1 in Fig. 7. Figures 8 show the area fraction as a function of the mass of a giant planet m_1, in the cases of $I = 0.05$ and $a_1 = 0.1$AU (Fig. 8a), and $a_1 = 5.0$AU (Fig. 8b). In these cases, $m_1 \sim 1M_{\rm J}$ is the most effective.

Equation (33) is rewritten as

$$m_{1r} \simeq \begin{cases} 1.7\left(\frac{\cos\epsilon_{\rm ini}}{\cos 25°}\right)\left(\frac{m_{\rm c}}{1M_\odot}\right)^{3/2}\left(\frac{a_1}{0.1{\rm AU}}\right)^{-2} \\ \times\left(\frac{a}{1{\rm AU}}\right)^{1/2}\left(\frac{D}{24{\rm hour}}\right)^{-1}[M_{\rm J}] \text{ for } a > a_1 \\ 2.2\left(\frac{\cos\epsilon_{\rm ini}}{\cos 25°}\right)\left(\frac{m_{\rm c}}{1M_\odot}\right)^{3/2}\left(\frac{a_1}{5{\rm AU}}\right)^{3} \\ \times\left(\frac{a}{1{\rm AU}}\right)^{-9/2}\left(\frac{D}{24{\rm hour}}\right)^{-1}[M_{\rm J}] \text{ for } a < a_1, \end{cases} \quad (35)$$

where m_{1r} is the mass of the giant planet at a_1 that causes spin-orbit resonances at a. The most effective m_1 is estimated as $\simeq 1.7M_{\rm J}$ for at $a_1 = 0.1$AU, and as $\simeq 2.2M_{\rm J}$ for $a_1 = 5$AU. These are consistent with Figs. 8. Figure 9 shows the area fraction with $\Delta\epsilon \geq 20°$ as a function of a_1 and m_1. The giant planets with $m_1 \gtrsim 1M_{\rm J}$ affect the obliquity of terrestrial planets in HZs when they are located at 0.05–0.1AU or at 3–5AU. The obliquity of terrestrial planets at ~ 1AU is hardly affected when the orbit of a giant planet is close enough to the HZ when $m_1 \gtrsim 1M_{\rm J}$. On the contrary, the orbit of the terrestrial planets become unstable when the giant planet is located in the vicinity of the HZ. The giant planets which cause the spin-orbit resonance are different from those which destabilize the orbits of the terrestrial planets.

Above estimation is valid for the systems with a single giant planet. When other giant planets are in the system and other resonant regions appear, the probability for terrestrial planets in a HZ to have large $\Delta\epsilon$ would generally increase, although modulation of resonant regions sometimes decreases the probability as seen in the case of Fig. 6c and Table I.

5. APPLICATIONS TO KNOWN EXTRASOLAR PLANETARY SYSTEMS

We apply the results in the previous section to the known extrasolar planetary systems to evaluate obliquity variations of possible terrestrial planets in their HZs. The samples of extrasolar planetary systems used here are listed in Tables II, III, and IV with relevant data on the stellar masses, and the planet's masses, semi-major axes and eccentricities. These data were taken from the the Extrasolar Planets Encyclopedia (http://cfa-www.harvard.edu/planets/).

In the current radial velocity surveys, only $m_{\rm p}\sin i$ ($m_{\rm p}$ is the planet's mass, and i is the inclination between the orbital and sky planes) are measured. Since we have little observational constraints on i, we adopt planetary masses corresponding to $i = 45°$, which means 1.4 times the minimum values assuming $i = 90°$. Because we are interested in the possible terrestrial planets on nearly circular orbits that have not been largely affected by close scattering or orbital resonances, we assume that the orbits of the terrestrial

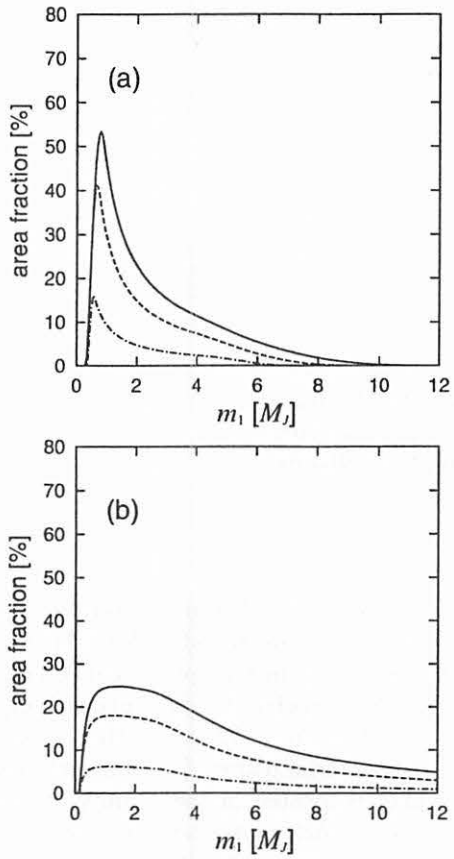

Fig. 8.— The area fraction with $\Delta\epsilon \geq 10°$ (solid line), $\geq 20°$ (dashed line), and $\geq 30°$ (dot-dashed line) as a function of mass of a giant planet m_1, in the case of $m_c = 1M_\odot$ and $I_0 = 0.05$. The semi-major axis of the giant planet a_1 are (a) 0.1AU and (b) 5.0AU.

planets are nearly on equatorial plane of original protoplanetary disks. The inclinations between the orbital plane of the giant planets and the original disks are not known. If orbital eccentricities e_p of the giant planets are produced by close scattering with other planets, the inclinations of the giant planets I would be in average $\sim e_p/2$ (Ida et al. 1993; Marzari and Weidenschilling 2002). The eccentricities of giant planets can be pumped up by disk-planet interactions or distant resonant perturbations by other planets. Then $I_p \sim e_p/2$ does not necessarily hold. However, we here adopt the simple assumption $I_p \sim e_p/2$. We will discuss the variety of choice of I_p later.

In Section 4, we adopted the region between 0.7AU and 1.3AU as a HZ. For the known extrasolar systems, however, we know their host star's masses, which predict the luminosity of the host stars. Using the predicted luminosity, we can estimate the range of HZs for individual systems. A variety of criteria have been used to define the boundaries of a HZ. According to Kasting et al. (1993), for the inner boundary of the HZ, we use the minimum distance from the host star where a runaway greenhouse effect occurs leading to the evaporation of all surface water. As for the outer boundary of the HZ, the maximum distance at which a cloud-free

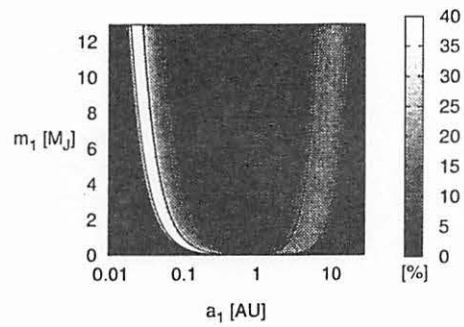

Fig. 9.— The area fraction with $\Delta\epsilon \geq 20°$ as a function of a_1 and m_1. The color bar indicates the area fraction in percent. The curves of constant fraction are drawn at 10 % and 30 %.

massive CO_2 atmosphere of the terrestrial planet can maintain a surface temperature of 273K. The HZs determined in this way are given as a function of stellar mass. In general, the boundaries of HZs move with stellar age because stellar luminosity changes with age. For simplicity, we use zero-age main sequence HZs here. The inner and outer radii of HZs are listed in the 7th column of Table II, III, and IV for each system.

As stated in Section 1, orbital stability of the possible terrestrial planets have been investigated by several groups. Among them, Menou and Tabachnik (2003) investigated the orbital dynamics of 85 extrasolar planetary systems, integrating 100 terrestrial planets (treated as test particles) in the HZs for 10^6 years. They found that orbital stability is correlated with the degree of overlap between a HZ and a gravitational zone of influence of a discovered giant planet, defined by the region extending from $R_{in} = (1 - e_p)a_p - 3R_{Hill}$ to $R_{out} = (1 + e_p)a_p + 3R_{Hill}$, where a_p and e_p are the semi-major axis, eccentricity of the giant planet and R_{Hill} is the planet's Hill radius defined by $R_{Hill} \equiv a_p(m_p/3m_c)^{1/3}$. Menou and Tabachnik (2003) classified orbital stability of the terrestrial planets in a HZ, based on the degree of overlap between the gas giant's zone of influence (ZI) and the system's habitable zone (HZ): Class I ($a_p \leq 0.25$ AU), Class II ($a_p > 0.25$ AU and no overlap between HZ and ZI), Class III ($a_p > 0.25$ AU and partial overlap between HZ and ZI), and Class IV ($a_p > 0.25$ AU and HZ is fully inside ZI). Menou and Tabachnik (2003) showed the probabilities for terrestrial planets to remain stable are 73.9 ± 8.3 % for Class I, 29.9 ± 17.3 % for Class II, 0.92 ± 2.31 % for Class III, and 0 % for Class IV. More orbits of terrestrial planets are unstable in the systems with larger overlap. The orbital classification (I–IV) are listed in the last column of Tables II, III, and IV in order to see the relation between orbital stability and obliquity variation.

TABLE II

EXTRASOLAR PLANETARY SYSTEMS IN GROUP A

system	M_* ($M_\odot$)	$M_p \sin i$ (M_{Jup})	a (AU)	e	HZ (AU)	$\Delta\epsilon \geq 10°$*1 (%)	$\Delta\epsilon \geq 20°$*2 (%)	$\Delta\epsilon \geq 40°$*3 (%)	class
HD46375	1.00	0.249	0.041	0.000	0.70/1.30	0.00	0.00	0.00	I
HD187123	1.06	0.520	0.042	0.030	0.75/1.40	0.00	0.00	0.00	I
HD209458	1.05	0.690	0.045	0.000	0.75/1.40	0.00	0.00	0.00	I
HD179949	1.24	0.840	0.045	0.050	1.10/2.25	0.00	0.00	0.00	I
HD75289	1.05	0.420	0.046	0.054	0.75/1.40	0.00	0.00	0.00	I
BD-10 3166	1.10	0.480	0.046	0.000	0.85/1.60	0.00	0.00	0.00	I
HD76700	1.00	0.197	0.049	0.000	0.70/1.30	0.00	0.00	0.00	I
51Peg	0.95	0.470	0.050	0.000	0.70/1.30	0.00	0.00	0.00	I
HD49674	1.00	0.120	0.057	0.000	0.70/1.30	0.00	0.00	0.00	I
HD168746	0.92	0.230	0.065	0.081	0.65/1.25	0.00	0.00	0.00	I
GI86	0.79	4.000	0.110	0.046	0.50/1.00	0.00	0.00	0.00	I
HD195019	1.02	3.430	0.140	0.050	0.70/1.30	0.00	0.00	0.00	I
rhoCrB	0.95	1.100	0.230	0.028	0.70/1.30	0.00	0.00	0.00	I
HD114762	0.82	11.000	0.300	0.334	0.50/1.00	0.00	0.00	0.00	III
HD121504	1.00	0.890	0.320	0.130	0.70/1.30	0.00	0.00	0.00	II
HD178911	0.87	6.292	0.320	0.124	0.60/1.20	0.00	0.00	0.00	II-III
HD52265	1.13	1.130	0.490	0.290	0.85/1.60	1.02	0.00	0.00	II
HD73526	1.02	3.000	0.660	0.340	0.70/1.30	0.00	0.00	0.00	III-IV
HD134987	1.05	1.580	0.780	0.240	0.75/1.40	0.00	0.00	0.00	III
HD40979	1.08	3.160	0.818	0.250	0.85/1.60	0.00	0.00	0.00	III
HD169830	1.40	2.960	0.823	0.340	1.40/3.00	6.61	0.00	0.00	II-III
HR810	1.03	2.250	0.925	0.161	0.70/1.30	0.00	0.00	0.00	IV
HD28185	0.99	5.700	1.030	0.070	0.70/1.30	0.00	0.00	0.00	IV
HD128311	0.80	2.630	1.060	0.210	0.50/1.00	0.00	0.00	0.00	IV
HD108874	1.00	1.650	1.070	0.200	0.70/1.30	0.00	0.00	0.00	IV
HD27442	1.20	1.430	1.180	0.020	0.93/1.80	0.00	0.00	0.00	III
HD114783	0.92	0.990	1.200	0.100	0.65/1.25	0.00	0.00	0.00	III-IV
HD20367	1.05	1.070	1.250	0.230	0.75/1.40	0.00	0.00	0.00	IV
HD19994	1.35	2.000	1.300	0.200	1.33/2.85	0.00	0.00	0.00	III
HD23079	1.10	2.540	1.480	0.060	0.85/1.60	0.00	0.00	0.00	III-IV
HD4028	0.93	0.810	1.690	0.040	0.65/1.25	0.25	0.16	0.00	II-III
HD10697	1.10	6.590	2.000	0.120	0.85/1.60	0.00	0.00	0.00	III-IV
HD196050	1.10	3.000	2.500	0.280	0.85/1.60	1.34	0.00	0.00	III-IV
HD216435	1.25	1.230	2.600	0.140	1.10/2.25	0.00	0.00	0.00	III-IV
HD30177	0.95	7.700	2.600	0.220	0.70/1.30	0.00	0.00	0.00	III-IV
HD23596	1.10	7.190	2.720	0.314	0.85/1.60	1.72	0.00	0.00	IV
HD72659	0.95	2.550	3.240	0.180	0.70/1.30	7.48	3.37	1.06	II-IV
GI777A	0.90	1.150	3.650	0.000	0.60/1.20	0.00	0.00	0.00	II
HD83443	0.79	0.350	0.038	0.080	0.50/1.00	9.77	2.99	0.00	I
		0.170	0.174	0.420					I
55Cnc	1.03	0.840	0.115	0.020	0.70/1.30	7.13	3.56	0.69	I
		0.210	0.241	0.340					I
		4.050	5.900	0.160					III

NOTE.—(*)The percentages indicate the fraction of the area where $\Delta\epsilon$ is larger than (1) 10°, (2) 20°, and (3) 40° in the area with D=8–72hours and a=0.7–1.3AU(HZ).

TABLE III

EXTRASOLAR PLANETARY SYSTEMS IN GROUP B

system	M_* ($M_\odot$)	$M_p \sin i$ ($M_{\rm Jup}$)	a (AU)	e	HZ (AU)	$\Delta\epsilon \geq 10^{\circ *1}$ (%)	$\Delta\epsilon \geq 20^{\circ *2}$ (%)	$\Delta\epsilon \geq 40^{\circ *3}$ (%)	class
B1									
Jupiter system	1.00	1.00	5.203	0.048	0.70/1.30	13.14	11.41	0.00	II
Tau Boo	1.30	3.870	0.046	0.018	1.25/2.70	11.74	3.99	0.00	I
HD130322	0.79	1.080	0.088	0.048	0.50/1.00	12.74	10.81	0.00	I
HD114386	0.75	0.990	1.620	0.280	0.50/1.00	20.14	3.89	1.35	III
B2									
70Vir	1.10	6.600	0.430	0.400	0.85/1.60	100.00	0.00	0.00	II-III
HD223084	1.05	1.210	0.440	0.480	0.75/1.40	100.00	0.00	0.00	II-III
GJ3021	0.90	3.320	0.490	0.505	0.60/1.20	100.00	0.00	0.00	III
HD8574	1.10	2.230	0.760	0.400	0.85/1.60	100.00	0.00	0.00	III
HD150706	0.98	1.000	0.820	0.380	0.70/1.30	100.00	0.00	0.00	IV
HD92788	1.06	3.800	0.940	0.360	0.75/1.40	100.00	0.00	0.00	IV
HD142	1.10	1.360	0.980	0.370	0.85/1.60	100.00	0.00	0.00	III-IV
HD177830	1.17	1.280	1.000	0.430	0.93/1.80	100.00	0.00	0.00	III-IV
HD4203	1.06	1.640	1.090	0.530	0.75/1.40	100.00	0.00	0.00	IV
HD210277	0.99	1.240	1.097	0.450	0.70/1.30	100.00	0.00	0.00	IV
HD147513	0.92	1.000	1.260	0.520	0.65/1.25	100.00	0.11	0.00	IV
HD141937	0.16	9.700	1.520	0.410	0.70/1.30	100.00	0.00	0.00	IV
HD213240	1.22	4.500	2.030	0.450	0.93/1.80	100.00	0.00	0.00	IV
HD190228	1.30	4.990	2.310	0.430	1.25/2.70	100.00	0.00	0.00	IV
HD136118	1.24	11.900	2.335	0.366	1.10/2.25	100.00	0.00	0.00	IV
HD50554	1.10	4.900	2.380	0.420	0.85/1.60	100.00	0.00	0.00	IV
HD106252	1.05	6.810	2.610	0.540	0.75/1.40	100.00	0.68	0.00	IV
HD33636	0.99	7.800	2.700	0.410	0.70/1.30	100.00	0.12	0.00	IV
HD39091	1.10	0.370	3.340	0.620	0.85/1.60	100.00	2.81	0.00	IV

TABLE IV

EXTRASOLAR PLANETARY SYSTEMS IN GROUP C

system	M_* ($M_\odot$)	$M_p \sin i$ (M_{Jup})	a (AU)	e	HZ (AU)	$\Delta\epsilon \geq 10^{\circ *1}$ (%)	$\Delta\epsilon \geq 20^{\circ *2}$ (%)	$\Delta\epsilon \geq 40^{\circ *3}$ (%)	class
HD68988	1.20	1.900	0.071	0.140	0.93/1.80	64.45	46.33	13.08	I
HD217107	0.98	1.280	0.070	0.140	0.70/1.30	65.18	44.54	12.56	I
HD108147	1.27	0.410	0.104	0.498	0.75/1.40	53.52	53.52	53.52	I
HD6434	1.00	0.480	0.150	0.300	0.70/1.30	90.31	51.10	21.68	I
HD16141	1.00	0.215	0.350	0.280	0.70/1.30	57.51	12.98	4.27	II
HD114729	0.93	0.900	2.080	0.330	0.65/1.25	55.49	5.09	2.25	III-IV
14Her	0.79	3.300	2.500	0.326	0.50/1.00	60.09	7.94	3.68	III-IV
HD216437	1.07	2.100	2.700	0.340	0.80/1.45	63.38	1.24	0.31	III-IV
Epsilon Eridani	0.80	0.860	3.30	0.608	0.50/1.00	83.62	82.37	47.07	III-IV
HD80606	0.90	3.410	0.439	0.927	0.60/1.20	100.00	100.00	0.00	II-III
HD89744	1.40	7.200	0.880	0.700	1.40/3.00	100.00	100.00	0.00	III
HIP75458	1.05	8.640	1.340	0.710	0.75/1.40	100.00	100.00	0.00	IV
HD222582	1.00	5.400	1.350	0.710	0.70/1.30	100.00	100.00	0.00	IV
16CygB	1.01	1.500	1.700	0.670	0.70/1.30	100.00	23.09	0.02	IV
HD2039	0.98	5.100	2.200	0.690	0.70/1.30	100.00	50.84	0.00	IV
Gliese 876	0.32	1.890	0.210	0.100	0.10/0.20	80.00	1.34	0.00	IV
		0.560	0.130	0.270					III-IV
HD37124	0.91	0.750	0.540	0.100	0.60/1.20	98.69	39.45	1.15	III
		1.200	2.500	0.690					III-IV
HD38529	1.39	0.780	0.129	0.290	1.40/3.00	100.00	99.98	2.60	I
		12.70	3.680	0.360					IV
HD74156	1.05	1.560	0.276	0.649	0.75/1.40	100.00	99.98	36.68	II
		7.500	3.470	0.395					IV
HD168443	1.01	7.700	0.290	0.529	0.70/1.30	100.00	71.83	1.33	II
		16.90	2.850	0.228					IV
HD82943	1.05	0.880	0.730	0.540	0.75/1.40	100.00	100.00	0.00	II-IV
		1.630	1.160	0.410					IV
HD12661	1.07	2.300	0.830	0.350	0.80/1.45	100.00	100.00	0.00	III-IV
		1.570	2.560	0.200					III-IV
HD160691	1.08	1.700	1.500	0.310	0.85/1.60	100.00	62.67	26.67	IV
		1.000	2.300	0.800					IV
47Uma	1.03	2.410	2.100	0.096	0.70/1.30	79.10	38.39	18.50	III-IV
		0.760	3.730	0.100					II
UpsAnd	1.30	0.690	0.059	0.012	1.25/2.70	100.00	47.28	0.00	I
		1.890	0.829	0.280					II
		3.750	2.530	0.270					IV

Tables II, III, and IV show the probability with $\Delta\epsilon \geq 10°, \geq 20°$ and $\geq 40°$ for terrestrial planets in HZs in 87 extrasolar planetary systems. Here, we consider spin periods of the terrestrial planets as 8–72 hours and the HZs listed in the 7th column in the Tables for each system. The extrasolar planetary systems can be classified into four distinct groups based on $\Delta\epsilon$, although the detailed values of the probability changes by different choices of the ranges of D and a, I, and $\sin i$.

About half of the systems show small obliquity variations ($\Delta\epsilon \leq 10°$) over the entire HZs (Group A). This group is mostly comprised of systems containing giant planets with small eccentricities. Corresponding small I make resonant regions narrow, resulting in the small probability. About 1/4 of the systems show large change of obliquity with more than 20° in their HZs (Group C). This group is mostly comprised of systems containing giant planets with $\sim 1M_J$ and semi-major axis $\sim$ 0.1AU, or planets with large eccentricities. In the systems containing giant planets with $m_p \sim 1M_J$ and $a_p \sim$ 0.1AU, resonant regions considerably overlap HZs, as shown in Fig. 6a. In the systems with giant planets on eccentric orbits, resonant regions are expanded by large inclinations inferred from the large eccentricities. All of the two giant planet systems except for HD83443 system, and a triple giant planets system, Ups And system, belong to Group C. The residual systems we call Groups B1 and B2, which show intermediate features between Group A and Group C. In the systems of Group B1, resonant regions and HZs partially overlap. We also list the result for the system which only contains Jupiter around a host star with $1M_\odot$ except for massless terrestrial planets (we call it "Jupiter system" hereafter). Jupiter system belongs to this group. In Group B2, resonant regions do not overlap with HZs, but the obliquity variation amplitude is not small enough: it is larger than 10° but smaller than 20° over the entire HZs. The systems in Group B2 contain giant planets with $e \sim$ 0.3–0.6, which causes large obliquity variations in non-resonant regions. The evaluated variation amplitude of obliquity may become small if the estimated orbital inclinations are reduced.

Both Group A and Group C include all the orbital stability classes. As expected from discussion in Section 5, large amplitude of obliquity variation is not necessarily associated with an unstable orbit. In general, if a giant planet is closer to the HZ and/or more massive, the orbits of terrestrial planets are more likely to be unstable. However, obliquity is less affected by spin-orbit resonances if the giant planet is closer to the HZ or more massive. More than 1/3 of the systems which have unstable orbits of terrestrial planets in the HZs (Class III or IV) show small obliquity variations. On the other hand, the terrestrial planets which has the stable orbits can have large obliquity variations. Nearly 1/3 of the systems in which the terrestrial planets have stable orbits in HZs (Class I or II) show large obliquity variations. The systems that have both stable orbits and small obliquity variations are only 1/5 of all the systems. Note that 2/3 of such systems are systems with the giant planet(s) with $a_p \lesssim$ 0.1AU.

In most of the multi-planet systems so far found, the obliquity of terrestrial planets in HZs would change by more than 20°. More resonant regions exist in multi-planet systems than in single-planet systems. In HD74156 system, it is the spin-orbit resonance with an eigenfrequency that causes the obliquity variation with $\geq 40°$. In 47Uma system, which contains giant planets relatively distant from the host star with small eccentricities, a secular resonance is located within its HZ, resulting in the large variation of obliquity. In HD82943 and HD160691 systems, their HZs are bounded by secular resonances. Only HD83443 and 55Cnc systems show small obliquity variations ($\Delta\epsilon \leq 10°$). In these systems, the orbit of terrestrial planets in their HZs are also stable. It should be noted that multi-planet systems in Group C contain giant planets with large eccentricities, which cause the large obliquity variations of terrestrial planets in HZ in non-resonant regions, as well as the resonant regions. Current surveys of the extrasolar planets are limited to the detection of planets located within 3–4 AU from their host stars. Planets on more distant orbits with small eccentricities will be detected as planets in new planetary systems or as additional planets in known planetary systems. As shown in Figure 7, distant giant planets have weaker effect on the obliquity of terrestrial planets in HZ than the giant planets at 2–4AU. Therefore we may find multiple giant planet systems whose HZs include the terrestrial planets with small obliquity variation, in future surveys.

6. DISCUSSION

We have evaluated the probability that terrestrial planets in HZs have large obliquity variations in 87 known extrasolar planetary systems. In future surveys, giant planets at $\gtrsim$ 5–10 AU could be detected as additional planets in known planetary systems. As suggested by the results in Fig. 9, however, such distant giant planets have less influence on the HZs, the results shown in Section 5 do not suffer from significant modification if additional giant planets are detected in future.

However, other terrestrial planets that may probably exist near or within a habitable zone affect the obliquity variations of a terrestrial planet in a HZ. As Figure 9 suggests, close planets with small masses can cause spin-orbit resonances. These effects may sometimes be more severe than those of giant planets. Indeed, Mars' obliquity is under the influence of other terrestrial planets, as well as Jupiter and Saturn (Ward 1974).

The effect of a satellite(s) cannot be neglected for the obliquity variation, if the satellite is as large as the Moon. Earth owes the stability of its spin axis to the existence of the Moon (Ward 1974; Laskar et al. 1993; Laskar 1996). Total torque that a terrestrial planet received is sum of the torques raised by other

objects in the system. In Earth's case, the torque by the Moon is twice as large as that exerted by Sun, which increases its precession constant by a factor of 3. This is equivalent to reducing the rotation period by a factor of 3 in the results in previous sections. As a result of this effect, Earth gets out of resonant regions. In the past, the Moon was closer to the Earth, so the lunar torque was stronger than the current one. Thus, the Moon has been stabilizing the Earth's obliquity.

There is an upper limit on orbital precession frequencies of terrestrial planets in a HZ for other planets to maintain the orbital stability of the terrestrial planets. Considering a giant planet far from the boundary of the HZ by $\sim 5R_{\rm Hill}$ ($R_{\rm Hill}$ is the Hill radius of the giant planet), which would marginally maintain the orbital stability, the orbital precession frequency of a terrestrial planet at 1AU is 50–100 $''$ yr^{-1}. Hence, 50–100 $''$ yr^{-1}may be close to the upper limit. Note that this value is almost the same order of the spin precession frequency at 1AU. If considerable torque by a satellite exerts on the terrestrial planet to pump up the spin precession frequency over the upper limit of the orbital precession frequency, spin-orbit resonance will not occur. So, a very large and/or very close satellite like the Moon would generally tend to stabilize obliquity of terrestrial planets.

Our analytical expressions of the obliquity variation of terrestrial planets can be applied to giant planets. Not only obliquity of terrestrial planets, but also that of giant planets is affected by spin-orbit resonance. Saturn's primordial obliquity may have been smaller and modified to the present value ($\sim 26°$) by spin-orbit resonance with Neptune (Hamilton and Ward 2002a,b,c). We investigated the obliquity variations of giant planets in known multiple-planet systems assuming rotation periods similar to Jupiter or Saturn ($\sim$ 10 hour), and found that no giant planets in multiple-planet systems so far found would be in spin orbit resonance.

As mentioned in Section 3, obliquity of the planets in a retrograde spin state is not affected by the spin-orbit resonance. Planetary spin caused by planetesimal accretion has two components: the systematic component produced by accumulation of a large number of small planetesimals, and the random component produced by small number of large impacts (e.g., Lissauer et al. 2000). The systematic component tends to result in relatively slow prograde spin. On the other hand, radom component can produce relatively rapid spin and does not have any preferred spin direction. For the terrestrial planets, it is expected that the random component is dominant (e.g., Lissauer et al. 2000). In the Solar System, however, three terrestrial planets have prograde spins. Primordial spin of Venus, which is the only terrestrial planet having a retrograde spin, could have been prograde until large obliquity variation and the dissipation of its thick atmosphere overturned the spin (Correia and Laskar 2001). If the planets are formed in retrograde spin state, they maintain the primordial obliquity.

As shown in Section 5, among the known extrasolar planetary systems, systems with short-period giant planets with semi-major axes $\lesssim$ 0.1AU are favorable sites for terrestrial planets to exist with orbital stability and small obliquity variations in HZs. However, short-period giant planets may have been formed in the region outside the HZs and migrated inward to the present locations by disk-planet interactions (Lin et al. 1996). It would not be easy for terrestrial planets in the HZs to survive during the passage of the giant planets. If terrestrial planets forms in a HZ from a residual protoplanetary disk after the passage, such terrestrial planets would stay in stable orbits with small obliquity variations.

7. CONCLUSION

We have investigated obliquity variations of possible terrestrial planets in habitable zones (HZs) in extrasolar planetary systems. The amplitude of obliquity variations may be one of the most important factors for land-based life to survive on the terrestrial planets.

We derived the analytical expression for the obliquity variations of terrestrial planets in the spin-orbit resonance region, as well as the expression in non-resonant region. The latter completely agrees with the formulae derived by Ward (1974). Analytically predicted amplitude of obliquity variations showed excellent agreement with the results obtained by numerically integrating the precession equation.

Using the analytical expressions, we statistically studied general properties of obliquity variations of terrestrial planets in a HZ perturbed by a giant planet(s). We presented the probability of terrestrial planets with prograde spin in the HZ having obliquity variation amplitude larger than given critical values. The results are as follows:

1. Largest obliquity variations are produced by giant planets as far from the habitable zone as the orbits of the terrestrial planets are stable.

2. Stability of the obliquity variations of a terrestrial planet is not associated with its orbital stability.

3. About half of the known extrasolar planetary systems show small obliquity variations of terrestrial planets ($\Delta\epsilon \leq 10°$) over the entire HZs.

4. The systems that have terrestrial planets with both small obliquity variations and stable orbits in the HZs are only 1/5 of the known extrasolar planetary systems.

5. In general, more planets (giant planets or other terrestrial planets) result in larger obliquity variations. Almost all of the known multiple-planet systems (except for HD83443 and 55Cnc systems) show large obliquity variations ($\Delta\epsilon \geq 20°$).

6. If a terrestrial planet on a stable orbit near 1AU has so large and/or so close satellite that it significantly enhances the precession rate of the spin axis of the terrestrial planet, obliquity variations may be significantly reduced.

Masses and orbital radii of the most effective giant planets for enhancing the obliquity variations are plotted in Figure 9. For example, in the system including a giant planet with $1M_J$ and with a HZ of 0.7–1.3AU, the obliquity of terrestrial planets in the HZ is most radically changed ($\Delta\epsilon \geq 20°$) if the giant planet orbits at $\sim$ 0.05–0.1AU or 3–5AU. If the mass of the giant planet is larger, the most effective location of the giant planet is further from the HZ. On the other hand, the orbits of the terrestrial planets in the HZ are destabilized if the giant planet is closer to the HZ or is more massive. The dependences on the masses and the orbital radii of perturbing planets are different between the orbital stability and the magnitude of the obliquity amplitude of terrestrial planets.

In the systems where planetary orbital migration has not occurred significantly, orbital configuration of planets may be likely to be in a marginally stable state. Then, the our results suggest that obliquity of a terrestrial planet tends to be near the spin-orbit resonances and often suffer large obliquity variations, as long as the spin of the terrestrial planet is prograde. Therefore, retrograde spin of the terrestrial planet or the existence of a large and/or close satellite that significantly pumps up spin precession rate might be essential for land-based life to survive on a terrestrial planet in a HZ.

APPENDIX: DERIVATION OF EQS. (9) AND (10)

We expand the precession equation,

$$\frac{d\hat{s}}{dt} = \alpha(\hat{s}\cdot\hat{n})(\hat{s}\times\hat{n}), \tag{1}$$

in terms of $I \ll 1$, in the Cartesian coordinates where the invariant plane is on the x-y plane (see Figure 1). In these coordinates, the spin vector $\hat{s}$ and the orbit normal $\hat{n}$ are given by

$$\hat{s} = \begin{pmatrix} \sin\theta\sin\psi \\ -\sin\theta\cos\psi \\ \cos\theta \end{pmatrix}, \tag{36}$$

$$\hat{n} = \begin{pmatrix} \sin I\sin\Omega \\ -\sin I\cos\Omega \\ \cos I \end{pmatrix}, \tag{37}$$

where θ is the angle between the equator and the reference plane, ψ is the longitude of the equator, I is the orbital inclination, and Ω is the longitude of the ascending node. The time derivative of $\hat{s}$ is given by

$$\frac{d\hat{s}}{dt} = \begin{pmatrix} \dot{\theta}\cos\theta\sin\psi + \dot{\psi}\sin\theta\cos\psi \\ -\dot{\theta}\cos\theta\cos\psi + \dot{\psi}\sin\theta\sin\psi \\ -\dot{\theta}\sin\theta \end{pmatrix}. \tag{38}$$

The vector product of $\hat{s}$ and $\hat{n}$ is

$$\hat{s}\times\hat{n} = \begin{pmatrix} -\sin\theta\cos\psi\cos I + \cos\theta\sin I\cos\Omega \\ \cos\theta\sin I\sin\Omega + \sin\theta\cos I\sin\Omega \\ -\sin\theta\sin\psi\sin I\cos\Omega + \sin\theta\cos\psi\sin I\sin\Omega \end{pmatrix}. \tag{39}$$

From the z component of Eq. (1), we obtain

$$\begin{aligned} \dot{\theta} &= \alpha\cos\epsilon\sin I(\sin\psi\cos\Omega - \cos\psi\sin\Omega) \\ &\simeq \alpha\cos\epsilon I(\sin\psi\cos\Omega - \cos\psi\sin\Omega) \\ &\quad + \mathcal{O}(I^2), \end{aligned} \tag{40}$$

with the assumption $I \ll 1$. Substituting $I\cos\Omega$ and $I\sin\Omega$ given by Eqs. (4) and (5) into the above equation, we obtain

$$\dot{\theta} \simeq \alpha\cos\epsilon\left[I_0\sin(\psi-\Omega_0) + \sum_{i=1}^{N_c} I_i\sin(\psi-\Omega_i)\right] + \mathcal{O}(I^2), \tag{41}$$

where $\Omega_0 = Bt+\gamma$ and $\Omega_i = f_i t + \gamma_i$.

From the x and the y components of Eq. (1), we obtain

$$\begin{aligned} \dot{\psi} &= \alpha\cos\epsilon[-\cos I \\ &\quad + \sin I\cot\theta(\cos\psi\cos\Omega + \sin\psi\sin\Omega)] \\ &\simeq \alpha\cos\epsilon[-1 \\ &\quad + I\cot\theta(\cos\psi\cos\Omega + \sin\psi\sin\Omega)] \\ &\quad + \mathcal{O}(I^2). \end{aligned} \tag{42}$$

With Eqs. (4) and (5), Eq. (42) is

$$\begin{aligned} \dot{\psi} &\simeq -\alpha\cos\epsilon + \alpha\cos\epsilon\cot\theta \\ &\quad \times\left[I_0\cos(\psi-\Omega_0) + \sum_{i=1}^{N_c} I_i\cos(\psi-\Omega_i)\right] \\ &\quad + \mathcal{O}(I^2). \end{aligned} \tag{43}$$

Substituting $\hat{s}$ and $\hat{n}$ given by Eqs. (36) and (37) into $\cos\epsilon = \hat{s}\cdot\hat{n}$ (Eq. 3),

$$\cos\epsilon = \cos\theta\cos I + \sin\theta\sin I\cos(\psi-\Omega). \tag{44}$$

Differentiating Eq. (44) with respect to t yields

$$\begin{aligned} \frac{d(\cos\epsilon)}{dt} &= -\dot{\theta}\sin\theta\cos I + \dot{\theta}\cos\theta\sin I\cos(\psi-\Omega) \\ &\quad - \frac{d}{dt}(\psi-\Omega)\sin\theta\sin I\sin(\psi-\Omega). \end{aligned} \tag{45}$$

Substituting Eqs. (40) and (11) into the above equation, and neglecting the higher terms than the second order of I, we obtain

$$\begin{aligned} \frac{d(\cos\epsilon)}{dt} &= I_0 B\sin\theta\sin(\psi-\Omega_0) \\ &\quad + \sum_{i=1}^{N_c} I_i f_i\sin\theta\sin(\psi-\Omega_i) \\ &\quad + \mathcal{O}(I^2). \end{aligned} \tag{46}$$

ACKNOWLEDGMENTS

We thank William Ward for useful comments on discussion about the known extrasolar planetary systems. We also thank Hidekazu Tanaka for valuable advice on the analytical formulation.

REFERENCES

Abe, Y. 1993. Physical state of very early Earth. *Lithos* **30**, 223–235.

Berger, A., J. Imbrie, J. Hays, G. Kukla and B. Saltzman eds. 1984. *Milankovitch and Climate — Understanding the Response to Astronomical Forcing.* D. Reidel, Norwell, Mass.

Berger, A. ed. 1989. *Climate and Geo-Science — A Challenge for Science and Society in the 21st Century.* Kluwer Academic Publishers, Dordrecht.

Brouwer, D., and G. M. Clemence 1961. *Methods of Celestial Mechanics.* Academic Press, New York.

Correia, A. C. M., and J. Laskar 2001. The four final rotation states of Venus. *Nature* **411**, 767–770.

Gehman, C. S., F. C. Adams, and G. Laughlin 1996. The prospects for Earth-like planets within known extrasolar planetary systems. *Publ. Astron. Soc. Pacific.* **108**, 1018–1023.

Hamilton, D. P., and W. R. Ward 2002a. The obliquities of the giant planets. *Bull. Am. Astron. Soc.* **33**, 1503(abstract).

Hamilton, D. P., and W. R. Ward 2002b. Obliquity of Saturn: Analytical model. *Bull. Am. Astron. Soc.* **34**, 2808(abstract).

Hamilton, D. P., and W. R. Ward 2002c. Obliquity of Saturn: Numerical model. *Bull. Am. Astron. Soc.* **34**, 2809(abstract).

Ida, S., E. Kokubo, and J. Makino 1993. The origin of anisotropic velocity dispersion of particles in a disc potential. *Mon. Not. R. Astron. Soc.* **108**, 875–889.

Ito, T., K. Masuda, Y. Hamano, and T. Matsui 1995. Climate friction: a possible cause for secular drift of the earth's obliquity. *J. Geophys. Res.* **100**, 15147–15161.

Jones, B. W., P. N. Sleep, and J. E. Chambers 2001. The stability of the orbits of terrestrial planets in the habitable zones of known exoplanetary systems. *Astron. Astrophys.* **366**, 254–262.

Jones, B. W., and P. N. Sleep 2002. The stability of the orbits of Earth-mass planets in the habitable zone of 47 Ursae Majoris. *Astron. Astrophys.* **393**, 1015-1026.

Kasting, J. F., D. P. Whitmire, and R. T. Reynolds 1993. Habitable zones around main sequence stars. *Icarus* **101**, 108–128.

Laskar, J., and P. Robutel 1993. The chaotic obliquity of the planets. *Nature* **361**, 608–612.

Laskar, J., F. Joutel, and P. Robutel 1993. Stabilization of the earth's obliquity by the moon. *Nature* **361**, 615–617.

Laskar, J. 1996. Large scale chaos and marginal stability in the Solar System. *Celes. Mech. Dyn. Astron.* **64**, 115–162.

Lin, D. N. C., P. Bodenheimer, and D. C. Richardson 1996. Orbital migration of the planetary companion of 51 Pegasi to its present location. *Nature* **380**, 606–607.

Lissauer, J. J., L. Dones, and K. Ohtsuki 2000. Origin and evolution of terrestrial planet rotation. In *Origin of Earth and Moon* (R. M. Canup, and K. Righter, Eds.), pp. 101–112. Univ. of Arizona Press, Tucson.

Marcy, G. W., R. P. Butler, and S. S. Vogt 2000. Sub-Saturn planetary candidates of HD 16141 and HD 46375. *Astrophys. J.* **536**, L43–46.

Marzari, F., and S. J. Weidenschilling 2002. Eccentric extrasolar planets: The jumping Jupiter model. *Icarus* **156**, 570–579.

Menou, K., and S. Tabachnik 2003. Dynamical habitability of known extrasolar planetary systems. *Astrophys. J.* **583**, 473–488.

Milankovitch, M. 1941. Kanon der Erdbestrahlung und seine Anwendung auf das Eiszeitproblem. *KanonKöniglich Serbische Academie Publication* **133**, Königlich Serbische Academie.

Noble, M., Z. E. Musielak, and M. Cuntz 2002. Orbital stability of terrestrial planets inside the habitable zones of extrasolar planetary systems. *Astrophys. J.* **572**, 1024–1030.

Touma, J., and J. Wisdom 1993. The chaotic obliquity of Mars. *Science* **259**, 1294–1297.

Ward, W. R. 1973. Large-scale variations in the obliquity of Mars. *Science* **181**, 260–262.

Ward, W. R. 1974. Climate variations on Mars 1. Astronomical theory of insolation. *J. Geophys. Res.* **79**, 3375–3386.

Ward, W. R. 1982. Comments on the long-term stability of the Earth's obliquity. *Icarus* **50**, 444–448.

Ward, W. R., and D. J. Rudy 1991. Resonant obliquity of Mars? *Icarus* **94**, 160–164.

Ward, W. R. 1992. Long-term orbital and spin dynamics of Mars. In *Mars*, p. 298–320. Univ. of Arizona Press, Tucson.

Ward, W. R., C. B. Agnor, and R. M. Canup 2002. Obliquity variations in planetary systems. *Lunar. Planet. Sci.* **XXXIII**, 2017(abstract).

This 2-column preprint was prepared with the AAS LaTeX macros v5.0.

太陽系内の平均運動共鳴
Mean motion resonances in the solar system

吉川　真（宇宙科学研究所†）
Makoto Yoshikawa (ISAS†)
3-1-1, Yoshinodai, Sagamihara, Kanagawa 229-8510, JAPAN
makoto@pub.isas.jaxa.jp

Abstract
In the solar system, there are many kinds of resonances, such as mean motion resonances, secular resonances, and spin-orbit resonances. In this paper, such resonances are briefly summarized first. Then the relationship between the distribution of asteroids and resonances are discussed and some examples of the orbital evolution of asteroids in mean motion resonances are shown. The mean motion resonances are very important not only for the stabilization of the system but also for the orbital evolution of the bodies in the solar system.

1．はじめに

太陽系には、太陽以外に惑星・衛星・小惑星・彗星・流星物質などが存在しているが、これらの運動には様々な特徴が見られる。その中でもこれらの天体の運動に普遍的に見られるものは、平均運動共鳴である。平均運動共鳴は、天体同士の公転周期の関係が整数比になるものであるが、平均運動共鳴にあることで系が安定化する場合もあれば、共鳴にあることで軌道が大きく変化してしまう場合もある。ここでは、太陽系天体の軌道進化を考える場合に重要な役割を果たすこの平均運動共鳴についてまとめてみることにする。以下では、まず太陽系内に見られる共鳴現象を概観し（2 節）、その後で特に小惑星についてその分布に共鳴がどのように影響しているのかをまとめてみる（3 節）。そして、共鳴にある小惑星の軌道進化について、いくつかの解析例を紹介する（4 節）。

2．太陽系内の共鳴現象

太陽系内の天体の運動には、様々な共鳴現象が見られるが、ここでは平均運動共鳴以外の共鳴も含めて、それぞれの天体ごとに見られる共鳴をまとめてみることにする。

(1) 水星
水星は、自転周期（58.65日）と公転周期（87.99日）の間に、2:3の共鳴関係がある。

---

†2003 年 10 月からは、それまでの宇宙科学研究所(ISAS)、航空宇宙技術研究所(NAL)、宇宙開発事業団(NASDA)が統合されて、宇宙航空研究開発機構(JAXA)となった。
JAXA：Japan Aerospace Exploration Agency

(2) 金星

金星は、ゆっくりと逆行自転しているのであるが、金星の自転周期・公転周期と地球の公転周期との間には、次のような関係があると言われている[1]。

$$\frac{\dfrac{1}{\text{金星の自転周期}} + \dfrac{1}{\text{地球の公転周期}}}{\dfrac{1}{\text{金星の公転周期}} - \dfrac{1}{\text{地球の公転周期}}} \sim 4$$

ただし、この関係は、近似的なものである。

(3) 地球

月が常にほぼ片側だけを地球に向けているが、これは周知のように、月の自転周期(27.3217日）が月の地球周りの公転周期（27.3217日）と一致しているためである。つまり、月の自転周期と月の公転周期とは1:1の共鳴状態にある。

また、地球の公転周期（1 年）と近い公転周期を持つ小惑星が存在することが知られており、コンパニオン小惑星と呼ばれることもある。例えば、:(3753)Cruithne や 2002 AA29 がそうであるが、これらは地球の公転周期に近い公転周期で運動しているが、公転周期が地球と完全に 1:1 になるような共鳴状態にはない。したがって、一時的にこのような軌道にある天体と考えられる。

(4) 火星

火星には2つの小さな衛星であるフォボスとダイモスがあるが、これらも地球の月と同様に公転周期と自転周期が同期している。このような自転と公転が同期している現象は、木星・土星・天王星・海王星にある衛星の多くに見られる現象である。

また、火星の公転運動と関係して、火星のトロヤ群（公転周期が 1:1 の共鳴状態）と思われる小惑星もいくつか発見されている。例えば、(5261)Eureka などがそうであるが、火星のトロヤ群（トロヤ群については、以下の木星の項を参照）においては、長期的に安定に存在するかどうかを確認する必要がある。(2003 年 11 月現在、Minor Planet Center のウエッブサイトでは、火星のトロヤ群のリストは削除されている。)

(5) 木星

木星には、現在、60個以上の衛星が発見されているが、衛星の公転周期について有名な共鳴は、イオとエウロパとカニメデの間に見られる共鳴である。これらの衛星の平均運動（n）の比は、

$$n_{Io} : n_{Europa} : n_{Ganimede} \sim 4 : 2 : 1$$

となっている。より厳密には、

$$n_{Io} - 3n_{Europa} + 2n_{Ganimede} = 0$$

という関係にある。(平均運動とは、平均の角速度のこと)

また、木星は、多くの小惑星と平均運動共鳴の関係にある。特にその数が多いのが1:1の共鳴にあるトロヤ群である。制限3体問題においては、その特殊解としてオイラーの直線解とラグランジュの正三角形解がある。正三角形解の方は安定であるが、木星の場合、太陽と木星を一辺とする正三角形の頂点付近に多数の小惑星が存在しており、これをトロヤ群と呼んでいるのである。これらの公転周期は木星の公転周期と同じであり、したがって1:1の共

鳴にあることになる。木星の前方（公転方向）にあるラグランジュ点（L_4）付近には、(588) Achillesをはじめとして1016個の小惑星が発見されている。また、木星の後方のL_5付近には、(617) Patroclusをはじめとして604個の小惑星が発見されている（2003年11月現在）。なお、1:1のトロヤ群以外に、木星といろいろな平均運動共鳴にある小惑星があるが、これは、小惑星の項で述べることにする。

木星については、土星との公転周期の比が2:5に近いという関係もある。これを平均運動で示せば $n_{Jupiter} : n_{Saturn} \sim 5 : 2$ となるが、これをla grande inégalité (the great inequality)と呼ぶ。太陽系の最大の惑星と2番目に大きい惑星とがこのような関係にあるために、惑星同士の摂動に大きな影響を及ぼしている。

(6) 土星

土星も多くの衛星を持ち、現在発見されているものは30個を越えている。土星の衛星間には多くの共鳴が見られる。それらを挙げると次のようになる。

$n_{Mimas} : n_{Tethys} = 2 : 1$

$n_{Enceladus} : n_{Dione} = 2 : 1$

$n_{Titan} : n_{Hyperion} = 4 : 3$

1:1共鳴またはそれに近いもの：

土星-Dione-Helene　：　正三角形

土星-Tethys-Telesto　：　正三角形

土星-Tethys-Calypso　：　正三角形

Prometheus と Pandora　：　同じ軌道上

なお、土星には美しい環が存在するが、環には微細な構造が見られる。例えば、衛星Mimasとの共鳴位置に空隙があることなどが知られている。

(7) 天王星

天王星にも多数（27個）の衛星が発見されているが、内側の衛星間には公転周期が2:1に近い関係がある。また、RosalindとCordeliaの衛星の間には、5:3の共鳴がある。さらには、Cordeliaとεリング、Opheliaとεリングにはそれぞれ、24:25と14:13の関係があると言われている。

(8) 海王星

海王星には、ラグランジュ点 L4 の位置にトロヤ群小惑星が１つ知られている。(2001 QR322)

(9) 冥王星

冥王星は、海王星の軌道の内側まで入り込むが、海王星と衝突する可能性はない。その理由としては、冥王星の軌道が海王星の軌道と立体的に交差しているということが挙げられるが、さらに、冥王星と海王星とが平均運動共鳴$n_{Neptune} : n_{Pluto} = 3 : 2$にあることも重要な理由である。この共鳴にあることで、海王星が冥王星と会合する場所が、冥王星と海王星の軌道が最接近する場所ではないところに保たれている。これらに加えて、冥王星の近日点の位置が黄道面内には来ないということも冥王星の軌道の安定化の要因となっている。

冥王星には、Charonという衛星があるが、この衛星の公転周期が冥王星の自転周期と一致している。つまり、Charonは、地球で言えばちょうど静止衛星のようになっているのである。

(10) 小惑星

すでに述べたように、小惑星には木星との平均運動共鳴が多数見られる。その様子は、小惑星の軌道長半径の分布を見ると顕著である。まず、小惑星帯では、木星と平均運動共鳴が起こるところは小惑星の数が少なくなり、分布のギャップが見られる。これをカークウッドギャップというが、小惑星と木星との平均運動の比がカークウッドギャップ では、4:1、3:1、5:2、7:3、2:1となっている。一方、小惑星帯の外側の領域では、逆に平均運動共鳴が起こるところに小惑星が集中して存在する傾向があり、3:2の共鳴がヒルダ群、4:3の共鳴がチューレ群と呼ばれている。もちろん、1:1の共鳴はトロヤ群である。

また、最近では海王星軌道近辺に多数（約800個）の小天体が発見されており、エッジワース・カイパーベルト天体と呼ばれている。このエッジワース・カイパーベルト天体の中には、海王星と平均運動共鳴にあるものがあることが知られている。

なお、小惑星の中には軌道が不安定なものがあり、惑星とクローズエンカウンターを起こすようなものがある。そのような天体の場合、一時的に惑星と平均運動共鳴状態になる場合がある。この他、小惑星帯では永年共鳴と呼ばれる共鳴もあるが、これについては、木下宙氏の論文を参照されたい。

(11) 彗星・流星物質

彗星は、小惑星のように小さな天体であるが、軌道の性質は小惑星とはかなり異なる。小惑星では、その大部分が安定であり、惑星に接近して軌道が不安定になるようなものの割合はかなり小さい。ところが、彗星の場合、軌道が長楕円であることもあって、惑星に接近して軌道が不安定に変化する場合が一般的である。その軌道が変化している過程で、一時的に惑星と平均運動共鳴状態になることがある。

流星物質の場合は、そのほとんどが彗星や小惑星から放出されたものと考えられるので、軌道運動も彗星や小惑星の場合と似たものになる。ただし、小さいために太陽輻射の影響を受けやすい。最近の研究では、たとえばしし座流星群に関連した流星物質の一部が惑星と共鳴状態にある可能性が高いことなどが指摘されている。

以上のように、太陽系には非常に多くの共鳴が存在している。これらの共鳴の多くは、軌道を安定化するために機能している。または、共鳴にあるがために、現在の軌道に存在していると言ってもよい。また、このように多彩な共鳴があるために、太陽系の力学は興味の尽きないものとなっているのである。

3．小惑星の分布と平均運動共鳴

2003 年 11 月現在、23 万個もの小惑星の軌道がカタログ化されており、また、確定番号が付いている小惑星も 7 万個に及ぶ。小惑星の個数は、ここ 5 年くらいの間に急増している。

小惑星の分布の様子を図にしたものが Fig.1 である。ここでは、2003 年 3 月初めの時点で発見されていた 21 万個余りの小惑星の位置を黄道面に投影したものが描かれている。このような図を描くと、小惑星帯は真っ黒になってしまう。もちろん、これは、小惑星を表す点を大きく描きすぎているためである。もし、大きさの比を実際のスケール比に合わせるとすると、小惑星を表す点は最大でも 40 ナノメートルくらいの大きさにする必要がある。印刷ではこれは無理である。実際の小惑星帯はこの図から想像されるようにぎゅうぎゅう詰めなのではなくて、逆に「すかすか」なのである。

Fig.1 には、小惑星帯を「真横」から見た図も描かれているが、小惑星帯が大体 2AU ほどの厚さをもっていることがわかる。

このような図は、小惑星の分布の様子を直感的に見るには便利な図であるが、力学的な特徴はあまり表現されていない。力学的な特徴で顕著なものは、Fig.1 の上の図で示されているように、木星軌道上で木星の前と後ろに一群の小惑星があることで、これは前節で述べたトロヤ群小惑星である。なお、木星の前（公転方向）にあるトロヤ群については、Fig.1 の下の図の左端に分離してプロットされているが、黄道面から離れた小惑星が比較的多いことが分かる。

この他の特徴としては、小惑星帯の縁について、外側の縁は木星軌道から 1.5 天文単位くらい離れたところにあるのに対して、内側の縁は火星軌道のすぐそばにあることが挙げられる。

力学的な特徴をよりはっきり知るためには、軌道要素の分布を見る必要がある。軌道要素についての詳細は関連する文献を参照してもらうとして、ここでは、名称のみを挙げることにする。代表的な軌道要素としては、軌道長半径（a）、軌道離心率（e）、軌道傾斜角（i）、近日点引数（ω）、昇交点経度（Ω）、近日点通過時刻（T_0）がある。

小惑星の軌道要素の分布には、いろいろな相関が見られる。ここでは、Fig.1 に示した小惑星について、a-e 平面と a-i 平面にプロットした図を示すことにする。

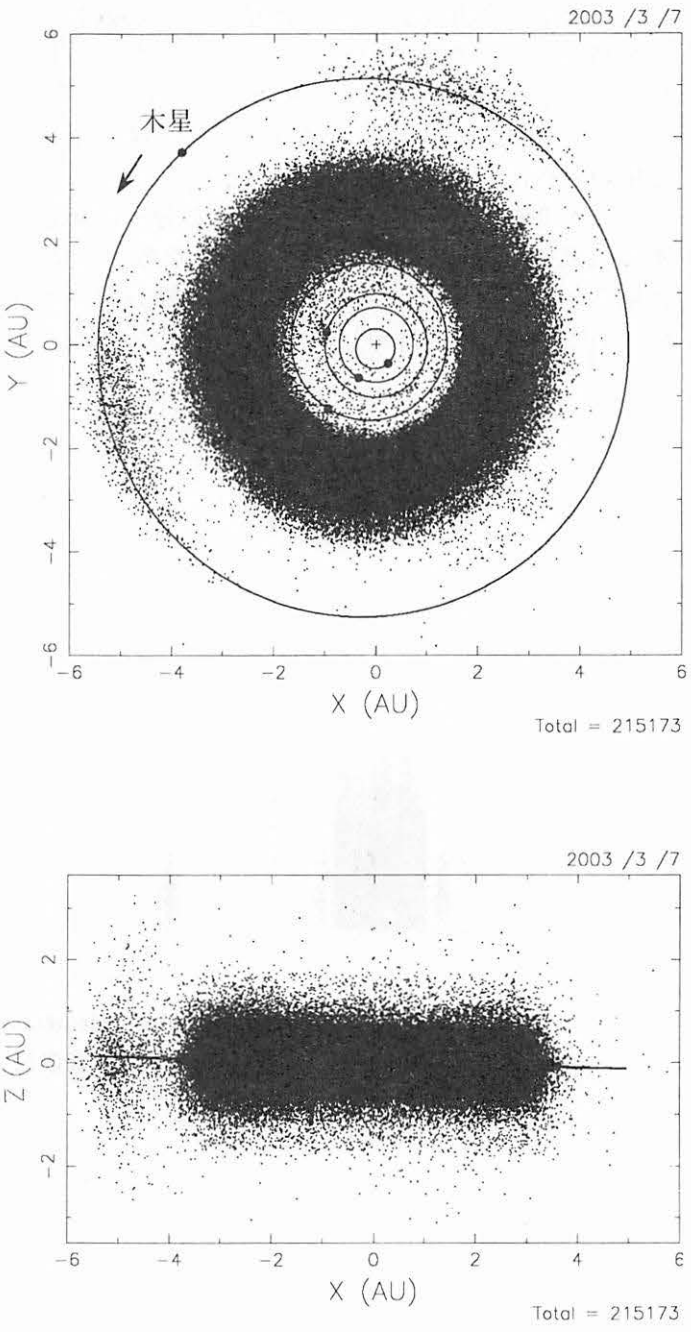

Fig.1 Distribution of asteroid: face on view (above) and edge on view (below).
小惑星の分布。太陽系を「真上」から見た図（上）と「真横」から見た図（下）。約 21 万 5 千個の小惑星の 2003 年 3 月 7 日現在の位置を示す。上の図で軌道は、内側から水星、金星、地球、火星、木星である。

Fig.2 は、a-e 平面上にプロットしたものであるが、大局的な分布としては、軌道長半径が大きくなるにつれて軌道離心率が小さくなる分布となっていることがわかる。これは、木星軌道になるべく接近しないような分布となっているためである。ただし、小惑星帯（a が 2AU～3.5AU 付

近）の外側（木星側）では、木星との平均運動共鳴であることにより、木星軌道と重なるような軌道にも小惑星が存在している。また、小惑星帯の中には縦方向に何本かすき間が見られるが、これがカークウッドギャップに対応するものである。

Fig.3 には、a-i 平面にプロットした図が示されている。a-i 平面にプロットすると、小惑星の分布にいくつかの構造があることがわかる。特に、軌道長半径が 2AU 付近で軌道傾斜角が 20 度を超えるあたりに孤立した分布があるが、この孤立した分布は、永年共鳴と平均運動共鳴（4:1）で作られているものである。なお、小惑星帯付近を拡大した図（Fig.3 右）を見るとカークウッドギャップによる縦方向のすき間以外に、分布の濃淡が見られるが、これは小惑星の「族（family)」によるものである。

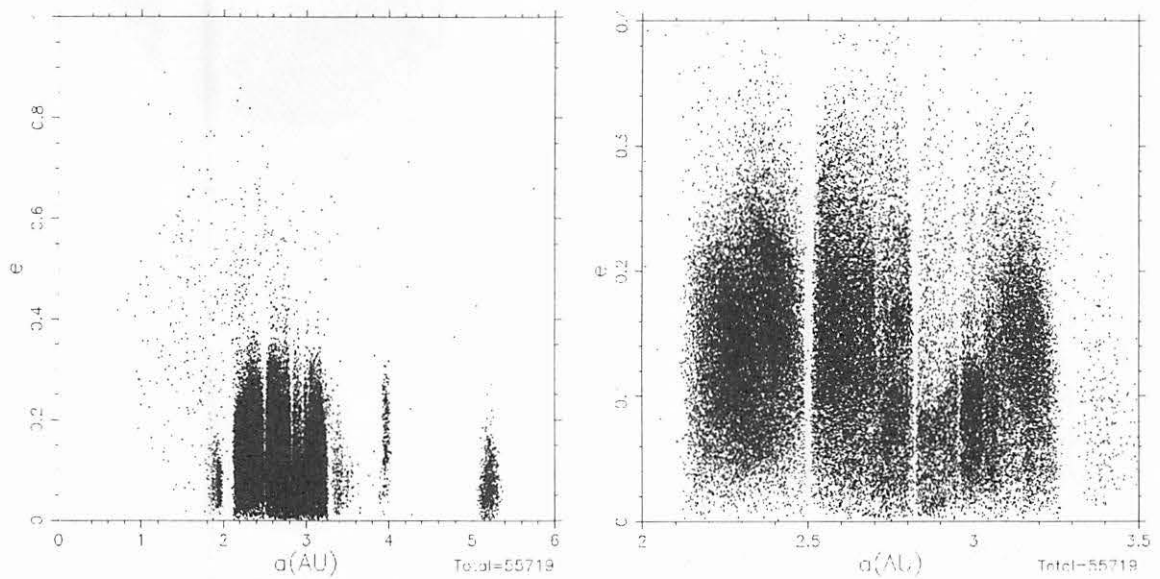

Fig.2 Distribution of orbital elements of asteroids in a-e plane.
a-e 平面上での小惑星の分布。（右の図は、左の図の部分の拡大）

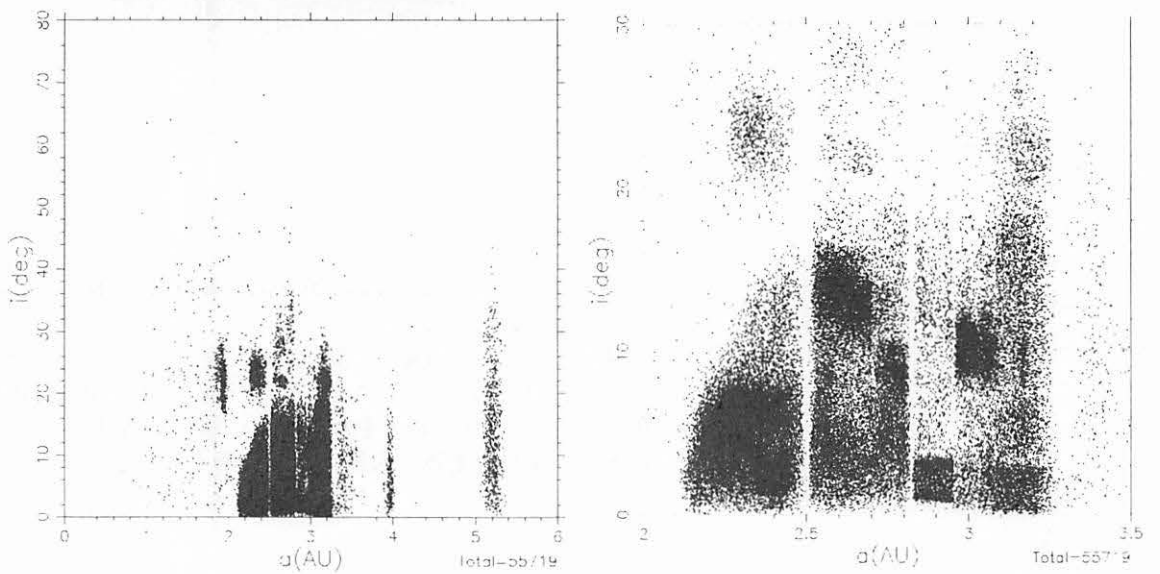

Fig.3 Distribution of orbital elements of asteroids in a-i plane.
a-i 平面上での小惑星の分布。（右の図は、左の図の部分の拡大）

さて、Fig.2 や Fig.3 でも平均運動共鳴による影響を見て取ることができるが、平均運動共鳴をよりはっきり見るためには、単に小惑星の軌道長半径の分布を見ればよい。これは、小惑星の公転周期が軌道長半径によって決まるためである。Fig.4 に軌道長半径の分布を示す。この図には、木星との平均共鳴の位置も描かれているが、小惑星帯では、平均共鳴の位置が分布のギャップや小惑星帯の両端に対応していることが分かる。また、小惑星帯の外側（木星側）では、平均運動共鳴の位置に小惑星が集まっていることがわかる。これらがすでに述べたカークウッドギャップや群である。

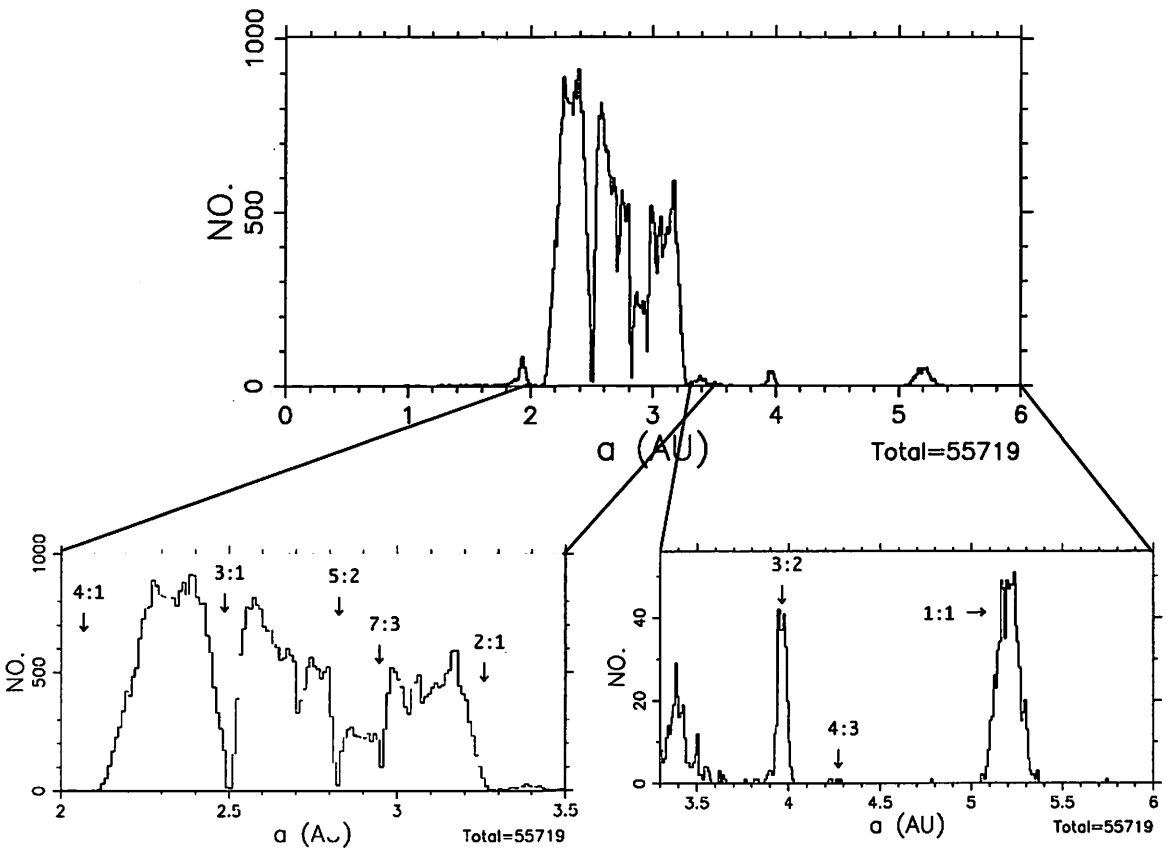

Fig.4 Distribution of semimajor axis of the numbered asteroids.
確定番号が付いた小惑星の軌道長半径の分布。下の図は上の図の部分の拡大。
また、図中の比の値は、小惑星と木星の平均運動の比。

なお、群については、群に属している小惑星だけの位置をプロットしてみても面白い。Fig.5 には、3:2 共鳴のヒルダ群と 1:1 共鳴のトロヤ群の分布を示す。これらの図は Fig.1 の上の図でこれらの群だけを選び出してプロットしたものである。ただし、ここでは、単純に軌道長半径の範囲を指定して選び出しただけであるので、厳密な意味での平均運動共鳴とはなっていない天体も含まれてしまっている可能性はある。ここでは、詳細は述べないが、共鳴状態にあるかどうかは、２つの天体の軌道によって定義されるある角度の振る舞いによって定義されるものである。なお、4:3 のチューレ群については、属する小惑星が数個しかないので、ここでは省略する。

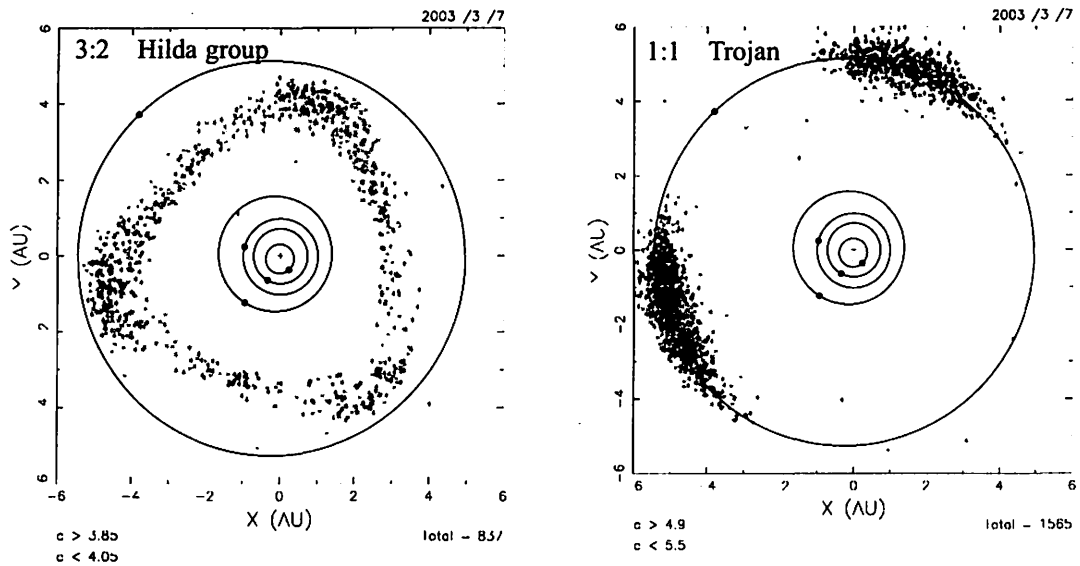

Fig.5 Distribution of Hilda group (left) and Trojan (right).
3:2 平均運動共鳴にあるヒルダ群（左）と 1:1 平均運動共鳴にあるトロヤ群の分布の様子。

さて、Fig.5 にあるヒルダ群の図を見ると、ヒルダ群小惑星が太陽系空間の中で大きな正三角形をつくるように分布していることが分かる。しかも、その正三角形の１つの頂点は、太陽を挟んで木星と正反対の位置にあり、残りの 2 つの頂点は、トロヤ群の位置にある。別の見方をすれば、ヒルダ群の小惑星の分布は木星本体が存在する場所からはなるべく離れるような分布になっていることになる。木星が公転していっても、木星に対するこの正三角形状分布の相対的な向きは変わらない。もちろん、１つ１つのヒルダ群小惑星は、この正三角形状の中を木星に対して動いていく。つまり、ヒルダ群小惑星は、木星軌道にかなり接近する場所があるが、木星本体には接近しないことになっているのである。このために、安定して存在していると考えられる。

トロヤ群については、すでに述べたように、木星の前後それぞれに一群の小惑星として分布している。この分布は、木星と太陽を一辺とする正三角形の頂点を中心にしている。これは、三体問題のラグランジュの正三角形解に対応したものである。トロヤ群小惑星は、木星と 1:1 の平均運動共鳴にあるので、単純に言えば、木星の前後にあるそれぞれの群は、木星が公転していくのに合わせて動いていくことになる。したがって、木星軌道上にあるが木星本体に接近することはなく、安定に存在できるのである。

4:3 共鳴にあるチューレついても、同様なことが言え、木星との接近をうまく回避することで、安定に存在している。ところが、4:3 にあるドン・キホーテという小惑星はその離心率が大きいため、安定している軌道とは言えない。もしかすると一時的に 4:3 共鳴にあるのかもしれない。

試みにこれら 3:2、4:3、1:1 共鳴にある小惑星を省いて Fig.1 に相当する図を作成してみたものが Fig.6 である（実際は、単純に軌道長半径が 3.85AU 以下のものに限ってプロットしたものである)。この図を見ると明らかのように、小惑星の分布は木星軌道から一様な距離だけ離れたところにきれいに分布していることが分かる。木星と平均運動共鳴のような特別な関係にないと、木星軌道のそばにまで達するような軌道に小惑星は安定に存在できないのである。

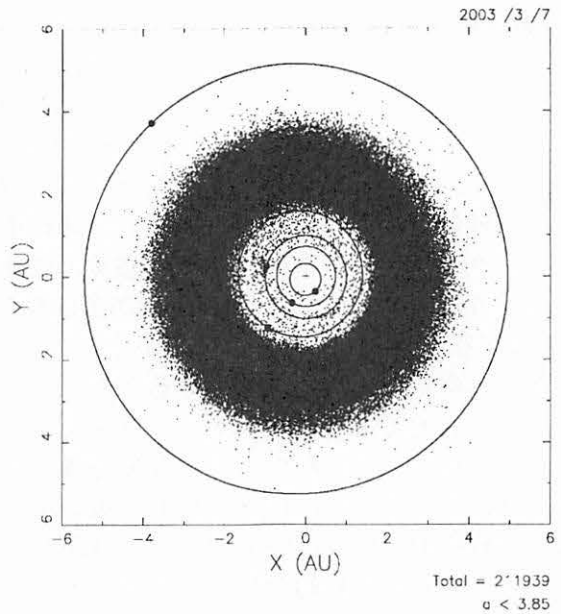

Fig.6 Distribution of asteroids with a <3.85.
ヒルダ群とトロヤ群を省いてプロットした小惑星の分布。
（実際には、単純に a<3.85AU という条件でプロットした。）

4．平均運動共鳴にある小惑星の軌道進化

小惑星は、惑星の摂動を受けながら太陽の周りを公転している。惑星の軌道進化を考える場合には、相互に引きあう効果を考慮する必要があるが、小惑星の場合には惑星（や太陽）からの引力を考慮するだけで、小惑星が惑星の運動に及ぼす影響は無視するのが一般的である。また、小惑星に働く力としては、万有引力以外に太陽光による圧力や輻射の影響がある。最近の研究では、長期的な軌道進化を考える場合には、これらの効果が重要であるということになってきている。ただし、ここでは万有引力のみを考慮することにする。

ほとんどの小惑星は共鳴状態にはなく、その軌道は惑星の摂動を受けて変化するものの、その変化の量は小さいのが一般的である。また、ある程度長期的に見れば、a、e、iの変化は周期的であり、平均すればほぼ同じ軌道にあると言ってよい。

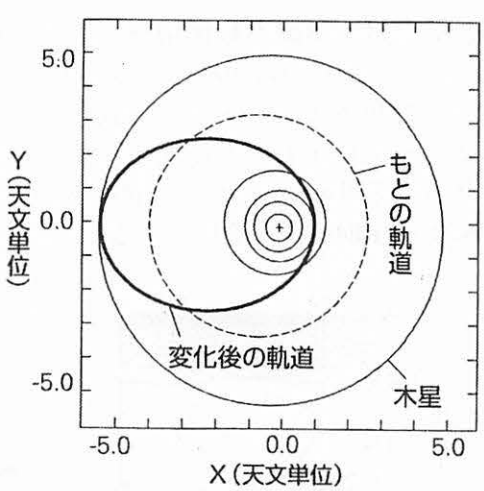

Fig.7 Typical orbital evolution of mean motion resonant asteroids.
平均運動共鳴にある小惑星の典型的な軌道進化。この図では、2:1 の平均運動共鳴にあった小惑星の軌道が大きく変化する様子が示されている。

ところが、共鳴状態にあると軌道進化の様相が大きく変わる場合がある。実際には、共鳴状態にある小惑星の軌道進化は複雑であり、共鳴の種類によっても異なるし、同じ共鳴でも初期条件によって異なる。しかし、共鳴にある小惑星について、最も典型的な軌道進化を挙

げるとすれば、その軌道離心率が大きく変化するということである。その様子を示したものが Fig.7 である。Fig.7 は、木星と 2:1 の平均運動共鳴にあると仮定された小惑星について実際に軌道計算で求められた軌道の変化を示したものである。この図で「もとの軌道」と書かれた軌道が初期の軌道で、計算を進めていくと、「変化後の軌道」とかかれた軌道にまで軌道が変わってしまうのである。この変化のタイムスケールは、数万年程度である。このケースでは、軌道が小惑星帯の外側近くにあった小惑星が、地球軌道付近にまで入り込むような軌道に変化している。つまり、これは、小惑星帯の小惑星が地球に衝突する可能性があることを意味している。このように、共鳴にあると、軌道の離心率や傾斜角が大きく変化することがある。ただし、軌道長半径は短周期で変動はするがその平均値は一定に保たれる。

このような共鳴状態にある小惑星の軌道進化を調べるときには、最近ではコンピュータによって数値積分を行うことが一般的である。コンピュータを使えば、いろいろな条件の計算が行えるからである。しかし、数値積分は解の大局的な振る舞いを知るのにはあまり適していない。解の大局的な振る舞いを知るためには、解析的な扱いができるのが好ましいのであるが、共鳴に関する場合には解析的な取り扱いも難しい場合がある。そこで、本来ならば解析的に式を展開していくべきところを数値的な平均化に置き換えて解の振る舞いを検討するやり方がある。これを半解析的方法と呼ぶこともある。

この半解析的な手法の一例を Fig.8（左端）に示す。これはヒルダ群（木星と 3:2 の平均共鳴）について、その軌道離心率の変化のし方を$\tilde{\omega}-\tilde{\omega}_J$の関数として表したものである。ここで$\tilde{\omega}$（パイと呼ぶ）は近日点経度であるが、その定義は、$\omega+\Omega$である。また、$\tilde{\omega}_J$は木星の近日点経度である。つまり、$\tilde{\omega}-\tilde{\omega}_J$は木星の近日点経度から計った小惑星の近日点経度である。この場合の半解析的モデルは、$\tilde{\omega}-\tilde{\omega}_J$と離心率の平面内で、これらの値が変化する様子を曲線として描いたことになる。つまり、変化のタイムスケールは分からないものの変化の仕方は分かるのである。

Fig.8 には、実際の数値積分で求められた軌道の例も示されている。離心率が小さい場合には、$\tilde{\omega}-\tilde{\omega}_J$が 0 から 360 度まで変化し、その値に応じて離心率が変化する様子が分かるが、これは半解析的モデルとよく一致している。また、離心率が大きい場合には$\tilde{\omega}-\tilde{\omega}_J$ が 180 度の周りを周回することになるが、その様子も数値結果と半解析的モデルで大体一致している（周回する中心がちょっと異なるが）。このように、半解析的モデルは、軌道変化の様子を理解する手助けになるのである。

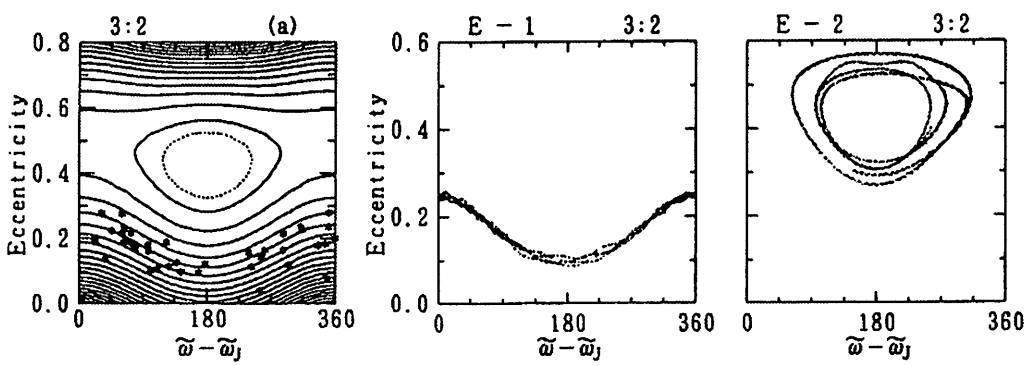

Fig.8 Orbit analysis for 3:2 mean motion resonance : Hilda group.

3:2 の平均運動共鳴にあるヒルダ群についての軌道解析。左端の図が半解析的モデルによる結果で、3:2 共鳴にある小惑星の離心率の変化の様子が分かる。実際に数値積分で求めた例が中央と右端の図で、半解析的モデルと比較的よく一致している。なお、左端の図には、実際のヒルダ群の軌道要素もプロットされている。（文献[2]より）

Fig.8 の半解析的モデルの図には、実際のヒルダ群の軌道要素もプロットされている。この図で、実際に存在するヒルダ群は、中央部分の離心率が大きくなる領域は避けて分布していることが分かる。3:2 の平均運動共鳴においては、離心率が大きく変化することになる場合とあまり変化しない場合とがあるが、実際に存在するヒルダ群は離心率があまり変化しない部分に存在しているのである。

同様な解析は、他の共鳴についても行うことができる。もう 1 例として、カークウッドギャップに相当する 5:2 平均運動共鳴の場合を示すと、半解析的モデルが Fig.9、それに対応した数値計算例が Fig.10 のようになる。数値積分で得られた軌道要素のパターンは、半解析的モデルで得られている曲線と似通っていることが分かる。また、この 5:2 平均運動共鳴の例では、小惑星の軌道離心率が 0.2 以下と小さかったとしても、急激に離心率が大きくなって 0.8 近くにまで増大することもあることを示している。

このような急激な離心率の増加が起こりうることを最初に示したのは、Wisdom[3]である。彼が数値計算で示した例を Fig.11 に示す。これは、3:1 の平均運動共鳴にある小惑星についての計算例で、最初のうちは軌道離心率が小さくてほぼ円に近い軌道であったが、突然、離心率が 0.35 くらいまで増大することが分かる。この計算結果は、カオスとも関連してその後、非常に多くの研究がなされるきっかけとなった。

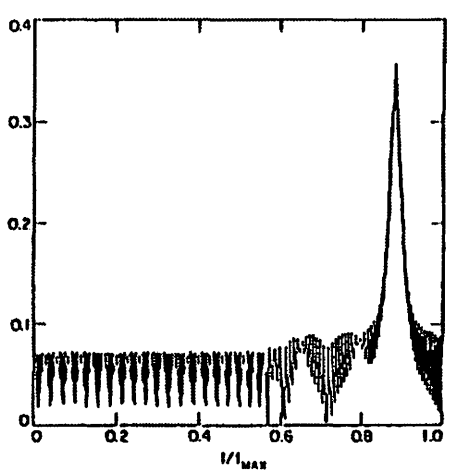

Fig.11 Eccentricity jump shown by Wisdom.
3:1 の平均運動共鳴にある小惑星が示した急な離心率の増加。J.Wisdom による。縦軸は離心率で横軸は時間を示す。横軸の最大値 1.0 は、約 250,000 年に相当する。(文献[3]より)

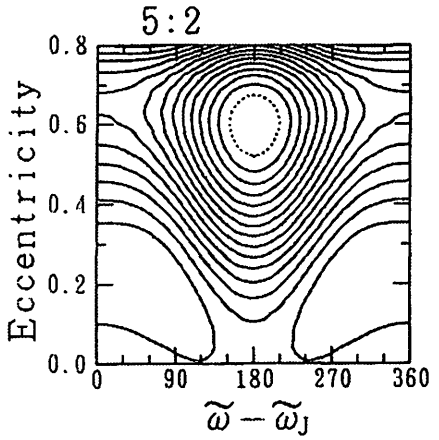

Fig.9 Semi-analytical model for the 5:2 mean motion resonance.
5:2 平均運動共鳴にある小惑星についての半解析的モデルの一例。(文献[2]より)

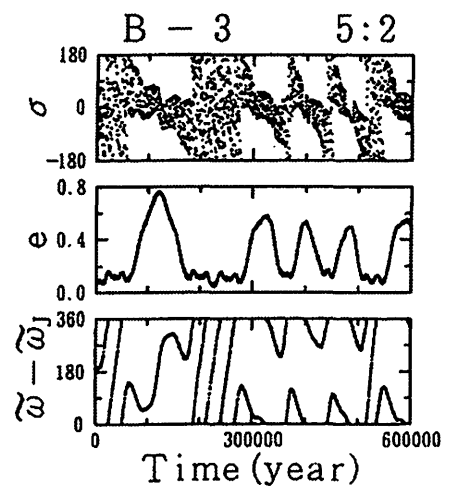

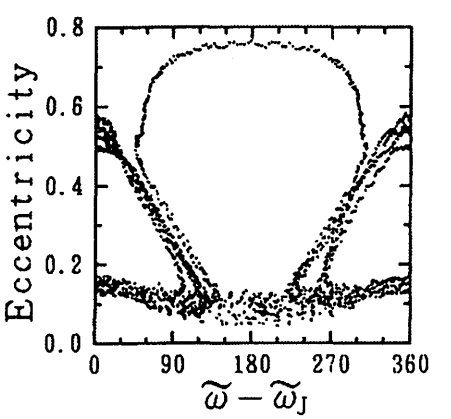

Fig.10 Orbital evolution of an asteroid in the 5:2 mean motion resonance by numerical integration.
5:2 平均運動共鳴にある小惑星について数値積分で求めた軌道進化の例。(文献[2]より)

ここでは、主に小惑星について述べてきた。それは、小惑星の場合にはその数が多いので、いろいろな共鳴の可能性があることと、共鳴の影響が分布等にはっきりと見えるためである。また、小惑星の場合には、共鳴状態が長く続く場合が多く、共鳴の効果が現れやすい。これに対して、似たような小天体である彗星では、一時的に共鳴状態に入ることはよくあるのだが、それが長続きすることは少ない。それは、彗星の場合には惑星に接近しやすいためである。惑星と接近すると、共鳴条件が崩れてしまうのである。一時的に共鳴状態になった例をFig. 12に示す。この例では、1000 年間ほど木星と 2:1 の平均運動共鳴にあったことになる。

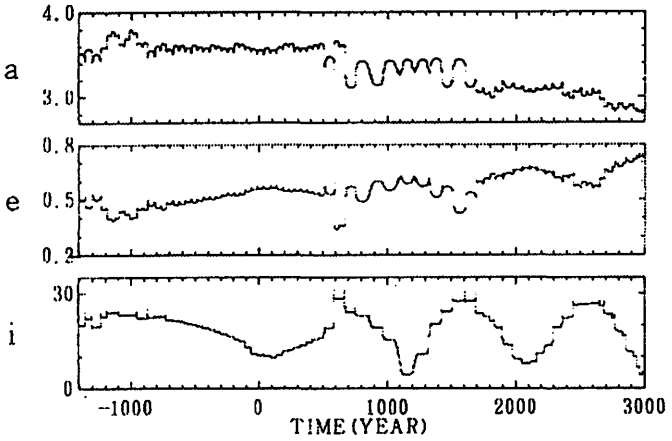

Fig.12 Example of temporal resonance shown by comet P/Tuttle-Giacobini-Kresak.
一時的に平均運動共鳴に捕らえられた例。タットル・ジャコビニ・クレサック彗星が西暦 1000 年前後で木星と 2:1 の平均運動に捕らえられている。横軸は西暦の年。(文献[4]より)

彗星と似たケースとしては、流星物質がある。流星物質についても、一時的には惑星と平均運動共鳴に入ることがあるが、惑星への接近や、太陽輻射圧などの影響によって共鳴状態から抜け出してしまう。

最後に、ここでは具体的には触れることができなかったが、衛星同士の平均運動共鳴や海王星と冥王星の 3:2 の平均運動共鳴がある。これらについては、共鳴状態にあることによって、系が安定に保たれているものと考えられる。実際、たとえば冥王星と海王星については長期的な数値積分がなされているが、平均してみるとそれらの軌道は現在のものから大きくずれることはない。

5．まとめ

太陽系には、多種多様な共鳴現象がある。それらが、太陽系の秩序を作ったり、太陽系天体の軌道進化に深くかかわったりしているのである。ここでは、共鳴についてほんの初歩的な一端を紹介したに過ぎない。是非、最近の成果[5]などを参考にして、共鳴の奥深さというものを知って欲しい。筆者自身も共鳴というものを改めて勉強し直してみようと考えている。

参考文献

[1]堀源一郎：太陽系 －その力学的秩序－、岩波新書、1976 年

[2]M.Yoshikawa: A survey of the motions of asteroids in the commensurabilities with Jupiter, *Astron. Astrophys.* **213**, 436-458 (1989).

[3]J.Wisdom: Chaotic Behavior and the Origin of the 3/1 Kirkwood Gap, *ICARUS* **56**, 51-74 (1983).

[4]T.Nakamura and M.Yoshikawa: COSMO-DICE: Dynamical investigation of cometary evolution, *Publ. Matl. Asron. Obs. Japan* **Vol.2**, 293-383 (1991).

[5]D.Nesvorny, S.Ferraz-Mello, M.Holman, and A.Morbidelli: Regular and Chaotic Dynamics in the Mean-Motion Resonances: Implications for the Structure and Evolution of Asteroid Belt, in *ASTEROIDS III*, The university of Arizona Press, 379-394 (2002).

Visualization of Lindblad and Corotation Resonance

Takaaki Takeda (takedatk@cc.nao.ac.jp)
National Astronomical Observatory, Mitaka, Tokyo 181-8588, Japan

We had made various animations about the orbital resonance phenomena. They are dedicated to visualize the perturbation potential and geometrical relationship between two bodies in orbital resonance. These animations are available at `http://th.nao.ac.jp/~kokubo/nbody2003/LindbladResonance/LindbladResonance_index_e.html` .

1. Introduction

The picture is worth a thousand words. Sometimes, images are very useful to comprehend physical or mathematical concepts, especially for young students. For dynamical phenomena, animations are often much better than motionless images.

Last year, we had made several animations about celestial mechanics, especially about orbital resonances. These animations visualize perturbation potential and geometrical relationship between the perturber and the perturbed bodies in resonance. Since the main theme of this symposium is the resonance phenomena, we made a presentation using these animations with educational purposes. This article is a summary of the presentation. All figures used in this article are snapshots of these animations. We recommend the readers to refer original animations rather than these motionless figures if possible. Full animations are available at `http://th.nao.ac.jp/~kokubo/nbody2003/LindbladResonance/LindbladResonance_index_e.html`.

2. Visualization of perturbing potential

We consider a system of two small objects m and m' which rotate around a central body in Keplerian motion. For simplicity we consider a coplanar case. We regards m' as a perturber, and assume that the perturber m' has only small eccentricity.

The perturbation potential is

$$\Psi(\mathbf{r}) = -\frac{Gm'}{|\mathbf{r}-\mathbf{r}'|} - Gm'\frac{\mathbf{r}\cdot\mathbf{r}'}{r'^3} \tag{1}$$

The leading term is the direct term, and the another term is the indirect term.

We use polar vector $\mathbf{r} = \mathbf{r}(r, \theta)$. We denote longitude of pericenter and mean longitude as λ and ϖ respectively. If $e = e' = 0$, location of the bodies are simply $\mathbf{r} = \mathbf{r}(r, \lambda)$ and $\mathbf{r}' = \mathbf{r}'(r', \lambda')$. In this case, the perturbation potential depends on r and $\lambda - \lambda'$ only. Expanding $\Psi(r, \lambda)$ in Fourier series,

$$\Psi = \sum_{m=0}^{\infty} \psi_m(r) \cos[m(\lambda - \lambda')]. \tag{2}$$

In Fig. 1, we show first two components, $\psi_1 \cos(\lambda - \lambda')$ and $\psi_2 \cos[2(\lambda - \lambda')]$, for example. The large white dot at the center is the central body. The potential between $0.3r'$ to $1.5r'$ is displayed in the figures. White implies that the potential is negative.

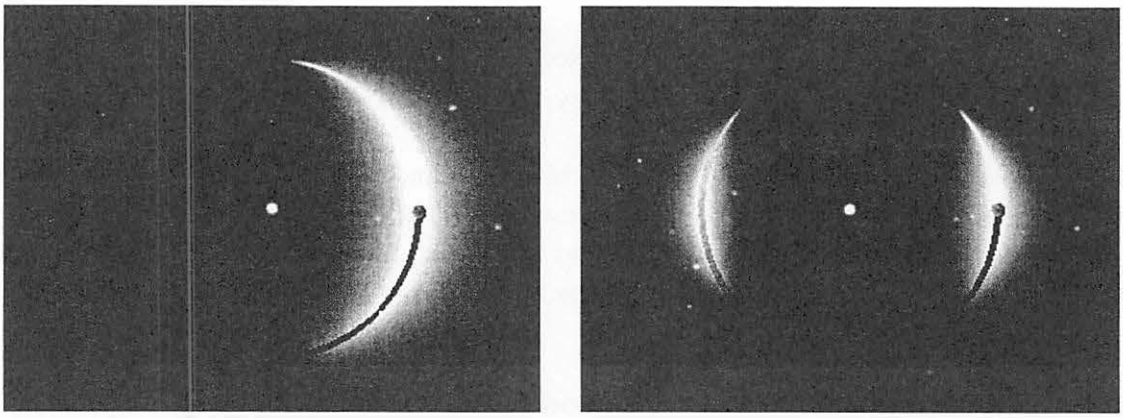

Fig. 1.— $m = 1$ and $m = 2$ component of perturbing potential. Black circle is the orbit of the perturber.

(red in original animations). The color strength expresses the depth of the potential. Where the potential is positive, we paint there black (green in original animations). The perturber is at the right side of the central body, and its orbit is drawn by black line (blue line in original animations). Note that m-th component has m nodes.

The superposition of every components from $m = 0$ to infinity approaches to the true potential Ψ, of course. Fig. 2 demonstrates that. It displayed the superposition of components $m = 1$, $m = 2$, and $m = 3$ (left panel), and the summation up to $m = 6$ (right panel). Since $m = 0$ component is everywhere negative, we excluded it for convenience of visualization.

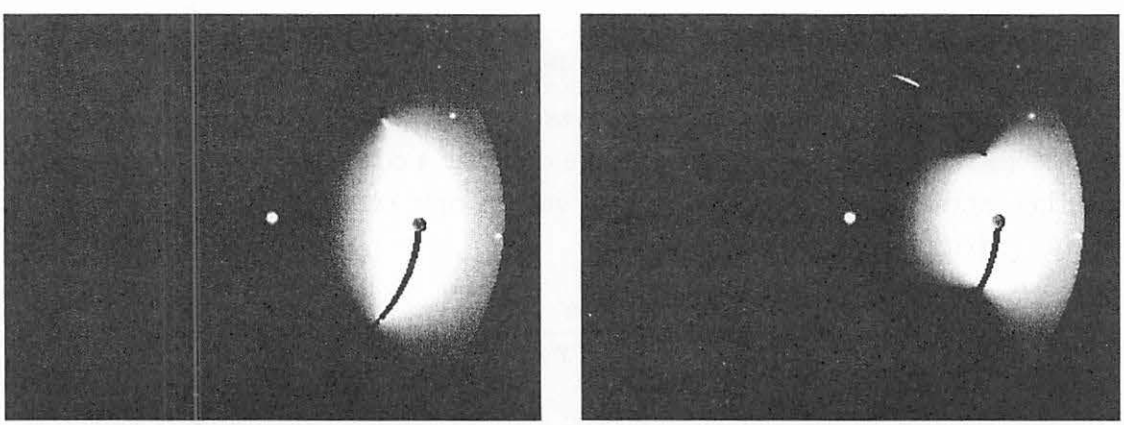

Fig. 2.— Left panel shows the superposition of components $m = 1$, $m = 2$, and $m = 3$, while right panel shows the superposition of components from $m = 1$ to $m = 6$.

When $e' = 0$, all components of perturbation potential rotate with the perturber, i.e., all components have pattern speeds $\Omega_{\rm p} = \Omega'$. However, if the perturber has eccentricity, it moves faster than the mean motion near the pericenter, while it moves slower near the apocenter. Thus, perturbation potential is no longer the superposition of the components with pattern speed $\Omega_{\rm p} = \Omega'$. This implies that the perturbation potential can no longer be expressed by $\lambda - \lambda'$ only. The information about the phase of epicycle motion $\lambda' - \varpi'$ is indispensable. Thus, the perturbation potential is expressed as,

$$\Psi = \sum_{m=0}^{\infty} \sum_{l=-\infty}^{\infty} \psi_{l,m}(r) \cos(m(\lambda - \lambda') + (m-l)(\lambda' - \varpi')) \tag{3}$$

See textbooks of celestial mechanics, such as Brouwer and Clemence (1961) or Murray and Dermott (1999), for the specific forms of $\psi_{l,m}(r)$. For example, we show $m = 2$, $(m - l) = \pm 1$ components in Fig. 3. In calculation for $\psi_{l,m}(r)$ here, we assumed that the orbits of the perturber and the perturbed body do not cross, so that it can not be applied in the region $r'(1 - e') < r < r'(1 + e')$.

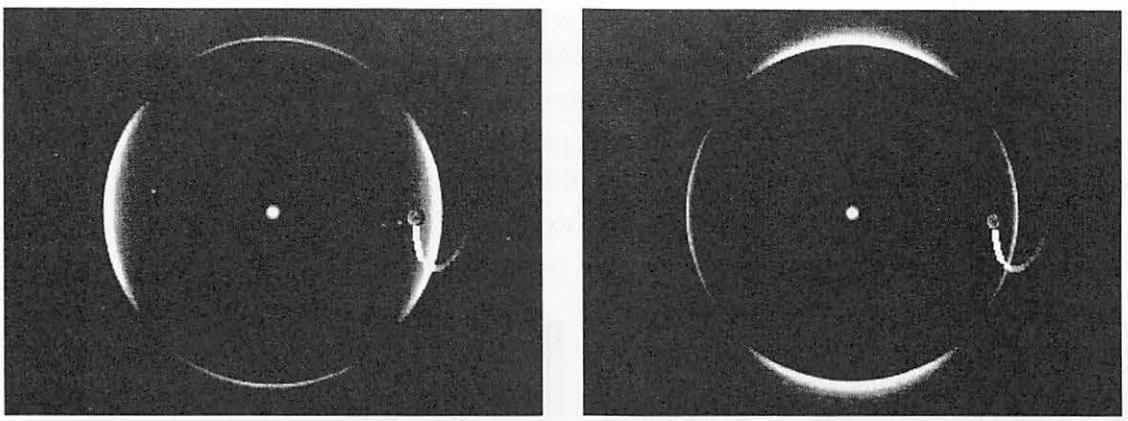

Fig. 3.— Left panel : $m = 2$, $m - l = -1$. Right panel : $m = 2$, $m - l = 1$. The lines are the orbit of the perturber in a frame which rotates with Ω'

In Fig. 3, the perturber is at the pericenter ($\lambda' = \varpi'$). As the time proceeds, the phase $\lambda' - \varpi'$ increases, while $\lambda - \lambda'$ is simply the angle between the two position vector of the (guiding center of) two bodies. Thus, the component $(m - l) < 0$ rotates faster than the perturber, while the component $(m - l) > 0$ rotates slower, or to opposite direction (see the animations). The $|m - l| = 1$ components shift their phases 2π in a time the perturber rotates a single epicycle motion. This implies that the lowest term of $|m-l| = 1$ components are proportional to e'.

Near the pericenter, the perturber moves faster than the mean motion, and it moves slower near the apocenter. It is interesting that the component $(m - l) = -1$, which rotate faster than the perturber, overwhelms the component $(m - l) = +1$ in the region $r < r'$, while the latter overwhelms the former in the region $r > r'$ (see the animations).

The important thing is that the perturbation potential is the superposition of many components which rotate with different pattern speeds. If the orbital or epicyclic frequency of a body coincides with the pattern speed of the perturbation potential, it is in the resonance.

3. Visualization of resonances, and pattern formation

If orbital frequency of the perturbed body coincides with the pattern speed of the perturbation potential ($\Omega = \Omega_p$), it is in the corotation resonance. In the case that $e' = 0$, the perturbation potential rotates with the perturber, so that the corotation resonance exits where $\Omega = \Omega_p = \Omega'$, i.e. semimajor axis $a = a'$. If the perturber has

eccentricity, the perturbation potential is the superposition of components with varied pattern speeds. Thus, corotation resonances exist even if $a \neq a'$.

In a frame which rotates with a body, or exactly speaking, with the guiding center of the body, the rotation speed of the perturbation potential is $\Omega_{\rm p} - \Omega$. Thus, the force the body feels has the frequency $m(\Omega_{\rm p} - \Omega)$. If the epicyclic frequency of the body κ coincides with the frequency of perturbing force, it is in the Lindblad resonance. The condition for the resonance is

$$m(\Omega_{\rm p} - \Omega) = \pm\kappa. \tag{4}$$

Note that $\kappa = \Omega$ in the case of Keplerian motion. If the perturbed body has eccentricity $e \neq 0$, its position can no longer be expressed as $\mathbf{r}(r, \lambda)$, which only represents the location of the guiding center. Thus, full disturbing function must be introduced for full description of the Lindblad resonance. However, our purpose here is to grasp the basic concept of resonance, we continue to use the perturbation potential.

As shown in eq. (4), there exist two Lindblad resonance for a single component of perturbation potential. Fig. 4. shows the example of two resonances, i.e., inner and outer Lindblad resonances. The perturbation potentials in the figure are $\psi_2 \cos[2(\lambda - \lambda')]$.

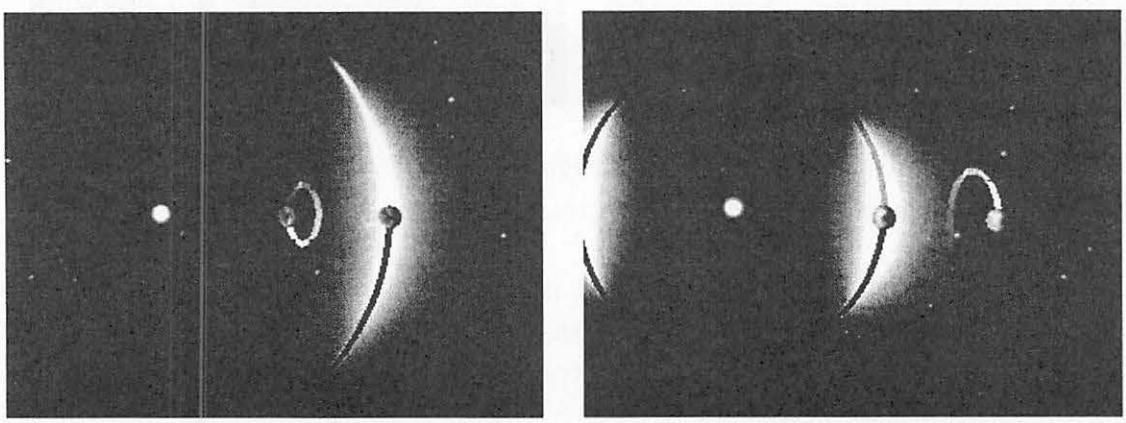

Fig. 4.— Left panel shows the inner Lindblad resonance, and right panel shows the outer Lindblad resonance.

Left panel shows the example of inner Lindblad resonance. The body and the perturber is in 2:1 commensurability. Consider that a body and a perturber are in conjunction at some time. In a time step of one orbital period of the body, the perturber moves to the opposite side of the body. However, since the perturbation potential is 2-fold, the body feels the same potential in the next cycle of epicyclic motion. In a frame rotating with the body, the perturbation potential rotates 180 deg in one epicyclic period (see the animation). Right panel shows an example of outer Lindblad resonance. The body and the perturber are in 2:3 commensurability. In a time step of one orbital period of the body, the perturber circulates the orbit 1.5 times. Thus, the perturber moves to the opposite side, and the body feels the same potential in the next cycle of epicyclic motion. In a frame rotating with the body, the perturbation potential rotates in opposite direction (see the animation).

Lindblad resonance is closely-related to the pattern formation in disk or ring system. The fact that the period of epicyclic motion coincides with the period of the perturbation potential leads to that in a frame rotating with the perturbation potential, the orbit of

the perturbed object closes. Fig. 5 is an example of such closed orbit in a frame rotating with Ω_p. Left panel shows the closed orbits of the bodies in inner and outer Lindblad resonances for $m = 2, (m - l) = 0$ component, and right panel shows the closed orbits for $m = 4, (m - l) = 0$ component.

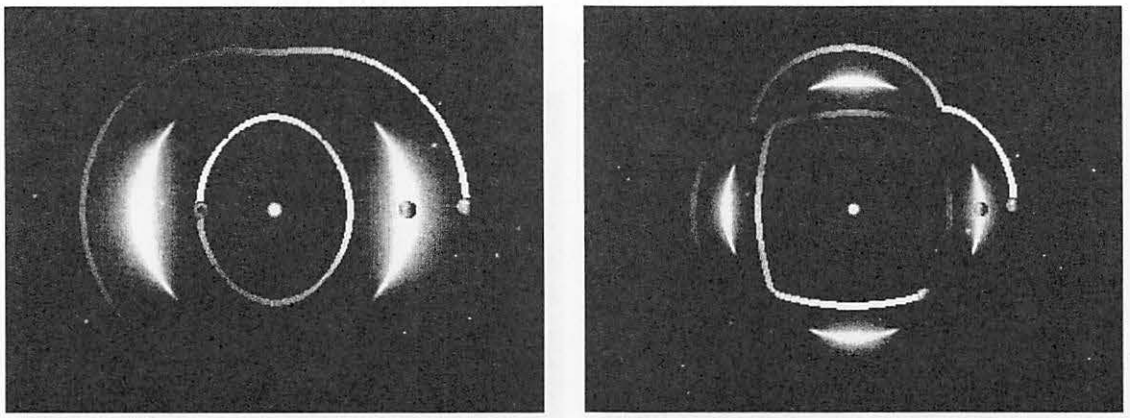

Fig. 5.— Examples of orbits which close in a frame rotates with pattern speed. Left panel shows m=2 orbits, and right panel shows m=4 orbits.

If many particles exist in a closed orbit, they form m-fold stream line. In Fig. 6, we show a ring of which all particles are on a $m = 2$ stream line. Of course, individual particles simply move on their own elliptic Kepler orbits in an inertial frame. However, the pattern rotates with the pattern speed Ω_p as a whole (see the animation). The right panel shows an example of pattern formation in numerical N-body simulation. The disk edge is truncated by a large satellite at 2:1 resonance. The form of the disk edge is elongated to an ellipse of $m = 2$ mode. This figure is formed using data of N-body simulation about the Moon accretion process from an impact generated debris disk (e.g. Ida et. al. 1997), based on the giant impact hypothesis (Cameron and Ward 1976, Hartmann and Davis 1975).

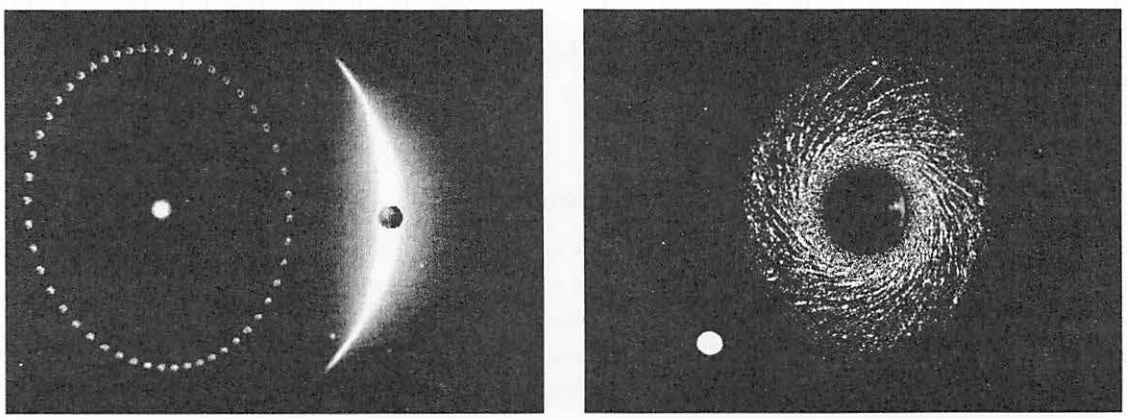

Fig. 6.— Left panel: stream line of $m = 2$ mode. Right panel: an example of pattern formation in numerical N-body simulation.

Orbital resonance phenomenon is also related to the spiral density wave. In a Keplerian disk, the width of region at which the condition $m(\Omega_p - \Omega) \sim \pm\kappa$ is satisfied is relatively narrow. However, rotation curve of a galaxy is not a Keplerian one. In a disk galaxy,

$\Omega - \kappa/2$ is relatively constant across much of the galaxy. Consider the case that $m(\Omega_{\rm p} - \Omega) \sim -\kappa$ is satisfied in relatively wide range of r, and $m = 2$ pattern is formed there. Setting up an aligned set of these stream lines, spiral patterns can be formed. (Fig.7, left panel). In the right panel, we distribute particles randomly along the streamlines. We can see density pattern of $m = 2$ mode. Density waves of this type are called kinematic density waves.

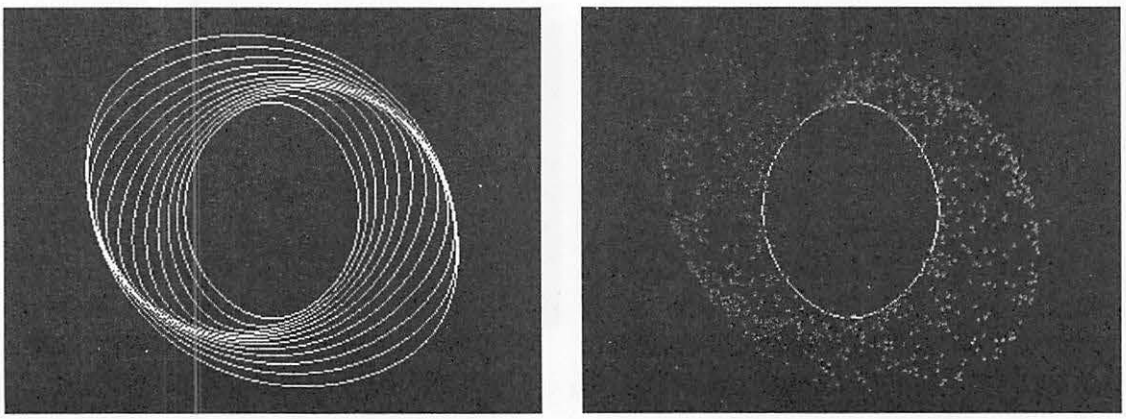

Fig. 7.— The formation of $m = 2$ spiral density pattern.

4. Summary

We made several animations about orbital resonance phenomena with an educational purpose. They are mainly dedicated to geometrical configures of resonances. As for the detailed dynamics of particles in resonances, see the textbooks such as Binney and Tremaine (1987) or Murray and Dermott (1999). Here, we have visualised following phenomena. 1) The perturbation potentials is the superposition of potentials with different pattern speeds. 2) If the orbital or epicyclic frequencies of the perturbed body coincide the pattern speed, the body is in resonance. 3) These resonance phenomena is closely related to the pattern formation mechanism. The animations for this presentation are available at a www site shown above.

References

Brouwer, D. and G. M. Cremence, 1961, *Methods of Celestial Mechanics* Academic Press, New York.

Cameron, A.G. and Ward W.R., 1976, The origin of the Moon. *Lunar Sci. Abs.* **7**, 120

Binney, J. and S. Tremaine, 1987, *Galactic Dynamics.* Princeton Univ. Press, Princeton.

Hartmann, W.K. and Davis, D.R. 1075, Satellite-sized planetesimals and lunar Origin *Icarus* **24**, 504.

Ida, S., Canup, R. M., and Stewart, G. R. 1997, Lunar Accretion from an impact-generated disk. *nat* **389**, 353.

Murray, C.D. and S.F. Dermott, 1999, *Solar System Dynamics.* Cambridge Univ. Press, Cambridge.

A Note on Secular Resonances

Hiroshi Kinoshita
National Astronomical Observatory
2-21-1 Osawa, Mitaka, Tokyo, Japan
e-mail: Kinoshita@nao.ac.jp

Abstract

The secular resonance (1:1 secular resonance), in which one eigen frequency of the dynamical system is equal to the other eigen frequency, does not take place in the mutually perturbed system such as a planetary system with finite mass. Secular resonances, in which angular variables with more than three are involved, might occur.

The 1:1 secular resonance takes place only in a restricted problem, in which the massless body is perturbed by the bodies whose motions are given of time.

The alignment of the pericenters of the planets, which is found in an extrasolar planetary system, is not a secular resonance. The alignment comes from the fact that the amplitude of one eigen frequency is larger than the sum of the amplitudes of other eigen frequencies.

1 introduction

A resonance arises when the mean motion of the linear combination of angle variables of the system $\theta = \sum_{i=1}^{n} j_i \theta_i$ becomes zero:

$$\frac{d\theta}{dt} = \sum_{i=1}^{n} j_i \frac{d\theta_i}{dt}. \tag{1}$$

From d'Alembert characteristic the summation of the coefficients of (1) is zero:

$$\sum_{i}^{n} j_i = 0, \tag{2}$$

When the angle θ includes the mean longitudes, the resonance is called as a motion resonance. When the angle θ does not includes the mean longitudes and consists of the longitudes of the pericenters and the nodes, the resonance is called as a secular resonance. Since the mean motion resonances are discussed by Yoshikawa somewhere in this proceeding, we only discuss the secular resonance and treat separately a mutually perturbed problem and a restricted problem.

2 Mutually Perturbed Problem

Here we discuss a system of planets with finite mass, which disturb each other.

2.1 Linear case

After eliminating the mean longitudes (short periodic terms) and assuming that the eccentricities and the inclinations of the planets are small , we develop the disturbing function to the second degree in the eccentricities and the inclinations. In stead of (e, ϖ) and (I, Ω), we introduce the following variables:

$$\begin{aligned} h &= e\sin\varpi, \quad & k &= e\cos\varpi \\ p &= \sin I\sin\Omega, \quad & q &= \sin I\cos\Omega. \end{aligned} \tag{3}$$

With use of these variables the equations of motion become linear for (h, k) and (p, q) and the motion in the orbital plane and the motion of the orbital plane are decoupled. In other words the motion of (e, ϖ) does not disturb the motion of (I, Ω) and vice versa.

The solution of the secular perturbation for a planetary system takes the following form (Brouwer and Clemence, 1961: Chapter 16):

$$e_i\sin\varpi_i = \sum_{j=1}^{n} M_{ij}\sin\theta_j, \tag{4}$$

$$e_i\cos\varpi_i = \sum_{j=1}^{n} M_{ij}\cos\theta_j, \tag{5}$$

where $\theta_j = g_j t + \beta_j$. In the above expressions g_j are the eigen frequencies, which are obtained from the following secular determinant:

$$|A - gU| = 0, \tag{6}$$

where A is a matrix of $n \times n$, of whose element A_{ij} is a function of only the semi-major axes and masses of n planets, the matrix A is symmetric, and U is a unit matrix.

The coefficients M_{ij} is a function of the initial values of e and ϖ and eigen vectors for (6). Here we implicitly assume that the secular determinant (6) does not have equal roots. The nonexistence of multiple roots has not been ascertained except for $n = 2$ and $n = 3$. The nonexistence for multiple roots for $n = 2$ is easily proved from non-zero of the determinant of the second-order equation derived from (6). Seeliger (1879) proved the nonexistence for equal roots for the case of $n = 3$. Darboux (1888) showed that there may be equal roots for the case of $n = 4$. Even though from the limited numerical experiment, I believe that the matrix A does not have equal roots.

When the secular determinant (6) has r-multiple roots ($r \geq 2$), in general the solution (4) and (5) has the mixed secular term, t^{r-1}. However, according to the theory of linear differential equations with constant coefficients (for example: Coddington and Levinson, 1955), when the matrix A in the secular determinant (6) is symmetric, the solution (4) and (5) does not have the mixed secular terms.

When a planetary system is composed of planets with large mass and planets with small mass and two eigen frequencies are close, the amplitude of the small planets corresponding to these eigen frequencies becomes large. For a planetary system which is composed of planets with same order mass, the enhancement of the amplitudes due to the closeness of two eigen frequencies is not large (Kinoshita 2001).

2.2 Alignment of Pericenters

The pericenters of outer two planets of υ Andromedae planetary system is corotating, which makes υ Andromedae planetary system stable. If this alignment is destroyed, the planetary system becomes unstable. This alignment of the pericenters are frequently called a secular resonance in the literature. Assuming that the eccentricities are small, we apply the linear secular perturbation theory to this system. As mentioned in Section 2.1 the secular determinant does not have equal roots for $n = 2$. We find for υ Andromedae planetary system

$$|M_{11}| = 0.1928 > |M_{12}| = 0.0955, |M_{21}| = 0.4404 > |M_{22}| = 0.0078 \tag{7}$$

(Kinoshita and Nakai, 2000). The first inequality in the above shows the amplitude for the eigen frequency g_1 is larger than that for g_2, which means that the longitude of the pericenter of the inner planet circulates with the mean motion g_1:

$$\varpi_1 = g_1 t + (periodic). \tag{8}$$

The second inequality (7) indicates also

$$\varpi_2 = g_1 t + (periodic). \tag{9}$$

The pericenters of two planets, therefore, corotates:

$$\varpi_1 - \varpi_2 = (periodic) \tag{10}$$

From this analysis, it is not appropriate to call this alignment of the pericenters a secular resonance.

The above discussions is easily extended to the alignment of r planets of a planetary system composed of n planets ($r \leq n$). If one of the amplitudes corresponding to eigen frequency g_1 is dominant such as

$$|M_{i1}| > \sum_{j=2}^{n} |M_{ij}| (i = 1, 2, ..., r), \tag{11}$$

the pericenters of r planets are in alignment.

The corotation or the alignment of the pericenters are found in other extrasolar planetary systems: such as GJ876 (Kinoshita and Nakai 2001,2002), HD82943 (Ji et al. 2003a, 2003b). Since the eccentricities of the planetary systems are large, the linear treatment up to the second degree in the eccentricities is not enough for the quantitative discussions. The numerical averaging method for the non-linear case, however, is very useful to know the global behavior, whose method is mentioned in Section 3.1.

2.3 Nonlinear case

As mentioned in Section 1.1, 1:1 secular resonance due to the fact that one eigen frequency of the system is equal to the other eigen frequency does not take place for the mutually perturbed system. Secular resonances other than 1:1 secular resonance might occur by taking into account higher degree in the eccentricities and the inclinations and in this case angular variables, whose number is more than three, are involved. Here we show one example from the motion of Pluto (Kinoshita and Nakai 1995,1996) The argument $\theta = \varpi_P - \varpi_N + 3(\Omega_P - \Omega_N)$ librates around 180° with a period of about 5.7×10^8yr. From the d'Alembert characteristics, the degree of this argument is 8 with respect to the eccentricities and the inclinations and the amplitude of this secular resonance is very small and this term does not give any important role of the stability of the motion of Pluto. Ito and Tanikawa (2002) carried out $\pm 5 \times 10^{10}$yr integration of outer planetary orbits and showed that the above critical argument θ alternates libration and circulation over a 10^{10}yr timescale. This means that the motion of the critical argument is very close to the separatrix region.

3 Restricted Problem

Here we discuss an orbital motion of a massless particle such as asteroids disturbed by planets and a rotational motion disturbed by the orbital motion.

3.1 Orbital Motion

The mathematical treatment of this case is similar to the case of n planets discussed in Section 2.1(Brouwer and Clemence, 1961: Chapter 16). The motion is considered to be the forced oscillation. The solution for (e, ϖ) is given by

$$h = e\sin\varpi = \nu\sin(gt+\beta) + \sum_{j=1}^{n} \frac{\nu_j}{g-g_j}\sin(g_j t + \beta_j), \tag{12}$$

$$k = e\cos\varpi = \nu\cos(gt+\beta) + \sum_{j=1}^{n} \frac{\nu_j}{g-g_j}\cos(g_j t+\beta_j), \tag{13}$$

where g is an eigen frequency for the small body, which depends on the masses of the disturbing planets and the semi-major axis of the small body and planets. When the higher degree terms with respect to e and i are included, g and s (the eigen frequency for (p,q)) do depend on a, e and i. Williams (1969) searched the locations in the asteroidal belt of the three secular resonances $g = g_5, g = g_6$, and $s = s_6$. Knežević (1991) found the locations of secular resonances in the region of $a = 2$ to 50 AU. Morbidelli and Henrard (1991) discussed the locations of secular resonances in the asteroidal belt with use of the Hamiltonian perturbation method. The eigen frequency g is sometimes called as a proper frequency.

When the proper frequency g is equal to one of eigen frequencies, a secular resonance occurs and a mixed secular term appears:

$$h = \nu\sin(gt+\beta) + \sum_{j=1,j\neq k}^{n} \frac{\nu_j}{g-g_j}\sin(g_j t+\beta_j) - \nu_k t\cos(g_k t+\beta_k) \tag{14}$$

$$k = \nu\cos(gt+\beta) + \sum_{j=1,j\neq k}^{n} \frac{\nu_j}{g-g_j}\cos(g_j t+\beta_j) + \nu_k t\sin(g_k t+\beta_k). \tag{15}$$

The last term of (14) and (15) is a mixed secular term, of which amplitude increases with time. We call the appearance of a mixed secular term a secular resonance.

When the higher degree terms with respect to e, I are taken into account, the amplitude does not become infinity and is suppressed at finite size. The analytical treatment becomes difficult since the coupling effect between the eccentricity and the inclination terms should be taken into account. As far as the linear treatment with respect the disturbing mass, we can treat the non-linear treatment with respect to the eccentricity and the inclination with use of the numerical averaging method. Reducing the number of degrees of freedom of the system by averaging numerically the Hamiltonian to one, we can draw the contour map of the Hamiltonian in (e,ϖ) plane or (I,Ω) plane. From this contour map we can know the global feature of the motion. One example for this application is given in the paper by Nakai and Kinoshita (1985), where the large change of the inclination of the Lost City meteorite is discussed. If the square of the disturbing mass is necessary, the problem becomes much more difficult mathematically.

The secular resonance in the restricted problem is reviewed by Scholl et al.(1989). The secular resonances in the region where the mean motion resonances take place are discussed by Morbidelli and Moons (1993) and Moons and Morbidelli (1995)

3.2 Rotational Motion Disturbed by Orbital Motion

A spin of a satellite or a planet can be treated as a restricted problem except Earth-Moon system. Here we assume that the rotational motion does not disturb the orbital motion and is disturbed by the orbital motion.

Using the canonical perturbation method, we get the first order solution of the rotational motion (see Appendix C):

$$\Delta h = \frac{1}{\sin I_s^*} \sum_{j=1}^{7} \frac{N_j s_j (\alpha - s_j \cos I_s^*)}{(s_j - \alpha \cos I_s^*)^2} \sin(s_j t + \delta_j - h^*), \tag{16}$$

$$\Delta I_s = -\sum_{j=1}^{7} \frac{N_j s_j}{s_j - \alpha \cos I_s^*} \cos(s_j t + \delta_j - h^*), \tag{17}$$

where $\alpha \cos I_s^*$ is the precessional rate of the figure axis.

From this equation the secular resonance occurs when the precession of the figure axis is equal to one of the eigen frequencies of the disturbing planets. More detailed discussion is given by Atobe somewhere in this proceedings .

Appendix

A: The Hamiltonian Referred to a Rotating Frame of Reference

This section is quoted from Kinoshita(1993).

Goldreich (1965) obtained the Hamiltonian referred to a moving reference frame from the Lagrangian. Here we give another derivation with use of a generating function of a canonical transformation.

Let $\mathbf{r} = (x, y, z)$ designate the position vector referred to the inertial frame and $\mathbf{r}' = (x', y', z')$ the position vector referred to the rotating frame. The transformation between $\mathbf{r}$ and $\mathbf{r}'$ is expressed with use of an orthogonal matrix A:

$$\mathbf{r}' = A\mathbf{r}, \qquad (A-1)$$

where the matrix depends explicitly on time. We introduce a canonical generating function F_2:

$$F_2 = (\mathbf{p}', A\mathbf{r}), \qquad (A-2)$$

where $\mathbf{p}'$ is the momentum vector conjugate to $\mathbf{r}'$ and the bracket means the inner product of two vectors. The generating function F_2 is also written as

$$F_2 = (\mathbf{r}, A^*\mathbf{p}'), \qquad (A-3)$$

where A^* is the transpose of A. The canonical transformations derived from F_2 are obtained from (A-2) and (A-3),

$$\mathbf{r}' = \frac{\partial F_2}{\partial \mathbf{p}'} = A\mathbf{r}, \qquad (A-1)$$

$$\mathbf{p} = \frac{\partial F_2}{\partial \mathbf{r}} = A^*\mathbf{p}'. \qquad (A-4)$$

Since the inverse of A^* is A itself, we have from (A-4)

$$\mathbf{p}' = A\mathbf{p}, \qquad (A-5)$$

which shows that the momentum vector is also obtained from the same transformation matrix A as the position vector. Since the generating function depends on time explicitly, the new Hamiltonian K referred to the rotating frame is obtained from

$$K = F + \frac{\partial F_2}{\partial t}, \qquad (A-6)$$

where F is the Hamiltonian referred to the inertial frame. Now we have to express the second term of (A-6) only in terms of $\mathbf{r}'$ and $\mathbf{p}'$:

$$\frac{\partial F_2}{\partial t} = (\mathbf{p}', \frac{dA}{dt}\mathbf{r}) = (\mathbf{p}', \dot{A}A^{-1}\mathbf{r}'). \qquad (A-7)$$

The matrix $\dot{A}A^{-1}$ is an anti-symmetric matrix and its independent three components are expressed with use of the rotational vector $\mathbf{R}$ of the rotating frame:

$$\dot{A}A^{-1} = \begin{pmatrix} 0 & R_{z'} & -R_{y'} \\ -R_{z'} & 0 & R_{x'} \\ R_{y'} & -R_{x'} & 0 \end{pmatrix}, \qquad (A-8)$$

where $R_{x'}$ is the component of the rotational vector around the x' axis. The derivation of (A-8) is found in textbooks on classical mechanics (for example Arnold 1974). Using (A-8), we get

$$\dot{A}A^{-1}\mathbf{r}' = -\mathbf{R} \times \mathbf{r}'. \qquad (A-9)$$

Using the relation of the scalar triple product, we have

$$\frac{\partial F_2}{\partial t} = -(\mathbf{p}', \mathbf{R} \times \mathbf{r}') = -(\mathbf{R}, \mathbf{r}' \times \mathbf{p}'), \qquad (A-10)$$

where $\mathbf{r}' \times \mathbf{p}'$ is the momentum vector $\mathbf{G}'$ referred to the rotating frame. Finally we have the Hamiltonian referred to the rotating frame as

$$K = F - (\mathbf{R}, \mathbf{G}') = F + E. \qquad (A-11)$$

Although we consider here a particle system, we can apply the same idea to a system of particles, and have the same form Hamiltonian for a rigid body. The textbook on classical dynamics by Landau and Lifshitz (1960) gives the Hamiltonian for a particle in a uniform rotating frame of reference in one of its exercises. Kozai and Kinoshita (1973) discussed an artificial satellite motion disturbed by nutation and precession of the Earth, in which equations of motion of the satellite referred to the equator were obtained from the equations of motion referred to the inertial reference frame.

B) An Explicit Hamiltonian for a rotational motion with respect to the moving orbital plane

We introduce Eulerian angles (ψ, θ, ϕ)(see Figure 1) and then the rotational matrix $\mathbf{R}$ is

$$\begin{aligned} R_{x'} &= \dot{\theta}\cos\phi + \dot{\psi}\sin\phi\sin\theta \\ R_{y'} &= -\dot{\theta}\sin\phi + \dot{\psi}\cos\phi\sin\theta \\ R_{z'} &= \dot{\phi} + \dot{\psi}\cos\theta. \end{aligned} \qquad (B-1)$$

The angular momentum vector $\mathbf{G}'$ of the spin of the planet is expressed in terms of Andoyer variables (Kinoshita 1972,1977) as follows:

$$G_{x'} = G\sin I_s \sin h$$

$$G_{y'} = -G \sin I_s \cos h \qquad (B-2)$$
$$G_{z'} = H = G \cos I_s.$$

Here G is the angular momentum, H is the z' component of the angular momentum vector, and h is a canonical conjugate variable of H (see Figure 1). The additional term $E = -(\mathbf{R}, \mathbf{G}')$ is explicitly expressed in the following form:

$$E = G \sin I_s(-\dot{\theta} \sin(h+\phi) + \dot{\psi} \sin\theta \cos(h+\phi)) - H(\dot{\phi} + \dot{\psi} \cos\theta). \qquad (B-3)$$

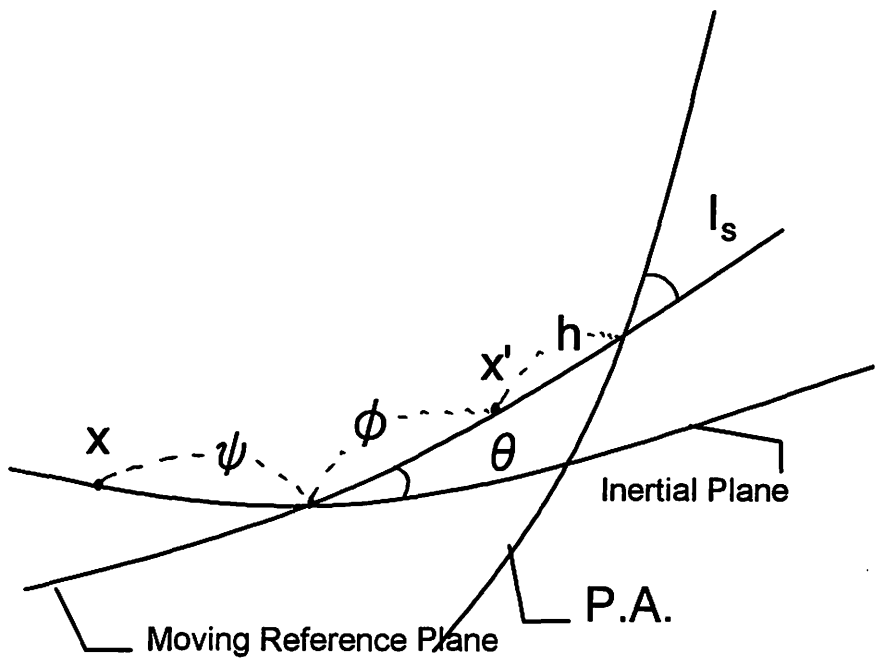

Figure 1:Reference Frames
P.A.=Plane perpendicular to the angular momentum vector.

C)Application to the spin motion disturbed by the orbital motion

Now we choose the Eulerian angles such as $\psi = \Omega, \theta = I, \phi = -\Omega$, where Ω is the longitude of node and I is the inclination of the planet's orbit(see Figure 2). Then E is transformed into

$$E = H(1 - \cos I)\dot{\Omega} + G \sin I_s(\sin I \cos(h-\Omega)\dot{\Omega} - \dot{I} \sin(h-\Omega)). \qquad (C-1)$$

Now we define variables p, q instead of Ω, I

$$p = \sin I \sin \Omega, q = \sin I \cos \Omega \qquad (C-2)$$

With use of p, q the E is transformed into

$$E = E_1 + E_2,$$

$$E_1 = G \sin I_s (-\sin h \frac{dq}{dt} + \cos h \frac{dp}{dt}), \qquad (C-3)$$

$$E_2 = G(1 - \cos I)(\dot{\Omega} \cos I - \dot{I} \sin I \sin(h - \Omega)).$$

The second term E_2 can be neglected in the following first-order discussions, since the orbital inclination of the planet is small and E_2 is second degree with respect to the orbital inclination.

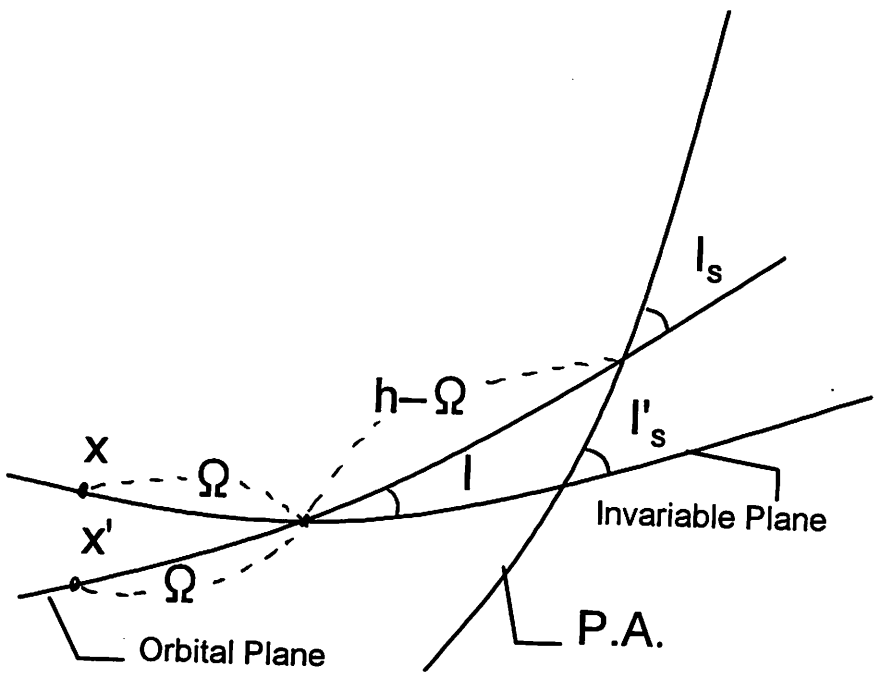

Figure 2:Reference Frames
P.A.=Plane perpendicular to the angular momentum vector.

The motion of the planet is expressed from the secular perturbation theory (Brouwer and Clemence 1961),

$$p = \sum_{j=1}^{7} N_j \sin(s_j t + \delta_j),$$

$$q = \sum_{j=1}^{7} N_j \cos(s_j t + \delta_j). \qquad (C-4)$$

Substituting (C-4) into (C-3) we obtain the additional term E

$$E = G \sin I_s \sum_{j=1}^{7} N_j s_j \cos(s_j t + \delta_j - h). \qquad (C-5)$$

The additional term E does not include short periodic terms whose arguments contains g and l, of which periods are a spin period and an Eulerian period, respectively. After the elimination of the short periodic terms the secular pert of the Hamiltonian K^* is

$$K^* = F^* = -\frac{1}{4}(1 - \frac{3}{2}\sin^2 J)\frac{C-A}{C} n^2 (1-e^2)^{-3/2}(3\cos^2 I_s^* - 1), \qquad (C-6)$$

which comes from the equatorial bulge of the planet and the number of degrees of freedom is reduced from three to one. The quantities A and C are the principal moments of inertia and n is the mean orbital motion of the planet. In (C-6) the constant term which does not include H is omitted and J is the angle between the figure axis and the angular momentum vector. When the dissipative mechanism exists, J approaches to zero. So we can neglet the term of $\sin^2 J$ and the figure axis coincides with the angular momentum axis.

The precession of the planet is

$$\frac{dh^*}{dt} = \frac{\partial F^*}{\partial H^*} = \alpha \cos I_s^*, \qquad (C-7)$$

and then

$$h^* = \alpha \cos I_s^* t + h_0^*, \qquad (C-8),$$

and

$$\alpha = -\frac{3}{2}\frac{C-A}{C}\frac{n^2}{\omega}(1-e^2)^{-3/2}, \qquad (C-9)$$

where ω is the spin rate of the planet.

Here we use a canonical perturbation method (Hori 1966) instead of solving directly the equations of motion for h, H, which are derived from the Hamiltonian K and are equivalent to the equations (25) and (26) obtained by Ward(1974). The determining function S which eliminates periodic terms from the Hamiltonian K is

$$S = \int E dt = G \sin I_s^* \sum_{j=1}^{7} \frac{N_j s_j}{s_j - \alpha \cos I_s^*} \sin(s_j t + \delta_j - h^*). \qquad (C-10)$$

Now we obtain the periodic perturbations of ΔH and Δh

$$\Delta H = -\frac{\partial S}{\partial h^*} = G \sin I_s^* \sum_{j=1}^{7} \frac{N_j s_j}{s_j - \alpha \cos I_s^*} \cos(s_j t + \delta_j - h^*) \qquad (C-11)$$

and

$$\Delta h = \frac{\partial S}{\partial H^*} = \frac{1}{\sin I_s^*} \sum_{j=1}^{7} \frac{N_j s_j (\alpha - s_j \cos I_s^*)}{(s_j - \alpha \cos I_s^*)^2} \sin(s_j t + \delta_j - h^*). \qquad (C-12)$$

The periodic perturbation of the inclination I_s is obtained from ΔH since G is constant:

$$\Delta I_s = -\frac{1}{G \sin I_s^*} \Delta H = -\sum_{j=1}^{7} \frac{N_j s_j}{s_j - \alpha \cos I_s^*} \cos(s_j t + \delta_j - h^*). \qquad (C-13)$$

The equations (C-12) and (C-13) are equivalent to the equations (36) and (32) derived by Ward(1974).

Next we obtain the inclination of the angular momentum axis I_s' referred to the inertial plane or the invariable plane. We put $I_S' = I_s + \delta I_s$ and get δI_s up to the first order:

$$\delta I_s = I \cos(h - \Omega) = q \cos h + p \sin h = \sum_{j=1}^{7} N_j \cos(s_j t + \delta_j - h^*), \qquad (C-13)$$

and the periodic variation of I_s' is

$$\Delta I_s' = \Delta I_s + \delta I_s = -\sum_{j=1}^{7} \frac{\alpha N_j \cos I_s^*}{s_j - \alpha \cos I_s^*} \cos(s_j t + \delta_j - h^*). \qquad (C-14)$$

references

Arnold,V.:1976,*Les Méthods Mathématiques de la Méchanique Classique*, NAUKA, Moscou, Chap.6.

Brouwer, D. and Clemence, G.M.: 1961, *Methods of Celestial Mechanics*, Academic Press, New York.

Coddington,E.A. and Levinson, N.:1955, *Theory of Ordinary Differential Equations*, McGraw Hill, New York.

Darboux,G.: 1888, *Oeuvres de Lagrange, XI*, Gauthier-Villars, Paris, 492, note 8.

Goldreich,P.:1965, Inclination of Satellite Orbits aabout an Oblate Precessing Planets, *Astron.J.*, **70**,5.

Hori,G.: Theory of General Perturbation with Unspecified Canonical Variable, *Publ. Astron. Soc. Japan*, **18**, 287-296.

Ito,T. and Tanikawa,K.:2002, Long-term Integrations and Stability of Planetary Orbits in Our Solar System, *Mon. Not. R. Astron. Soc*, **336**, 483-500.

Ji,J., Kinoshita,H., Liu,L., Li,G. and Nakai,H.:2003a, The Apsidal Antialignment of the HD82943 System, in*Pro. IAU Colloquium No.189*,in press.

Ji,J., Liu,L., Kinoshita,H., Zhou,J., Nakai,H., and Li,G.: 2003b, The Librating Companion in HD 37124, HD 12661, HD 82943, 47 Uma and GJ 871: Alignment or Antialignment, *Astroph. J.*, **591**, L57-L60.

Kinoshita,H.:1972, First-order perturbations of the two finite body problem, *Publ. Astron. Soc. Japan*, **24**, 423-457.
Kinoshita,H.:1977, Theory of the Rotation of the Rigid Earth,*Celest.Mech.*, **15**, 277-326.
Kinoshita,H.:1993, Motion of the Orbital Plane of a Satellite due to a Secular Change of the of the Obliquity of its Mother Planet, *Celest.Mech.*, **57**, 359-368.
Kinoshita,H. and Nakai,H.:1995, Long-Term Behavior of the Motion of Pluto over 5.5 Billion Years, *Earth, Moon & Planets*, **72**, 165-173.
Kinoshita,H. and Nakai,H.:1996, The Motion of Pluto Over the Age of the Solar System, in *the proceedings of IAU Symposium No.172 " Dynamics, Ephemerides and Astrometry in the Solar System"*,61-70 .
Kinoshita,H. and Nakai,H.: 2000,Stability Mechanism of Planetary System of υ Andromedae, in *Proc. IAU Symposium No. 201*, in press.
Kinoshita,H.:2001, Does a Secular Resonance Take Place for a Planetary System?, in *Proc. 33rd Symp. Celest. Mech. ed. Kokubo et al.*,158-165.
Kinoshita,H. and Nakai,H.:2001,Stability Mechanism of GJ876 Planetary System, in *Proc. 33rd Symp. Celest. Mech. ed. Kokubo et al.*,166-179.
Kinoshita,H. and Nakai,H.:2002,Dynamical Stability of Planetary System of GJ876, in *Proc. 34th Symp. Celest. Mech. ed. Kokubo et al.*,199-225.
Knežević,Z., Milani,A., Farinella,P., Froeschle,Ch., and Froeschle,Cl.:1991, Secular Resonances from 2 to 50 AU, *ICARUS*, **93**, 316-330.
Kozai,Y. and Kinoshita,H.:1973,Effects of motion of the equatorial plane on the orbital elements of an earth satellite, *Celest.Mech.*, **7**, 356-366.
Landau,L.D. and Lifshitz,E.M.:1960, *Mechanics*, Pergamon Press, London, p.133.
Moons,M. and Morbidelli,A.:1995, Secular Resonances in Mean Motion Commensurabilities:The 4/1, 3/1, 5/2, and 7/3 Cases, *ICARUS*, **114**, 33-50.
Morbidelli,A. and Henrard,J.:1991, Secular Resonances in the Asteroid Belt:Theoretical Perturbation Approach and the Problem of their Location, *Celest. Mech. Dyn. Astron.*, **51**, 131-167.
Morbidelli,A. and Moons,M.:1991, Secular Resonances in Mean Motion Commensurabilities:The 2/1 and 3/2 Cases, *ICARUS*, **102**, 316-332.
Nakai,H. and Kinoshita,H.: 1985, Secular Perturbations of asteroids in secular resonance, *Celest. Mech.*, **36**, 391-407.
Scholl,H., Froeschle,C.H., Kinoshita,H., Yoshikawa,M. and Williams,J.G.,1989: Secular Resonances, *in Asteroids II*, ed. by Gehrels, The University Of Arizona Press,845-861.
Seeliger, H.: 1878, Ueber die Gleichung, von deren Wurzeln die saecularen Veränderungen der Planetenbahnelemente abhängen, *Astro. Nachr.*, **93**, 353-364.
Ward,W.:1974,Climatic Variations on Mars 1. Astronomical Theory of Insolation, *J. Geophys. Res.*, **79**, 3375-3386.
Williams,J.G.:1969, Secular Perturbations in the Solar System, *Ph. D. Dissertation*, University of California, Los Angels.

古在機構 (共鳴)
Kozai Mechanism ("Resonance")

小久保英一郎 (国立天文台)
Eiichiro Kokubo (National Astronomical Observatory)

Abstract

I briefly summarize the concept of the Kozai mechanism in which an asteroid with high eccentricity and inclination shows the libration of argument of pericenter around $\pi/2$ or $3\pi/2$ under the perturbation of Jupiter. The derivation of the disturbing function and the Hamiltonian map are presented. I also show the examples of the numerical integration.

1 はじめに

太陽 (中心天体)-木星 (摂動天体)-小惑星 (テスト粒子) 系のような制限3体問題を考える。このとき軌道離心率と軌道傾斜角の大きな小惑星の近点引数は、ある条件下で$\pi/2$ もくは $3\pi/2$ のまわりを秤動 (振動) することが知られている (Kozai 1962)。この秤動はしばしば古在共鳴と呼ばれる。しかし、後で示すようにこれは物理的な意味での共鳴ではない。なのでここでは古在機構と呼ぶことにする。

古在機構の応用範囲は広い。太陽系では上記の小惑星の場合だけでなく、太陽-惑星-惑星、太陽-惑星-彗星、惑星-太陽-衛星などの系に応用されている。また、近年発見されている太陽系以外の惑星系でも、中心星-惑星-惑星、主星- 伴星-惑星 (連星系) などの系に応用されている。

ここでは簡単に永年摂動論の考え方と古在機構の概念について解説し、数値計算例を示す。より詳しくは、原論文 (Kozai 1962) や文献 (Kinoshita & Nakai 1991, 1999) などを参照して欲しい。

2 モデル

a	semimajor axis
e	eccentricity
i	inclination
Ω	longitude of ascending node
ω	argument of pericenter
ϖ	longitude of pericenter

n	mean motion
l	mean anomaly
f	true anomaly

表 1: List of symbols.

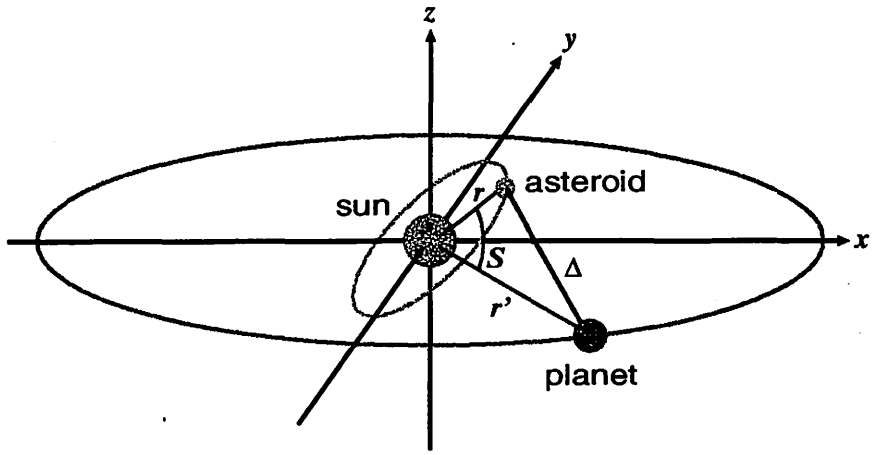

図 1: Schematic illustration of the model.

ここでは摂動天体が被摂動天体の外側にある場合を考える。例として太陽 (中心天体)-惑星 (摂動天体)-小惑星 (テスト粒子) の制限 3 体問題を考える (図 1)。他の系の場合はそれぞれ対応する天体に読みかえればよい。

太陽 (質量 m) のまわりに小惑星 (質量 0、位置$\boldsymbol{r}$) がある。惑星 (質量 m'、位置$\boldsymbol{r}'$) は小惑星から十分に遠いとする。表 1 に軌道要素の記号をまとめる。以下でプライム (') なしは小惑星、プライムつきは惑星の軌道要素を表すとする。

3 小惑星の運動方程式

惑星の軌道面を x-y平面とし ($i' = 0$)、座標原点を太陽にとる。小惑星の運動方程式は

$$\frac{d^2\boldsymbol{r}}{dt^2} = -k^2 m \frac{\boldsymbol{r}}{r^3} + \frac{\partial R}{\partial \boldsymbol{r}} \tag{1}$$

となる。ここで k^2は重力定数である。惑星の摂動を表す摂動関数 Rは

$$R = k^2 m' \left(\frac{1}{\Delta} - \frac{\boldsymbol{r}\cdot\boldsymbol{r}'}{r'^3} \right) \tag{2}$$

である。Δは惑星と小惑星間の距離で

$$\Delta^2 = (x - x')^2 + (y - y')^2 + z^2 = r^2 + r'^2 - 2rr' \cos S \tag{3}$$

である。ここで Sは太陽から見た惑星と小惑星のなす角度である (図 1)。式 (2) の右辺第 1 項が摂動の直接項、第 2 項は間接項 (惑星が太陽をゆらす効果) である。$\cos S$を球面三角公式の余弦定理を使って書き変えると

$$\cos S = \cos(\omega + f)\cos(\omega' + f') + \sin(\omega + f)\sin(\omega' + f')\cos i \tag{4}$$

となる。

小惑星の単位質量当たりのハミルトニアンは2体問題のハミルトニアン $F_{\rm K}$ と摂動関数を使って

$$F = F_{\rm K} - R(\boldsymbol{r}, t) = -\frac{k^2 m}{2a} - R(\boldsymbol{r}, t) \tag{5}$$

と書ける。これは保存量ではないことに注意。

4 摂動関数の展開

惑星の軌道半径が小惑星の軌道半径より十分大きい ($r' \gg r$) として

$$\frac{r'}{\Delta} = \left[1 + \left(\frac{r}{r'}\right)^2 - 2\frac{r}{r'}\cos S\right]^{-1/2} \tag{6}$$

をルジャンドル多項式を使って展開する。展開して $(r/r')^2$ の項までを取ると

$$\frac{r'}{\Delta} \simeq 1 + \left(\frac{r}{r'}\right) P_1(\cos S) + \left(\frac{r}{r'}\right)^2 P_2(\cos S) \tag{7}$$

となる。これを使うと摂動関数は

$$R \simeq \frac{k^2 m'}{r'}\left[\left(\frac{r}{r'}\right)^2 P_2(\cos S)\right] = \frac{k^2 m' a^2}{a'^3}\left[\left(\frac{r}{a}\right)^2 \left(\frac{a'}{r'}\right)^3 \left(-\frac{1}{2} + \frac{3}{2}\cos^2 S\right)\right] \tag{8}$$

となる。ここで摂動関数の中で小惑星の運動に寄与しない $k^2 m'/r'$ を無視した。また、間接項 $(\boldsymbol{r}\cdot\boldsymbol{r}'/r'^3)$ は $P_1(\cos S) = \cos S$ の項と相殺してしまうので、摂動には効かない。

5 摂動関数の軌道平均

軌道の長期的な変化を見るため、摂動関数を軌道平均して短周期項を落す。これは惑星を軌道の形のリングに近似することに対応する。周期 T の軌道での軌道平均を以下のように表す。

$$\frac{1}{T}\int_0^T dt = \frac{1}{2\pi}\int_0^{2\pi} dl \equiv \langle\rangle_l \tag{9}$$

小惑星と惑星の軌道運動で平均すると摂動関数は

$$\begin{aligned}\langle\langle R\rangle_{l'}\rangle_l &\simeq \frac{k^2 m' a^2}{a'^3}\left[-\frac{1}{2}\left\langle\left\langle\left(\frac{r}{a}\right)^2\left(\frac{a'}{r'}\right)^3\right\rangle_{l'}\right\rangle_l + \frac{3}{2}\left\langle\left\langle\left(\frac{r}{a}\right)^2\left(\frac{a'}{r'}\right)^3\cos^2 S\right\rangle_{l'}\right\rangle_l\right] \\ &= \frac{m'}{m+m'}\frac{n'^2 a^2}{\eta'^3}\left[\frac{1}{8}\left(1+\frac{3}{2}e^2\right)(3\cos^2 i - 1) + \frac{15}{16}e^2\cos 2\omega \sin^2 i\right]\end{aligned} \tag{10}$$

となる。ここで、$k^2(m+m') = n'^2 a'^3$ を使った。また、$\eta = \sqrt{1-e^2}$ である。摂動関数を見てわかるようにここまでの展開では摂動関数に被摂動天体の Ω や摂動天体の ϖ' が現れない、つまり軸対称な摂動関数 (リングポテンシャル) になっている。

軸対称な摂動関数の下では角運動量の z成分が保存する。この場合、角運動量 L_zは

$$L_z = \sqrt{k^2 m a(1-e^2)}\cos i \tag{11}$$

である。

6 ラグランジュの惑星方程式

ラグランジュの惑星方程式から軌道平均後の小惑星の運動方程式は

$$\frac{da}{dt} = 0 \tag{12}$$

$$\frac{de}{dt} = -\frac{\eta}{na^2 e}\frac{\partial\langle R\rangle}{\partial\omega} \tag{13}$$

$$\frac{di}{dt} = \frac{\cot i}{na^2\eta}\frac{\partial\langle R\rangle}{\partial\omega} \tag{14}$$

$$\frac{d\omega}{dt} = \frac{\eta}{na^2 e}\frac{\partial\langle R\rangle}{\partial e} - \frac{\cot i}{na^2\eta}\frac{\partial\langle R\rangle}{\partial i} \tag{15}$$

$$\frac{d\Omega}{dt} = \frac{1}{na^2\eta\sin i}\frac{\partial\langle R\rangle}{\partial i} \tag{16}$$

となる。これ以降簡単のため $\langle\langle\rangle_{l'}\rangle_l$を単に $\langle\rangle$ と表す。

$\dot{a}=0$($\langle R\rangle$ に元期近点離角σが現れない) から小惑星の軌道長半径に永年変化がないことがわかる。

長期的に見て$\dot{\omega}=0$、つまり、近点引数に永年変化がない場合が古在機構である。このとき$\dot{\varpi}=\dot{\omega}+\dot{\Omega}=\dot{\Omega}$になっている。このために共鳴と呼ばれることがある。しかし、これは外力の振動数と系の固有振動数が一致するという意味での共鳴の条件とは違う。

普通は運動方程式 (13)-(16) を数値的に積分して軌道進化を計算するが、木下、中井はヤコビ楕円関数を用いて解析解を与えている (Kinoshita & Nakai 1999)。

7 ハミルトニアンマップ

小惑星のハミルトニアンを軌道平均すると

$$\langle F\rangle = -\frac{k^2 m}{2\langle a\rangle} - \langle R\rangle \tag{17}$$

となる。これは時間に陽に依存しないので保存量となる。今の場合 a は一定なので $\langle R\rangle$ が保存することになる。$\langle R\rangle$ をさらに簡単にした R^*を

$$R^* = (2+3e^2)(3\cos^2 i - 1) + 15e^2\cos 2\omega\sin^2 i \tag{18}$$

と定義する。

角運動量の z成分の保存を使うことによって R^*から i を消去することができる。角運動量の z成分保存から

$$\eta \cos i = \text{const.} \equiv \pm\sqrt{h} \tag{19}$$

となる。これを使うと R^*は

$$R^* = (2+3e^2)\left(\frac{3h}{\eta^2}-1\right) + 15e^2\left(1-\frac{h}{\eta^2}\right)\cos 2\omega \equiv c \tag{20}$$

となり、e とωだけの関数になる。角運動量 (h) を与え、$\omega - e$ 面でエネルギー (c) の等値線 (等ハミルトニアン線) を描いたものをハミルトニアンマップと呼ぶ。等ハミルトニアン線から、小惑星の運動を解かなくても e とωの大局的なふるまいを知ることができる。すなわち、軌道平均後のハミルトニアンは保存するので、e とωは等ハミルトニアン線にそって変化する。

式 (20) をωについて解くと

$$\omega = \frac{1}{2}\arccos\alpha \tag{21}$$

$$\alpha = \frac{c(1-e^2)-(2+3e^2)(3h-1+e^2)}{15e^2(1-e^2-h)} \tag{22}$$

となる。e の取り得る範囲は $|\alpha| \leq 1$ で決まる。また、式 (19) より $0 < i < \pi/2$ なら $e_{\max}$ のとき $i_{\min}$となり$\pi/2 < i < \pi$なら $e_{\max}$のとき $i_{\max}$となる。

8 数値計算例

近点引数が秤動する場合と回転する場合について、ハミルトニアンマップと軌道積分の例を示す。太陽のパラメータは $m = 1.0$、惑星のパラメータは $m' = 0.001$、$a' = 5$、$e' = 0$ である。また、小惑星の初期軌道要素は $a_0 = 2.5$、$e_0 = 0.3$、$i_0 = 1.0$、$\Omega_0 = 0$ で、$h = 2.7$ となる。軌道積分は小惑星の周期で約 4×10^4周期行なっている。

秤動 (libration)

初期の$\omega_0 = 1.0$ のとき、$c = -0.68$ となる。この場合、ωは$\pi/2$ 近傍で秤動が可能である (図 2)。この秤動が古在機構である。このとき a、e、i には永年変化はない (図 2 左)。これは長周期ではエネルギーが保存し、かつ角運動量の z成分が保存しているためである。

軌道積分による小惑星の$\omega - e$ 面での進化がほぼ等ハミルトニアン線にそっていることがわかる (図 2 右)。ずれは摂動関数の導出で無視した高次の項の影響である。

ハミルトニアンマップを見てわかるように、秤動領域の中心部には軌道がほとんど変化しない、つまり軌道の安定領域が存在する。

秤動する場合について可能な最大離心率 $e_{\max}$を求める。$\omega_0 = \pi/2$ で e が最小値 e_0をとり、このときの軌道傾斜角を $i_0(< \pi/2)$ とする。$\omega = \pi/2$、つまり e が最小と最大のときの

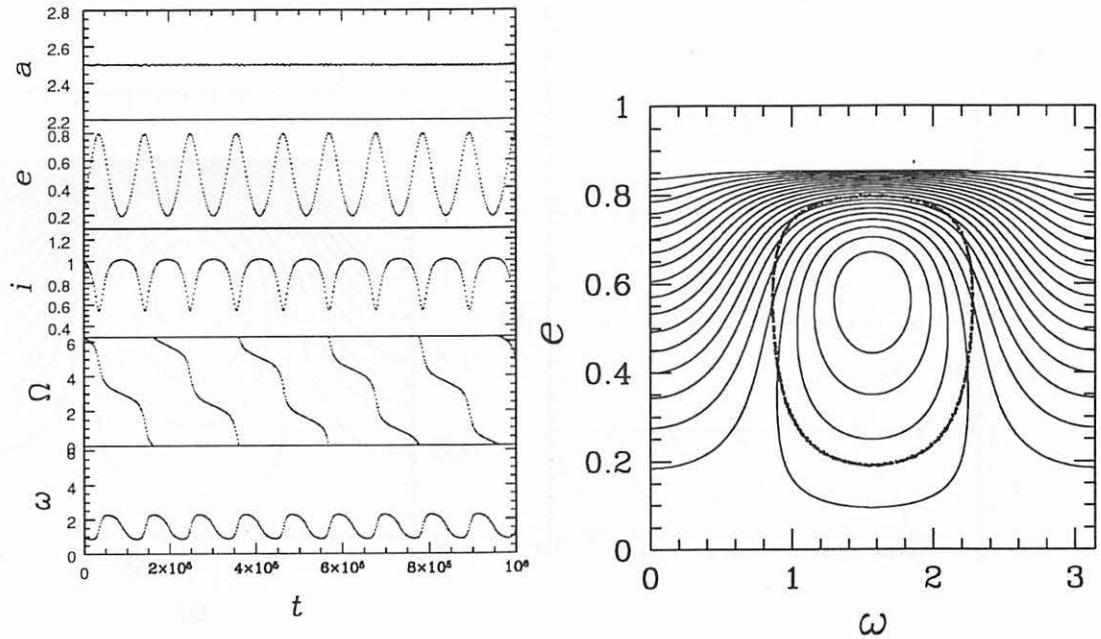

図 2: Orbital evolution for the libration case ($h = 2.7$ and $c = -0.68$). Time evolution of the orbital elements (left) and the Hamiltonian map (right). The dots on the Hamiltonian map show the results of the numerical integration.

式 (19) と式 (20) を連立させて e について解くと $e_{\max}$ が得られ

$$e_{\max} = \sqrt{1 - \frac{5}{3}\cos^2 i_0} \tag{23}$$

となる。これから秤動する領域が存在するための初期の i_0 の条件は

$$i_0 \geq \arccos\sqrt{\frac{3}{5}} = 0.68472\ (39.2315^\circ) \tag{24}$$

となる。

回転 (circulation)

初期の $\omega_0 = 0.0$ のとき、$c = 0.67$ となる。この場合、ω は秤動せず回転する (図 3)。この場合も秤動と同じように a、e、i に永年変化はない (図 3 左)。やはり等ハミルトニアン線と軌道進化がほぼ合っていることがわかる (図 3 右)。

秤動と回転の境界領域では e が大きく変化する領域がある。この領域では初期に e が 0 に近くても、1 に近いところまで大きくなることが可能である。この現象が古在共鳴と呼ばれる場合もあるので注意されたい。

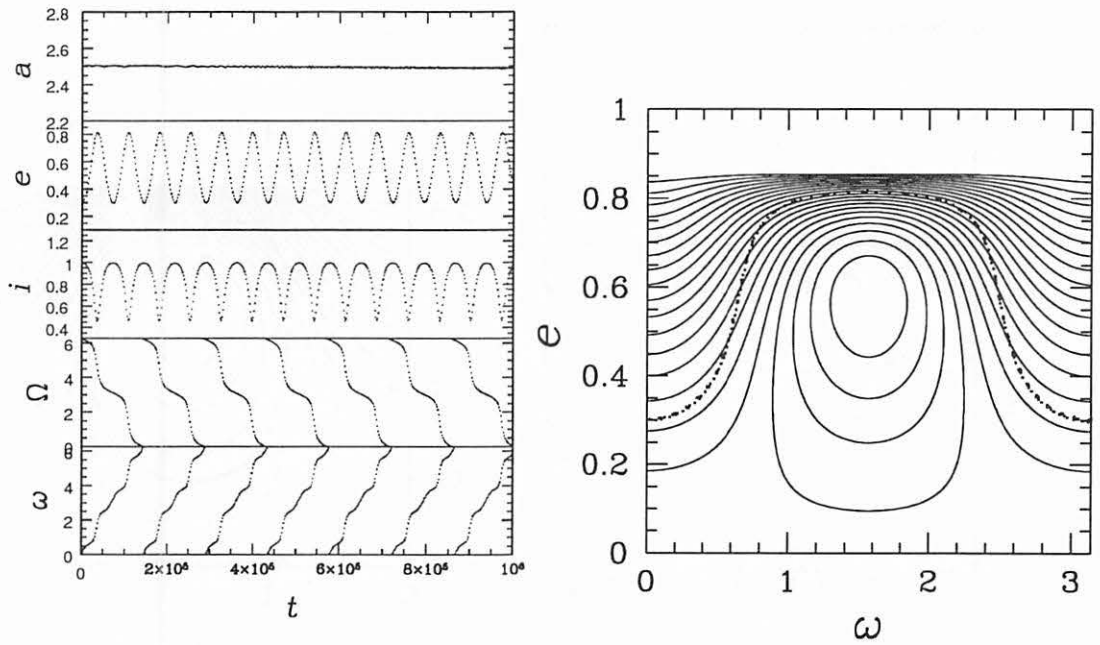

図 3: The same as Fig.2 but for the circulation case ($h = 2.7$ and $c = 0.67$).

まとめ

古在機構は、制限 3 体問題で大きな軌道離心率と軌道傾斜角をもつテスト粒子の近点引数が$\pi/2$もしくは$3\pi/2$まわりで秤動する、というものである。永年摂動論を用いるとこれを理論的に説明することができる。制限 3 体問題における永年摂動論で、r/r'は 2 次、eとiは 4 次までの摂動関数の特徴は次のようになる。

- 軸対称である。すなわち角運動量のz成分が保存する。
- 保存量である。すなわちエネルギーが保存する。

この摂動関数のもとでテスト粒子の軌道要素の永年変化を計算し、近点引数が秤動する場合が古在機構である。ちなみに、先に述べたように古在機構は物理的な意味での共鳴ではないし、もちろん永年共鳴でもない。

近年、古在機構は、摂動天体が被摂動天体の内側にある場合、平均運動共鳴と同時に起きる場合、摂動天体と被摂動天体の軌道が交差している場合、さらに制限問題ではない場合などにまで拡張されている。ここでは取り上げないが、興味があれば最近の論文を読んでみて欲しい。

参考文献

Kozai, Y., 1962, Secular Perturbation of Asteroids with High Inclination and Eccentricity, AJ, 67, 591

Kinoshita, H., Nakai, H., 1991, Secular Perturbation of Fictitious Satellites of Uranus, Celest. Mech. & Dyn. Astr., 52, 293

Kinoshita, H., Nakai, H., 1999, Analytical Solution of the Kozai Resonance and its Application, Celest. Mech. & Dyn. Astr., 75, 125

謝辞

本稿をまとめるにあたり、木下宙氏から貴重な意見をいただいた。ここに感謝する。

Long-term Evolution of Stellar Self-Gravitating System away from the Thermal Equilibrium : connection with non-extensive statistics

Atsushi Taruya*

Research Center for the Early Universe, School of Science, University of Tokyo, Tokyo 113-0033, Japan

Masa-aki Sakagami†

Department of Fundamental Sciences, FIHS, Kyoto University, Kyoto 606-8501, Japan

Abstract

With particular attention to the recently postulated introduction of a non-extensive generalization of Boltzmann-Gibbs statistics, we study the long-term stellar dynamical evolution of self-gravitating systems on timescales much longer than the two-body relaxation time. In a self-gravitating N-body system confined in an adiabatic wall, we show that the quasi-equilibrium sequence arising from the Tsallis entropy, so-called *stellar polytropes*, plays an important role in characterizing the transient states away from the Boltzmann-Gibbs equilibrium state.

PACS numbers: 98.10.+z, 04.40.-b, 05.70.-a, 64.60.Fr

*Electronic address: ataruya@utap.phys.s.u-tokyo.ac.jp

†Electronic address: sakagami@phys.h.kyoto-u.ac.jp

I. INTRODUCTION

The long-term evolution of self-gravitating many-body system is an old problem with a rich history in astrophysics. The problem, in nature, involves the long-range nature of attractive gravity and is fundamentally connected with statistical mechanics and thermodynamics. Historically, the important consequence from the thermodynamical arguments has arisen in 1960s, known as the *gravothermal catastrophe*, i.e., thermodynamic instability due to the negative specific heat[1]. Originally, the gravothermal catastrophe has been investigated in a very idealized situation, i.e., a stellar system confined in a spherical cavity[2]. Owing to the maximum entropy principle, the existence of an unstable thermal state has been found from the standard analysis of statistical mechanics with a particular attention to the Boltzmann-Gibbs(BG) entropy:

$$S_{\rm BG} = -\int d^3\boldsymbol{x} d^3\boldsymbol{v}\, f(\boldsymbol{x},\boldsymbol{v}) \ln f(\boldsymbol{x},\boldsymbol{v}), \tag{1}$$

where $f(\boldsymbol{x},\boldsymbol{v})$ denotes the one-particle distribution function defined in phase-space $(\boldsymbol{x},\boldsymbol{v})$.

Since 1960s, the standard approach using the BG entropy has dramatically improved our view of the late-time phase of the globular cluster as a real astronomical system[3], however, from a thermodynamic point of view, peculiarities of the thermal property in self-gravitating systems such as negative specific heat, as well as the non-equilibrium properties away from the BG state have not yet been understood completely.

In this Letter, aiming at a better understanding of the (non-equilibrium) thermodynamic properties of stellar self-gravitating systems, we present a set of long-term N-body simulations, the timescale of which is much longer than the relaxation time. With a particular emphasis to the recent application of the non-extensive generalization of BG statistics, we focus on the stellar dynamical evolution in an isolated star cluster before self-similar core-collapse[4]. We show that the quasi-equilibrium sequence arising from the Tsallis entropy[5] plays an important role in characterizing the non-equilibrium evolution of a self-gravitating system.

II. N-BODY SIMULATIONS

The N-body experiment considered here is the same situation as investigated in classic papers ([2], see also Ref.[6]). That is, we confine the N particles interacted via Newton

TABLE I: Initial distributions and their evolutionary states

run #	initial distribution	parameters	# of particles	transient state	final state
A	stellar polytrope($n = 3$)	$D = 10,000$	2,048	stellar polytrope	collapse
B1	stellar polytrope($n = 6$)	$D = 110$	2,048	stellar polytrope	collapse
B2	stellar polytrope($n = 6$)	$D = 10,000$	2,048	stellar polytrope	collapse
C1	Hernquist model	$a/r_e = 0.5$	8,192	stellar polytrope	collapse
C2	Hernquist model	$a/r_e = 1.0$	8,192	none	isothermal

gravity in a spherical adiabatic wall, which reverses the radial components of the velocity if the particle reaches the wall. Without loss of generality, we set the units as $G = M = r_e = 1$, where G is gravitational constant, M and r_e is the total mass of the system and the radius of the adiabatic wall, respectively. Note that the typical timescales appearing in this system are the free-fall time, $T_{\rm ff} = (G\rho)^{-1/2}$, and the global relaxation time driven by the two-body encounter, $T_{\rm relax} = (0.1N/\ln N)T_{\rm ff}$ [1], which are basically scaled as $T_{\rm ff} \sim 1$ and $T_{\rm relax} \sim 0.1N/\ln N$ in our units. To perform an expensive N-body calculation, we used a special-purpose hardware, GRAPE-6, which is especially designed to accelerate the gravitational force calculations for collisional N-body systems[7]. With this implementation, the 4th-order Hermite integrator with individual time step[8] can work efficiently, which is suited for probing the relaxation process in denser core regions with an appropriate accuracy. We adopt the Plummer softened potential, $\phi = 1/\sqrt{r^2 + \epsilon^2}$ with a softening length ϵ of 1/512 and 1/2048.

In the present numerical simulation, the choice of the initial condition is an important step. Here, we set the initial distribution to the stationary state of Poisson-Vlassov equation, i.e., dynamical equilibrium for a spherical system with isotropic velocity distribution. According to the Jeans theorem[1], the one-particle distribution function $f(\boldsymbol{x}, \boldsymbol{v})$ can be expressed as a function of specific energy, $\varepsilon = v^2/2 + \Phi(r)$ with r and Φ being the radius and the gravitational potential. Then keeping the energy and the mass constant, the thermal equilibrium of ordinary extensive statistics derived from the maximum entropy principle of the BG entropy (1) reduces to the exponential distribution, so-called *isothermal* distribution given by $f(\varepsilon) \propto e^{-\beta\varepsilon}$, which effectively satisfies the equation of state, $P(r) \propto \rho(r)$, where $P(r)$ is pressure and $\rho(r)$ is mass density[1, 2].

On the other hand, as another possibility, one considers the extremum state of Tsallis' non-extensive entropy [5]:

$$S_q = -\int d^3\boldsymbol{x}d^3\boldsymbol{v}\,[\{f(\boldsymbol{x},\boldsymbol{v})\}^q - f(\boldsymbol{x},\boldsymbol{v})]/(1-q), \tag{2}$$

which might be of particular importance in describing the quasi-equilibrium state away from the BG state[9]. In this case, the maximum entropy principle leads to the power-law distribution, $f(\varepsilon) \propto (\Phi_0 - \varepsilon)^{1/(q-1)}$ [10–13], referred to as the *stellar polytrope*[1]. It satisfies the polytropic equation of state, $P(r) \propto \rho(r)^{1+1/n}$, and the polytrope index n is related to the q-parameter as $n = 1/(q-1) + 3/2$[14]. Provided the polytrope index n, the equilibrium structure can be determined by solving the Láne-Emden equation [15] and using this solution, the relationship between the dimensionless energy $\lambda \equiv -r_e E/(GM^2)$ and the density contrast $D \equiv \rho_c/\rho_e$, the core density divided by the edge density, can be drawn (see Fig.1, [16]). Note that the limit $n \to \infty$ (or $q \to 1$) corresponds to the isothermal distribution derived from the BG entropy (1).

Table I summarizes the list of the five simulation runs. A more systematic study of the systems with several initial conditions is now in progress and the details of the results will

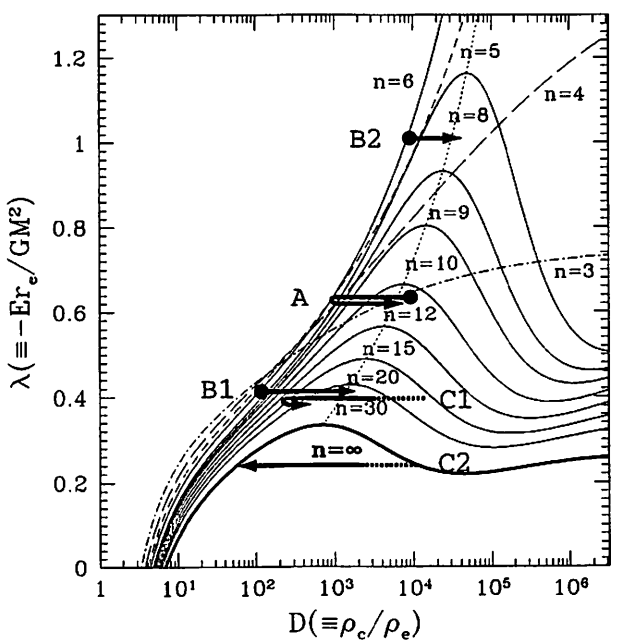

FIG. 1: Equilibrium sequences of stellar polytrope and isothermal distribution ($n = \infty$) in the energy-density contrast relation, $\lambda \equiv -r_e E/(GM^2)$ v.s. $D \equiv \rho_c/\rho_e$. The thick arrows denote the evolutionary tracks in each simulation run.

be reported elsewhere. In Table I, in addition to the stellar polytropic initial state, we also consider the Hernquist model[17], which was originally introduced to account for the empirical law of observed elliptical galaxies[1].

III. RESULTS

It has been recently discussed in [11–13] that the thermodynamic structure of the stellar polytropic distribution can be consistently characterized by the non-extensive framework of the thermostatistics. According to their results, the stellar polytrope confined in an adiabatic wall is shown to be thermodynamically stable when the polytrope index $n < 5$. In other words, if $n > 5$, a stable equilibrium state ceases to exist for a sufficiently large density contrast $D > D_{\rm crit}$, where the critical value $D_{\rm crit}$ given by a function of n is determined from the second variation of entropy around the extremum state of Tsallis entropy, $\delta^2 S_q = 0$[11, 13]. The dotted line in Fig.1 represents the critical value $D_{\rm crit}$ for each polytrope index, which indicates that the stellar polytrope at low density contrast $D < D_{\rm crit}$ is expected to remain stable. Apart from the BG state, one might expect that the stellar polytrope acts as a thermal equilibrium.

Of course, this naive expectation is not correct at all. Indeed, the numerical simulations reveal that the stellar polytropic distribution gradually changes with time, on the timescale of two-body relaxation. Further, it seems that the gravothermal instability appears at relatively smaller values of D than the predicted one, $D_{\rm crit}$, which might be partially ascribed to the non-stationarity of the background stellar polytrope. Physically, the core-collapse phenomenon due to the gravothermal catastrophe follows from the decoupling of the relaxation timescales between the central and the outer parts, whose behavior sensitively depends on the physical property of heat transport[18]. In a rigorous sense, the thermodynamic prediction might lose the physical relevance, however, focusing on the evolutionary sequence, we found that the transient state starting from the initial stellar polytrope can be remarkably characterized by a sequence of stellar polytropes (run A, B1 and B2). This is even true in the case starting from the Hernquist model (run C1).

Let us show the representative results taken from run A (Fig.2). Fig.2(a) plots the snapshots of the density profile $\rho(r)$, while Fig.2(b) represents the distribution function $f(\varepsilon)$ as a function of the specific energy ε. Note that just for illustrative purpose, each output

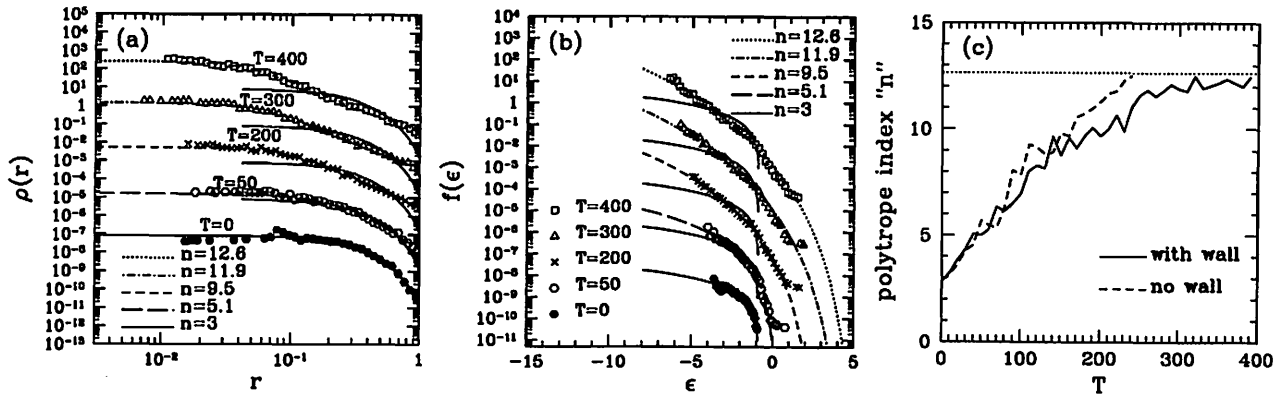

FIG. 2: Results from simulation run A. (a) Snapshots of density profile $\rho(r)$. (b) Snapshots of one-particle distribution function $f(\varepsilon)$. (c) The time evolution of the polytrope index for run A with and without the boundary of adiabatic wall.

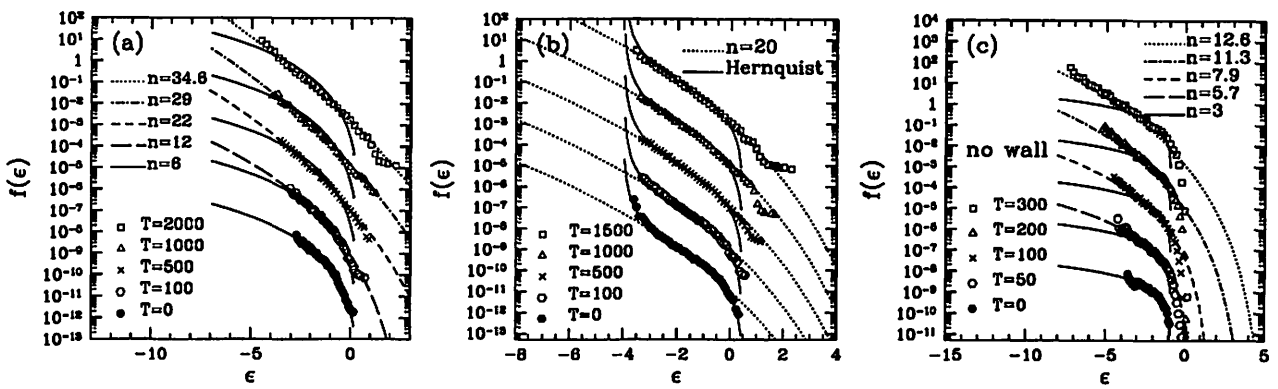

FIG. 3: Evolution of one-particle distribution function in other models. (a) Run B1. (b) Run C1. (c) Run A removing the adiabatic wall.

result is artificially shifting to the two-digits below. Only the final output with $T = 400$ represents the correct scales. In each figure, solid lines mean the initial stellar polytrope with $n = 3$ and the other lines indicate the fitting results to the stellar polytrope by varying the polytrope index n[19]. Note that the number of fitting parameters just reduces to one, i.e., the polytrope index, since the total energy is well-conserved in the present situation. Fig.2 shows that while the system gradually deviates from the initial polytropic state, the transient state still follows a sequence of stellar polytropes. The fitting results are remarkably good until the time exceeds $T \simeq 400$, corresponding to $15T_{\rm relax}$. Afterwards, the system enters the gravothermally unstable regime and finally undergoes the core-collapse.

Now, focus on the evolutionary track in each simulation run summarized in the energy-

density contrast plane (Fig.1), where the filled circle represents the initial stellar polytrope. Interestingly, the density contrast of the transient state in run A initially decreases, but it eventually turns to increase. The turning-point roughly corresponds to the stellar polytrope with index $n \sim 5 - 6$. Note, however, that the time evolution of polytrope index itself is a monotonically increasing function of time as shown in Fig.2(c), apart from the tiny fluctuations. This is indeed true for the other cases, indicating the Boltzmann H-theorem that any of the self-gravitating systems tends to approach the BG state. A typical example is the run C2, which finally reaches the stable BG state. However, as already shown in run A, all the systems cannot reach the BG state. Fig.1 indicates that no BG state is possible for a fixed value $\lambda > 0.335$[2], which can be derived from the peak value of the trajectory. Further, stable stellar polytropes cease to exist at high density contrast $D > D_{\rm crit}$. In fact, our simulations starting from the stellar polytropes finally underwent core-collapse (runs A, B1 and B2). Though it might not be rigorously correct, the predicted value $D_{\rm crit}$ provides a crude approximation to the boundary between the stability and the instability.

Fig.3 plots the snapshots of the distribution function taken from the other runs. The initial density contrast in run B1 (Fig.3(a)) is relatively low ($D = 110$) and thereby the system slowly evolves following a sequence of stellar polytropes. After $T = 2000 \sim 74 T_{\rm relax}$, the system begins to deviate from the stable equilibrium sequence, leading to the core-collapse. Another noticeable case is the run C1 (Fig.3(b)). The Hernquist model as initial distribution of run C has cuspy density profile, $\rho(r) \propto 1/r/(r+a)^3$, which behaves as $\rho \propto r^{-1}$ at the inner part [17]. The resultant distribution function $f(\varepsilon)$ shows a singular behavior at the negative energy region, which cannot be described by the power-law distribution. Soon after a while, however, the gravothermal expansion[6] takes place and the flatter core is eventually formed. Then the system settles into a sequence of stellar polytropes and can be approximately described by the stellar polytrope with index $n = 20$ for a long time. Thus, as long as the stellar system confined in an adiabatic wall is concerned, the stellar polytrope can be regarded as a quasi-attractor and a quasi-equilibrium state.

Of course, these remarkable features could be an outcome in a very idealized situation and one suspects that quasi-equilibrium state of stellar polytrope cannot hold if we remove the boundary of the adiabatic wall. As a demonstration, Fig.3(c) plots the results removing the boundary, in which the initial state is the same distribution as in run A. As is expected, the high-energy particles freely escape outwards from the central region and the resultant

distribution function $f(\varepsilon)$ sharply falls off at the energy region $\varepsilon \sim 0$, indicating that the density contrast D becomes effectively large. Thus, compared to the system confined in the wall, the removal of the boundary makes the stellar system unstable and the core-collapse takes place earlier. Nevertheless, focusing on the inner part of the denser region, the evolution of the core is not significantly affected by the escape particles at the outer part and can be fitted by a sequence of stellar polytropes (see also the dashed line in Fig.2(c)). The successful fit to the density profile $\rho(r)$ almost remains the same. Hence, the stellar polytrope characterized by the Tsallis entropy can be even realized in a realistic situation removing the boundary of the adiabatic wall.

IV. SUMMARY

We have performed a set of numerical simulation of long-term stellar dynamical evolution away from the BG state and found that the transient state of the system confined in an adiabatic wall can be remarkably fitted by a sequence of stellar polytropes. This is even true in the case removing the outer boundary. Therefore, the stellar polytropic distribution can be a quasi-attractor and a quasi-equilibrium state of a self-gravitating system.

Alternative characterization of the transients away from the BG state might be possible besides the q-exponential distribution of stellar polytropes. For an empirical characterization of observed structure, the one-parameter family of truncated exponential distributions, so-called King model has been used in the literature[1, 3, 20]. Also, the sequence of King model has been found to characterize the evolutionary sequence of density profile for isolated stellar systems without boundary[4]. We have also tried to fit the simulation data to the King model. Similarly to the stellar polytrope, the King model accurately describes the simulated density profile $\rho(r)$ confined in an adiabatic wall, however, it fails to match the simulated distribution function $f(\varepsilon)$, especially at the cutoff energy scales. Therefore, from the quantitative description of the entire phase-space structure, the power-law distribution of the stellar polytropes can be a better characterization of the quasi-equilibrium state and this could yield an interesting explanation of the origin of the empirical King model.

Acknowledgments

We are grateful to T. Fukushige for providing us the GRAPE-6 code and for his constant supports and helpful comments. We also thank to J. Makino for fruitful discussion especially on the applicability of equilibrium sequences of stellar polytrope. Numerical computations were carried out at ADAC (the Astronomical Data Analysis Center) of the National Astronomical Observatory of Japan. This research was supported in part by the grant-in-aid from Japan Society of Promotion of Science (No.1470157).

---

[1] J. Binney and S. Tremaine, *Galactic Dynamics*, (Princeton Univ. Press, Princeton, 1987); L. Spitzer, *Dynamical Evolution of Globular Clusters*, (Princeton Univ. Press, Princeton, 1987).

[2] V.A. Antonov, Vest. Leningrad Gros. Univ. **7**, 135 (1962); D. Lynden-Bell and R. Wood, Mon. Rot. R. Astron. Soc. **138**, 495 (1968).

[3] G. Meylan and D.C. Heggie, Astron. Astrophys. Rev. **8**, 1 (1997).

[4] H. Cohn, Astrophys. J. **242**, 765 (1980).

[5] C. Tsallis, J. Stat. Phys. **52**, 479 (1988).

[6] H. Endoh, T. Fukushige and J. Makino, Publ. Astron. Soc. Japan **49**, 345 (1997).

[7] J. Makino, in J. Makino and P. Hut (Eds.), Proc. IAU Symp. **208**, *Astrophysical Supercomputing using Particle Simulations*, in press.

[8] J. Makino and S.J. Aarseth, Publ. Astron. Soc. Japan **44**, 141 (1992).

[9] C. Tsallis, Braz. J. Phys. **29** 1; S. Abe and Y. Okamoto (Eds.), *Nonextensive Statistical Mechanics and Its Applications* (Springer, Berlin, 2001).

[10] A.R. Plastino and A. Plastino, Phys. Lett. A **174**, 384 (1993).

[11] A. Taruya and M. Sakagami, Physica A **307**, 185 (2002).

[12] A. Taruya and M. Sakagami, Physica A **318**, 387 (2003).

[13] A. Taruya and M. Sakagami, Physica A **322**, 285 (2003).

[14] The relation between the polytrope index n and the q-parameter may change, depending on the choice of the statistical average: standard linear means[10, 11] or normalized q-values[13]. Here, we simply adopt the result using the standard linear mean.

[15] S. Chandrasekhar, *Introduction to the Study of Stellar Structure*, (Dover, New York, 1939).

[16] The energy-density contrast relation in Fig.1 is essentially the same one as obtained from the analysis using the standard linear means (Fig.2 of Ref.[11]) and that using the normalized q-values (Fig. 3 of Ref.[13]). This means that the thermodynamic stability in a system confined in an adiabatic wall does not depend on the choice of the statistical average (see Ref.[13] for details).

[17] L. Hernquist, Astrophys. J. **356**, 359 (1990).

[18] J. Makino and P. Hut, Astrophys. J. **383**, 181 (1991).

[19] In fitting the simulation data to the stellar polytrope, we first quantify the radial density profile $\rho(r)$ from each snapshot data. Selecting the 100 points from it at regular intervals in logarithmic scale of radius r, the results are then compared with the Emden solutions, fixing the energy λ and varying the polytrope index n.

[20] I.R. King, Astron. J. **71** 64 (1966).

On the "stellar dynamical" evidences for massive black holes

Junichiro Makino
Department of Astronomy, University of Tokyo, 7-3-1 Hongo,
Bunkyo-ku,Tokyo 113-0033, Japan

May 13, 2003

Abstract

We critically examine recent claims that globular clusters M15 and G1 of M31 contains massive central black holes. For both clusters, we performed detailed N-body simulations with realistic effects like the stellar mass loss due to stellar evolution are taken into account. In the case of M15, we found neutron stars and massive white dwarfs concentrate to the center through mass segregation, resulting in a sharp increase in M/L toward the center. While consistent with the presence of a central black hole, the Hubble data can also be explained by this central concentration of neutron stars and massive white dwarfs. In the case of G1, the effect of the mass segregation is not significant, because the relaxation time of G1 is longer than the Hubble time. Even so, we found that our simulation model can perfectly reproduce the observed properties of G1 such as the luminosity profile, velocity dispersion profile, rotation profile and ellipticity profile. Though it's unclear why the existence of the black hole was concluded in the case of G1, simulation models clearly show that black holes are not necessary to explain observations.

1 初めに

Gerssen et al. (2002) は球状星団 M15 に 3,000 太陽質量程度のブラックホールを発見したと報告した。また、Gebhardt et al. (2002) は、M31 内に球状星団 G1 に、2×10^4 太陽質量のブラックホールを発見したと報告した。これらはいずれもハッブル宇宙望遠鏡によって星団中心部の星の速度分布を求めて、それを説明するにはブラックホールが必要であると結論している。

もしもこれらの主張が本当であるなら、球状星団の中に、恒星質量よりもはるかに大きなブラックホールを発見した最初の例となる。これは球状星団の形成、進化という観点からも、また、銀河中心の巨大ブラックホールの形成過程の理解という観点からも極めて重要である (Ebisuzaki et al., 2001)。

しかし、これらの報告は、にわかには信じ難いものでもある。 M15 の中心密度は確かに高いが、これは従来典型的な post-collapse 球状星団として理解されてきていた。 G1 は有限サイズのコアを持つ、キングモデルで十分フィットできる星団であり (Meylan et al., 2001; Djorgovski et al., 1997)、その中心に巨大ブラックホールがあるというのは非常にありそうなことではない。

そこで、我々は、現実的な N 体計算の結果と観測で得られた密度、速度プロファイル等を比較することで、観測の説明にブラックホールが必要かどうかを検証することを試みた。

方法、結果の詳細は既に雑誌論文 (Baumgardt et al., 2003a,b) で報告したので、ここでは仮定と結論を簡単に紹介する。詳しくは元論文を参照して欲しい。以下、2 節で M15 の場合、3 節で G1 の場合の検証について説明し、最後に 4 節で我々の結果の意味するところについて議論する。

2 M15

2.1 観測「事実」と解釈

まず、観測からどのような論理でブラックホールの存在が結論されるかをまとめておく。

球状星団なので、分布は球対称であるとして、速度分布は等方的であると仮定する。表面測光 (実際には、 M15 の場合には巨星の star count) から、半径方向の投影された輝度分布が求められるので、球対称を仮定して空間的な輝度分布、すなわち星の数密度分布が求められる。

次に、速度分散プロファイルを求める。 M15 の場合には、個々の星がハッブルでは分解できるので、分光観測からそれぞれの視線速度を求め、星団全体の平均の視線速度からのずれの分散を計算して速度分散プロファイルを求めることができる。

さて、恒星系力学の初歩を学んだ人ならだれでも知っているように[1] 、ジーンズの定理を使うと、ある恒星のグループについて数密度分布と速度分散の分布が分かれば、星団全体の質量分布を決めることができる。 M15 の場合、速度分散が決められるのも、数密度が決められるのも巨星段階の明るい星だけだが、それから「全体の質量分布」がどうなっているか分かるのである。 従って、原理的には質量分布を直接求めて、中心にブラックホールがあるかないかが決められる。

「原理的には」と書いたのはもちろん実際にはそんなにうまくいかないからである。輝度分布はともかく、速度分散はノイズが極めて大きい。特に中心付近では、巨星の数自体が少なくなってくるのでどんなに精密な観測をしても small-N ゆらぎのために精度が上がらない。このため、ブラックホールがあるかないかという議論は、実際には以下のような手順でなされることになる。

1. 適当な M/L (質量-輝度比) プロファイルを仮定して、輝度分布から質量分布を求め、求まった質量分布から速度分散の分布を求める。
2. この時に、中心に適当な質量のブラックホールを仮定する。
3. M/L 全体に掛ける係数とブラックホールの質量をふってみて、χ^2 値がもっとも良いモデルが「観測結果」であると信じる。

つまり、観測事実とブラックホールの間には、以下のような仮定やモデルがはいっているのである。

[1] 知らない人は牧野の講義ノート
http://grape.astron.s.u-tokyo.ac.jp/pub/people/makino/kougi/stellar_dynamics/kougi.html
でも見て下さい

1. 空間分布は球対称である

2. 速度分散は等方的である

3. モデルとして使った M/L のプロファイルは正しい (誤差をもたない)

実際にはこれらの仮定が本当かどうかはわからないわけだが、それによる不確定性は χ^2 値、つまりは結果のエラーバーには全くはいってこないことに注意して欲しい。こんなことは実際に観測をしている人にはいうまでもないことかもしれないが、理論家には観測からなされる主張の何が仮定で何が事実であるかを見極めるのは必ずしも容易なことではない。

さて、理論家の側から見ると、上の 3 つの仮定のうち最初の 2 つは、熱力学的な緩和時間が短い球状星団の中心部に対しては極めて妥当なものである。これに対し、 M/L のプロファイルには注意が必要である。

M15 の場合、星団全体の緩和時間が宇宙年齢よりもかなり短い。もちろんこのために中心部が重力熱力学的崩壊 (core collapse) しているわけである。緩和時間が短いので、重い星は mass segregation により中心部に沈む。年齢がほぼ宇宙年齢である球状星団では、もっとも重い星は初期に出来た中性子星や重い白色矮星である。現在巨星である星は生まれた時の質量が 0.8 太陽質量程度であり、光っている星の中ではもっとも重いが 1.4 太陽質量の中性子星や、それに近いところまで分布する白色矮星に比べると軽い。

このことは、もちろん Gerssen 他にも理解されていて、彼らは M/L について 2 通りの仮定を置いている。一つはもっとも単純だが現実的とはいいがたい M/L が一定という仮定である。もうひとつは、Indiana 大学の Haldan Cohn のグループが軌道平均 Fokker-Plank 方程式を数値的に解いて、 M15 の 1997 年当時の観測データを再現したモデルで求まった M/L プロファイルである (Dull et al., 1997)。これは適当な初期質量関数から、星団全体で中性子星、白色矮星の割合を仮定し、見える星は 0.8 太陽質量から下であると仮定して、つまり、球状星団ができた時から「現在の」質量関数であったとして進化計算させたモデルであり、中心にブラックホールは存在しない。

Gerssen 他はこの両方のモデルで、ブラックホールの質量の推定値についてほぼ同じ結果を得た。非常に違う仮定で同じ結果を得たので、彼らはブラックホールがあるのは確実であると判断したのであろう。

しかし、良く考えてみると、 M/L について非常に違う仮定をしたにもかかわらずブラックホールの質量が同じになるというのは奇妙なことである。実際、Dull 他は 1997 年当時の輝度分布と速度分散分布を両方再現するようにモデルを構成したのだから、 1997 年に求まっていた速度分散分布とハッブルを使って改善したものの違い程度しかブラックホールはでてこないはずである。

では、速度分散の違いはどの程度かというと、確かにハッブルによって今までよりも中心近くの星が観測できて、速度分散のグラフが中心まで延びたが、実は比べてみるとその延び方は Dull 他の Fokker-Planck 計算の結果とほとんどずれないものだった[2] 。

さて、なにが問題だったのだろう？

[2] なお、こう書いてしまうともう Gerssen 他の計算は何か間違っているに決まっていて、N 体計算で何かする必要などなかったのではないかと思うかもしれない。後から考えるとそういう面もなくはないが、我々がこの辺の事情を完全に理解したのは論文を投稿してからであった。

2.2 シミュレーションモデル

人の観測結果 (とその解釈) と、それとは別の人の理論計算を比べていても今一つ要領を得ないので、理論計算のほうは自前で準備してみることにした。 M15 は典型的な PCC (Post-core-collapse) 球状星団なので、我々が、というか Holger Baumgardt が計算した現実的な球状星団の進化のサーベイ計算 (Baumgardt and Makino, 2003) の中から、銀河中心からの距離が類似でやはり PCC の状態、正確には現在まさに collapse した瞬間であるものを持ってきた。初期質量関数等は業界標準なものであり、特に M15 に合わせたパラメータチューニング等は行っていない。

星団の質量や速度分散などは完全に同じではない (粒子数がそもそも少ないため) ので、我々が目的としたのは精密な定量的比較というよりは、シミュレーションで作った星団を、Gerssen 他と可能な限り「同じように」観測したらどう見えるかということである。なお、とりあえず中心にブラックホールができない進化モデルを考えた。これは、人工的にブラックホールができなくしたという意味ではなく、現在ちょうど最初の collapse にあるような進化シナリオではブラックホールはできないことがわかっている。最初から非常に中心密度が高く、数百万年で collapse するようなシナリオではブラックホールができる可能性がある (Ebisuzaki et al., 2001) が、今回はとりあえず通常のシナリオを採用した。

2.3 モデルと観測の比較

シミュレーションで出来た星団の「観測」結果を図 1 に示す。

エラーバーつきの点は、巨星の速度分散の観測結果である。 1 パーセクから内側で、中心にむかってゆっくりと上がっていることがわかる。 Gerssen 他の観測結果と定性的な特徴は非常に良く合っている。破線は、 M/L 一定として輝度分布から速度分散を求めた結果である。 下から順に、中心ブラックホールとして 0, 40, 80 および 120 太陽質量を仮定した。これでは 80 太陽質量程度がもっとも良くあっていることがわかる。我々のモデル星団の質量は M15 の 1/40 程度なので、 M15 に換算すると 3,000 太陽質量となり Gerssen 他の結果と妙に良くあっている。

いうまでもないが、我々のシミュレーションモデルでは中心にブラックホールはない。 80 太陽質量のブラックホールがでてきたのは、純粋に M/L 一定の仮定のためである。実線で示したのが、 M/L 一定の仮定をおかず、実際の質量分布から求めたジーンズ方程式を使って求めた速度分散である。当然の結果であるが、これは速度分散の「観測」結果と極めて良く一致しており、ブラックホールは必要ではない。

2.4 解釈

シミュレーションからはっきり確認できたことは、標準的なシナリオに従って進化した、collapse した球状星団を持ってきて、 M/L 一定として解析するとブラックホールの存在が結論されるということである。もうひとつ、ある意味もっと重要なことは、シミュレーション結果は M15 の定性的な特徴を極めて良く再現した、特に速度分散や輝度密度のべき等をほぼ完璧に再現したということで、これは標準的な球状星団のシナリオに対する強力なサポートになっている。

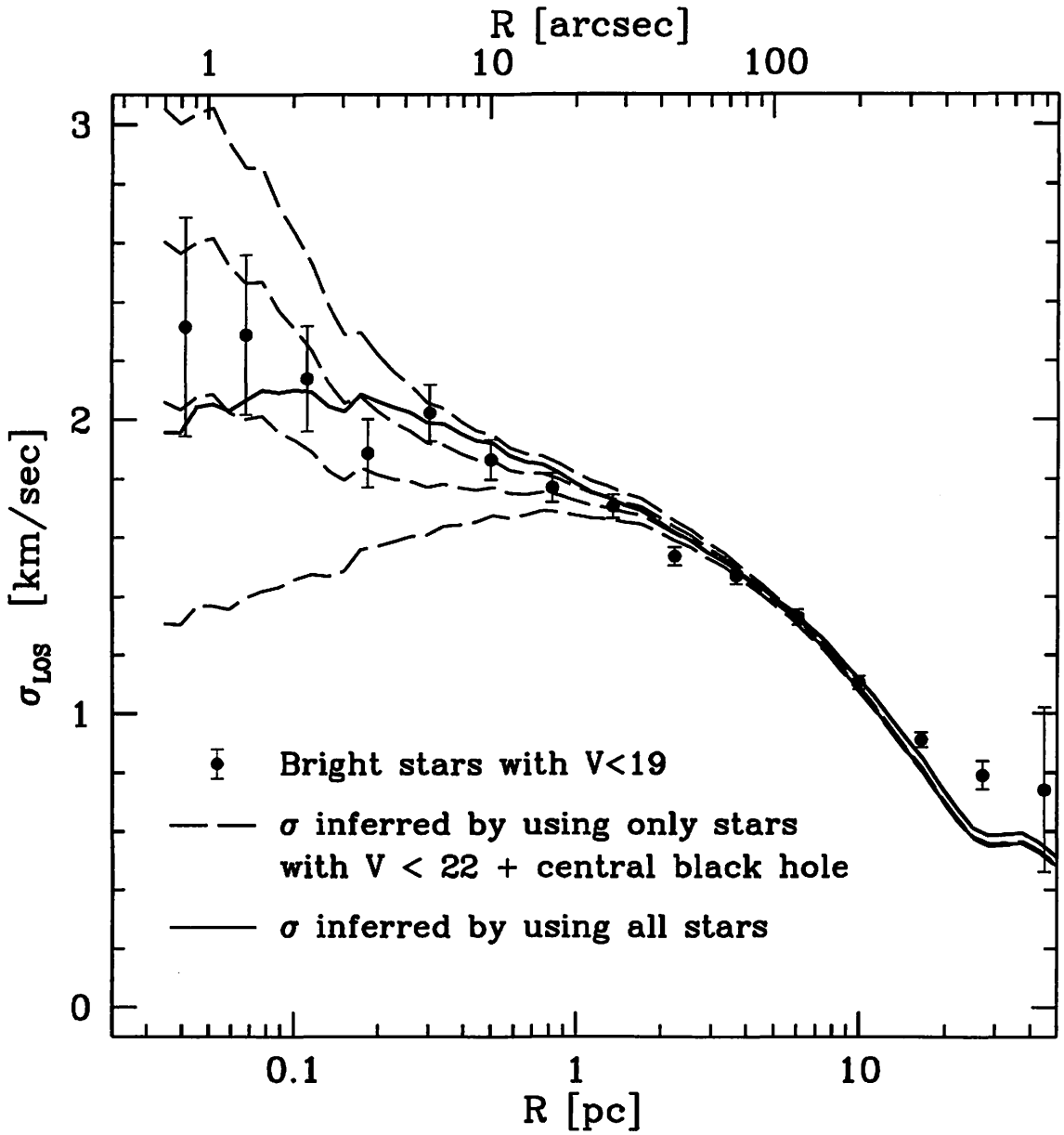

Figure 1: Line-of-sight velocity dispersion of the $V < 19$ stars in the N-body simulations (filled circles), and inferred from the stellar number density and cluster potential (solid and dashed curves). The solid curve shows the inferred velocity dispersion of stars with $V < 22$, using the potential calculated from all stars. Dashed curves are calculated using the potential determined from stars with $V < 22$, assuming a constant M/L, together with central point masses of (bottom to top) 0, 40, 80 and 120 $M_\odot$. The value of M/L is chosen to fit the measured velocity dispersion between 1 and 10 pc from the cluster center. For constant assumed M/L, the best fit has $M_{BH} \sim 80 M_\odot$.

ともかく、M/L 一定の解析ではそこにはないブラックホールがあることになってしまうので、これは駄目である。既に述べたように Gerssen 他は M/L にモデル計算の結果をいれた解析もやっているわけだが、これはどう考えても正しく計算できていれば M/L 一定の時よりもブラックホールの質量が小さくならないといけないので、あまり変わらないという結果になったのは、おそらく彼らの計算が間違っているからと考えるべきであろう。

我々は上のように考えて論文を投稿し (Baumgardt et al., 2003a)、Gerssen と共著者にはプレプリントを送った。すると、数時間のうちに「M/L モデルをいれた計算には間違いがあって、現在再計算中だ」と返事があり、さらにその数時間後にはその再計算の結果が投稿され、プレプリントサーバーにも登録されていた (Gerssen et al., 2003)。

間違いは一体どういうものであったかというと、Dull 他の論文の M/L のグラフの横軸の目盛りが約 3 倍間違っていて、そのグラフを信用したので M/L が大きい領域の半径をそれだけ小さく見積もっていた、つまりは中心部で M/L が大きくなるのがほとんど計算に入っていなかったというものである。なるほど、M/L が一定の計算と同じ結果になったはずである。

Gerssen 他の修正版の論文には、ブラックホールの質量は小さいけど存在はしてると主張されているが、1σ エラーバーのほうが質量よりも大きく、これはブラックホールの質量に上限値をつけただけの結果と解釈するのが普通である。いいかえれば、現在の観測結果をもっとも普通に解釈すると、M15 の中心に巨大ブラックホールは存在しない。

3 G1

では G1 についてはどうであろうか？細かいことは省略するが、G1 についても我々のシミュレーションではブラックホールなしで密度、速度分散を再現できた。なお、G1 は非常に緩和時間が長く、回転しておりかなり偏平である。回転速度、偏平度についても、初期に適当に角運動量を与える、具体的には同じ質量のキングモデルを off-center な放物軌道から合体させた初期条件から初めることで非常に良く再現できた。

Gebhardt の主張 (private communication) は、速度分散の 4 次のモーメントがブラックホールがないと説明できないというものである。もちろん、4 次のモーメントが信頼できる精度で決まっていれば、それはかなり有力な根拠になる。しかし、彼らのデータ (未発表) を見た限りでは、4 次のモーメントがブラックホールの影響がないはずのかなり外側でも有意に正の値を持っており、ベースラインの設定等の観測データの処理の段階で問題があったことを示唆する結果になっている。

4 考察

結局、M15、G1 のどちらでも、ブラックホールがないシミュレーションモデルで観測結果を非常に良く説明できる。このことからブラックホールがないと結論できるわけではもちろんないが、少なくとも現在の観測データからブラックホールがあると結論できないということは間違いないであろう。

M15 のほうは間違いの原因もはっきりしていて他に影響するようなものではないので問題はないが、G1 のほうは原因がはっきりしないだけに影響範囲がはっきりしない。G1 でブラックホール質量の推定に使われたのは、いわゆる Nukers[3] が使ってきた彼らにとっては標準的なツールボックスである。そして、G1 についての彼らの結果は 2σ レベルであり、多くの楕円銀河についての彼らの結果に比べて特に悪い結果ではない。ということは、逆にいえば例えば Magorrian et al. (1998) の結果の相当数は G1 と同様なものである可能性がある。これについては、理論、観測の両面から検証を行っていく必要があるだろう。

References

Baumgardt, H., and Makino, J. 2003, *MNRAS*, 341, 247.

Baumgardt, H., Hut, P., Makino, J., McMillan, S.L.W., and Portegies Zwart, S.F. 2003a, *ApJ*, 582, L21

Baumgardt, H., Makino, J., Hut, P., McMillan, S.L.W., and Portegies Zwart, S.F. 2003b, *ApJ*, 589, L25.

Djorgovski, S. G., et al. 1997, *ApJ*, 474, L19

Dull, J. D., Cohn, H. N., Lugger, P. M., Murphy, B. W., Seitzer, P. O., Callanan, P. J., Rutten, R. G. M., and Charles, P. A. 1997, *ApJ*, 481, 267

Ebisuzaki, T., Makino, J., Tsuru, T. G., Funato, Y., Portegies Zwart, S. F., Hut, P., McMillan, S. L. W., Matsushita, S., Matsumoto, H., and Kawabe, R. 2001, *ApJ*, 562, L19

Gebhardt, K., Rich, R. M., and Ho, L. C. 2002, *ApJ*, 578, L41

Gerssen, J., van der Marel, R. P., Gebhardt, K., Guhathakurta, P., Peterson, R., and Pryor, C. 2002, *AJ*, 124, 3270.

Gerssen, J., van der Marel, R. P., Gebhardt, K., Guhathakurta, P., Peterson, R., and Pryor, C. 2003, *AJ*, 125, 376.

Magorrian, J., Tremaine, S., Richstone, D., Bender, R., Bower, G., Dressler, A., Faber, S. M., Gebhardt, K., Green, R., Grillmair, C., Kormendy, J., and Lauer, T., *AJ*, 115, 2285.

Meylan, G., Sarajedini, A., Jablonka, P., Djorgovski, S. G., Bridges, T., and Rich, R. M. 2001, *AJ*, 123, 830

[3] Gebhardt, Faber, Magorrian, Richston ら、ハッブルでの光学観測から楕円銀河の中心ブラックホールを研究しているグループ

Formation of non-gaussian velocity distribution after the collapse in self-gravitating system

Naoko Kanaeda[1], Osamu Iguch,[2] and Yasuhide Sota[3]

Department of Physics, Ochanomizu University, 2-1-1 Ohtuka, Bunkyo, Tokyo, 112-8610, Japan

Abstract

We study the statistical properties of particles in stationary state after the cold collapse in 3-dimentional self-gravitating system. We investigate two models, spherical collapse(SC) and collision of two clusters(CC) as simple examples. In both cases, the non-gaussian velocity distribution are observed in case of small virial ratio. Using mass ratio defined by mass m enclosed in a sphere of radius r, we find that the quantities such as the density profile or the velocity dispersion against mass ratio seems to be stationary in both cases. We examine the properties by dividing the systems into several shells with equal mass. The velocity distribution in each shell is gaussian and the velocity dispersion decreases linearly up to 0.7 mass ratio.

1 Introduction

Gravitational collapse is intrinsic in a gravitational system and plays an important role in forming the astronomical objects such as galaxies or large scale structures. So it seems important to get the knowledge of the statistical properties during and after such a collapse.

It is well known that universal density profile appears during the collapse of dark matter halo in cosmological N-body simulation [1]. The orgin of the universal profiles have been examined from the viewpoint of self-similarity but have not yet been clearly understood [2]. It is also known that luminosity profile for elliptical galaxies can be well represented by the $r^{1/4}$ law [3] [9]. Albada showed that this universal profile is well attained after the cold collapse of the matters in N-body simulation[4].

So far density profile or velocity dispersion have been mainly examined in these N-body simulations[10] [11] [12]. Howerver, the gravitational system are expected to have more intrinsic statististical characters, because of its specific properties such as long range interaction and negative specific heat[13] or gravotharmal catastrophe[7] [8].

For example, 1-dimensional sheet model, where each sheet interacts with others with long range interaciton, shows the fractal structure after the collapse with initial small virial ratio [5]. In this model, however, the specific heat is positive and all of the sheets are gravitationally bounded because of its interaction form contrary to real 3-dimentional gravitational system. In the system with negative specific heat, on the other hand, the particles are separated into central core and outer halo parts. In halo parts, the particles are too loosely bounded to be in tharmal equillibrium and expected to show the exotic character such as non-Gaussian veloicty distribution [6]. So the system may show the characteristic properties during and after the gravitational collapse not only in the density profile, but also in the velocity distribution.

Here from this motivation, we examine the cold collapse simulation mainly from the viewpoint of velocity distribution. We treat the case with small virial ratio to reexamine the Albada's typical case and the case of cold collapse with zero initial virial ratio and the collision of the two clusters.

2 model and initial conditions

2.1 model

In this paper, we examine two models, spherical collapse (SC) and collision of two clusters (CC), in 3 dimentional self-gravitating system.

[1]kanaeda@degway.phys.ocha.ac.jp
[2]osamu@phys.ocha.ac.jp
[3]sota@cosmos.phys.ocha.ac.jp

RUN	vr	N	ϵ
$SC1$	0.0	5000	10^{-4}
$SC2$	0.1	5000	10^{-2}
$CC1$	1.4	1000	10^{-4}
$CC2$	1.4	10000	10^{-4}

Table 1: Initial conditions in our simulations. vr, N, and ϵ denotes the virial ratio, the total number of particles, and the softening parameter of the gravitational interraction respectively.

In case of SC, initially we distribute the particles with gaussian velocity distribution uniformly in sphere with radius R_s.

In case of CC, initially two clusters is at rest and the distance between two clusters is $6R_s$. Each cluster is a sphere with radius R_s and contains half of the total number of particles in the system. In each cluster, the particles with gaussian velocity distribution are distributed uniformly.

The equation of motion for the i-th particles in these systems is

$$m\frac{d^2\boldsymbol{x}_i}{dt^2} = -Gm^2\sum_{i\neq j}^{N}\frac{\boldsymbol{x}_i - \boldsymbol{x}_j}{(|\boldsymbol{x}_i - \boldsymbol{x}_j|^2 + \epsilon^2)^{\frac{3}{2}}}, \tag{1}$$

where $\boldsymbol{x}_i$ are the position of i-th particle, G is the gravitational constant, m is the mass of each particle, and ϵ is a softening parameter.

In our simulation, we employed the units, $G = 1, M := Nm = 1, R_s = 1$. Then the dynamical time of the system t_{dyn} is,

$$t_{dyn} := \sqrt{\frac{R_s^3}{GM}}, \tag{2}$$

2.2 Initial Conditions

All parameters of our simulations are summarized in Table 1. SC1 and SC2 are the case of SC and CC1 and CC2 are the case of CC.

3 results

In this section, we show the results of the simulation calcurated by use of Nbody2h, Aarseth Code developed by Sverre Aarseth[14]. The error of the total energy of the system for our simulation is less than 0.1 percent.

3.1 The time evolution of the system

We show the time evolution of the system. The typical exsamples of the time evolution are shown in Fig.1 and Fig.2.

In the case of SC, the particles are initially distributed in sphere uniformly (Fig.1-a) and collapse at $t \sim 1t_{dyn}$. After collapse (Fig.1-b), some of the particles were bounded gravitationally and some of them escaped toward outside.

In the case of CC, two clusters is initially at rest (Fig.2-a) and are approaching each other and collide at $t \sim 20t_{dyn}$. After the collision (Fig.2-b), the system seems to be stationary during our simulation $t = 300t_{dyn}$.

In Fig.3, we show the time evolution of the virial ratio (a) and the velocity dispersion (b, c, d) for run SC1. After the collapse or collision ($t > t_{dyn}$), the system seem to be statinary in terms of the virial ratio and the velocity dispersion.

The time evolution of the density profile for run SC1 and run CC2 is shown in Fig.4(a) and (b) respectively. From Fig.4(a), in the case of the zero viral ratio ($vr = 0$), the high density region move

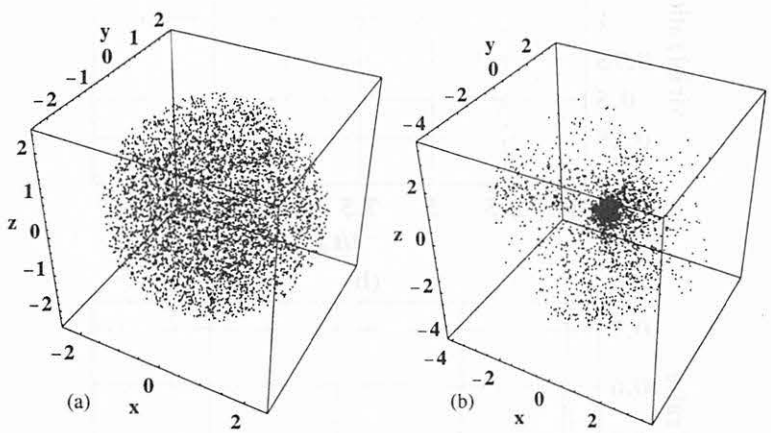

Figure 1: Snapshot in the (x, y, z) space for run SC1. Each dot in these boxies denotes the position of particles. (a) and (b) shows the snapshot at $t = 0t_{dyn}$ and $t = 2t_{dyn}$ respectively.

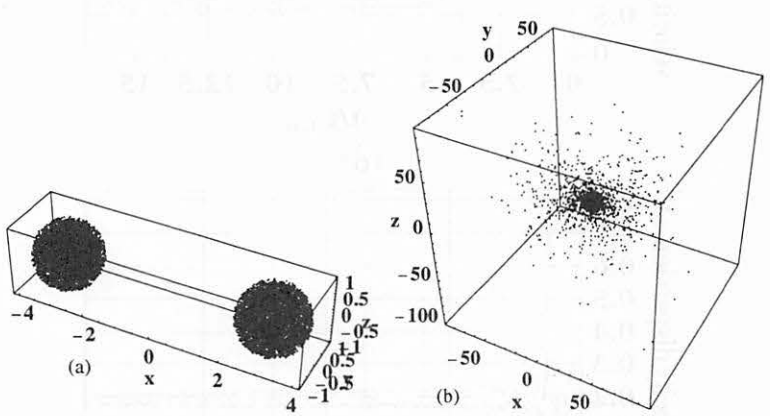

Figure 2: Snapshot in the (x, y, z) space for run CC2. Each point in these boxies denotes the position of particles. (a) and (b) shows the snapshot at $t = 0t_{dyn}$ and $t = 100t_{dyn}$ respectively.

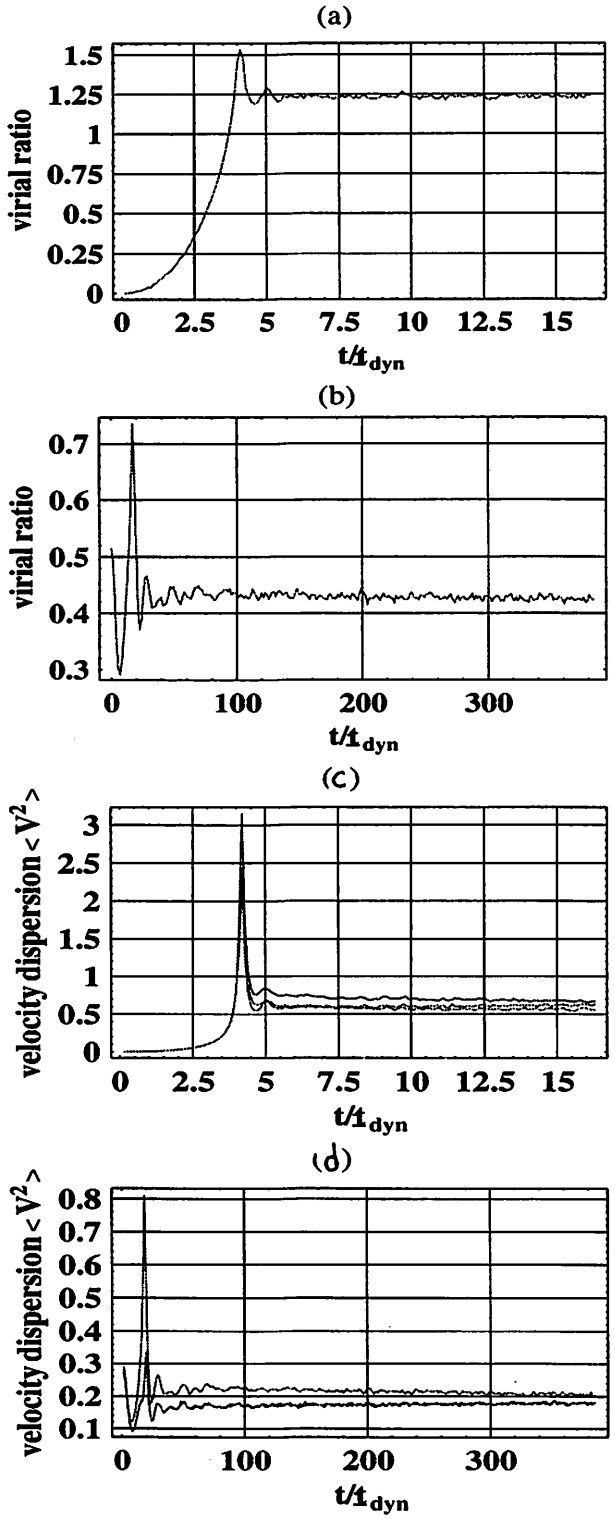

Figure 3: Time evolution of the virial raito and velocity dispersion for run SC1 and run CC2. (a)virial ratio for run SC1, (b)the velocity dispersion for run SC1, (c)the velocity dispersion for run CC2, and (d)the velocity dispersion for runCC2.

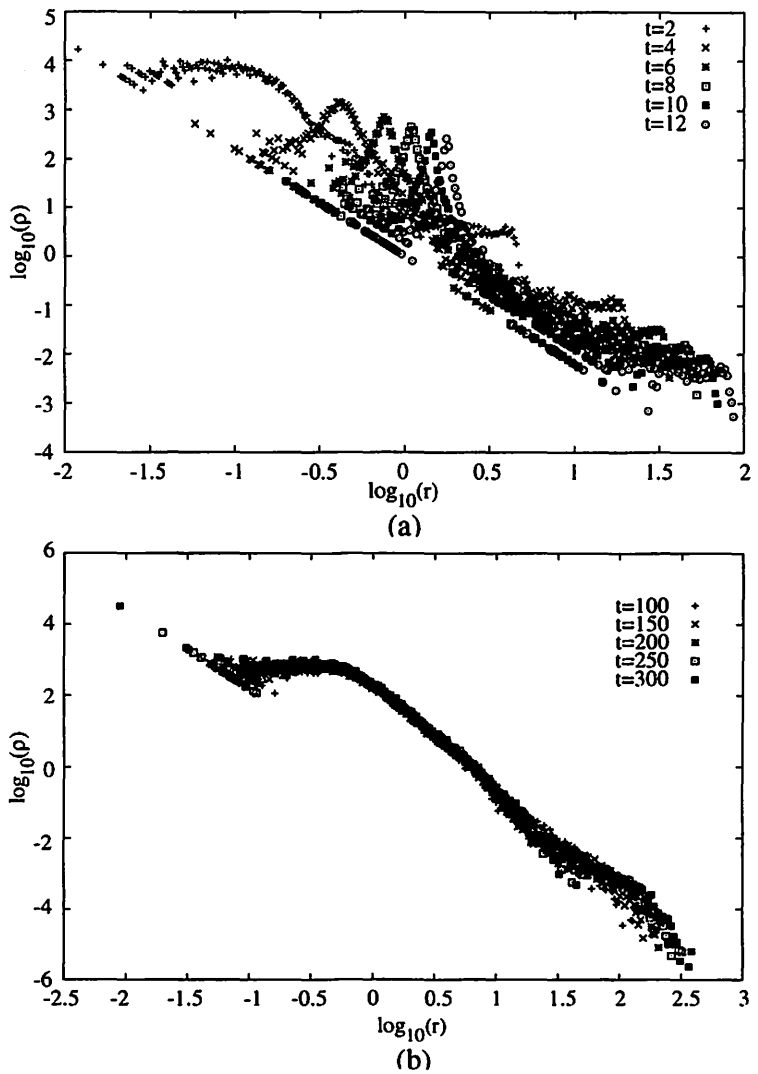

Figure 4: Linear-log plot of the time evolution of the density profile $\rho(r)$ for run SC1 (a) and run CC2 (b).

toward outside of the system and the system expands. On the other hand, for run SC2, CC1, and CC2, the density profile seems to be stationary.

3.2 Non-gaussian velocity distribution

Here, we discuss the velocity distribution after a collapse or a collision. After collapse, the velocity distribution becomes non-gaussian and seem to be universal in both cases(in our simulations, we use the chi-square test to fit the function to the velocity distribution).

In order to show non-guassianity, we fit the data with the gaussian funtion. Both numerical data and fitted gaussian funtion are shown in Fig.5. Figs.5-a and 5-b are the case of run SC1 and run CC2 respectively. In both cases, the velocity distribution deviates from gaussian distribution on the whole part of f(v). We suppose that the non-gaussian velocity ditribution is a characteristic property of the self-grabitating system after the cold collapse.

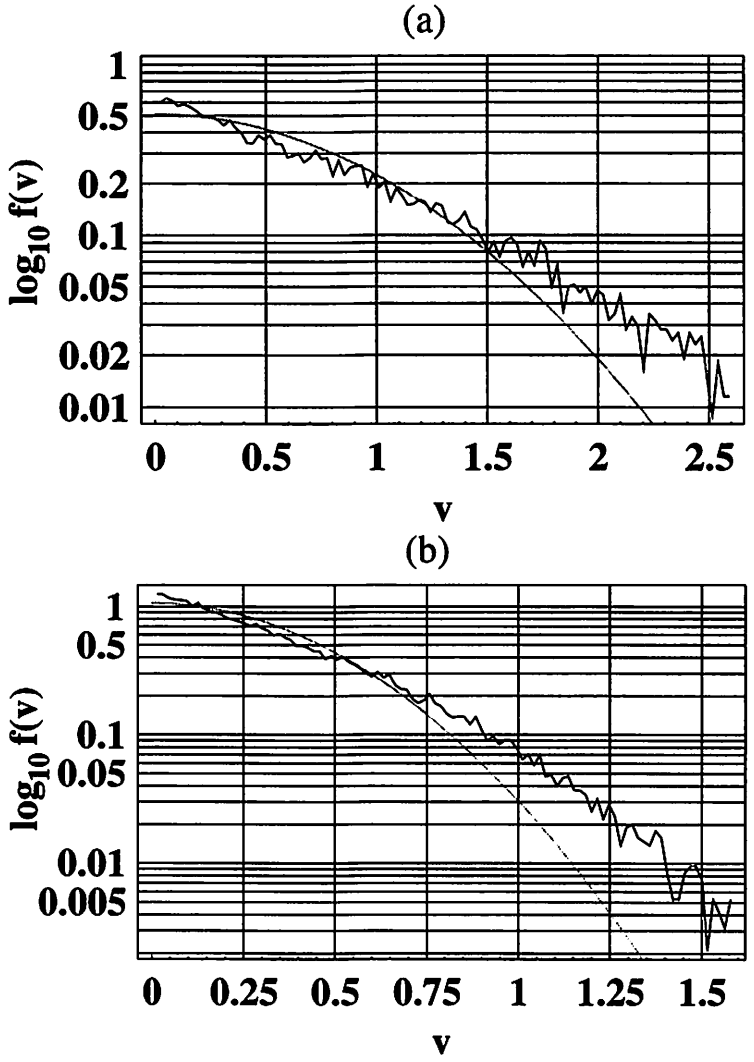

Figure 5: Linear-log plot of observed stable non-gauss velocity distribution for run SC1 and CC2 at t=$100t_{dyn}$. Vertical axis represents the log of velocity distribution function and horizonal axis represents the absolute value of the velocity. Black line is fitting gaussian function. Figures (a) and (b) shows for run SC1 and run CC2 respectively.

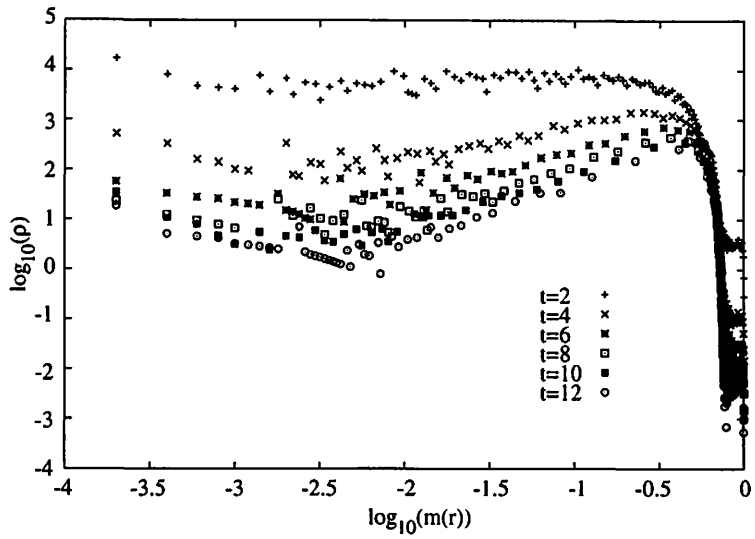

Figure 6: Log-log plot of the time evolution of the density profile ρ against the mass ratio $m(r)$ for run SC1.

3.3 the properties in the shell

We divide the system into several shells and examine some properties in these shells. Each shell contains 10 percent of the total mass of the system. Using the mass ratio $m(r)$ enclosed in a sphere of radius r replacing the radius r, we examine the properties in each shell.

The density profile against mass ratio$m(r)$ for run SC1 are shown in Fig.6. From Fig4, the density profile is not stationary after the collapse. However, the density profile against the mass ratio seems to be stationary. It suggests that the system evolves self-similarlly after the collapse in the case of zero virial ratio.

We investigate the velocity distribution in each shell. The velocity distribution in each shell for SC1(a) and CC2(b) are shown in Fig.8. The velocity distribution in inner shells up to 0.7 mass ratio seems to be gaussian in both cases. On the other hand, the velocity distribution in outer shells from 0.8 mass ratio, seems to deviate from gaussian.

In Fig.9, we show the gradient of the velocity dispersion against mass ratio. The figure(a) shows run SC1 and the figure(b) shows run CC2. In case of CC2, the velocity dispersion decreases linear on the whole part of mass ratio. In case of SC1, the velocity dispersion seems to be linear where the σ^2 nears 0. So, we introduce the function whose velocity dispersion decreases lineary and the local velocity distribution is gaussian. We expressed it as follows,

$$f(v_i) = a\int_0^{T_0} exp(-v_i^2/2T)dT = a[\sqrt{\frac{2T_0}{\pi}}e^{-\frac{v_i^2}{2T_0}} - |v_i|[1 - Erf(\frac{|v_i|}{\sqrt{2T_0}})]] \quad (3)$$

where suffix i is x, y or z and T means the velosity dispersion, a and T_0 are fitting parameters.

Then, we fit the non-gaussian velocity distribution with this function. In Figure 10, we show the non-gaussian velocity distribtuion fitted with this function and gaussian. The figure (a) shows for run SC1 and (b) figure shows for run CC2. This function seems to fit better than gaussian. The chi-square value of this function is less than that of gaussian in all cases during calculation time.

4 Summary and discussion

In this paper, we investigate the statistical properties especially for the velocity distribution after cold collapse in 3-dimensional self-gravitating system. We examin two models, spherical collapse (SC) and

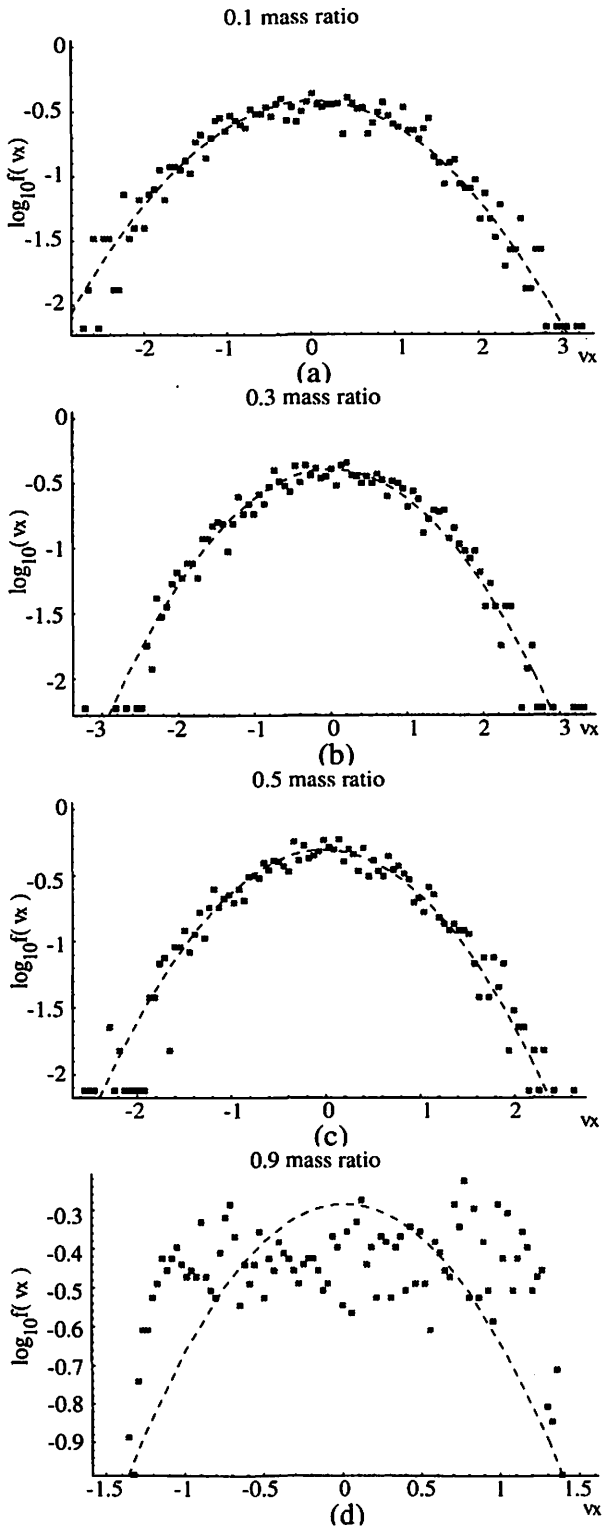

Figure 7: The velocity distribution in each shell. The vertical axis represents the log of velocity distribution and the horizonal axis represents the velocity v_x. Figure (a), (b), (c) and (d) shows the velocity distribution in 0.1, 0.3, 0.5 and 0.7 mass ratio respectively.

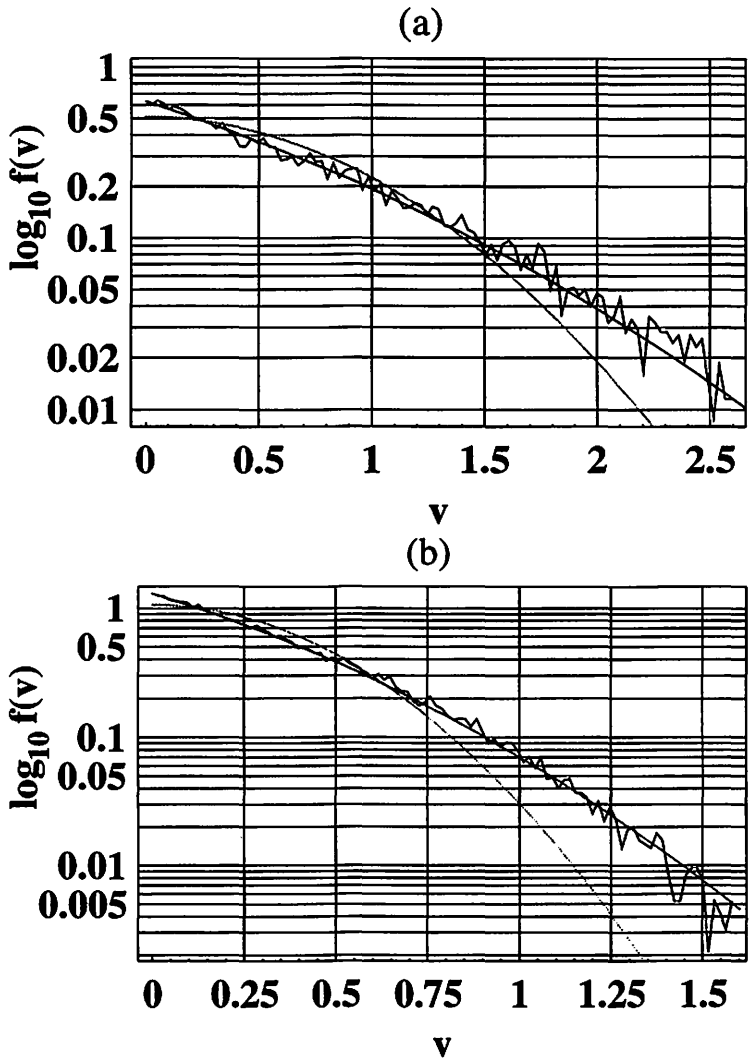

Figure 8: Linear-log plot of bserved stable non-gauss velocity distribution for run SC1 (a) and CC2 (b) at t=$100t_{dyn}$. The vertical axis represents the log of velocity distribution function. Axis of abscissas represents the absolute value of the velocity of components. Black line is the fitting function we use in this paper and gray line is fitted gaussian function. Light gray line is the fitted exponential function.

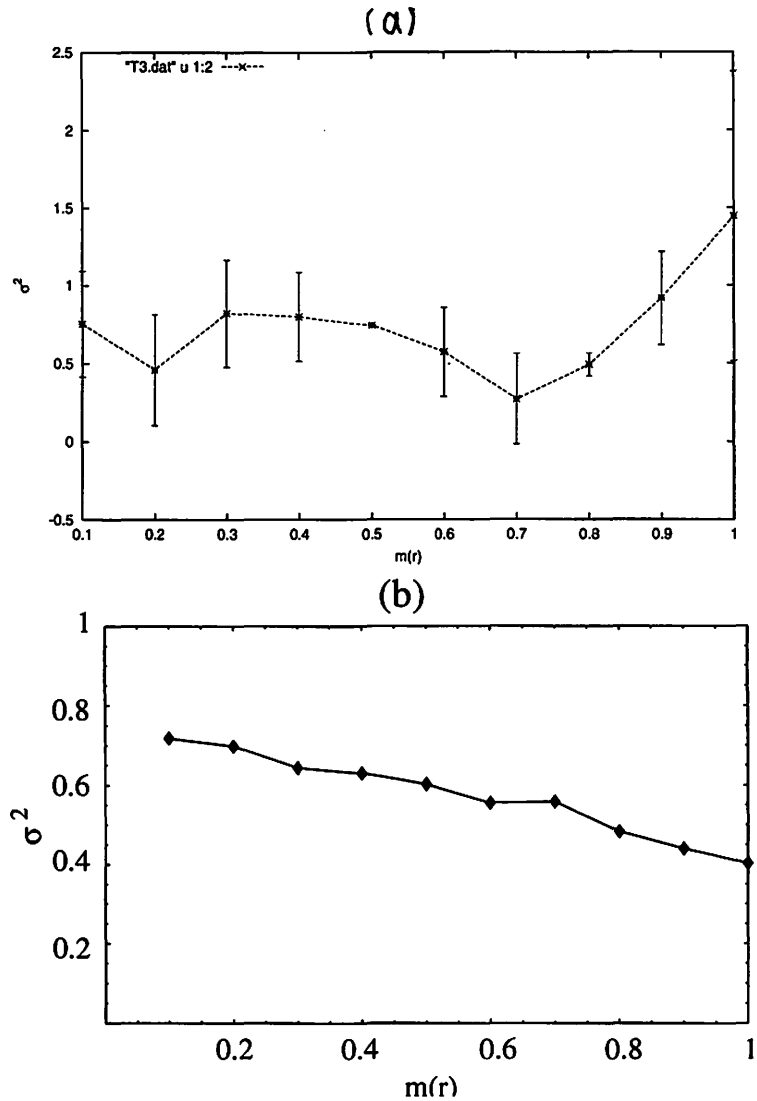

Figure 9: The velocity dispersion against the mass ratio. Figure (a) shows run SC1 and Figure (b) shows run CC2

collision of two clusters (CC).

After the collapse or the collision, the velocity distribution become non-gaussian and seems to be statinory during our simulation.

As for time evolution of the system, the velocity dispersion or virial ratio seems to be constant after collapse or collision. However, the time evolution of density profile are not always stationary. In the case of SC with the zero virial ratio $vr = 0$, the high density region moves toward outside.

We divide the systems into several shells and examine the properties in each shell. Using the mass ratio replacing with the radius, the density profile against the mass ratio seems to be stationary for SC with $vr = 0$. It means that the time evolution of the density profile has self-similary. Then, we examine the other properties in shells. The velocity distribution in shells are gaussian up to 0.7 mass ratio. In addition, the velocity dispersion decreas linearly in terms of mass ratio. So, we make the fitting function supposing that the velocity dispersion of the system decreases lineary and local velocity distribution is gaussian. We fit the non-gaussian velocity distribution with this function and gaussian. We find that this function fits better than gaussian judging by the chi-square test.

From the investigation in term of mass ratio, the quantities against mass ratio show a good behavior. Thus, as for the properties of the system after the cold collapse, the analysis by use of mass ratio might

have an advantage. The stationarity of the quantities against mass ratio also implies that the state after the cold collapse has self similarity. We interest in the relation between the linearity of the gradient of velocity dispersion and the self-similarity appeared in viewpoint of mass ratio.

Acknowledgements

We would like to thank professor M. Morikawa greatly for his detailed comments and suggestions. We also thank to T. Tatekawa and A. Nakamichi for advices and on using n-body code. We also thank to professor N. Gouda for discussion.

References

[1] Navarro J. F. , Frenck C. S. and White S. D. M, Astrophys. J. ,**490** (1997) 493,

[2] Fukushige T. and Makino J. , Astrophys. J. ,**557**(2001) 533.

[3] G de Vaucouleurs, Mon. Not. R. Astr. Soc. **113**(1953)134D.

[4] Van Albada, Mon. Not. R. Astr. Soc. ,**201** (1982), 939.

[5] H. Koyama and T. Konishi, Phys. Lett. A **295**(2002) 109.

[6] Y. Sota , O. Iguchi, M. Morikawa and T. Tatekawa and K. Maeda, Phys. Rev. E **64**(2001) 056133.

[7] Lynden Bell, Mon. Not. R. Astr. Soc. **136** (1967), 101-121.

[8] Lynden-Bell and Rodger Wood, Mon. Not. R. astr. Soc. **138** (1968), 495-525.

[9] James and Binney & Scotto Tremaine, 1987, Glactic Dynamics, Princeton.

[10] S. J. Aarseth and James Binney,Mon. Not. R. Astr. Soc. **185** (1978)227-244.

[11] A. May and T. S. Albada, 1984, MNRAS. 209. 15.

[12] David Merrit, Scott Tremaine and Doug Johnstone, 1989MNRAS, 236, 829-841.

[13] T. Padmanabhan, 1990, physics report, 188, 285.

[14] S. Aarseth, 1985, Direct Method for N-body Simulation in Multiple Time Scales, Academic Press.

一次元シート系におけるフラクタル構造と膨脹則
Fractal Structure in one-dimensional sheet model and expansion law

立川 崇之，前田 恵一
Takayuki Tatekawa and Kei-ichi Maeda
Department of Physics, Waseda University, 3-4-1 Okubo, Shinjuku-ku, Tokyo 169-8555, JAPAN
(May 7, 2003)

一次元シートモデルは重力の性質を解析するための簡単なモデルとして，昔から扱われてきた．宇宙膨張を考慮した一次元シート系について，我々は過去にフラクタル的な密度ゆらぎから成長した構造のフラクタル性，特にフラクタル次元の時間変化について解析し，初期密度ゆらぎのパターンのフラクタル次元によらず，形成される構造のフラクタル次元が収束する事を示した．その後，特徴的なスケールを持たない構造が，宇宙膨張のない一次元シート系でも形成される事が報告された．今回は宇宙膨張の規則を変えた場合の，一次元シート系の解析を行う．

One-dimensional sheet model was handled as an easy model to analyze the nature of the gravity from the old days. For one-dimensional sheet model with cosmic expansion, we analyzed evolution of fractal dimension of structure formed from primordial fractal density fluctuation. We found that the fractal dimension of nonlinear structure is independent of fractal dimension of initial pattern. Recently, the scale-free structure formed in one-dimensional sheet model without cosmic expansion. In this paper, we analyze one-dimensional sheet model with other expansion rate.

I. INTRODUCTION

一次元シートモデルは重力の性質を解析するための簡単なモデルとして，昔から扱われてきた．特にここで扱う宇宙膨張入りのシートモデルは，宇宙の大規模構造形成を考察する際の簡単なモデルとして解析がなされている．まず構造形成の摂動論である Zel'dovich 近似 [9] が，一次元シート系の厳密解を与える事が知られており，半解析的手法により厳密に時間発展を追う事が可能である．初期の研究として，初期密度揺らぎがスケールフリーのスペクトルで与えられた時，時間発展によりシートの交差が起きた後は，初期条件に依存せずに一定のベキをもつスペクトルが現れる事が示された [2]．また，スペクトルにカットオフを含む場合にも，初期条件に依存しない新たなスペクトルが現れる事が示されている [8]．

我々はかつて，初期密度揺らぎをフラクタル的にした場合の振る舞いを解析した [7]．一様・等方で平坦な膨張宇宙において，初期の密度ゆらぎによる重力不安定から構造が形成されたと考え，解析的な方法による時間発展を行った．初期条件として与えるフラクタルパターンは，フラクタル次元の異なるいくつかのモデルを考慮したが，十分に時間が経過した後の非線形構造のフラクタル次元はほぼ同じ値で落ち着くという傾向が見られた．

一方，宇宙膨張を含まないシート系についても，様々な解析がなされている．例えば系の長時間発展においては，局所的な緩和と大局的な緩和という二つの緩和が存在する事，大局的な緩和のタイムスケールに至っても，その後も系がカオス的遍歴を辿るという事等である．さらに最近では，このシート系においても一時的ではあるが，シートの空間二点相関関数がベキ的になるという，スケールフリーな構造の形成が報告されている．

ここで新たな疑問が生じる．フラクタル構造を形成する際，宇宙膨張の効果は重要なのであろうか．宇宙膨張を含まないシート系で，ベキ的な相関を持つ構造が現れる事が最近報告されている．この報告によると，ベキ的な相関が見られる構造が形成されるものの，相関関数のベキは時間変化し，最後には構造が消えてしまう．宇宙膨張の有無によって構造は劇的に変わるのだろうか．

本研究では，背景時空の膨張則を変えて構造がどのように形成されるかに迫る．従来の研究では，シートの運動を記述する運動方程式と，宇宙膨張を記述する Friedmann 方程式を連立させて解いていた．ここでは Friedmann 方程式を連立させる代わりに，背景時空の膨張を設定し，この膨張則を運動方程式に代入してシートの運動を考える．今回は，膨張が時間のベキの形で書かれる場合を考えた．

時間発展により，質量密度の高い領域が現れる．一定の密度以上の領域のみを取り出し，モノフラクタル次元を求めた．時間発展は，シートが最初に交差する時刻の数百倍のタイムスケールまで行った．結果として，このタイムスケールでは膨張則の違いによる構造のフラクタル次元の違いが大きく現れなかった．長時間の発展を行い，膨張則の違いがどのように構造に影響するかを考えていく事が必要と考えられる．

II. 時間発展の方程式

ここでは背景時空の膨張則を変えた場合の方程式とその解を示す．従来の研究では，シートの運動を記述する運動方程式と，背景時空の膨張則を与える Friedmann 方程式を両立させて解いていた．背景時空の膨張に乗った系での基礎方程式は，以下のようになる [5].

$$\frac{\partial \delta}{\partial t} + \frac{1}{a}\nabla \cdot \{\mathbf{v}(1+\delta)\} = 0 \tag{1}$$

$$\frac{\partial \mathbf{v}}{\partial t} + \frac{1}{a}(\mathbf{v}\cdot\nabla)\mathbf{v} + \frac{\dot{a}}{a}\mathbf{v} = -\frac{1}{a}\nabla\phi - \frac{1}{a\rho}C_s^2\rho_b\nabla\delta \tag{2}$$

$$\nabla^2\phi = 4\pi G\rho_b a^2\delta \tag{3}$$

$$\delta \equiv \frac{\rho-\rho_b}{\rho_b}$$

$$\phi = \Phi - \frac{2}{3}\pi G a^2\mathbf{x}^2\rho_b$$

ρ_b は平均密度，a は背景時空の膨張を記述するスケールファクターである．これらの方程式系に対し，次のように摂動を与える．

$$\mathbf{x} = \mathbf{q} + \mathbf{S}(t,\mathbf{q}) \tag{4}$$

$\mathbf{x}$ ： 共動座標 (Eular 座標)

$\mathbf{q}$ ： 粒子の Lagrange 座標, $(\nabla \times \mathbf{S} = 0)$

つまり粒子の一様分布からの微小変位を摂動として与え，運動方程式を解く．この摂動による近似法を Lagrange 近似といい，特に一次の摂動だけを取り出す近似法を Zel'dovich 近似という [9]．特に一次元シート系の場合には，Zel'dovich 近似は厳密解を与える．

以後は一次元シート系の場合に話を限って進める．摂動に関する方程式は以下のようになる．

$$\ddot{S}(t,q) + 2\left(\frac{\dot{a}}{a}\right)\dot{S}(t,q) - \frac{3}{2}\left(\frac{\dot{a}}{a}\right)^2\dot{S} = 0 \tag{5}$$

従来の研究では，この a の振る舞いを Friedmann 方程式を解く事により与えていた．平坦な宇宙モデルでの Friedmann 方程式は

$$2\frac{\ddot{a}}{a} + \left(\frac{\dot{a}}{a}\right)^2 = 0 \tag{6}$$

で与えられ，圧力が物質の質量密度に比べて十分小さい物質優勢の平坦な宇宙モデルでは，

$$a \propto t^{2/3} \tag{7}$$

となる．

本研究では，Friedmann 方程式を用いず膨張則を別に与える事にした．具体的には，膨張則が時間のべきに従う以下の式で与える．

$$a(t) = \left(\frac{t}{t_0}\right)^n \tag{8}$$

(8) を運動方程式 (5) に代入すると，その解は以下のようになる．

$$S(q,t) = D_+(t)S_1(q) + D_-(t)S_2(q) \tag{9}$$

$$D_+(t) \equiv \left(\frac{t}{t_0}\right)^{(1-2n+\sqrt{10n^2-4n+1})/2} \tag{10}$$

$$D_-(t) \equiv \left(\frac{t}{t_0}\right)^{(1-2n-\sqrt{10n^2-4n+1})/2} \tag{11}$$

例として $n = 2/3$ の場合を考えてみると，この解は

$$D_+(t) \equiv \left(\frac{t}{t_0}\right)^{2/3} \tag{12}$$

$$D_-(t) \equiv \left(\frac{t}{t_0}\right)^{-1} \tag{13}$$

となり，以前の研究で扱った解に一致する．また，膨張を止めた $n = 0$ の場合には

$$D_+(t) \equiv \left(\frac{t}{t_0}\right)^{1} \tag{14}$$

$$D_-(t) \equiv \left(\frac{t}{t_0}\right)^{0} = \text{const.} \tag{15}$$

となる．普通の一次元シート系と解の形が異なるのは，本モデルでは質量分布そのものではなく，質量分布のゆらぎが重力不安定を引き起こすようになっているからである．

シートが交差するまでは解は解析的に記述できる．二枚のシートが交差する際は，解の再構成を行い速度を入れ替える．つまり，$q = q_1$ と $q = q_2$ に対応する二枚のシートが $t = t_x$ に入れ替わる時は

$$x(q_1, t_x) \to x(q_2, t_x), v(q_1, t_x) \to x(q_2, t_x)$$
$$x(q_2, t_x) \to x(q_1, t_x), v(q_2, t_x) \to v(q_1, t_x)$$

なる入れ替えの操作を行い，解を再構成する．

この操作を繰り返していく事により，シート系の時間発展は解析的に解く事が出来る．

III. フラクタル次元

フラクタルとは，特徴的な長さを持たない図形や構造，現象などを総称したもので，自己相似性が重要な特徴として挙げられる．着目している構造について，ある一部分がそれよりも大きい部分，または全体と相似関係にあるということである．自然現象においてフラクタル性を確かめるにはフラクタル次元を計算する必要がある．

フラクタル次元は数学的に厳密な定義があるが，自然現象を解析する際には非常に扱いにくい．そこで次元の定義を実用的なものに改良する必要がある．改良された次元の定義はいくつかあるが，ここでは本研究で用いた Box-counting の方法を紹介する [1], [6]．この方法はフラクタル性が存在する範囲が有限である，自然界での現象への応用に優れている．

Box-counting の方法は以下の通りである．d 次元 Euclid 空間に存在する図形を一辺の長さが r の d 次元立方体で分割し，考えている図形の一部を含むような立方体の数 $N(r)$ を数え上げていく方法である．r をいろいろと変えた場合に

$$N(r) \propto r^{-D} \tag{16}$$

なる関係が満たされた場合，この図形のフラクタル次元は D 次元であるという．この方法を Box-counting の方法という．この方法は曲線や立体などに適用されるだけではなく，例えば川のように分岐をたくさん含むような図形の解析にも適用できる．本研究でもこの Box-counting の方法を用いてフラクタル次元の計算を行う．図 1 ではフラクタル図形である Sierpinski gasket を分割したものを例として示す．

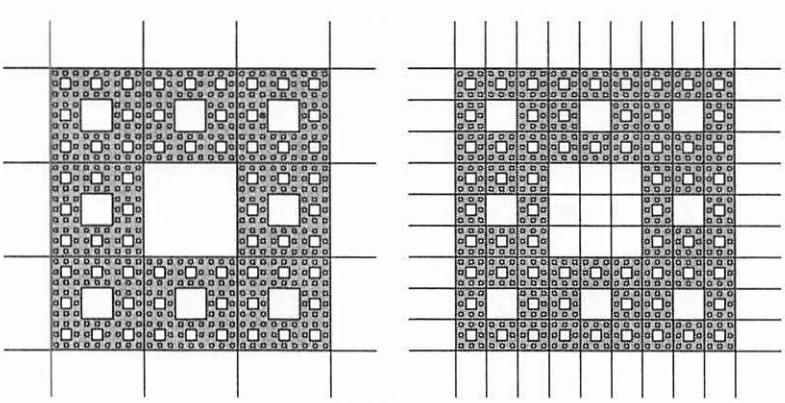

(a) (b)

FIG. 1. (a) The structure is divided into 8 cubes. (b) The structure is divided into 64 cubes.

(16) で定義される次元 D をモノフラクタル次元と呼ぶ．Box-counting の方法による次元の定義の拡張として，マルチフラクタル次元が存在する．モノフラクタル次元は，構造を立方体に分割した際，立方体が構造を含むかどうかだけで次元を計算していた．マルチフラクタル次元ではさらに，存在する構造の密度などの濃淡までを考慮する．

本研究ではモノフラクタル次元での解析のみ行う．マルチフラクタル次元の計算は今後の研究で行う予定である．

IV. 構造のフラクタル次元の時間変化

本研究では簡単な場合として空間一次元モデルを考えた．つまり，シート状の物質がシートと垂直方向にのみ運動するモデルである．初期にフラクタル的な密度ゆらぎを与えた場合に，時間発展でどのような構造が形成されていくかについて，質量分布のモノフラクタル次元を求めた．

フラクタル的な初期条件として Cantor 集合を応用したものを用いた．ただし，数学的に定義された Cantor 集合では無限小までフラクタル性が存在するが，現実の宇宙ではそのような事はあり得ないと考え下限を与えた．モデル全体のスケールを L とした時に，下限となるスケールが $10^{-3}L$ 程度になるようなモデルを考えた．つまり Cantor 集合を形成する操作を行う際に，線分を取り除く回数を有限でとどめる．以後，このスケール L は宇宙の膨張に乗った共動座標で取り扱う事にする．そうすれば，時間発展の結果によりスケールが変化しても座標変数の値を大きく変える事がなくなる．本研究では 1/10 ずつ線分を取り除く操作を 7 回繰り返した集合を用いた．この Cantor 集合のフラクタル次元は

$$D = \frac{\log 2}{\log 20/9} \simeq 0.868 \tag{17}$$

である．

線分を取り除いた領域を密度ゆらぎが負 (δ_-)，線分が残った領域を密度ゆらぎが正 (δ_+) としたモデルを与えた（図 2）．δ_+, δ_- は一定値としている．ここで作ったモデルの外側は，今考えたモデルが Cantor 集合の規則にしたがって分布していると考える．モデル間の密度揺らぎは 0 とする．時間発展の初期にはそれぞれのモデルが独立に構造を形成していくが，十分に時間が経過すると複数のモデルが合体する事がある．

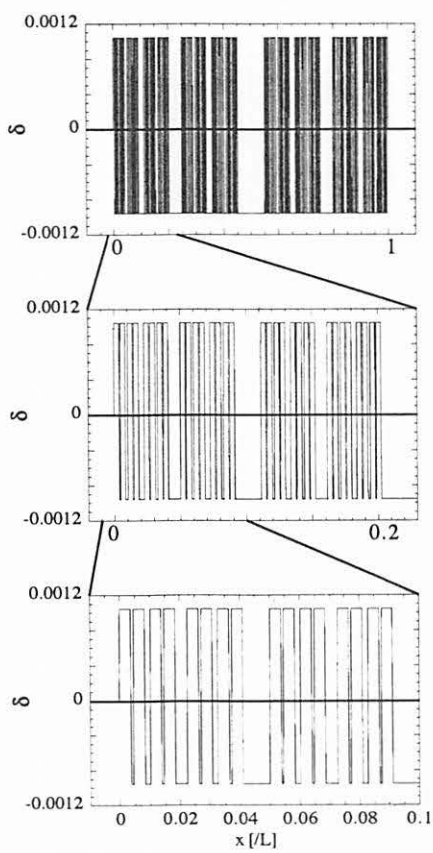

FIG. 2. Primordial density fluctuaion

まず，構造のフラクタル次元を計算する．フラクタル次元の計算方法としては，密度ゆらぎが $\delta \geq 1$ である領域を Box-counting の方法で拾い集める方法を用いた．$\delta \geq 1$ である領域は構造形成の理論でいう非線形領域であるため，線形理論で扱えないような領域に着目すれば，観測で確認されるような構造が存在するところを取り上げる事ができるだろうと考えたからである．

Box-counting の方法を用いる際，shell crossing までは構造の最小のスケール，すなわちモデルとして与えた Cantor 集合の最小の線分の長さを下限として計算した．この線分の長さは自己重力による収縮により時間変化する．shell crossing 後は構造が複雑に入り組むようになるので，最小のスケールとしては $2^{-16}L$ を下限として計算した．上限は Box の数が少なくなるために生じる誤差を避けるため，$10^{-1}L$ 程度とした．すなわちモデル全体を 10 個程度に区切るスケールである．

今回は膨張則を変えた 6 通りのモデルを考えた．すなわち

$$a \propto t^n \quad \left(n = \frac{1}{6}, \frac{1}{3}, \frac{1}{2}, \frac{2}{3}, \frac{5}{6}, 1\right) \tag{18}$$

という膨張則の場合である．$a = 2/3$ が平坦な宇宙である Einstein-de Sitter 宇宙モデルに対応する．

結果を図 3 に示す．これらの図は，最初にシートが交差する時刻を $\tau = 1$ で規格化し，$\tau = 100$ までのモノフラクタル次元の変化をプロットしたものである．膨張則の違いによるフラクタル次元の変化，安定性はまだはっきりしていない．今後構造がどのようになっていくかは長時間の発展が必要である．

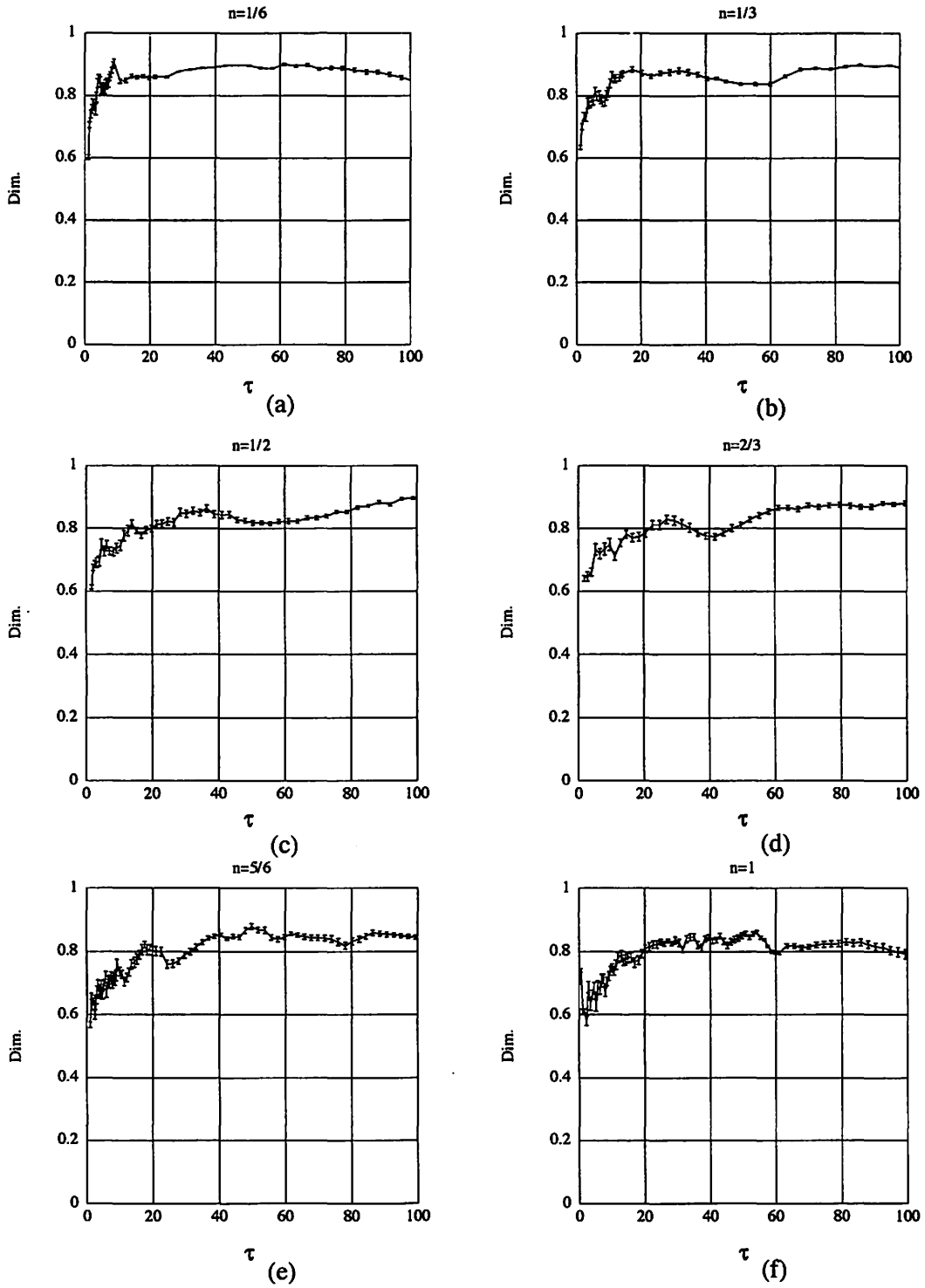

FIG. 3. The evolution of mono-fractal dimension of nonlinear ($\delta \geq 1$) structure. These figures show time evolution until $\tau = 100$. We set $\tau = 1$ as first shell-crossing time. (a) $n = 1/6$ case. (b) $n = 1/3$ case. (c) $n = 1/2$ case. (d) $n = 2/3$ case. (e) $n = 5/6$ case. (f) $n = 1/6$ case.

V. CONCLUSION

本研究では線分を 1/10 ずつ取り除く Cantor 集合を用いて初期密度ゆらぎを与えた．最初に密度が発散する時間の 100 倍まで発展させ比較したところ，膨張則による構造の違いははっきりと現れなかった．だが，膨張の入っていない一次元シート系では，free fall time の数百万倍にも及ぶ長時間の発展で，大局的な緩和が発見されている．膨張を含むモデルでこのような長時間の発展を行った場合，構造はどのようになっていくのか，膨張則の違いがどのように現れるのかという疑問がある．今後は長時間の発展を行って構造を解析する必要がある．

解析手法に関して，本研究では密度が高い領域の分布に対してモノフラクタル解析を行った．宇宙膨張を考慮した一次元シート系において，マルチフラクタル解析による構造の次元を求めた研究がなされている [4]．彼等はマルチフラクタル次元が収束する事を主張し，特にモノフラクタル次元は 0.6 程度になるとしているが，この研究では長時間の発展を行っていない．長時間の緩和によりマルチフラクタル次元が収束していくのか，初期条件の依存性が現れるのかどうかを今後調査していく予定である．

---

[1] K. Falconer, *Fractal Geometry*, (Wiley 1990).
[2] N. Gouda and T. Nakamura, Prog. Theor. Phys. **79** (1988) 765; Prog. Theor. Phys. **81** (1989) 633.
[3] H. Koyama and T. Konishi, Phys. Lett. A **279** (2001) 226; Europhys. Lett. **58** (2002) 356; Phys. Lett. A **295** (2002) 102.
[4] B. N. Miller and J. L. Rouet, Phys. Rev. **E65** (2002) 056121.
[5] P. J. E. Peebles, *The Large Scale Structure of the Universe*, (Princeton University Press 1981).
[6] 高安　秀樹, フラクタル, (朝倉書店 1986)
高安　秀樹, フラクタル科学, (朝倉書店 1987)
[7] T. Tatekawa and K. Maeda, Astrophys. J. **547** (2001) 531.
[8] T. Yano and N: Gouda, Astrophys. J. Supp. (1999).
[9] Ya. B. Zeldovich, Astron. Astrophys. **5** (1970) 84.

Formation and Evolution of a Globular Cluster System

Tsuyoshi Sakamoto [1] and Masashi Chiba [2]

Abstract

We present the dynamical evolution of a globular cluster system in disk galaxies, for the purpose of setting important limits on its initial state, i.e., the initial mass function of globular clusters, their spatial distribution, and velocity anisotropy, thereby allowing us to elucidate the initial state of a host galaxy where a cluster system resides. A globular cluster system is also a good mass tracer of its host galaxy, whereby the effects of its dynamical evolution must be properly taken into account for the correct, unbiased mass estimate.

Based on this motivation, we develop semi-analytical models for the dynamical evolution of a globular cluster system embedded in various galactic potentials. In sharp contrast to simple spherical models examined previously, our models fully take into account the non-spherical nature of a galactic potential, i.e., the presence of a galactic disk component which strongly affects the dynamical evolution of globular clusters in the course of their orbital motions. In an axisymmetric potential which allows an explicit evaluation of the so-called third integral of motions, we consider the several mass-loss processes of globular clusters, including the effects of stellar evolution in cluster stars, their two-body gravitational relaxation, and gravitational shocks acting on a cluster.

1 Introduction

A globular cluster is a spherical, compact stellar system consisting of 10^3 to 10^6 stars and constitutes one of the fundamental building blocks of the Universe. Such clusters are not distributed uniformly across the Universe but are mostly found around brighter, more massive galaxies with various morphological types, such as elliptical galaxies, lenticular galaxies, disk galaxies, irregular galaxies, and dwarf galaxies. Thus, each galaxy is surrounded by a group of several to ten thousand globular clusters, which is called *a globular cluster system* (hereafter referred to as a GCS for simplicity).

Globular clusters in a GCS are usually as old as Hubble time, and hence a GCS plays important roles in studying when, where, and how globular clusters formed. Studies of a

[1] Department of Astronomical Science, The Graduate University for Advanced Studies, Mitaka, Tokyo 181-8588, Japan

[2] National Astronomical Observatory, Mitaka, Tokyo 181-8588, Japan

GCS are also closely associated with the most important issue in galactic astronomy, i.e., when and how a galaxy formed, where a GCS is found. In particular, various properties of globular clusters in each GCS, such as their total number, mass function, spatial and kinematic structures, age distribution, and metallicity (color) distribution, provide us with useful information on the formation of a GCS in each host galaxy as well as the early evolution of a host galaxy itself.

Furthermore, since a globular cluster is so compact and intrinsically bright, it is relatively easy to identify itself and to obtain its spectroscopic data in both our Galaxy and other external galaxies. In particular, based on a plenty of intrinsically bright horizontal-branch stars found in a cluster and the (rather tight) linear relation between the absolute magnitude of such a stellar population and its metallicity, it is possible to obtain the accurate distance to each globular cluster. Thus, combined with spatial and kinematical information of clusters, such as their positions and radial velocities inside its host galaxy, studying a GCS is important in clarifying another fundamental issue in galactic astronomy, i.e., the determination of the global mass distribution of a galaxy, especially the distribution of dark matter.

1.1 Observed properties of globular clusters in various galaxies

Advent of high-resolution observation by the HST and 8-10m class ground-based telescopes has made it possible to resolve extragalactic globular clusters in more distant galaxies, i.e., those outside the Local Group. In particular, surveys of globular clusters in several clusters of galaxies were made, where various morphological types of galaxies are available, thereby enabling us to compare the properties of globular clusters among galaxy types. However, the observations of extragalactic globular clusters are yet incomplete, especially in spiral galaxies: the detection of globular clusters in such galaxies is generally difficult because of uneven luminosity distribution of galactic disks mainly due to extinction by interstellar dust. On the other hand, the lack of dust extinction in elliptical galaxies makes their luminosity distribution smooth and thus makes it easy to identify globular clusters distributed over such smooth luminosity systems. Thus, more cluster samples have been available for elliptical galaxies than for spiral galaxies and this observational bias should be remarked for any statistical analyses of globular clusters.

Nonetheless, several characteristic properties of clusters, such as their color distribution and luminosity function, have been accumulated for various types of host galaxies. For instance, the color distribution of clusters in most of giant galaxies, i.e., disk and elliptical

galaxies, is characterized by a bimodal function, as found in the MW and M31 (Goudfrooij et al. 2003). Also, the luminosity function of clusters in most of such (isolated) galaxies has a Gaussian-like form with a peak located at the same absolute magnitude as that of the MW globular cluster system. It is worth noting here that in merging galaxies like the Antennae galaxy, there is no apparent peak in luminosity functions of globular clusters; they appear to follow a simple, power law-like function with abundant faint clusters (Zhang & Fall 1999). Even for non-merging galaxies showing similarly a Gaussian-like function of clusters, their total number appears to depend rather strongly on a type of galaxies: in giant galaxies, the total number of clusters in early-type galaxies ($\sim$ a few $\times$1000) is about ten times as large as that in late-type galaxies ($\sim$ a few $\times$100), whereas only several clusters are found in dwarf galaxies (Goudfrooij et al. 2003).

Now that several key properties of extragalactic globular clusters are available, such as their total number, luminosity function, and metallicity (color) distribution, as described above, it is intriguing to address the question, *what causes the resemblance or difference in the properties of globular cluster systems among various galaxies?* Clarifying this issue is of great importance as it is closely related to the origin of globular cluster systems in various galaxies.

1.2 Dynamical evolution of a globular cluster system

During their life time, globular clusters are subject to various mass-loss processes, as will be described in more details in the next section. In order to utilize such clusters as probes of galactic past and/or dynamics, it is important to understand how the various properties of a GCS undergo time evolution, depending on its initial condition and galactic environment.

Most of the previous theoretical works on a GCS have mainly focused on the change of the mass function of its member clusters as a result of several mass-loss processes, based on several methods, such as semi-analytic method, Fokker-Planck code, and N-body simulation (e.g., Fall & Zhang 2001, hereafter FZ01). For instance, based on their semi-analytic model, FZ01 investigated the evolution of the mass function for a GCS over the period of 12 Gyr, on the assumption that its initial mass function takes either of four different functional forms: a simple power law, truncated power law, lognormal function, or Schechter function. They showed that all of the models starting from different initial mass functions appear to develop a single peak in the mass function, and that the position of this peak is remarkably close to that as observed in the MW globular cluster system. FZ01 also considered two different kinematic structures for the initial set up of a GCS,

isotropic velocity distribution of clusters over all radii (Model A) and radially anisotropic velocity distribution, where its degree of anisotropy is made larger with increasing distance from the galactic center (Model B). Although both models result in the mass function which is approximately in agreement with that in the MW, Model B appears to yield a mass function which resembles that in the MW more closely than Model A, when the radial distribution of the mass function is also considered.

While the evolution of the mass function of a GCS has been studied well, our understanding of the evolution of its spatial and kinematic structures inside a host galaxy is yet highly limited; only a few studies have focused on the issues, based on a simple assumption for galactic environment (e.g., Baumgardt 1998). For instance, in the work of Baumgardt (1998), the evolution of a GCS was followed in a simple, spherical dark halo, where the spatial and velocity distributions of clusters were modeled as a power-law density distribution with various indices and various degree of velocity anisotropy, respectively. It was shown that clusters are destroyed more effectively in inner parts of a galaxy than its outer parts by galactic tides, so that their density distribution is made flat in all of the models he considered. He also found that as clusters on radial orbits come close to the galactic center and thus are preferentially destroyed, their velocity distribution is made more tangentially anisotropic in inner parts of a host galaxy, while its outer parts remain unchanged.

It is worth noting here that several mass-loss processes of clusters depend on the change of external gravitational force acting on them during the course of their orbital motion, i.e., the detailed form of gravitational potential in a host galaxy. Hence, an assumption of a spherical potential adopted above is too simple to apply to actual galaxies holding bulge and disk components: such non-spherical parts of a gravitational potential strongly affect the evolution of a GCS. However, comprehensive studies of these effects on the evolution of spatial and kinematic structures of a GCS are yet lacking, so that it remains unclear how such a general consideration of galactic environment affects the evolution of a GCS, or conversely the initial state of a GCS by tracing back its evolution. Therefore, it is yet unsettled as to how many clusters were existing before they disappeared by their dynamical evolution, or in other words, how many clusters formed in each host galaxy. This indicates that more detailed studies for the evolution of a GCS are required for the purpose of setting useful limits on the formation process of globular clusters in a galaxy.

1.3 Motivation for this study

As described in previous subsections, the data of extragalactic globular clusters have been accumulated and their statistical properties have been understood gradually. However, our understanding of their evolutionary process is yet limited to some specific aspects, such as the evolution of a mass function for clusters, while the effects of their spatial and velocity distributions are neglected for the sake of simplicity. For this reason, our knowledge on the initial state of a GCS, including its mass function and total number of clusters as well as their spatial and kinematic structures in each host galaxy, is yet highly limited. Also, the evolution of a GCS affects its dynamical state inside a host galaxy, so that the mass determination based on a GCS as a dynamical tracer of a galaxy ought to be modified; it is yet unknown how much evolutionary correction is required for the mass estimate when using a GCS.

Motivated by this backgound, we construct general dynamical models for a GCS, so as to follow the evolution of its mass function, spatial distribution, and kinematic structure, depending on initial settings of a GCS and its surrounding environment in a host galaxy.

In this paper, we consider only a *disk galaxy* as a host of a GCS for the following three reasons. (1) Compared to elliptical galaxies, dynamical structure of a disk galaxy is accurately determined from the analysis of its rotation curve. (2) Detailed dynamical properties of globular clusters are available in the nearest disk galaxies, i.e., in the MW and M31, as opposed to clusters in more distant, early-type galaxies, where no dynamical data are available. (3) If one follows the hypothesis that an elliptical galaxy formed from the major merger between two disk galaxies, then the evolutionary properties of a GCS in a disk galaxy are keys to understanding those of a GCS in an elliptical galaxy.

2 Galactic potential

We adopt an axisymmetric gravitational potential for the orbit calculation of a globular cluster in a host galaxy. We then set a distribution function of clusters, which follows isolating integrals of cluster motion in a consistent manner.

It is well known that for an axisymmetric gravitational potential, two classical integrals exist, i.e., the orbital energy, E, and the angular-momentum component parallel to the symmmetry axis, L_z, whereas no general expression exists for the third integral, I_3, which is thus estimated numerically in most cases. If a distribution function of clusters depends only on E and L_z, their velocity dispersions $< V_\varpi^2 >$ and $< V_z^2 >$ in cylindrical coordinates

(ϖ, z) ought to be identical and thus lack generality for the application to actual cluster systems. However, it is also known that an exact third integral is available if a gravitational potential is of Stäckel form, for which the Hamilton-Jacobi equation separates in ellipsoidal coordinates. Every orbit in this type of potential possesses three exact isolating integrals of motion, E, I_2, and I_3, which are known explicitly. Therefore, we adopt Stäckel potential as the galactic potential in our following calculations.

We define prolate spheroidal coordinates as the triple (λ, ϕ, ν), where ϕ is the azimuthal angle in cylndrical coordinates (ϖ, ϕ, z) and λ and ν are the two roots for τ of

$$\frac{\varpi^2}{\tau + \alpha} + \frac{z^2}{\tau + \gamma} = 1, \tag{2.1}$$

with $-\gamma \leq \nu \leq -\alpha \leq \lambda$. The parameters α and γ are constants and give foci ($\varpi = 0$, $z = \pm\Delta$) of the spheroids of constant λ and the hyperboloids of constant ν in the plane of $\phi = constant$ for $\Delta = (\gamma - \alpha)^{1/2}$. The relations between (λ, ν) and (ϖ, z) are given by

$$\varpi^2 = \frac{(\lambda + \alpha)(\nu + \alpha)}{\alpha - \gamma}, \quad z^2 = \frac{(\lambda + \gamma)(\nu + \gamma)}{\gamma - \alpha}. \tag{2.2}$$

An axisymmetric gravitational potential of Stäckel type, V, is written in the coordinates as

$$V(\lambda, \nu) = -\frac{(\lambda + \gamma)G(\lambda) - (\nu + \gamma)G(\nu)}{\lambda - \nu} \equiv -\psi, \tag{2.3}$$

where $G(\tau)$ is an arbitrary function and ψ is the relative potential. We take

$$G(\tau) = G_d(\tau) + G_h(\tau), \tag{2.4}$$

where $G_d(\tau)$ and $G_h(\tau)$ are the contribution from the disk and the dark halo, respectively. Following Vedel and Sommer-Larsen (1990), we adopt the perfect oblate spheroid for $G_d(\tau)$,

$$G_d(\tau) = \frac{2G}{\pi} \frac{M_d}{\sqrt{\tau + \gamma}} \arctan \sqrt{\frac{\tau + \gamma}{-\gamma}}, \tag{2.5}$$

where G is the gravitational constant and M_d is the total mass of the disk, whereas for $G_h(\tau)$, the s=2 model of de Zeeuw, Peletier, and Franx (1986) is adopted,

$$\begin{aligned} G_h(\tau) \;=\; & -4\pi G \rho_0 \gamma_h \left[\ln\left(\frac{\alpha_h}{\gamma_h}\right) - \frac{\tau + 2\gamma_h - \alpha_h}{2(\tau + \gamma_h)} \ln\left(\frac{\tau}{-\gamma_h}\right) + \frac{2\gamma_h - \alpha_h}{\sqrt{-\gamma_h}} \right. \\ & \left. \times \left(\frac{1}{\sqrt{\tau + \gamma_h}} \arctan \sqrt{\frac{\tau + \gamma_h}{-\gamma_h}} - \frac{1}{\sqrt{\gamma_h - \alpha_h}} \arctan \sqrt{\frac{\gamma_h - \alpha_h}{-\gamma_h}} \right) \right], \end{aligned} \tag{2.6}$$

where ρ_0 is the mass density of the halo at the galactic center. The parameters γ_h and α_h are arbitrary and play the same role as γ and α, respectively, in defining the current

prolate spheroidal coordinates. In order to make this combined potential of Stäckel form, we choose the coordinates so that the focus of the disk is identical to that of the halo,

$$\gamma_h = \gamma - b, \ \alpha_h = \alpha - b, \tag{2.7}$$

where b is an arbitrary parameter. From Eqs. (2.6) and (2.7), $G_h(\tau)$ is written as

$$\begin{aligned} G_h(\tau) &= -4\pi G\rho_0(\gamma - b)\left[\ln\frac{\Delta^2 - \gamma - b}{-\gamma + b}\right. \\ &\quad -\frac{\tau + \gamma + \Delta^2}{2(\tau+\gamma)}\ln\frac{\tau + b}{-\gamma + b} + \frac{\Delta^2 + \gamma - b}{\sqrt{-\gamma + b}} \\ &\quad \left.\times\left(\frac{1}{\sqrt{\tau+\gamma}}\arctan\sqrt{\frac{\tau+\gamma}{-\gamma+b}} - \frac{1}{\Delta}\arctan\frac{\Delta}{\sqrt{-\gamma+b}}\right)\right]. \end{aligned} \tag{2.8}$$

This potential is characterized by Δ, M_d, ρ_0, the axial ratio of the disk, $q_d(\equiv\sqrt{\gamma/\alpha})$, and the axial ratio of the halo near the galactic center, $q_h(\equiv\sqrt{\gamma_h/\alpha_h})$.

As a standard model for this type of galactic potential, we adopt the following parameters after some experiments: $\Delta = 4$ kpc, $M_d = 6\times10^{10}\ M_\odot$, $\rho_0 = 5.89\times10^7\ M_\odot\text{kpc}^{-3}$, $(-\gamma)^{1/2} = 0.125$ kpc, $(b-\gamma)^{1/2} = 3.75$ kpc, resulting in $q_d = 0.031$, $q_h = 0.68$. Based on this standard model, we plot, in Fig. 2.1, the rotation curve and vertical density distribution at the solar radius ($\varpi = 8$ kpc). It follows that the rotation curve is approximately flat outside $\varpi \approx \Delta$ and its value at the solar radius is given as $V_c \approx 219$ km s^{-1}. Also, the local density at the solar radius, ρ_{local}, (including both disk and dark halo contributions) is given as $\rho_{local} = 0.13\ M_\odot\text{pc}^{-3}$. For other galactic potentials, we will change the values of Δ, M_d and ρ_0 to see the effects of various galactic environments on the final results.

In this Stäckel-type potential, the equations of motion of a globular cluster are given as

$$p_\tau^2 = \frac{1}{2(\tau+\alpha)}\left[G(\tau) - \frac{I_2}{\tau+\alpha} - \frac{I_3}{\tau+\gamma} - \epsilon\right], \ \tau = \lambda, \nu \tag{2.9}$$

$$p_\phi^2 = L_z^2 = 2I_2, \tag{2.10}$$

where ϵ, I_2, and I_3 are three isolating integrals allowed by the potential, i.e.,

$$\epsilon = -H \tag{2.11}$$

$$H = \frac{p_\lambda^2}{2P^2} + \frac{p_\phi^2}{2\varpi} + \frac{p_\nu^2}{2R^2} - \psi(\lambda,\nu) \tag{2.12}$$

$$P^2 = \frac{\lambda - \nu}{4(\lambda+\alpha)(\lambda+\gamma)}, \ R^2 = -\frac{\nu - \lambda}{4(\nu+\alpha)(\nu+\gamma)} \tag{2.13}$$

$$I_2 = \frac{1}{2}L_z^2, \tag{2.14}$$

$$I_3 = \frac{1}{2}(L_x^2 + L_y^2) + \Delta^2\left[\frac{1}{2}v_z^2 - z^2\frac{G(\lambda) - G(\nu)}{\lambda - \nu}\right], \tag{2.15}$$

where $\mathbf{L} = (L_x, L_y, L_z)$ is the angular momentum in rectangular coordinates. The velocities of a globular cluster on an orbit characterized by the integrals (ϵ, I_2, I_3) can be expressed as

$$v_\lambda = \pm\sqrt{\frac{2(I_3^+ - I_3)}{\lambda - \nu}}, \quad v_\phi = \pm\sqrt{\frac{2I_2}{\varpi}}, \quad v_\lambda = \pm\sqrt{\frac{2(I_3 - I_3^-)}{\lambda - \nu}}, \tag{2.16}$$

where

$$I_3^+(\epsilon, I_2, \lambda) = (\lambda + \gamma)[G(\lambda) - \epsilon] - \frac{\lambda + \gamma}{\lambda + \alpha}I_2 \tag{2.17}$$

$$I_3^-(\epsilon, I_2, \nu) = (\nu + \gamma)[G(\nu) - \epsilon] - \frac{\nu + \gamma}{\nu + \alpha}I_2. \tag{2.18}$$

Having obtained the form of a galactic potential, we assume that the orbital structure of the initial globular cluster system follows a phase space distribution function which depends only on isolating integrals, ϵ, I_2, and I_3:

$$f(\epsilon, I_2, I_3) = \begin{cases} (e^{\epsilon/\sigma_c} - e^{\epsilon_0/\sigma_c^2})e^{-[2(I_2+I_3)]/2\sigma_c^2 r_A^2}, & \epsilon \geq \epsilon_0 \\ 0, & \epsilon < \epsilon_0 \end{cases} \tag{2.19}$$

where σ_c is a characteristic velocity, r_A is the core radius, and ϵ_0 is minus the cutoff energy (Vedel and Sommer-Larsen 1990). In a spherical potential, this distribution function yields velocity dispersions $\sigma_r = \sigma_c$ and $\sigma_T = \sigma_c[1 + (r/r_A)^2]^{-1/2}$ in the radial and transverse directions, respectively, where r_A marks the transition from a nearly isotropic to a predominantly radial velcity dispersion. The number density distribution corresponding to the distribution function is written as

$$\rho(\varpi, z) = \frac{2\sqrt{2}}{\varpi}\int_{\epsilon_0}^{\psi(\varpi,z)} d\epsilon \int_0^{I_2^+(\epsilon,\lambda,\nu)} \frac{dI_2}{\sqrt{I_2}} \times \int_{I_3^-(\epsilon,I_2,\nu)}^{I_3^+(\epsilon,I_2,\lambda)} \frac{f(\epsilon, I_2, I_3)dI_3}{\sqrt{(I_3^+ - I_3)(I_3 - I_3^-)}}. \tag{2.20}$$

In a spherical logarithmic potential, $\psi = V_c \log r$, $\rho(r)$ is simply given as

$$\rho(r) \propto [1 + (r/r_A)^2]^{-1} r^{-\gamma_g} \tag{2.21}$$

with $\gamma_g = (V_c/\sigma_c)^2$.

As a standard model for the initial distribution of a globular cluster system, we adopt the following parameters: $\epsilon_0 = \psi(\varpi = 250 \text{ kpc}, z = 0 \text{ kpc})$, $r_c = 5$ kpc, and σ_c=145

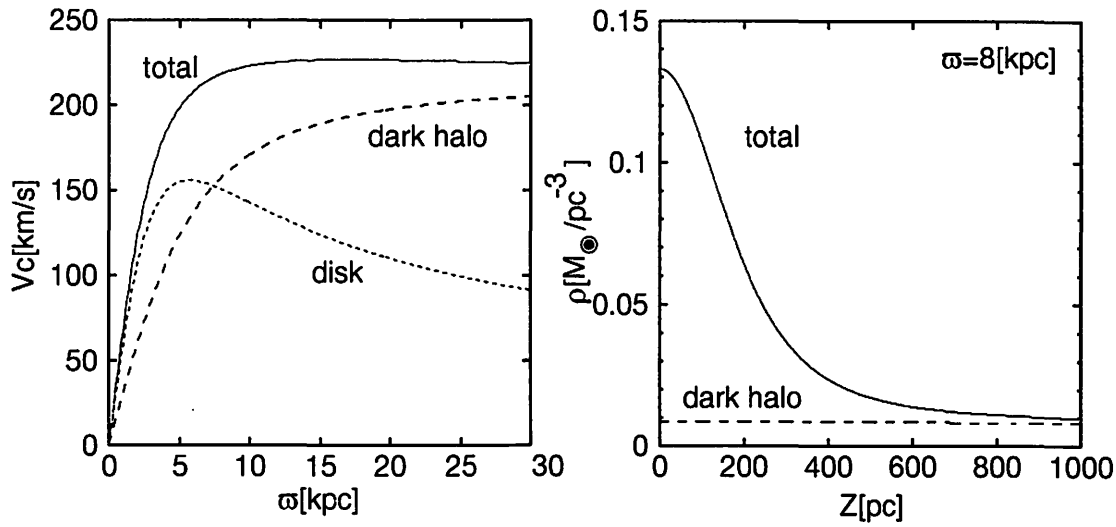

Figure 2.1: Rotation curve for a standard potential of a galaxy (left panel) and its vertical density distribution at $\varpi = 8$ kpc (right panel).

km s^{-1}, resulting in $\gamma_g \approx 2.3$. For other initial distributions of cluster systems, we will change only the value of r_A, i.e., the location of transition between a nearly isotropic and predominantly radial velcity dispersions.

3 Mass-loss process of a globular cluster

In the course of its orbital motion, a globular cluster is subject to various disruptive processes on various timescales. Stellar evolutionary processes, i.e., a combination of supernovae, stellar winds, and other ejecta, remove mass from a globular cluster on a short timescale ($t \lesssim$ few $\times 10^8$ yr). On long timescales ($t \gtrsim$ few $\times 10^8$ yr), there exit three different dynamical processes which also remove mass from a globular cluster. As the first process, internal relaxation by two-body scattering, i.e. two-body ralaxation, causes some stars, especially low-mass stars, to gain enough energy to escape from the cluster. As the second process, when a cluster orbits around a host galaxy, it experiences a time-dependent tidal field, which may vary rapidly when it passes rapidly near the bulge or through the disk that stars in the outer parts of the cluster cannot respond adiabatically. The corresponding change in the energy of stars (heating and relaxation) causes some of them to escape from the cluster. These effects are known respectively as bulge and disk shocks and more generically as gravitational shocks. As the third process, the deceleration of a cluster induced by

the wakes of stars and dark matter particles in a host galaxy behind it, dynamical friction, causes the cluster to spiral toward the galactic center, where it may be destroyed by the strong tidal field. We note that the effects of dynamical friction on a cluster depend on its mass and the position in the host galaxy, and it is especially important *only if* clusters are located near the galactic center; most of them orbiting in the outer parts of the Galaxy are not spiraled toward the galactic center by dynamical friction. More specifically, following the simple analysis of Fall and Zhang (2001, hereafter FZ01), which evaluated the disruption time t_{df} by dynamical friction for the globular clusters in the Milky Way, the vast majority of them have $t_{df} > 20$ Gyr. Thus, we neglect dynamical friction in calculating mass loss of a globular cluster.

In our model for the evolution of a globular cluster, we consider three processes that reduce the mass of a cluster: (1) evaporation driven by two-body relaxation, (2) evaporation driven by gravitational shocks, and (3) mass loss driven by stellar evolution (supernovae, stellar winds, and other ejecta). These processes may be correlated and mutually reinforcing in a realistic globular cluster, but we assume that they operate independently each other in order to simplify our calculation of mass loss of a cluster. Thus, following many previous studies (see Spitzer 1987, FZ01), we write

$$\dot{M} = -[\nu_{ev}(t) + \nu_{sh}(t) + \nu_{se}(t)]M, \quad . \tag{3.1}$$

where $\nu_{ev}(t)$, $\nu_{sh}(t)$, and $\nu_{se}(t)$ are fractional rates of two-body relaxation, gravitational shocks, and stellar evolution, respectively.

The fractional rate of mass loss by stellar evolution, $\nu_{se}(t)$, depends on the age of a cluster and the stellar initial mass function. We compute $\nu_{se}(t)$ from the Leitherer et al. (1999) model with the Salpeter initial stellar mass function. We find that, following the model of stellar evolution, the mass of a cluster drops approximately exponentially with time over the period of $t \lesssim 3 \times 10^8$ yr, reaching about 60 % of its initial value, and then remains unchanged in the later stages.

The effects of the two stellar dynamical processes, two-body relaxation (ν_{ev}) and gravitational shocks (ν_{sh}), respectively, can be analytically written as

$$\nu_{ev} = \frac{\xi_e}{t_{rh}} = \frac{7.25\xi_e m G^{1/2} \ln\Lambda}{M^{1/2} k^{3/2} r_t^{3/2}}, \tag{3.2}$$

$$\nu_{sh} = \frac{\epsilon_h \kappa_s \bar{A}}{t_{sh}} = \frac{6.67\epsilon_h \kappa_s \bar{A} g_m^2 k^3 r_t^3}{GMP_\phi V_z^2}, \tag{3.3}$$

(Spitzer 1987; FZ01). In Eq. (3.2), ξ_e is the fraction of stars that escape from a cluster per half-mass relaxation time t_{rh} by two-body scattering, r_t is the tidal radius of a cluster,

Table 1: the parameters of mass-loss calculation of a globular cluster

ξ_e	0.045
k	0.145
m	0.7 $M_\odot$
κ_s	1
$\ln \Lambda$	12
ϵ_h	7/3

k relates its tidal radius with the half-mass radius, i.e., $r_h = kr_t$, m is mean stellar mass, and $\ln \Lambda$ is the Coulomb logarithm. We adopt $\xi_e = 0.045$ and $k = 0.145$ (Hénon 1961), as obtained from the self-similar evolution of a tidally limited cluster (with a single stellar mass) by two-body relaxation alone. In Eq.(3.3), t_{sh} is the gravitational shock heating time for first-order energy changes in the impulse approximation (Ostriker, Spitzer, & Chevalier 1972), $\bar{A}$ is a correction for partial adiabatic (i.e. nonimpulse) response averaged over all stars in a cluster. The parameter ϵ_h accounts approximately for the addition of second-order energy changes, also known as shock-induced relaxation (Spitzer & Chevalier 1973; Kundić & Ostriker 1995). The other parameter κ_s relates the fractional change in energy caused by gravitational shocks to the corresponding fractional change in mass, i.e. $\dot{M}/M = \kappa_s \dot{E}/E$, where $\dot{E}$ and E are the total energy change and the total energy of a cluster, respectively. Also, in Eq.(3.3), V_z is the vertical component of the velocity of a cluster relative to the disk, P_ϕ is the azimuthal period of its orbit around the host galaxy, and g_m is the maximum vertical acceleration caused by the disk. The adopted values of parameters in Eqs.(3.2) and (3.3) are summarized in Table 1.

4 Numerical modeling of dynamical mass-loss processes

In order to simplify the calculation of these two dynamical processes, we adopt several numerical approximation as follows.

(i) Method for calculating a tidal radius

First, we assume that each cluster has an outer, limiting radius r_t determined by the tidal field of a host galaxy at the pericenter of its orbit and that each cluster evolves

at constant mean density, as derived from $\bar{\rho} = M/(4\pi r_t^3/3)$. In the case of a spherical galactic potential, the pericentric distance from the galactic center remains unchanged at each passage, so that a cluster on such an orbit may hold a constant mean density, $\bar{\rho}$, as determined from r_t estimated as

$$r_t = \left(\frac{GM}{\omega^2 - d^2\Phi/dr^2} \right)^{1/3}, \tag{4.1}$$

where ω is its angular velocity, and Φ is the galactic potential (King 1962). For non-spherical cases as assumed here, where the pericenter differs at each orbital passage, we assume that a cluster is supposed to have a constant mean density as well, as determined from the smallest tidal radius r_t, i.e., when cluster's orbit holds the smallest pericenter, and that Eq.(4.1) for a spherical limit yet provides us with an approximate estimator of r_t in non-spherical cases.

Taylor & Babul (2001, hereafter TB01) also adopted Eq.(4.1) for their axisymmetric model, where the asphericity of the potential was averaged to estimate $d^2\Phi/dr^2$, i.e.,

$$\frac{d^2\Phi}{dr^2} = \frac{d^2\Phi_{sph}}{dr^2} = \frac{d}{dr}\left[\frac{GM(<r)}{r^2} \right], \tag{4.2}$$

where Φ_{sph} is the spherical potential with the same total mass $M(<r)$ interior to r as the axisymmetric density distribution. However, the calculation of this $M(<r)$ is tedious as the potential we adopt is complex, while this method of estimating r_t is not necessarily accurate. We instead obtain a differential equation for $d^2\Phi/dr^2$ at the position of a cluster center and solve it in a self-consistent manner: we first obtain the gravitational force f

$$f = \left(\frac{d\Phi}{dr} \right)_{\theta,\phi} = \left(\frac{\partial\Phi}{\partial R} \right)_Z \frac{R}{r} + \left(\frac{\partial\Phi}{\partial Z} \right)_R \frac{Z}{r} \tag{4.3}$$

at four points $(R \pm \delta R, Z)$, $(R, Z \pm \delta Z)$ near the center of the cluster (R, Z), where δR and δZ are infinitesimal, and then calculate $d^2\Phi/dr^2$ at the center of the cluster (R, Z),

$$\left.\frac{d^2\Phi}{dr^2}\right|_{(R,Z)} = \left.\left(\frac{df}{dr} \right)_{\theta,\phi}\right|_{(R,Z)} = \left.\left(\frac{\partial f}{\partial R} \right)_Z\right|_{(R,Z)} \frac{R}{r} + \left.\left(\frac{\partial f}{\partial Z} \right)_R\right|_{(R,Z)} \frac{Z}{r}. \tag{4.4}$$

For the comparison between the above two different methods to estimate $d^2\Phi/dr^2$, we use a perfect oblate spheroid as a gravitational potential, where the surfaces of constant density are all similar concentric ellipsoids, and calculate $d^2\Phi/dr^2$ at specific points in the perfect oblate spheroids with various axial ratio q of the mass density. Fig.4.1 shows

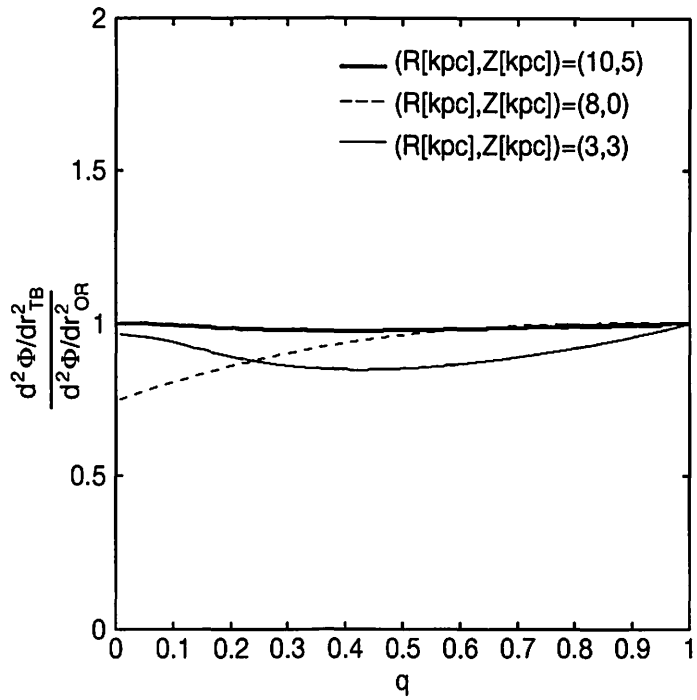

Figure 4.1: Ratio between $d^2\Phi/dr^2$ obtained from Taylor & Babul's (2001) and our methods for the perfect oblate spheroids with axial ratio q of mass density at some points (R [kpc], Z [kpc])=(10,5), (8,0), and (3,3) in the potential.

the ratio between $d^2\Phi/dr^2$ obtained from TB01's and our methods for the perfect oblate spheroids with various axial ratios q of mass density. The thick solid, thin solid, and dashed lines denote (R [kpc], Z [kpc]) = (10, 5), (8,0), and (3,3) in cylindrical coordinates in the potential, respectively. At (R [kpc], Z [kpc]) = (10, 5), $d^2\Phi/dr^2$ obtained from our method agrees with that obtained from TB01's method in all axial ratios q of mass density. At the closer point ((R [kpc], Z [kpc]) = (3, 3)) to the galactic center and at the point ((R [kpc], Z [kpc]) = (8, 0)) near the disk, the ratio decreases with decreasing axial ratio q. However, since the minimum of this ratio is ~0.75 at $q \sim 0$ and (R [kpc], Z [kpc]) = (8, 0), the tidal radius obtained from our method almost agrees with that obtained from TB01's method, independent of the position in the host galaxy and the axial ratio of mass density of it.

With the constant density assumption for it as discussed above, Eq.(3.1)-(3.3) take the form

$$\dot{M} = -\mu_{ev} - \nu_{sh} M, \tag{4.5}$$

$$\mu_{ev} = 269\xi_e (G\bar{\rho})^{1/2} m \ln\Lambda, \tag{4.6}$$

$$\nu_{sh} = \frac{4.84 \times 10^{-3} \epsilon_h \kappa_s \bar{A} g_m^2}{G\bar{\rho} P_\phi V_z^2}, \tag{4.7}$$

where μ_{ev} and ν_{sh} are constants. The coefficients $\bar{A}$ and g_m in Eq.(4.7) of gravitational shocks depend on the galactic potential and the orbit of a cluster. Since the inclination of a cluster's orbit on the disk varies with time in an axisymmetric potential, we determine $\bar{A}$ and g_m at each passage through the disk as described below.

(ii) Method for calculating the effect of gravitational shock

To evaluate Eq.(4.7), we adopt the following approximation. The quantity g_m denotes the maximum vertical acceleration caused by the disk,

$$g_m = \left.\frac{\partial\Phi}{\partial Z}\right|_{(R_i, S_i)}, \tag{4.8}$$

where R_i is R at ith passage through the disk, and S_i is Z at which a cluster starts to feel ith gravitational (disk) shock. In order to determine S_i on an orbit of a cluster in our adopted gravitational potential, we identify the beginning of shocks under the condition of rapid shocks, i.e.,

$$t_{sh} < t_{cross} \tag{4.9}$$

where t_{cross} denotes a typical crossing time of stars at half-mass radius r_h of a cluster and t_{sh} a shock crossing time estimated at ith passage through the disk

$$t_{cross} = \left(\frac{r_h}{r_t}\right)^{3/2}\left(\frac{GM}{r_t^3}\right)^{-1/2} \tag{4.10}$$

$$t_{sh} = \frac{S_i}{V_{Z,i}}, \tag{4.11}$$

so that

$$S_i = V_{Z,i}\left(\frac{r_h}{r_t}\right)^{3/2}(G\bar{\rho})^{-1/2}, \tag{4.12}$$

where $V_{Z,i}$ is V_Z at ith passage through the disk. It is worth noting that this height S_i depends on both the average density of a cluster and its vertical velocity to the disk V_Z: a more massive cluster with higher velocity through the disk has larger height S_i.

Using the height S_i, the average adiabatic correction factor $\bar{A}$ is written as

$$\bar{A} = \frac{\int_0^{r_t} r^2(A_1[x(r)] + A_2[x(r)])\rho(r)r^2dr}{\int_0^{r_t} r^2\rho(r)r^2dr}, \tag{4.13}$$

$$A_1(x) = A_2(x) = (1+x^2)^{-3/2}, \tag{4.14}$$

$$x = \omega(r)t_{sh} = \frac{\omega(r)S_i}{V_{Z,i}} \tag{4.15}$$

$$\omega(r) = \left(\frac{r}{r_t}\right)^{-3/2} \tag{4.16}$$

where $A_1(x)$ and $A_2(x)$ are the local adiabatic correction factors for the first- and second-order energy changes by gravitational shocks, respectively, and $\rho(r)$ is the density distribution of stars in a cluster. We approximate that all clusters at a given time have the density distribution

$$\rho(r) \propto \frac{1}{r^2}\left(1-\frac{r}{r_t}\right)\left(\frac{GM}{r_t^3}\right)^{1/2}, \tag{4.17}$$

(FZ01). Its density distribution is the same as that of the King (1966) model, $\rho(r) \propto (\frac{1}{r}-\frac{1}{r_t})^{5/2}$ for $r \to r_t$, in the outer region of a cluster, whereas in the inner region, it has a singular behavior appropriate for core collapse models, $\rho(r) \propto r^{-2}$ for $r \to 0$ (Spitzer 1987, FZ01). The half-mass radius of our adopted density distibution of a cluster is $r_h = 0.18r_t$, reasonably close to that of the Hénon model ($r_h = 0.145r_t$).

Thus, in this simplified model for the mass-loss of a cluster, Eq.(4.5) has the exact solution at $T_{d,i} \le t \le T_{d,i+1}$,

$$M(t) = \begin{cases} M(0) - \mu_{ev}t - M_{se}, & i = 0 \\ M(T_{d,i}) - \frac{\mu_{ev}}{\nu_{sh,i}}\{\exp[\nu_{sh,i}(t-T_{d,i})] - 1\}\exp[-\nu_{sh,i}(t-T_{d,i})], & i \neq 0 \end{cases} \tag{4.18}$$

where $T_{d,i}$ denotes the epoch of the ith passage through the disk, $M(T_{d,i})$ is the mass of a cluster at $t = T_{d,i}$, $\nu_{sh,i}$ is fractional rate of gravitational shock at $T_{d,i} \leq t \leq T_{d,i+1}$, and M_{se} is total mass-loss by stellar evolution for $t \lesssim 3 \times 10^8$ yr.

In contrast to our method for dealing with gravitational shock as described above, TB01 made a different approach to the issue, based on the method which reproduces mass loss of a satellite galaxy calculated by N-body simulation. Their method is summarized as follows. Firstly, they identify rapid shocks on the condition that shock timescale is shorter than the satellite's internal orbital period. Secondly, they divide the gravitational shock into a series of n discrete time steps of length Δt, and in going from t_n to t_{n+1}, the energy change $\Delta W(t_n \rightarrow t_{n+1})$ of the satellite galaxy in a single time step is

$$\Delta W(t_n \rightarrow t_{n+1}) = \frac{1}{2}(\Delta t)^2 A_{tid}(t_n) \cdot \left[2 \sum_{i=0}^{n-1} A_{tid}(t_i) + A_{tid}(t_n) \right], \tag{4.19}$$

where $A_{tid}(t_i)$ is the tidal acceleration at t_i. The acceleration A_{tid} at the center of the satellite galaxy is written as

$$A_{tid}(t) = x(t) \cdot [\nabla g]_{(x=0)} = g_{a,b} x_b(t) e_a, \tag{4.20}$$

where g is the galactic gravitational field, $g_{a,b} = \partial g_a / \partial x_b$ evaluated at $x = 0$, e_a is the unit vector in x_a-direction, repeated indices a, b indicate summation over the three Cartesian coordinates. Thus, taking the dot product in Eq. (4.19) and averaging over a sphere of radius r gives

$$\Delta W_{tid}(t_n \rightarrow t_{n+1}) = \frac{1}{6} r^2 (\Delta t)^2 \left[2 g_{a,b}(t_n) \sum_{i=0}^{n-1} g_{a,b}(t_i) + g_{a,b}(t_n) g_{a,b}(t_n) \right], \tag{4.21}$$

with 18 terms from two summations over a and b. In an axisymmetric potential, a and b are R and Z in cylindrical coordinates, thus $g_{a,b}$ obtained from TB01's method includes g_{RR}, g_{RZ} and g_{ZZ}, whereas $g_{a,b}$ obtained from our method only includes g_{ZZ}. From Eq.(4:21), the energy change ΔE by gravitational shock is written as

$$\Delta E = \epsilon_h A_{1,TB}(x_h) \Delta W_{tid}(t_n \rightarrow t_{n+1}), \tag{4.22}$$

$$A_{1,TB}(x_h) = (1 + x_h^2)^{-\gamma}, \tag{4.23}$$

$$x_h = \omega(r_h) t_{sh}, \tag{4.24}$$

where $A_{1,TB}(x_h)$ is the first local adiabatic correction factor at the half-mass radius of the satellite galaxy. Thirdly, they calculate the change $\Delta \bar{\rho}_{r,sat}$ in mean density of the satellite

galaxy inside radius r, in the absence of shell crossing,

$$\Delta\bar{\rho}_{r,sat} \propto \Delta\left[\frac{M(<r)}{r^3}\right] \propto -\frac{\Delta r}{r^4} \propto -\frac{\Delta E(r)}{r^2}, \tag{4.25}$$

which is independent of radius r. Finally, they apply the tidal stripping,

$$\rho_{r,sat}(<r_t) = \eta\bar{\rho}_{gal}(<r) \tag{4.26}$$

$$\eta \equiv \frac{\rho_{r,sat}(<r_t)}{\rho_{gal}(<r)} = \frac{r^3}{r_t^3}\frac{M_{sat}}{M(<r)} = \frac{r^3}{GM(<r)}\left(\omega - \frac{d^2\Phi}{dr^2}\right), \tag{4.27}$$

to the new, heated density profile to determine how much mass is lost.

In order to highlight the difference between TB01's and our methods, we calculate the mass-loss rate of a cluster by gravitational shock alone as obtained from TB01's and our methods. In this calculation, we calculate only $A_1(x)$ in our method and adopt 3/2 as γ in TB01's method. Fig.4.2a shows a typical orbit of a cluster obtained with the integrals $\epsilon = 1.$, $I_2 = 0.5$, and $I_3 = 0.7$. Given the shape of an orbit, Fig.4.2b shows how the cluster evolves by gravitational shock alone, based on our method (thick solid line), TB01's method with all $g_{a,b}$ (thin solid line), and TB01's method with g_{zz} alone (dashed line). In this figure, the normalized factor M_0 corresponds to the initial mass of a cluster, which is $10^5 M_\odot$, and $M(t)$ is the mass of a cluster at time t. It follows from the figure that the ratio M/M_0 decreases approximately linearly with time and it reaches about 0.95 at t =13 Gyr. This ratio obtained from our method almost agrees with that calculated by TB01's method with g_{zz} alone and also almost agrees with that calculated by TB01's method with all $g_{a,b}$. Thus, even for other types of orbits, the effect of gravitational shock in our method is expected to agree with that in TB01's method with $g_{a,b}$.

(iii) Mass loss of a cluster in the current model

To summarize, we develop the method to calculate the mass loss of a globular cluster by three different processes, (1) stellar evolution, (2) two-body relaxation, and (3) gravitational shocks, in an axisymmetric potential consisting of the disk and dark halo components. Based on various approximation as described so far, we present the time evolution for the mass of a cluster. Fig.4.3 shows how a globular cluster having the orbit given in Fig.4.2a and the initial mass of $M_0 = 10^5 M_\odot$ evolves with time by the three processes in our model. In this figure, thick solid line shows the combined effect of stellar evolution, two-body relaxation, and gravitational shocks, whereas thin solid and dahed lines, respectively, considers only the two-body relaxation and gravitational shocks. Firstly, from the comparison between thin solid line and dashed line, it is found that the mass loss by

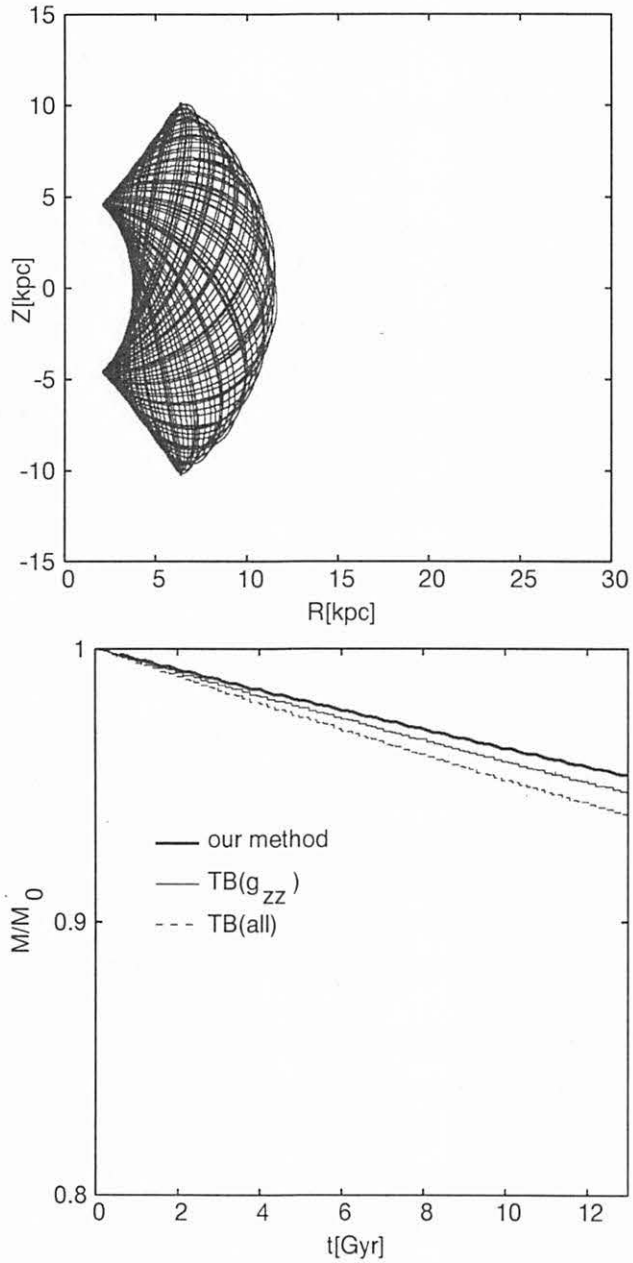

Figure 4.2: (a)Orbit of the cluster with $\epsilon = 1.$, $I_2 = 0.5$, and $I_3 = 0.7$. The initial position of the cluster lies on $(R[\mathrm{kpc}], \mathrm{Z}[\mathrm{kpc}]) = (8, 5)$. (b)Ratio $M(t)/M_0$ of a cluster with the orbit (a) in our method (thick solid line), TB01's method with all $g_{a,b}$ (thin solid line), and TB01's method with g_{ZZ} alone (dashed line). The mass M_0 and $M(t)$ are the initial mass of a cluster, $10^5 M_\odot$ and the mass at time t.

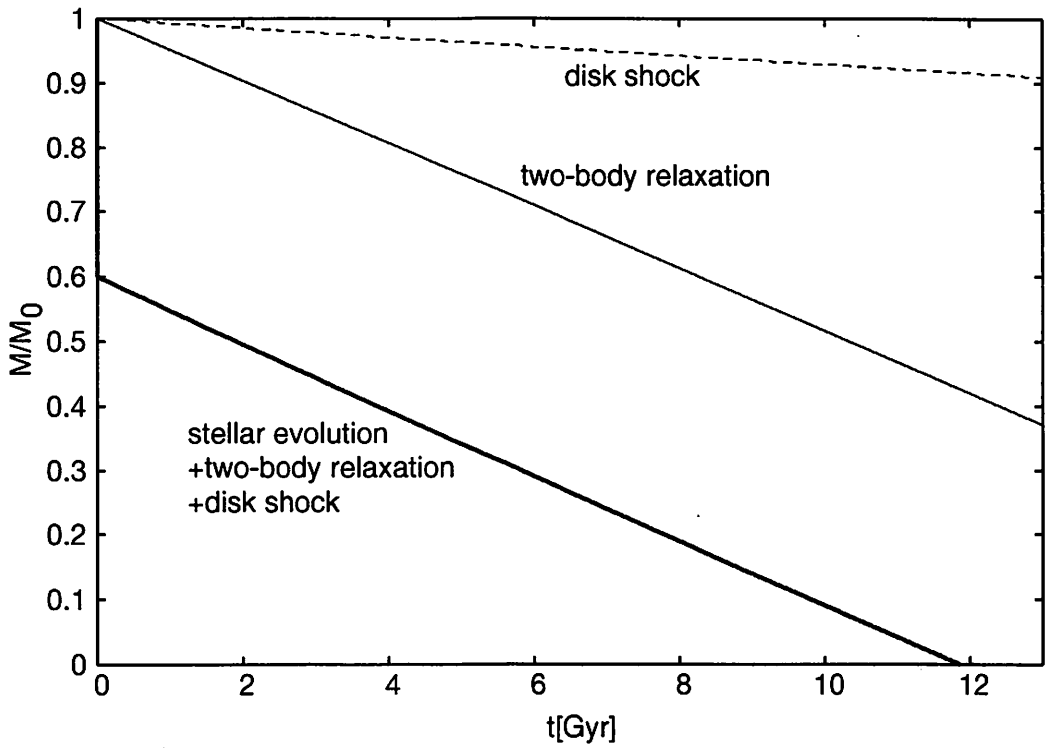

Figure 4.3: Time evolution for the mass of a cluster having the orbit given in Fig.4.2a and the initial mass of $10^5 M_\odot$. Thick solid line shows the combined evolution of stellar evolution, two-body relaxation, and gravitational shocks, whereas thin solid and dahed lines, respectively, considers only the two-body relaxation and gravitational shocks.

gravitational shocks is much smaller than that by two-body relaxation and is relatively less important at later stages. Secondly, as found from thick solid line, the mass of a cluster shows a rapid decline as a result of stellar evolution until it reaches about 60% of its initial mass and then shows an approximately exponential decline with time mainly by two-body relaxation.

References

[1] Baumgardt, H., 1998, A&A, 330, 480

[2] Dejonghe, H., & de Zeeuw, T., 1988, ApJ, 333, 90

[3] de Zeeuw, T., 1985, MNRAS, 216, 273

[4] de Zeeuw, T., Peletier, R., & Franx, M., 1986, MNRAS, 221, 1001

[5] Fall, S. M., & Zhang, Q., 2001, ApJ, 561, 751 (FZ01)

[6] Goudfrooij, P., Strader, J., Brenneman, L., et al, 2003, MNRAS, 343, 665

[7] Harris, W. E., 1991, ARAA, 29, 543

[8] Hénon, M., 1961, Ann, d'Astrophys, 24, 369

[9] King, I., 1962, AJ, 67, 471

[10] King, I., 1966, AJ, 71, 64

[11] Kundić, T., & Ostriker, J. P., 1995, ApJ, 438, 702

[12] Larsen, S. S., Forbes, D. A.,& Brodie, J. P., 2001, MNRAS, 327, 1116

[13] Leitherer, C., Schaerer, Goldader, J. D., et al., 1999, ApJS, 123, 3

[14] Murali, C., & Weinberg, M. D., 1997a, MNRAS, 288, 749

[15] Murali, C., & Weinberg, M. D., 1997b, MNRAS, 288, 767

[16] Murali, C., & Weinberg, M. D., 1997c, MNRAS, 291, 717

[17] Okazaki, T., & Tosa, M., 1995, MNRAS, 274, 48

[18] Ostriker, J. P., Spitzer, L., & Chevalier, R. A.,1972, ApJ, 176, L51

[19] Perrett, K. M., Bridges, T. J., Hanes, D. A., Brodie, J. P., Carter, D., 2002, AJ, 123, 2490

[20] Spitzer, L., 1987, Dynamical Evolution of Globular clusters, Princeton Univ, Press, Princeton

[21] Spitzer, L., & Chevalier, R. A., 1972, ApJ, 183, 565

[22] Taylor, J. E., & Babul, A., 2001, ApJ, 559, 716

[23] Vedel, H., & Sommer-Larsen, J., 1990, ApJ, 359, 104

[24] Vesperini, E., 1997, MNRAS, 287, 915

[25] Vesperini, E., 1998, MNRAS, 299, 1019

[26] Vesperini, E., Zepf, S. E., Kundu, A., & Ashman, K. M., 2003, ApJ, 593, 760

[27] Taylor, J. E. & Babul, A., 2001, ApJ, 559, 716

[28] Zhang, Q., & Fall, S. M., 1999, ApJ, 527, L81

Kinematics of Tidal Debris from Omega Centauri's Progenitor Galaxy

Arihiro Mizutani[1], Masashi Chiba[2], and Tsuyoshi Sakamoto[1]

ABSTRACT

We present the kinematic properties of a tidally disrupted dwarf galaxy in the Milky Way, based on the hypothesis that its central part once contained the most massive Galactic globular cluster, ω Cen. Dynamical evolution of a self-gravitating progenitor galaxy that follows the present-day and likely past orbits of ω Cen is calculated numerically and the kinematic nature of their tidal debris is analyzed, combined with randomly generated stars comprising spheroidal halo and flat disk components. We show that the retrograde rotation of the debris stars at ~ -100 km s^{-1} accords with a recently discovered, large radial velocity stream at ~ 300 km s^{-1} towards the Galactic longitude of $\sim 270°$. These stars also contribute, only in part, to a reported retrograde motion of the outer halo at the North Galactic Pole. The prospects for future debris searches and the implications for the early evolution of the Galaxy are briefly presented.

Subject headings: Galaxy: formation — globular clusters: individual (ω Centauri) — stars: kinematics

1. INTRODUCTION

Omega Centauri, the most massive globular cluster in the Milky Way, is unique in terms of its metallicity content, internal kinematics, and structure. Unlike other Galactic globular clusters, ω Cen shows a wide spread in metallicity (e.g. Norris, Freeman, & Mighell 1996), with a main metal-poor component at [Fe/H]$\simeq -1.6$, a second smaller peak at [Fe/H]$\simeq -1.2$, and a long tail extending up to [Fe/H]$\simeq -0.5$. The metal-rich population holds a low velocity dispersion and no sign of rotation, in contrast to the rotating metal-poor population. Furthermore, the metal-rich stars in ω Cen are largely enhanced in s-process elements relative

[1]Department of Astronomical Science, The Graduate University for Advanced Studies, Mitaka, Tokyo 181-8588, Japan; mizutnar@cc.nao.ac.jp

[2]National Astronomical Observatory, Mitaka, Tokyo 181-8588, Japan

to those in globular clusters and field stars with similar metallicities (e.g. Norris & Da Costa 1995), thereby suggesting that the ejecta from low-mass, asymptotic giant branch (AGB) stars had to be retained and incorporated into the next-generation stars.

In spite of its large mass (5×10^6 $M_\odot$), it has been demonstrated by Gnedin et al. (2002) that ω Cen is not unique in its ability to retain the AGB ejecta as found for other clusters. An isolated formation of ω Cen is thus unlikely, because the enriched gas would easily be lost by encountering the Galactic disk. The most viable explanation for the uniqueness of ω Cen is that it was once the dense nucleus of a dwarf galaxy (Freeman 1993). A gravitational potential provided by progenitor's stellar system and dark matter (as suggested from dwarf spheroidal galaxies in the Local Group, Mateo 1998) would help retaining the enriched gas and let the cluster being self-enriched at least over a few Gigayears.

If this hypothesis is the case for the origin of ω Cen, the question arises: *where and in what form does the stellar system of its progenitor galaxy remain?* Dinescu (2002) first investigated this issue, by examining the possible signature of the progenitor's tidal debris among nearby metal-poor stars in the catalog of Beers et al. (2000, B00). She identified a group of stars with $-2.0 <$[Fe/H]≤ -1.5, which departs from the characteristics of the inner Galactic halo but has retrograde orbits similar to ω Cen. Her simplified disruption model of the progenitor galaxy demonstrated that trailing tidal debris, having orbital characteristics similar to the cluster, can be found in the solar neighborhood, although the concrete spatial distribution and kinematics of the debris stars remain yet unclear.

This work motivates us to conduct an N-body simulation for the tidal disruption of ω Cen's progenitor galaxy, to obtain the characteristic structure and kinematics of its debris stars and compare with various observations showing signatures of recent merging events in the Milky Way (Gilmore, Wyse, & Norris 2002, GWN; Kinman et al. 2002, K02; Chiba & Beers 2000, CB). In particular, we show that a recently identified stream of stars at heliocentric radial velocity of $\sim$ 300 km s^{-1} (GWN) is a natural outcome of the current disruption model, without affecting local halo kinematics near the Sun and microlensing optical depth towards the Large Magellanic Cloud (LMC).

2. SIMPLE DYNAMICAL MODEL OF A PROGENITOR GALAXY

We calculate the dynamical evolution of an orbiting dwarf galaxy in a fixed external gravitational potential representing the Milky Way. The potential consists of three parts: a spherical Hernquist bulge $\Phi_b(r)$, a Miyamoto-Nagai disk $\Phi_d(R, z)$, and a logarithmic dark halo $\Phi_h(r)$, where r is the Galactocentric distance and (R, z) denote cylindrical coordinates.

Each is given as, $\Phi_b(r) = -GM_b/(r+a)$, $\Phi_d(R,z) = -GM_d/\sqrt{R^2+(b+\sqrt{z^2+c^2})^2}$, and $\Phi_h(r) = v_h^2/2\ln(r^2+d^2)$, where $M_b = 3.4\times10^{10}$ M$_\odot$, $a = 0.7$ kpc, $M_d = 10^{11}$ M$_\odot$, $b = 6.5$ kpc, $c = 0.26$ kpc, $v_h = 186$ km s^{-1}, and $d = 12$ kpc. This choice yields a circular velocity of 228 km s^{-1} at the solar circle of $R_\odot = 8$ kpc and a flat rotation curve outside $R_\odot$.

We set self-gravitating particles in the dwarf galaxy following a King model, where the central density, central velocity dispersion, and core radius are given as 0.3 M$_\odot$ pc^{-3}, 18.1 km s^{-1}, and 0.56 kpc, respectively. In addition, a particle with the mass of 5×10^6 M$_\odot$ representing ω Cen is placed at the center of the galaxy to trace its orbit. This setting yields the total mass of the galaxy as $M_{tot} = 5.79\times10^8$ M$_\odot$. A part of the mass is provided by stars, which is roughly estimated from the mean metallicity of stars in ω Cen ($\langle$[Fe/H]$\rangle \sim -1.6$), combined with the metallicity-luminosity relation for the Local Group dwarfs (Côté et al. 2000) and the mass-to-light ratio (assuming $M/L \sim 4$ obtained for ω Cen, Meylan et al. 1995), yielding $M_{stars} \sim 10^7$ M$_\odot$. Thus, our model galaxy is largely dominated by a dark component, in agreement with the observed large M/L in dwarfs (Mateo 1998). The galaxy is represented by a collection of 10^4 particles and the self-gravity is calculated in terms of a multiple expansion of the internal potential to fourth order (Zaritsky & White 1988).

In the course of its orbital motion, a dwarf galaxy is disrupted by Galactic tides, whereas its dense core is expected to survive and follow ω Cen's orbit. While our calculation in a fixed Galactic potential neglects dynamical friction against progenitor's orbit, the effect is only modest for the system of $\lesssim 10^8$ M$_\odot$ (Zhao 2002), especially during a few orbital periods required for tidal disruption. We thus examine two representative orbits for the progenitor, model 1 and 2: model 1 follows the current orbit of ω Cen, whereas for model 2, we calculate an orbit back to the past over ~ 2 Gyr from its current position and velocity by fully taking into account dynamical friction and then set a progenitor galaxy on its non-decaying orbit. These two models provide us with satisfactory information on the generic properties of a tidally disrupted progenitor and we postulate that the realistic nature of their debris is midway between these model predictions. We calculate ω Cen's orbit, based on the distance[3] from the Sun $D = 5.3\pm0.5$ kpc, position $(l,b) = (309°, 15°)$, proper motion $(\mu_\alpha\cos\delta, \mu_\delta) = (-5.08\pm0.35, -3.57\pm0.34)$ mas yr^{-1}, and heliocentric radial velocity $v_{los} = 232.5\pm0.7$ km s^{-1} (Dinescu, Girard, & van Altena 1999). This orbit for model 1 is characterized by frequent disk crossings with a period of $\tau_{orb} = 0.8\times10^8$ yr, retrograde motion, and apo and pericentric distances $(r_{apo}, r_{peri}) = (6.4, 1.1)$ kpc. For model 2, we obtain $\tau_{orb} = 1.5\times10^8$ yr and $(r_{apo}, r_{peri}) = (11.3, 3.0)$ kpc. In both experiments, we adopt

[3]We estimate this distance, based on the Harris (1996) data and the relation between absolute magnitude of cluster horizontal branch and metallicity derived by Carretta, Gratton, & Clementini (2000).

the same progenitor mass M_{tot} and place it at apocenter to maximize its survival chances[4].

Figure 1 shows the spatial distribution of the tidally disrupted debris. Upper (middle) panel shows model 1 (model 2) after the 1.37 (1.86) Gyr orbital excursion of the progenitor galaxy. Lower panel shows the orbit of the galaxy center. In the course of the orbital motion of the galaxy, its structure is made elongated along the orbit induced by Galactic tides, in particular at its pericenter passages, and then the particles are spread out to form the tidal streams along the orbit. A rosette-like feature of the debris becomes steady after about eight orbital periods. Model 1 results in more compact distribution than model 2, which reflects the difference in orbital radii.

Figure 2 shows the velocity distributions of the debris particles in cylindrical coordinates (v_R, v_ϕ, v_z). As is evident, model 1 and 2 provide essentially the same debris kinematics: most remarkable is a sharply peaked v_ϕ distribution at ~ -100 km s^{-1}, arising from a retrograde orbit of a progenitor. These kinematics suggest that the difference in model 1 and 2 resides only in the spatial extent of the debris.

3. EFFECTS OF DEBRIS ON GALACTIC KINEMATICS

3.1. Method for kinematic analysis

In order to assess the reality of the debris stars in light of observed stellar kinematics in the Milky Way, we analyze the kinematics of both the simulated debris and other Galactic stars generated randomly by a Monte Carlo method. The metal-poor halo is modeled as a flattened spheroid $\rho \propto (R^2+z^2/q^2)^{-3.5/2}$, where q is an axis ratio ranging 0.55-0.7, anisotropic velocity ellipsoid $(\sigma_R, \sigma_\phi, \sigma_z) = (154, 121, 96)$ km s^{-1}, and small mean rotation $\langle v_\phi \rangle = 24$ km s^{-1}, as found for halo stars with [Fe/H]< -2 near the Sun (CB). Thin and thick disks are modeled as $\rho \propto \exp(-R/R_d)\,\mathrm{sec}^2(z/z_d)$, where $R_d = 3.5$ kpc and $z_d = 0.3$ (1) kpc for thin (thick) disk. Both disks rotate at 200 km s^{-1}, having velocity ellipsoids of $(34, 25, 20)$ km s^{-1} and $(46, 50, 35)$ km s^{-1} for thin and thick disks, respectively (CB). The relative fraction of each component is fixed using observed local densities near the Sun, in such a manner that the halo and thick-disk densities at $D < 1$ kpc are 0.2 % and 2 % of the thin-disk density, respectively (e.g. Yamagata & Yoshii 1992).

In our model of ω Cen's progenitor galaxy, the self-gravitating particles represent both

[4]For model 1, this initial mass may be too large as an as-yet-undisrupted galaxy (Zhao 2002), so the debris density in model 1 can be overly represented.

stars and dark matter. We note that a correct estimate for the fraction of stars is uncertain, because their M/L ratio as well as the amount of dark matter in the progenitor is unavailable. As a useful method to incorporate this ambiguity for the current kinematic analysis, we set a parameter f as the fraction of the debris particles relative to halo stars near the Sun, *when all of the particles are regarded as stellar ones.* By this, the normalization of the halo density is obtained for the given debris particles.

A typical value of f for the conversion of the simulated particles to the stars is estimated in the following manner. Model 1 (model 2) yields 21 (74) particles at $D < 2$ kpc, giving the mass density of $\rho_g = 0.4(1.3) \times 10^{-4}$ $M_\odot$ pc^{-3} near the Sun, whereas the total mass density and metal-poor halo density have been derived as 8×10^{-3} $M_\odot$ pc^{-3} (Gates, Gyuk, & Turner 1995) and 6.4×10^{-5} $M_\odot$ pc^{-3} (Gould, Flynn, & Bahcall 1998), respectively. Then, if the debris stars (with $M_{stars} \sim 10^7$ $M_\odot$) are distributed in the same manner as the simulated particles (with $M_{tot} = 5.74 \times 10^8$ $M_\odot$), which would be a reasonable approximation in view of the dissipationless nature of stars, the mass density of the debris stars in the solar neighborhood can be estimated as $(M_{stars}/M_{tot})\rho_g = O(10^{-6})$ $M_\odot$ pc^{-3}, which is about 1 % of the halo density. Thus, f, defined here as debris fraction at $D < 2$ kpc, is expected to be of order of a few percents.

3.2. GWN's radial velocity survey

Recently, GWN reported a spectroscopic survey of ~ 2000 F/G stars down to $V = 19.5$ mag, in the direction against Galactic rotation $(l, b) = (270°, -45°)$ and $(270°, +33°)$, where radial velocities, v_{los}, in combination with distances largely reflect orbital angular momentum. The v_{los} distribution of the stars a few kpc from the Sun shows two stellar streams at $v_{los} \sim 100$ km s^{-1} and ~ 300 km s^{-1}, which are not explained by known Galactic components. While the stream at $v_{los} \sim 100$ km s^{-1} was reproduced by their model of a merging satellite in prograde rotation, the stream at $v_{los} \sim 300$ km s^{-1} remains yet unexplained.

Figure 3a shows the v_{los} distribution for the debris stars of model 2 and halo stars of $q = 0.7$ (i.e. without disks) at $1 < D < 5$ kpc, $260° < l < 280°$, and two fields for b. Figure 3b shows when disk stars are incorporated. As is evident, the debris stars from ω Cen's progenitor form a local peak at $v_{los} \sim 300$ km s^{-1}, which is provided by many stars having $v_\phi \sim -100$ km s^{-1}. This is in good agreement with the $v_{los} \sim 300$ km s^{-1} stream discovered by GWN. A more flattened halo than the case $q = 0.7$ yields a higher peak, since the density contrast of the debris relative to halo is made higher in this survey region. It is worth noting that model 1 yields essentially the same v_{los} distribution as model 2, reflecting the same velocity distribution, although to attain the same peak height at ~ 300 km s^{-1}, f

be a few factor larger and the selected range of l be a few degree higher than the respective values in model 2, because of less number of debris stars near the Sun. This rule applies to other considerations below as well.

3.3. Kinematics at the North Galactic Pole

Majewski (1992) suggested that the outer halo at the North Galactic Pole (NGP) shows a retrograde rotation $\langle v_\phi \rangle \simeq -55$ km s^{-1} at $z > 4$ kpc. Also, K02 reported that their sample of horizontal branch stars at $2 < z < 12$ kpc shows a retrograde rotation at $\langle v_\phi \rangle \simeq -65$ km s^{-1}. On the other hand, halo stars near the Sun show no retrograde rotation (CB).

To investigate the role of the debris stars in this issue, we select those of model 2 and randomly generated stars at $b > 70°$ and $2 < D < 5$ kpc (resembling K02's selection). Since the observational determination of full space velocities involves rather inaccurate information of proper motions compared to radial velocities, we convolve the velocity distribution of stars with a Gaussian distribution for velocity errors, having 1 σ of a typical 30 km s^{-1} error. The resulting velocity distribution shows a non-Gaussian feature owing to the presence of the debris stars: the v_ϕ distribution holds an extra peak at ~ -100 km s^{-1} in addition to the $v_\phi \sim 20$ km s^{-1} peak, where the former amplitude becomes comparable to the latter one at f of a few percents, whereas for v_R and v_z, the velocity distributions are made slightly asymmetric. However, the change of $\langle v_\phi \rangle$ by the inclusion of the debris stars with $f = 5$ % amounts to only -19 (-14) km s^{-1} for $q = 0.55$ (0.7), which are still insufficient for explaining the reported $\langle v_\phi \rangle = -35 \sim -65$ km s^{-1}. Also, if we extend the selection of the stars at higher z or instead consider model 1, the changes of $\langle v_\phi \rangle$ become smaller than the above mentioned values, because there are no debris stars in our current model. Thus, it is safe to conclude that the debris stars contribute only in part to a reported retrograde motion at the NGP.

3.4. Local halo kinematics and microlensing towards LMC

We select the nearby debris and halo stars at $6.5 < R < 9.5$ kpc, $z < 4$ kpc, and $D < 4$ kpc (as was drawn by CB), convolve the velocities with a Gaussian error distribution of 1 $\sigma = 30$ km s^{-1}, and compare with the corresponding stars with [Fe/H]≤ -2 in B00. It follows that the non-Gaussian feature in velocities is much weaker than that at the NGP: the change of $\langle v_\phi \rangle$ for $f = 5$ % is only -9 (-10) km s^{-1} in model 1 (model 2). This is due to the smaller debris fraction near $z = 0$ than at high $|z|$.

The effects of the debris stars on the microlensing optical depth towards LMC, τ, are

modest as well. Following the Gould (1999) prescription for τ and investigating the debris within $10° \times 10°$ centered at LMC, we arrive at $\tau \lesssim 10^{-7} f$, thereby indicating that τ provided by the debris stars is much smaller than the observed τ of $O(10^{-7})$.

4. DISCUSSION

We have demonstrated that our fiducial models of an orbiting dwarf galaxy that once contained ω Cen predict a sequence of tidal streams in retrograde rotation and their existence is imprinted in kinematics of nearby stars, especially in the direction against Galactic rotation (GWN) and at the NGP (K02), while local halo kinematics and microlensing towards LMC remain unchanged. The streams are mostly distributed inside the solar circle, as suggested from the current orbit of ω Cen (Dinescu 2002). In contrast to the Sgr dwarf galaxy having polar orbit, the orbit of ω Cen's progenitor galaxy is largely affected by a non-spherical disk potential, where the orbital plane exhibits precession with respect to the Galactic Pole, causing self-crossing of tidal streams in the disk. The projection of the orbit perpendicular to the disk shows an 'X'-like feature, thereby leaving denser streams at high $|z|$ than at low $|z|$ for a given radius. This explains the significance of the debris at the NGP compared to the solar neighborhood.

Existing kinematic studies of Galactic stars to search for a signature of ω Cen's progenitor galaxy are yet confined to nearby stars, where the significance of the debris streams is modest, as shown here. Searches of stars inside the solar circle are more encouraging (Fig. 1), in particular in the directions of $l \sim 320°$ and $l \sim 50°$, where we expect the presence of high-velocity streams at $v_{los} = 200 \sim 300$ km s^{-1} and $-400 \sim -300$ km s^{-1}, respectively. Future radial velocity surveys of these fields including the sample of the Sloan Digital Sky Survey or planned RAdial Velocity Experiment are worth exploring in this context. Also, detailed abundance studies of candidate stream stars will be intriguing, because such stars may exhibit different abundance patterns from field halo stars, as found in dwarf galaxies (Shetrone, Côté, & Sargent 2001).

A yet unsettled issue is the origin of a progenitor satellite orbiting inside the solar circle, because dynamical friction alone from the present-day *smooth* Galactic components is insufficient for shrinking the orbit if it was born at a large distance (say, ~ 50 kpc) from Galactic center (Zhao 2002). One of the possibilities to preclude it may be that the merging of a satellite occurred while the Milky Way was still in the process of halo formation via hierarchical merging of several subgalactic clumps; successive gravitational interaction among clumps may help reducing the orbital angular momentum of a progenitor efficiently. Also, a progenitor may have formed in the vicinity of the proto-Galaxy, where the environment of a

strong tidal field promotes the formation of a compact M32-like galaxy (Burkert 1994) and its high density affords the survival chances until the epoch of the Galactic disk formation. Then, if a progenitor retained gas, growing Galactic tides induce the infall of gas into the progenitor center and trigger the formation of a globular cluster there (Bekki & Chiba 2002) similar to ω Cen. The story is yet speculative but worth pursuing based on sophisticated numerical codes for Galaxy formation.

We are grateful to the anonymous referee for helpful comments. M.C. thanks Kenji Bekki and Tim Beers for useful discussions.

REFERENCES

Beers, T. C., Chiba, M., Yoshii, Y., Platais, I., Hanson, R. B., Fuchs, B., & Rossi, S. 2000, AJ, 119, 2866 (B00)

Bekki, K., & Chiba, M. 2002, ApJ, 566, 245

Burkert, A. 1994, MNRAS, 266, 877

Carretta, E., Gratton, R.G., & Clemintini, G. 2000, MNRAS, 316, 721

Chiba, M., & Beers, T. C. 2000, AJ, 119, 2843 (CB)

Côté, P., Marzke, R. O., West, M. J., & Minniti, D. 2000, ApJ, 533, 869

Dinescu, D. I. 2002, in ASP Conf. Ser. 265, Omega Centauri: A Unique Window into Astrophysics, ed. F. van Leeuwen, J. D. Hughes, & G. Piotto (San Francisco: ASP), 365

Dinescu, D. I., Girard T. M., & van Altena, W. F. 1999, AJ, 117, 1792

Freeman, K. C. 1993, in ASP Conf. Ser. 48, The Globular Cluster-Galaxy Connection, ed. G. H. Smith & J. P. Brodie (San Francisco: ASP), 608

Gates, E. I., Gyuk, G., & Turner, E. 1995, ApJ, 449, L123

Gilmore, G., Wyse, R. F. G., & Norris, J. E. 2002, ApJ, 574, L39 (GWN)

Gnedin, O. Y., Zhao, H.-S., Pringle, J. E., Fall, S. M., Livio, M., & Meylan, G. 2002, ApJ, 568, L23

Gould, A. 1999, ApJ, 525, 734

Gould, A., Flynn, C., & Bahcall, J. N. 1998, ApJ, 503, 798

Harris, W. E. 1996, AJ, 112, 1487

Kinman, T. D., Cacciari, C., Bragaglia, A., Buzzoni, A., & Spagna, A. 2002, in Galactic Dynamics Workshop, in press (astro-ph/0211243) (K02)

Majewski, S. R. 1992, ApJS, 78, 87

Mateo, M. 1998, ARA&A, 36, 435

Meylan, G., Mayor, M., Duquennoy, A., & Dubath, P. 1995, A&A, 303, 761

Norris, J. E., & Da Costa, G. S. 1995, ApJ, 447, 680

Norris, J. E., Freeman, K. C., & Mighell, K. L.1996, ApJ, 462, 241

Shetrone, M. D., Côté, P., & Sargent, W. L. W. 2001, ApJ, 548, 592

Yamagata, T., & Yoshii, Y. 1992, AJ, 103, 117

Zaritsky, D., & White, S. D. M. 1988, MNRAS, 235, 289

Zhao, H.-S. 2002, in ASP Conf. Ser. 265, Omega Centauri: A Unique Window into Astrophysics, ed. F. van Leeuwen, J. D. Hughes, & G. Piotto (San Francisco: ASP), 391

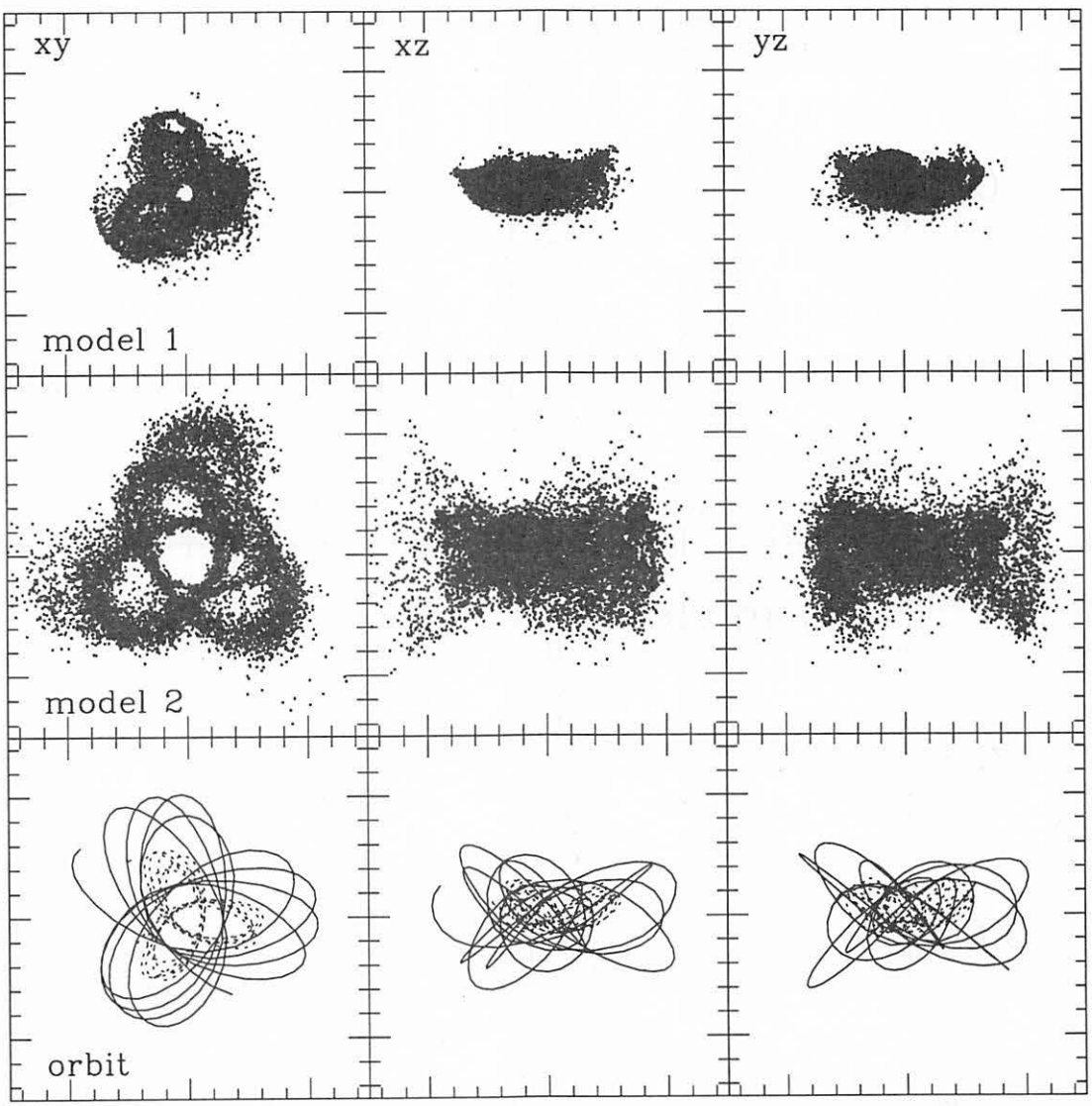

Fig. 1.— Upper panel: spatial distribution of the debris particles at 1.85 Gyr, projected onto xy plane (left), xz plane (middle), and yz plane (right). A frame measures 15 kpc on a side of each panel. The Sun is located at $(x, y, z) = (-8, 0, 0)$ kpc and the xy plane corresponds to the disk plane. Lower panel: orbital motion of a central particle (corresponding to ω Cen) over 1.85 Gyr in the same planes.

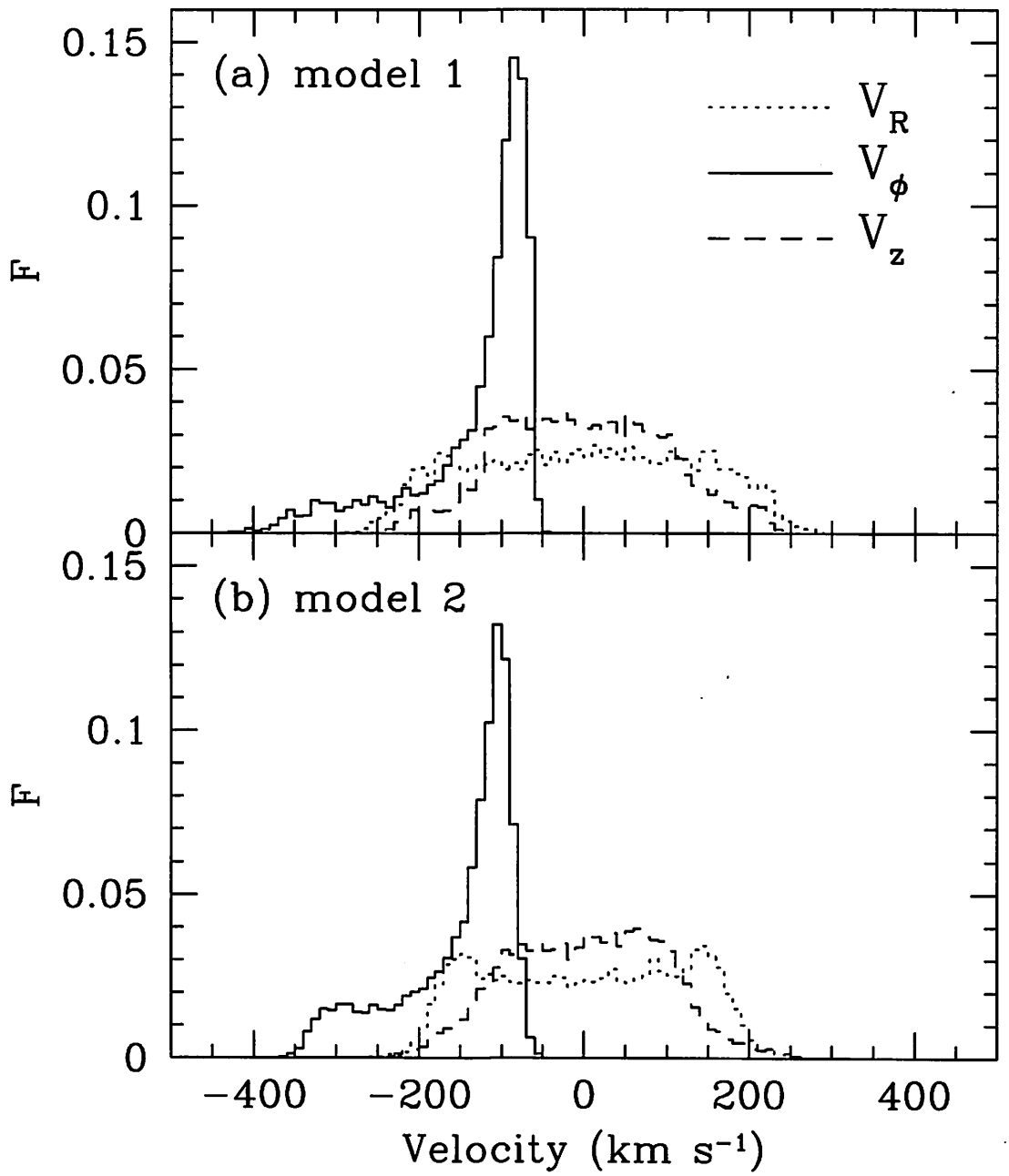

Fig. 2.— Velocity distribution of the debris particles in cylindrical coordinates, v_R (dotted line), v_ϕ (solid line), v_z (dashed line).

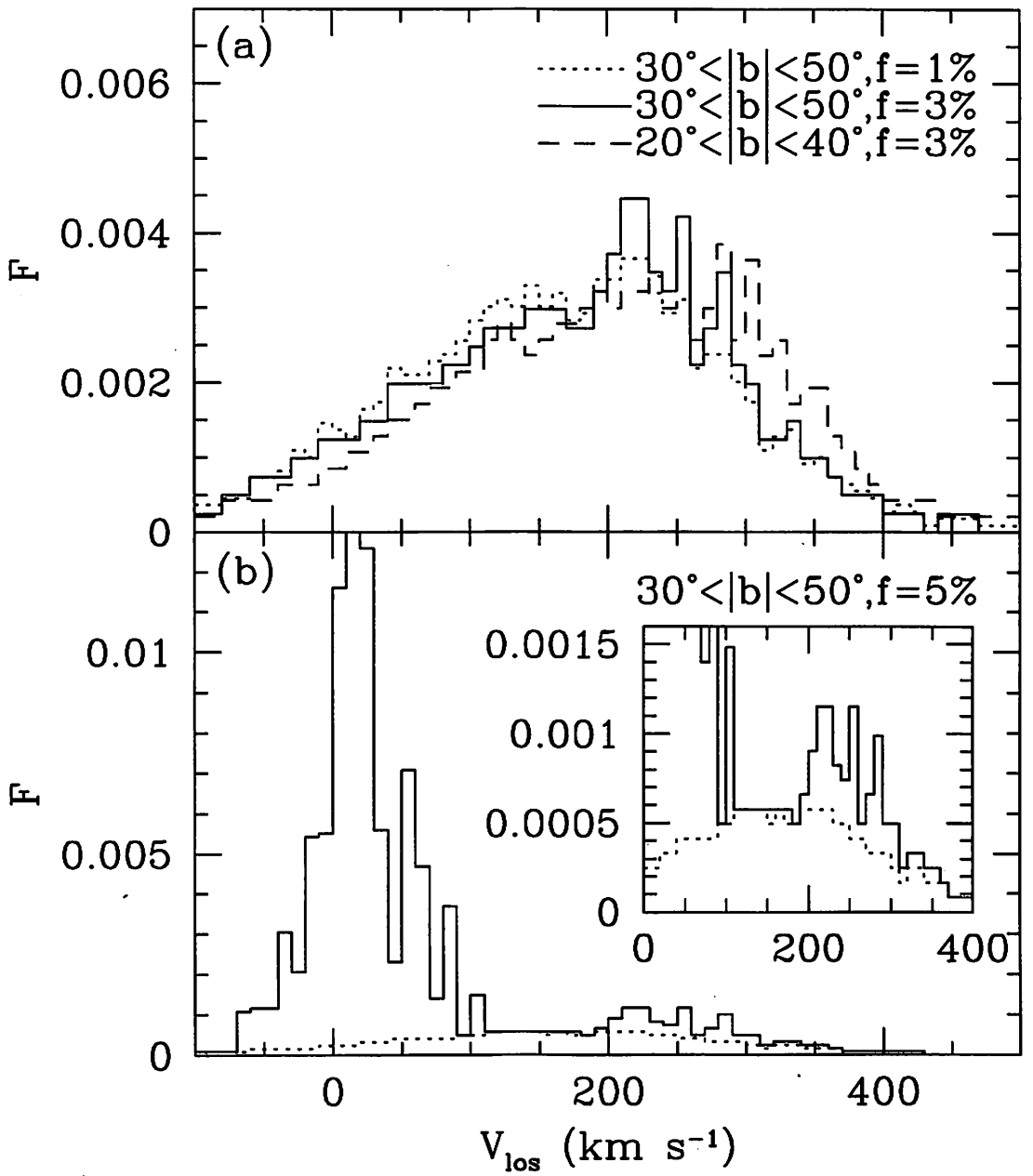

Fig. 3.— (a) Distribution of the heliocentric radial velocities in the direction of the Gilmore, Wyse, and Norris (2002) survey, for the debris stars and randomly generated halo stars with axis ratio of $q = 0.7$. In this plot, we select the stars at $0.5 < D < 5$ kpc in the fields of $30° < |b| < 50°$ (with $f = 1$ % and $f = 3$ % for dotted and solid histograms, respectively) and $20° < |b| < 40°$ (with $f = 3$ %: dashed histogram). (b) The same as (a) but incorporating the randomly generated disk stars as well for $30° < |b| < 50°$ with $f = 3$ % (solid histogram). Dotted histogram denotes the case for the metal-poor halo alone.

Formation of Terrestrial Planets in a Dissipating Gas Disk with Jupiter and Saturn

Junko Kominami and Shigeru Ida

Department of Earth and Planetary Sciences,
Tokyo Institute of Technology,
Ookayama, Meguro-ku, Tokyo,152-8551, Japan
Telephone:+81-3-5734-2620
Fax:+81-3-5734-3538

kominami@geo.titech.ac.jp

ida@geo.titech.ac.jp

ABSTRACT

We have performed N-body simulations on final accretion stage of terrestrial planets, including the eccentricity and inclination damping effect due to tidal interaction with a gas disk and the effect of secular perturbations by Jupiter and Saturn. In the final stage, terrestrial planets are formed through coagulation of protoplanets of about the size of Mars. They would collide and grow in a decaying gas disk. Kominami & Ida (2002, Icarus 157, 43-56) showed that it is plausible that Earth-sized, low-eccentricity planets are formed in a mostly depleted gas disk. However, four or five small protoplanets remain. In the final stage of terrestrial planetary formation, it is likely that Jupiter and Saturn are already formed. When Jupiter and Saturn are included, their secular perturbations pump up eccentricities of protoplanets and tend to reduce the number of final planets in the terrestrial planet regions. We did 10 simulations with time-independent gas surface density and 4 simulations with exponentially decaying gas surface density with Jupiter and Saturn. Most of the simulations of time-independent gas model resulted in the formation of Earth-sized, low-eccentricity planet. However, 4 or 5 small protoplanets still tend to remain; the final planets' number is not reduced significantly by including the effect of Jupiter and Saturn. Simulations with decaying gas model resulted in formation of 2 - 3 large mass planets with high eccentricities. The result is similar to the gas free cases.

1. Introduction

Numerical simulations predict accretion of about twenty Mars-sized protoplanets ($\sim 0.1 M_\oplus$) with almost circular orbits from a planetesimal swarm in terrestrial planet regions (Weidenschilling et al. 1997, Kokubo & Ida 1998, 2000). Mutual gravitational interaction between the protoplanets (Chambers et al. 1996) and/or the effect of the giant planets increase the eccentricities of the protoplanets on a time scale of $10^5 - 10^7$ years (Nagasawa et al. 2000, Ito & Tanikawa 1999) to cause orbit crossing of the protoplanets. The protoplanets start to collide and grow to the size of the Earth and Venus.

If only the mutual gravitational interaction between the prototplanets are considered, the resulting planets have relatively high eccentricities compared to those of Earth and Venus (Chambers and Wetherill 1998, Agnor et al. 1999). These high eccentricities are the remnant of orbital crossing. Collisional damping is not strong enough to reproduce relatively small eccentricities ($\lesssim 0.03$) which are comparable to time-averaged eccentricities of Venus and Earth. However, it is reasonable to assume that leftover planetesimals and remnant disk gas still exist during this stage. Gravitational interactions with the planetesimals and/or the disk gas damp the eccentricities (and inclinations).

Kominami & Ida (2002 ; hereafter refer to as KI02) carried out N-body simulations starting from Mars-sized protoplanets including the eccentricity damping due to disk gas and showed that if orbit crossing occurs when a gas disk with $\sim 10^{-3} - 10^{-4}$ times the minimum mass model (Hayashi 1981) is left, planets with $m \sim M_\oplus$ and $e \lesssim 0.03$ are formed. Such small amount of gas is enough to damp the eccentricities of the formed Earth-sized planets (KI02, Agnor & Ward 2002).

Although KI02 showed that one or two Earth-sized planets with low eccentricities can be reproduced, in most of the simulations, four to five Mars-sized planets remained. The averaged number of final planets was ~ 7, which is greater than that of the present terrestrial planets in our Solar system, which is 4. Meanwhile, asteroid belt was assumed to be depleted in all calculations by gas giant planets in KI02. They gravitationally perturb the asteroidal bodies, increase the eccentricities of the bodies and make them eject from the asteroid belt region (Chambers & Wetherill 2001, Petit et.al. 2001, Chambers & Cassen 2002). Moreover, they consider the stage when disk gas is mostly depleted in KI02. Hence, it is more consistent with the reality to assume that Jupiter and Saturn have already been present during the final stage of terrestrial planet formation. The effect was not included in KI02.

In this paper, we present the simulations with Jupiter and Saturn. The perturbations from the giant planets pump up eccentricities of the protoplanets, which may enhance the collisions between the protoplanets, and may result in less number of final planets. We did

10 simulations using time-independent gas surface density model and compared the results without Jupiter and Saturn (KI02). Four simulations are done using exponentially decaying gas surface density model as well.

In section 2, we explain the calculation method and initial conditions. The simulations results are discussed in section 3. Section 4 is summary and discussion.

2. Calculation Method and Model

2.1. Orbital Integration

We integrate orbits with 4th order Hermite scheme (Makino & Aarseth 1992) and hierarchical individual time step (Makino 1991) as in KI02. The equation we used is

$$\frac{\mathrm{d}\boldsymbol{v}_j}{\mathrm{d}t} = -\frac{GM_\odot}{|\boldsymbol{r}_j|^3}\boldsymbol{r}_j - \sum_{j\neq k}\frac{GM_j}{|\boldsymbol{r}_j-\boldsymbol{r}_k|^3}(\boldsymbol{r}_j-\boldsymbol{r}_k) + \boldsymbol{f}_{\mathrm{GD}} - \sum_k \frac{GM_k}{|\boldsymbol{r}_k|^3}\boldsymbol{r}_k. \tag{1}$$

The first term is the gravity from the sun. The second term is the mutual gravity between the protoplanets, the third term expresses the damping of eccentricities and inclinations due to the disk, which we will explain in section 2.2, and the last one is an indirect term. Last term was omitted in KI02, since they only dealt with Mars-sizes protoplanets; they did not include Jupiter and Saturn. However, since we include Jupiter and Saturn in the present paper, the indirect term cannot be neglected.

When protoplanets collide, perfect accretion is assumed. The physical radius of a protoplanet is determined by its mass M and internal density ρ_{p} as

$$r_{\mathrm{p}} = \left(\frac{3}{4\pi}\frac{M}{\rho_{\mathrm{p}}}\right)^{1/3}. \tag{2}$$

We adopt 3 gcm^{-3} as for ρ_{p}.

2.2. Gravitational Gas Drag

We consider the damping of orbital eccentricities and inclinations due to disk-planet interaction, which we call "gravitational drag", as in KI02. Gravitational drag is more effective than aerodynamic gas drag for protoplanets larger than Moon (Ward 1993). We assume that Jupiter and Saturn do not interact with the disk because they would form a gap in the disk around their orbits wide enough to make the drag force ineffective.

The gravitational drag force $\boldsymbol{f}_{\rm GD}$ is expressed as

$$\boldsymbol{f}_{\rm GD} = -\frac{\boldsymbol{v} - \boldsymbol{v}_{\rm gas}}{\tau_{\rm damp}}, \tag{3}$$

(KI02), where $\boldsymbol{v}$ and $\boldsymbol{v}_{\rm gas}$ are velocities of a protoplanet and the gas respectively. We here assume the gas motion is non-inclined circular Keplerian motion. Damping time scale of gravitational drag is

$$\tau_{\rm damp} \simeq \left(\frac{M_\odot}{M}\right)\left(\frac{M_\odot}{\Sigma_{\rm gas} r^2}\right)\left(\frac{c_{\rm s}}{v_{\rm kep}}\right)^4 \Omega_{\rm kep}^{-1}, \tag{4}$$

where Σ is the surface density of the gas disk, $c_{\rm s}$ is sound velocity of disk gas and $\Omega_{\rm kep}$ is Keplerian frequency (Ward 1989, 1993, Artymowitz 1993). Supposing the minimum mass disk model with gas surface density given by $\Sigma^{\rm min} = 1700\,(r/1{\rm AU})^{-3/2}\,{\rm gcm}^{-2}$ (Hayashi 1981),

$$\tau_{\rm damp} \simeq 0.5 \times 10^3 \left(\frac{M}{M_\oplus}\right)^{-1}\left(\frac{r}{1{\rm AU}}\right)^2\left(\frac{\Sigma}{\Sigma^{\rm min}}\right)^{-1} {\rm years}. \tag{5}$$

In the cases with a decaying gas disk, we assume exponential decay of the gas surface density as

$$\Sigma(t) = \Sigma_0 \exp\left(-\frac{t}{\tau_{\rm gas}}\right), \tag{6}$$

where $\tau_{\rm gas}$ is a constant depletion time scale. As a consequence, damping time scale lengthens as

$$\tau_{\rm damp}(\Sigma(t)) = \tau_{\rm damp}(\Sigma_0) \exp\left(\frac{t}{\tau_{\rm gas}}\right). \tag{7}$$

2.3. Initial Conditions

(i) Distribution of protoplanets

As in KI02, 15 protoplanets are placed in nearly circular and coplanar orbits with orbital separation (Δa_0) that is given by $\alpha r_{\rm H}$, where α a is constant in each simulation, which ranges from 6 to 12. $r_{\rm H}$ is mutual Hill radius which is defined as

$$r_{\rm H} = \left(\frac{2m}{3M_\odot}\right)^{1/3} r \simeq 0.007\left(\frac{m}{0.2M_\oplus}\right)^{1/3} r, \tag{8}$$

where m is the mass of the each protoplanet. We use equal mass for each protoplanet, $m = 0.2M_\oplus$. The total mass of 15 protoplanets is $3M_\oplus$.

Table I
Maximum and Minimum Semi-major Axis of the Initial Condition

$\Delta a_0(r_H)$	a_{min} (AU)	a_{max} (AU)
6	0.73	1.37
7	0.70	1.43
8	0.66	1.51
9	0.63	1.59
10	0.60	1.67

Table I shows the initial semimajor axes of innermost and outermost protoplanets. The ranges of initial radial distributions of the protoplanets are comparable to or slightly smaller than the present terrestrial planet region. The initial angular distribution is set to be random.

In calculations using time-independent gas model, initial e and i are ~ 0.01 to skip orbitally stable stage, as KI02 did.

In simulations using decaying disk gas, initial eccentricities and inclinations are about 10^{-4}. When the disk gas is still abundant, gravitational drag is so strong that eccentricities and inclinations are kept in this level. As the disk gas decays, distant perturbations between the protoplanets and the perturbations from Jupiter and Saturn pump up the eccentricities to allow orbit crossing.

(ii) Distribution of Jupiter and Saturn
Masses of Jupiter and Saturn are $317.8M_\oplus$ and $95.2M_\oplus$ respectively. Their eccentricities, inclinations, longitude of perihelion, longitude of ascending node, and longitude are taken from planetary orbital elements at the epoch of J2000 (JD 2451545.0) with respect to the mean ecliptic and equinox of J2000. Their eccentricities are ~ 0.05 and their inclinations are ~ 0.03.

3. Results

3.1. Constant Disk Gas

We did 10 simulations using time-independent gas surface density model. In order to compare the results with KI02, the amount of gas is fixed to $\Sigma_{gas} = 2.5 \times 10^{-4}\Sigma^{min}(\tau_{damp} = 10^7 \text{years})$. As explained in section 2, drag force is neglected for Jupiter and Saturn. The initial eccentricities and the inclinations of the protoplanets are ~ 0.01.

The results are shown in Table II.

Table II
Simulation Results with Jupiter and Saturn with Constant Gas

with Jupiter and Saturn					without Jupiter and Saturn	
Run	$\Delta a_0(r_H)$	n_{final}	$M_{max}(M_\oplus)$	e_{max}	n_{final}^{ngp}	$M_{max}^{ngp}(M_\oplus)$
G6	6	5	1.2	0.034	4	1.2
G6$_*$	6	5	1.0	0.016	6	1.2
G7	7	5	1.0	0.017	4	1.8
G7$_*$	7	6	1.4	0.027	8	1.2
G8	8	7	1.0	0.015	7	0.8
G8$_*$	8	6	1.4	0.017	7	1.4
G9	9	7	1.2	0.025	9	1.0
G9$_*$	9	6	0.8	0.051	6	1.4
G10	10	7	0.6	0.021	7	1.4
G10$_*$	10	6	1.0	0.041	7	1.0

First column indicates the name of the simulations. The letter G, in the simulation name, indicates that these are the runs with giant planets. The number after the letter shows the initial separation Δa_0, scaled by r_H. Angular distribution is given randomly and $*$ is for a different angular distribution type. n_{final} is the number of final planets. M_{max} is the largest final planet in each run. e_{max} is its time averaged eccentricity, taken after the isolation takes place. If there are more than one largest planets, the average is taken within the same mass. For comparison, the results of simulations without Jupiter and Saturn (n_{final}^{ngp},M_{max}^{ngp}) are also listed.

The initial conditions of the protoplanets are the same as those of the corresponding runs by KI02. Nine out of ten runs resulted in formation of largest planets with $M_{max} \geq 0.8 M_\oplus$. Since there is forced eccentricity due to Jupiter and Saturn, Earth's eccentricity librates between ~ 0.01 and ~ 0.06. Thus it is possible for the time averaged eccentricities of the planets to be $\sim 0.03 - 0.04$. Most simulations resulted in $e_{max} \leq 0.04$. Hence, formation of Earth-sized, low-eccentricity planets are highly possible. However, too many small planets still tend to remain. The average and the variance of final number of planets are

$$\bar{n}_{final} = 6.0 \pm 0.8. \tag{9}$$

Ones without the giant planets are

$$\bar{n}_{final}^{ngp} = 6.5 \pm 1.6. \tag{10}$$

Although the perturbations of Jupiter and Saturn slightly reduce the number of final planets, the reduction is not enough for $\bar{n}_{final}$ to be consistent with the present terrestrial planets.

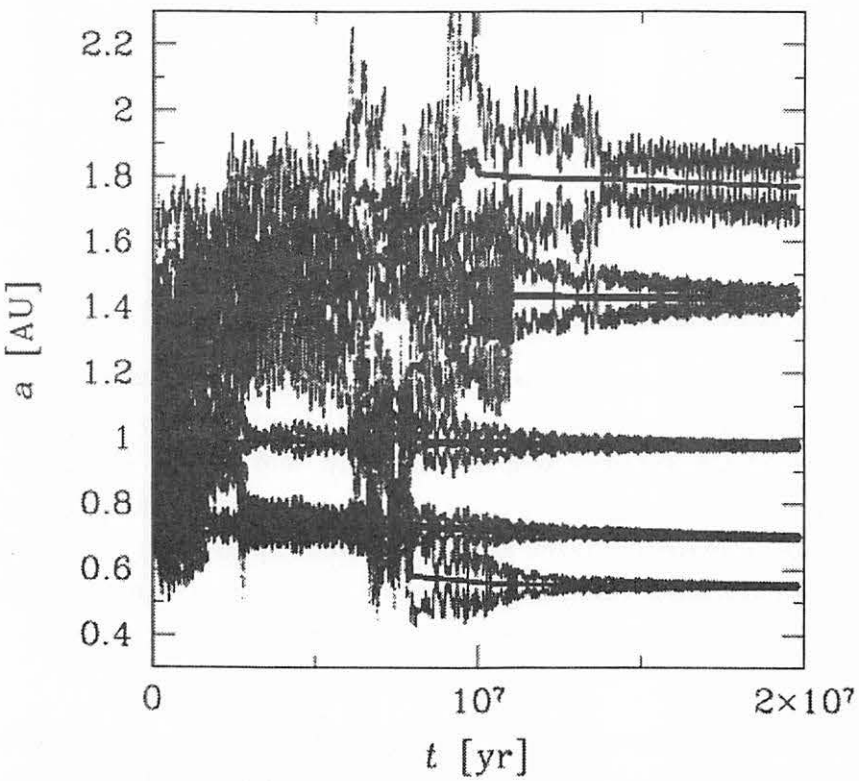

Fig. 1.— Orbital evolution of run G6$_\star$. Semimajor axis, pericenters and apocenters are plotted.

Typical orbital evolution with Jupiter and Saturn is shown in Fig.1. This is the result of run G6$_*$. Although secular perturbations of Jupiter and Saturn generally prolong orbit crossing periods by a factor 2 - 3, they do not enhance collisions between distant protoplanets. The reasons is as follows.

Figure 2 shows the forced eccentricity of a test particle in a system with Jupiter and Saturn. The forced eccentricity is $\sim 0.02 - 0.04$ except at secular resonances, which reduces orbitally stable period ($\tau_{\rm cross}$) (Yoshinaga et.al., 1999). However, it is smaller than the eccentricities pumped up by close encounters between protoplanets themselves during orbit crossing, which are $\sim 0.1 - 0.2$. If protoplanets are included, the forced eccentricity is modulated. The forced eccentricity at $t = 1 \times 10^6$ years of run G6$_*$ is shown in Fig.3. The solid line represents the forced eccentricity of a test particle. Filled dots are the eccentricities of the protoplanets at $t = 1 \times 10^6$ yr. Although number of secular resonances increases, the resonant widths are small. Moreover, the time scale for orbital changing is shorter than excitation time scales of the resonances. Hence, the secular resonances do not work effectively to pump up eccentricities during the orbit crossing periods. Other than the regions of the resonances, the forced eccentricity is $\sim 0.02 - 0.04$. Hence, in the orbit crossing stages, the perturbations due to Jupiter and Saturn do not significantly pump up eccentricities compared with close encounters between the protoplanets. Since radial excursions of the protoplanets are not enlarged by the inclusion of the giant planets, the number of final planets does not decrease.

3.2. Decaying Disk Gas

We have also done 4 simulations with Jupiter and Saturn using the decaying gas model. The initial conditions, the gas depletion time scale and the results are listed in Table III.

Table III
Simulation Results with Jupiter and Saturn with Decaying Gas

Run	$\Delta a_0(r_{\rm H})$	$\tau_{\rm gas}$(years)	$n_{\rm final}$	$M_{\rm max}(M_\oplus)$	$e_{\rm max}$
GD8	8	2×10^6	2	1.6	0.11
GD8$_*$	8	3×10^6	2	1.4	0.21
GD9	9	3×10^6	3	1.6	0.21
GD11	11	1×10^6	2	1.8	0.21

The results of the simulations using the decaying gas model (indicated by D), with Jupiter and Saturn (indicated by G). Notations used are the same as in Table II.

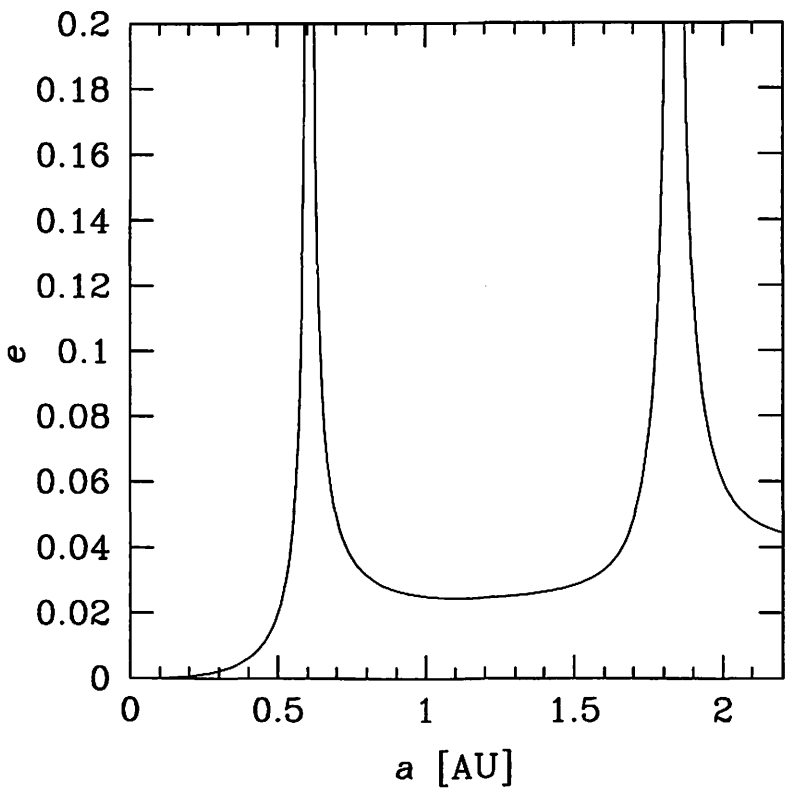

Fig. 2.— Forced eccentricity of a test particle in a system of Jupiter and Saturn only. Forced eccentricity of the region around 1AU is $\sim 0.02 - 0.04$.

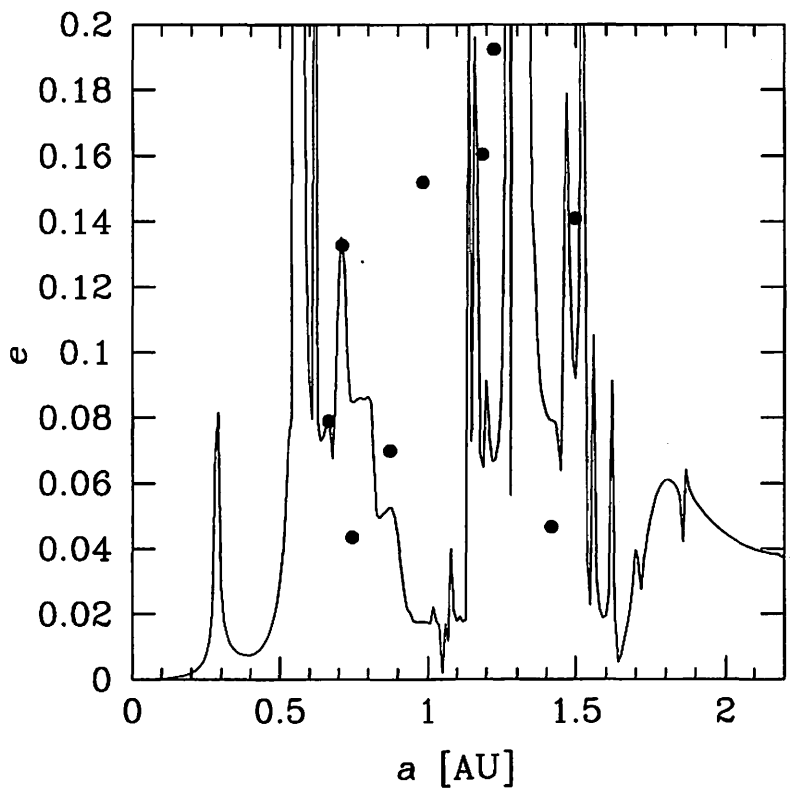

Fig. 3.— Forced eccentricity of a test particle of the system of $G6_*$, at $t = 1 \times 10^6$ yr. Solid line is forced eccentricity of test particles, calculated analytically. The dots represent a and e at the instant.

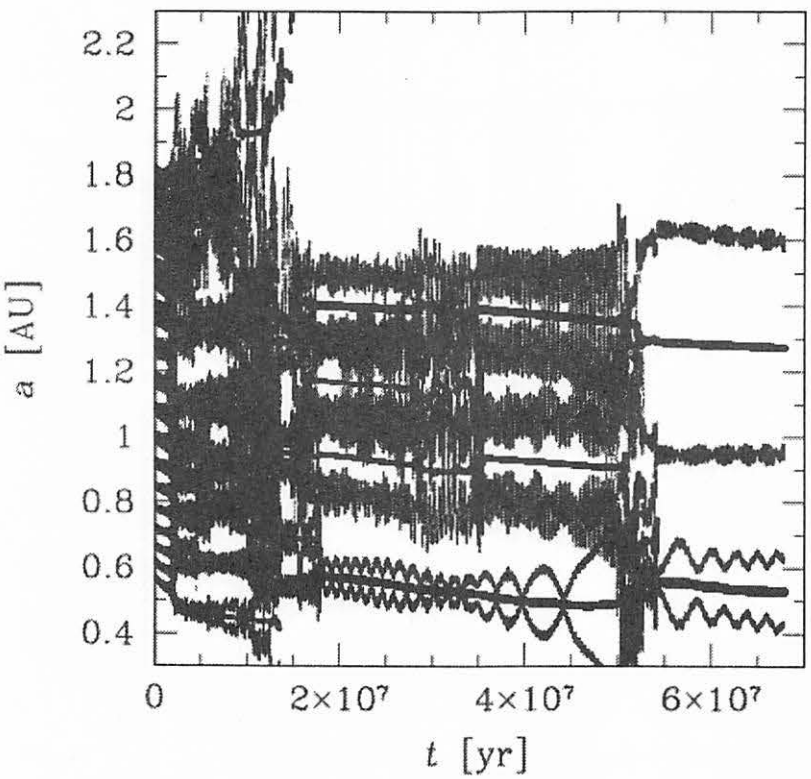

Fig. 4.— Orbital evolution of run GD11. Semimajor axis, pericenters and apocenters are plotted.

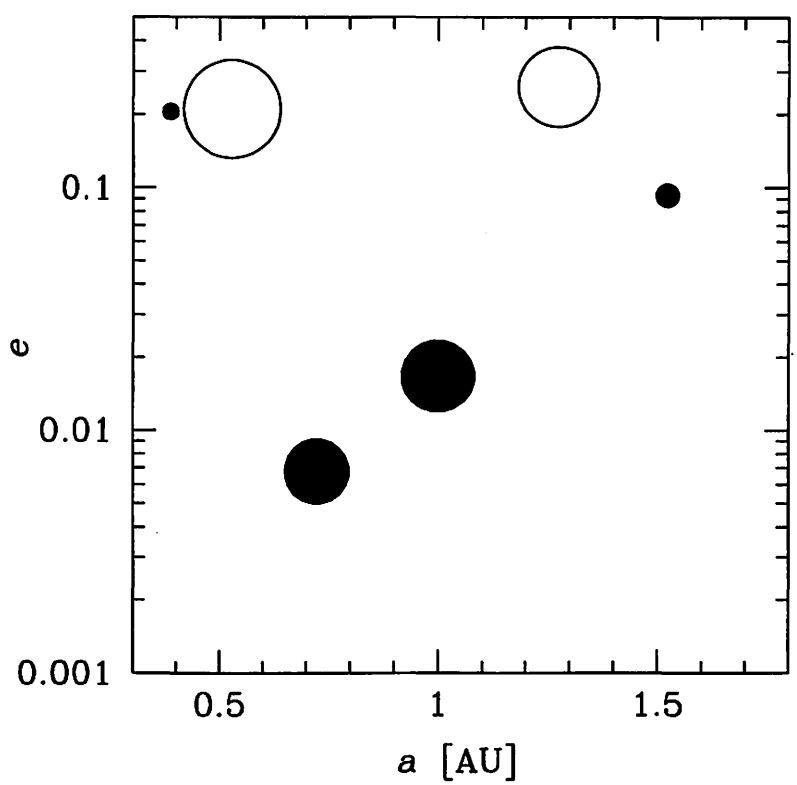

Fig. 5.— Final planets of run GD11. Area of the circle is proportional to the planets' mass. Filled circles are terrestrial planets.

A couple of large planets with large eccentricities ($\gtrsim 0.1$) are formed as in gas free cases (Chambers & Wetherill 1998). Typical orbital evolution is shown in Fig.4, which is the result of run GD11. In all cases, we found repeated orbit crossing periods. Such trend was not found in the results without giant planets as in KI02. When the isolation takes place, the amount of gas left is very little. In this case, $\Sigma(t \lesssim 5 \times 10^7 \text{years}) \lesssim 10^{-23}\Sigma_{\rm H}$. Therefore, there is almost no eccentricity damping force left. Final planets of GD11 are shown in Fig.5. The masses and eccentricities are too large compared to the terrestrial planets in our solar system.

Inclusion of Jupiter and Saturn shortens the orbitally stable period, $\tau_{\rm cross}$ (Ito & Tanikawa, 1999). We confirmed that $\tau_{\rm cross} \sim$ a few $\times 10^5$ years. Because $\tau_{\rm cross}$ is relatively short even after accretion expands orbital separation, orbit crossing periods repeat. In this case, disk gas is almost completely depleted before the final orbit crossing period. Hence, the final results are similar to the results in gas free cases: A few large planets with too large eccentricities are formed. If eccentricities of Jupiter and Saturn are reduced, $\tau_{\rm cross}$ is not shortened so much and the results are similar to those without Jupiter and Saturn.

4. Conclusion and Discussion

Gravitational drag from disk gas lowers the eccentricities of the planets after they are formed (KI02, Agnor & Ward 2002). KI02 confirmed through N-body simulations that Earth-sized planets with low eccentricities, which are consistent with Earth and Venus in the present Solar system, are formed if a mostly depleted gas disk is considered. KI02 adopted time-independent gas density in most of their simulations. It is likely that Jupiter and Saturn have already formed in the orbit crossing stage in such a mostly depleted gas disk, although KI02 did not include the giant planets.

In this paper, we investigate the effect of disk gas and perturbations from Jupiter and Saturn on the final accretion stage of terrestrial planets from Mars-sized protoplanets. We carried out 10 simulations using the time-independent gas model and 4 simulations using the exponentially decaying gas model. Although the perturbations from Jupiter and Saturn enhance collisions of the protoplanets, a reduction in the number of final planets is not significant. Total number of final planets is ~ 6.0 in the cases with Jupiter and Saturn, whereas it is ~ 7.0 if Jupiter and Saturn are not included. Orbital separation of final planets (equivalently, number of the final planets) are determined by eccentricities during orbit crossing. Magnitude of the eccentricities during orbit crossing is $\sim 0.1 - 0.2$. Such

high eccentricities are caused by close encounters between the protoplanets. Meanwhile, forced eccentricity caused by Jupiter and Saturn is $\sim 0.02 - 0.04$, except for the resonance regions. Since the time scale of the orbits to change is short and protoplanets do not remain in the resonance region long enough in the orbit crossing stage, the resonances do not work effectively. Thus, perturbations from Jupiter and Saturn do not have a large effect during the accretion of the protoplanets.

Simulations of the decaying gas model with Jupiter and Saturn result in formation of large mass and large eccentricity planets. This is because of the shortened orbitally stable stage by the perturbations. Orbitally stable period is followed by orbital crossing stage. Orbital crossing repeats until the planets become isolated even with high eccentricities. By the time they are isolated, the amount of gas left is so small that it can not damp the eccentricities of the planets.

The orbit crossing with perturbations from Jupiter and Saturn in a decaying gas disk may be realistic. However, our simulation results show that the planets' eccentricities remain high in such a case. In order for the eccentricities to be damped, other damping source should be present. For example, dynamical friction from the left over planetesimals may be effective.

Another possibility is that Jupiter and Saturn did not effect the protoplanets' orbital evolution. If the eccentricities of Jupiter and Saturn were lower than present ones during the orbit crossing, the effect of their secular perturbations is weak and $\tau_{\rm cross}$ is not shortened. On the other hand, if the gas decayed more rapidly in terrestrial planet region than in giant planet region, terrestrial planets can be formed before the gas giant planets fully grow. In such cases, Earth-sized, low-eccentricity planets are reproduced. However, there remains a difficulty that numerous small bodies may be left.

Orbital evolution of asteroid belt bodies may also have to be considered. Bodies in asteroid belt are likely to be strongly perturbed by Jupiter and Saturn (Chambers & Wetherill 2001, Chambers & Cassen 2002, Petit et.al. 2001). Such bodies can effect the planets in the terrestrial planet region.

REFERENCES

Agnor, C. B., R. M. Canup, and H. F. Levison 1999. On the character and consequences of large impacts in the late stage of terrestrial planet formation. *Icarus*,**142**,219-237.

Agnor, C. B., and Ward, W. R. 2002. Damping of terrestrial-planet eccentricities by density-wave interactions with a remnant gas disk. *APJ*,**567**,579-586.

Artymowicz, P. 1993. Disk-satellite interacton via density wave and the eccentricity evolution of bodies embedded in disks. *Astron. J.*,**419**,166-180.

Chambers, J. E., G. W. Wetherill, and A. P. Boss 1996 The stability of multi-planet systems. *Icarus*,**119**,261-268.

Chambers, J. E., and G. W. Wetherill 1998. Making the terrestrial planets: N-body integrations of planetary enbryos in three dimensions. *Icarus*,**136**,304-327.

Chambers, J. E., and G. W. Wetherill 2001. Planets in the asteroid belt *Meteoritics & Planetary Science*,**36**,381-399

Chambers, J. E., and P. Cassen 2002. The effects of nebula surface density profile and giant-planet eccentricities on planetary accretion in the inner solar system Authors: *Meteoritics & Planetary Science*,**37**,1523-1540

Hayashi, C. 1981. Structure of the solar nebula, growth and decay of magnetic fields and effects of magnetic and turbulent viscosities on the nebula. *Prog. Theor. Phys. Suppl.*,**70**,35-53.

Ito, T., and K. Tanikawa 1999. Stability and instability of the terrestrial protoplanet system and their possible roles in the final stage of planet formation. *Icarus*,**139**,336-349.

Iwasaki, K., H. Emori, K. Nakazawa, and H. Tanaka, 2002. Orbital stability of a protoplanet system under the drag force proprotional to the random velocity. *PASJ*,**54**,471-479

Kokubo, E., and S. Ida 1998. Oligarchic growth of protoplanets. *Icarus*,**131**,171-178.

Kokubo, E., and S. Ida 2000. Formation of protoplanets from planetesimals in the solar nebula. *Icarus*,**143**,15-27.

Kominami, J., and S. Ida 2002. The effect of tidal interaction with a gas disk on formation of terrestrial planets *Icarus*,**157**,43-56

Makino, J. 1991. Optimal order and time-step criterion for Aarseth-type N-body intergrators. *A.P.J*,**369**,200-212.

Makino, J., and S. J. Aarseth 1992. On a hermite integrator with Ahmad-Cohen scheme for gravitational many-body problems. *Publ. Astron. Soc. Jpn.*,**44**,141-151.

Nagasawa, M., H. Tanaka, and S. Ida 2000. Orbital evolution of asteroids during depletion of solar nebula. *Astron. J.*,**119**,1480-1497.

Petit, Jean-Marc, A. Morbidelli, J. Chambers 2001. The Primordial Excitation and Clearing of the Asteroid Belt *Icarus*,**153**,338-347

Ward, W. R. 1989. On the rapid formation of giant planet cores. *Astrophys.J.Lett*,**345**,L99-L102.

Ward, W. R. 1993. Density Wave In The Solar Nebula: Planetesimal Velocities. *ICARUS*,**106**,274-287.

Weidenschilling, S. J.,D. Spaute, D. R. Davis, F. Marzari, and K. Ohtsuki 1997. Accretional evolution of a planetesimal swarm. 2. The terrestrial zone *Icarus*,**128**,429-455.

Yoshinaga, K., E. Kokubo, and J. Makino 1999. The stability of protoplanet systems. *Icarus*,**139**,328-335.

Migration mechanism of proto-Neptune

Keisuke Takahashi* and Sei-ichiro Watanabe*

* Department of Earth and Planetary Sciences, Nagoya University

Abstract: The outer giant planet, Neptune pose a challenge to theories of Solar-System formation. Because of the long dynamical timescales and a low primordial density of material, it takes so long time (longer than age of the sun) to form such large body. On the other hand, a large number of trans-Neptune objects are found to have orbits that are commensurate with the 3:2 mean motion resonance of Neptune's orbit. These fact indicates that Neptune migrated outward at its formation stage and KBOs are captured and dragged at that time. Neptune need to gain angular momentum to migrate outward, and there are tow possibility of the source, disk gas and planetesimals. We assume that the source of angular momentum are planetesimals based on research of Ida et al.(2000). Their N-body simulations indicated that Neptune will migrate toward the direction where surface density of planetesimals are denser. But they could not determine the direction of migration because they neglect the effect of other giant planet. So we investigate the motion of the planetesimals around Proto-Neptune under Jupiter's gravitational effect using α-hermite integrator, because it determine the exchange of angular momentum. As a result, we find that Jupiter's scattering is effective for planetesimals whose angular momentum are reduced by interaction with Neptune because their perihelion are close to Jupiter's orbit. They are scattered by Jupiter to the region where they will not be able to regain angular momentum from proto-Neptune, so proto-Neptune migrate toward outward.

1 Introduction

In a recent research, more than 170 trans-Neptunian objects have been found. Among them, the semi-major axis (a), eccentricity (e), and inclinations (i) of nearly 120 Trans-Neptunian objects have been determined. And Nearly 50 objects have a similar orbit that are commensurate with the 3:2 mean-motion resonance of Neptune's orbit, but rarely with the 2:1. On the other hand, Neptune cannot accumulate at present orbit (30.1AU) in the present theory of formation of Solar System.

There is the model to solve both problems, that is Neptune's outward migration model. This model is like that Planetesimals were captured into Neptune's resonant configuration when it migrated outward from its cradle. In this model, formation time will be shortened by to form Neptune at inner of the solar system. But, in spite of some research try to solve this problems (Fernandez & Ip 1984), It is still rested problems how migrated the Neptune.

Ida et al. (2000) suggest the scenario that Neptune migrate by exchange the angular momentum with planetesimals. Their results are that Neptune's migrate by that scenario is possible and direction is determined by surface density of planetesimals, migrate toward greater surface density. But they didn't consider the effect of

other giant planets and can't determine which direction Neptune migrate toward. So, our purpose is to find the mechanism that can determine the direction of the migration using restricted 4-body calculations.

2 The Model

Our scenario of the Neptune's migration is based on gravitational interaction with the planetesimals. But a planet can't yean asymmetry of motion of the planetesimals around planet. So we investigate the situation that two planets exist around the central star in keplarian motion. To fit this model to our problems, inner planet is Jupiter, outer planet is Neptune, respectively (hereafter we call that). We neglect the effect of gas drag, effect of interaction between planetesimals, and effect of other planet's gravity to see Jupiter's effect purely. In our scenario, mass of Neptune and orbital elements of Neptune (semi-major axis and eccentricity) should be parameters, but we almost fix them in this research. We assume that Jupiter has present orbital elements and present mass, and Neptune's orbital elements are a = 12AU, e = 0.0, and has present mass.

2.1 Fundamental equation

Equation of the motion in the restricted 4-body simulations are given like that. m is the mass, r is the distance to planetesimal, 1 is about central star, 2 is about inner planet, 3 is about outer planet, respectively.

$$\frac{d^2\boldsymbol{r}}{dt^2} = -\sum_{j=1}^{3} \frac{Gm_j}{r_j^3}\boldsymbol{r}_j \tag{1}$$

We research the motion of the planetesimals by calculate this equation using alpha hermite integrator (Kokubo et al. 1998).

2.2 Parameters

Planetesimals in keplarian motion in one plane have a four orbital elements that semi-major axis (a), eccentricity (e), degree of pericenter (ω), initial phase. We put 360 planetesimals par 1 degree for initial phase to each a,e. To determine the dividing number of initial phase, we need a statistic reference because of restricted 4-body simulations behave chaotic for little difference of initial condition. Our reference in this research is the number of unstable planetesimals. The ratio of unstable planetesimals never changed for more dividing number. And we unificate the initial degree of the perihelion for each planets because of the synodic period of each planets in this time is 16.6 year and that is too shorter than the time scale of migration ($10^{6\sim7}$), effect of initial degree of perihelion are smoothing.

We also fix degree of pericenter of planetesimals because it rotate very fast ($\sim 10^2$year) by the effect of planets, there are no affect to several statistic quantities in assumed time scale of migration ($10^6 \sim 10^7$year).

3 Results

From some calculations, we can understand the aspects of the planetesimal's motion. There is stable region between Jupiter and Neptune. Focus to the effects of the Jupiter, there are tow leading effects, supply and remove

planetesimals to or from Neptune's encounter zone. In next subsections, we objectify the supplement and removal effect by the Jupiter's gravity and show the pattern diagram.

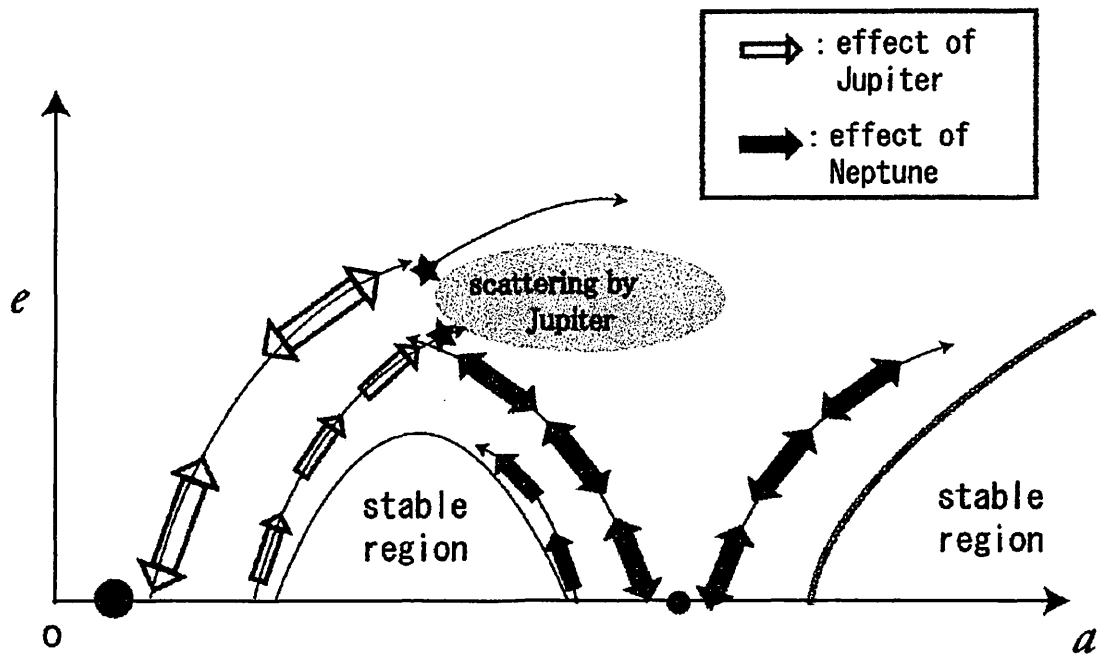

Figure 1: Aspects of the Motion of the planetesimals under the gravity of two giant planets in a-e plane

3.0.1 Supplement effect

Supplement has a major pattern in our model. Planetesimals are scattered by Jupiter from the inner side of the stable region. Angular momentum exchange ratio in such high eccentricity region is less than low eccentricity region, but it's difficult to stay low region because of the strong affection of the Neptune. And low eccentricity region can't gain the planetesimals by the effect of Jupiter, so higher eccentricity region is important for the exchange of the angular momentum. But, suplyed planetesimals also remove same region after experience some interaction with Neputne. Remove at same point indicates that total exchange of angular momentum with Neptune is almost 0. So, supplement effect by Jupiter can be neglected.

Additionally, supplement and removal effects in the outer close encounter zone is only by the exchange with the inner region.

3.0.2 removal effect

By experience some strong interaction with Neputune, planetesimals around moves along Jacobi potensial's contour. This line close to Jupiter while eccentricity get higher and higher, consequently Jupiter's effects get higher and higher, finally they scattered from encounter zone of Neptune.

There are two principal patterns, First, delete by Jupiter after excited the eccentricity by Neptune. Second, delete by Jupiter after supplied by Jupiter. In first pattern, planetesimals have lost their angular momentum by

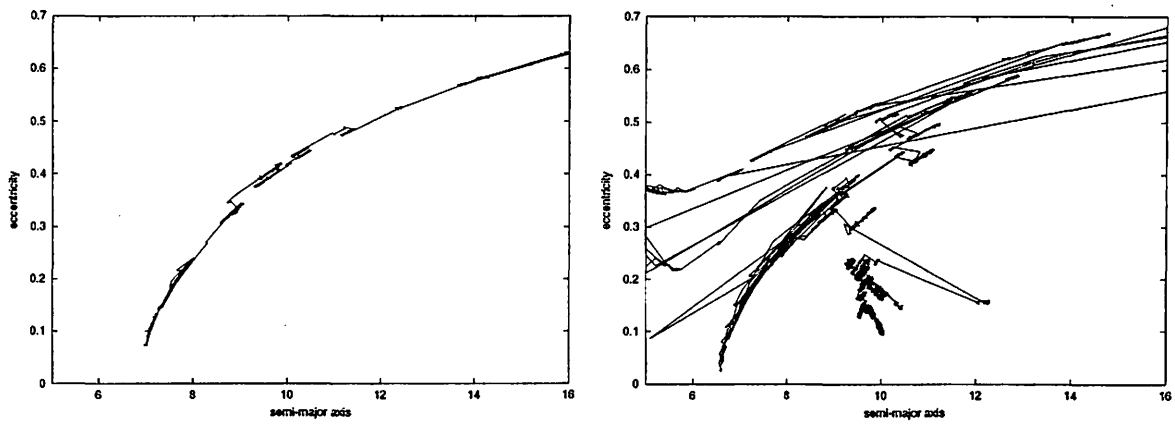

Figure 2: Typical motion of the planetesimals. Left figure shows supplement by Jupiter, and right one shows removed by Jupiter.

giving to Neptune. And, some of them gain angular momentum from Jupiter and removed from this system. Accordingly, angular momentum have moved from Jupiter to Neptune. And in anyway, planetesimals can't deplete Neptune's angular momentum because removal effect act only for inner branch of the encounter zone. It indicate that Neptune migrate outward certainly.

By the neglecting effect, gravitational interactions between planetesimals (like N-body simulations), gas drag, planetesimals may supply from the lower region. It may make variation of the velocity of migration,.

3.1 Velocity of migration

Inner branch of the encounter zone (especially at high eccentricity region) is affected by both Neptune and Jupiter. Removal effect is strong there, and it determine the migration velocity of the Neptune. We calculate the removal ratio of planetesimals around Neptune.

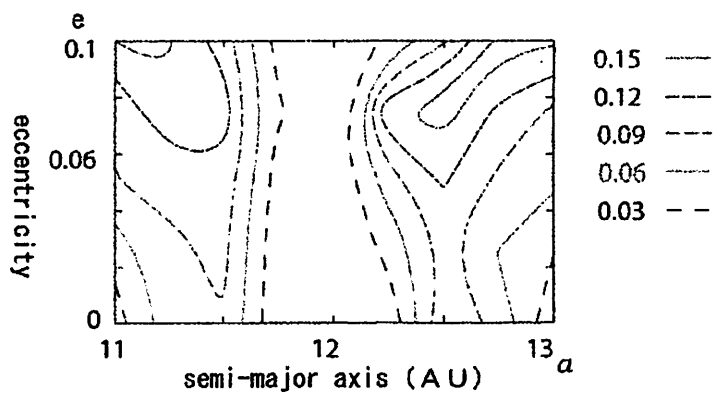

Figure 3: Contour of removal ratio around Neptune in a-e plane.

This contour shows that over 15% of planetesimals were sent to high eccentricity region (belting Jupiter's effect) in 10^4years and removed from encounter zone of Neptune by Jupiter's scattering. These planetesimals are

sent to high eccentricity region by Neptune, therefor Neptune exchanges angular momentum with planetesimals. To calculate the migration velocity of Neptune, we make tow following assumption. First, all Juipter's scattering are occur at $e = 0.18, a = 10.5$AU. Second, there are rested planetesimals that 20% of Hayashi model (Hayashi et al. 1981). By multiplying the ratio of Jupiter's scattering, we estimate that Neptune's migration velocity is $0.02\text{AU}/10^4 year$. But it's a very rough estimation, so we should estimate more strictly in future work.

4 Summary

We have investigated the migration mechanism of Neputne using restricted 4-body simulation. If Jupiter existed inner of the Neptune, planetesimals around Neptune were avoided return path to encounter zone of Neptune by scattering of Jupiter. And by the asymmetry of Jupiter's effect, only inner planetesimals scattered when its angular momentum are minimum in that region. This fact indicate that all planetesimals scattered by Jupiter gives angular momentum to Neptune, and Neptune will migrate toward outward. But there are many neglecting effect. To build up the migration theory of Neptune, we need more calculations.

The Evidence of an Early Stellar Encounter and Orbital Evolution due to Gas Drag in Edgeworth Kuiper Belt Objects.

Hiroshi Kobayashi

1. INTRODUCTION

More than 800 objects are observed in Edgeworth-Kuiper belt (EKB). EKB objects (EKBOs) are divided into three dynamical classes: resonant EKBOs, classical EKBOs (CEKBOs), and scattered EKBOs (Jewitt & Luu 2000). Figure 1 shows the distribution of eccentricities e and inclinations i of EKBOs. Inclinations are scaled in units of radians with respect to the ecliptic plane in this paper. The filled circles show the multiple observed objects and the dot lines and the dashed lines show the locus of orbits with perihelia q at 30AU and 35AU, respectively. The resonant EKBOs are in mean motion resonance with Neptune. Most of them are in the 3:2 mean motion resonance ($\simeq$ 39.5AU) with Neptune. They are also called Plutinos, since Pluto are also in the 3:2 resonance. The scattered EKBOs have perihelia q of 30-35AU because Neptune located about 30AU greatly scattered them (Duncan *et al.* 1995). The CEKBOs have semimajor axes beyond 42AU and perihelia beyond 35AU.

Although objects with small eccentricity e and semimajor axes a between 36 and 39AU are dynamically stable (Duncan *et al.* 1995), there are few objects observed in this region. This may be because of an outward orbital migration of Neptune. The outward orbital migration of Neptune results in the 3:2 resonance passing in the region between 36 and 39AU and then the objects in the region are thought to be captured by the 3:2 resonance (e.g., Malhotra 1993; 1995; Ida *et al.* 2000). The outward migration of 7AU can pump up e up to 0.3, which explains large eccentricities of Plutinos.

The CEKBOs are dynamically excited, but they cannot be pumped up by present planetary perturbations and resonances (e.g., Malhotra *et al.* 2000; Kuchner *et al.* 2002). Their i are distributed up to 0.6 while their e are smaller than 0.2 because of the constraint on q. In the CEKBOs, there are two inclination-population, i.e., $i \sim e$ and $i \gg e$ (Brown 2001). Levison & Stern (2001) suggest that larger objects tend to have large i. The CEKBOs are discovered to have a within 50AU. There are some previous studies on the excitation of CEKBOs. (a) Petit *et al.* (1999) proposed that Earth-size protoplanets scattered by Neptune would pump up e and i of CEKBOs. (b) According to Thommes *et al.* (2002), a proto-Neptune forms near Jupiter and it is scattered by Jupiter during gas accretion of Jupiter. Then, the scattered proto-Neptune pumps up e and i of CEKBOs (Thommes *et al.*

2002). (c) An early stellar encounter is also proposed as a possible mechanism pumping up e and i of CEKBOs (Ida *et al.* 2000 here after ILB00). (d) The sweeping secular resonances in EKB during the depletion of the solar nebula would excite CEKBOs, too (Nagasawa & Ida 2000). Though they adopt the midplane of nebula disk is set at the ecliptic plane, Nagasawa *et al.* (2002) also show the sweeping secular resonance can pump up i if the midplane is set at the invalid plane of solar system. (e) Gomes (2003) suggests that the outward orbital migration of Neptune can form the objects with large i, $e \gtrsim 0.2$, and $a \gtrsim 42$AU. Neptune scatters the objects during its outward migration and orbits of the scattered objects evolve due to mean motion, Kozai, secular resonances. They have large i and the objects that is originally in EKB have small i.

All of mechanisms can pump up e and i. In the mechanisms (a), (b), and (c), i are pumped up as large as e. They cannot explain the objects with $i \gg e$. In the mechanism (d), i can be pumped up much larger than e. In this case, there are few objects with small i. In mechanism (e), there are objects with $i \gg e$. However, the objects with large i and $a \geq 42$AU have e larger than 0.2. It is difficult for each of mechanisms to explain the two inclination-population. The depletion of CEKBOs beyond 50AU could be caused by an early stellar encounter. A stellar encounter can pump up e and i in outer region. Most of observations are near the ecliptic plane. Then, the objects with large i are rarely observed ILB00. In the other mechanisms, the objects beyond 50AU have small e and i. Thus, the other mechanisms cannot explain the depletion of EKBOs beyond 50AU.

In general, stars are born as members of an open cluster. Stellar clusters would evaporate on timescales more than 10^8 years (Kroupa 1995; 1998). This evaporation would be caused by gravitational interactions between stars, so that many stars experience gravitational perturbations of the other stars during the evaporation. More than half of T Tauri stars have protoplanetary disks (e.g., Beckwith and Sargent 1996), which would eventually form planetary systems on timescales 10^6-10^9 years (e.g., Safronov 1969; Wetherill 1980; Hayashi *et al.* 1985). Planetary systems would be affected by stellar encounters more or less during their formation stage.

A stellar encounter pumps up e and i of objects in outer region ILB00. In inner region, the gravitational potential of the central star is deep and then the objects are not significantly perturbed. A stellar encounter results in a steep increase of e and i with semimajor axes in $a \gtrsim 0.3D$, where D is a pericenter distance of a passing star. In outer region, the relative velocity between objects are large after a stellar encounter. The collision between the objects are destructive. As a result, collisions between objects lead to growth in inner region. In outer region, collisions are destructive and planet formation is inhibited. Then, the collisions lead to dust production (formation of dust-debris disk) and the remaining large objects become

CKBOs.

The depletion CEKBO beyond 50AU can be explained only by an early stellar encounter, because a stellar encounter lead to a steep increase in e and i with semimajor axes. Though a stellar encounter can pump up e and i larger than 0.1, it is not clarified whether it can explain the two inclination-populations or not. After strong excitation by a stellar encounter, most of the excited objects have i as large as e. Such objects are dynamically unstable, because their perihelia are close to Neptune's orbit (e.g., Duncan *et al.* 1995). After an early stellar encounter, however, the orbits of CKBOs can evolve due to some effects, such as hydrodynamical gas drag and collision. In the previous studies on the CEKBOs, the gas drag effects were examined. At the first step, we investigate the orbital evolution of EKBOs due to hydrodynamical gas drag. We also examine the possibility that the gas drag changes the objects with $i \sim e$ into the objects with $i \gg e$.

Adachi *et al.* (1976 hereafter AHN) examined the damping rate of e, i, and a due to gas drag in the case of small e and i. Though the results by AHN is not valid for dynamically excited CEKBOs, we roughly estimate the gas drag effect on the EKBOs by the use of their results. When we consider the minimum-mass solar nebula model, according to AHN, the damping time of e and i is roughly given by

$$\frac{\tau_0}{e+i} =\simeq 2.3 \times 10^8 \left(\frac{e+i}{0.1}\right)^{-1} \left(\frac{d}{100\ \mathrm{km}}\right) \left(\frac{a}{40\mathrm{AU}}\right)^{7/4} \left(\frac{\sigma(40\mathrm{AU})}{7\mathrm{gcm}^{-2}}\right)^{-1} \mathrm{yr}. \qquad (1)$$

where d and $\sigma(40\mathrm{AU})$ are the radius of a object and surface density of nebula disk at 40AU, respectively. It is longer than the nebula life time that is $\sim 10^7$ years. The surface density at 40AU can be higher and then gas drag is effective. In the case of the minimum-mass solar nebula model, σ is in proportion to $r^{-1.5}$. The model of accretion disks is recently that $\sigma \propto r^{-1}$ and this power-law exponent is consistent with observation rather than that of the minimum-mass solar nebula. Adapting the surface density at 1AU of the minimum-mass solar nebula model, the damping time in EKB is $10^7 yr$ in the case of $\sigma \propto r^{-1}$. It follows that the gas drag significantly damps e and i in the disk model. The estimation by AHN is not valid if e and i are large. The orbital evolution of objects with large e and i need be investigate in detail.

In this paper, we investigate the orbital evolution of a object after a stellar encounter. due to gas drag while AHN examined the case of small e and i. Especially as for i, they assumed that $i \ll H/a \ll 1$, where H is the scale height of nebula disk (see Eq. 8). Inaba *et al.* (2000) modified the formulae by AHN in the case of small e and i. We analytically derive the changes in a, e, and i due to gas drag in two cases of large eccentricities and inclinations. We will see that the gas drag effect is stronger than the estimation by AHN in the case of large e. If vertical altitudes in orbits, ia, are larger the disk scale height, the damping

due to gas drag would be weak. We will show that the gas drag effect is stronger than the estimation by AHN, in the case of large e and i. We also construct a simple interpolation formulae, using the analytical results in these three limited cases. Using these interpolation formulae, we investigate the orbital evolution of objects with large e and i in outer region. We discuss gas drag can form two inclination-population.

In §2, we invsetigate the effect of a stellar enounter on a planetesimal disk. In §3, we derive analytical expressions of changes in a, e, and i due to gas drag in limiting cases. We construct the interpolation formulae. Using the interpolation formulae, we investigate the orbital evolution of objects beyond 42AU in §4. We also investigate the orbital evolution, starting from the distribution of objects after a stellar encounter in §5. Finally, we conclude and discuss our findings in §6.

2. DYNAMICS OF A STELLAR ENCOUNTER

2.1. CALCULATION MODEL AND BASIC EQUATION

We model a planetesimal disk as non-self-gravitating, collisionless particles that initially have coplanar circular orbits around a primary (host) star, because two-body relaxation time and mean collision time between planetesimals are much longer than an effective encounter time scale that is comparable to Kepler time scale at pericenter distance (D) of the encounter (for example, it is $\sim 10^3$ years for $D \sim 100$AU). We also neglect hydrodynamical gas drag, because the damping time due to the drag [$\simeq 10^7$-$10^8(d/100\mathrm{km})$ yr at 40AU] is longer than the effective encounter time $\sim 10^3$ years for size $d > 10$cm at 40AU; we are considering planetesimals with the sizes of EKBOs (100km). The particulate disk encounters a hypothetical passing star. Note that the gravitational relaxation, collision and the drag can be important when we consider planet formation on a longer time scale after the stellar passing. We will investigate the effect of gas drag after a stellar encounter in long time 5. The equation of motion of a planetesimal in the heliocentric frame (the frame with the primary star at center) is

$$\frac{d^2\mathbf{r}_j}{dt^2} = -\frac{GM_1}{|\,\mathbf{r}_j\,|^3}\mathbf{r}_j + \frac{GM_2}{|\,\mathbf{R}-\mathbf{r}_j\,|^3}(\mathbf{R}-\mathbf{r}_j) - \frac{GM_2}{|\,\mathbf{R}\,|^3}\mathbf{R}, \tag{2}$$

where M_1 and M_2 are masses of the primary and the passing stars, $\mathbf{r}_j$ and $\mathbf{R}$ are position vectors of the planetesimal j and the passing star. The first term in the r. h. s. is force to produce Kepler motion around the primary star, and the second and third terms are direct and indirect perturbing forces of the passing star.

We scale length by pericenter distance D of the stellar encounter, mass by the primary

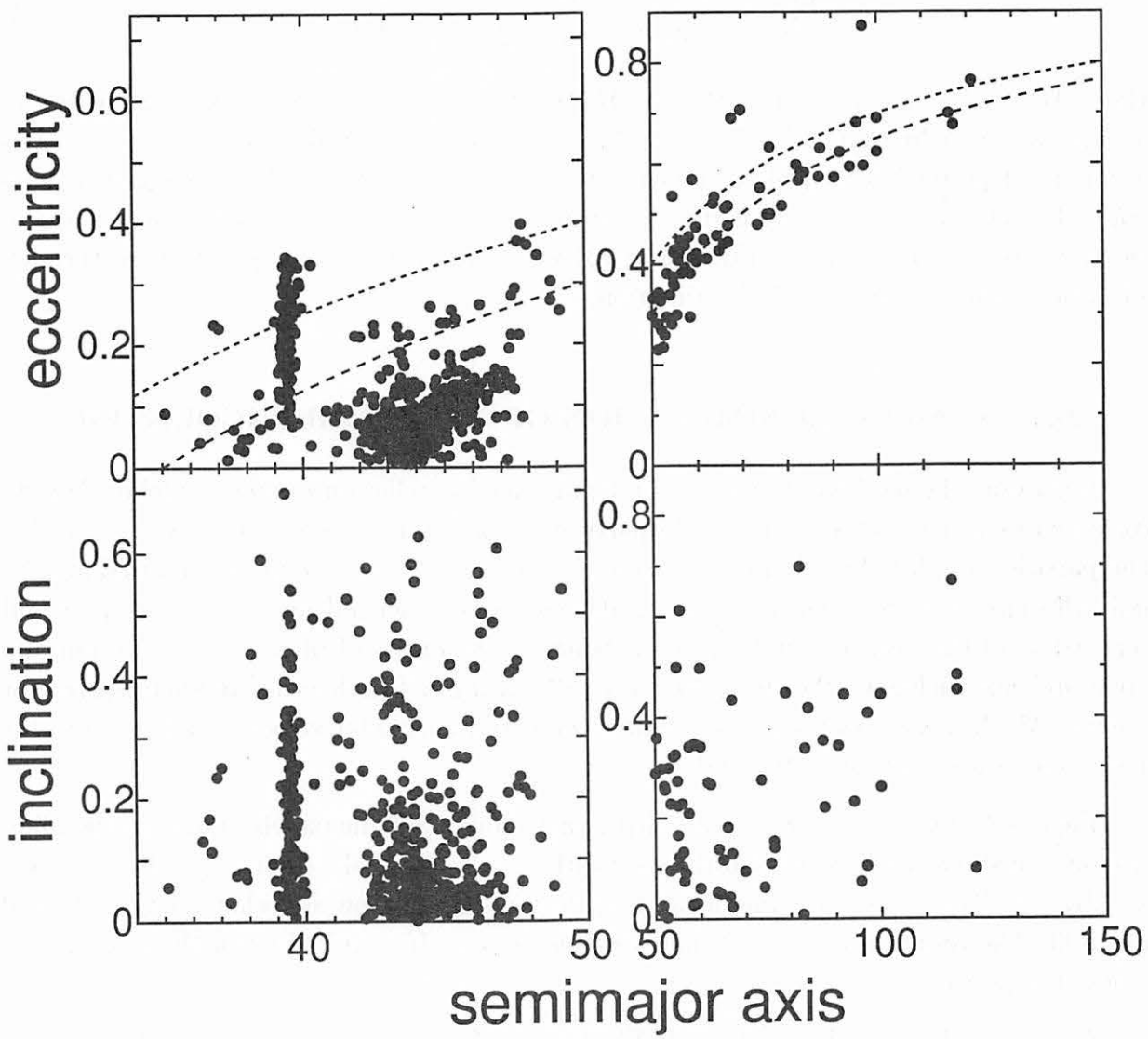

Fig. 1.— In left side panels, e (top) and i (bottom) of the classical objects and the resonant objects as a function of a. In right side panels, e (top) and i (bottom) of scattered objects as a function of a. The locus of orbits with q at 30AU (dot lines) and 35AU (dushed lines) are also plotted in top panels.

star mass M_1, and time by $\Omega_{\rm kep}^{-1}$ where $\Omega_{\rm kep}$ is Keplerian frequency at $a = D$ given by $\sqrt{GM_1/D^3}$. Equation (2) is then transformed to

$$\frac{d^2\tilde{\mathbf{r}}_j}{d\tilde{t}^2} = -\frac{\tilde{\mathbf{r}}_j}{|\,\tilde{\mathbf{r}}_j\,|^3} - \frac{M_*(\tilde{\mathbf{r}}_j - \tilde{R})}{|\,\tilde{\mathbf{r}}_j - \tilde{R}\,|^3} - \frac{M_*\tilde{R}}{|\,\tilde{R}\,|^3}, \tag{3}$$

where $M_* = M_2/M_1$, $\tilde{\mathbf{r}}_j = \mathbf{r}_j/D$, $\tilde{\mathbf{R}} = \mathbf{R}/D$, and $\tilde{t} = \Omega_{\rm kep}t$. Thus the parameters of encounters are inclination (i_*) relative to the initial planetesimal disk, eccentricity (e_*), and argument of perihelion (ω_*) of orbit of the passing star, and the scaled passing star mass (M_*). The encounter geometry is illustrated in Fig. 3. We calculate changes in e and i of the planetesimals according to Eq. (2) or (3) with various encounter parameters, through orbital integration and analytical estimation.

2.2. NUMERICAL SIMULATION OF A STELLAR ENCOUNTER

Regarding the method of numerical integration of a stellar encounter, we follow ILB00. We integrated orbits of 10,000-100,000 particles with surface number density $n_s \propto a^{-3/2}$. The particles are distributed in the region $a/D = 0.05$-0.8. Since we neglect mutual gravity and collisions of planetesimals, the particular choice of a-dependence of n_s and outer and inner edges of the disk does not affect the results. The orbits of planetesimals are initially circle and not inclined. We integrated Eq. (3), using a fourth order predictor-corrector scheme. Much more variations of encounter geometry, encounter velocity, and passing star mass were examined than ILB00 did.

Figures 4 show time evolution of e (left panels) and i (middle panels) and corresponding face-on snapshots (right panels) in the case with $e_* = 1$ (parabolic orbit), $i_* = 30°$, $\omega_* = 0°$, and $M_* = 1$. The (a) top, (b) middle and (c) bottom panels show snapshots at $\tilde{t} = -1.33$, 0 and 1.33. The resultant e and i of planetesimals are mostly acquired when the passing star is near the pericenter.

The pumped-up e and i are shown in Fig. 2.2, as a function of the scaled initial semimajor axis a/D, in the case with $i_* = 5°$ and $\omega_* = 90°$. (M_*, e_*) = (1,1), (0.2,1) and (1,5) in Figs. 2.2a, 2.2b and 2.2c, respectively. In all cases, we find three characteristic regions of pumped-up e and i. In the inner region at $a/D \lesssim 0.1$-0.3, e and i are in proportion to $(a/D)^{5/2}$ and $(a/D)^{3/2}$, respectively. In the outer region at $a/D \gtrsim 0.1$-0.3, e and i have steeper a-gradient and divergence due to initial mean anomaly of planetesimals. In the outermost region, e of many planetesimals, is greater than 1, that is, the particles are ejected from the system. ILB00 also found these features. We find that $e \propto (a/D)^{5/2}$ and $i \propto (a/D)^{3/2}$ always hold. Kobayashi & Ida (2001) analytically derive pumped-up e and i. Especially $e_* = 1$, the

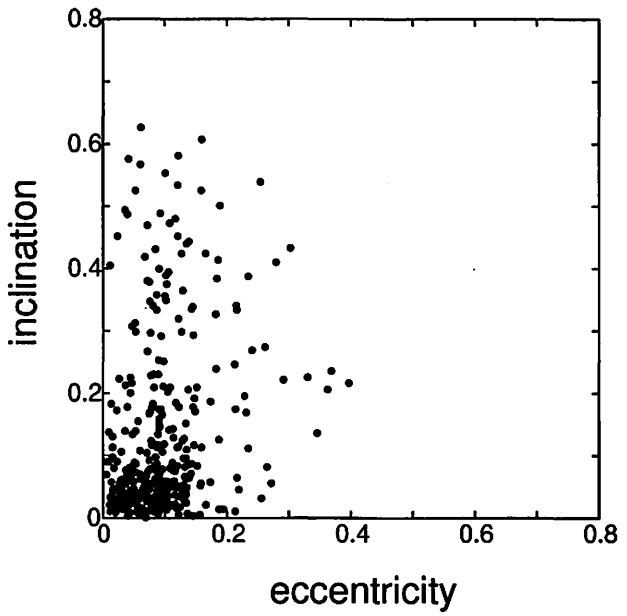

Fig. 2.— $e \times i$ of the classical objects.

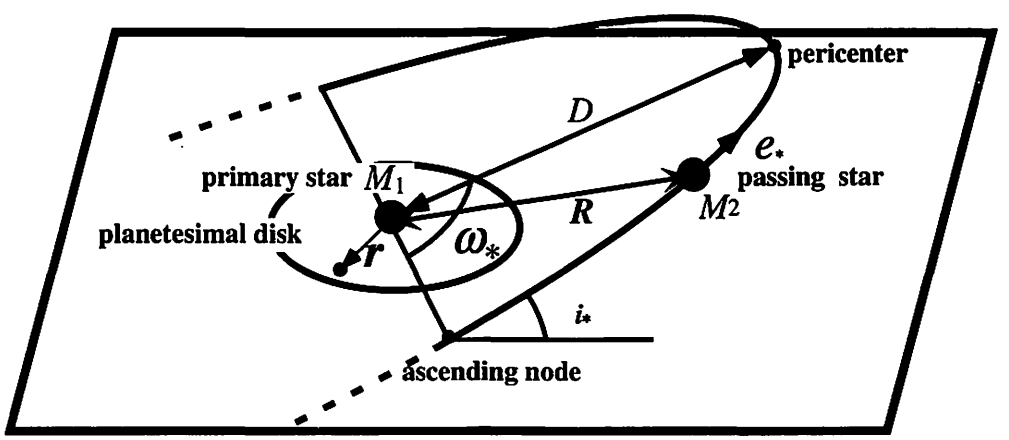

Fig. 3.— Encounter configuration in the frame centered at the primary star with mass M_1. The orbit of the passing star with mass M_2 is characterized by pericenter distance D, eccentricity e_*, inclination i_* and argument of perihelion ω_*. If length and mass are scaled by D and M_1, the encounter parameter are M_* ($= M_2/M_1$), e_*, i_* and ω_*.

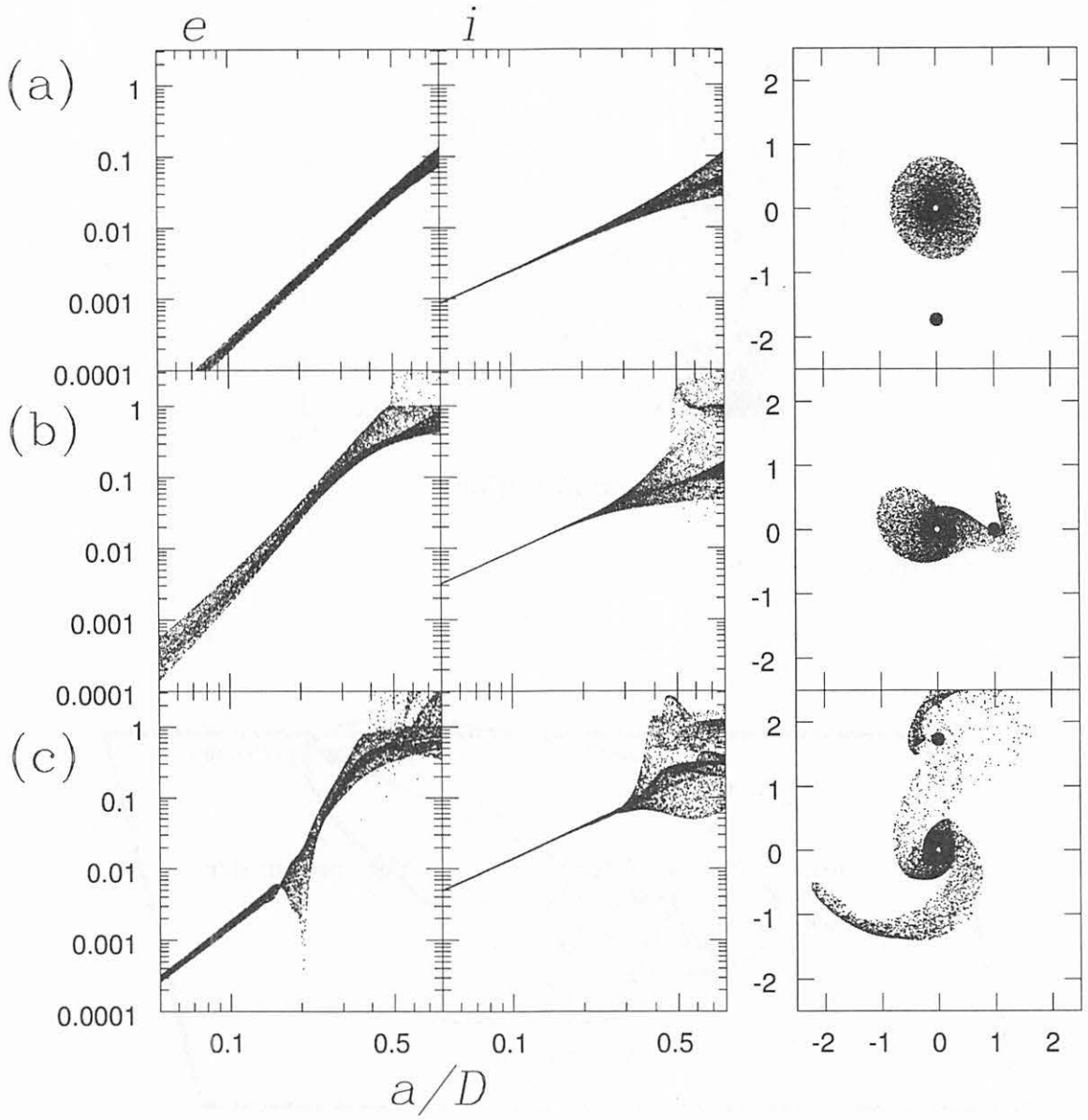

Fig. 4.— Left and center panels are the time evolution of orbital eccentricity e and inclination i of particles as a function of scaled initial semimajor axis a/D. Time proceeds from (a) top to (c) bottom panels. The right panels are face-on snapshots of the disk particles (small dots) and the passing star (filled circle).

formulae is given as

$$e \simeq \frac{15\pi}{32\sqrt{2}}\frac{M_*}{\sqrt{1+M_*}}\left(\frac{a}{D}\right)^{\frac{5}{2}} \times \left[\cos^2\omega_*\left(1-\frac{5}{4}\sin^2 i_*\right)^2 + \sin^2\omega_*\cos^2 i_*\left(1-\frac{15}{4}\sin^2 i_*\right)^2\right]^{\frac{1}{2}}, \quad (4)$$

$$i \simeq \frac{3\pi}{8\sqrt{2}}\frac{M_*}{\sqrt{1+M_*}}\left(\frac{a}{D}\right)^{\frac{3}{2}}|\sin 2i_*|. \quad (5)$$

Note that the dashed lines with triangles are the analytical formulae in inner region. Figures 2.2 show larger M_* and/or smaller e_* produce larger e and i. The agreement between the numerical and analytical results imply that e and i are scaled by $M_*/\sqrt{M_*+1}$. The dependence on e_* is a more complicated form (Kobayashi & Ida 2001, in Appendix)

Figures 6 show the dependence of i_*, in the case with $\omega_* = \pi/2$, $e_* = 1$ and $M_* = 1$. We set i_* as $\pi/6$ (Fig. 6a), $\pi/4$ (Fig. 6b), $\pi/3$ (Fig. 6c), $\pi/2$ (Fig. 6d) and $5\pi/6$ (Fig. 6e). An encounter with $0 \leq i_* < \pi/2$ is a prograde encounter relative to rotation of the planetesimal disk and one with $\pi/2 \leq i_* \leq \pi$ is retrograde. A prograde encounter lead to a steep increase in e and i with a/D in outer region ($a/D \gtrsim 0.3$). The pumped-up i is larger than 0.6 (largest inclination of EKBOs). In the outer regions, pumped-up e and i depend not only on initial radial position but also on azimuthal position of planetesimals. Inclinations are distributed widely with same a. Most of objects with larger i have e larger than 0.2. Thus, they are dynamically unstable for $q < 35$AU and they cannot be CEKBOs. The prograde encounter with $D = 100$-150AU can pump up i as large as 0.6. Retrograde encounters and a encounter with $i_* = \pi/2$ lead to less steep a/D-gradient than that in prograde encounters in the outer region ($a/D \gtrsim 0.2$-0.3). In this case, encounters pump up i lower. Thus, the close encounters with $D \lesssim 60$AU need to pump up i as large as 0.6 in EKB and there are few planetesimals with low i.

Figure 7 shows e and i of planctesimals in the region of classical EKB (a =42-48AU, $q > 35$AU). In the case of small D, the excitation of a stellar encounter is large in the region, because the region between 42-48AU coincide with the outer region where e and i steeply increase with semimajor axes. The pumped-up i are up to 0.6 with D = 100-120AU (see Figs. 7a and 7b). The close encounter with 100-120AU can pump up i as large as largest i of CEKBOs, but there are few objects with small i and small e. On the other hand, the encounters with large D pump up i as large as 0.1 (see Figs. 7c and 7d). The distribution of e and i is narrow in the region of EKB with large D, since pumped-up e and i are almost dependent on radial position only in inner region.

In the outer and outermost regions, pumped-up e and i depend not only on initial radial

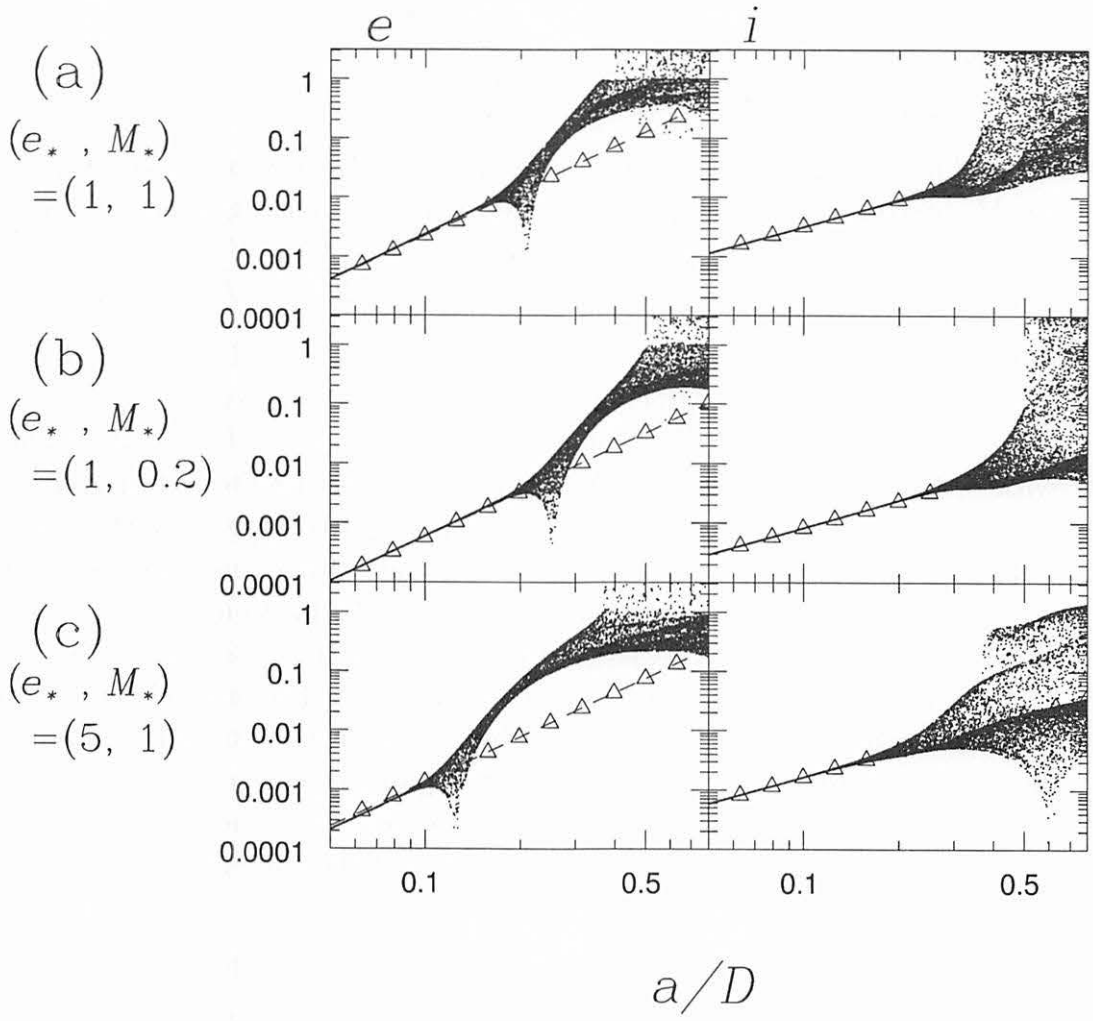

Fig. 5.— (a)Orbital eccentricity e and inclination i of particles pumped-up by a passing star, as a function of initial scaled semimajor axis a/D, in the case with $i_* = 5°$, $\omega_* = 90°$, $e_* = 1$ and $M_* = 1$. (b)The results with $e_* = 1$ and $M_* = 0.2$ (i_* and ω_* are the same). (c)The result with $e_* = 5$ and $M_* = 1$. Dashed lines with triangles express analytical expression given by Eqs. (4) and (5). The dashed lines (in particular, for i) are almost indistinguishable from the numerical results in the inner region.

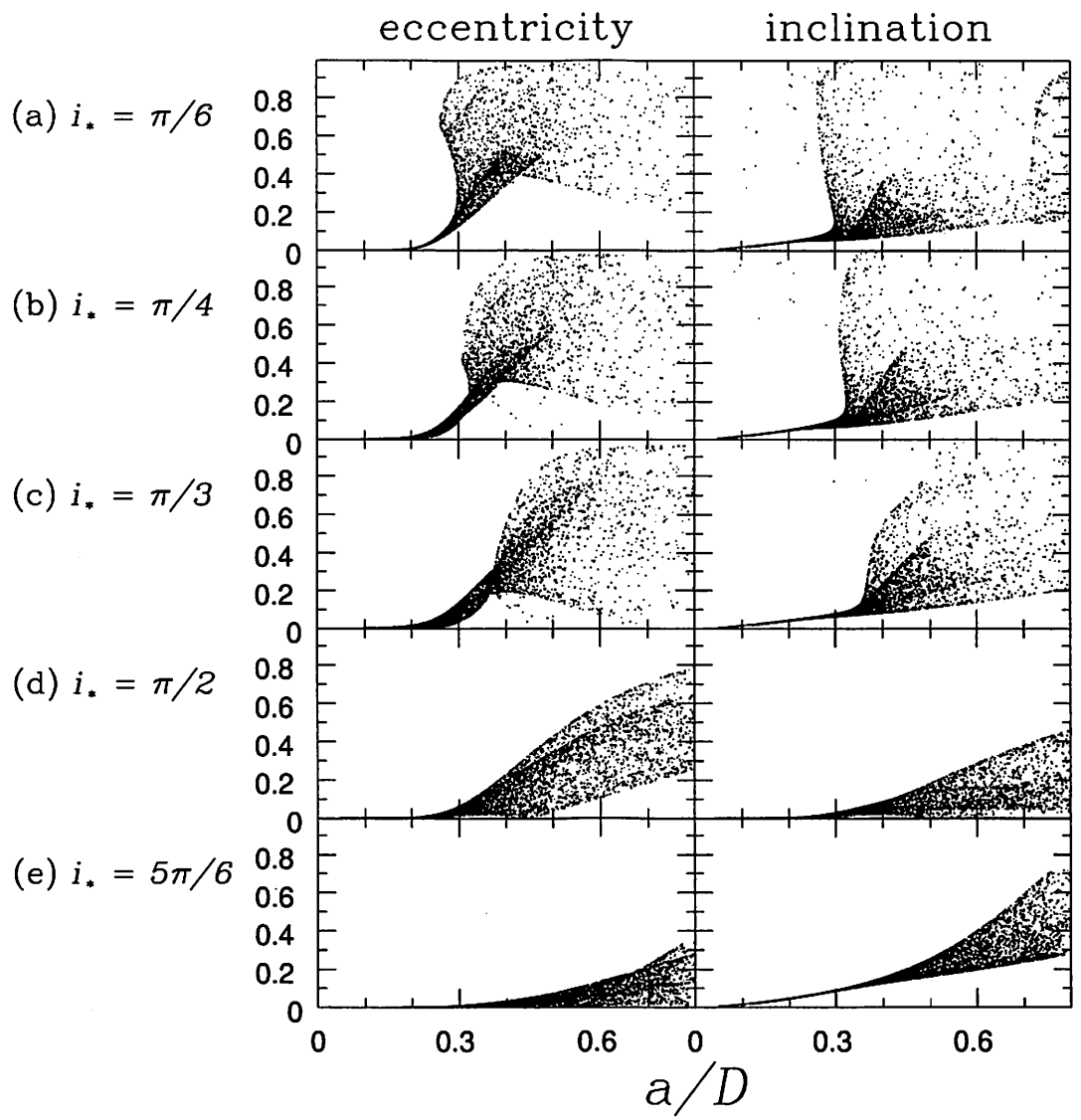

Fig. 6.— Orbital eccentricities e and inclinations i of particles pumped-up by a passing star, as a function of scaled semimajor axis a/D, in the case with $\omega_* = 90°$, $e_* = 1$ and $M_* = 1$. Orbital inclination of the passing star is (a) $\pi/6$, (b) $\pi/4$, (c) $\pi/3$, (d) $\pi/2$ and (e) $5\pi/6$.

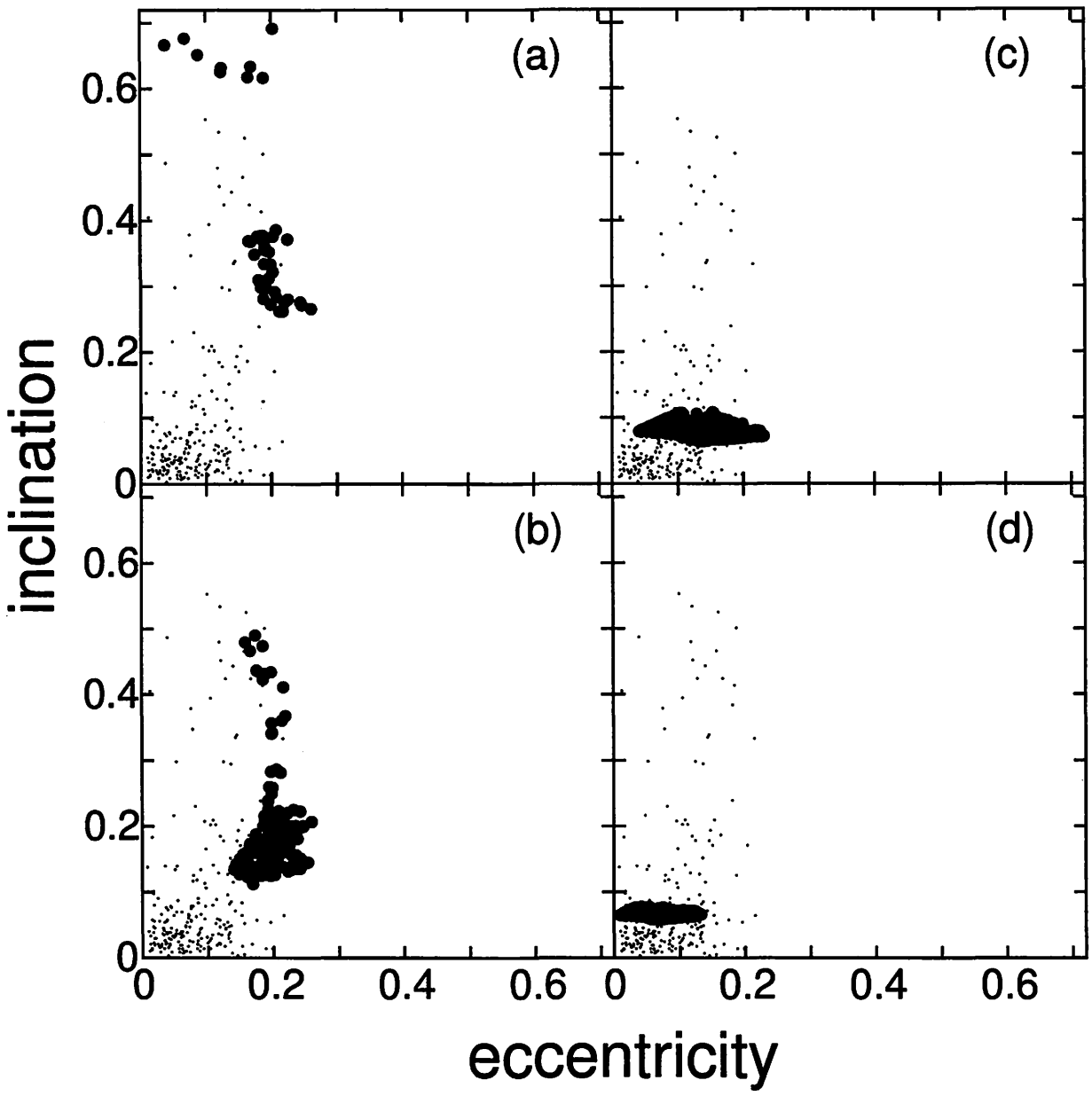

Fig. 7.— Orbital eccentricities e and inclinations i of planetesimals pumped-up by a passing star in the region of EKB (42-48AU), in the case with $i_* = \pi/3$, $\omega_* = \pi/2$, $e_* = 1$ and $M_* = 1$. We adopt pericenter distance D of the passing star as (a) 100AU, (b) 120AU, (c) 140AU, and (d) 160AU.

position but also on azimuthal position of planetesimals. In the case of a prograde encounter, particles in the near side of the disk at pericenter passage are affected by resonances while ones in the far side are hardly affected. In these region, Keplerian angular velocity of planetesimals is not large enough compared with the angular velocity of the passing star, so that such asymmetry remains. In the case of a retrograde encounter, only far-side planetesimals are affected. Note that particles with very small e and i exist at resonant points depending on the azimuthal position, which might be able start runaway accretion.

A stellar encounter can cause disk truncation. Many particle are unbound ($e \gtrsim 1$) at $a/D \gtrsim 0.3$ after the prograde encounter, in the case with $M_* = 1$, $e_* = 1$ (Fig. 4c). Some particles are captured by the passing star during a prograde encounter. Their eccentricities are usually close to unity in the frame in which the passing star is at center. (If the passing star also has a planetesimal disk, some planetesimals are captured by the primary star.) Note that exact amount of the disk truncation and the capture depends on the radius of outer edge of the disk relative to D. Such strong encounters would have the depletion of CEKBOs beyond 50AU. A stellar encounter results in dividing into three region: the planet formation region, the region of EKB, and the truncation region, that is, in the inner region (small e and i), outer region (e and $i \gtrsim 0.1$), and outermost region ($e \sim 1$). It is not clear whether the planetesimals excited by a stellar encounter can become CEKBOs or not. We need to investigate the orbit evolution of planetesimals in long time after a stellar encounter. In next section, we investigate the orbital evolution of objects (planetesimals) with large e and i due to gas drag.

3. CHANGES IN ORBITAL ELEMENTS DUE TO GAS DRAG

3.1. NEBULA DISK MODEL AND GAS DRAG LAW

First, we describe the nebula disk model we adopt. We consider a passive nebula disk rotating around a central star with mass M. We assume that the nebula disk is axisymmetric and in a steady state. To describe the disk, we use a cylindrical coordinate system (r, θ, z). The central star is located at the origin of the coordinate system, the z axis is chosen to coincide with the rotation axis of the disk. In this coordinate system, the gas velocity $\mathbf{v}_{\rm gas}$, has only the θ-component. That is, $\mathbf{v}_{\rm gas} = (0, r\Omega_{\rm gas}, 0)$, where $\Omega_{\rm gas}$ is the angular velocity of the gas. The angular velocity $\Omega_{\rm gas}$ and the gaseous density of the nebular disk ρ, is described by Euler's equation

$$(\mathbf{v}_{\rm gas} \cdot \nabla)\mathbf{v}_{\rm gas} = -\frac{1}{\rho}\nabla p - \nabla\left(-\frac{GM}{\sqrt{r^2+z^2}}\right), \tag{6}$$

where G and P are the gravitational constant and the gas pressure, respectively. We further assume that the disk is geometrically thin and vertically isothermal. Thus we adopt the isothermal equation of state, $p = c^2\rho$, where c is the isothermal sound speed. Under these assumptions, we obtain the gas density ρ from the z-component of Eq. (6) (Hayashi *et al.* 1985), as

$$\rho = \frac{\sigma}{\sqrt{\pi}H} \exp\left(-\frac{z^2}{H^2}\right), \tag{7}$$

where $\sigma(r)(= \int_{-\infty}^{\infty} \rho dz)$ is the surface density of the nebula disk; the disk scale height H is given by

$$H = \sqrt{2}c/\Omega_{\rm K}; \tag{8}$$

and $\Omega_{\rm K} = (GM/r^3)^{1/2}$ is Keplerian angular velocity. For the simplicity, the r-dependences of σ and c are assumed as $\sigma \propto r^{-\alpha}$, $c \propto r^{-\beta}$, respectively. In the minimum-mass solar nebula model, for example, the surface density and the isothermal sound velocity is given by

$$\sigma = 1.7 \times 10^3 \left(\frac{r}{1{\rm AU}}\right)^{-3/2} [{\rm g\ cm^{-3}}], \tag{9}$$

$$c = 9.9 \times 10^4 \left(\frac{r}{1{\rm AU}}\right)^{-1/4} [{\rm cm\ s^{-1}}]. \tag{10}$$

At 40AU, σ is 6.7 g cm^{-3}. In the case of $\alpha = 1$, σ is 43 g cm^{-3}. The angular velocity $\Omega_{\rm gas}$ is obtained from the r-component of Eq. (6) as (e.g., Tanaka *et al.* 2002)

$$\Omega_{\rm gas} = \Omega_{\rm K}\left[1 - \frac{1}{4}\left(\alpha + \beta + \frac{3}{2}\right)\frac{H^2}{r^2} - \frac{\beta}{2}\frac{z^2}{r^2}\right], \tag{11}$$

In the derivation of Eq. (11), the terms of $O(z^4/r^4)$ and the higher are neglected. This neglection is valid even for investigation of the gas drag effect on highly inclined orbits since it is not necessary to consider the gas drag (and the nebula gas) at a high altitude such as $z \gg H$ because of a low gas density. We consider the objects of which size is larger than 10 km-size. The gas drag force per unit mass can be written as (AHN)

$$F_i = A\rho \mid \mathbf{u} \mid u_i, \tag{12}$$

with $A = C_D\pi d^2/2m$, where d and m are the radius and the mass of the object. The relative velocity between a object and gas, $\mathbf{u}$, is given by $\mathbf{u} = \mathbf{v} - \mathbf{v}_{\rm gas}$, where $\mathbf{v}$ is the velocity of the body. In general, the non-dimensional drag coefficient, $C_{\rm D}$, is dependent on Mach number $Ma = u/c$ and Reynolds number $Re = 2\rho u d/\mu$, where μ is viscosity (AHN). In the case with $d \gtrsim$ 10km and a of 40AU, $C_{\rm D}$ is from 1 to 2. $C_{\rm D}$ is 2 in the limit of $Ma \gg 1$. In the case with $d \lesssim$ 10km and a of 40AU, $C_{\rm D}$ is dependent on u (Stokes law). In this paper, we consider the orbital evolution of CEKBOs whose sizes are generally 100km and

C_D is independent of u. Since the relative velocity u_i roughly given by $(e+i)v_K$, we can estimate Mach number as $Ma \sim (e+i)v_K/c$. When e or i is greater than 0.1 at 40AU, Ma is larger than 1. Then, according to AHN, the value of C_D is $C_D \simeq 2$. In §4, we took C_D as 2. Using Eqs. (7), (11), and (12), we can evaluate the drag force on the object by the nebula disk. The ratio of this gas drag force and gravity force of central star is $2 \times 10^{-6} C_D (a/40\mathrm{AU})(\rho/10^{-14}\mathrm{g\ cm}^{-3})(d/10\mathrm{km})^{-1}[(e+i)/0.1]^2$. The gas drag force is much smaller than the gravity force, and the time scale of change in orbital elements caused by gas drag force is much longer than Kepler time.

3.2. GENERAL EXPRESSIONS FOR THE CHANGE IN a, e AND i

We examine the time variations of a, e, i , and the argument of perihelion ω of a object due to the gas drag force. These time variations are described by using Gauss's equations (e.g., Brouwer and Clemence 1961):

$$\frac{da}{dt} = \frac{2}{na}\left(F_R \frac{ae}{\sqrt{1-e^2}} \sin f + F_\phi \frac{a^2\sqrt{1-e^2}}{R}\right), \tag{13}$$

$$\frac{de}{dt} = \frac{\sqrt{1-e^2}}{na}\left[F_R \sin f + F_\phi(\cos f + \frac{e+\cos f}{1+e\cos f})\right], \tag{14}$$

$$\frac{di}{dt} = \frac{1}{na\sqrt{1-e^2}} F_\zeta \frac{R}{a}\cos(f+\omega), \tag{15}$$

$$\frac{d\omega}{dt} = \frac{\sqrt{1-e^2}}{ena}\left[-F_R\cos f + F_\phi \sin f \frac{2+e\cos f}{1+e\cos f} + eF_\zeta \frac{\cot i}{1+e\cos f}\sin(f+\omega)\right], \tag{16}$$

where f and n are the true anomaly and the mean motion, and (R, ϕ, ζ) is the cylindrical coordinate system of which the R-ϕ plane is the orbital plane of the object. The gas velocity in this coordinate,

$$v_{\mathrm{gas},R} = 0, \tag{17}$$

$$v_{\mathrm{gas},\phi} = r\Omega_{\mathrm{gas}}(r,z)\frac{\cos i}{\chi}, \tag{18}$$

$$v_{\mathrm{gas},\zeta} = -r\Omega_{\mathrm{gas}}(r,z)\frac{\cos(f+\omega)\sin i}{\chi}, \tag{19}$$

where $\chi = [1-\sin^2(f+\omega)\sin^2 i]^{1/2} = r/R$.

Using Eq. (12) and the velocities of gas and a object, we can rewrite Eqs. (13)-(16) as

$$\frac{da}{dt} = -A\rho u \frac{2a}{1-e^2}\left[1+2e\cos f+e^2-(1+e\cos f)^{3/2}\kappa\cos i\right], \tag{20}$$

$$\frac{de}{dt} = -A\rho u\left[2\cos f+2e-\frac{2\cos f+e+e\cos^2 f}{(1+e\cos f)^{1/2}}\kappa\cos i\right], \tag{21}$$

$$\frac{di}{dt} = -A\rho u\frac{\cos^2(f+\omega)}{(1-e^2)(1+e\cos f)^{1/2}}\kappa\sin i, \tag{22}$$

$$\frac{d\omega}{dt} = -A\rho u\frac{1}{e}\left[2\sin f+\frac{e\sin 2(f+\omega)-2\sin f(2+e\cos f)}{2\sqrt{1+e\cos f}}\kappa\cos i\right], \tag{23}$$

where ρ, κ, and u are given by

$$\rho = \rho_0(a)\left(\frac{(1-e^2)\chi}{1+e\cos f}\right)^{-\alpha+\beta-\frac{3}{2}}\exp\left(-\frac{a^2(1-e^2)^2\sin^2(\omega+f)\sin^2 i}{2h^2(1+e\cos\omega)^2}\right), \tag{24}$$

$$\kappa = \frac{\Omega_{\rm gas}}{\Omega_{\rm K}\chi^{3/2}}, \tag{25}$$

$$\begin{aligned} u &= |\,\mathbf{u}\,| \\ &= \frac{v_{\rm K}(a)}{\sqrt{1-e^2}}[1+2e\cos f+e^2 \\ &\quad -2(1+e\cos f)^{3/2}\kappa\cos i+(1+e\cos f)\kappa^2\chi^2]^{1/2}. \end{aligned} \tag{26}$$

When e is large, the change in the perihelion distance q due to gas drag can be large. We can obtain the change in q in form of Eq. (20) and (21),

$$\frac{dq}{dt} = -A\rho u q\left[2\frac{1-\cos f}{1+e}-\frac{1+2\cos f+e\cos^2 f}{\kappa}\cos i\right]. \tag{27}$$

We consider the changes in a, e, i, ω, and q averaged over one orbital period. The averaged changes are defined as

$$\left\langle\frac{da}{dt}\right\rangle = \frac{1}{T_{\rm K}}\int_0^{T_{\rm K}}\frac{da}{dt}dt = \frac{1}{2\pi}\int_0^{2\pi}\frac{da}{dt}\frac{(1-e^2)^{3/2}}{(1+e\cos f)^2}df. \tag{28}$$

We also take time-averaging in e, i and ω in same method. Since the gas drag force being much smaller than gravity force of the central star for the object with $d \gtrsim 10$km, we can assume that a, e, i and ω is almost constant in one orbital period. Then, in the RHSs of Eqs. (20)-(23) and (27), only the true anomaly f is dependent on t at the averaging.

Using Eqs. (20)-(22), AHN derived the averaged changes in a, e and i, in the case with $e \ll 1$ and $i \ll H/a$. They considered that $\Omega_{\rm gas} = \Omega_{\rm K}(1-\eta)$ and neglected the dependence of z so that η depends a only. Inaba *et al.* (2000) modified their results in the form

$$\frac{\tau_0}{a}\left\langle\frac{da}{dt}\right\rangle = -2\left\{[(0.97e)^2+(0.64i)^2+\eta^2]^{1/2}\eta + [0.16(\alpha-\beta)+0.59]e^3\right\}, \quad (29)$$

$$\frac{\tau_0}{e}\left\langle\frac{de}{dt}\right\rangle = -[(0.77e)^2+(0.64i)^2+(1.5\eta)^2]^{1/2}, \quad (30)$$

$$\frac{\tau_0}{i}\left\langle\frac{di}{dt}\right\rangle = -\frac{1}{2}\{[0.77e(1-0.16\cos 2\omega)]^2+(0.85i)^2+\eta^2\}^{1/2}, \quad (31)$$

where τ_0 and η are defined as

$$\tau_0 = \frac{1}{A\rho v_{\rm K}} \quad (32)$$

$$\eta = \frac{1}{4}\left(\alpha+\beta+\frac{3}{2}\right)\left(\frac{H}{r}\right)^2. \quad (33)$$

In the case with small e and i, the damping timescale due to gas drag is expressed as $\tau_0 v_{\rm K}/u \sim \dot{a}/\eta a \sim \dot{e}/e \sim \dot{i}/i$. The term of e^3 in Eq. (29) is neglected in this estimate. In the case with large e, da/dt is much larger than the estimate (see §4). We can estimate the damping timescale due to gas drag, using τ_0. In the minimum mass solar nebula model, for example, τ_0 is given by:

$$\tau_0 \simeq 2\times 10^7 \left(\frac{C_{\rm D}}{2}\right)^{-1}\left(\frac{d}{100\ {\rm km}}\right)\left(\frac{a}{40{\rm AU}}\right)^{13/4}\left(\frac{\rho_{\rm mat}}{1{\rm gcm}^{-3}}\right)\left(\frac{\sigma(40{\rm AU})}{6.8{\rm gcm}^{-2}}\right)^{-1}{\rm yr}. \quad (34)$$

In this case, the damping timescale for $e \sim i \sim 0.1$, that is $u \sim 0.1 v_{\rm K}$, is $\sim 10^8$ years and much longer than nebula life time ($\sim 10^7$ years). We also consider the nebula of which α is 1 and surface density at 1AU is same as the minimum-mass solar nebula. In this case, τ_0 is given by 4×10^6 years for object with 100km at 40AU. In this case, the damping time is comparable to the nebula life time for the object with e, $i \sim 0.1$.

Equations (29)-(31) are valid for small e and i. If i of a object is large enough, the object goes at a high altitude where the gas density is extremely low. AHN do not consider this effect. In present study, we derive analytical expressions of the changes in the cases that e is large and that i is large. We will further make the interpolation formulae from the analytical results.

3.3. CASE OF LARGE ECCENTRICITY AND SMALL INCLINATION

Here we consider the case that e is almost equal to unity and i is much smaller than unity. Expanding Eqs. (20)-(23) with respect to $(1-e^2)$, and keeping only the lowest order terms of $(1-e^2)$, we can rewrite Eqs. (20)-(23) as

$$\frac{da}{dt} = -\frac{a}{\tau_0}(1-e^2)^{-\alpha+\beta-3}\Psi(f), \tag{35}$$

$$\frac{de}{dt} = -\frac{1}{\tau_0}(1-e^2)^{-\alpha+\beta-2}\Psi(f), \tag{36}$$

$$\frac{di}{dt} = -\frac{i}{\tau_0}(1-e^2)^{-\alpha+\beta-2}[\Phi_1(f)+\Phi_2(f)\cos 2\omega+\Phi_3(f)\sin 2\omega], \tag{37}$$

$$\frac{d\omega}{dt} = -\frac{1}{\tau_0}(1-e^2)^{-\alpha+\beta-2}[\Theta_1(f)\sin 2\omega+\Theta_2(f,\omega)], \tag{38}$$

where

$$\Psi(f) = 2(1+\cos f)^{\alpha-\beta+3}(2-\sqrt{1+\cos f})\sqrt{3-2\sqrt{1+\cos f}}, \tag{39}$$

$$\Phi_1(f) = \frac{1}{2}(1+\cos f)^{\alpha-\beta+3/2}\sqrt{3-2\sqrt{1+\cos f}}, \tag{40}$$

$$\Phi_2(f) = \frac{1}{2}(1+\cos f)^{\alpha-\beta+3/2}\sqrt{3-2\sqrt{1+\cos f}}\cos 2f, \tag{41}$$

$$\Phi_3(f) = \frac{1}{2}(1+\cos f)^{\alpha-\beta+3/2}\sqrt{3-2\sqrt{1+\cos f}}\sin 2f, \tag{42}$$

$$\Theta_1(f) = \frac{1}{2}(1+\cos f)^{\alpha-\beta+2}\sqrt{3-2\sqrt{1+\cos f}}\cos 2f, \tag{43}$$

$$\Theta_2(f,\omega) = (1+\cos f)^{\alpha-\beta+5/2}\sqrt{3-2\sqrt{1+\cos f}} \times\left[2\sin f+\frac{\sin 2f\cos 2\omega-2\sin f(2+\cos f)}{2\sqrt{1+\cos f}}\right]. \tag{44}$$

In Eqs. (35)-(38), we neglected the terms of $O(i^2)$ and the higher. The changes in a, e, and i caused by the large e are much larger than the difference between the nebula gas velocity and Keplarian velocity, we can consider that $\mathbf{v}_{\rm gas}$ is equal to $\mathbf{v}_{\rm K}$. To take the orbital average on Eqs. (35)-(38), we only have to integrate functions dependent on f over the orbital period. That is,

$$\left\langle\frac{da}{dt}\right\rangle = -\frac{a}{\tau_0}(1-e^2)^{-\alpha+\beta-3/2}\bar{\Psi}, \tag{45}$$

$$\left\langle \frac{de}{dt} \right\rangle = -\frac{1}{\tau_0}(1-e^2)^{-\alpha+\beta-1/2}\bar{\Psi}, \tag{46}$$

$$\left\langle \frac{di}{dt} \right\rangle = -\frac{i}{\tau_0}(1-e^2)^{-\alpha+\beta-1/2}(\bar{\Phi}_1 + \bar{\Phi}_2 \sin^2\omega), \tag{47}$$

$$\left\langle \frac{d\omega}{dt} \right\rangle = -\frac{1}{\tau_0}(1-e^2)^{-\alpha+\beta-1/2}\bar{\Theta}_1 \sin 2\omega, \tag{48}$$

where

$$\bar{\Psi} = \frac{1}{2\pi}\int_0^{2\pi} \Psi(f)(1+\cos f)^{-2} df, \tag{49}$$

$$\bar{\Phi}_1 = \frac{1}{2\pi}\int_0^{2\pi} \Phi_1(f)(1+\cos f)^{-2} df, \tag{50}$$

$$\bar{\Phi}_2 = \frac{1}{2\pi}\int_0^{2\pi} \Phi_2(f)(1+\cos f)^{-2} df, \tag{51}$$

$$\bar{\Theta}_1 = \frac{1}{2\pi}\int_0^{2\pi} \Theta_1(f)(1+\cos f)^{-2} df. \tag{52}$$

As Φ_3 and Θ_2 are odd function on f, their integrations disappear. These $\bar{\Psi}$, $\bar{\Phi}_1$, $\bar{\Phi}_2$ and $\bar{\Theta}_1$ can be expressed as functions of $\alpha-\beta$, by the use of the Gamma and Hypermetric functions. However, since these expressions are very complex, we only show them as a function of $\alpha-\beta$ in Fig. 8. In the minimum-mass solar nebular model, $\alpha-\beta$ is 5/4 and, then, $\bar{\Psi} = 4.94$, $\bar{\Phi}_1 = 2.24$, $\bar{\Phi}_2 = -0.49$, and $\Theta = -0.40$.

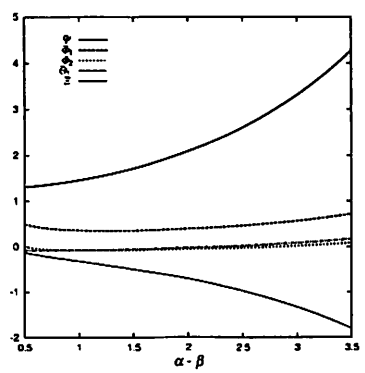

Fig. 8.— $\bar{\Psi}$ (solid line), $\bar{\Phi}_1$ (dashed line line), $\bar{\Phi}_2$ (short dashed line), $\bar{\Theta}_1$ (dot and dashed line), and $\bar{\Xi}$ (dot line) as functions of $\alpha-\beta$.

In order to evaluate the change in q, using Eqs. (45) and (46) are not valid. We remain the higher order of $(1-e^2)$ than Eqs. (45) and (46), and obtain

$$\left\langle \frac{dq}{dt} \right\rangle = -\frac{q}{2\pi\tau_0}(1-e^2)^{-\alpha+\beta-1/2}\bar{\Xi}, \tag{53}$$

where

$$\bar{\Xi} = \int_0^{2\pi} (1+\cos f)^{\alpha-\beta}[1-\cos f-(1+\cos f)^{3/2}]\sqrt{3-2(1+\cos f)}df. \tag{54}$$

The function $\bar{\Xi}$ are also shown in Fig. 8. In the minimum-mass solar nebular model, $\bar{\Xi}$ is -2.6 and q increases due to gas drag in the case with large e.

Figures 9 show the changes in a, e, and i, as functions of $e/(1-e^2)$, in the case of $i = 0.01$. The filled circles, the short dashed lines, and the dashed line show the result of the numerical orbital integration, Eqs. (29)-(31), and Eqs. (45)-(47), respectively. In the case of small e, Eqs. (29)-(31) are agrees with the numerical integral. In the case that e is very close to unity, that is, $1-e^2 \ll 1$, Eqs. (45)-(47) are consistent with the numerical result, and we can derive the excellent equations for changes in a, e, and i, in the case with large e and small i.

3.4. CASE OF LARGE INCLINATION

Next, we consider highly inclined orbits where $a\sin i$ is much larger than H. Object with such a large inclination penetrates the nebula disk twice per an orbital period, i.e., at the ascending and the descending nodes. We only have to examine the gas drag effect at the penetrations. We first examine the penetration at the ascending node ($f \simeq \omega$) in this case, Since, on highly inclined orbits, the duration of a penetration is much shorter than the orbital period, the only density ρ is dependent on time during a penetration in the RHSs of Eqs. (20)-(23). Expanding ρ with $f+\omega$ and putting $f = -\omega$ in other factors in RHSs of Eqs. (20)-(23), we have

$$\frac{da}{dt} = -\frac{2a\tilde{r}^{-\beta+5/2}}{\tau_0(1-e^2)^{3/2}} I(\omega) \exp\left(-\frac{a^2(1-e^2)^2(f+\omega)^2\sin^2 i}{H^2(1+e\cos\omega)^2}\right), \tag{55}$$

$$\frac{de}{dt} = -\frac{\tilde{r}^{-\beta+5/2}}{\tau_0\sqrt{1-e^2}} J(\omega) \exp\left(-\frac{a^2(1-e^2)^2(f+\omega)^2\sin^2 i}{H^2(1+e\cos\omega)^2}\right), \tag{56}$$

$$\frac{di}{dt} = -\frac{\tilde{r}^{-\beta+5/2}\sin i}{\tau_0(1-e^2)^{3/2}} K(\omega) \exp\left(-\frac{a^2(1-e^2)^2(f+\omega)^2\sin^2 i}{H^2(1+e\cos\omega)^2}\right), \tag{57}$$

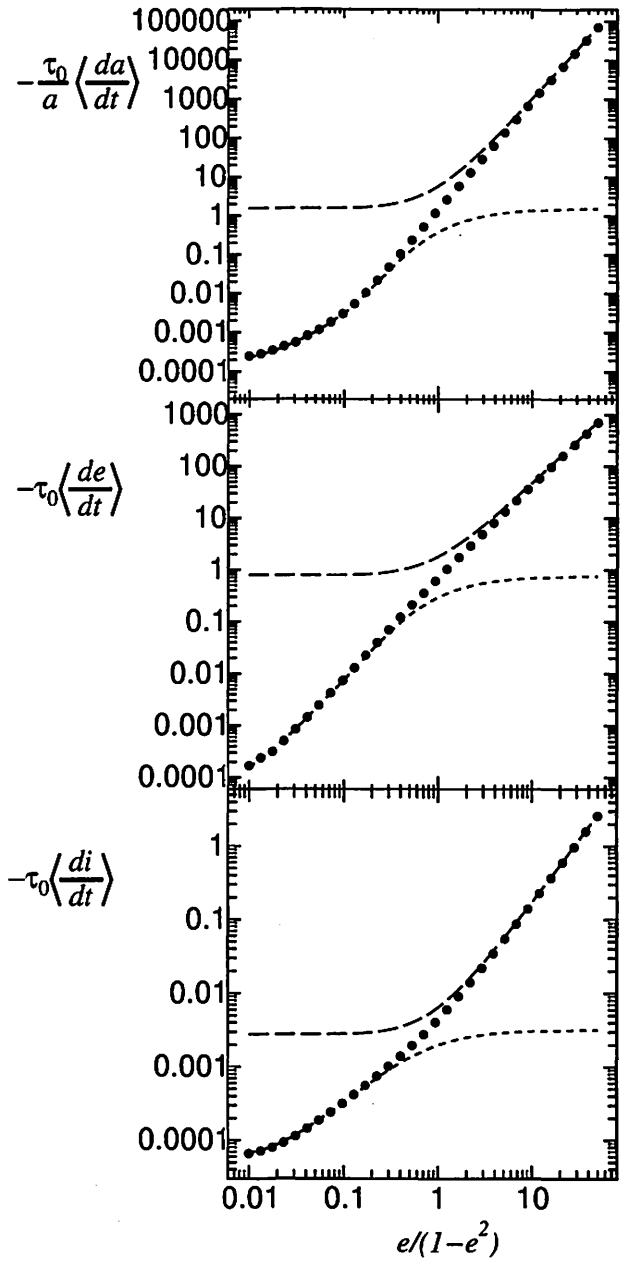

Fig. 9.— The changes in a, e, and i, as a function of the initial $e/(1-e^2)$, in the case with $i = 0.01$, $\alpha = 1.5$, and $\beta = 0.25$. The filled circles, the dashed lines, and the short dashed lines show the numerical result, Eqs. (45)-(47), and Eqs. (29)-(31), respectively.

$$\frac{d\omega}{dt} = -\frac{\tilde{r}^{-\beta+5/2}}{\tau_0(1-e^2)^{1/2}}L(\omega)\exp\left(-\frac{a^2(1-e^2)^2(f+\omega)^2\sin^2 i}{H^2(1+e\cos\omega)^2}\right), \tag{58}$$

where

$$I(\omega) = \tilde{r}^{-\alpha+1}\tilde{u}[1+2e\cos\omega+e^2-(1+e\cos\omega)^{3/2}\cos i], \tag{59}$$

$$J(\omega) = \tilde{r}^{-\alpha+1}\tilde{u}\left[2(e+\cos\omega)-\left(\cos\omega+\frac{\cos\omega+e}{1+e\cos\omega}\right)\sqrt{1+e\cos\omega}\cos i\right], \tag{60}$$

$$K(\omega) = \tilde{r}^{-\alpha+2}\tilde{u}\sqrt{1+e\cos\omega}, \tag{61}$$

$$L(\omega) = \tilde{r}^{-\alpha+1}\tilde{u}\left[\cos\omega\sin\omega+\frac{\cos\omega+e}{1+e\cos\omega}\sqrt{1+e\cos\omega}(\sqrt{1+e\cos\omega}-\cos i)\right], \tag{62}$$

and

$$\tilde{r} = \frac{1-e^2}{1+e\cos\omega}, \tag{63}$$

$$\tilde{u} = \sqrt{2+3e\cos\omega+e^2-2(1+e\cos\omega)^{3/2}\cos i}. \tag{64}$$

In the above, we also assumed that $\mathbf{v}_{\rm gas} = \mathbf{v}_{\rm K}$, since the difference, $\mathbf{v}_{\rm gas} - \mathbf{v}_{\rm K}$, is negligible compared with the large relative velocity $\mathbf{u}$ in this case. In order to obtain the averaged changing rate of the orbital elements from Eqs. (55)-(58), we only have to integrate the exponential functions with respect to f. The integration at the penetration at the ascending node yields:

$$\int_{-\omega-\pi/2}^{-\omega+\pi/2}\exp\left(-\frac{a^2(1-e^2)^2(f+\omega)^2\sin^2 i}{H^2(1+e\cos\omega)^2}\right)df \tag{65}$$

$$\simeq \int_{-\infty}^{\infty}\exp\left(-\frac{a^2(1-e^2)^2(f+\omega)^2\sin^2 i}{H^2(1+e\cos\omega)^2}\right)d(f+\omega) \tag{66}$$

$$= \frac{H(1+e\cos\omega)\sqrt{\pi}}{a(1-e^2)\sin i}. \tag{67}$$

On the other hand, as for the changes at penetration at the descending node, we can obtain them, by replacing ω by $\omega+\pi$ in (55)-(58). Summing up the changes at two penetrations, we finally obtain the averaged change as

$$\left\langle\frac{da}{dt}\right\rangle = -\frac{a}{\tau_0}\frac{H_0}{\sqrt{\pi}a(1-e^2)^2\sin i}[I(\omega)+I(\omega+\pi)], \tag{68}$$

$$\left\langle\frac{de}{dt}\right\rangle = -\frac{1}{\tau_0}\frac{H_0}{\sqrt{\pi}a(1-e^2)\sin i}[J(\omega)+J(\omega+\pi)], \tag{69}$$

$$\left\langle \frac{di}{dt} \right\rangle = -\frac{1}{\tau_0} \frac{H_0}{\sqrt{\pi} a (1-e^2)^2} [K(\omega) + K(\omega+\pi)], \tag{70}$$

$$\left\langle \frac{d\omega}{dt} \right\rangle = -\frac{1}{\tau_0} \frac{H_0}{\sqrt{\pi} a (1-e^2) \sin i} [L(\omega) + L(\omega+\pi)], \tag{71}$$

$$\left\langle \frac{dq}{dt} \right\rangle = -\frac{q}{\tau_0} \frac{H_0}{\sqrt{\pi} a (1-e^2) \sin i} [N(\omega) + N(\omega+\pi)], \tag{72}$$

where

$$N(\omega) = \frac{I(\omega)}{1+e} - J(\omega) \tag{73}$$

and $H = H_0 (a/a_0)^{\beta-3/2}$. In minimum-mass solar nebula model, if we take a_0 as 1AU, H_0 is 0.047. We derive dq/dt from $(1-e)da/dt - ade/dt$.

In Fig. 10, we show the changes in a, e, and i of a object due to gas drag, as functions with i, in the case of $e = 0.1$ and 0.9. The disk scale height H is in proportion to $r^{-1.25}$ and we take H as 0.1 at initial a of a objects. The filled circles and the dashed line with two dots are the numerical integrations and Eqs. (68)-(71), respectively. When $i \gg H$, Eqs. (68)-(71) are valid for any e. When e is small, Eqs. (68)-(71) are rewritten

$$\left\langle \frac{da}{dt} \right\rangle = -\frac{2\sqrt{2} H_0 (1-\cos i)^{3/2}}{\sqrt{\pi} \tau_0 \sin i}, \tag{74}$$

$$\left\langle \frac{de}{dt} \right\rangle = -\frac{\sqrt{2} H_0 (1-\cos i)^{1/2}}{\sqrt{\pi} \tau_0 a \sin i} \left[(2-\cos i) + 2\left(\alpha - \frac{1}{4}\right)(1-\cos i)\cos^2\omega \right] e, \tag{75}$$

$$\left\langle \frac{di}{dt} \right\rangle = -\frac{\sqrt{2} H_0 (1-\cos i)^{1/2}}{\sqrt{\pi} \tau_0 a}, \tag{76}$$

$$\left\langle \frac{d\omega}{dt} \right\rangle = -\frac{H_0 (1-\cos i)^{1/2} \sin 2\omega}{\sqrt{2\pi} \tau_0 a \sin i}, \tag{77}$$

$\langle dq/dt \rangle$ is equal to $\langle da/dt \rangle$ in this case. Eqs. (74)-(77) show that the changes in a, i, and ω are independent of e and that the change in e is proportional to e, when e is small and i is much larger than H/a.

3.5. GENERAL FORMULAE OF THE ORBITAL CHANGES

We derived the formulae for the changes in orbital elements in three limited cases that $e \ll 1$ and $i \ll H/a$; $1-e \ll 1$ and $i \ll H/a$; $i \gg H/a$. Interpolating the three cases,

we construct general formulae which is valid for any e and i. The way of interpolation is not unique. We choose a accurate and simple formulae, comparing with results of numerical orbital integrations.

At first, we consider the case of $i \ll H/a$. As interpolation formulae between Eqs. (29)-(31) and (45)-(47), we adopt the following expressions:

$$\left\langle \frac{da}{dt} \right\rangle = -2\frac{a}{\tau_0}\left\{ \left[(0.97e)^2 + (0.64i)^2 + \eta^2\right]^{1/2} \eta + [0.16(\alpha-\beta)+0.59]e^3 \right\} (1-e^2)^{-\alpha+\beta-3/2}, \quad (78)$$

$$\left\langle \frac{de}{dt} \right\rangle = -\frac{e}{\tau_0}\left[(0.77e)^2 + (0.64i)^2 + (1.5\eta)^2\right]^{1/2} (1-e^2)^{-\alpha+\beta-1/2}, \quad (79)$$

$$\left\langle \frac{di}{dt} \right\rangle = -\frac{i}{2\tau_0}\left[(0.77e)^2 + (0.85i)^2 + \eta^2\right]^{1/2} (1.37 - 0.21\cos 2\omega)(1-e^2)^{-\alpha+\beta-1/2}, \quad (80)$$

$$\left\langle \frac{dq}{dt} \right\rangle = (1-e)\left\langle \frac{da}{dt} \right\rangle - a\left\langle \frac{de}{dt} \right\rangle. \quad (81)$$

As readily seen, the above expressions are reduced to Eqs. (29)-(31) in the limit of $e \ll 1$. In Figs. 11, we show the changes in a, e, and i of a object, as functions with e, in the case with $i = 0.01$, $\beta = 0.25$, and $\alpha = 1.5$ and 1. The changes given by Eqs. (78)-(80) completely agree with those of the numerical integrations in the whole range of e. Though these formulae do not have accuracy in large e, this method is experientially correct at $\alpha - \beta = 0.5$-3 in 30%, in the case with $e < 0.9$. However, the change in q derived from da/dt and de/dt does not agree with numerical integrals with this accuracy in the case with large e (see Fig. 12).

Next, we construct a general formula connecting Eqs. (78)-(80) to Eqs. (68)-(70). As for the change in a,

$$\ln\left\langle \frac{da}{dt} \right\rangle = \begin{cases} \ln\left\langle \frac{da}{dt} \right\rangle_{(78)} & \left(i \le \frac{H}{2a}\right) \\ \left[\ln\left(\frac{2i}{H}\right)\ln\left\langle \frac{da}{dt}\right\rangle_{(68)}\Big|_{i=\frac{2H}{a}} + \ln\left(\frac{2H}{i}\right)\ln\left\langle \frac{da}{dt}\right\rangle_{(78)}\Big|_{i=\frac{H}{2a}}\right]/\ln 4 & \left(\frac{H}{2a} < i < \frac{2H}{a}\right) \\ \ln\left\langle \frac{da}{dt} \right\rangle_{(68)} & \left(i \ge \frac{2H}{a}\right) \end{cases} \quad (82)$$

We also take interpolation in e and i in the same way. Figure 12 shows the changes in a, e, i, and q of a object, as functions of initial i, in the case with initial e of 0.1, 0.3, and 0.7,

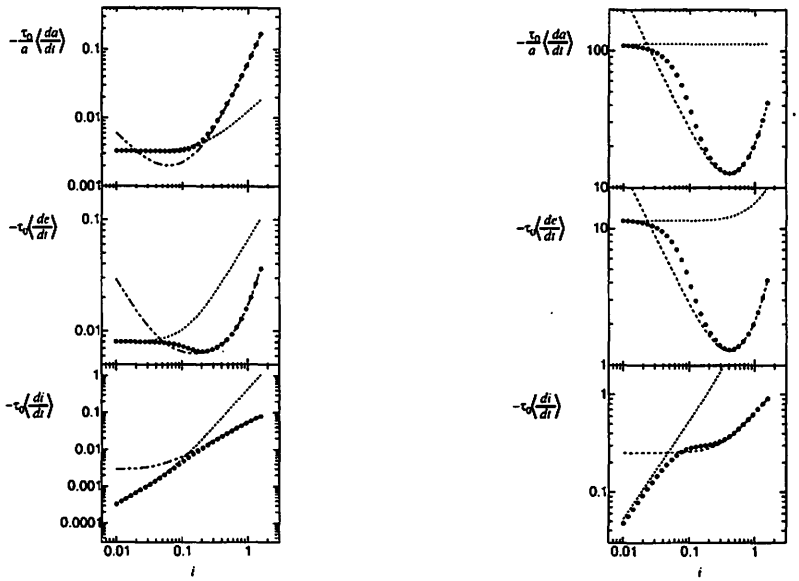

Fig. 10.— The changes in a, e, and i, as a function of the initial i, with initial $e = 0.1$ (left panels) and $e = 0.9$ (right panels) in the case of disk thickness $\delta = 0.1$ at initial a, $\alpha = 1.5$, and $\beta = 0.25$. The filled circle, the dot lines, and the 2-dot dashed lines show the numerical result, Eqs. (78)-(80), and Eqs. (68)-(70), respectively.

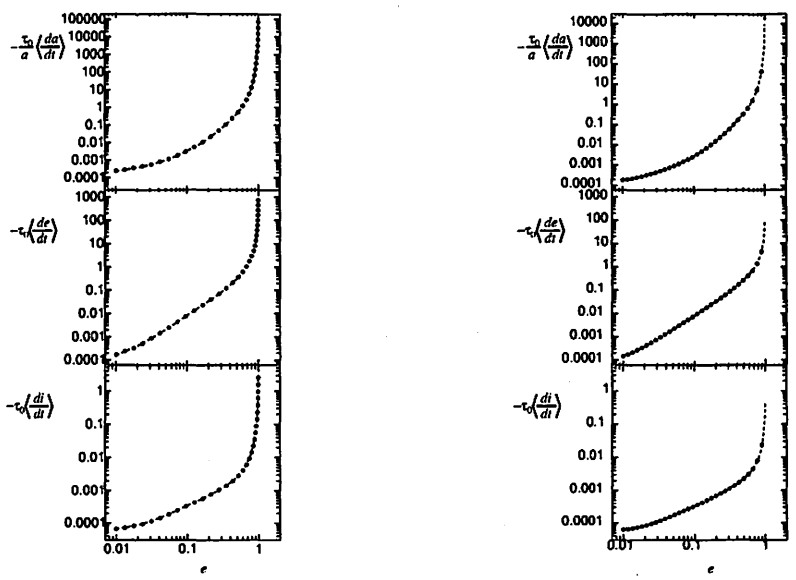

Fig. 11.— The changes in a, e, and i as functions of e with $\alpha = 1.5$ (left pannels) and $\alpha = 1$ (right pannels) in the case of $i = 0.01$, and $\beta = 0.25$. The filled circles and the dashed lines show numerical integrations and Eqs. (78)-(80), respectively.

and $H(a)/a = 0.1$ at initial a of the objects, $\alpha = 1.5$, and $\beta = 0.25$. We derive $\langle dq/dt \rangle$ from the changes in a and e. As for the changes in a, e, and i of a objects, the general formulae (interpolation formulae) agree with the numerical integrations within the accuracy of 30%. In the case with large e, the change in q does not agree well, because Eqs. (78)-(80) have small disagreement for large e and i and this disagreement becomes large to calculate the change in q.

4. ORBITAL EVOLUTION OF OBJECTS DUE TO GAS DRAG

CEKBOs are dynamically stable, and they have a between 42AU and 48AU and their q are larger than 35AU. In this section, we discuss that the change in the orbital distribution of CEKBOs due to gas drag. By using the obtained general formulae in §3.5, we investigate the orbital evolution of a object due to gas drag. We treat ω as a constant value, because ω does not change so much. When the objects have large e and i, gas drag can valuably damp e and i of the objects, even if objects are in the region of EKB. At first, we fix the radii of objects are 100km that is typical values of EKBOs. The strength of gas drag force is related to e, i, and τ_0 which depends on the nebula density and the radius of a objects (see Eq. 32). Thus the orbital change due to gas drag is almost governed by e, i, and the ratio of τ_0 to time for which the orbit has been influenced by gas drag. The results with d 100km after 1×10^7 years are similar to the results with d 10km after 1×10^6 years.

In Fig. 13, we show the variation of a, e, and i of the object which initially have e and i of 0.3, and a of 48AU in the case with $\alpha = 1$ and 1.5. Filled circles and open circles show the orbits in each 1×10^7 years in the case of $\alpha = 1.5$ and $\alpha = 1$, respectively. We assume the surface density at 1AU is 1.7×10^3g cm^{-3} in both of cases (Hayashi *et al.* 1985). The variations of a, e, and i are small in the case with $\alpha = 1.5$. On the other hand, a is damped about 5AU in 3×10^7 years in the case with $\alpha = 1$. Eccentricities and inclinations are also damped half of the initial value. The orbit crosses the line with q at 35AU, because q increase about 3AU in 3×10^7 years. Its orbit become dynamical stable. The damping in e and i accompanies strongly damping in a. If the gas drag damping is effective for CEKBOs, they would come from the outer region.

Figure 14 shows the orbital evolution of objects in e-i plane. Each of objects initially has q of 35AU and filled circles show the orbits in each 1×10^7 years in the case of $\alpha = 1$. These paths in e-i plane is almost same for any initial a, because the ratio between the damping in e and i due to gas drag are mainly dependent on e and i and the dependences of α, β, ω, and H/a is small. If objects have i as large as e, damping in e is as fast as than damping in i. Thus, gas drag does not make objects with $i > 2e$ from objects with $i \sim e$. If we consider

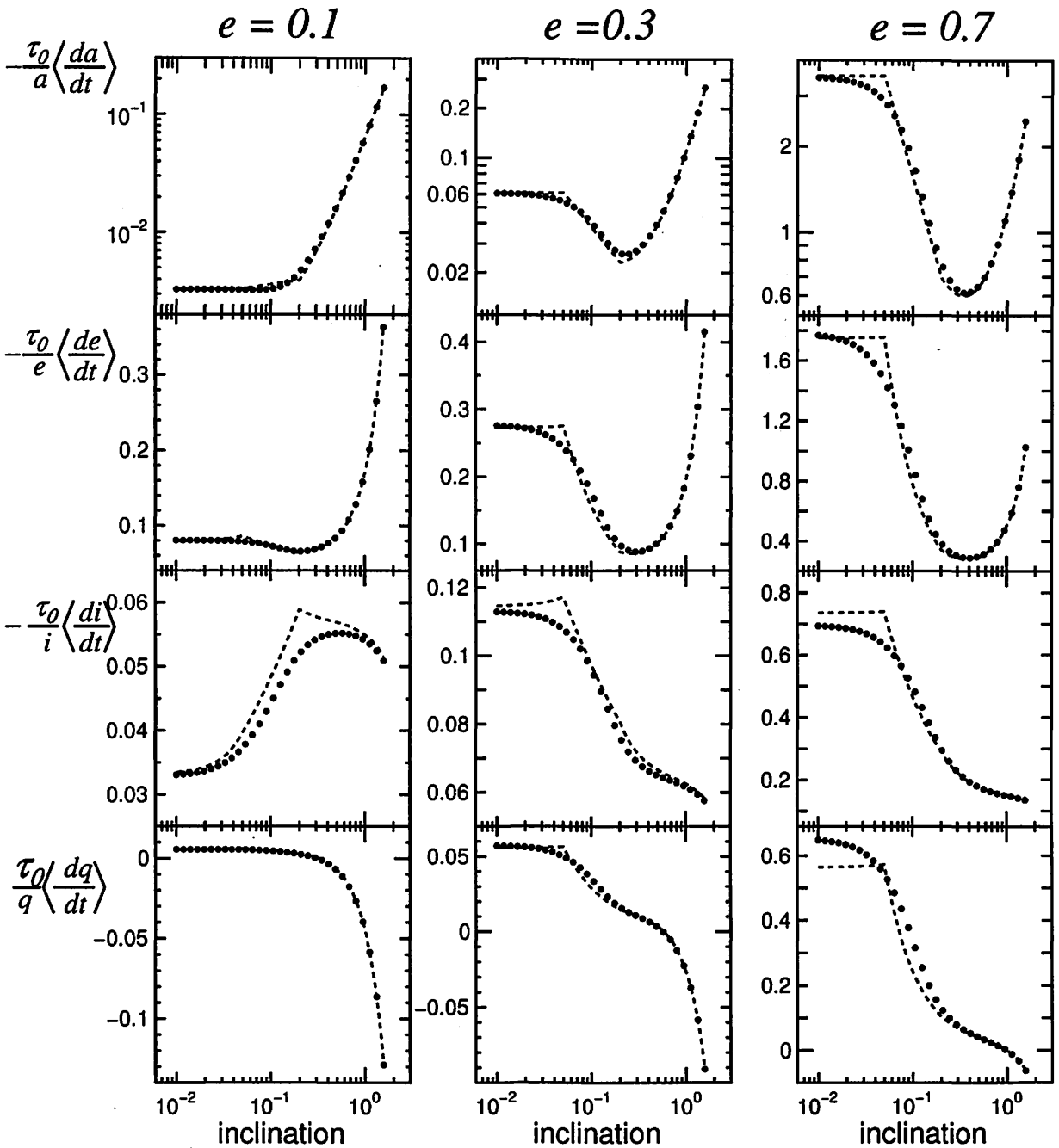

Fig. 12.— The changes in a, e, i, and q as functions of i in the case with $e = 0.1$, 0.3, and 0.5. The full circle plots and the dashed lines show numerical integrations and Eqs. (82), respectively. As for the line of the change in q, we calculate from Eqs. (82).

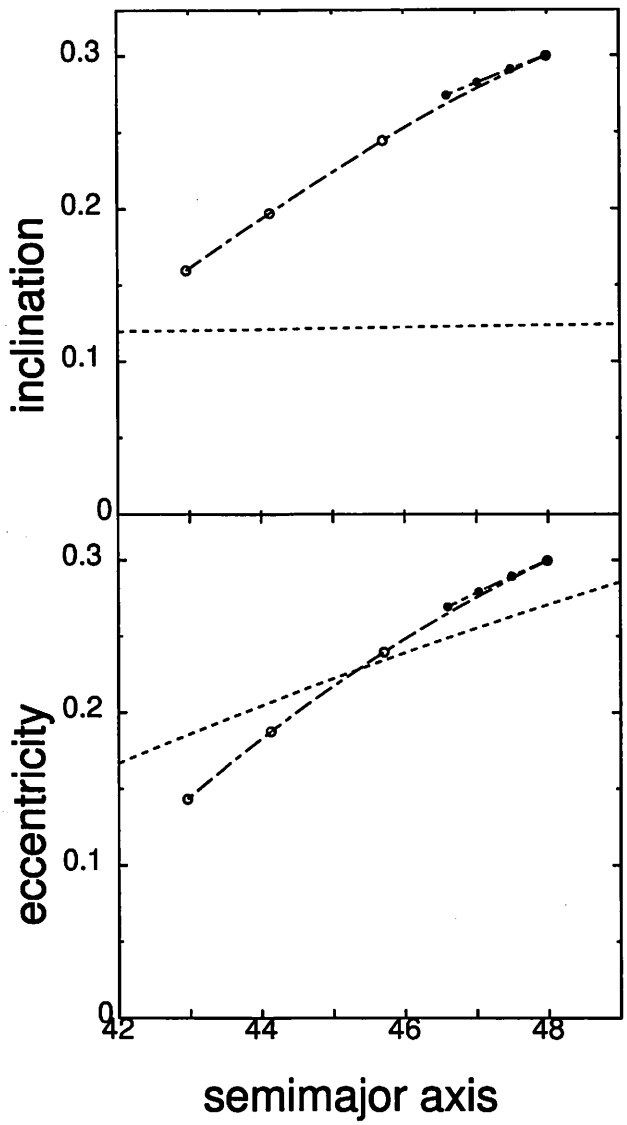

Fig. 13.— Orbital evolution of objects in a-e and a-i plane. Short dashed lines with 2 dots show orbital evolution of a object in the case with $\alpha = 1.5$. Filled circles show orbits of the object per 10^7 years. Short dashed lines with a dot and open circles show same ones, except for $\alpha = 1$.

the orbital evolution due to gas drag only, CEKBOs having $i \gg e$ also had $i \gg 2e$ in past. In Fig. 14, the damping time of objects with $i \gg e$ is shorter than the damping time of the others. It does not mean that the damping in i is fast for the CEKBOs with large i. The perihelia of objects with $i \gg e$ decrease due to gas drag (see Fig. 12). Then, they migrate to the region inside 35AU. In the case of $i \gg e$, the objects with $q \lesssim 35$AU can be CKBOs due to gas drag. The objects with initially $q \gtrsim 35$AU can be in EKB due to gas drag.

Levison & Stern (2001) suggest that large objects tend to have large inclination. Inclination is mainly smaller than 0.1 for small objects with $d \lesssim 200$km. The dumping time in i is so long for objects with $i \lesssim 0.1$ that gas drag cannot form the objects with $i \lesssim 0.1$ from the objects with $i \gtrsim 0.2$. This result shows that the objects with small i originally have small i. This follows that gas drag cannot form such a correlation between inclination and size.

Figures 15 (left panels) shows that orbital changes in a, e, and i of CEKBOs ($a > 42$, $q > 35$) are integrated over inverse time in 3×10^7yr in the case with $\alpha = 1.5$, using the general formulae in §3.5. We adopt the radii of CEKBOs calculated from their absolute magnitudes under assumption that the albedos of CEKBOs are 0.04. The gas drag with $\alpha = 1.5$ does not greatly change the orbital distribution of CEKBOs in 3×10^7 years. We also investigate the orbital evolution of CEKBOs in the case with $\alpha = 1$ (see Fig. 15 center panels). In this case, CEKBOs with $e \geq 0.1$ radially migrate by more than 5AU and were beyond 50AU in 3×10^7 years ago. They are significantly damped e. Then, they had correlation between e and a and the large e tend to be far from Sun. The objects which migrate beyond 50AU had $i \geq 0.3$ and $i \leq 0.2$. Inclinations are damped larger than e, in the case of $i \gg e$. On the other hand, e are damped larger than i, in the case of $i \ll e$. The gas drag dose not significantly change the ratio of e to i. The objects beyond 50AU and perihelia at 30-35AU have small i. On the other hand, the objects beyond 50AU and large i have $q \gtrsim 35$. In the case of $i \gg e$, q decrease due to gas drag (see Fig. 12). The objects scattered by Neptune have q at 30-35AU and large i. If they radially migrate to EKB due to gas drag, they cannot be CEKBOs for $q \gtrsim 35$AU. We investigate the case that surface density is enlarged 3 times (see Fig. 15 right panels). Some objects migrate from the region beyond 1000AU and they had $e \gtrsim 0.9$. Our assumption that gas nebula dose not cut off lead to the objects with a beyond 1000AU. Even if gas nebula has higher density, gas drag cannot significantly change the ratio of e to i. Finally, it is difficult for gas drag to from two inclination-population ($i \sim e$ and $i \gg e$) from the distribution with $e \sim i$, such as the distribution after a stellar encounter. On the other hand, gas drag can form the correlation between a and e and an early stellar encounter can pump up larger e in outer region (Kobayashi & Ida 2001 and see Fig. 6). A stellar encounter which can pump up i larger than e may be able to form the orbital distribution of CEKBOs due to gas drag.

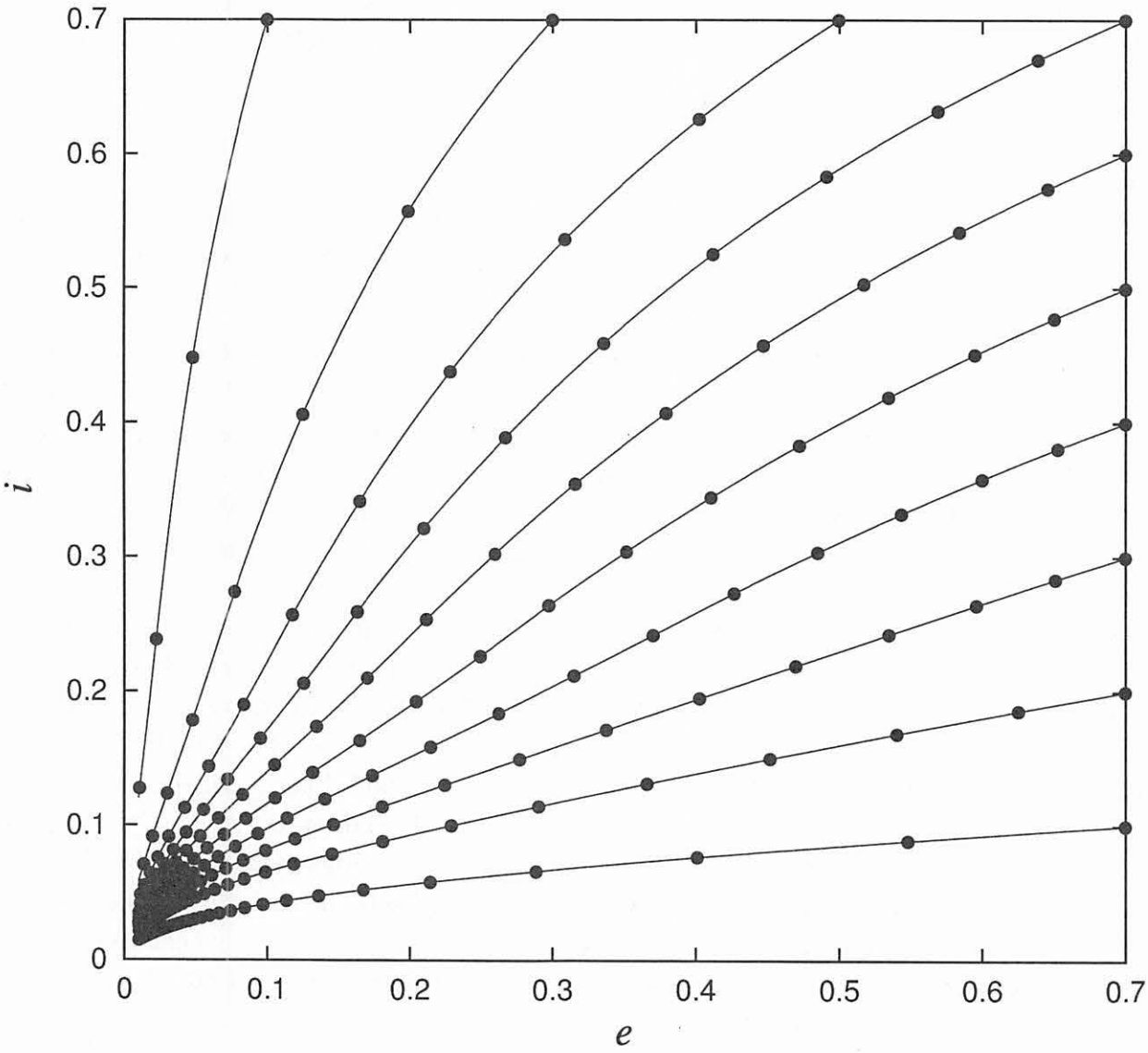

Fig. 14.— Orbital evolution of objects in e-i plane in the case of $\alpha = 1$. The objects initially have $q = 35$AU.

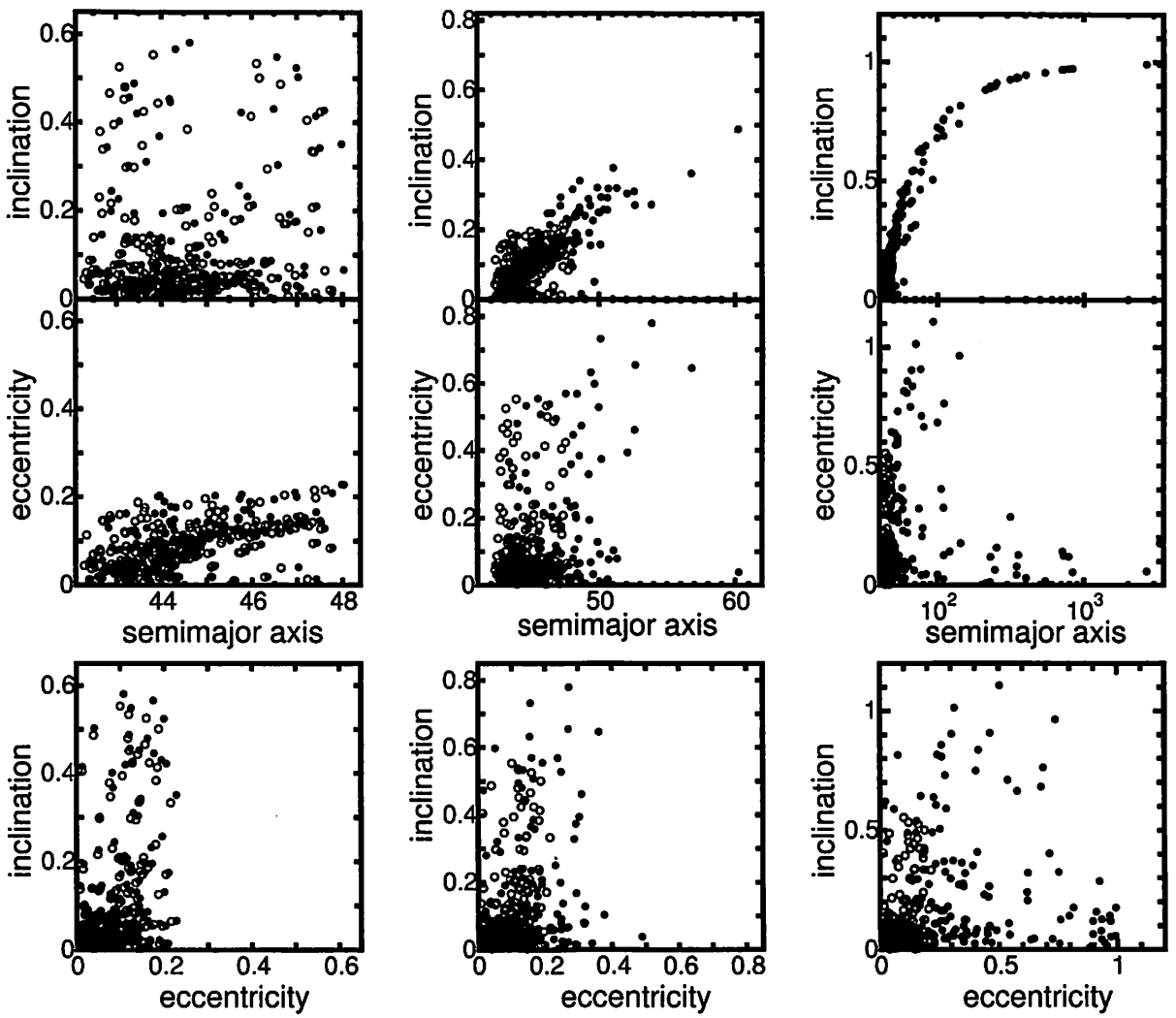

Fig. 15.— $a \times e$, $a \times i$, and $e \times i$ with $\alpha = 1.5$ (left panels), $\alpha = 1$ (center panels), and three times higher density than case of $\alpha = 1$. Filled circles show EKBOs in $1 \times 3 \times 10^7$ years ago. Open circles show the orbits of current EKBOs.

5. THE EFFECT OF GAS DRAG AFTER AN EARLY STELLAR ENCOUNTER

In this section, we also investigate the orbital evolution due to gas drag, starting from the resultant distribution of objects after the stellar encounter. We assume the time dependence of nebula density depletion given by

$$\rho(t) = \exp\left(-\frac{t}{t_{\rm d}}\right), \tag{83}$$

where $t_{\rm d}$ is the depletion timescale of nebula (the nebula life time). We mainly adopt $t_{\rm d}$ as 3×10^7 years. We also adopt the radii of the excited objects as 100km and the nebula model similar to in §4. We investigate the cases with $\alpha = 1.5$ and 1, too.

The result after the orbital evolution due to gas drag are shown in Fig. 16 in the case of $\alpha = 1.5$, starting from the resultant distribution of objects after the stellar encounter with $D = 140$AU, (a) $i_* = \pi/6$, (b) $i_* = \pi/4$, (c) $i_* = \pi/3$, (d) $i_* = \pi/2$, and (e) $i_* = 5\pi/6$. We use the objects with a_i between 40-80AU, where a_i is samimajor axis of objects before a stellar encounter. The objects with e highly pumped-up by a stellar encounter migrate to inner region, since they pass in nebula with high density at their q. The objects with large e are provided to the inner region. This follows the growth rates of planets could become faster. On the other hand, in the case of $a \gtrsim 40$AU and $e \lesssim 0.4$, their orbits do not change significantly. The orbital distribution in the region of classical EKB is not change significantly (see Fig. 17). Thus, the formation of two inclination-population is difficult in the case of $\alpha = 1$.

In Fig. 18, we also show the result after orbital evolution due to gas drag with $\alpha = 1$. The objects, even if $e \lesssim 0.2$ and $a \gtrsim 40$, can migrate significantly, in the case of the prograde encounter. In the cases of $i_* = \pi/6$ and $\pi/4$, there are few objects with $i \gtrsim 0.2$. In this case, the stellar encounter highly pumps up not only i but also e. Gas drag force is strong for the objects with large e, and then i are dumped greatly due to the strong gas drag. On the other hand, in the case of $i_* = \pi/3$, the stellar encounter pumps up i highly and e moderately for some objects. Thus, gas drag is not so strong for the objects. The objects migrate from the region beyond 50AU to the region of EKB. This can be the objects with large i and small e. In the cases of $i_* = \pi/2$ and $i_* = 5\pi/6$, the orbits do not significantly change due to gas drag because e pumped-up by the stellar encounter are small. If the stellar encounter is closer, the orbits are affected by gas drag.

In Fig. 19, we show e and i in the region of classical EKB ($a = 42$-48AU, $q > 35$AU) after the orbital distribution due to gas drag with $\alpha = 1$, starting from the result of the stellar encounter with $i_* = \pi/3$, $\omega_* = \pi/2$, (a) $D = 100$AU, (b) $D = 120$AU, (c) $D = 140$AU,

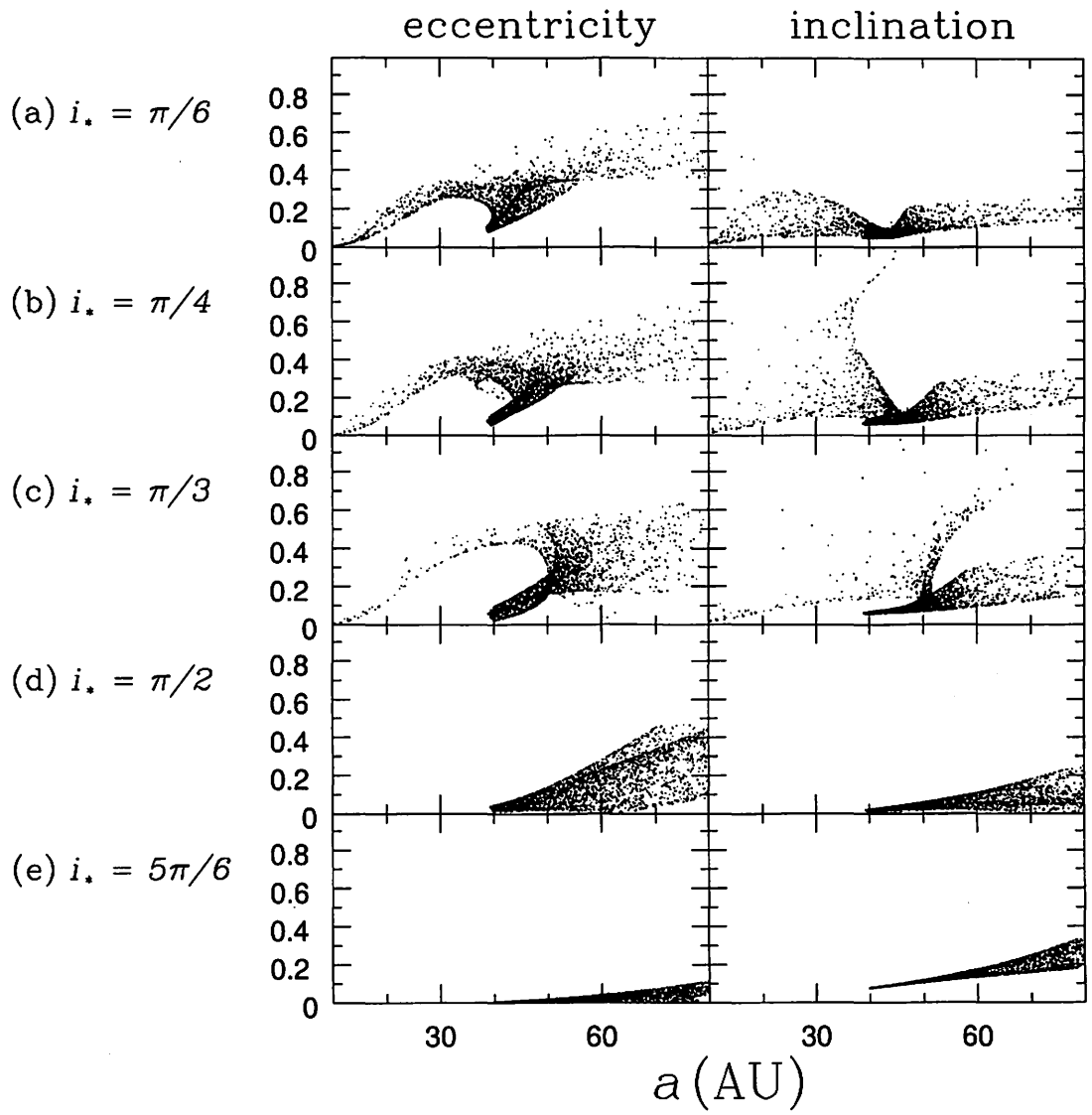

Fig. 16.— Orbital eccentricities e and inclinations i of objects damped due to gas drag, as a function of semimajor axis a, in the case of $\alpha = 1.5$, after stellar encounters with $\omega_* = 90°$, $e_* = 1$ and $M_* = 1$. Orbital inclination of the passing star is (a) $\pi/6$, (b) $\pi/4$, (c) $\pi/3$, (d) $\pi/2$ and (e) $5\pi/6$.

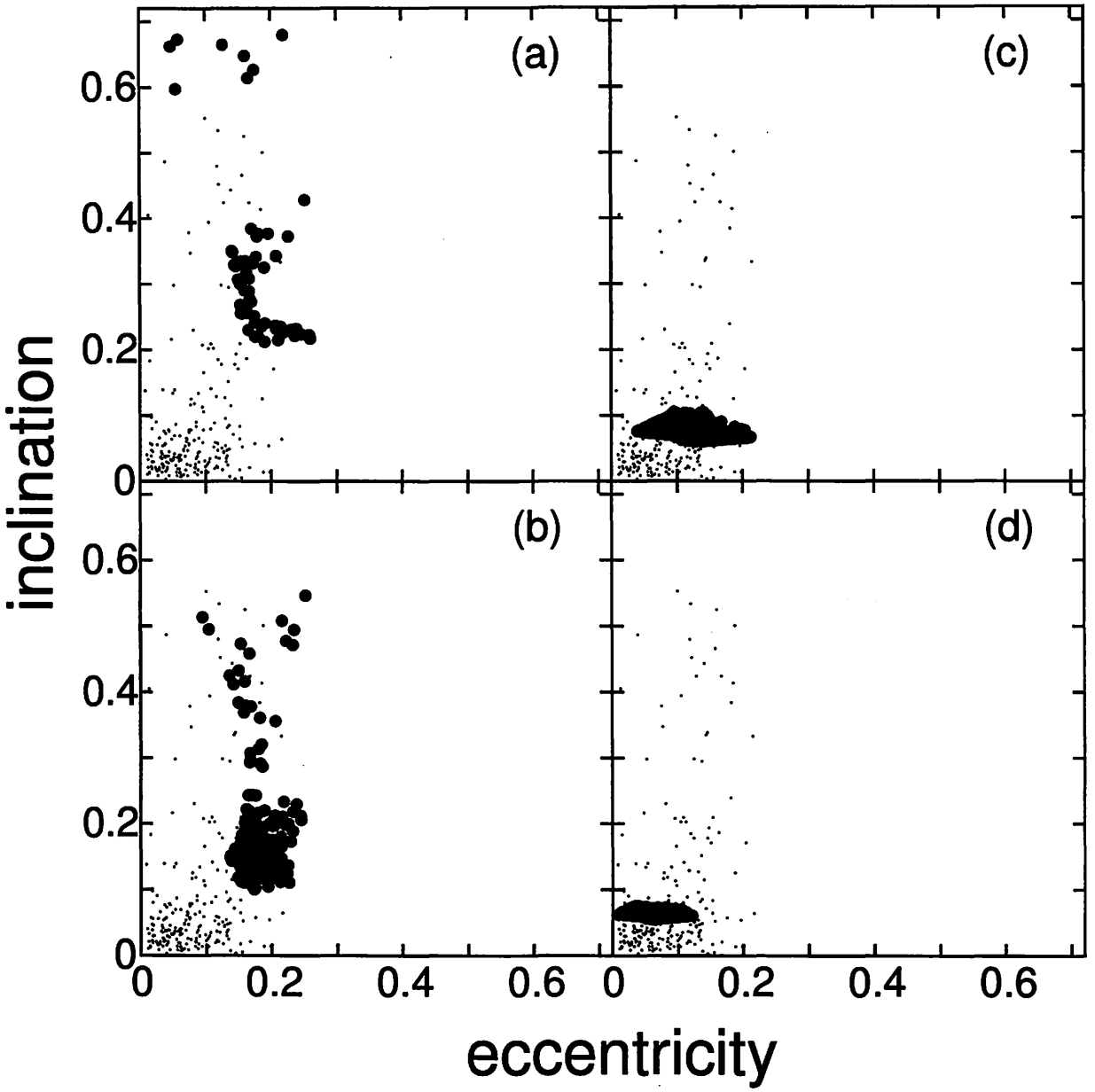

Fig. 17.— Filled circles are eccentricities and inclinations in the region of classical EKB (a = 42-48AU, $q > 35$AU) in the case with $\alpha = 1.5$. The pericenter distance of the stellar encounter is (a) $D = 100$AU, (b) $D = 120$AU, (c) $D = 140$AU, and (d) $D = 160$AU. Dots are the orbit of current EKBOs.

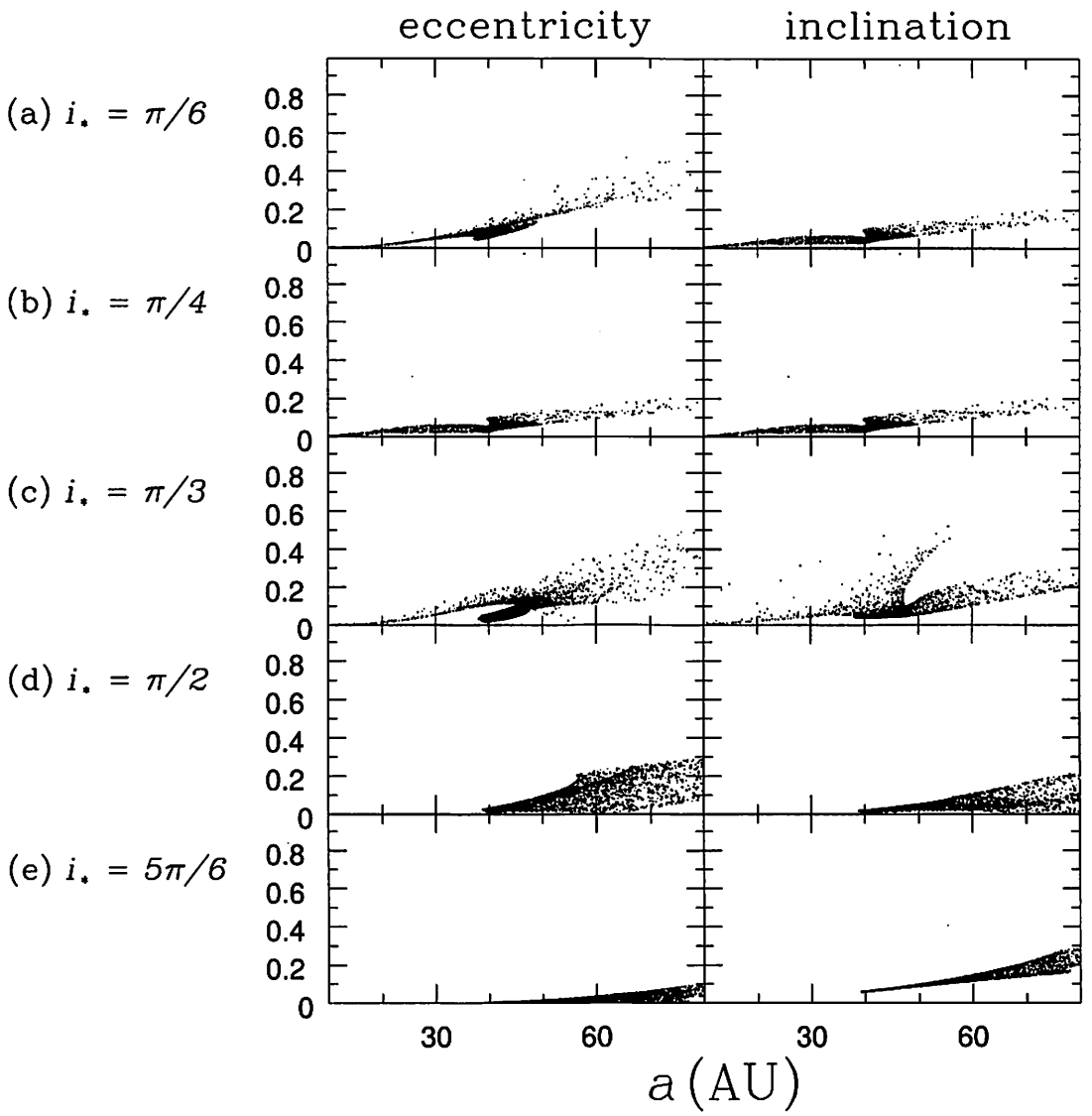

Fig. 18.— Same one as Fig. 16, except for $\alpha = 1$.

and (d) D = 160AU. In close encounter, there are objects with larger i. In the case of D = 100-120AU, i is as large as i of hot population in CEKBOs. Though there are some objects with $i \lesssim 0.2$, there are few objects with e and $i \simeq 0.1$. In the case of D = 140AU, there are objects with small e and i and objects with large i and small e, but the largest i is smaller than largest i of EKBOs. In close encounter, the number of objects with small i and small e increase due to gas drag. On the other hand, the number of objects with large i increase due to gas drag in the case of D = 140-160AU (compare Fig. 7 and 19). The objects with large e and i or with large e and small i migrate valuably (see §4). Then, the objects with low i or high i increase in inner region (see §4). This effect can form the two-inclination population.

6. DISCUSSION

Our simulations show that an early stellar encounter combined with the orbital evolution due to gas drag can explain the two inclination population of classical Edgeworth-Kuiper belt objects (CEKBOs). A stellar encounter pumps up e and i with steep a-gradient. The objects with small i and large e or with large i and moderate e, can migrate to the region of EKB from the region beyond 50AU due to gas drag. There are some problems to explain the orbital distribution of CEKBOs. The stellar encounter with $D \simeq$ 100AU can pump up i up to 0.6 in the region of EKB and gas drag can form objects with i 0.6. In this case, there are few objects with e, $i \leq 0.1$. On the other hand, if the stellar encounter have $D \simeq$ 140AU, some objects objects have $i > 2e$ and other objects have $i \sim e$, in the region. In this case, largest i is smaller than 0.6. Thus, we may need to consider other effect on the orbital evolution of EKBOs.

Collisions between objects can change the orbits of objects. The collisional timescale is given by 4.3×10^9 years, assuming that objects with radii 100km is consist of all solid matter in the minimum-mass solar nebula model. This follows the objects have collided in age of solar system. If we assume $\alpha = 1$ and adopt the surface density at 1AU in minimum-mass solar nebula model, the collisional timescale is 5×10^8 years. The number of objects decreases for the truncation of stellar encounter and the migration of gas drag. Though the collisional timescale become longer, the objects can be affected by the collisions. After an early stellar encounter, collisions are destructive in the region of EKB (Kobayashi & Ida 2001). We have a scenario that the objects initially have same sizes as largest current EKBOs. An early stellar encounter pumps up e and i and gas drag form the objects with large i and small i. Though a stellar encounter with $D \simeq$ 100AU cannot form the objects with $i \lesssim 0.1$, the collisions between the objects dump i and produce the objects with $i \lesssim 0.1$.

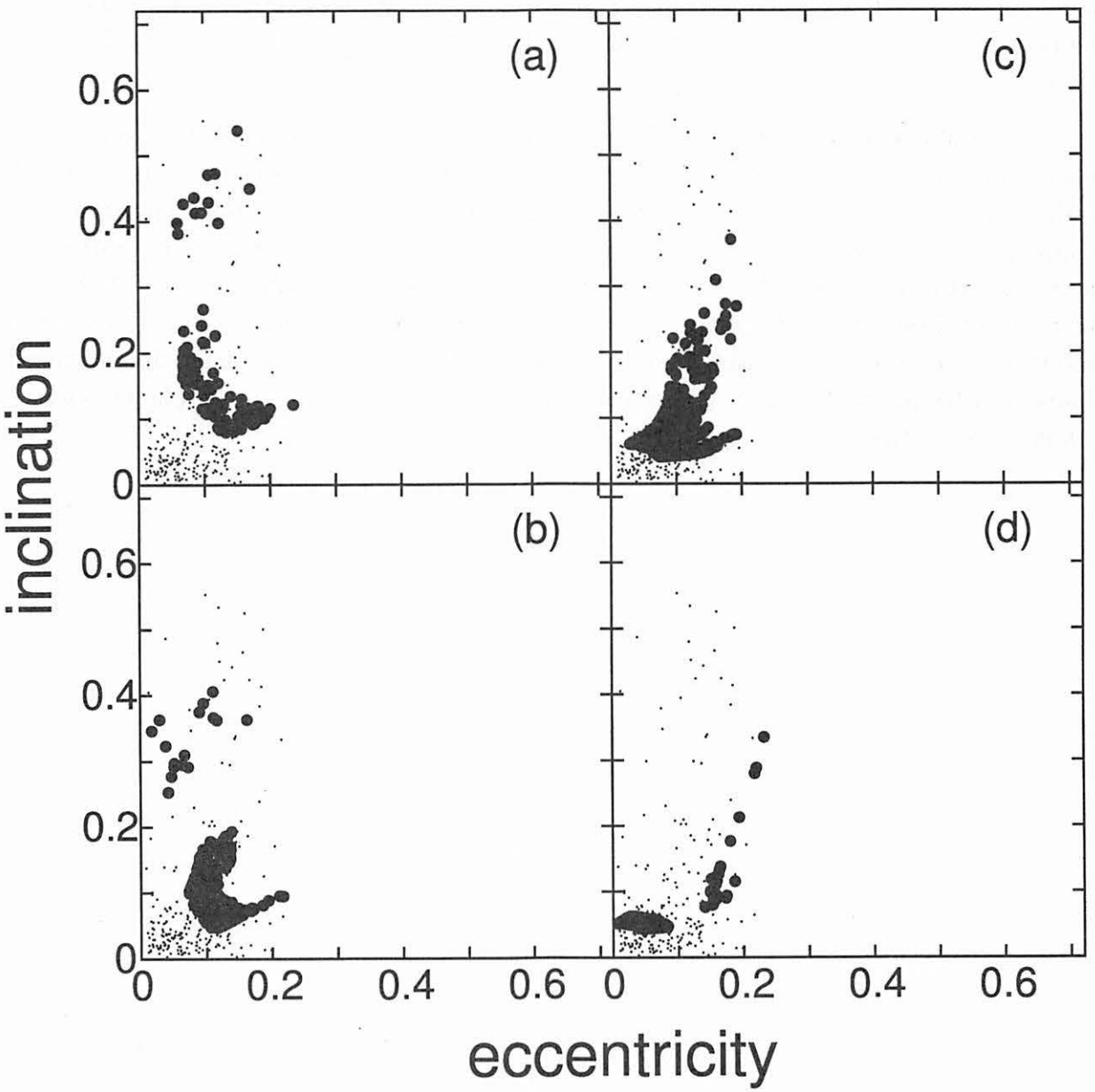

Fig. 19.— Same one as Fig. 17, except for $\alpha = 1$.

The objects which avoid the collisions are larger and have high i. The collisions produce small objects. The small objects collide more frequently. The large objects remain and small objects become smaller. After all, the objects become smaller and migrate to inner region due to gas drag or Poynting-Robertson light drag. The amount of EKBOs is much less than the minimum-mass solar nebula. The amount of EKBOs may be able to decrease for these effect.

Our results show the objects with large e in outer region can migrate to inner region. Inner planets can feed the migrating objects and then the growth of planets can be faster. A further important point is that gas drag is stronger for small objects. A stellar encounter can pump up e and i of objects in outer region and collisions between the objects are destructive there (Kobayashi & Ida 2001). The destructive collisions can produce small objects and then the small objects are migrate faster to inner region due to strong gas drag. Collisional growth between the small objects and a protoplanet that has an atmosphere are enhanced (Inaba and Ikoma 2003). These effects may speed up the accretion of outer planet, such as Uranus and Neptune.

REFERENCES

Adachi, I., Hayashi, C., and Nakazawa, K. 1976. The gas drag effect on the elliptical motion of a solid body in the primordial solar nebula. *Prog. Theor. Phys.* **56** 1756-1771.

Beckwith,S. V. W., and A. I. Sargent 1996. Circumstellar disks and the search for neighbouring planetary systems. *Nature* **383**, 139-144.

Brouwer, D., and G. M. Clemence, 1961. *Methods of Celestial Mechanics.* Academic Press, New York.

Brown, M. E. 2001. The Inclination Distribution of the Kuiper Belt. *Astron. J.*, **121**, 2804-2814.

Duncan M. J., H. F. Levison, S. M. Budd 1995. The Dynamical Structure of the Kuiper Belt. *Astron. J.* **110**, 3073-3081.

Duncan M. J. and H. F. Levison 1997. A Scattered Comet Disk and the Origin of Jupiter Family Comet. *Science* **276**, 1670-1672.

Gomes R. S. 2003. The origin of the Kuiper Belt high-inclination population. *Icarus* **161**, 404-418.

Hayashi, C., K. Nakazawa, and Y. Nakagawa 1985. Formation of the solar system. In *Protostars and Planets II* (D. C. Black and M. S. Matthews, Eds.), pp. 1100-1153. Univ. of Arizona Press, Tucson.

Ida, S., J. Larwood, and A. Burkert 2000. Evidence for Early Stellar Encounters in the Orbital Distribution of Edgeworth-Kuiper Belt Objects. *Astrophys. J.* **528** 351-356.

Ida, S., G. Bryden, D. N. C. Lin, and H. Tanaka 2000. Orbital Migration of Neptune and Orbital Distribution of Trans-Neptunian Objects. *Astrophys. J.* **534**, 428-445.

Inaba, S., H. Tanaka, K. Nakazawa, G. Wetherill, and E. Kokubo 2001. High-Accuracy Statistical Simulation of Planetary Accretion: II. Comparison with N-Body Simulation. *Icarus* **149**, 235-250.

Inaba, S. and M. Ikoma 2003. Enhanced collisional growth of a protoplanet that has an atmosphere *Astron. and Astrophys.* **410**, 711-723.

Jewitt, D. C. and J. X. Luu 2000. Physical Nature of the Kuiper Belt. In *Protostars and Planets IV* (V. Mannings, A. P. Boss and S. S. Russell, Eds.), pp. 1201-1229. Univ. of Arizona Press, Tucoson.

Kitamura, Y., M. Momose, S. Yokogawa, R. Kawabe, M. Tamura, and S. Ida 2002. Investigation of the Physical Properties of Protoplanetary Disks around T Tauri Stars by a 1 Arcsecond Imaging Survey: Evolution and Diversity of the Disks in Their Accretion Stage. *Astrophys. J.* **581**, 357-380.

Kobayashi, H. and S. Ida 2001. The Effects of a Stellar Encounter on a Planetesimal Disk. *Icarus* **153** 416-429.

Kroupa, P. 1995. The dynamical properties of stellar systems in the Galactic disc. *Mon. Not. R. Astron. Soc.* **277** 1507-1521.

Kroupa, P. 1998. On the binary properties and the spatial and kinematical distribution of young stars. *Mon. Not. R. Astron. Soc.* **298**, 231-242.

Kuchner, M. J., M. E. Brown, and M. Holman 2002 Long-Term Dynamics and the Orbital Inclinations of the Classical Kuiper Belt Objects. *Astron. J.* **124**, 1221-1230.

Levison, H. and A. Stern 2001. On the Size Dependence of the Inclination Distribution of the Main Kuiper Belt. *Astron. J.* **121** 1730-1735.

Lissauer, J. J., and G. R. Stewart, 1993. Growth of planets from planetesimals. In *Protostars and planets III* (E. H. Levy and J. Lunine, Eds.), pp. 1061-1088. Univ. of Arizona Press, Tucson.

Malhotra, R., 1993. The Origin of Pluto's Peculiar Orbit *Nature*, **365** 819-821

Malhotra, R., 1995 The Origin of Pluto's Orbit: Implications for the Solar System Beyond Neptune. *Astron. J.*, **110** 420-429.

Malhotra, R., M. J. Duncan, and H. F. Levison Dynamics of the Kuiper Belt. In *Protostars and Planets IV* (V. Mannings, A. P. Boss and S. S. Russell, Eds.), pp. 1231-1254. Univ. of Arizona Press, Tucoson.

Nagasawa, M. and S. Ida, 2000. Sweepig Secular Resonances in the Kuiper Belt Caused by Depletion of the Solar Nebula. *Astron. J.*, **120** 3311-3322.

Nagasawa, M., S. Ida, and H. Tanaka, 2002. Excitation of Orbital Inclinations of Asteroids during Depletion of a Protoplanetary Disk: Dependence on the Disk Configuration. *Icarus*, **159** 322-327.

Petit, J., A. Morbidelli, and G. Valsecchi 1999. Large Scattered Planetesimals and the Excitation of the Small Body Belts. *Icarus* **141** 367-387.

Safronov, V. S. 1969. *Evolution of the Protoplanetary Cloud and Formation of the Earth and Planets.* Nauka Press, Moscow.

Tanaka, H., T. Takeuchi, and W. Ward 2002. Three-Dimensional Interaction between a Planet and an Isothermal Gaseous Disk. I. Corotation and Lindblad Torques and Planet Migration. *Astrophys. J.* **565** 1257-1274.

Thommes, E., M. Duncan, and Levison, H. 2002. The Formation of Uranus and Neptune among Jupiter and Saturn. *Astron. J.* **123** 2862-2883.

Wetherill, G. W. 1980. Formation of the terrestrial planets. *Annu. Rev. Astron. Astrophys.* **18**, 77-113.

Three-Body Affairs in the Outer Solar System

Yoko Funato
General System Studies, University of Tokyo, Tokyo 153, Japan
funato@chianti.c.u-tokyo.ac.jp

Junichiro Makino
Department of Astronomy, University of Tokyo, Tokyo 113, Japan

Piet Hut
Institute for Advanced Study, Princeton, NJ 08540, USA

Eiichiro Kokubo & Daisuke Kinoshita
National Astronomical Observatory, Tokyo 180, Japan

Recent observations[1, 2, 3] have revealed an unexpectedly high binary fraction among the Trans-Neptunian Objects (TNOs) that populate the Kuiper Belt. The TNO binaries are strikingly different from asteroid binaries in four respects[2]: their frequency is an order of magnitude larger, the mass ratio of their components is closer to unity, and their orbits are wider and highly eccentric. Two explanations have been proposed for their formation, one assuming large numbers of massive bodies[4], and one assuming large numbers of light bodies[5]. We argue that both assumptions are unwarranted, and we show how TNO binaries can be produced from a modest number of intermediate-mass bodies of the type predicted by the gravitational instability theory for the formation of planetesimals[6]. We start with a TNO binary population similar to the asteroid binary population, but subsequently modified by three-body exchange reactions, a process that is far more efficient in the Kuiper belt, because of the much smaller tidal perturbations by the Sun. Our mechanism can naturally account for all four characteristics that distinguish TNO binaries from main-belt asteroid binaries.

The TNO binary 1998WW31 has[2] a mass ratio $m_2/m_1 \sim 0.7$, eccentricity $e \sim 0.8$, semimajor axis $a \sim 2 \times 10^4$ km, and inferred radii $r_1 \sim 1.1 r_2 \sim 10^2$ km, hence $a/r_1 > 10^2$, in stark contrast to main belt asteroid binaries[7], where $m_2/m_1 \ll 1$, $e \sim 0$, and $a/r_1 \lesssim 10$.

Asteroid binaries are probably formed by collisions[8], as in the leading scenario for the formation of the Moon[9, 10]. The observed characteristics, $m_2/m_1 \ll 1$, $e \sim 0$, and

$a/r_1 \lesssim 10$, are all natural consequences of this scenario[11]. For a different scenario for 1998WW31, we can look at dynamical binary formation in star clusters, where there are three channels: 1) tidal capture[12]; 2) three-body binary formation[13]; and 3) exchange reactions[13].

Channel 1 is analogous to the standard scenario for asteroid binary formation. It will indeed occur: each TNO has grown through accretion, and much of this accretion has happened through collisions with an object comparable in mass to the growing TNO itself[14, 15].

Channel 2 would require a near-simultaneous encounter of three massive objects with low enough velocities to allow an appreciable chance to leave two of the objects bound. For this to work, the random velocities of the most massive objects should be significantly lower than their Hill velocities. Under such conditions, this channel could play a role, as pointed out by Goldreich *et al.*[5], who assumed that there are $\sim 10^5$ 100 km–sized object embedded in a sea of small ($<$ 1km) objects. This assumption, however, is at odds with Goldreich and Ward's theory for the formation of planetesimals[6] through gravitational instability, and it is hard to see how objects in the Kuiper Belt could form from non-gravitational coagulation, because the time scales are far too long[16]. In contrast, the gravitational instability theory predicts the size of the initial bodies to be $10 - 100$km. Starting with these larger bodies would make channel 2 ineffective, because the velocity dispersion would be higher than the Hill velocity[14, 17].

Recently, Weidenschilling[4] proposed a variation on the idea of using interactions between three unbound bodies in order to create a binary. He studied how a third massive body could capture the merger remnant from a collision of two massive bodies if the third body were near enough during the time of the collision. This mechanism seems unlikely to work, however, since it requires a number density of massive objects about two orders of magnitude higher than the value consistent with present observations[5].

Goldreich *et al.*[5] have proposed another mechanism, based on the dynamical friction from a sea of smaller bodies that can turn a hyperbolic encounter between two massive bodies into a bound orbit under favorable conditions. Effectively, this mechanism makes use of a superposition of three-body encounters, since each light body interacts independently with the two heavier ones, and in that sense it is another variant on channel 2. As we mentioned above, the gravitational instability theory for the formation of planetesimals[6] would exclude the existence of such a sea of small objects, and since the alternative theory of nongravitational agglomeration does not seem to work, we will explore the consequences of dropping channel 2.

Channel 3 can operate on the binaries formed through channel 1, so we should check whether channel 1 and 3 together produce the right binaries in the right numbers.

Starting with the first task, consider a relatively massive TNO primary in a binary orbit with a much less massive secondary. If the binary encounters a particle with a mass m that is comparable to the mass of the primary component ($m_1 \sim m \gg m_2$), the most likely result is an exchange reaction, in which the incoming object replaces the original secondary[18]. Figure 1 shows an example of such a reaction.

The binding energy of the binary will not change much during the exchange, hence $m_1 m_2/a_0 \approx m_1 m/a$ where a is the new semimajor axis after the exchange.

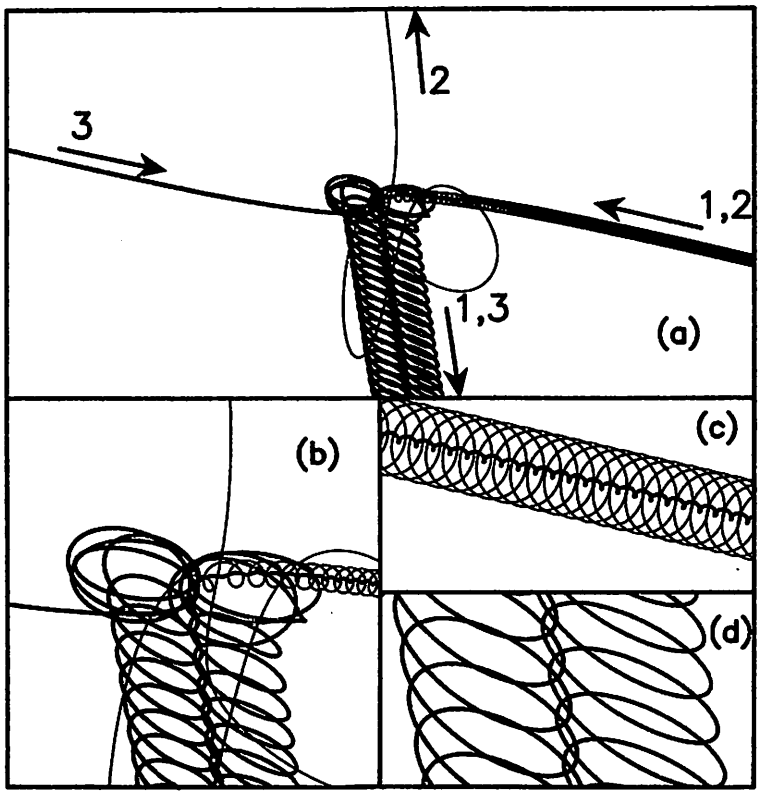

Figure 1: An example of a binary–single-body exchange interaction, in the '(massive, light) meets massive' category discussed in this paper. Bodies 1 and 2 have masses $m_1 = 1$ and $m_2 = 0.1$, respectively, forming a binary with an initially circular orbit. Body 3, with mass $m_3 = 1$, encounters the binary on an initially parabolic orbit. In panel (a), the whole scattering process is shown. Panel (b) shows the complex central interaction in more detail, while panels (c) and (d) show the orbits of the initial and final binary, respectively. Note that the final binary orbit is highly eccentric and much wider than the initial circular binary orbit.

channel:	(a)	(b)	(c)	(d)	(e)	(f)
process:	(1,3),2	(2,3),1	(1+2,3)	(1+3,2)	(2+3,1)	no binary
σv^2:	12.1	1.3	0.9	1.3	0.9	1.2

Table 1: Cross sections σ for various configuration-changing channels in binary–single-body scattering. The gravitational focusing factor v^2 is scaled out in order to obtain finite values in the parabolic limit, where v is the initial relative velocity between binary and single body at infinity. We use units in which $G = m_1 = m_3 = a = 1$, where G is the gravitational constant, m_1 and m_3 are the masses of the heaviest body in the binary and the single body, respectively, and a is the initial semi-major axis of the binary. The mass of the lighter body in the binary is $m_2 = 0.05$. The radii are $r_1 = r_3 = 0.05$ and $r_2 = r_1(m_2/m_1)^{1/3} \approx 0.01842$. The scattering processes are coded as follows: (x, y) indicates a binary in the final state with components x and y, while a $p + q$ indicates the product of a merger between bodies p and q. A single body z in the final state is indicated by $(,), z$. The physical meaning of the six channels is as follows: (a) an exchange reaction resulting in a massive–massive binary; (b) an exchange reaction resulting in a massive–light binary; (c) a merger resulting in a massive–massive binary; (d) a merger resulting in a twice-as-massive–light binary; (e) a merger resulting in a massive–massive binary; (f) no binary is left, after three-body merging or two-body merging followed by escape.

This implies $a/a_0 \approx m/m_2 \gg 1$. Under the impulse approximation, the interaction happens in a space small compared to the distance a_0 to the primary. Conservation of specific angular momentum of the system gives $m_2 a_0(1 - e_0) \approx ma(1 - e)$ which gives $1 - e \approx m_2/m \ll 1$.

We have run a series of scattering experiments to obtain the relevant cross sections, for an initial binary with mass ratio of 20 : 1 and semimajor axis $a_0 = 20r_1$, where r_1 is the radius of the primary. These values are typical for main-belt binary asteroids, with $m_2/m_1 < 0.1$, and separations $5 - 40$ times the radius of the primary. We choose parabolic relative orbits for the single body approaching the binary, with periastron distances uniformly distributed between 0 and $20a_0$. We only followed the system as long as all three bodies stayed within their Hill radius, $1000a_0$.

Table 1 gives cross sections for processes in which initial binary membership is altered. Channels (a), (c) and (e) result in binaries with two massive components, and together comprise about 80% of the total cross section. We checked these results through a comparison with the starlab three-body scattering package[19].

In figure 2 the distribution for the semi-major axis is strongly peaked at $a = 20$, in good agreement with the simple argument presented above. Similarly, the eccentricity peaks at 0.95, as expected. We assumed $r_1 = 75$km, the estimated radius of the primary of 1998WW31. In figure 3, the orbital elements of 1998WW31 are consistent with the binary having formed through the processes modeled here.

We now confront our second task: to check whether the exchange channel is efficient enough to produce the observed binaries. Starting with TNOs of intermediate mass, as predicted by Goldreich and Ward's theory for the formation of planetesimals[6], the heaviest TNOs will accrete mass primarily through collisions with TNOs of comparable mass[14, 15]. Many of these collisions are of the 'giant impact' type

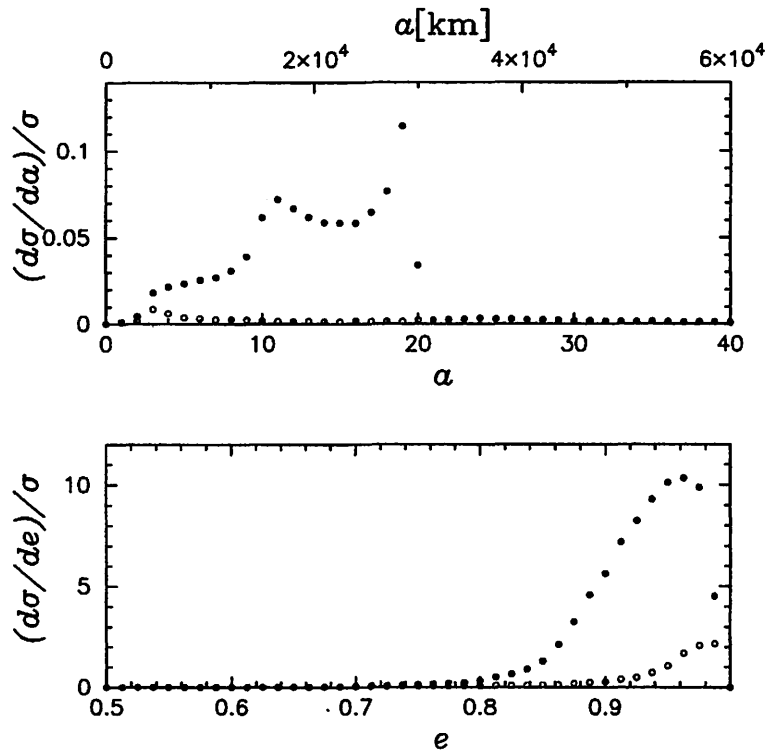

Figure 2: Normalized differential cross sections for the formation of a 'massive-massive' binary, under the conditions specified in the text (channels a, c and e in table 1), with respect to the semi-major axis a (top panel), and eccentricity e (bottom panel) of the final binary. The initially circular binary has $a = 1$ in the dimensionless units used for $d\sigma/da$, while the physical units are given for reference at the top of the figure. The filled points are the total values for the differential cross sections, while the open circles are the contributions from the merger channels (c and e in table 1). Note the double-peaked structure in the top panel: the sharp peak toward $a \sim 20$ arises from non-resonant exchanges, where the final binary has an energy comparable to that of the initial binary; the broad peak around $a \sim 10$ arises from resonant exchanges, where the memory of the initial binary is wiped out, leading on average to more strongly hyperbolic escape in which a harder binary is formed.

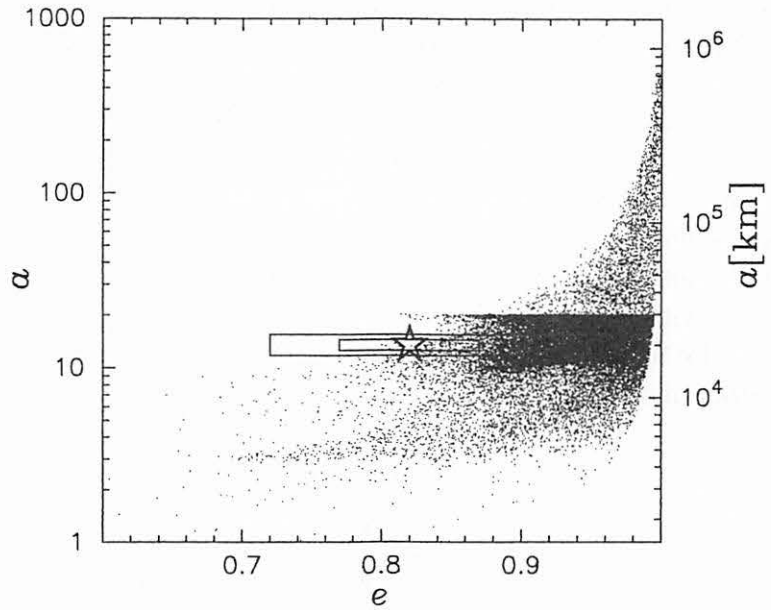

Figure 3: Orbital properties of 'massive-massive' binaries formed in our scattering experiments: a and e have the same meaning and units as in fig. 2. Contributions from exchange reactions, channel (a) in table 1, are limited by energy conservation to $a \lesssim 20$, and give rise to the horizontal rim in the middle of the figure. Contributions involving mergers, channels (c) and (e) in table 1, can lead to a values all the way to the Hill radius $a \approx 10^3$, but are limited by angular momentum conservation to increasingly high e for increasing a. The star symbol shows the observed orbit for 1998WW31. Boxes around the star indicate the observational 1- and 2-σ error bars.

that form a tight circular strongly unequal-mass binary (channel 1). Let us estimate what fraction of encounters between comparable-mass TNOs will give rise to 'giant impact' type binaries, and how long such binaries survive on average before they are destroyed again.

We assume that one in three collisions between comparable TNOs gives rise to a binary. When no binary is produced, we have to wait for a typical time T until another major collision occurs. When a binary is formed, gravitational focusing implies a cross section for three body interactions of order a_0. Therefore, our newly-formed binary will undergo an exchange reaction on a time scale $(r/a_0)T \ll T$, leading to a significant increase in a. Strong three-body interactions will subsequently occur on a much shorter time scale $(r/a)T \ll T$. As a result, the semimajor axis will shrink systematically, while the 'thermal' distribution $f(e) = 2e$ favors high eccentricity[13].

When the orbit becomes small enough, $r/a \sim 0.03$, the chance for collisions in resonant encounters becomes significant[20]. Let us assume that an exchange reaction turns a 'giant impact' binary into a binary with a semi-major axis of $a \sim 300r$. Each subsequent strong encounter will on average decrease a by a factor[21] ~ 1.2. After a dozen encounters, $a \sim 30r$ and collision is likely to occur. The time scale for each encounter to occur is $\sim (r/a)T$. The waiting time for the last encounter in this series to occur is $(1/30)T$, while each previous waiting time was less by a factor 1.2. Summing this series, we get a total waiting time of $(T/30)/(1-(1/1.2)) = 0.2T$ before

a collision between two or three massive TNOs. If all three collide, we are back where we started, and the resulting system may be a single body (with an assumed chance of 2/3) or a strongly unequal-mass binary (chance 1/3). If two of the bodies collide, the third one may remain in orbit, or it may escape. In the latter case, we again are back where we started. In the former case, we still have an equal-mass and likely highly eccentric wide binary.

Under these assumptions, in 1/3 of the cases, we wind up with an equal-mass TNO binary with the observed properties for a period $\sim 0.2T$, compared to a 2/3 chance to wind up with a single TNO for a period $\sim T$. This allows us to derive the rate equation for the formation and destruction of the binaries. If we denote by N_S and N_B the number of single bodies and the number of binaries, respectively, we have

$$\begin{aligned} \frac{dN_B}{dt} &= \frac{1}{3}N_S - \frac{1}{0.2}\frac{2}{3}N_B \\ \frac{dN_S}{dt} &= -\frac{dN_B}{dt} \end{aligned}$$

if we measure time in unit of T. So for the stationary state we have $dN_B/dt = dN_S/dt = 0$, and $N_B = 0.2N_S/2 = 0.1N_S$. Therefore, the binary fraction is $\sim 10\%$. When accretion in the Kuiper belt region diminished, the number of single and binary objects was frozen, with a ratio similar to this steady-state value.

While our arguments are only approximate, it is clear that after cessation of the accretion stage at least several percent or more of the TNOs were accidentally left in such a binary phase. The fact that more than 1% of the known TNOs are found to be in wide roughly equal-mass binaries is thus a natural consequence of *any* accretion model *independent of the assumed parameters* for the density and velocity dispersion of the protoplanetary disk or the duration of the accretion phase. As a corollary, we predict that future discoveries of TNO binaries will similarly show roughly equal masses, large separations, and high eccentricities.

We conclude that we have found a robust and in fact unavoidable way to produce the type of TNO binaries that have been found, as long as we start from the plausible assumption that TNOs were formed through gravitational instabilities[6].

1. Burnes, J. A., Science, 297, 942-943 (2002).
2. Veillet C., et al., Nature, 416, 711-713 (2002).
3. Margot, J-L., Nature, 416, 694-695, (2002).
4. Weidenschilling, S. J., Icarus, 160, 212-215 (2002).
5. Goldreich, P., Lithwick, Y., and Sari, R., Nature, 420, 643-646 (2002).
6. Goldreich, P. and Ward, W. R., ApJ, 183, 1051 (1973).
7. Margot, J-L., Nolan, M. C., Benner, L. A. M., Ostro, S. J., Jurgens, R. F., Giorgini, J. D., Stade, M. A., and Campbell, D. B., Science, 296, 1445-1447, (2002).

8. Merline, W. J. et al. in Asteroids III (eds Bottke, W. F., Cellino, A., Paolicchi, P. & Binzel, R. P.) (in the press).

9. Hartmann, W. K. and Davis,D. R., Icarus, 24, 504-515 (1975).

10. Kokubo, E., Ida, S., Makino, J. Icarus, 148, 419–436, (2000).

11. Durda, D. D., Bottke, W. F., Asphaug, E., and Richardson, D. C., Bull. Am. Astron. Soc., 33, 1134 (2001).

12. Fabian, A.C., Pringle, J.E. & Rees, M.J., MNRAS 172, 15P (1975).

13. Heggie, D.C., MNRAS, 173, 729 (1975).

14. Kokubo, E. and Ida, S., Icarus, 131, 171 (1998).

15. Makino, J., Fukushige, T., Funato, Y., & Kokubo, E., New Astronomy, 3, 411-416 (1998)

16. Wetherill, G.W., Annu. Rev. Earth Planet. Sci. 18, 205 (1990).

17. Kenyon, S. J.and Luu, J. X., Astronomical Journal, 115, 2125 (1998).

18. Spitzer, L., "Dynamical evolution of globular clusters", Princeton, NJ, Princeton University Press, (1987).

19. McMillan, S. & Hut, P., Astrophysical Journal, 467, 348-358 (1996).

20. Hut, P. and Inagaki, S., Astrophysical Journal, 298, 502-520 (1985).

21. Heggie, D.C. & Hut, P. *The Gravitational Million-Body Problem* [Cambridge Univ. Pr.], Ch. 23 (2003).

Acknowledgements We acknowledge helpful comments on our manuscript by Peter Goldreich and Roman Rafikov.

Gravitational interaction between a planet and an optically thin protoplanetary disk

M. Ito and H. Tanaka
Dept. of Earth and Planetary Sciences, Tokyo Institute of Technology.

伊東　真史
東京工業大学　大学院理工学研究科　地球惑星科学専攻

Abstract

We investigate gravitational interaction between a planet and an optically thin protoplanetary disk, taking account of radiative transfer. A planet excites two density waves on both sides of the planet orbit due to Lindblad resonances. The outer density wave exerts a negative torque on the planet while the inner density wave exerts a positive torque. The sum of the two torque gives the net torque on the planet. As a first step, we examine one of the torques (one-side torque) in the present study. In most previous studies of density waves, the isothermal equation of state has been assumed.In this study, solving the energy equation in the linear calculation, we examine the effect of energy transfer on the wave excitation. In protoplanetary disks, the energy is transfered is by radiation and the radiative transfer is governed by dust opacity. At the stage of planet formation, the dust opacity is expected to be sufficiently low because of dust growth and planetesimal formation. Thus we assume an optically thin gaseous disk. The efficiency of radiative transfer increases with the amountof dust in optically thin disks. We consider the amount of dust as a parameter and calculate the one-side torque on a planet. Due to radiative transfer, the values of the one-side torque is deviated only by about 10% from the isothermal case. However, it is also found that the gas in the Hill sphere of the planet has a large contribution on the one-side torque.This large contribution in the Hill sphere may change the net torque sufficiently.

0.1 はじめに

原始惑星系円盤と惑星の重力相互作用は、惑星形成理論において非常に重要な物理現象の一つである。ガス円盤の中で、太陽の周りを公転する惑星があるとすると、惑星の内側と外側を流れるそれぞれのガスは、惑星によって引き寄せられ惑星の内側と外側それぞれに密度波を形成する。Goldreich & Tremaine(1979,1980) では片側の密度波が惑星に与えるトルクを線形計算により明らかにした。惑星の外側に励起される密度波は惑星に負のトルクを与え、回転運動を妨げる。また、惑星の内側に励起される密度波は惑星に正のトルクを与える。それぞれの密度波が惑星に与えるトルクは互いに打ち消しあい、その絶対値の差が、惑星が受ける正味のトルクとなる。Ward(1986) は惑星にかかる"差のトルク"を算出し、その結果、惑星が太陽方向に落下する時間を 10^6 年 ($1M_{earth}$,5AU) と見積もった。一方で木星の固体コアの集積時間は 10^7 年と見積もられていることから、コアは集積する前に太陽に落下してしまうことになる。この問題は惑星落下問題と呼ばれている。Tanaka et al(2002) は三次元のガス円盤における線形計算を行った。従来の研究でなされていた二次元のガス円盤に対する結果に比べ、惑星落下時間は長くなるものの、コアの集積時間に比べては依然として短いままである。

従来のガス円盤と惑星の重力相互作用における研究においては、等温の状態方程式を用いていた。しかし、ガス円盤内にダストが浮遊しているような場合、ダストの輻射効果を考えエネルギー輸送の効果を考える必要があると考えられる。本稿ではダスト輻射の効果が、原始惑星系円盤と惑星の重力相互作用に与える影響を調べる。ダスト輻射によるエネルギー方程式を解き、最初の段階として、片側の密度波が惑星に与えるトルクを線形計算する。

0.2 モデルと基礎方程式

惑星の集積が進んだ、惑星形成の後期の段階では、ガス円盤の光学的厚さは十分薄いものと考えられる。光学的に薄い場合、ガス円盤内のダストは輻射により円盤の外にエネルギーを放射する。ダストは同時に太陽放射によるエネルギーを吸収している。

ガス単位質量当たりに含まれるダストが、単位時間に輻射により放射するエネルギー j は、放射する光の振動数 ν に依存する。プランクのミーンオパシティー κ_p を用いると、

$$j = \int_0^\infty j_\nu = 4\kappa_p \sigma_{SB} T^4, \tag{1}$$

と書ける。σ_{SB} はステファン-ボルツマン定数である。

ρ、p、T をそれぞれ、ガス円盤の密度、圧力、温度とし、φ を重力ポテンシャルとする。さらに T_0 を擾乱 (惑星) がない場合の温度とすると、ガス円盤の満たす方程式系は以下のようになる。

$$\frac{\partial \rho}{\partial t} + \nabla \cdot (\rho \boldsymbol{v}) = 0, \tag{2}$$

$$\frac{\partial \boldsymbol{v}}{\partial t} + (\boldsymbol{v}\cdot\nabla)\boldsymbol{v} = -\frac{1}{\rho}\nabla p - \nabla\varphi, \tag{3}$$

$$\frac{\partial T}{\partial t} + (\boldsymbol{v}\cdot\nabla)T = -\frac{p}{c_v\rho}\nabla\cdot\boldsymbol{v} - \frac{4\kappa_p\sigma_{SB}}{c_v}(T^4 - T_0^4), \tag{4}$$

$$p = \frac{k}{m_M}\rho T. \tag{5}$$

k、m_M はそれぞれボルツマン定数、平均分子量、c_v は単位質量当たりの定積比熱である。

擾乱を与えることで生じる各物理量 X の摂動量を X_1 とする。(2)〜(5) を線形化し、摂動量 X_1 を、円筒座標系の θ 方向 z 方向に対して次のように展開する。

$$X = X_0 + X_1 \tag{6}$$

$$= X_0 + \sum_{m=1}^{\infty}\sum_{n=1}^{\infty} Re[X_{1,m,n}H_n(Z)e^{im(\theta-\Omega_p)t}]. \tag{7}$$

$Z = z/h$(h はガス円盤のスケールハイト) とし、$H_n(Z)$ はエルミート多項式、Ω_p は惑星の角速度である。(7) を用いて展開することにより、シェアリングシートモデル内で、各モード m、n の満たす方程式系 (本稿では $n = 0$ の場合を扱う) が得られる。r_p を惑星の軌道半径とし、$x = (r - r_p)/h$、$\tilde{k}_\theta = mr_p/h$ と定義すると、(2)〜(5) は、

$$\frac{3}{2}\tilde{k}_\theta x(i\tilde{v}_{r,m,n=0}) + 2\tilde{v}_{\theta,m,n=0} = \frac{\partial}{\partial t}(\tilde{p}_{m,n=0} + \tilde{\varphi}_{m,n=0}), \tag{8}$$

$$\frac{3}{2}\tilde{k}_\theta x\tilde{v}_{\theta,m,n=0} + \frac{1}{2}(i\tilde{v}_{r,m,n=0}) = k(\tilde{p}_{m,n=0} + \tilde{\varphi}_{m,n=0}), \tag{9}$$

$$\frac{3}{2}\tilde{k}_\theta x\tilde{\rho}_{m,n=0} + \frac{\partial}{\partial t}(i\tilde{v}_{r,m,n=0}) = \tilde{k}_\theta\tilde{v}_{\theta,m,n=0}, \tag{10}$$

$$\frac{3}{2}\tilde{k}_\theta x\tilde{T}_{m,n=0} = (\gamma-1)\frac{3}{2}\tilde{k}_\theta x\tilde{\rho}_{m,n=0} - \zeta i\tilde{T}_{m,n=0}, \tag{11}$$

$$\tilde{p}_{m,n=0} = \tilde{\rho}_{m,n=0} + \tilde{T}_{m,n=0}, \tag{12}$$

となる。$\tilde{\rho}$、$\tilde{p}$、$\tilde{T}$ はそれぞれの摂動量を非摂動量で規格化し、$\boldsymbol{v}$ の摂動量は音速で規格化した。γ はガスの比熱比である。さらに無次元量 ζ は、

$$\zeta = \frac{16\sigma_{SB}T_0^3}{c_v\Sigma_0\Omega_p}\tau, \tag{13}$$

と定義される。Σ_0 はガスの面密度の非摂動量、τ は光学的厚さである。ζ は惑星の公転周期と輻射による熱の冷却時間の比のオーダーになっている。ζ が大きい極限でガスは等温的、ζ が小さい極限でガスは断熱的になる。ζ をパラメータとして (8)〜(12) を解く。

0.3 結果

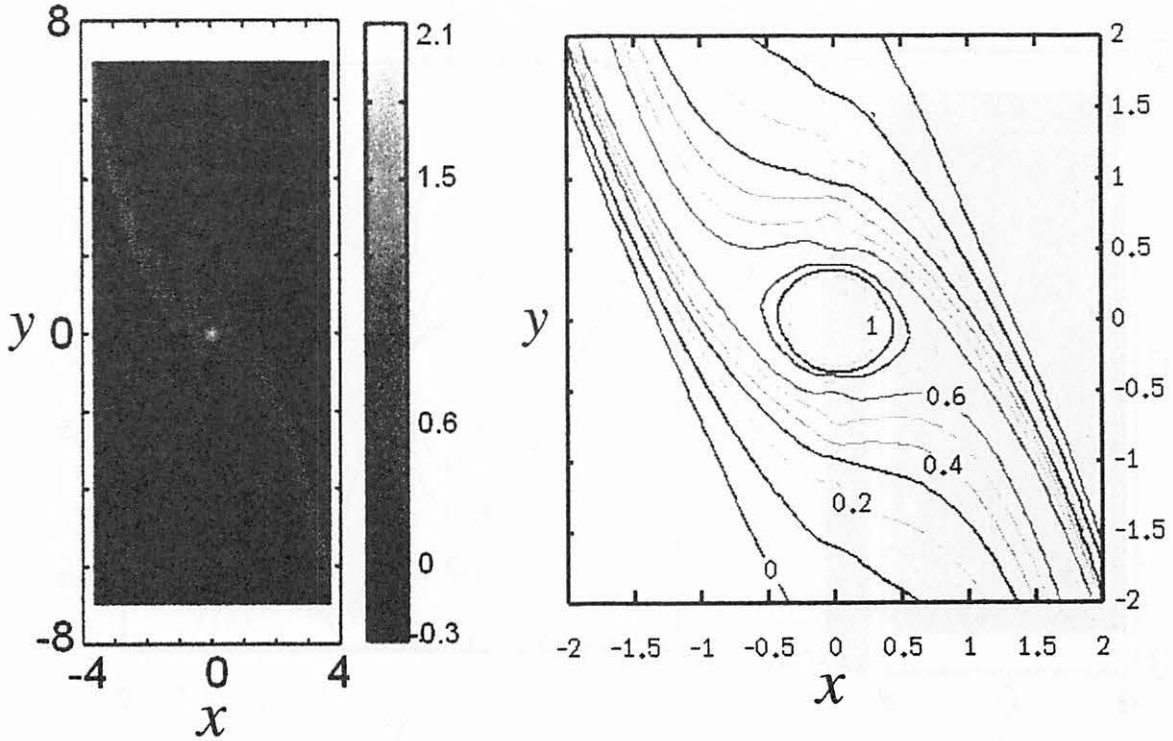

Figure 1. Distributions of the surface density perturbaion in the isothermal disk. The planet is located at the origin. The right panel shows the contours of closer views around planet in the case of isothermal

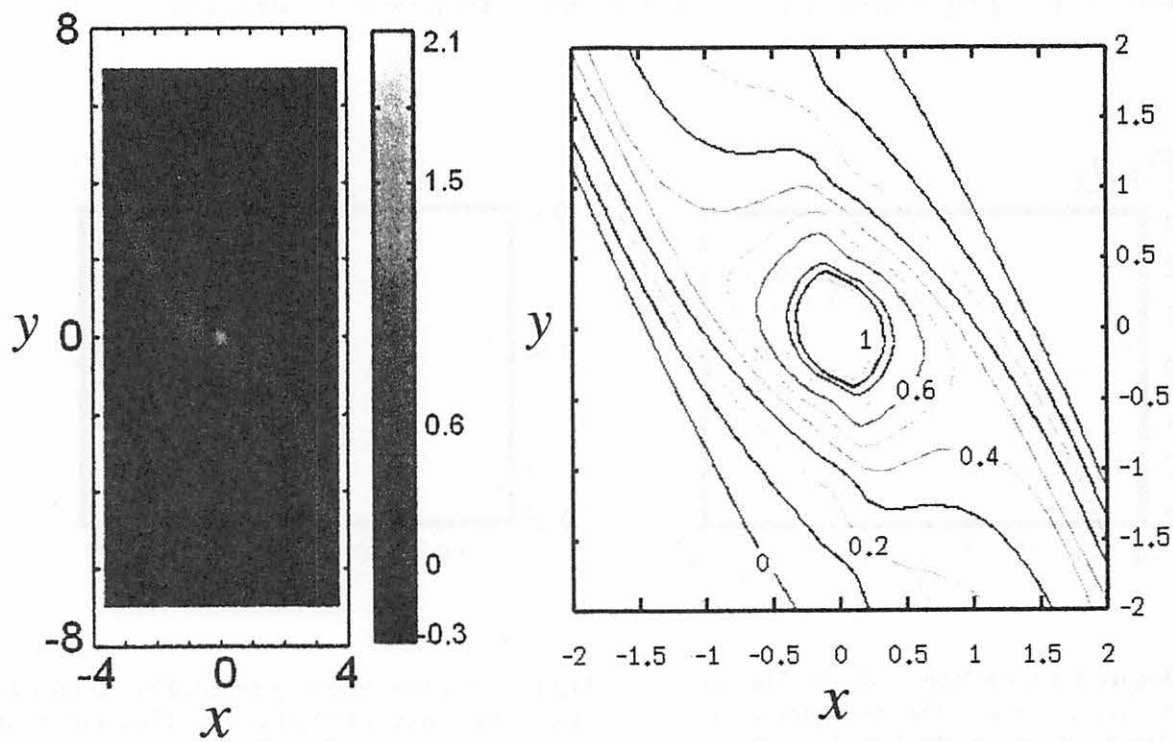

Figure 2. Distributions of the surface density perturbaion in the optically thin disk with ζ =1. The planet is located at the origin. The right panel shows the contours of closer views around planet in the case of ζ =1.

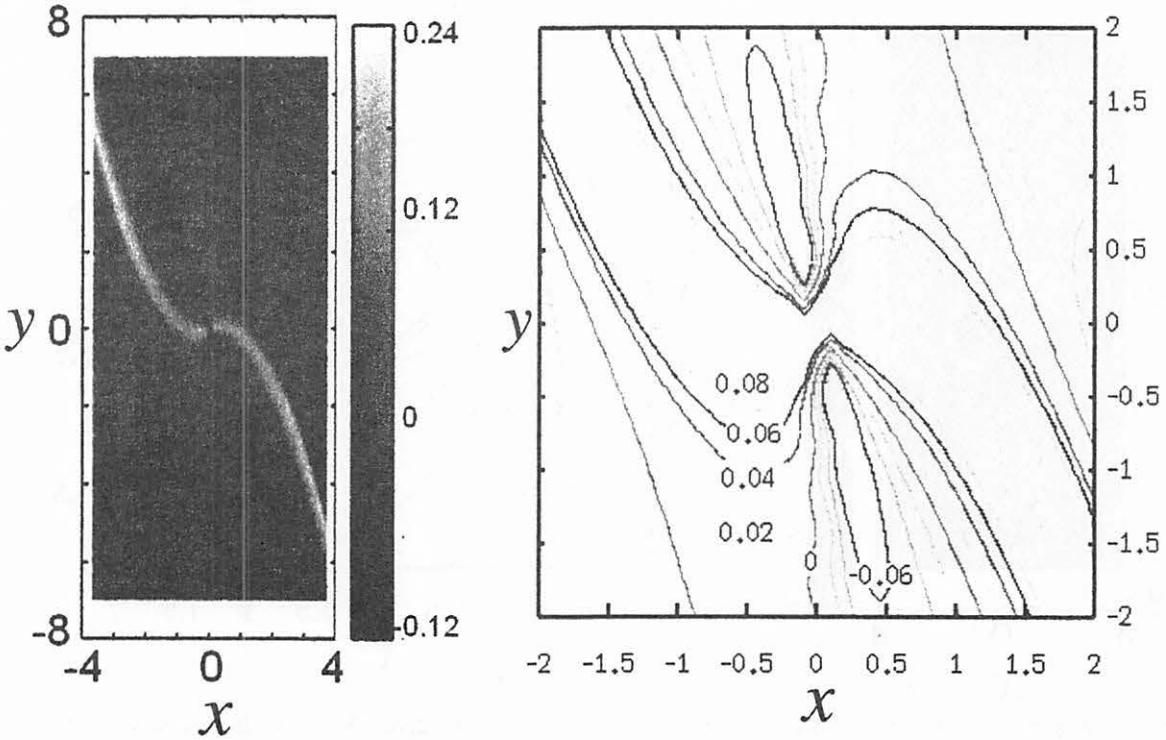

Figure 3. Distributions of the temperature perturbaion in the optically thin disk with ζ =1. The planet is located at the origin. The right panel shows the contours of closer views around planet in the case of ζ =1.

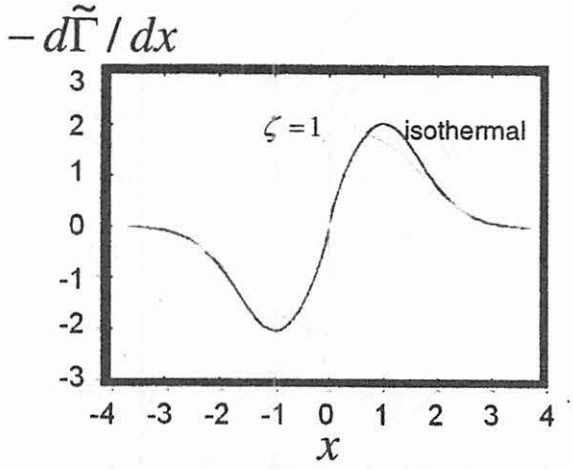

Figure 4. Torque density $d\tilde{\Gamma}/dx$. The planet is located $x = 0$. The lines represent torque densities in case of $\zeta = 1$ and isothermal one, respectively.

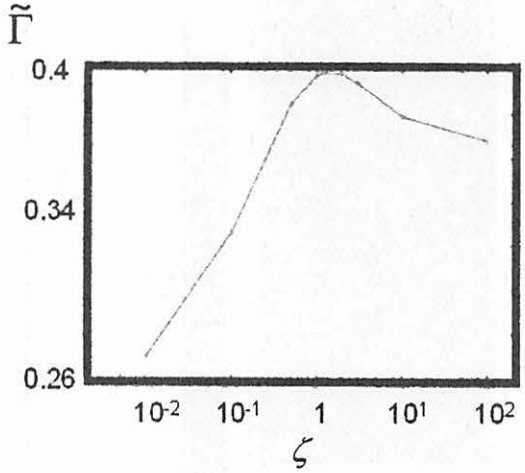

Figure 5. The one-sided torque exerted by 3D (n = 0) disks on the planet as a function of ζ . The dot represent torques in optically thin disks. The line parallel to x-axis gives torque in an isothermal disk.

fig1、fig2 は惑星近傍における面密度の摂動量の分布である。y 軸は惑星回転方向の距離をスケールハイト h で規格化したものである。fig1 は等温の場合、fig2 は $\zeta=1$ の場合である。fig3 は惑星近傍における、温度の摂動量の分布をあらわす（$\zeta=1$ の場合)。$\zeta=1$ の場合を等温の場合と比較すると、密度波を通過した後のガスが低温度、高密度の領域を作っていることがわかる。密度波を通過するガスは、密度波通過の際に密度が上がるため、圧縮されて温度が上がる。温度があがると輻射によりエネルギーが放出される。密度波通過後のガスは、密度波を通過する前に比べてエネルギーを放出した分、低温になり fig3 に見られるような領域を作る。等温的な場合はエネルギーの放出が非常に早いため、温度は変化せずこのような領域はできない。また断熱的な場合は温度が上がってもエネルギーを放出しないため、密度波を通過したガスは通過前と同じ温度に戻り低温領域は形成されない。この領域は輻射効果を考えることで初めて得られる結果である。

fig4 は惑星にかかるトルク Γ の動径方向依存性 $d\Gamma/dx$ をあらわしている。$d\Gamma/dx$ 及び Γ は次のように定義される。

$$d\Gamma/dx = r_p \int_{-\infty}^{\infty} dy \int_{-\infty}^{\infty} dz\ \rho \frac{\partial \varphi_p}{\partial y}, \tag{14}$$

$$\Gamma = -\int_0^{\infty} \frac{d\Gamma}{dx} dx. \tag{15}$$

$\tilde{\varphi}_p$ は惑星のポテンシャルである。惑星は等温の場合、惑星からスケールハイト程離れたところ（$x=1$）から強くトルクを受けている事がわかる。輻射が効果的に働く場合、惑星は等温の場合に比べ、非常に惑星に近い位置からもトルクを受けている。これは fig2、fig3 でみられる低温度、高密度領域が惑星に付加的なトルクを与えるためである。片側の密度波から惑星が受けるトルクは、ζ が 1 付近でピークをもつ（fig5)。これは輻射による熱の冷却時間が惑星の公転周期と同程度であるため、輻射が効果的に働き、低温度、高密度領域が形成され惑星に付加的なトルクを与えるためである。

0.4 まとめと今後の課題

本稿ではダスト輻射効果が原始惑星系円盤と惑星の重力相互作用に与える影響を調べた。ζ をパラメータとして、断熱的なガス円盤から等温的なガス円盤に励起される片側の密度波から惑星が受けるトルクを線形計算した。その結果、輻射による熱の冷却時間が惑星の公転周期と同程度のところで、ピークをもつことが分かった。片側から受けるトルクの量としては、等温の時に比べ１．１倍であるが、トルクの受ける位置は等温の場合と比べると非常に近い位置にあることがわかった。

ガス円盤は、動径方向に対して密度勾配や温度勾配などをもつ。惑星にかかる"差のトルク"は、惑星の両側にあるガス円盤の密度や温度が違うことから生じる。片側の密度波から惑星が受けるトルクの位置が、輻射の効果によって大きく変わるという結果は、惑星の両側における輻射効果の違いを考慮することで、"差のトルク"が大きく変わる可能性があることを示している。

0.5 参考文献

[1] Peter Goldreich and Scott Tremaine 1979. The excitation of density waves at the Lindblad and corotation resonances by an external potential

[2] Peter Goldreich and Scott Tremaine 1980. Disk-satellite interactions

[3] Hidekazu Tanaka.,Taku Tanaka and William R. Ward 1998. Three-dimensional interaction between aplanet and an isothermal gaseous disk

[4] William R. Ward 1986. Density Waves in the Solar Nebula: Differential Lindblad Torque

惑星と光学的に薄い円盤との重力相互作用

酒井 圭、田中 秀和

東京工業大学大学院 理工学研究科 地球惑星科学専攻

Abstract

原始惑星と光学的に薄い原始惑星系円盤との重力相互作用について、シアリングシートモデルを用いた局所3次元流体シミュレーションにより調べた。本研究では、光学的に薄い原始惑星系円盤中の放射によるエネルギー輸送を考慮に入れた。原始惑星形成以前の段階で、ダストのオパシティーは原始惑星系円盤中におけるダスト成長や微惑星形成により十分小さくなっていると考えられる。それゆえに、原始惑星形成時には、原始惑星系円盤が光学的に十分薄いという仮定は理にかなっている。光学的に薄い円盤から惑星が受ける片側トルクについて、様々な光学的厚さの場合に対して計算した。光学的に薄い円盤では、密度波における放射冷却の影響により密度波の後面で前面よりも温度が低くなることが明らかになった。衝撃波による加熱は放射冷却よりも効果は低かった。惑星周辺の密度分布は放射冷却により対照的ではなくなり、結果として、惑星は等温の場合に比べて余分なトルクを受けることがわかった。トルクの増加は冷却時間がケプラー周期と同じくらいの時に最大となる。また、惑星質量の減少と共にトルクは増加する。3倍の地球質量をもつ惑星の場合には、片側トルクの増加は最大で等温の場合の40%にもなる。放射冷却は差のトルクや惑星の落下時間にも大きな影響を及ぼしうるであろう。

1 Introduction

原始惑星と原始惑星系円盤との重力相互作用は惑星系形成理論における重要な物理過程のひとつである。惑星と円盤との相互作用は主に線形解析によって調べられてきた。それによると、惑星は原始惑星系円盤中に密度波を励起し、密度波と重力的に相互作用を行なう。その結果、重力的なトルクが励起された密度波による反作用として惑星に働く。正のトルクは惑星軌道より内側の円盤から働き、外側の円盤からは負のトルクが働く。これらのトルクがお互いに打ち消し合えば、惑星が受ける正味のトルクはゼロとなり我々は落下問題に悩まされることもない。円盤の動径方向の変化を考慮に入れ円盤から受ける正味のトルクを見積もると、惑星軌道の減衰時間は、木星型惑星のコア質量（10倍の地球質量）の原始惑星が5 AUにある場合で10^5年と見積もられる。この軌道減衰時間は原始惑星の形成時間に比べ十分に短い。それゆえに、惑星と円盤との相互作用は惑星形成理論における深刻な問題のひとつである。

2 Disc model

原始惑星系円盤中でダストは互いに衝突合体を繰返し、様々なサイズをもつようになる。10^4年の集積後にはほとんどのダスト半径は5.2 AUで1 cmに達している。光学的な厚さについて荒い見積もりを行なうために、ダストサイズは一様でパラメータとして与える。ここでは、ダストの微惑星形成や動径方向への移動は無視する。これらの仮定のもとで、円盤のオパシティーは5.2 AUで0.1 μm、100 μm、1 cmの半径をもつダストの場合にそれぞれ8.2、0.90、0.0075 $\mathrm{cm^2\,g^{-1}}$と見積もられる。円盤の光学的厚さは1 cmサイズのダストの場合に5.2 AUで1.1となる。

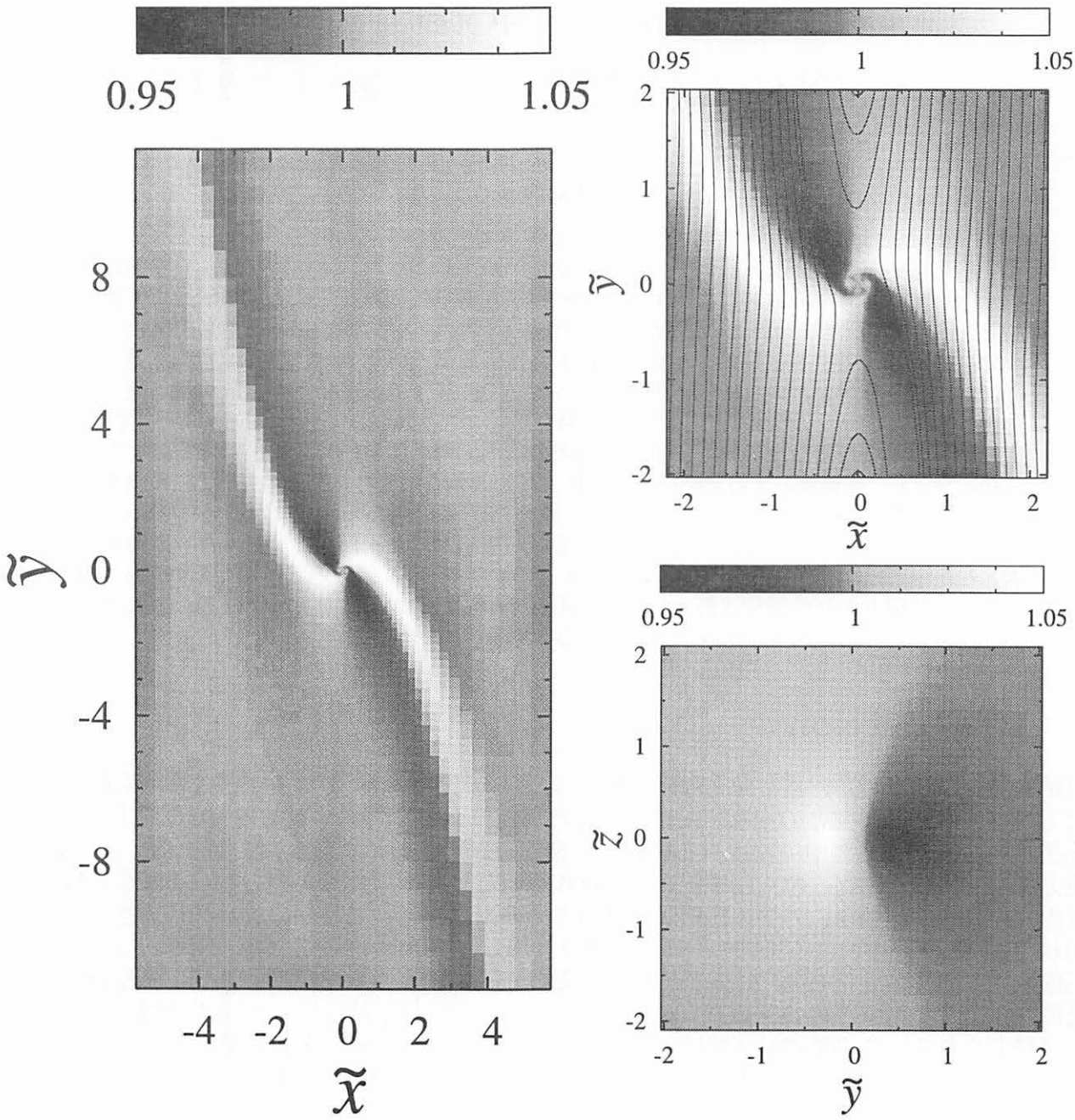

Figure 1: 光学的に薄い円盤における温度分布。惑星は原点に位置している。左図は赤道面における計算領域全体の温度であり、右上図は惑星近傍の温度である。流線が右上図には重ねて描かれている。右下図は $\tilde{x} = -0.5$ の平面における温度分布を表している。

この光学的厚さの見積もりは、微惑星形成や動径方向の移動を無視しているため、原始惑星系円盤における上限値である。惑星形成以前に、これらの効果によりダストの面密度は桁で小さくなっており、光学的厚さも同様に小さくなることを示唆している。ダストの面密度が1/10倍においては、1 cmサイズの円盤の光学的厚さは3 AUより外側では1よりも十分に小さくなる。従って、光学的に薄い円盤における惑星と円盤との相互作用を考えることは重要である。

3 Summary

惑星と光学的に薄い円盤との円盤との相互作用について、3次元流体シミュレーションによって調べた。エネルギー方程式に放射輸送の効果を考慮に入れ、放射が密度波の励起に及ぼす効果について調べた。主な結果をまとめると以下の通りである。

1. 光学的に薄い円盤における密度波は放射冷却を引き起こす。放射冷却のために、密度波の後面における温度は前面よりも低くなる（Figure 1）。結果、密度分布は傾斜し余分なトルクが惑星に加えられる。惑星の極近傍では流れは惑星にバウンドされガスはほぼ等温になる。この領域は惑星にトルクを及ぼさない。

2. 放射輸送の効率は放射による冷却時間とケプラー周期との比で定義され、惑星が受けるトルクは輸送効率によっては等温の場合よりも大きくなる。輸送効率が高い極限では等温場合のトルクに収束し、低い極限では断熱に収束する。

3. 惑星質量が軽い場合は、放射冷却やトルクは非常に大きくなる。これは小さなボンディ半径により密度分布の傾斜が惑星の非常に近傍で起きることによる。

Kepler要素に対するPoisson括弧の直接計算法
Direct Calculation Method of the Poisson Parentheses for the Keplerian Elements

井上　猛　（京都産業大学）
T. Inoue
Kyoto Sangyo University

Abstract. The equations for the variation of arbitrary constants are expressed with the aid of the Poisson parentheses. Various methods widely used to obtain these equations inevitably contain the tedious calculations of the superfluous Lagrange brackets.

Here, we present a method which enables us to obtain the equations of the variation for the Keplerian elements without any aid of the Lagrange brackets, that is to say, one is directly capable to calculate the Poisson parentheses, also in the case of arbitrary intermediary orbits.

We introduced the rectangular unit vectors $\vec{P}^*$, $\vec{Q}^*$ and $\vec{R}$ with which the radius vector $\vec{r}$ and the velocity vector $\vec{V}$ are expressed as follows :

(43) $\vec{r} = r \cdot \vec{P}^*$ and (44) $\vec{V} = \sqrt{\left\{\frac{\mu}{p}\right\}} \cdot \left\{ e \sin f \cdot \vec{P}^* + \xi \cdot \vec{Q}^* \right\}$

The desired partial derivatives of the Keplerian elements with respect to the radius vector and the velocity vector are straightforwardly obtained as :

(48) $\frac{\partial a}{\partial \vec{r}} = \frac{2\xi^2}{\eta^4} \vec{P}^*$ and (49) $\frac{\partial a}{\partial \vec{V}} = \frac{2e \sin f}{n\eta} \vec{P}^* + \frac{2\xi}{n\eta} \vec{Q}^*$

(63) $\frac{\partial \omega}{\partial \vec{r}} = \frac{\xi \sin f}{pe} \vec{P}^* + \frac{(-\xi + \eta^2)}{pe^2} \vec{Q}^* + \frac{\cos i}{p \sin i} (\cos \psi + e \cos \omega) \vec{R}$

(66) $\frac{\partial M}{\partial \vec{V}} = \frac{\eta^2(\xi^2 - \xi - 2e^2)}{n a e^2 \xi} \vec{P}^* - \frac{\eta^2(\xi + 1) \sin f}{n a e \xi} \vec{Q}^*$

These are four examples among twelve partial derivatives.

The Poisson parentheses should be calculated through the scalar product of these derivatives. The Poisson parenthesis(a, e) will be given as an example.

(67) $(a, e) = \left(\frac{\partial a}{\partial \vec{r}} \cdot \frac{\partial e}{\partial \vec{V}}\right) - \left(\frac{\partial a}{\partial \vec{V}} \cdot \frac{\partial e}{\partial \vec{r}}\right) =$

$$= \frac{2\xi \sin f}{n a \eta^3} \{\xi - \xi + \eta^2 - \eta^2\} = 0$$

It is profoundly desirable to construct the equations of the variation of the arbitrary constants through the present maneuver.

1．「要素変化の式」の導出に際して、通常の方法では、Lagrange括弧の計算は不可欠である。最終的な表式は、総てが Poisson括弧で表わされるのであるから、仲介役としてのLagrange括弧の計算を必要としない方法が在るならば、それは「優れたもの」と言うべきである。此の事を念頭に置きつつ工夫を凝らした結果、 Poisson括弧を直接的に計算する方法を確立する事が出来たのである。二体問題の系を「人工系」に選んだ際の“新変数”即ち、Kepler要素に対して、具体的な導出の方法を提示する。此の様な事が可能となったのも、「定数変化の方法」に関して、充分に理解を深める事が出来て居たからである。
☆　井上猛：『定数変化法と云うもの』　第27回天体力学研究会集録　p. 155, 1995

先ずは、我々が用いる「Kepler要素の表記」を示す目的で、二体問題の解表式を以下に挙げて置く。

$$(1)\qquad u - e\sin u = M = n(t-\tau) = \int_{t_*}^{t} n\,dt + \chi$$

$$(2)\qquad n \equiv \sqrt{\{\mu / a^3\}}$$

$$(3)\qquad \mu \equiv G(m_{太陽} + m_{惑星})$$

$$(4)\qquad \tan(f/2) = \sqrt{\{(1+e)/(1-e)\}}\tan(u/2)$$

$$(5)\qquad \psi \equiv \omega + f$$

$$(6)\qquad r = a(1 - e\cos u)$$

$$(7)\qquad \phi = \Omega + \tan^{-1}(\cos i \tan\psi)$$

$$(8)\qquad \theta = \sin^{-1}(\sin i \sin\psi)$$

此処に、Kepler要素 ： a、e、i ； Ω、ω、τは、それぞれが次の意味を有するとした：

a ：軌道長半径　　e ：離心率　　i ：軌道傾斜角

Ω ：昇交点黄経　　ω ：近日点引数　　τ：近日点通過の時刻

以下に於ては、直交座標系に準拠した「位置」と「速度」の利用が、計算に取って甚だ好都合なので、次の形の表式を掲げて置く事にする。

$$(9)\qquad \vec{r} = \begin{pmatrix} x \\ y \\ z \end{pmatrix} = a(\cos u - e)\cdot\vec{P} + a\eta \sin u\cdot\vec{Q}$$

$$(10)\qquad \vec{V} = \begin{pmatrix} V_x \\ V_y \\ V_z \end{pmatrix} = -\frac{\sqrt{\{\mu a\}}}{r}\sin u\cdot\vec{P} + \frac{\sqrt{\{\mu a\}}\,\eta}{r}\cos u\cdot\vec{Q}$$

$$(11)\qquad \eta \equiv \sqrt{\{1-e^2\}}$$

量 $\vec{P}$ および $\vec{Q}$ は、$\vec{R}$と共に、軌道のヴェクトル定数と呼ばれて居る互いに直交する単位ヴェクトルを表わす。

$$(12)\quad \vec{P} = \begin{pmatrix} \cos\Omega\cos\omega - \sin\Omega\sin\omega\cos i \\ \sin\Omega\cos\omega + \cos\Omega\sin\omega\cos i \\ \sin\omega\sin i \end{pmatrix}$$

$$(13)\quad \vec{Q} = \begin{pmatrix} -\cos\Omega\sin\omega - \sin\Omega\cos\omega\cos i \\ -\sin\Omega\sin\omega + \cos\Omega\cos\omega\cos i \\ \cos\omega\sin i \end{pmatrix}$$

$$(14)\quad \vec{R} = \begin{pmatrix} R_x \\ R_y \\ R_z \end{pmatrix} = \begin{pmatrix} \sin\Omega\sin i \\ -\cos\Omega\sin i \\ \cos i \end{pmatrix}$$

2．通常の方法に於ては、直ちに上記の式群を計算して行くのであるが、我々の方法ではこれらを要素に付いて解いた次の形のものを用意してから、計算に取り掛かるのである。

$$(15)\quad a = \left(\frac{2}{r} - \frac{V^2}{\mu}\right)^{-1}$$

$$(16)\quad e\sin u = \frac{(\vec{r}\cdot\vec{V})}{\sqrt{\{\mu a\}}}$$

$$(17)\quad e\cos u = 1 - \frac{r}{a}$$

$$(18)\quad M = u - e\sin u$$

$$(19)\quad \cos i = \frac{x V_y - y V_x}{\sqrt{\{\mu a\}}\eta}$$

$$(20)\quad \sin\Omega\sin i = + \frac{y V_z - z V_y}{\sqrt{\{\mu a\}}\eta}$$

$$(21)\quad \cos\Omega\sin i = - \frac{z V_x - x V_z}{\sqrt{\{\mu a\}}\eta}$$

$$(22)\quad \sin\omega\sin i = \frac{z}{r}\cos u - \sqrt{\left\{\frac{a}{\mu}\right\}}\, V_z \sin u$$

$$(23)\quad \cos\omega\sin i = \frac{z}{r}\frac{\sin u}{\eta} + \sqrt{\left\{\frac{a}{\mu}\right\}}\, V_z \frac{\cos u - e}{\eta}$$

$$(24)\quad r = \sqrt{\{\vec{r}\cdot\vec{r}\}} = a(1 - e\cos u)$$

$$(25)\quad V = \sqrt{\{\vec{V}\cdot\vec{V}\}} = \frac{2\mu}{r} - \frac{\mu}{a}$$

実は、ヴェクトル $\vec{P}$ 及び $\vec{Q}$ の中の角度 ω の所を、これに真近点離角 f を加えた量 ψ に置き換えたもので考える方が好都合なのである。量 ψ は、(5)式で定義して置いた。

$$(26)\quad \vec{P}^{*} \equiv \begin{pmatrix} +\cos\Omega\cos\psi - \sin\Omega\sin\psi\cos i \\ +\sin\Omega\cos\psi + \cos\Omega\sin\psi\cos i \\ \sin\psi\sin i \end{pmatrix}$$

$$(27)\quad \vec{Q}^{*} \equiv \begin{pmatrix} -\cos\Omega\sin\psi - \sin\Omega\cos\psi\cos i \\ -\sin\Omega\sin\psi + \cos\Omega\cos\psi\cos i \\ \cos\psi\sin i \end{pmatrix}$$

ヴェクトル $\vec{R}$ は、(14)式で与えられるものを、その儘の形で用いる。

3．要素変化の式そのものは、既に良く知られて居るものである。此処で問題にしようとして居るのは 「Poisson括弧のみに依拠」した形で、その導出が可能なものなのか否かを知る事である。そこで、問題とする要素変化の式を、先ずは書いて置く事にする。

$$(28)\qquad \dot{\zeta}_h = -\sum_{k=1}^{6}(\zeta_h, \zeta_k)\frac{\partial \varepsilon R}{\partial \zeta_k} \quad , \qquad (h = 1, 2, \cdots, 6)$$

此処では、要素に次の対比を課して、表記の簡便化を図った。

$$(29)\qquad \begin{matrix} \zeta_1 & \zeta_2 & \zeta_3 & \zeta_4 & \zeta_5 & \zeta_6 \\ a & e & i & \Omega & \omega & \tau \end{matrix}$$

量 εR は、摂動函数を表わす。

$$(30)\qquad \varepsilon R = \varepsilon R(\zeta_1, \zeta_2, \zeta_3; \zeta_4, \zeta_5, \zeta_6; t)$$

量 (ζ_h, ζ_k) は、 Poisson括弧を表わす。具体的な内容は、次式で与えられる。

$$(31)\quad (\zeta_h, \zeta_k) = \frac{\partial \mathcal{Z}_h}{\partial x}\frac{\partial \mathcal{Z}_k}{\partial V_x} - \frac{\partial \mathcal{Z}_h}{\partial V_x}\frac{\partial \mathcal{Z}_k}{\partial x} + \frac{\partial \mathcal{Z}_h}{\partial y}\frac{\partial \mathcal{Z}_k}{\partial V_y} - \frac{\partial \mathcal{Z}_h}{\partial V_y}\frac{\partial \mathcal{Z}_k}{\partial y} + \\ + \frac{\partial \mathcal{Z}_h}{\partial z}\frac{\partial \mathcal{Z}_k}{\partial V_z} - \frac{\partial \mathcal{Z}_h}{\partial V_z}\frac{\partial \mathcal{Z}_k}{\partial z} \quad , \quad (h, k = 1, 2, \cdots, 6)$$

此処で、$\mathcal{Z}_h$ と表記したものは、要素 ζ_hを、位置ヴェクトル$\vec{r}$、速度ヴェクトル$\vec{V}$及び時間 t に付いて解いた時の函数を表わす。

$$(32)\qquad \zeta_h = \mathcal{Z}_h(x, y, z; V_x, V_y, V_z; t) \quad , \quad (h = 1, 2, \cdots, 6)$$

処で、此の函数 $\mathcal{Z}_h$は、どの様にして定められたのであろう？ 実は、話の順序が逆になって居たのである。二体問題の解表式(1)～(14)を、表式中に含まれて居る積分定数に付いて解いた式群(15)～(23)が、外ならぬ当該函数 $\mathcal{Z}_h$を定めるのである。従って、積分定数たるKepler要素 ：$a, e, i; \Omega, \omega, \tau$ に対して、次の関係式が先ず初めに書かれるべきであったのである。

$$(33)\qquad c_h = \mathcal{Z}_h(x, y, z; V_x, V_y, V_z; t) \quad , \quad (h = 1, 2, \cdots, 6)$$

此処で、c_h と表記したものは、未だ定数で有る事を強調した処のKepler要素を表わす。対比は、以下の如くである。

$$(34)\qquad \begin{matrix} c_1 & c_2 & c_3 & c_4 & c_5 & c_6 \\ a & e & i & \Omega & \omega & \tau \end{matrix}$$

本来なら、(33)式に於ける位置ヴェクトルおよび速度ヴェクトルの文字表記は、(32)式のそれとは、異なるもので書き表わされなければならないのであるが、煩瑣を避ける目的で同一文字で済ませた。何はともあれ、函数 $\mathcal{Z}_h$は、(33)式に依って与えられるのである。従って、此の函数が、次の関係式を満たすのは明らかな事である。

$$(35)\qquad \dot{c}_h = \frac{\partial \mathcal{Z}_h}{\partial x}\dot{x} + \frac{\partial \mathcal{Z}_h}{\partial y}\dot{y} + \frac{\partial \mathcal{Z}_h}{\partial z}\dot{z} + \frac{\partial \mathcal{Z}_h}{\partial V_x}\dot{V}_x + \frac{\partial \mathcal{Z}_h}{\partial V_y}\dot{V}_y + \frac{\partial \mathcal{Z}_h}{\partial V_z}\dot{V}_z + \\ + \frac{\partial \mathcal{Z}_h}{\partial t} \equiv 0 \quad , \qquad (h = 1, 2, \cdots, 6)$$

摂動が存在して居る場合には、只今の積分定数 c_hを、新変数 ζ_hに置き換えると共に位置ヴェクトルおよび速度ヴェクトルが満たす、運動方程式を考慮するのであった。

4．与えられた運動方程式が、次の形のものであるとする。

$$(36)\qquad \dot{x}=V_x-\frac{\partial\,\varepsilon R^*}{\partial V_x}\ ,\quad \dot{y}=V_y-\frac{\partial\,\varepsilon R^*}{\partial V_y}\ ,\quad \dot{z}=V_z-\frac{\partial\,\varepsilon R^*}{\partial V_z}\ ;$$

$$(37)\qquad \dot{V}_x=-\frac{\mu}{r^3}x+\frac{\partial\,\varepsilon R^*}{\partial x}\ ,\quad \dot{V}_y=-\frac{\mu}{r^3}y+\frac{\partial\,\varepsilon R^*}{\partial y}\ ,\quad \dot{V}_z=-\frac{\mu}{r^3}z+\frac{\partial\,\varepsilon R^*}{\partial z}$$

此処で、量 εR^* は、位置ヴェクトルおよび速度ヴェクトルを引数とした時の摂動函数を表わして居る。

$$(38)\qquad \varepsilon R^*=\varepsilon R^*(x,y,z;V_x,V_y,V_z;t)$$

二体問題の系を「人工系」としたのであるから、(32)式で与えられる要素 ζ_h に対する時間的な変化は以下の様になる。

$$(39)\qquad \begin{aligned}\dot{\zeta}_h&=\frac{\partial \mathcal{Z}_h}{\partial x}\dot{x}+\frac{\partial \mathcal{Z}_h}{\partial y}\dot{y}+\frac{\partial \mathcal{Z}_h}{\partial z}\dot{z}+\frac{\partial \mathcal{Z}_h}{\partial V_x}\dot{V}_x+\frac{\partial \mathcal{Z}_h}{\partial V_y}\dot{V}_y+\frac{\partial \mathcal{Z}_h}{\partial V_z}\dot{V}_z+\frac{\partial \mathcal{Z}_h}{\partial t}=\\&=\left\{\frac{\partial \mathcal{Z}_h}{\partial x}V_x+\frac{\partial \mathcal{Z}_h}{\partial y}V_y+\frac{\partial \mathcal{Z}_h}{\partial z}V_z+\right.\\&\left.+\frac{\partial \mathcal{Z}_h}{\partial V_x}\left(-\frac{\mu}{r^3}x\right)+\frac{\partial \mathcal{Z}_h}{\partial V_y}\left(-\frac{\mu}{r^3}y\right)+\frac{\partial \mathcal{Z}_h}{\partial V_z}\left(-\frac{\mu}{r^3}z\right)+\frac{\partial \mathcal{Z}_h}{\partial t}\right\}+\\&-\frac{\partial \mathcal{Z}_h}{\partial x}\frac{\partial\,\varepsilon R^*}{\partial V_x}-\frac{\partial \mathcal{Z}_h}{\partial y}\frac{\partial\,\varepsilon R^*}{\partial V_y}-\frac{\partial \mathcal{Z}_h}{\partial z}\frac{\partial\,\varepsilon R^*}{\partial V_z}+\\&+\frac{\partial \mathcal{Z}_h}{\partial V_x}\frac{\partial\,\varepsilon R^*}{\partial x}+\frac{\partial \mathcal{Z}_h}{\partial V_y}\frac{\partial\,\varepsilon R^*}{\partial y}+\frac{\partial \mathcal{Z}_h}{\partial V_z}\frac{\partial\,\varepsilon R^*}{\partial z}\end{aligned}$$

上で、中括弧 {･･･}の中の量は、函数 $\mathcal{Z}_h$の定め方から(35)式の適用を受け、零となる。摂動函数 εR^* と εRの偏微分係数の間には、次の関係が存在して居る。

$$(40)\qquad \frac{\partial\,\varepsilon R^*}{\partial V_x}=\sum_{k=1}^{6}\frac{\partial\,\varepsilon R}{\partial\zeta_k}\frac{\partial \mathcal{Z}_k}{\partial V_x},\quad \frac{\partial\,\varepsilon R^*}{\partial V_y}=\sum_{k=1}^{6}\frac{\partial\,\varepsilon R}{\partial\zeta_k}\frac{\partial \mathcal{Z}_k}{\partial V_y},\quad \frac{\partial\,\varepsilon R^*}{\partial V_z}=\sum_{k=1}^{6}\frac{\partial\,\varepsilon R}{\partial\zeta_k}\frac{\partial \mathcal{Z}_k}{\partial V_z}\ ;$$

$$(41)\qquad \frac{\partial\,\varepsilon R^*}{\partial x}=\sum_{k=1}^{6}\frac{\partial\,\varepsilon R}{\partial\zeta_k}\frac{\partial \mathcal{Z}_k}{\partial x},\quad \frac{\partial\,\varepsilon R^*}{\partial y}=\sum_{k=1}^{6}\frac{\partial\,\varepsilon R}{\partial\zeta_k}\frac{\partial \mathcal{Z}_k}{\partial y},\quad \frac{\partial\,\varepsilon R^*}{\partial z}=\sum_{k=1}^{6}\frac{\partial\,\varepsilon R}{\partial\zeta_k}\frac{\partial \mathcal{Z}_k}{\partial z}$$

只今の関係を、(39)式に考慮すれば、以下の結果を得る。

$$(42)\qquad \begin{aligned}\dot{\zeta}_h&=-\sum_{k=1}^{6}\left(\frac{\partial \mathcal{Z}_h}{\partial x}\frac{\partial \mathcal{Z}_k}{\partial V_x}+\frac{\partial \mathcal{Z}_h}{\partial y}\frac{\partial \mathcal{Z}_k}{\partial V_y}+\frac{\partial \mathcal{Z}_h}{\partial z}\frac{\partial \mathcal{Z}_k}{\partial V_z}\right)\frac{\partial\,\varepsilon R}{\partial\zeta_k}+\\&+\sum_{k=1}^{6}\left(\frac{\partial \mathcal{Z}_h}{\partial V_x}\frac{\partial \mathcal{Z}_k}{\partial x}+\frac{\partial \mathcal{Z}_h}{\partial V_y}\frac{\partial \mathcal{Z}_k}{\partial y}+\frac{\partial \mathcal{Z}_h}{\partial V_z}\frac{\partial \mathcal{Z}_k}{\partial z}\right)\frac{\partial\,\varepsilon R}{\partial\zeta_k}=\\&=-\sum_{k=1}^{6}(\zeta_h,\zeta_k)\frac{\partial\,\varepsilon R}{\partial\zeta_k}\ ,\qquad (h=1,2,\cdots,6)\end{aligned}$$

斯くして、(28)式に与えて置いた要素変化の式を何の曖昧さも無く導き出す事が出来た。此の表式自体は、既に良く知られたものであって、何ら新しいものでは無い。肝心なのは此処に登場して来る偏微分係数を、直接的に計算する方法を提示する事である。

5．先に、(26)式および(27)式で、軌道のヴェクトル定数に準ずる、軌道面内に位置する単位ヴェクトル $\vec{P}^*$および $\vec{Q}^*$を定義して置いた。これを用いる時は、位置ヴェクトルや速度ヴェクトルが、次の形に書き表わされる事になる。

(43) $$\vec{r} = r \cdot \vec{P}^*$$

(44) $$\vec{V} = \sqrt{\left\{\frac{\mu}{p}\right\}} \cdot \left\{ e \sin f \cdot \vec{P}^* + \xi \cdot \vec{Q}^* \right\}$$

(45) $$p \equiv a(1 - e^2)$$

(46) $$\xi \equiv \frac{p}{r} = 1 + e \cos f$$

以上の準備が整いさえすれば、後は、平易かつ機械的な計算を進めて行くのみである。我々の様に直角座標を用いた場合は、一つの成分に対する偏微分係数を計算すれば、残る成分に対しても、同型の結果が得られる様になって居る事が多いのである。

一例として、長半径ａの偏微分係数の計算要領を、エネルギー積分に着目して示す。

(47) $$-\frac{\mu}{2a} = \frac{1}{2} V^2 - \frac{\mu}{r}$$

$$\frac{\mu}{2a^2} \frac{\partial a}{\partial x} = \frac{\mu}{r^2} \frac{x}{r} \quad , \qquad \frac{\partial a}{\partial x} = 2 \frac{a^2}{r^2} \frac{x}{r} = \frac{2\xi^2}{\eta^4} P_x^*$$

(48) $$\frac{\partial a}{\partial \vec{r}} = \frac{2\xi^2}{\eta^4} \vec{P}^*$$

$$\frac{\mu}{2a^2} \frac{\partial a}{\partial V_x} = V_x \quad , \quad \frac{\partial a}{\partial V_x} = \frac{2a^2}{\mu} \sqrt{\left\{\frac{\mu}{p}\right\}} \left\{ e^* \sin f \cdot P_x + \xi \cdot Q_x^* \right\}$$

(49) $$\frac{\partial a}{\partial \vec{V}} = \frac{2e \sin f}{n\eta} \vec{P}^* + \frac{2\xi}{n\eta} \vec{Q}^*$$

次には e sin uおよび e cos uを、$\vec{r}$および$\vec{V}$に付いて偏微分して行く。此処にはuの偏微分係数のみを書いて置く事にする。

(50) $$e \frac{\partial u}{\partial \vec{r}} = -\frac{\xi e \sin f}{p e \eta} \vec{P}^* + \frac{\eta^2(\xi - \eta^2)}{p e \eta} \vec{Q}^*$$

(51) $$e \frac{\partial u}{\partial \vec{V}} = \frac{\xi(\xi + \eta^2 - 2)}{n a e \xi} \vec{P}^* - \frac{(\xi + \eta^2) e \sin f}{n a e \xi} \vec{Q}^*$$

残る要素の計算に必要となる、補助量に対する偏微分係数の結果を列挙して置こう。

(52) $$\frac{\partial p}{\partial \vec{r}} = 2 \vec{P}^* + 2e \vec{P} \quad , \qquad \frac{\partial p}{\partial \vec{V}} = -\frac{2\eta^3}{n\xi} \vec{Q}^*$$

(53) $$\frac{\partial f}{\partial \vec{r}} = -\frac{\xi e \sin f}{p e^2} \vec{P}^* + \frac{\{(2 - \eta^2)\xi - \eta^2\}}{p e^2} \vec{Q}^*$$

(54) $$\frac{\partial f}{\partial \vec{V}} = \frac{\eta\xi(\xi - 1)}{n a e^2 \xi} \vec{P}^* - \frac{\eta(\xi + 1) e \sin f}{n a e^2 \xi} \vec{Q}^*$$

6．本小論では、要素τの代りに平均近点離角Mを用いる事にした。此の事は、本質的な困難を惹起したりをしないばかりか、寧ろ、見通しの良い結果を与えて呉れるのである。

何はともあれ、計算結果を一括列挙してみるならば、以下の様になる。

(55) $$\frac{\partial a}{\partial \vec{r}} = \frac{2\xi^2}{\eta^4}\vec{P}^*$$

(56) $$\frac{\partial a}{\partial \vec{V}} = \frac{2e \sin f}{n\eta}\vec{P}^* + \frac{2\xi}{n\eta}\vec{Q}^*$$

(57) $$\frac{\partial e}{\partial \vec{r}} = -\frac{\xi(\xi-\eta^2)}{pe}\vec{P}^* + \frac{\sin f}{a}\vec{Q}^*$$

(58) $$\frac{\partial e}{\partial \vec{V}} = \frac{\eta \sin f}{na}\vec{P}^* + \frac{\eta(\xi^2-\eta^2)}{na e\xi}\vec{Q}^*$$

(59) $$\frac{\partial i}{\partial \vec{r}} = \frac{1}{p}(\sin\psi + e\sin\omega)\vec{R}$$

(60) $$\frac{\partial i}{\partial \vec{V}} = \frac{\cos\psi}{na\xi}\vec{R}$$

(61) $$\frac{\partial \Omega}{\partial \vec{r}} = -\frac{1}{p\sin i}(\cos\psi + e\cos\omega)\vec{R}$$

(62) $$\frac{\partial \Omega}{\partial \vec{V}} = \frac{\eta \sin\psi}{na\sin i\,\xi}\vec{R}$$

(63) $$\frac{\partial \omega}{\partial \vec{r}} = \frac{\xi \sin f}{pe}\vec{P}^* + \frac{(-\xi+\eta^2)}{pe^2}\vec{Q}^* + \frac{\cos i}{p\sin i}(\cos\psi + e\cos\omega)\vec{R}$$

(64) $$\frac{\partial \omega}{\partial \vec{V}} = \frac{\eta(-\xi+1)}{nae^2}\vec{P}^* + \frac{\eta(\xi+1)\sin f}{nae\xi}\vec{Q}^* - \frac{\eta\cos i\sin\psi}{na\xi\sin i}\vec{R}$$

(65) $$\frac{\partial M}{\partial \vec{r}} = -\frac{(\xi+e^2)\sin f}{ae\eta}\vec{P}^* + \frac{\eta(\xi-1)}{ae^2}\vec{Q}^*$$

(66) $$\frac{\partial M}{\partial \vec{V}} = \frac{\eta^2(\xi^2-\xi-2e^2)}{nae^2\xi}\vec{P}^* - \frac{\eta^2(\xi+1)\sin f}{nae\xi}\vec{Q}^*$$

これが総てである。量 $\vec{P}^*$、$\vec{Q}^*$、$\vec{R}$ が、互いに直交する単位ヴェクトルである事の故にPoisson括弧の計算は、極めて容易なものとなるのである。

此の様な「優れたもの」が、これ迄に提案されなかったと云うのは、甚だ不可解な事と言うべきであろう。

7．最早、説明の必要は無い処であるが、一例として括弧（a，e）を計算して置く。

$$(67)\qquad (a,e) = \left(\frac{\partial a}{\partial \vec{r}} \cdot \frac{\partial e}{\partial \vec{V}}\right) - \left(\frac{\partial a}{\partial \vec{V}} \cdot \frac{\partial e}{\partial \vec{r}}\right) =$$

$$= \left(\frac{2\xi^2}{\eta^4}\vec{P}^* \cdot \frac{\eta \sin f}{na}\vec{P}^* + \frac{\eta(\xi^2-\eta^2)}{na e \xi}\vec{Q}^*\right) +$$

$$- \left(\frac{2e \sin f}{n\eta}\vec{P}^* + \frac{2\xi}{n\eta}\vec{Q}^* \cdot \frac{\xi(\xi-\eta^2)}{pe}\vec{P}^* + \frac{\sin f}{a}\vec{Q}^*\right) =$$

$$= \frac{2\xi^2}{\eta^4}\frac{\eta \sin f}{na} - \frac{2e \sin f}{n\eta}\frac{\xi(\xi-\eta^2)}{pe} - \frac{2\xi}{n\eta}\frac{\sin f}{a} =$$

$$= \frac{2\xi \sin f}{na\eta^3}\{\xi - \xi + \eta^2 - \eta^2\} = 0$$

以下、同様の単純計算を行ないさえすれば、次の良く知られた結果に到達する。

$$(68)\qquad (a,M) = -\frac{2}{na}$$

$$(69)\qquad (e,\omega) = \frac{\eta}{na^2e}$$

$$(70)\qquad (e,M) = -\frac{\eta^2}{na^2e}$$

$$(71)\qquad (i,\Omega) = \frac{1}{na^2\eta \sin i}$$

$$(72)\qquad (i,\omega) = -\frac{\cos i}{na^2\eta \sin i}$$

要素変化の式を書いて、終る事にする。

$$(73)\qquad \dot{a} = \frac{2}{na}\frac{\partial \varepsilon R}{\partial \chi}$$

$$(74)\qquad \dot{e} = \frac{\eta^2}{na^2e}\frac{\partial \varepsilon R}{\partial \chi} - \frac{\eta}{na^2e}\frac{\partial \varepsilon R}{\partial \omega}$$

$$(75)\qquad \frac{di}{dt} = \frac{\cos i}{na^2\eta \sin i}\frac{\partial \varepsilon R}{\partial \omega} - \frac{1}{na^2\eta \sin i}\frac{\partial \varepsilon R}{\partial \Omega}$$

$$(76)\qquad \dot{\Omega} = \frac{1}{na^2\eta \sin i}\frac{\partial \varepsilon R}{\partial i}$$

$$(77)\qquad \dot{\omega} = \frac{\eta}{na^2e}\frac{\partial \varepsilon R}{\partial e} - \frac{\cos i}{na^2\eta \sin i}\frac{\partial \varepsilon R}{\partial i}$$

$$(78)\qquad \dot{\chi} = -\frac{\eta^2}{na^2e}\frac{\partial \varepsilon R}{\partial e} - \frac{2}{na}\left(\theta\frac{\varepsilon R}{\partial a}\right)$$

唐突に、近日点通過の時刻τの代りに、量χが現われて居るが、既に、（1)式で定義して置いたので混乱は無いであろう。一連の偏微分係数を求める際に、特に平均近点離角Mを用いたので、斯う云う事も容易に行なえたと云う次第である。

此処に述べた Poisson括弧を直接的に計算する方式が、教育の場などで広く行なわれる事を切望する。任意の中間軌道に対しても、本法の適用は勿論可能である。　(03506ma)

Return of shepherding satellites

Hiroshi Daisaka and Junichiro Makino

Department of Astronomy, Graduate School of Science, University of Tokyo, 7-3-1 Hongo, Bunkyo-ku, Tokyo 113-0033, Japan
Telephone:+81-3-5841-4274
Fax:+81-3-5841-4252

daisaka@astron.s.u-tokyo.ac.jp

makino@astron.s.u-tokyo.ac.jp

ABSTRACT

We have investigated the evolution of a satellite-ring system in order to understand the mechanism of the formation and maintenance of the Uranian eccentric rings, by performing N-body simulations of the system in which ring particles are confined by two shepherding satellites inside and outside of the ring. Our simulations demonstrated that under certain conditions the initially circular ring and satellites become eccentric, and remain to be eccentric. To our surprise, the self-gravity of ring particles, which is essential in the self-gravity model originally proposed by Goldreich & Tremaine (1979a,b) has a little effect on our simulated eccentric ring. We also performed numerical simulations of a simple system in which satellites move on fixed orbits and only inelastic collision of particles is taken into account. Even in such a system, we found that the initially circular ring becomes eccentric, and that properties of the ring is explained by the effect of the forced oscillation by a perturbing satellite. This result implies that the effect of secular perturbation with satellites and ring and inelastic collisions of ring particles are keys for the formation of eccentric ring in our simulation. These effects might play an important role on the formation and maintenance of the Uranian eccentric rings.

Subject headings: planetary rings, Uranus, N-body simulation

1. Introduction

One of the most striking features of the Uranian ring system is that some of rings, at least 6, 5, 4, α, β, ϵ-rings, are eccentric (e.g., French et al. 1991). The existence of the

eccentric rings is truly surprising, because it requires the pericenter of ring particles with different orbital periods to behave in exactly the same way under dispersive effects such as quadrapole moment of Uranus, which precesses the longitude of the pericenter of a ring particle, ϖ, depending on its semimajor axis, a. If the eccentricity, e, and inclination, i, are small enough ($e, i << 1$), the precession rate is expressed as

$$\frac{d\varpi}{dt} \simeq \frac{3}{2} J_2 R^2 (GM)^{1/2} a^{-7/2}, \tag{1}$$

where G is the gravitational constant, and, M, R, and J_2 are the mass, radius, and non-dimensional harmonic coefficient of the potential of Uranus. For the ϵ-ring, the difference between the angles of the pericenter of the innermost particle and that of the outermost particle undergoes one full rotation in about 200 years. Thus, it seems unlikely that the eccentric ring survives for a long time without an additional contribution.

In order to explain these eccentric rings, various theorical models have been proposed. One is a theory based on the self-gravity of the ring, originally proposed by Goldreich & Tremaine (1979a,b) (also, see Borderies, Tremaine, & Goldreich (1983)). In this model, the self-gravity of ring particles locks their apsides against the differential precession. This model is widely accepted, since the model can give some observable prediction which is consistent with observations. However, it also has consequences which contradict with observations (e.g., French et al. (1991); Graps et al. (1995)). Recently, in order to solve such problems, this model was extended to take into account the effect of particle collision, and predicted much larger mass for the α-ring (Chiang & Goldreich 2000; Mosqueira & Estrada 2002). Kozai (1992, 1993) proposed another model, in which eccentric rings are maintained by the forced oscillation of ring particles caused by undiscovered shepherding satellites in eccentric orbits. In this model, it is assumed that apsidal motions of the ring particles and the satellites completely synchronize with each other. It has been unclear whether or not any of these theories correctly accounts for the formation and survival of the eccentric rings.

We studied the evolution of a ring-satellite system in which a narrow ring is confined by two shepherding satellites orbiting around an oblate central planet, by performing direct N-body simulations. This is a setting similar to Kozai's model, but we have not made any assumption on the eccentricity of shepherding satellites. In our model, the orbits of satellites evolve through interaction with the ring and the other satellite. In our simulations, gravitational interaction and physical (inelastic) collision between ring particles are taken into account. For calculation of the gravitational interactions, we used GRAPE-6 (Makino, Fukushige, & Namura 2002), which allow us to do simulations for a long time with a large number of particles.

In the next section, we describe the simulation method and the ring-satellite model. In

section 3, we describe our numerical results. The main finding is that an initially circular ring becomes eccentric, even though initially both the ring and orbits of both satellites are circular. In section 4, we show the effect of secular perturbations from satellites on our eccentric ring by simulations in which satellites move in fixed orbits. Section 5 is for discussions.

2. Model

2.1. Simulation method

We consider motion of particles under a potential of a oblate central body, taking into account mutual interactions of particles through the gravitational force and the direct collision. The orbit of particles is calculated by integrating the equation of motion with the forth-order P(EC)^2 Hermite scheme (Kokubo, Yoshinaga, & Makino 1998). For calculation of the gravitational force between ring particles, GRAPE-6, a special purpose computer for calculating gravitational force (Makino, Fukushige, & Namura 2002), is used. In our simulation, collision is detected as overlapping of particles. By assuming a free-slip, hard-sphere collision model, we calculate post-collisional velocity with restitution coefficient in normal direction, ε. For simplicity, we use velocity-independent restitution coefficient and $\varepsilon = 0.01$, which is needed to keep ring particles within a narrow region. For details, see Daisaka & Makino (2002).

2.2. Ring-Satellite model

The ring consists of N equal-mass, equal-size particles. For our standard simulations, $N = 10^4$ and $m_p = 10^{-10}M$, where N is the number of ring particles and m_p is the mass of a ring particle, so that the mass of the ring is $m_r = 10^{-6}M$. To determine the size of the ring particles, we assume that their density is given by $\rho/(Ma_0^{-3}) = 1.54$, where a_0 is the central value of the semi-major axis of ring particles. This roughly corresponds to the typical value for icy particles at the location of the ϵ-ring of Uranus. Initially, ring particles have the semi-major axis uniformly distributed in $[a_0 - W/2, a_0 + W/2]$, where we take $W = 0.02a_0$ for our standard runs. Initial eccentricities and inclinations of ring particles are $0.1h_r$, where $h_r = (2m_p/3M)^{1/3}$ is the reduce Hill radius of ring particles. Other orbital elements are chosen randomly.

Two satellites have the same mass, $m_s = 10^{-6}M$. Thus, the total mass of the ring and the mass of one satellite is the same. We placed two satellites in circular orbits inside and

outside the ring, with radial distance $\Delta a = 5h_s a_0$, where $h_s = (m_s/3M)^{1/3}$ is the reduced Hill radius of the satellite. The synodic time of these satellites is about $20T_K$. For the J_2 term of the potential of Uranus, we use $J_2(R/a_0)^2 = 8.95 \times 10^{-3}$. This value is similar to the value at the ϵ-ring of Uranus. The precession period is $\sim 750T_K$.

3. Result

3.1. Formation of Eccentric Rings

Figure 1 shows the result of the standard simulation. Initially the ring is circular, and the ring particles form a straight line in cylindrical coordinates at $t = 0$. At $t = 600T_K$, the ring is still circular. At $t = 3000T_K$, however, the sinusoidal distortion of the distribution is clearly be seen. In this case, the distribution of the eccentricity vector is offset from the origin, indicating that the pericenters of ring particles are aligned and the ring becomes eccentric. After the formation, the eccentric ring is maintained for a long time but the eccentricity and the longitude of pericenter change with time ($t = 6000, 19735$, and $40000T_K$ in Fig. 1).

Figure 2 shows the time evolution of global ring characteristics. The eccentricity of the ring in Fig. 2(a) is defined as an average of the scalar product of the eccentricity vector of a ring particle and an unit vector with the direction of the pericenter of the ring, $(\cos\varpi_{ring}, \sin\varpi_{ring})$ (see below). In Fig. 2(a), we can see that the eccentricity of the ring grows rapidly for $t = 1000$ to $4000T_K$, which corresponds to the growth of the eccentric ring seen in Fig. 1. After the initial growth of the eccentricity, it exhibits a complex quasi-oscillatory behavior. The timescale of the oscillation is clearly related to that of the relative rotation of apsides of the ring and the inner and outer shepherding satellites. Comparison of Fig. 2(a) with Fig. 2(c), and (d) suggests that the eccentricity takes maximal values at times when the angle of apsides between the outer satellite and the ring is minimum (~ 0) and the angle between the inner and the ring is maximum ($\sim \pi$). In Fig. 2(b), the longitude of the pericenter of the ring is defined simply as $\varpi_{ring} = \tan^{-1}(< \sin\varpi > / < \cos\varpi >)$, where "<>" means the average over ring particles. It is tricky to take an average of ϖ because it is an angle variable with indeterminacy of $2\pi n$, where n is an integer. We also plot the deviation of the pericenter from average in Fig. 2(b). This quantity is useful to see whether the ring is eccentric or not. It should be ~ 1.8 when the ring is circular. As the system evolves($t > 1000T_K$), the deviation becomes much smaller than 1.8, indicating that the apsides of ring particles aligned with each other.

In Fig. 2(a), the eccentricity of the ring shows quasi-periodic oscillations, but with the

magnitude of average eccentricity slowly decreasing in time. This decrease is probably the result of the increase of the separation between the satellites and the ring shown in Fig. 2(e). The center of the ring and its width plotted in Fig. 2(e) are defined as the average of the semimajor axes of ring particles ($< a >$) and its dispersion ($\sqrt{< a^2 > - < a >^2}$). As the system evolves, satellites slowly go away from the ring.

Figure 2(b) indicates that the eccentric ring is precessing at an almost constant rate. The precessing period obtained from this figure is $6.8 \times 10^2 T_K$. Those for for satellites inside and outside are $5.7 \times 10^2 T_K$ and $8.2 \times 10^2 T_K$, respectively. The period calculated purely from the J_2 contribution of the potential of the plants are $7.45 \times 10^2 T_K$, $6.47 \times 10^2 T_K$, and $8.53 \times 10^2 T_K$, for the ring and the satellites, respectively. Thus, our numerical values are in good agreement with the simple theoretical estimate. The complete synchronization of the apsidal motion, which was assumed in Kozai's model (Kozai 1992, 1993), does not take place in our eccentric ring.

3.2. Effect of the self-gravity of ring particles

In the self-gravity model (Goldreich & Tremaine 1979a,b; Borderies, Tremaine, & Goldreich 1983; Chiang & Goldreich 2000; Mosqueira & Estrada 2002), the self-gravity of ring particles is essential to maintain a common apsidal motion of the ring particles, providing counteraction against the differential precession due to J_2. As a consequence, rigid precession of the ring is realized. In order to see how the self-gravity work in our simulated eccentric ring, we perform a simulation in which the self-gravity of ring particles is neglected.

Figure 3 is the result of the simulation with the same parameters used in the standard run but neglecting the self-gravity of ring particles. This figure provides the evidence that even in ring particles without the self-gravity the formation and maintenance of the eccentric ring, and the common apsidal motion of ring particles are realized. The timescale of the growth of the eccentric ring is also similar to that in the standard run. These results suggest that in our simulated eccentric ring, the self-gravity of the ring has little effect on the growth of the eccentricity and on apse alignment of ring particles.

4. Secular perturbations from satellites

The behavior of the eccentricities of the ring and satellites seen in our simulations, for example, a maximum in the ring's eccentricity seems to coincide with a minimum in the eccentricities of the satellites, reminds us of importance of secular perturbations from

ring and satellites. However, only the secular perturbations can not explain our simulated eccentric ring, because another effect is also important on the dynamical evolution of the system. In fact, the distant encounters between the ring and satellites should give rise to the evolution of the semimajor axes of the satellites (Daisaka & Makino 2002).

In order to separate the effect of secular perturbations from satellites on our eccentric ring, we performed numerical simulations of a simple ring-satellite model in which satellites move in fixed orbits and only inelastic collision of ring particles is taken into account.

We considered the simplest case in which a one satellite moves in an eccentric orbit while the other moves in a circular orbit. The inclinations of the satellites are set to be zero. Such a modeling of a ring-satellites system is similar to that used in Kozai (1992, 1993).

We performed simulations with different sets of $(e_{s,in}, e_{s,out}, \Delta a)$, where $e_{s,in}$ and $e_{s,out}$ are the eccentricities of an inner and outer satellite, respectively, and Δa is radial distance of the inner or outer satellite from the ring. In the simulations, we used a smaller number of ring particles ($N = 5000$) than used in the standard run ($N = 10000$), in order to reduce computational time.

The results obtained from a simulation with $(e_{s,in}, e_{s,out}, \Delta a) = (0.25\ h_s,\ 0,\ 5\ h_s a_0)$, i.e., in the case where the inner satellite moves in the eccentric orbit while the outer in the circular orbit, can be seen in Fig. 4 and Fig. 5, which show the time evolution of particle distributions in space and in the eccentricity vectors and that of the orbital elements of the ring, respectively. Even in this case, the ring becomes eccentric and it is maintained for long time, as seen in the standard run. Also, particle distributions in the eccentricity vectors shift from the origin and move counterclockwise around the origin, indicating that there is a tendency for the ring particles to have a common apsidal motion. This apsidal motion is not independent of that of the perturbing satellite. Figure 5 (c) exhibits libration of $\varpi_{s,in} - \varpi_{ring}$ around zero after $t > 30000 T_K$. This indicates a tendency for the apse of the ring to be locked by that of the perturbing satellite. On the other hand, such phenomena did not occur when $e_{s,in}$ and $e_{s,out}$ are zero. Figure. 6 and Fig. 7 are the results of a simulation with $(e_{s,in}, e_{s,out}, \Delta a) = (0,\ 0,\ 5\ h_s a_0)$, i.e., in the case where both satellites have circular orbits. In this case, e_{ring} is very small, and the deviation of the pericenter of the ring almost keeps to be ~ 1.8, indicating that the ring is still circular.

From simulations with $e_{s,in}$ or $e_{s,out}$ large enough to make a ring eccentric, we obtained a time-averaged value of e_{ring} and its dispersion to compare with the forced eccentricity derived by secular perturbation theory (Daisaka & Makino 2002). In Fig. 8, we plot a normalized ring eccentricity e_{ring}/e_s by dots with error-bars obtained from the simulations and the forced eccentricity by solid line, as a function of the normalized semimajor axis of the perturbing

satellite (a/a_0). This figure shows a good agreement between e_{ring} and e_{forced}. Figure 8 also shows a peak close to $\sim -5h_s a_0$, which corresponds to the location of the secular resonance. Since in the simulation of Fig. 4 we put the inner satellite with the eccentricity close to this location, the ring's eccentricity could be enhanced largely by the effect of the secular resonance.

Thus, if we consider the simple system of a ring and satellites, the secular perturbations should provide a good approximation to our eccentric ring.

5. Discussion

Secular perturbations from satellites might explain the eccentric ring in the standard run where we allow the satellites to evolve freely. However, we have to explain how the satellites increase in their eccentricities. Also, we have to understand the effect of inelastic collisions of ring particles on the formation and maintenance of the eccentric ring. To address these points, we are currently constructing a simplified analytic model.

REFERENCES

Borderies, N., Goldreich, P.,& Tremaine, S. 1983, AJ, 88, 1560

Chiang, E. I., & Goldreich, P. 2000, ApJ, 540, 1084

Daisaka, H., & Makino, J., submitted to ApJ

French, R. G., Nicholson, P. D., Porco, C. C., & Marouf E. A. 1991, in Uranus, ed. J. T. Bergstralh, E. D. Miner, & M. S. Matthews (Tucson: Univ. Arizona Press), 327

Graps, A. L., Showalter, M. A., Lissauer, J. J., & Kary, D. M. 1995, AJ, 109, 2262

Goldreich, P.,& Tremaine, S. 1979a, Nature, 277, 97

Goldreich, P.,& Tremaine, S. 1979b, AJ, 84, 1638

Goldreich, P.,& Tremaine, S. 1981, ApJ, 243, 1062

Kozai, Y. 1992, PASJ, 44, 135

Kozai, Y. 1993, PASJ, 45, 263

Kokubo, E., Yoshinaga, K., & Makino, J. 1988, MNRAS, 297, 1067

Makino, J., Fukushige, T.,& Namura, K., in preparation

Mosqueira, I.,& Estrada, P. R. 2002, Icarus, 158, 545

Murray, C. C.,& Dermott, S. F. 1999, Solar System Dynamics, Cambridge Univ. Press

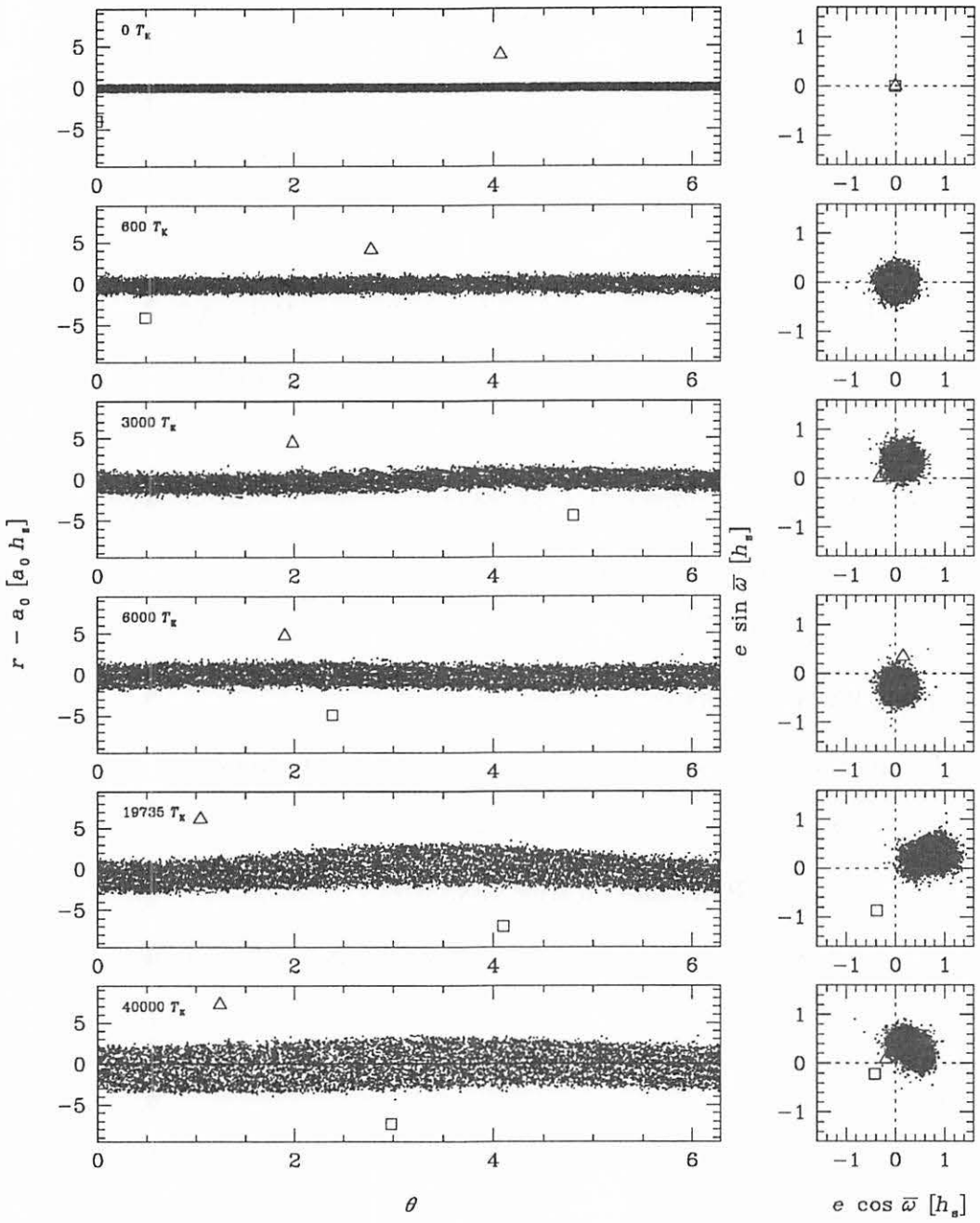

Fig. 1.— Formation and evolution of an elliptical ring in a system with 10000 identical, spherical, inelastic, and self-gravitating particles with shepherding satellites orbiting around a non-spherical central planet. Left panels are spatial distributions in cylindrical coordinates. Vertical axis shows the difference of semi-major axis $\Delta a = a - a_0$, where a_0 is the central value of the semi-major axis of ring particles at $t = 0$. It is scaled by the Hill radius $h_s = (m_s/3M)^{-1/3} = 6.93 \times 10^{-3}$. Right panels are distributions in the plane of the eccentricity vector $(e\cos\varpi, e\sin\varpi)$. The inner and outer satellites are denoted by an open circle and triangle, respectively.

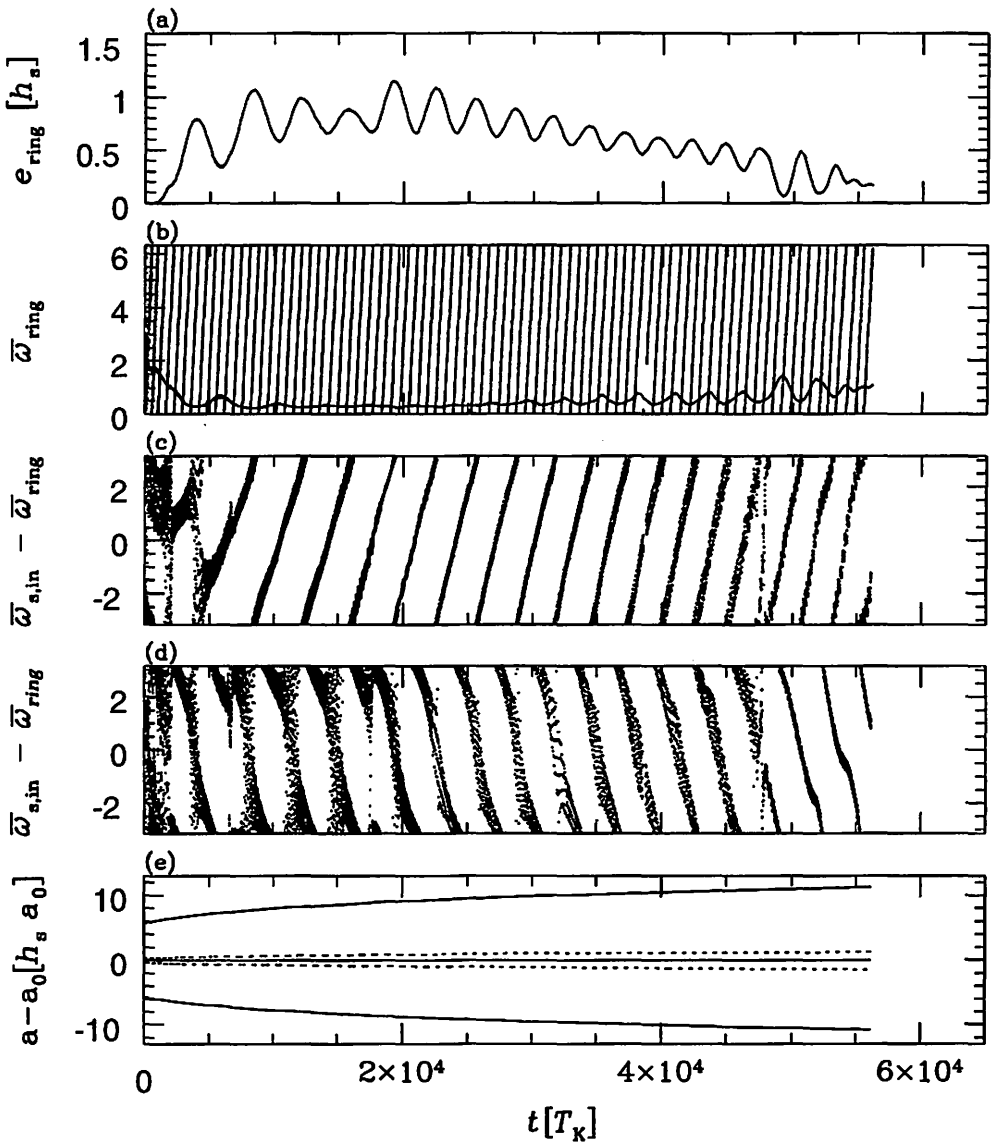

Fig. 2.— The time evolution of orbital elements of ring particles and satellites in the simulation of Fig. 1. (a)The eccentricity of the ring. (b)The longitude of the pericenter of the ring (dots) and its deviation from the average (line). (c)The phase difference of the pericenter of the inner satellite from that of the ring. (d)The phase difference of the pericenter of the outer satellite from that of the ring. (e)The semimajor axes of satellites(upper and lower lines), the average of the semimajor axis of ring particles (solid line around $a - a_0 = 0$), and its dispersion (broken lines).

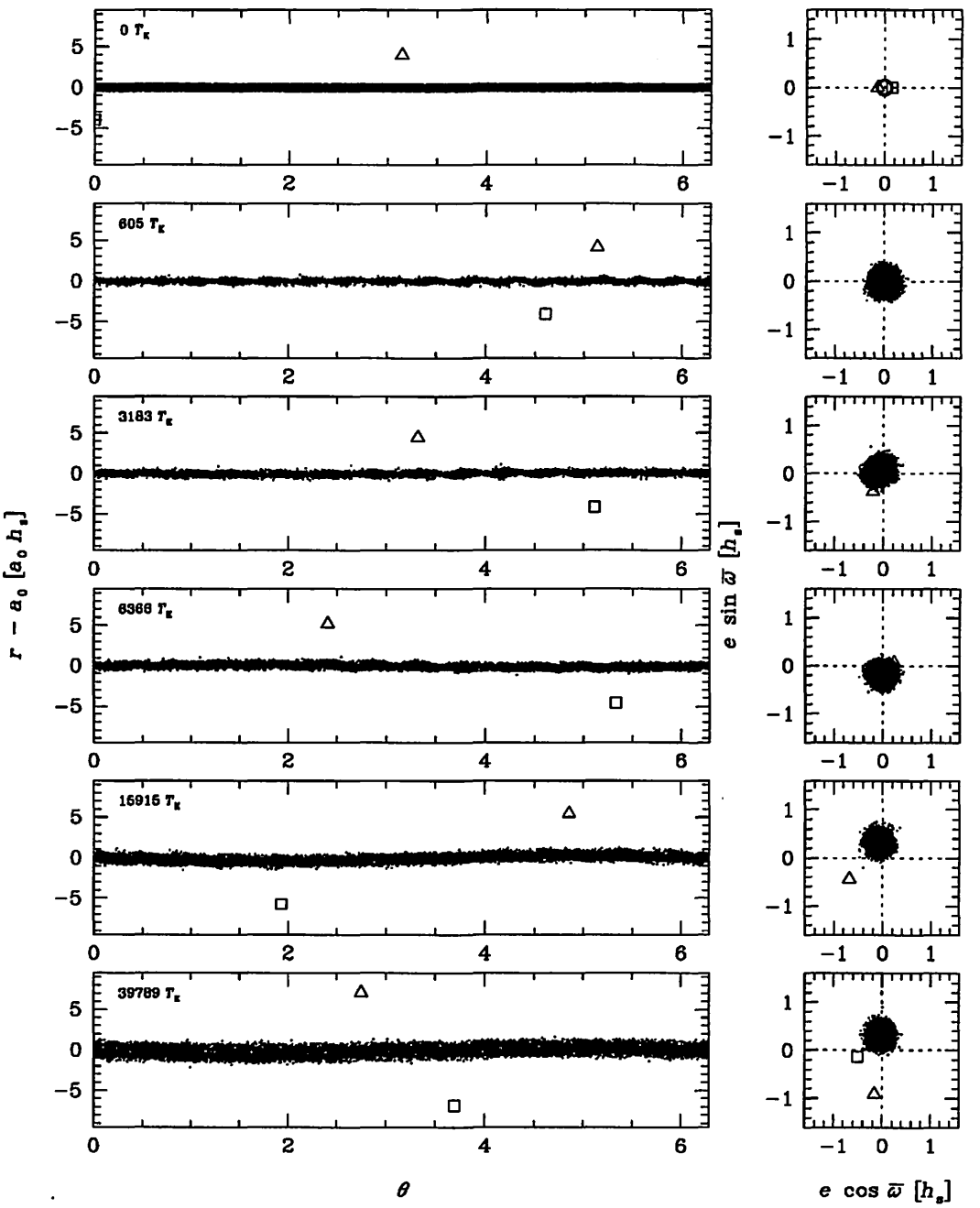

Fig. 3.— Formation and evolution of an elliptical ring in the case where the self-gravity of ring particles is ignored. Parameters used in this simulation is the same as these used in Fig. 1.

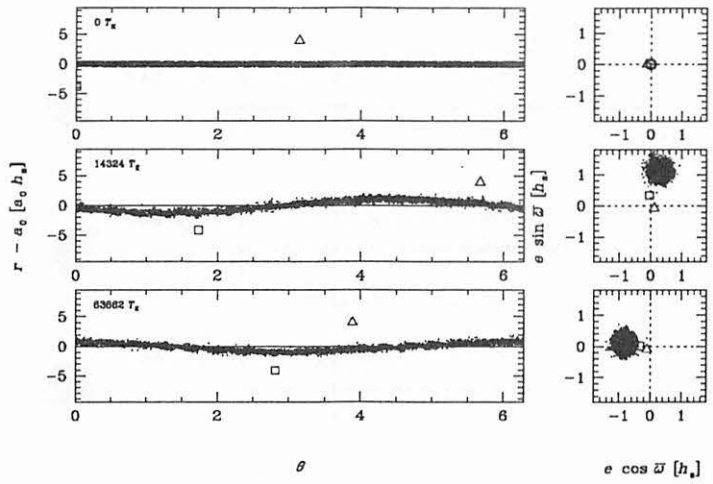

Fig. 4.— Particle distributions in space and in the eccentric vectors in the case where the inner satellite moves in an eccentric orbit while the outer in a circular orbit.

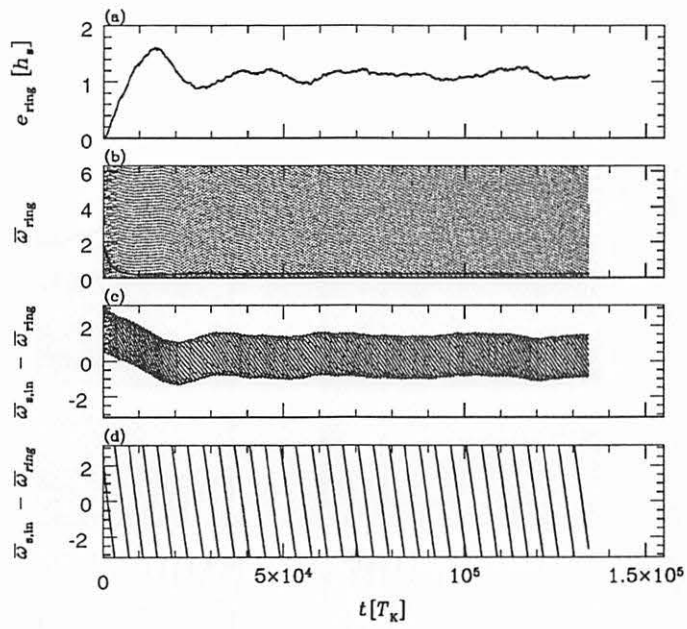

Fig. 5.— The time evolution of orbital elements of ring particles and satellites in the simulation of Fig. 4. (a)The eccentricity of the ring. (b)The longitude of the pericenter of the ring (dots) and its deviation from the average (line). (c)The phase difference of the pericenter of the inner satellite from that of the ring. (d)The phase difference of the pericenter of the outer satellite from that of the ring.

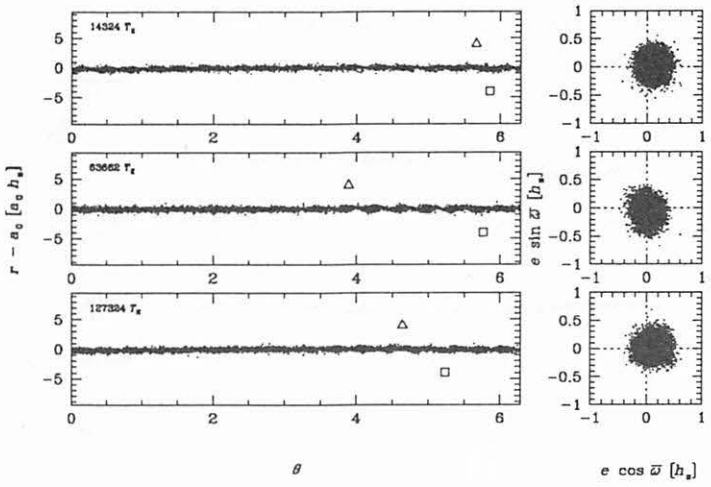

Fig. 6.— Same as Fig. 4 but in the case where both satellites have zero-eccentricity.

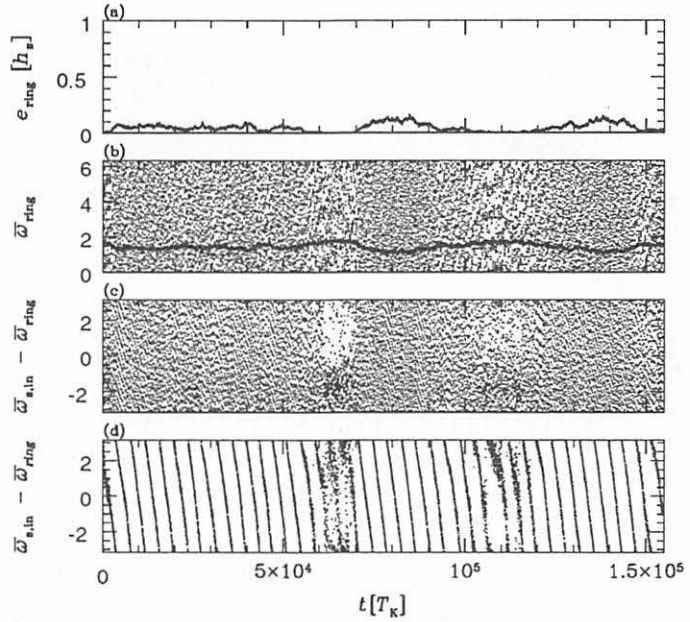

Fig. 7.— Same as Fig. 5 but in the case where both satellites have zero-eccentricity.

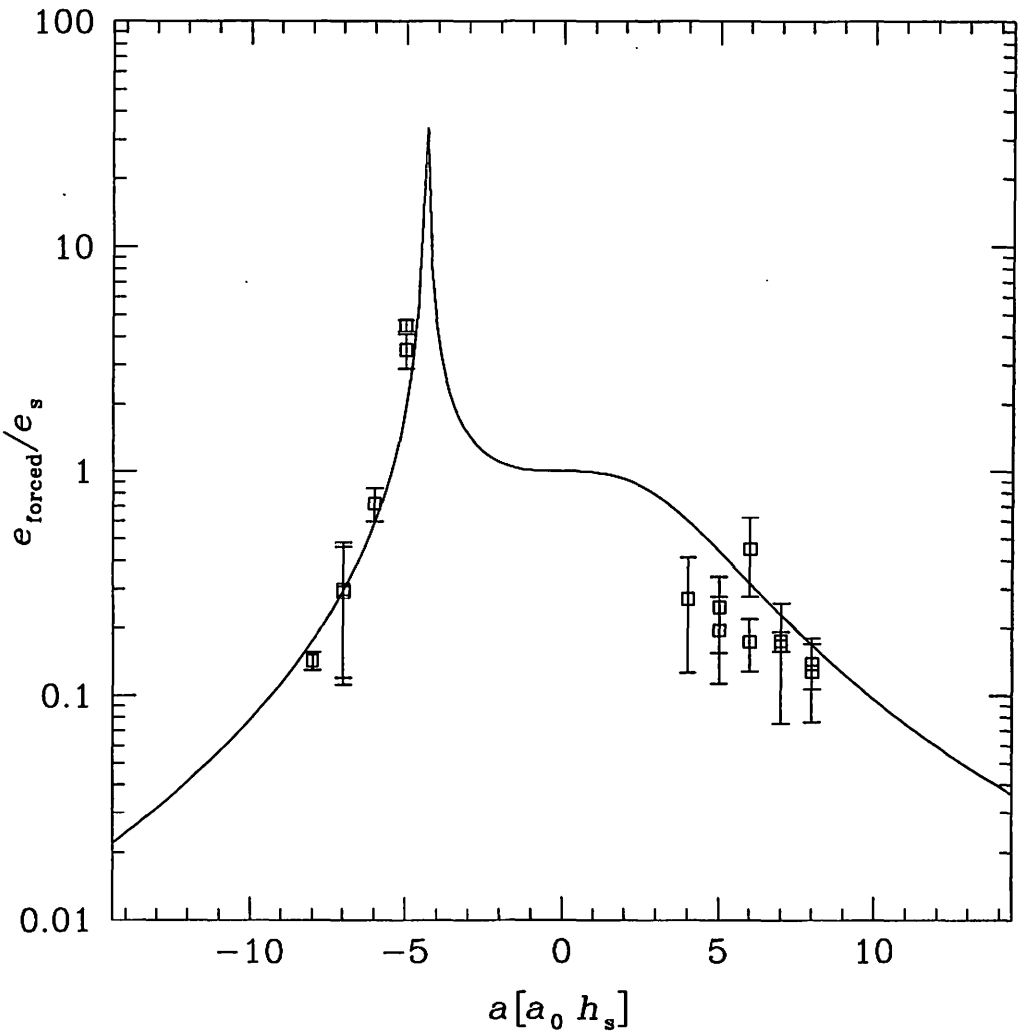

Fig. 8.— Comparison of the ring's eccentricity obtained from the simulations in which both satellites move on fixed orbits (dots), with the forced eccentricity derived by secular perturbation theory (line). Note that a peak close to $-5h_s a_0$ indicates the location of secular resonance.

水星近日点黄経に於ける余剰永年変化問題への最終解答
Final Answer to the Problem of the Excess Secular Variation in the Longitude of the Perihelion of Mercury

井上　猛　（京都産業大学）
T. Inoue
Kyoto Sangyo University

Abstract. Since 1991, we continuously examine the problem of the excess secular variation in the longitude of the perihelion of Mercury. The existence of this peculiar motion was pointed out for the first time by Le Verrier in 1859. Then Newcomb afirmed this phenomenon in 1895. This amount is about 43 arc seconds per century. We know well "the widely accepted fact" that this problem has been totally solved by the Einstein's general theory of relativity in 1915.

Our constant examination for this problem made able us to reveal the truth. That is to say, there existed "a tiny mistake" in the theories of the motion of Mercury established by Le Verrier and Newcomb.

This is "the very reason" why such an excess advance appears in the motion of Mercury. Our result shows that the Newtonian Mechanics is perfect at least to describe the motion of this planet.

1．「惑星運動の理論」は、太陽と着目惑星とから成る「二体問題の系」を先ずは積分しそこでの積分定数を新変数として書かれた「要素変化の式」を通して、総ての天体に依る作用を取り込む形で構成されて居る。運動理論の中に現われる数値は、観測を通して定められるべき性質のものである。然し、現実には総ての天体の影響を内包した状況下でしかこれらを決定する事は出来ない。それでは「二体問題の系」と云うのは謂わば絵に描いた餅でしか無いのであろうか？　そんな事は無い！　観測的に決定された数値の中に“紛れ込んで居る摂動の部分”は、理論の助けを借りて、排除して行けば良い事になって居る。最初に「水星の近日点黄経ϖに、“余剰の”永年変化が存在する」と云う事を言い出したLe Verrierの場合とても、状況は全く同じであった。

水星の運動が一平面内に限って行なわれるとしても、問題の本質を見失う事は無いので平面極座標（r, ϕ）を導入する。rは動径を、ϕは黄経を表わす。我々も、Le Verrierに倣って、離心率eの二次以上の微小量は無視して、楕円軌道を次の形に書く。

(1)　：$\phi = \varpi + M + 2e \sin M$

(2)　：$r = a(1 - e \cos u)$

此処で、aは長半径を、ϖは近日点黄経を、Mは平均近点離角を表わす。

2．水星の黄経φおよび動径ｒを与える運動理論は、極めて複雑な三角函数の組合せから成って居る。更に、これに多数の数表を併用して行かなければならない様になって居る。

然し、我々が問題とする対象は意外と“単純”であって、Le Verrierが与えたものから引用しても以下の様である。

(3)　$\phi_{\text{観測}} = \varpi + M + 2e_{\text{楕円}} \sin M + S \sin M$

(4)　$r_{\text{観測}} = a(1 - e_{\text{楕円}} \cos u) + C_{\text{金星}} \cos M$

(5)　$S \equiv S_{\text{金星}} + (S_{\text{地球}} + S_{\text{木星}})$

此処に、量ＳやＣ金星などは、Le Verrierに依って、次の様に与えられて居るものである。

惑　星	黄経の摂動　δφ sin M の係数	動径の摂動　δｒ cos M の係数
金　星	$S_{\text{金星}}$: +0.″065 2528	$C_{\text{金星}}$: -0.″011 4015
地　球	$S_{\text{地球}}$: +0.″017 7139	＊　＊　＊
木　星	$S_{\text{木星}}$: +0.″032 0147	＊　＊　＊
総　和	S : +0.″114 9815	$C_{\text{金星}}$: -0.″011 4015

本小論で扱って居る精度からすれば、上の関係式は、次の形に書き表わす事も出来る。

(6)　$\phi_{\text{観測}} = \varpi + M + 2e_{\text{観測}} \sin M$

(7)　$r_{\text{観測}} = a(1 - e_{\text{動径}} \cos u)$

但し、次の関係を仮定した。

(8)　$e_{\text{観測}} \equiv e_{\text{楕円}} + \frac{S}{2}$

(9)　$e_{\text{動径}} \equiv e_{\text{楕円}} - \frac{C_{\text{金星}}}{a}$

観測的に離心率の値を決定するには、「中心差」の表式に着目するのが良いであろう。上記の(6)式が、将に此の表式に外ならないので、これに依って量$e_{\text{観測}}$の値を、観測的に決定する事が出来る。量Ｓは、理論の方から知る事が出来るので、(8)式に依って直ちに楕円軌道の離心率$e_{\text{楕円}}$の値を知る事が出来る。

処が、惑星運動理論の大御所たる Le Verrier も Newcombも此の手順を踏んでは居ないのである。何故か？　それは、深い考えが有っての事なのであろうが、実際問題としては量Ｓの推定が、意外に困難なものなのかも知れない。何はともあれ「彼らが、どんな風に運動理論を構築して行ったか」は、我々にも充分に窺い知る事が出来るのである。それが可能であったればこそ、彼らが建設した理論の中の誤りも発見する事が出来たのである。「彼ら」と一括りにして言ったが、Le Verrierの理論の建設の仕方と Newcombのそれとの間には明確な違いが存して居るのである。

3. Le Verrierが、どの様に扱ったかを見て行く事にしよう。「中心差」の表式に着目し観測から“離心率$e_{観測}$”の値を入手する。その数値から、地球と木星に依る摂動分を差し引いて、次式で与えられる“離心率$\tilde{e}$”を定める。

(10) $$\tilde{e} \equiv e_{観測} - \frac{1}{2}(S_{地球} + S_{木星})$$

只今の量$\tilde{e}$には、未だ金星に依る影響が含まれて居る。金星の影響を除去するのに、彼は「二通り」に修正を施して、二個の“離心率”を設定して行くのである。

(11) $$e_L \equiv \tilde{e} - \frac{S_{金星}}{2}$$

(12) $$e_r \equiv \tilde{e} + \frac{C_{金星}}{a}$$

具体的な数値を与えてみる。

(13) $$-\frac{S_{金星}}{2} = -0.''032\ 626$$

(14) $$+\frac{C_{金星}}{a} = -0.''029\ 453$$

両者の差は僅少である。

(15) $$+\frac{C_{金星}}{a} - \left\{-\frac{S_{金星}}{2}\right\} = +0.''003\ 173$$

Le Verrierは、「二体問題」の解を、「中心差」及び「動径」に対し、平均近点離角に関する Fourier級数に展開する。その時に、「中心差」の展開には“離心率e_L” を用い「動径」の展開には“離心率e_r” を用いるのである。「差が小さいから、構わない」と見做したのであろう。その解表式に金星に依る摂動を加味して行くのである。その様子を「中心差」及び「動径」で見てみるならば以下の如しである。

(16) $$\phi_L = \varpi + M + 2e_L \sin M + S_{金星} \sin M$$

(17) $$r_L = a_L(1 - e_r \cos u) + C_{金星} \cos M$$

これは、何の事は無い、単に一つの楕円軌道を計算したに過ぎない事になって居る。動径r_Lの表式では、長半径を a_Lと表記して置いた。

(18) $$\dot{\phi}_L = \varpi + M + 2\tilde{e} \sin M$$

(19) $$r_L = a_L(1 - \tilde{e} \cos u)$$

彼は、更に $S_{地球}$ 及び $S_{木星}$ に依る影響を、黄経ϕ_L の表式に追加して行くのである。

次には、 Newcombの扱いに付いて見て行く。彼は、観測される黄経$\phi_{観測}$を、楕円軌道で以て表現すべく、次の様な扱いをした。

(20) $$e_N \equiv e_L + \frac{S}{2} \quad , \quad S = S_{金星} + (S_{地球} + S_{木星})$$

これに依る時は、黄経ϕの方は、関与する惑星の摂動を総て取り込んで居るのであるから問題は全く無い。然し、此の離心率 e_Nを、動径 r の計算にも用いて居るのである。

Newcombが、黄経ϕおよび動径rを計算する為に用いた表式を書き出して置く。

(21) $\phi_N = \varpi + M + 2e_N \sin M$

(22) $r_N = a_N(1 - e_N \cos u)$

此処で用いた長半径 a_Nは、Le Verrierの a_Lと、次の関係を有する。

(23) $a_N \left(1 + \frac{1}{2} e_N^2\right) = a_L \left(1 + \frac{1}{2} e_L^2\right)$

これは、Le Verrierが、水星の質量を太陽の質量の三百万分の一である、と仮定したのに対して、Newcombは、六百万分の一であると仮定した事に起因するものである。

4. Le Verrierの理論構成の仕方と Newcombのそれとの間には“明確な差異が存在”して居るのであるが、要するに「一つの楕円軌道を計算したに過ぎない」と云う点からすれば「両人とも同じである」と言っても過言では無い。

我々は、(15)式に与えられて居る「金星の影響に於ける“差”」は確かに僅少であるがLe Verrierの理論の精度からすれば「これを無視する事は許されない」と云う事を指摘し此の差異に着目して『中間軌道』の導入を図ったのであった。

(24) $u - e \sin u = M \quad , \quad M = \int_{t_0}^{t} n\,dt + \chi$

(25) $n \equiv \sqrt{\{\mu_N / a_N^3\}} \quad , \quad \mu_N = G(m_{太陽} + m_{水星})$

(26) $\tan(f/2) = \sqrt{\{(1+e^*)/(1-e^*)\}} \cdot \tan(u/2)$

(27) $e^* \equiv e + \Delta E \quad , \quad \Delta E \equiv S_{地球} + S_{水星}$

(28) $r = a_N\{1 - (e - \Delta e) \cos u\}$

(29) $\phi = \varpi + f$

(30) $p_r = n a_N (e - \Delta e) \sin u / (1 - e \cos u)$

(31) $p_\phi = n r^2 \sin f / \{\sin u (1 - e \cos u)\}$

(32) $\Delta e \equiv \frac{C_{金星}}{a} + \frac{S_{金星}}{2}$

何の故に此の様なものを導入したかと言えば、これに依って(3)式(4)式が表わして居る真の黄経ϕおよび動径rが、所与の精度で表現され得るからである。加えて、此の『中間軌道』を用いるならば、「要素変化の方法」に依る摂動計算が精密かつ容易に実行可能となるからである。上で、単にeと表記したものは、(11)式で与えられる e_Lの意味に解すべきものである。

Le Verrierも Newcombも共に、二体問題の系を「人工系」に選び、Kepler要素に対する摂動計算を行なって「前進量の存在」を主張したのであった。

水星の運動を“正しく表現して居る”我々の『中間軌道』が、二体問題の系と如何なる関係にあるかは明らかにされなければならない重要事項である。そこで、二体問題の系を「人工系」に選び、積分定数たる楕円要素に対して「変化の式」を解いて行ってみる。

此の立場に立つ時は、次の εR_Nが、Kepler要素に対する「摂動函数」となる。

$$(33)\quad \varepsilon R_N = \mu_N \frac{\Delta e}{e}\left\{\frac{1}{a_N} - \frac{3}{r} + \frac{a_N}{r^2} + \frac{a_N^2(1-e^2)}{r^3}\right\} + \\ + \mu_N \frac{\Delta E}{e}\left\{-\frac{a_N}{r^2} + \frac{a_N^2(1-e^2)}{r^3}\right\}$$

特に知りたいのは、近日点黄経 ϖ に於ける永年変化 $\delta\varpi_{(s)}$ である。そこで、摂動函数 εR_N の永年部 $\varepsilon R_{N(s)}$ を抽出して調べてみる事にしよう。

$$(34)\quad \varepsilon R_{N(s)} = \mu_N \frac{\Delta e}{e}\left\{-\frac{2}{a_N} + \frac{2}{a_N\eta}\right\} + \mu_N \frac{\Delta E}{e} \times 0$$

$$(35)\quad \delta\varpi_{(s)} = \frac{\Delta e}{e}\cdot\frac{2}{1+\eta}\cdot\left\{\frac{1}{\eta} + \frac{e^2}{\eta^2}\right\}\cdot n(t-t_0)$$

$$(36)\quad \boxed{\delta\varpi_{(s)} : +43.374\ 8296\text{秒角/世紀}}$$

これで見れば、「正しい軌道」は、静止した楕円軌道に対して近日点黄経 ϖ に上記の一世紀当り43秒角の前進を有するが如きものであると云う事が明らかになった。

Le Verrierも Newcombも、我々の『中間軌道』に於ける微小量 Δeの存在を、無視して居るのである。これでは、43秒角/世紀 の不足分が出たとしても不思議は無い訳である。

惑星摂動を「正しく」考慮しさえすれば、“世紀の難問 : 43秒角/世紀 の不足”なるものも雲散霧消して仕舞うのは「火を見るよりも明らか」である。これを以て、一先ずは当該問題に終止符を打つ事としたい。

本小論では、参考文献を逐一挙げる事をしなかた。それは、既に第24回天体力学研究会集録から第34回天体力学研究会集録に至る間の、我々の主張を繰り返しつつ整理したのが本報告であるとの認識に立ったからである。然し、それでは拠り所の無いになって仕舞うので、一つだけ挙げて置く事にする。

井上猛 : 2000 第32回天体力学研究会集録 p. 147 ~ p. 158
水星近日点前進の問題 Newcombの場合

(03511D)

Kreutz 群のサブグループ
Subgroups of The Kreutz Sungrazers

住 谷　秀 夫　（大阪音楽大学）
Hideo Sunitani
Osaka College of Music

Abstract

Kreutz studied several comets that had similar orbital elements in the 19th century, and he pointed out existence of comet group. Therefore, these comets were called the Kreuts comet group. The orbital characteristic of the Kreutz comet group has a very small perihelion distance. Furthermore, their comets have a strong correlation between argument of perihelion and longitude of ascending node.

Until C/1970K1, 8 sungrazers were observed from the ground. Two spacecrafts, SOLWIND and SMM, discovered 16 sungrazers during 1979 to 1989. SOHO spacecraft detected about 500 sungrazers, and orbital elements of 454 sungrazers were published.

D-criterion defined by Jöpek was used as the orbital similarity of two comets. Using the cluster analysis, 478 sungrazers classified 6 subgroups. Subgroup ① and Subgroup ② correspond to Marsden's Subgroup I and Subgroup II. Subgroup ③ and Subgroup ④ consist of only one comet, C/1984O2 and C/1997M5, respectively. These two sungrazers have the maximum perihelion distance or the minimum inclination. Because these orbital elements include a problem, these sungrazers are not subgroup. There are 6 or 7 members constituting Subgroup ⑤ and Subgroup ⑥, it should be recognized as new subgroups if sungrazers of these subgroups increase.

1．Kreutz群

彗星群は近日点あるいは遠日点の方向がほぼ同じで、軌道要素が互いに良く似ているような彗星から構成されている。Kreutz 群は彗星群の中で最も有名であり、そのメンバーも最多である。

Kreutz 群に属する彗星の軌道の特徴を挙げると次のようになる。

1）近日点距離qが小さい

2）逆行軌道である

3）近日点引数ωと昇交点黄経Ωに線形関係がある

1）の近日点距離qの分布は、Fig.1 に示すように、その多くは太陽半径の 2 倍以内にある。これは、太陽コロナの中を通過するほどであり、太陽を掠める彗星群という別名も、この特徴に由来する。半数以上の彗星は太陽半径の1.0 ～ 1.2 倍の範囲にある。太陽半径の2倍以上の近日点距離を持つ彗星は 3 彗星であり、最大値は 3.3 倍である。逆に、太陽半径より小さな近日点距離を持つ彗星も 4 彗星あり、これらは太陽と衝突する軌道を持つことになる。

Fig. 2 は軌道傾斜角iの分布である。143 ～ 144° 付近に集中している。しかし、130° 以下の彗星もある。

3）の線形関係については、Fig.3 に示すように、相関係数 r=0.9751 とかなり強い相関がある。

Fig.1 Histgram of Perihelion Distnce

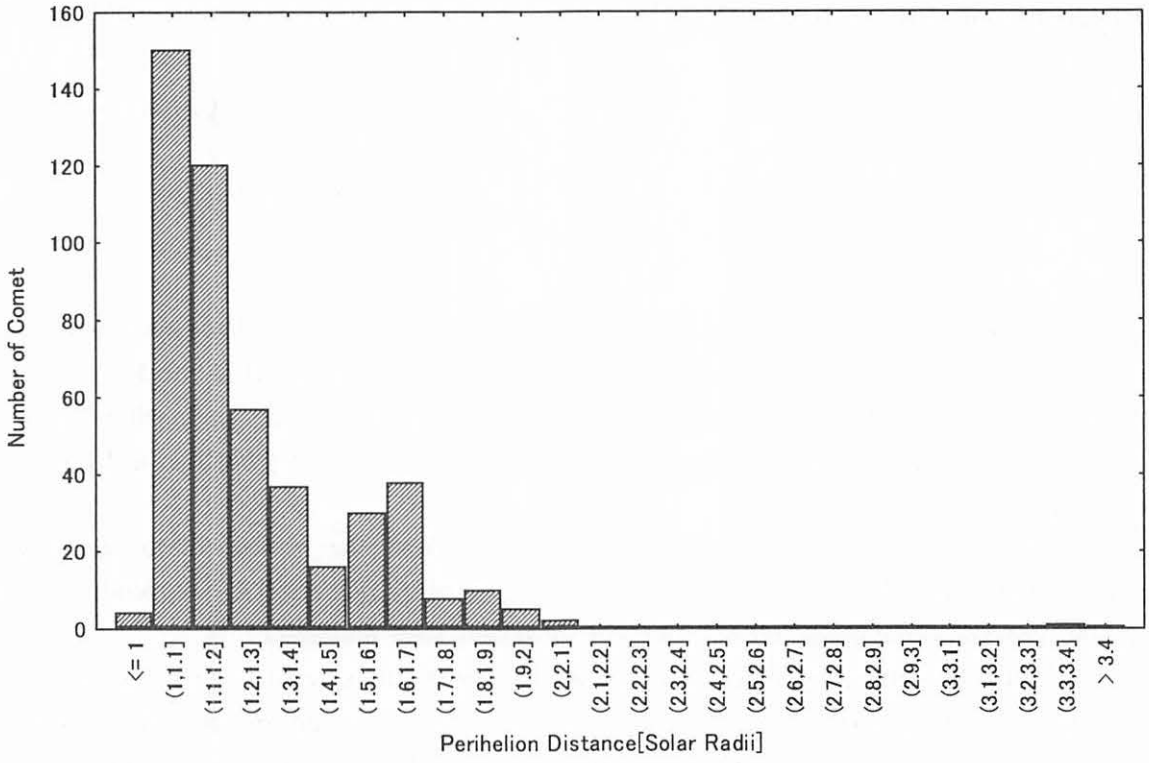

Fig.2 Histgram of Orbital Inclination

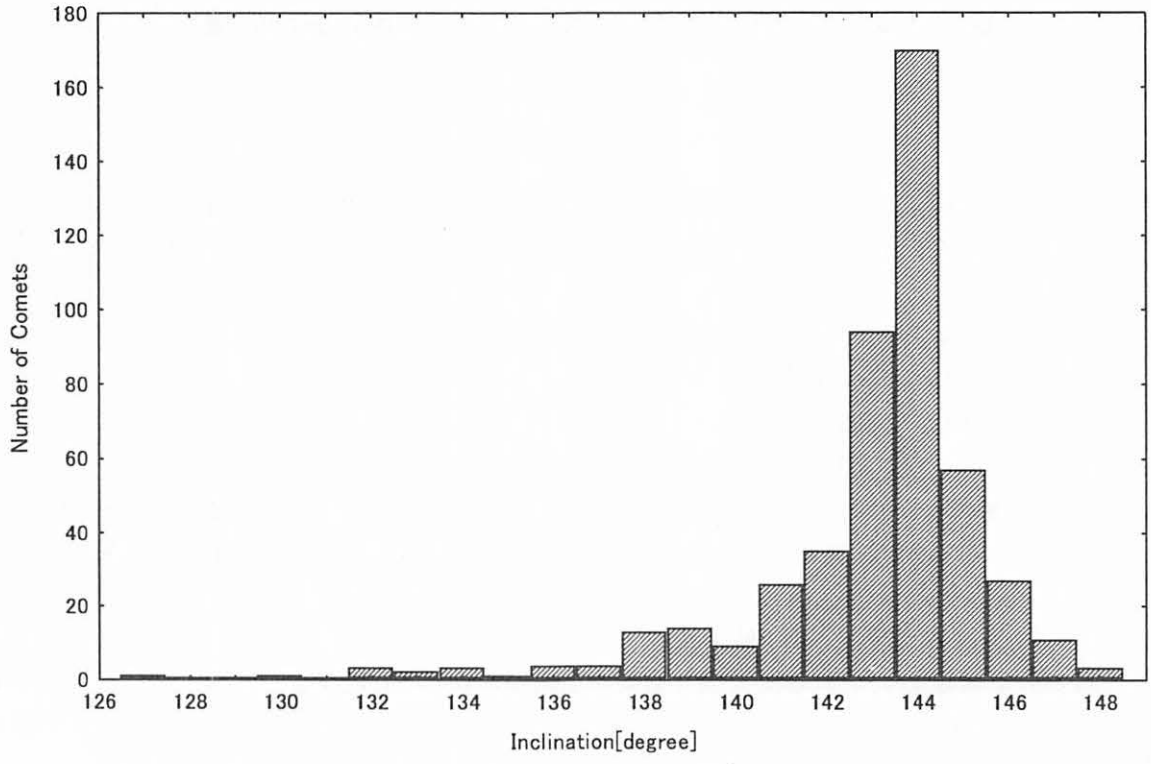

回帰直線は$\Omega = 91.167+1.149\ \omega$となる。ただし、$\omega < 45°$ではこの関係からはずれる彗星も存在している。

これらの特徴と、近日点の座標を使用すれば、Kreutz群の判定に使用できるだろう。

Kreutz群に属する彗星は、C/1970K1までは地上から観測された彗星だけであった。1970年以降のKreutz群の彗星は、すべて太陽観測用の探査機に搭載されたコロナグラフのCCDによる画像から発見されている。特に、1996年以降SOHOによって多くの彗星が発見されている。これらの彗星はすべて近日点通過前に発見されているものの、近日点を無事に通過した彗星は皆無である。

このKreutz群が、C/1882R1やC/1965S1が分裂したこともあり、母彗星からの分裂を繰り返すことで形成されたことは疑いようがない。このため、Kreutz群はさらにサブグループに分類できることが指摘されている。Marsden(1989)は、Subgroup IとSubgroup IIに分け、C/1970K1をSubgroup II aと分類した。

SOHOによって発見されたKreutz群の彗星も含めると、Marsdenの分類によるサブグループはどうなるのか、という点について、これまでSOHOの彗星が43彗星の場合(1998)、191彗星の場合(2000)で、サブグループを調査してきた。しかし、彗星の軌道要素が改良されたことや、その分布が拡大することもあり、これらの結果は同じような結果にはならなかった。SOHOによる彗星の発見は続いており、新しいSOHOの彗星も含めてサブグループをもう一度考えてみたい。

2. サンプル数

地上から観測されたKreutz群の彗星をTable 1の8彗星とした。Kreutz群の可能性がある彗星はこれら以外にもあるが、本稿では割愛した。

1979～1989年にかけて、人工衛星のSOLWINDとSMMに搭載されたコロナグラフの画像から、1等級から－4等級の彗星がそれぞれ6彗星と10彗星の合計16彗星を発見した。これらと比較すると、Biesecker et al.(2001)の光度観測の結果では、SOHOで発見されている彗星の多くは5～7等級で、微光なものが多い(。これは、SOLWINDやSMMに搭載されたCCDに比べて感度が向上したことや、C2 、C3と呼ばれる視野が異なる2つのコロナグラフを搭載していることもある。さらに、SOHOの画像がインターネット上で公開されており、多くのアマチュアがこの画像から彗星を探索できるからである。

2003年2月末現在、SOHOによって発見され、その軌道要素が公表されたKreutz群の彗星は454彗星である(ただし、研究会以降、4月末までに新たに10彗星の軌道要素がMPECで公表されている)。

したがって、Kreuz群の彗星数を本稿では合計478彗星とする。

3. 軌道要素の類似性と解析方法

近日点通過時刻を除く軌道要素の類似性を考えるために、Jöpek(1993)の式を使用することにした。この式は、流星の軌道を求めた際に、母彗星の軌道との類似性を調査して、関連性を確認するための式である。Southwarth & Hawkinsが考案した式と、Drummondの式を検討してJöpekが再構成した式である。もし、Dの値が0なら同一の軌道になる。

彗星Aと彗星Bの軌道の類似性Dの値を軌道要素で表すと次式のようになる。

Fig. 3 Correlation between Argument of Perihelion and Longitude of Ascending Node

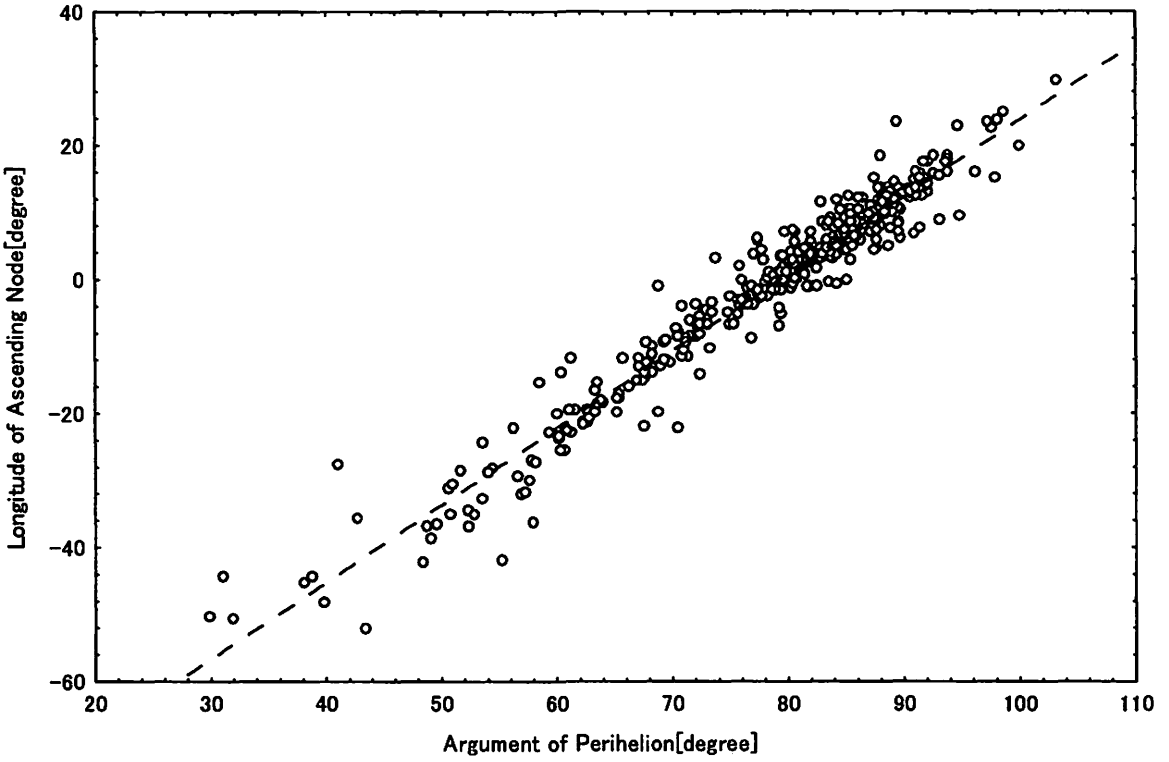

Table 1 Orbital Elements of Kreutz Sungrazers Observed from the Ground (J2000.0)

Comet	q [AU]	e	ω [degree]	Ω [degree]	i [degree]	L [degree]	B [degree]	Marsden's Subgroup
C/1843D1	0.0055	0.9999	82.64	3.53	144.35	282.56	35.31	I
C/1880C1	0.0055	1.0	86.25	7.78	144.67	282.37	35.25	I
C/1887B1	0.0048	1.0	83.51	4.59	144.38	282.55	35.35	I
C/1963R1	0.0051	0.9999	86.16	7.94	144.58	282.65	35.33	I
C/1882R1	0.0078	0.9999	69.59	347.66	142.01	282.94	35.23	II
C/1945X1	0.0075	1.0	72.06	351.20	141.87	283.57	35.97	II
C/1965S1	0.0078	0.9999	69.05	346.99	141.86	282.95	35.22	II
C/1970K1	0.0089	1.0	61.29	337.01	139.07	282.95	35.07	IIa

$$D^2 = (e_B - e_A)^2 + \left(\frac{q_B - q_A}{q_B + q_A}\right)^2 + \left(2\sin\frac{I_{BA}}{2}\right)^2 + \left(\frac{e_B + e_A}{2}\right)^2 \left(2\sin\frac{\Pi_{BA}}{2}\right)^2$$

$$\left(2\sin\frac{I_{BA}}{2}\right)^2 = \left(2\sin\frac{i_B - i_A}{2}\right)^2 + (\sin i_B \sin i_A)\left(2\sin\frac{\Omega_B - \Omega_A}{2}\right)^2$$

$$\Pi_{BA} = (\omega_B - \omega_A) + 2\arcsin\left(\cos\frac{i_B + i_A}{2}\sin\frac{\Omega_B - \Omega_A}{2}\sec\frac{I_{BA}}{2}\right)$$

サブグループを探るために、群平均法を使った階層的クラスター分析を行った。群平均法では D^2 を用いて計算するため、Jöpek による軌道の類似性 D^2 を 478 彗星の全組み合わせで求め、類似行列を作成した。

階層的クラスター分析では、まず 478 彗星を 478 のサブグループと考える。そして、D^2 の小さなペアほど、軌道が互いに類似していることから、これらは同じサブグループに属するものとして融合する。この融合されたサブグループと他のサブグループとの D^2 の値を再計算する必要がある。この計算に幾つかの方法があり、サブグループ間の値をメンバー数を考慮した平均を使って計算する群平均法を今回は用いた。

なお、今回のサンプル数になると、パソコン用の統計用ソフトでは計算ができなくなったため、今回は自作のプログラムを使用した。

5. 結果

群平均法による階層的クラスター分析の結果をデンドログラム(Fig.3)で示す。この図から、サブグループの関係がわかることになる。

階層的クラスター分析では、最終的にいくつのクラスターに分類するかということは不明であるが、今回は Marsden の Subgroup Ⅰ、Ⅱとの対応も考慮して、サブグループ①と②が融合する前の状態で6つのサブグループとした。

Table 2 にサブグループのメンバーを、そしてサブグループごとの軌道要素の平均値を Table 3 に示す。

このうち、①、②のサブグループは、以前から指摘されていたサブグループで、Marsden の Subgroup ⅠとⅡに対応する。特に、サブグループ①の彗星は②の彗星と比べて約3倍の数になっており、Fig. 5 に見られるように、明確な集団を形成している。このサブグループ①が母彗星の主核と考えればよいだろう。サブグループ②の彗星では分布が拡がっており、小さな集団が偏在しており、Marsden が Subgroup Ⅱ a とした C/1970K1 はサブグループ②の中に含まれている(なお、研究会以降に軌道要素が公表された 10 彗星を加えても、サブグループの数は変化せず、サブグループ①に 6 彗星、サブグループ②に 4 彗星が加わる)。

③と④のサブグループに含まれるのは1彗星のみである。特に、③の C/1984O1 は最後に融合が起こる。この彗星の近日点距離が最大になっているためであろう。Marsden(1989)の文献では、この彗星の軌道要素が不確実と述べている。また、④の C/1997M5 の軌道要素では、軌道傾斜角が 127° と最小の値になっており、近日点の方向も他の彗星とは異なっている。このため、これらをサブグループとするには無理がある。むしろ、軌道要素に問題があると考えるべきだろう。

Tavle 2 Members of Subgroups

Subgroup	Comet										
①	1843D1	1880C1	1887B1	1963R1	1981V1	1987T2	1987U4	1988M1	1988Q1	1988T1	1988U1
	1988W1	1989L1	1989N3	1989S1	1996A2	1996B4	1996B5	1996E2	1996F2	1996H1	1996L1
	1996M1	1996M2	1996Q2	1996Q3	1996R4	1996V1	1996X1	1996X2	1996Y1	1996Y2	1997G3
	1997G4	1997G5	1997G6	1997J4	1997K1	1997K4	1997K6	1997L4	1997N3	1997P1	1997Q2
	1997R2	1997R3	1997S3	1997T2	1997T4	1997T5	1997T6	1997T7	1997T8	1997U2	1997U3
	1997U4	1997U5	1997U6	1997U7	1997V2	1997V4	1997V6	1997W1	1997W2	1997W3	1997X1
	1997X3	1997X4	1997Y1	1997Y2	1998A1	1998B2	1998E1	1998F2	1998G2	1998G5	1998G6
	1998G8	1998H2	1998H3	1998H4	1998H5	1998H6	1998J2	1998J3	1998J4	1998K7	1998K8
	1998K9	1998K10	1998K11	1998K12	1998K14	1998K16	1998K17	1998L2	1998L3	1998L4	1998L5
	1998L6	1998L9	1998M8	1998M10	1998U6	1998V1	1998V2	1998V3	1998V4	1998V7	1998W4
	1998W5	1998W6	1998X3	1998X4	1998X5	1998X7	1998X8	1998X9	1998X11	1998X12	1999C1
	1999E2	1999G2	1999G5	1999H2	1999H4	1999H5	1999H6	1999H8	1999J1	1999J7	1999J8
	1999J9	1999J10	1999J11	1999J12	1999J13	1999K1	1999K9	1999K10	1999K11	1999K14	1999K15
	1999K17	1999L1	1999M1	1999M2	1999N1	1999N3	1999O1	1999O3	1999P3	1999P4	1999Q1
	1999Q2	1999Q3	1999R3	1999R4	1999S1	1999S5	1999S6	1999S7	1999U6	1999U7	1999U8
	1999U9	1999V2	1999V3	1999V4	1999W1	1999W2	1999Y3	2000A2	2000B1	2000B5	2000B6
	2000B7	2000C6	2000D1	2000E1	2000F1	2000H2	2000H3	2000H4	2000H5	2000J3	2000J4
	2000J6	2000J7	2000K3	2000K4	2000K5	2000K6	2000K7	2000K8	2000L1	2000L2	2000L4
	2000M1	2000M2	2000M3	2000M6	2000M7	2000M8	2000M9	2000N1	2000N2	2000N3	2000P1
	2000P2	2000T1	2000T3	2000T4	2000T5	2000U1	2000U4	2000V1	2000V3	2000W2	2000W4
	2000W5	2000X1	2000X2	2000X3	2000X5	2000X8	2000Y8	2000Y9	2001A3	2001A4	2001C2
	2001C3	2001F2	2001G2	2001H3	2001H4	2001H6	2001H7	2001J2	2001J4	2001J5	2001K2
	2001K8	2001K9	2001K10	2001L1	2001L3	2001L4	2001L5	2001L7	2001L8	2001L9	2001L11
	2001M2	2001M3	2001M4	2001M5	2001M7	2001M8	2001M9	2001M11	2001O1	2001R2	2001R3
	2001R5	2001S2	2001T2	2001T6	2001T7	2001U1	2001U2	2001U3	2001U4	2001U5	2001U8
	2001U9	2001U10	2001V2	2001V3	2001V4	2001V5	2001W3	2001W4	2001X5	2001Y2	2001Y5
	2002C3	2002C4	2002D1	2002E1	2002E3	2002F2	2002F3	2002G2	2002G4	2002H3	2002H4
	2002H6	2002H7	2002J1	2002J2	2002J6	2002J7	2002K3	2002K5	2002K7	2002K8	2002K9
	2002K10	2002L1	2002L2	2002L3	2002L4	2002L6	2002L7	2002L8	2002M1	2002M5	2002M6
	2002M7	2002M8	2002N1	2002O1	2002O2	2002O3	2002P2	2002Q7	2002Q11	2002Q12	2002Q13
	2002R6	2002R7	2002S2	2002S3	2002S6	2002S8	2002S9	2002S10	2002T3	2002U1	2002U3
	2002U4	2002U5	2002U7	2002U8	2002U9	2002V3	2002X3	2002X4			
②	1882R1	1945X1	1965S1	1970K1	1979Q1	1981B1	1981O1	1983S2	1996B3	1996D1	1996O1
	1996O2	1996O3	1996O4	1996S3	1997B2	1997B3	1997H3	1997J3	1997K3	1997K5	1997K7
	1997L3	1997L5	1997M1	1997M3	1997M4	1997P3	1997Q1	1997R1	1997S1	1997S2	1997V3
	1997V5	1997X5	1997X6	1997Y3	1998F1	1998G4	1998G7	1998K13	1998K15	1998L1	1998L7
	1998L8	1998M7	1998M9	1998V6	1998V9	1998X6	1998X10	1999C2	1999G3	1999G4	1999H7
	1999H9	1999K13	1999L4	1999L5	1999L6	1999L7	1999L8	1999M4	1999O2	1999P2	1999P5
	1999U5	1999X2	2000D3	2000F2	2000G3	2000H6	2000H7	2000J5	2000L3	2000L5	2000M4
	2000M5	2000U2	2000U3	2000V2	2000W3	2000X6	2000X7	2001B3	2001C6	2001G3	2001H1
	2001H8	2001J3	2001K4	2001K6	2001K7	2001L2	2001L6	2001M6	2001R4	2001U7	2001V1
	2001X4	2001X6	2001X7	2001Y3	2001Y4	2002G5	2002H1	2002J3	2002J8	2002K6	2002L5
	2002M2	2002M3	2002M4	2002Q14							
③	1984O2										
④	1997M5										
⑤	1997U1	2000F3	2000T6	2000Y4	2001C4	2002H5					
⑥	1998V5	1999K12	2002L6	2002X4	2000Y5	2001H2	2001X9				

Fig. 4 Dendrogram

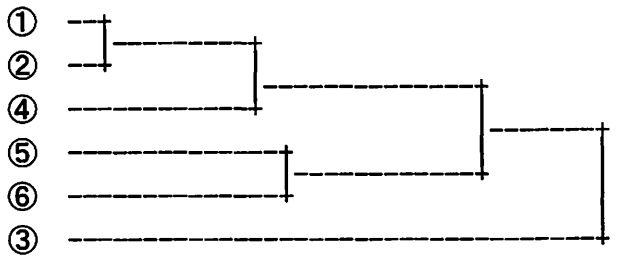

Table 3 Average Orbital Elements of Subgroups(J2000.0)

Subgroup	q [AU]	ω [degree]	Ω [degree]	i [degree]	L [degree]	B [degree]	Number of Comets
①	0.0055±0.000	84.28±5.48	5.67± 6.65	143.94±1.67	282.59±2.46	35.67±1.87	349
②	0.0071±0.001	67.98±9.84	346.77±12.32	142.99±3.48	283.75±3.55	33.22±3.28	114
③	0.0154	56.67	330.44	136.39	282.69	35.19	1
④	0.0059	71.88	351.32	127.42	289.62	49.01	1
⑤	0.0052±0.000	52.63±5.63	319.98± 7.22	135.46±3.81	276.90±5.46	33.71±3.71	6
⑥	0.0069±0.000	35.83±4.69	315.45± 7.81	143.33±2.01	285.30±6.15	20.34±1.91	7

Fig. 5 Plot of Argument of Perihelion against Perihelion Distance

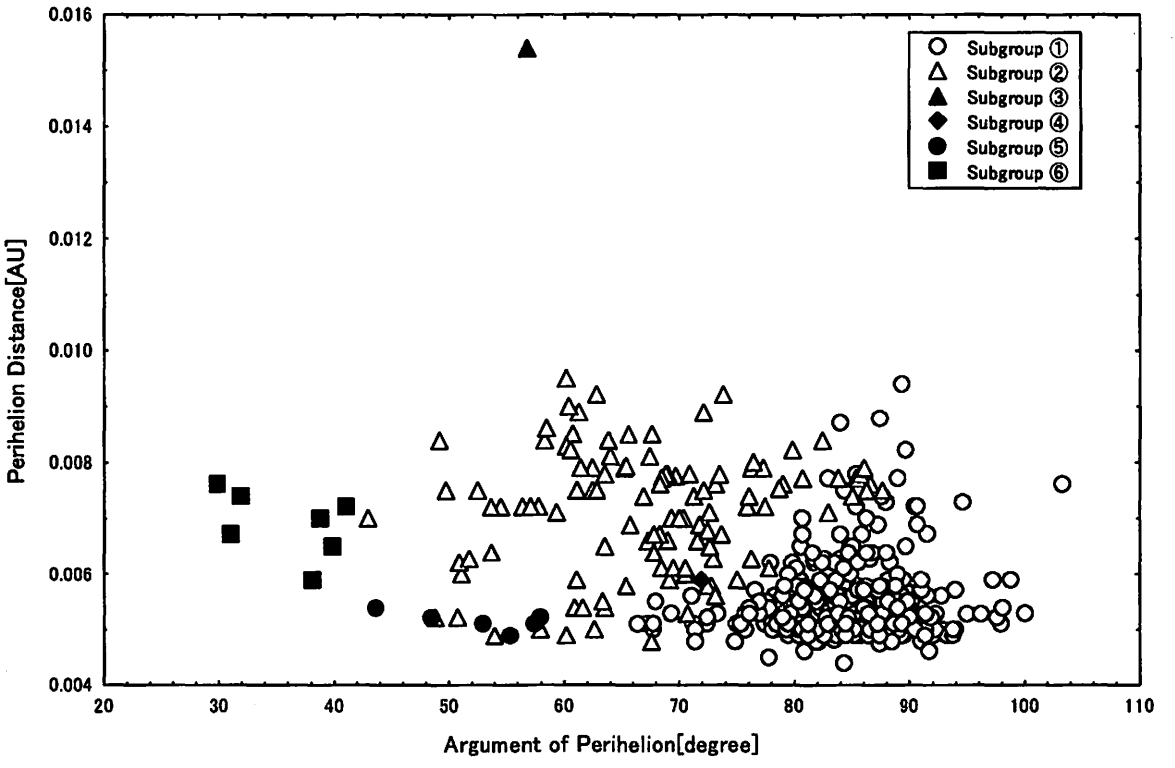

⑤と⑥のサブグループでは、それぞれ 6 彗星と 7 彗星が属している。これらの彗星は、一般に近日点引数が小さい値を持っている。特に、サブグループ⑥の彗星は⑤の彗星よりも小さくなり、Kreutz 群の特徴とした、近日点引数と昇交点黄経の線形関係からもややずれる傾向が見られる。サブグループ⑤の彗星は近日点距離がサブグループ①に近いものの、軌道傾斜角が小さくなっている。このような点からすると、これらの彗星の軌道が改良される可能性もある。しかし今後、同様の軌道を持つ彗星が新たに発見されるなら、新たなサブグループと考える必要があろう。

6. まとめ

Kreutz 群の 478 彗星に対して、Jöpek の軌道の類似度 D から類似行列を求め、群平均法を用いた階層的クラスター分析によって、サブグループを分類した。

サブグループ①、②は以前から指摘されていたサブグループⅠ、Ⅱに対応する。この他のサブグループは、軌道要素のいずれかに特異な値を持っていることから分類されたといえるだろう。サブグループ③、④は1彗星しかなく、軌道の精度に問題があり、これらはサブグループとは認めがたい。サブグループ⑤、⑥のメンバーは多くはないが、今後これらに属する彗星が増加するなら新たなサブグループとなるだろう。

SOHO による Kreutz 群の彗星は依然続いている。SOHO の活動が停止する前に、C/1965S1 のように、近日点を無事に通過するような彗星が出現することを期待したい。

参考文献

- B.G.Marsden(1967) *Astronomical Journal*, vol.72, pp.1170-1183.
- B.G.Marsden(1989) *Astronomical Journal*, vol.98, pp.2306-2321.
- 住谷秀夫(1998) 大阪音楽大学研究紀要第 37 号, pp.89-108.
- 住谷秀夫(2000) 大阪音楽大学研究紀要第 39 号, pp.25-44.
- D.A Biesecker et al.(2002) *Icarus*, vol.157, pp323-348.
- T.J.Jöpek(1993) *Icarus*, vol.106, pp.603-607.

カイパーベルト帯における共鳴構造
Resonance Structure in Kuiper Belt

中井宏、木下宙（国立天文台）
H. Nakai and H. Kinoshita
National Astronomical Observatory

Abstract

We investigate the resonance structure of the Edgeworth-Kuiper belt objects, which consist of 46 numbered and about 525 unnumbered asteroids discovered until now (January 6, 2003) and obtained the following results:

- All stable orbits with high eccentricity are trapped in the mean motion resonance (MMR) with Neptune.
- In the 1:2 MMR, the libration centers of the critical argument are $180° \pm \Delta\sigma$ and $\Delta\sigma$ depends on the eccentricity and inclination. On the other hand, the libration center of other MMR is 180° or 0°.
- In the Kozai resonance, the libration center of the argument of perihelion is 90° or 270° for the 2:3 MMR, for the 1:2 case, the libration center depends on the angular momentum and the libration center of critical argument.
- For some orbits that approach Uranus, the eccentricity and inclination are in opposite phases, and the period of the eccentricity change is equal to the half period of the argument of perihelion. When the asteroid approaches Uranus, the eccentricity becomes small and inclination becomes large, therefore, the asteroid passes through Uranus with a high velocity at a large inclination. The asteroids with such a feature avoid a close approach with Uranus, then the orbits become stable.

1 はじめに

エッジワース・カイパーベルト領域における小惑星の発見数は570個を超え、この領域にもメインベルトと同様な分布構造が明らかになってきた。多数のテスト天体の軌道進化から共鳴構造を明らかにする試みがDuncan *et al.*(1995),Fuse（1999）等により行われ、またIda *et al.*(2000), Chiang *et al.*(2002)等は海王星の移動から小惑星の分布を説明している。ここでは実際に観測された小惑星（2003年1月現在番号付き46個、番号なし約525個）の分布や軌道の特徴について検討し、軌道が安定になる機構について調べた。

2 数値積分

数値積分法として外挿法を用いた。摂動天体は木星、土星、天王星、海王星の4天体とし、小惑星の質量は0とした。摂動天体の初期値はDE405から求め、小惑星はMinor Planet Centerのdistant.arc(2003年1月6日）を用いた。積分期間は番号付き小惑星は1000万年、番号の付けられていない小惑星は500万年とした。

図1は数値積分で求めた小惑星の500万年間の平均の軌道長半径と離心率の分布である。積分期間中、軌道が大きく乱れた約70個の小惑星は取り除いている。大きな菱形は解析的手法で求めた海王星との平均運動共鳴の領域を示している。45AU付近には4:7(43.73AU)と8:15(45.78AU)共鳴だけを示しているがその間には5:9 (44.56AU), 6:11 (45.10AU), 7:13 (45.49AU)等の共鳴領域が重なっていて、それぞれ、5個、2個、4個の小惑星が海王星との平均運動共鳴の関係になっている。図中の点線は小惑星の近日点距離が天王星、海王星軌道と交差する離心率を示している。図中◇印は海王星と平均運動共鳴にあり、離心率(e)、軌道傾斜角(i)、近日点引数(ω)の周期が同期している（昇交点経度(Ω)の周期もこれらの周期に近い）もので、これらの小惑星の近日点は天王星と海王星の軌道の中間付近まで近ずく。＋印は平均運動共鳴にあり古在共鳴であるもの、○印は平均運動共鳴になるもの、□, △印はそれぞれν_{18}永年共鳴、ν_8永年共鳴になる小惑星を示している。また、*印は近日点の動きが遅く、古在共鳴かどうかが明確に判断出来ないものを表している。小黒□印は軌道は安定であるが臨界引数が秤動していない(海王星と平均運動共鳴にない）小惑星である。2:3、1:2平均運動共鳴で、近日点が海王星軌道と交差する離心率領域の小惑星の中には古在共鳴（＋印）になるものがある。しかし、4:7,2:5平均運動共鳴では軌道が交差する離心率より小さい離心率の領域で古在共鳴の小惑星が存在する。ν_{18}, ν_8永年共鳴の周期は非常に永いので、500万年の積分期間ではν_{18}, ν_8永年共鳴かどうかを明確に決定できていない可能性がある。

海王星軌道に接近する可能性のあるもので安定な軌道はすべて海王星と平均運動共鳴の関係になっている。特に、2:3平均運動共鳴領域には小惑星が集中し、$\tilde{\varpi} \simeq 0(e, i, \omega$が同期している）の小惑星や古在共鳴の小惑星が数多く存在する。このような集中はメインベルトにおける木星との3:2平均運動共鳴（ヒルダ群）領域の小惑星の集中と類似している。

3-1 平均運動共鳴

海王星との主な平均運動共鳴の内で、3:4,2:3,1:2,2:5の各平均運動共鳴領域での臨界引数(σ)と軌道長半径(a)の関係をそれぞれ図2,3,4,5に示す。解析的手法で求めた摂動関数の等ポテンシャル曲線は吉川（1990）がメインベルトにおける平均運動共鳴の解明に用いた方法で求めている。ここでは摂動天体として海王星だけを考慮している。図中の点は数値積分で求めた実際の小惑星1995DA2(3:4共鳴)、Pluto(2:3共鳴)、1996TR66(1:2共鳴)、1999DE9(2:5共鳴)の臨界引数と軌道長半径の関係で、短周期成分は平均操作で取り除いている。

臨界引数が秤動するための軌道長半径の変動幅は2:3平均運動共鳴の場合、図3-a,b,c,dに示すように、離心率(e)が0.1のとき、$39.1 < a < 39.7$、小惑星の近日点が海王星軌道と交差する離心率($\simeq 0.24$)に近いeが0.25のとき、$38.6 < a < 40.2$と大きくなる。それ以上に離心率が大きくなり、eが0.4となると$39.0 < a < 39.8$となりaの変動幅は小さくなる。同様に、他の共鳴においても図2,4,5に示すように、離心率の増加につれて、臨界引数が秤動するための軌道長半径の振幅Δaは増加し、小惑星の軌道が海王星の軌道と交差する離心率付近で、Δaは最大になる。それより大きな離心率ではΔaは小さくなる。

臨界引数の秤動中心は3:4(図2),2:3(図3),2:5平均運動共鳴(図5)の場合、離心率が小さいときは180°、離心率が非常に大きくなると0°へと変化する。これに対して、1:2平均運動共鳴(図4)では$e = 0.1$のとき180°(図4-a)であるが、$e = 0.25$になると秤動中心は二つに分かれ約70°と290°となる(図4-b)。180°からのずれ$\Delta\sigma$は図4-b,c,dに示すように、離心率により変化する。また、この$\Delta\sigma$は軌道傾斜角によっても変化する。このように臨界引数の秤動中心が$180° - \Delta\sigma, 180° + \Delta\sigma$に分離するため1:2平均運動共鳴では系の状況により臨界引数は$180° - \Delta\sigma$、180°、$180° + \Delta\sigma$の回りを秤動する場合がある。1:2平均運動共鳴における臨界引数の秤動中心が変化する例として小惑星2001UP18の500万年間の軌道要素を図6-a,b,c,dに示す。図6-eは数値積分で求めた$a : \sigma$の関係を解析的手法で求めた等ポテンシャル曲線上に重ねて図示したものである。図6-a,d,eの軌道長半径と臨界引数の値は平均操作により短周期成分を消去している。この例では、臨界引数は110°、180°、250°の回りを秤動している。

このように、1:2平均運動共鳴では臨界引数の秤動中心が分離する。このことは他の共鳴と大きく異なる点である。

3-2 古在共鳴

図7は2:3平均運動共鳴領域で、$\Theta(= \sqrt{1 - e^2}\cos i)$を変化させたときの解析的手法で求めた近日点引数($\omega$)と離心率($e$)の関係を示している。図は臨界引数($\sigma$)が180°の回りを秤動すると仮定して描いている。図7-a,b,cに示すようにΘが小さくなると、90°(270°)の回りの近日点引数が秤動するための離心率の変動が$0.18 < e < 0.30$(図7-a), $0.15 < e < 0.33$(図7-b), $0.13 < e < 0.37$(図7-c)と変化する。このように、Θを変化させながら離心率の変動幅をまとめたものが古在共鳴の領域(図7-d)となる。図7-bには、Plutoの数値積分の結果を点で重ねて描いている。

図8は1:2平均運動共鳴領域で、Θを変化させたときのωとeの関係である。臨界引数の秤動中心は図4-cから約290°であるので、図8-a,b,c,dは全て臨界引数の秤動中心を290°と仮定して描いている。Θが0.935と大きい場合は、ωの秤動中心は明確に現れない(図8-a)。しかし、図8-b,cに示すように、Θが0.896, 0.814と小さくなってくると、ωの秤動中心は$e \simeq 0.4, \omega \simeq 144°(324°)$に現れてくる。図8-dは臨界引数の秤動中心を290°と仮定したときの、近日点引数が144°(324°)の回りを秤動するときの古在共鳴領域である。図8-bに実際の小惑星1996TR66の数値積分から求めたω:のeの関係を描いている。数値積分と解析的手法による結果は良く一致している。

近日点引数の秤動中心はΘやσの秤動中心の値に依存する。このため、1:2平均運動共鳴では、古在共鳴における近日点引数の秤動中心は90°(270°)と異なる値となる。このことは2:3平均運動共鳴と大きく異なる点である。

3-3 天王星軌道に接近する小惑星の軌道

図1の◇印で示した小惑星は近日点距離が海王星軌道の内側で、天王星に接近する可能性のある小惑星の一群である。例として、図9に小惑星2002GM32(2:3平均運動共鳴)の軌道要素を示している。これらの軌道の特徴は離心率(e)と軌道傾斜角(i)が逆位相で

その2倍の周期が近日点引数 (ω) の周期に一致している (図 9-b,c,d,h,i)。また、昇交点経度 (Ω) の周期は近日点引数 (ω) の周期に近い (図 9-j)。これらの小惑星が天王星の軌道面に接近したとき、近日点引数は 0° となり (図 9-h,i)、このとき離心率は最小 ($e = 0.34$) になり、軌道傾斜角は最大 ($i = 29.5°$) になる。このため天王星の軌道面近くでは、小惑星は最大の近日点距離 ($26.1AU$) になるため、天王星軌道から出来るだけ離れたところを最大の軌道傾斜角 (29.5°) で横切ることになる。天王星から離れた軌道は海王星に接近する軌道であるが、平均運動共鳴により海王星との接近を回避している。これらは軌道の安定化機能として働いている。

このような軌道の分布を調べるために、初期値として a=39.45AU (2:3 平均運動共鳴)、$\omega = 90°$、$\Omega = 270°$、$\sigma = 180°$ とし、e を $0 \sim 0.6, i$ を $0 \sim 60°$ まで変化させたテスト天体について、数値積分を行い、古在共鳴と上で述べた安定化機構 ($\dot{\varpi} \simeq 0$) の働く初期値の領域を求めた。その結果が図 10 である。積分期間は 500 万年である。+印は平均運動共鳴であり古在共鳴になる領域、◇ 印は平均運動共鳴であり $\dot{\varpi} \simeq 0$ になる領域、· は平均運動共鳴領域、黒 □ 印は臨界引数が秤動しない (2:3 平均運動共鳴にない) 領域、× 印は軌道長半径の変動幅が ± 2AU を超えた領域を表している。実線は図 7-d と同じ図で、解析的手法で求めた古在共鳴の領域である。近日点引数の動きは離心率が大きくなれば, 順行で周期が短くなる。一方、昇交点経度の動きは逆行で殆ど一定の周期であるために、$\dot{\varpi} \simeq 0$ となるのは、古在共鳴になる離心率より少し大きな離心率の領域となる。この領域が上で述べた安定化機構の領域である。数値積分の結果と解析的手法との結果は良く一致している。

4 まとめ

小惑星は様々な機構によって惑星との大接近を回避している。従来から知られていた平均運動共鳴、古在共鳴とは別に、天王星の影響を小さくする機構や、1:2 共鳴における秤動中心が他の共鳴とは異なる例が見つかった。今回明らかになった事を以下に示す。

- 現在までに発見されたエッジワース・カイパーベルト小惑星の中で、離心率が大きくて軌道が安定なものは全て海王星と平均運動共鳴の関係になっている。

- 臨界引数の秤動中心は 1:2 平均運動共鳴以外は 180° か 0° であるが、1:2 平均運動共鳴では $180° \pm \Delta\sigma$ となり、$\Delta\sigma$ は離心率、軌道傾斜角の値に依存する。

- 平均運動共鳴と古在共鳴が同時に生ずる場合、近日点引数の秤動中心は $\Theta(= \sqrt{1-e^2}\cos i)$ や臨界引数の秤動中心の値に依存する。このため、1:2 平均運動共鳴時の古在共鳴の近日点引数の秤動中心は 90°(270°) と異なった値になる。

- 天王星に接近し、安定な軌道は離心率 (e) と軌道傾斜角 (i) が逆位相で、それらの 2 倍の周期が近日点引数 (ω) の周期に一致する。これにより、小惑星が天王星の軌道面に接近した場合、出来るだけ大きな近日点距離のところを、最大の軌道傾斜角で横切ることになり、天王星の影響を小さくしている。これも軌道安定化機構となっている。

5 終わりに

小惑星の軌道は惑星に接近しない様々な機構が働いていて、軌道を安定に保っている。小惑星の分布構造を明らかにするだけでなく、今までに知られていなかった安定化機構を調べるためにも、エッジワース・カイパーベルト小惑星の発見数の増加とともに、高精度の軌道要素の決定が重要である。

6 参考文献

Chiang,E.I.,& Jordan,A.B. : 2002, On the Plutinos and Twotinos of the Kuiper Belt, *AJ*,**124**,3430.

Duncan,M.J.,Levison,H.F.,& Budd,S.M. :1995,The Dynamical Structure of the Kuiper Belt,*AJ*,**110**,3073.

Fuse, T. : 1999, Dynamical Structure of Edgeworth-Kuiper Belt Objects in/around Mean Motion Resonances with Neptune, thesis for a doctorate at the Graduate University for Advanced Studies.

Ida, S.,Bryden,G.,Lin,D.N.C.,& Tanaka, H. : 2000,Orbital Migration of Neptune and Orbital Distribution of Trans-Neptunian Objects,*ApJ*,**534**,428.

MPC :2003,Distant minor planets(Centaurs and transneptunians).

Standish,E.M. : 1998, JPL Planetary and Lunar Ephemerides,DE405/LE405, JPL Interoffice Memorandum,IOM 312.F-98-048.

Yoshikawa, M. : 1990, Motions of Asteroids at the Kirkwood Gaps
I. On the 3:1 Resonance with Jupiter, *Icarus*, **87**, pp.78-102.

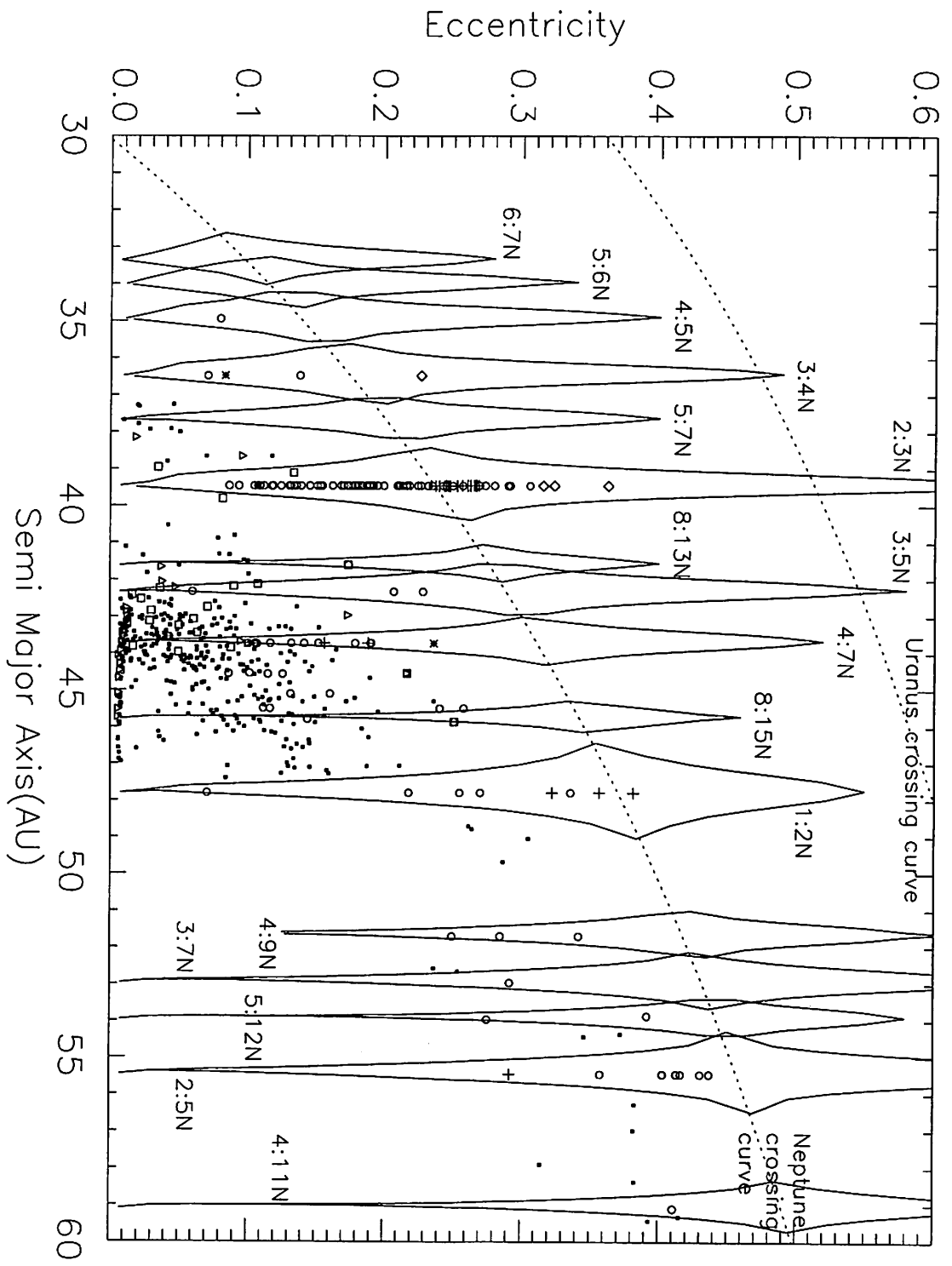

Figure 1. The regions of mean motion resonance(MMR) with Neptune.
The diamond-like curves are borders of MMR with Neptune. The dot curves show the Neptune-crossing curve and Uranus-crossing curve. The symbol of $\diamond$ means the changes of e,i,and ω of the asteroid are synchronized. The symbols of +, and $\bigcirc$ denote Kozai resonance, and mean motion resonance respectively. The symbols of $\square$, and $\triangle$ denoteν_{18} secular resonance,and ν_8 secular resonance respectively. The small black square indicates that an asteroid is not in MMR with Neptune.

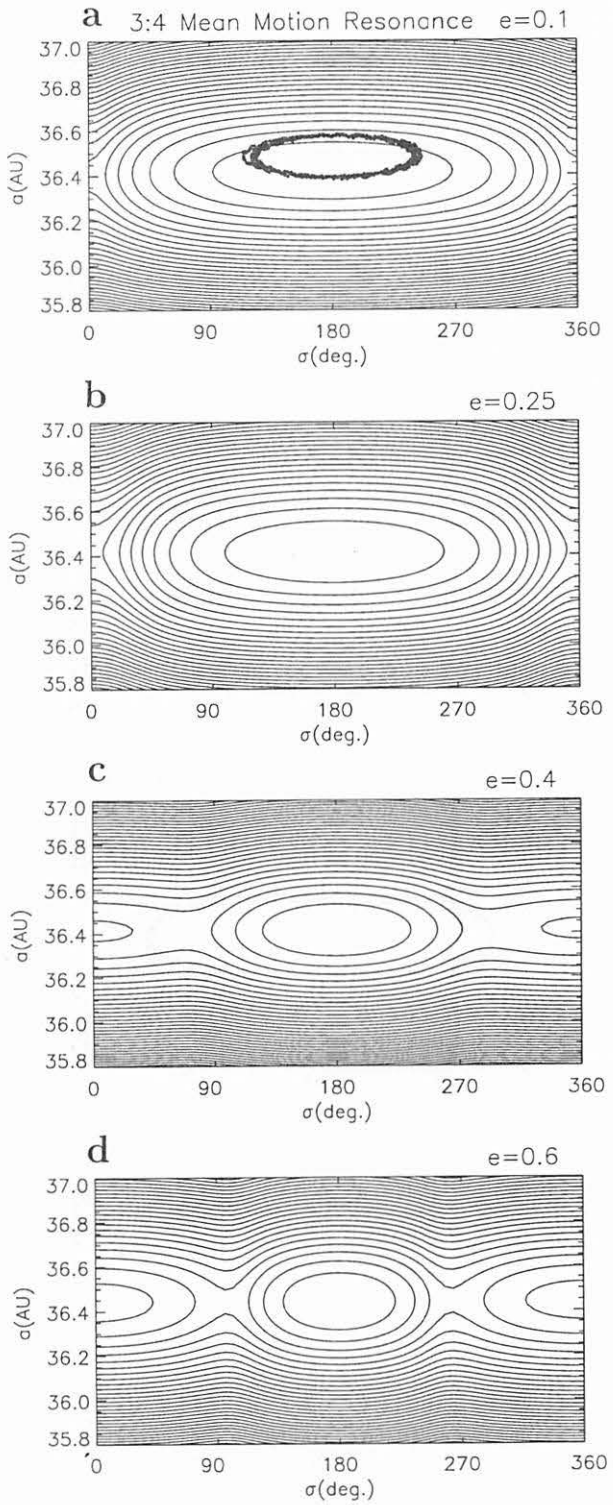

Figure 2. The equi-potential curves of 3:4 MMR. The variations of a and σ are obtained by the semianalytical method(Yoshikawa). Four panels are for four values of e. The dots in Fig. 2-a show the solution by numerical integration for 1995DA2.

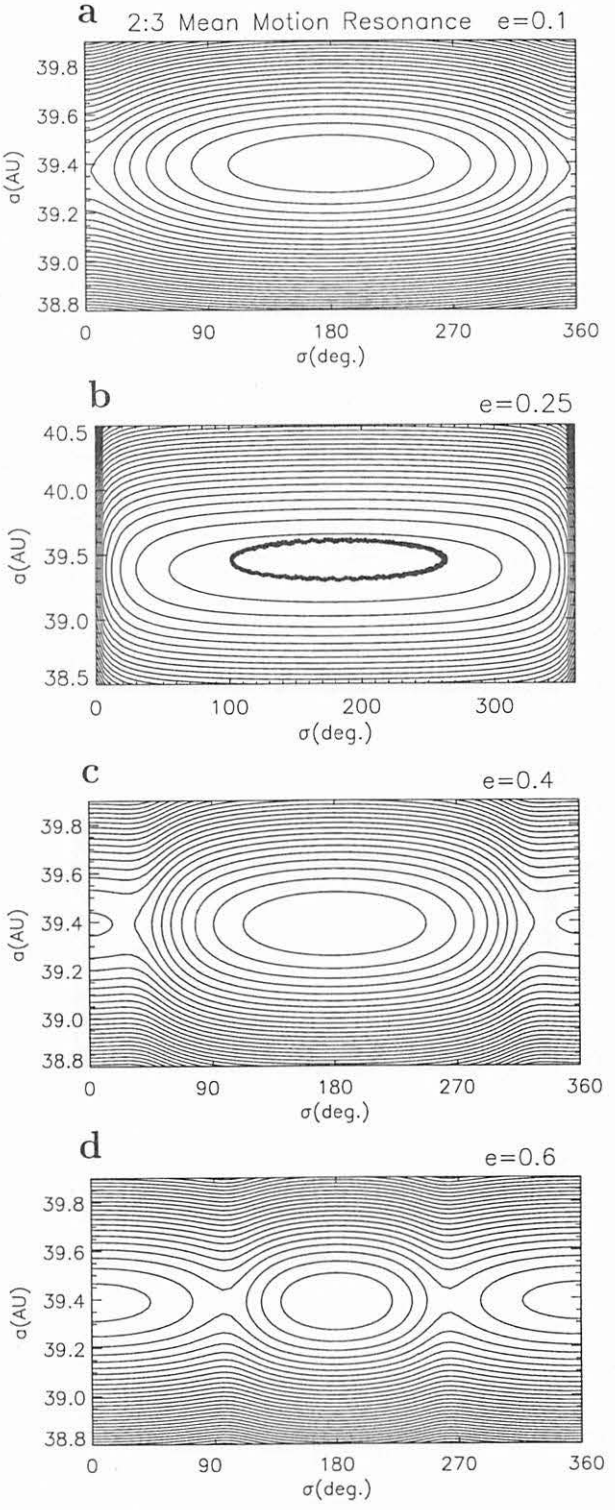

Figure 3. The equi-potential curves of 2:3 MMR. The dots in Fig. 3-b show the solution by numerical integration for Pluto. See the legend of Fig. 2.

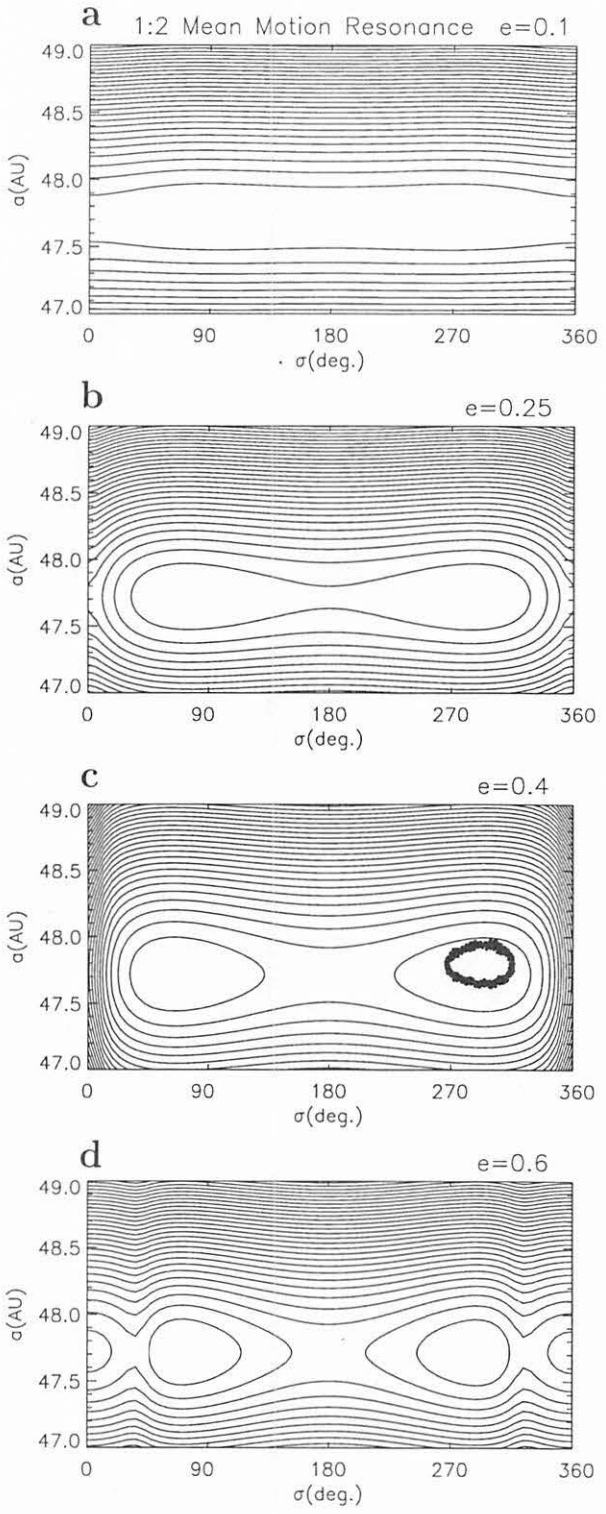

Figure 4. The equi-potential curves of 1:2 MMR. The dots in Fig. 4-c show the solution by numerical integration for 1996TR66. See the legend of Fig. 2.

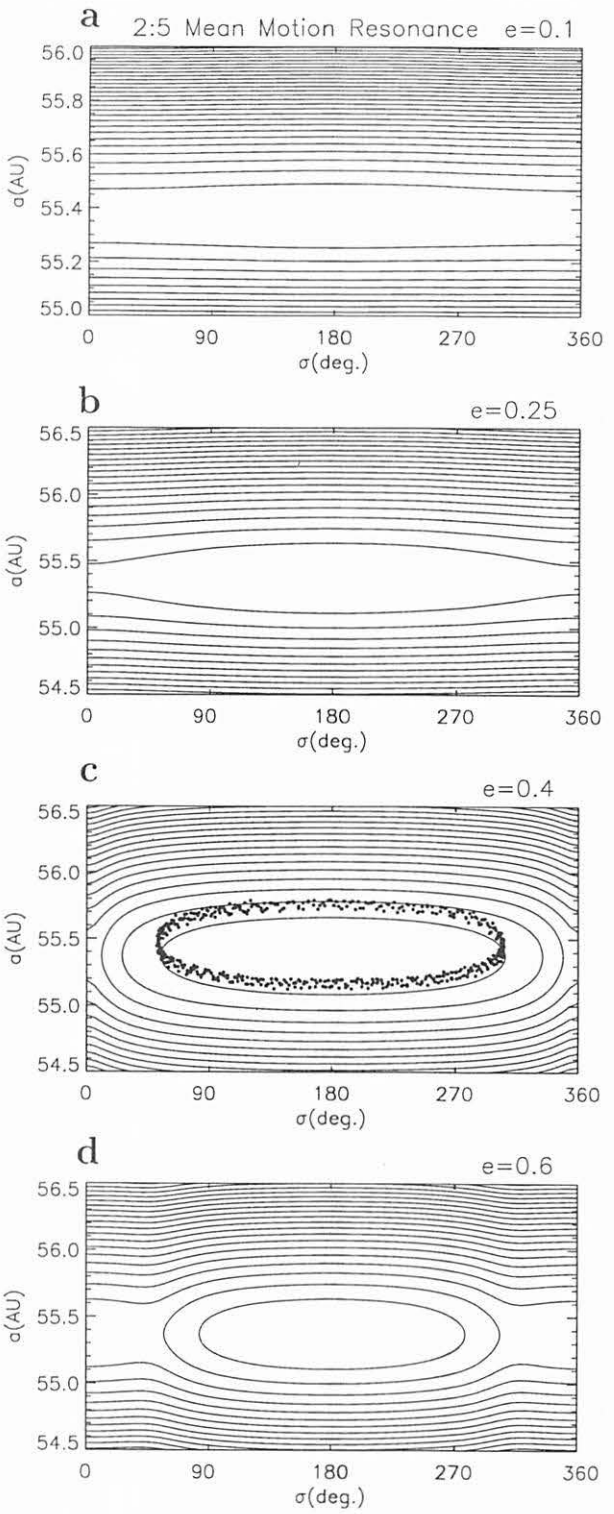

Figure 5. The equi-potential curves of 2:5 MMR. The dots in Fig. 5-c show the solution by numerical integration for 1999DE9. See the legend of Fig. 2.

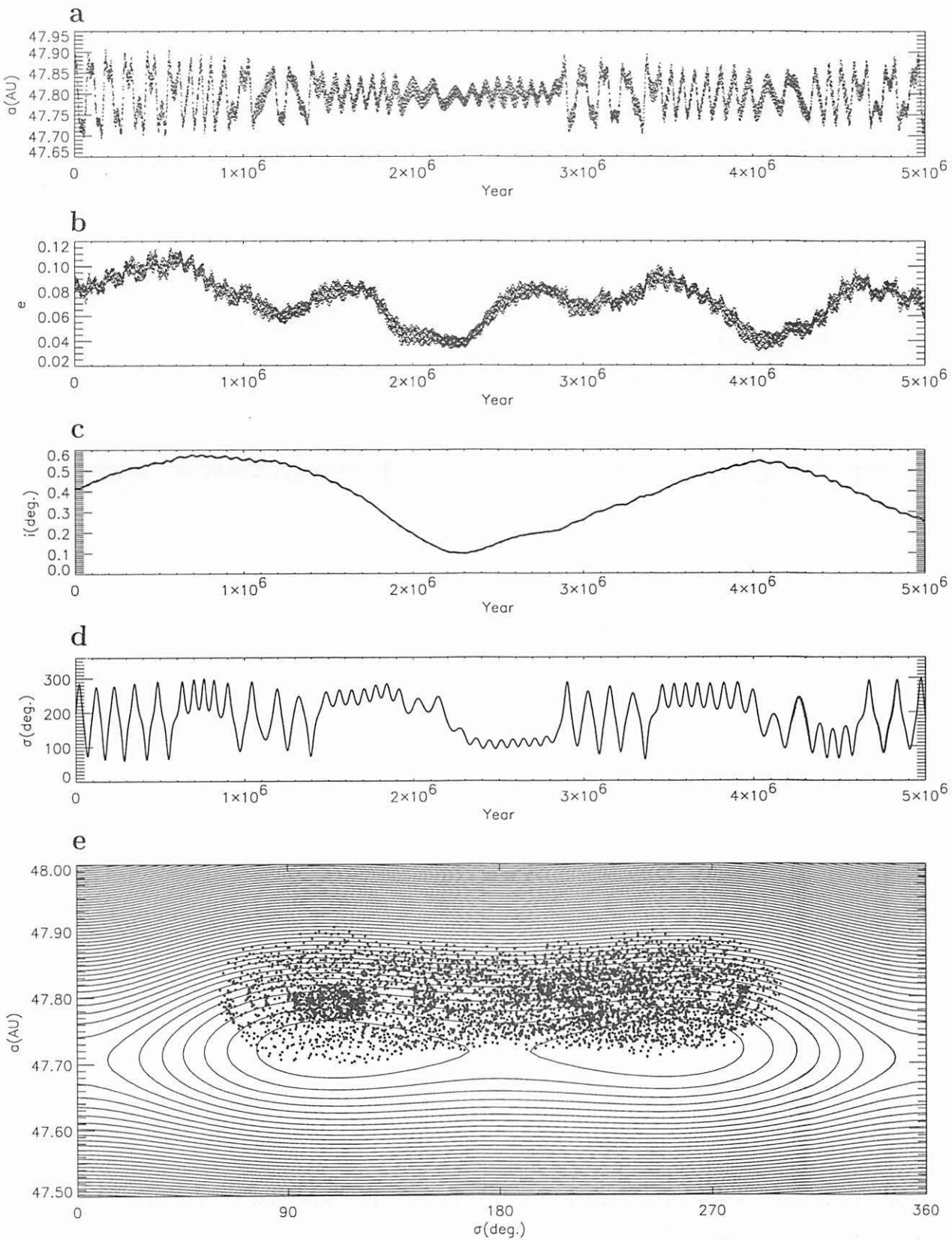

Figure 6. The orbital evolution of 2001UP18 in the 1:2 MMR and the equi-potential curve. The libration center of critical argument changes around $110°, 180°$ or $250°$ one after another. The dots in Fig. 6-e show the solution by numerical integration.

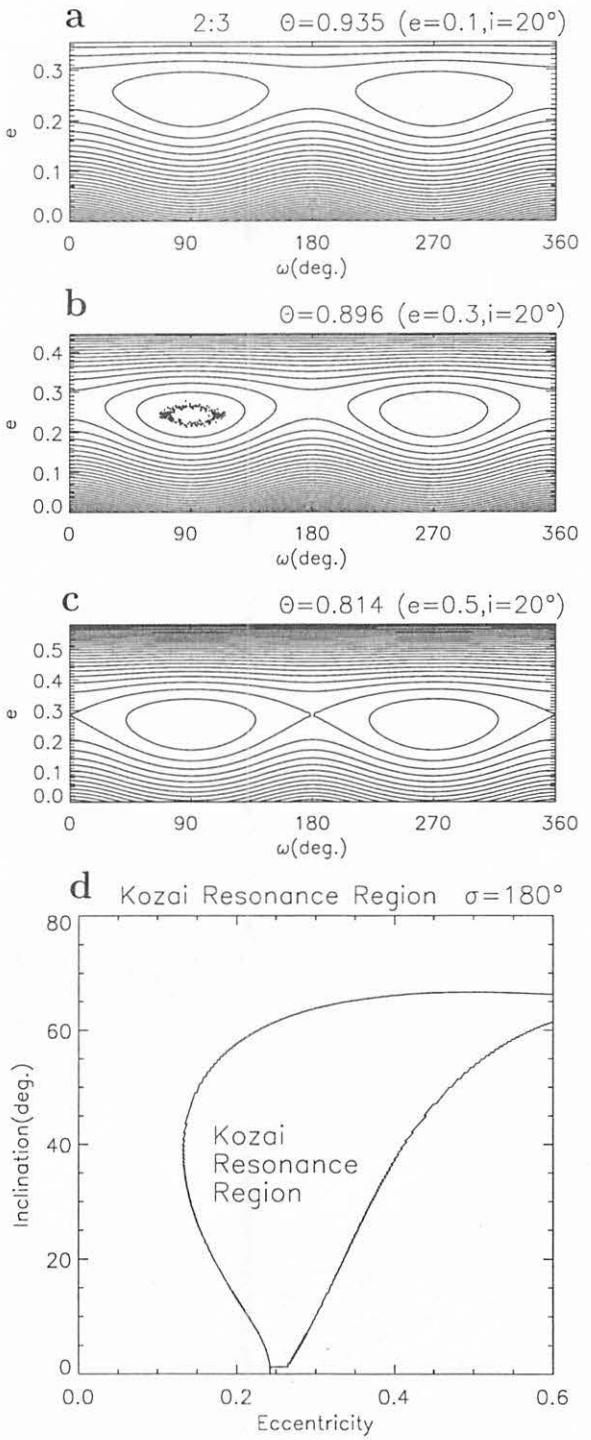

Figure 7. The equi-potential curves and Kozai resonance region for the 2:3MMR. The variations of e and ω are obtained by a semianalytical method. The first three panels(a,b,c) show for three values of $\Theta(=\sqrt{1-e^2}\cos i)$. It is assumed that σ librates around 180°. The dots in Fig. 7-b show the solution by numerical integration for Pluto.

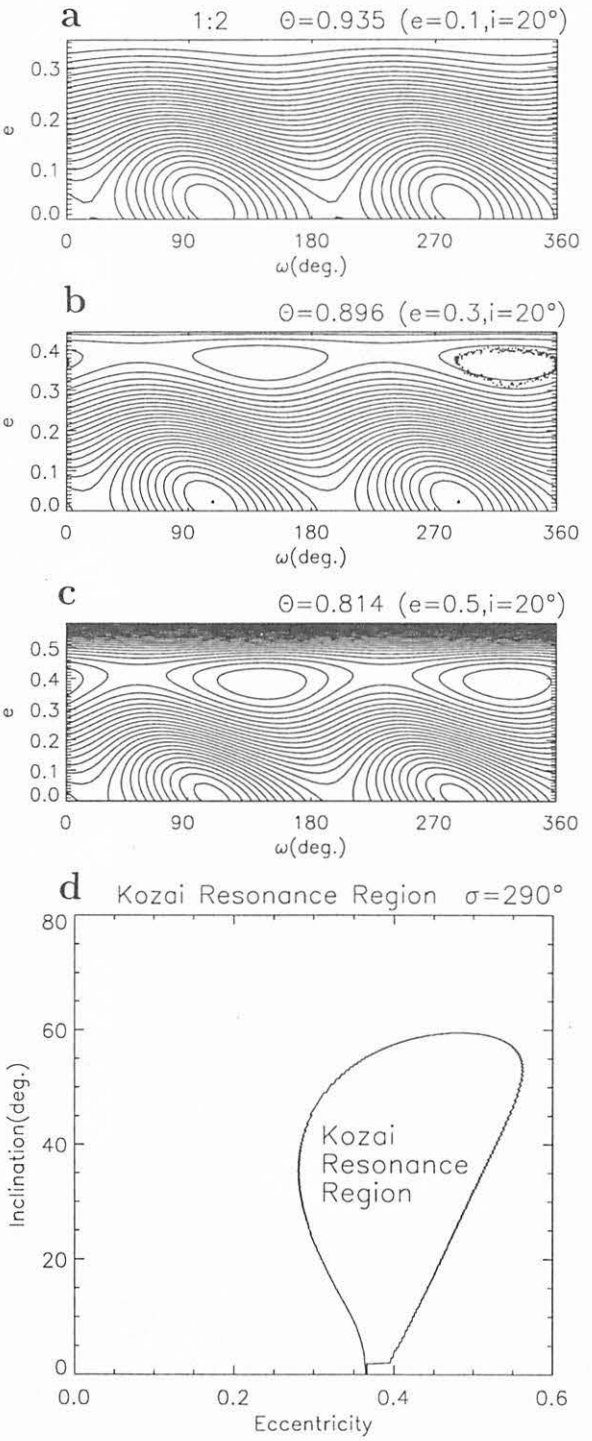

Figure 8. The equi-potential curves and Kozai resonance region for the 1:2MMR. It is assumed that σ librates around 290°. The dots in Fig. 8-b show the solution by numerical integration for 1996TR66. See the legend of Fig. 7.

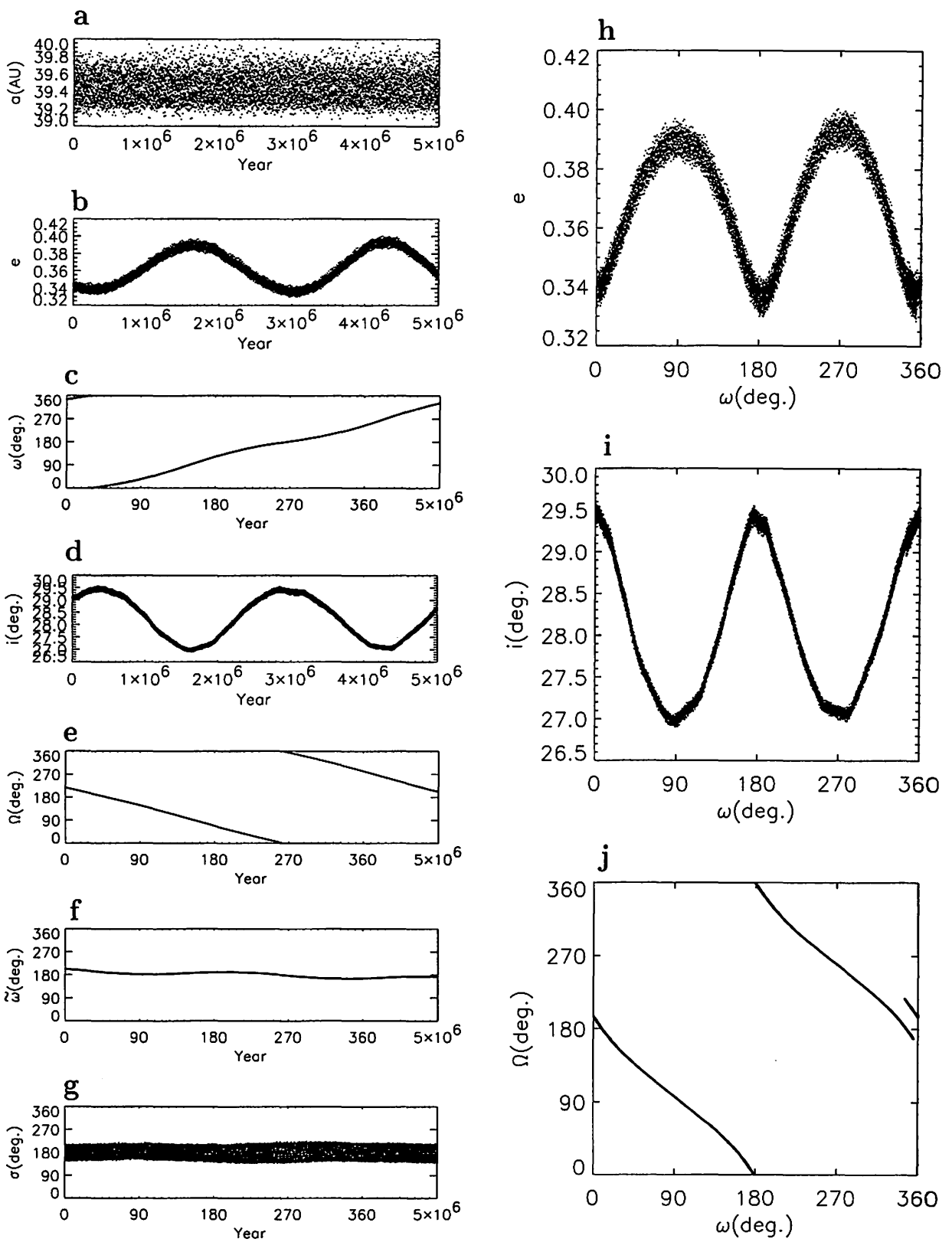

Figure 9. Example of orbital changes of 2002GM32($\dot{\varpi} \simeq 0$).
The phases of variations of eccentricity and inclination are opposite, and the period of eccentricity change is equal to the half period of the argument of perihelion. Moreover, it is almost equal to the phase of ω and Ω.

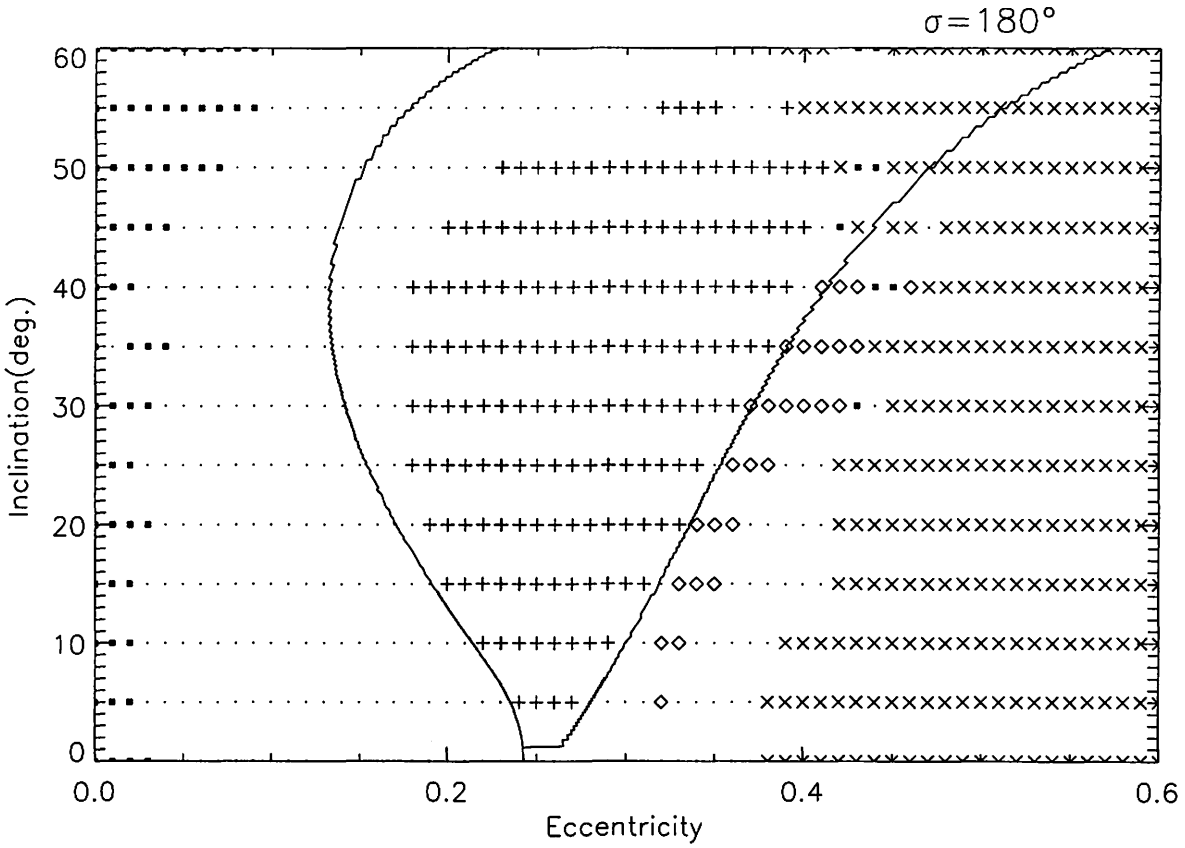

Figure 10. Motions in the e-i plane for the 2:3 MMR.
The initial values are a=39.45AU,$\omega = 90°, \Omega = 270°, \sigma = 180°$. In the region indicated by + signs, ω librates about 90°(Kozai resonance). $\diamond$ signs, dots, and small black squares indicate $\dot{\varpi} \simeq 0$, the libration of σ about 180°(2:3MMR),and the circulation of σ respectively. $\times$ signs indicate Δa(the variation of the semi-major axis) > 2 AU. Two solid curves are the borders of Kozai resonance that obtained by a semianalytical method.

Candidate Centaurs Trapped in Mean Motion Resonances with a Giant Planet

Y. Masaki[(1)] and H. Kinoshita[(2)]

([1]) National Astronomical Observatory, Japan, [1]
ymasaki@gsi.go.jp
([2]) National Astronomical Observatory, Japan,
2-21-1, Osawa, Mitaka, Tokyo, 181-8588, Japan
Kinoshita@nao.ac.jp

ABSTRACT

We investigated the dynamical evolution of Centaurs moving in the region of the giant planets. Perturbations from four major planets (Jupiter, Saturn, Uranus and Neptune) were included. We have found that $2000QC_{243}$ [2] is trapped in a 5:4 mean motion resonance with Uranus and $2001XZ_{255}$ is also locked in a 4:3 resonance. Both Centaurs are moving between the orbits of Saturn and Uranus. They leave the resonances after a few hundred thousand years. Some other Centaurs (10199 Chariklo and 1994TA) also show the resonant character. Their orbital elements (except for Chariklo) are not well determined. However, the region between Saturn and Uranus may play the role of a temporary reservoir for Centaurs.

1 Introduction

For the past several years, automated observational systems operated all over the world have detected a tremendous number of asteroids and revealed their orbital nature. As of August 2003, 65,000 or more objects had been registered as 'numbered asteroids,' and more than a hundred thousand bodies remain unnumbered.

The increase in orbital information enables us to depict the distribution of minor bodies in the Solar system. Most cataloged objects classified as asteroids populate the region between Mars and Jupiter, forming the 'main belt.' Since the 1990s, another type of small objects has also been detected in the far-Neptunian region. These are called Edgeworth-Kuiper belt objects (EKBOs).

The dynamics of main belt asteroids (MBAs) and EKBOs have been intensively studied by many astronomers. We can see some dynamical structures in the distribution of these objects. Mean motion resonances with Jupiter (for MBAs) or Neptune (for EKBOs) make eminent gaps or groups.

[1] Present address:
Space Geodesy Research Division, Geographical Survey Institute,
1, Kitasato, Tsukuba, Ibaraki, 305-0811, Japan

[2] Recently, $2000QC_{243}$ is registered as a numbered body, (54598).

However, some minor objects, classified as Centaurs, are distributed in the region of the giant planets (between Jupiter and Neptune). We can only find some tens of objects with the semimajor axis a of $6 < a < 30$ AU, including unnumbered objects. (2060) Chiron is the first detected body in this region and shows cometary activity (e.g. Tholen et al. (1988)). Due to its high eccentricity, its orbital evolution shows a chaotic nature (Oikawa & Everhart (1979)). The discoveries of other Centaurs have stimulated the studies of their dynamical evolution and lifetimes (e.g. Asher et al. (1994); Dones et al. (1996)). Today, it is believed that Centaurs are in the transitional state from EKBOs to short periodic comets.

We integrated the equations of motion of 44 numbered and unnumbered Centaurs in the giant planets region. We have found that some Centaurs are temporarily locked in a mean motion resonance with Uranus. (For the main belt asteroids, similar numerical simulations have already been reported (e.g. Kozai & Nakai (2002)).) Centaurs $2000QC_{243}$ and $2001XZ_{255}$ have the semimajor axes of $\sim$ 16AU, located in the region between Saturn and Uranus. Both have low orbital eccentricities ($e \sim 0.2$ and $e \sim 0.05$), in contrast to other Centaur objects (e.g. $e \sim 0.7$). We have found that critical arguments librate around 0 degrees for several hundred thousand years. The Centaurs (10199) Chariklo and 1994TA also show the resonant character.

2 Methods of Analysis

Now we consider the motion of Centaurs around the Sun under the perturbations of the four giant planets (Jupiter, Saturn, Uranus and Neptune). We treat Centaurs as massless particles.

The orbital data of Centaurs are obtained through the internet from the MPCORB database maintained by The IAU Minor Planet Center. [3] Additional data on the accuracy of the ephemeris are also available from this database. Positions and velocities of the disturbing planets at the epoch of the MPCORB data are obtained from the DE405 ephemeris supplied by JPL.

We integrated equations of motion by extrapolation (Bulirsch-Stoer) code for 1 Myr forward and backward. We adopted heliocentric coordinates and an invariable plane based on the four planets as the reference plane for outputting results. We selected 44 Centaurs whose osculating semimajor axis at the epoch lies in the range of $6 < a < 35$ AU for our calculation.

In advance, we monitored the orbital elements (especially the semimajor axis) of each Centaur to judge whether it is likely to be in a resonant state or not. Next, we checked the critical argument appropriate for the resonance.

[3] The URL is `http://cfa-www.harvard.edu/iau/mpc.html` .

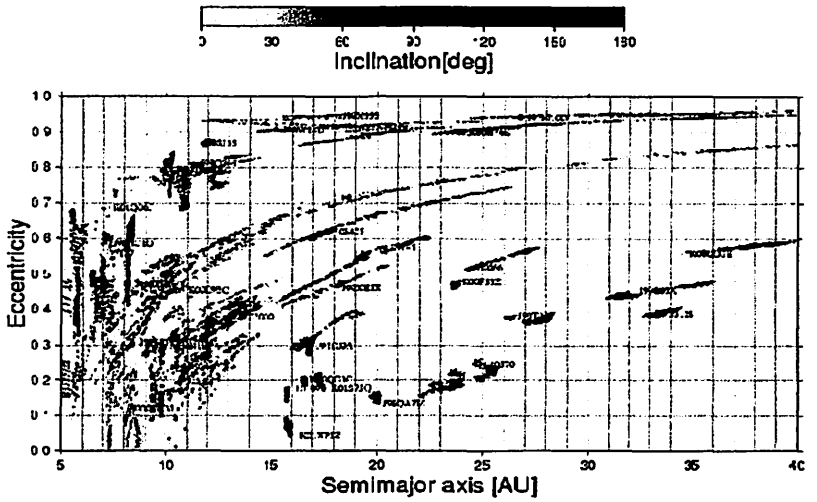

Figure 1: Orbital evolution of Centaurs during the next 50 000 years. Most objects between Jupiter and Neptune rapidly change their orbital elements, due to close encounters with nearby planets. Centaurs trapped in mean motion resonances with Uranus shows slow orbital evolution, compared to others.

3 Results

Fig. 1 shows orbital evolution of 44 Centaurs that we have examined. We plot the evolutional tracks on an (a, e)-plane during the next 50,000 years. Most objects rapidly change their orbital elements due to gravitational interaction with giant planets, especially Jupiter and Saturn. When Centaurs are scattered by a nearby giant planets, their orbital elements move on a curved line on an (a, e)-plane. This is because the Jacobi integral is conserved during close encounter, if we can regard the system as a restricted three-body problem.

However, Centaurs which have small eccentricities in the region between Saturn and Uranus, orbital evolution is relatively small in contrast to other Centaurs. We have found that some Centaurs of this type show resonant nature with Uranus.

4 Centaurs in resonant state

We have found that $2000QC_{243}$ and $2001XZ_{255}$ are temporarily locked in a mean motion resonance with Uranus at present. We also see the resonant character in

Table 1: Osculating elements of Centaurs $2000QC_{243}$, $2001XZ_{255}$, (10199) Chariklo and 1994TA. The original data are listed in The MPCORB database (Version: Aug. 18, 2002) maintained by The IAU Minor Planet Center. See also `http://cfa-www.harvard.edu/iau/info/MPOrbitFormat.html` for further explanations of each item.

Item	$2000QC_{243}$	$2001XZ_{255}$	(10199)	1994TA
Semimajor axis a[AU]	16.4958326	16.0429096	15.8285197	16.8097671
Eccentricity e	0.2016333	0.0438819	0.1738749	0.2996731
Inclination I[deg]	20.77197	2.60700	23.36552	5.39557
Longitude of the ascending node Ω[deg]	337.84861	77.81235	300.39518	137.75032
Argument of the perihelion ω[deg]	152.51174	294.46211	241.33396	154.36691
Mean anomaly at the epoch l_0 [deg]	222.34865	87.69243	351.03363	92.42874
Epoch [JD]	2452400.50	2452400.50	2452400.50	2452400.50
Number of oppositions	3	1	5	5
Uncertainty parameter	3	6	2	2
RMS residual [arcsec]	0.44	0.15	0.50	0.65

(10199) Chariklo and 1994TA, but for a shorter duration. Their orbital elements are listed in Table 1.

The evolution of the osculating elements of the first two Centaurs is shown in Fig. 2. We extracted data in the range of 0.1 Myr forward and backward for the plotting. The bottom panels of the figures show the critical arguments: $\sigma = 5\lambda_U - 4\lambda - \varpi$ for $2000QC_{243}$ and $\sigma = 4\lambda_U - 3\lambda - \varpi$ for $2001XZ_{255}$, where λ and ϖ are the mean longitude and the perihelion longitude of the Centaurs and λ_U is the mean longitude of Uranus.

The semimajor axes for these resonances obtained from Kepler's third law are 16.6 AU (for the 5 : 4 resonance) and 15.9 AU (for the 4 : 3). The osculating elements listed in Table 1 are slightly different from these values, but this difference is due to the resonant libration.

Since the critical arguments exhibit librations around 0 degrees, both Centaurs are trapped in a first order $(p : (p-1))$ mean motion resonance. Therefore, longitudinal conjunctions between the Centaur and Uranus occur around the perihelion passage of the Centaur, to avoid a close approach to Uranus.

However, neither can stay in the resonances eternally. They leave this resonant state after ~ 0.1 Myr for $2001XZ_{255}$ and ~ 0.8 Myr for $2000QC_{243}$. These two Centaurs are temporarily locked in these resonances.

Due to the secular or longer periodic perturbations from the nearby giant planets, their orbits are successively changed. For a longer timespan (such as the period of the apsidal motion; the order of 10^5 years), their orbital eccentricities

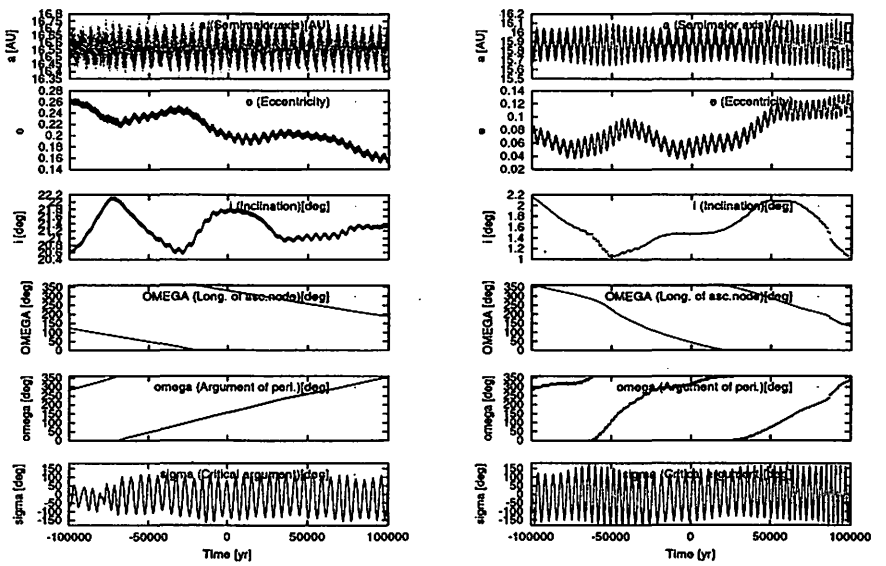

(a)2000QC$_{243}$ (b)2001XZ$_{255}$

Figure 2: Numerically integrated orbital elements of (a)2000QC$_{243}$ and (b)2001XZ$_{255}$. The bottom panels show the critical arguments: $\sigma = 5\lambda_U - 4\lambda - \varpi$ for 2000QC$_{243}$ and $\sigma = 4\lambda_U - 3\lambda - \varpi$ for 2001XZ$_{255}$. They librate around 0 degrees.

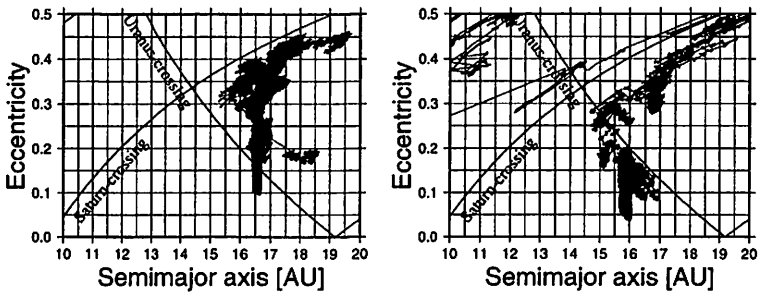

(a)2000QC$_{243}$ (b)2001XZ$_{255}$

Figure 3: Orbital evolution on an (a,e) plane. The plotted data cover from -1 Myr to +1 Myr. For convenience, the planet-crossing curves are also shown. For drawing these curves, we assume that the Centaur and giant planets are moving on a common plane and the planetary eccentricities are fixed to the present values.

increase irregularly. After these Centaurs leave the resonance, the protection mechanism against the approach to Uranus also collapses. Successive large perturbations from Uranus accelerate their orbital evolution. Finally, their orbits become planet(Saturn or Uranus)-crossing. After leaving the resonances, their orbital evolution shows chaotic behavior.

Evolutional tracks of these orbits on an (a,e) plane (the semimajor axis versus the eccentricity) are shown in Fig. 3. The orbit of 2000QC$_{243}$ has evolved from a Saturn-crossing one to its present state. After the orbit leaves the resonant state, Uranian perturbations strongly affect its evolution. For 2001XZ$_{255}$, the orbital eccentricity decreases over the past few hundred thousand years, locked in a resonant state. After a collapse of the resonant mechanism, the close approaches to Uranus accelerate its orbital evolution and the orbit plunges into a chaotic track.

However, due to uncertainties of the provisional orbital data and chaotic orbital evolution caused by repeated close approaches to the giant planets, these evolutional tracks do NOT perfectly depict their evolutional tracks.

Some other Centaurs also show a resonant character, but for shorter durations. The numbered Centaur (10199) Chariklo had locked in a 4:3 resonance in the past (see Fig. 4). The critical argument $\sigma = 4\lambda_U - 3\lambda - \varpi$ is librating around 0 degree. 1994TA is in an 11:9 resonance (the semimajor axis is $\sim$ 16.8 AU) at present. Interestingly, the critical argument contains the longitude of the perihelion of Uranus ϖ_U; i.e. $\sigma = 11\lambda_U - 9\lambda - 2\varpi_U$. It librates around 180 degrees. The resonant state only lasts for a few tens of thousands of years.

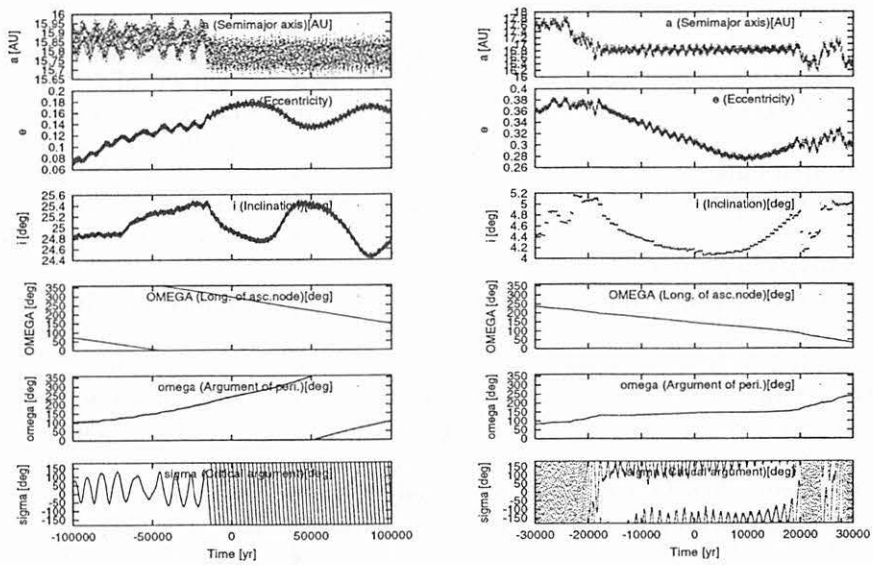

(a) (10199) Chariklo

(b) 1994TA (-30 Kyr to + 30Kyr)

Figure 4: Numerically integrated orbital elements of (a) (10199) Chariklo and (b)1994TA (-30 Kyr to + 30Kyr). The bottom panels show the critical arguments of $\sigma = 4\lambda_U - 3\lambda - \varpi$ for (10199) Chariklo and $\sigma = 11\lambda_U - 9\lambda - 2\varpi_U$ for 1994TA. (10199) Chariklo is not in the resonance at present.

5 Clone Tests

Up to August 2002, orbital elements of $2000QC_{243}$ and $2001XZ_{255}$ are NOT well-determined because observational arcs are too short to permit their determining (see Table 1). Especially, the elements of $2001XZ_{255}$ are derived from only one oppositional season of observation, and they contain orbital fitting errors. After more observations are made, their elements may change from the current provisional values.

Hereafter, we assess the tolerance to the change in the present orbital elements to keep the system in a resonant state.

We introduce some sets of 'clones' whose semimajor axis and eccentricity are changed by a small amount from the MPC data. We numerically integrated for 50,000 years and monitored the critical argument whether a clone is in the resonance or not. The results, plotted on a (t, σ) plane (the time versus the critical argument), are shown in Fig. 5 (a) for $2000QC_{243}$ and Fig. 5 (b) for $2001XZ_{255}$. Each panel corresponds to one clone; the horizontal axis spans from 0 to 50,000 years (10,000 years per grid) and the vertical axis spans from -180 to 180 degrees (90 degrees per grid).

The results show that even if the semimajor axis is shifted by $\Delta a = +0.05$ AU for $2000QC_{243}$, the resonant character still holds for at least 50,000 years. The initial eccentricity is larger by $\Delta e = +0.04$ than the current value, and the system stays in the resonance. For $2001XZ_{255}$, a smaller semimajor axis is preferred for the system holding the resonant state. The resonant nature is not sensitive to the change in the eccentricity. However, these integrations also indicate that if the current provisional elements contain large uncertainties, these Centaurs do not librate in the mean motion resonances.

We also check the effect of ambiguity in the argument of the perihelion because, for a nearly circular orbit, the perihelion is hardly determined. Therefore, we shift the value by a small amount and monitor the critical argument. (Generally speaking, the longitude of the celestial body is well-determined even in the case of a circular orbit. Therefore, we adjust the mean anomaly at the initial epoch so as not to change the initial mean longitude when we shift the argument of the perihelion). We confirmed that the resonant nature is not sensitive to small errors in the argument of the perihelion.

6 Discussion

Do other faint and unknown Centaurs stay around the region between Saturn and Uranus? Does the resonance play the role of a (temporary) reservoir for some Centaurs?

Since most Centaurs have highly eccentric and/or planet-crossing orbits, their orbits are rapidly changed by strong perturbations from giant planets. However, a slightly eccentric orbit in the Saturn-Uranus region shows slower

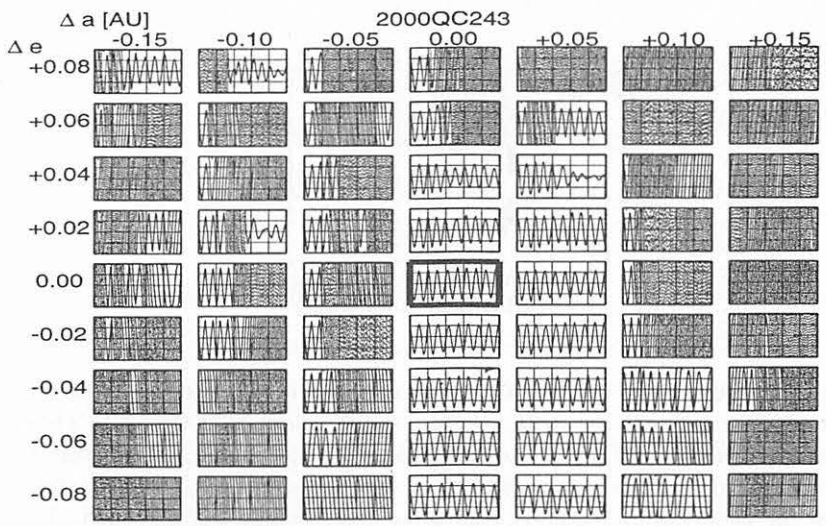

(a)2000QC$_{243}$

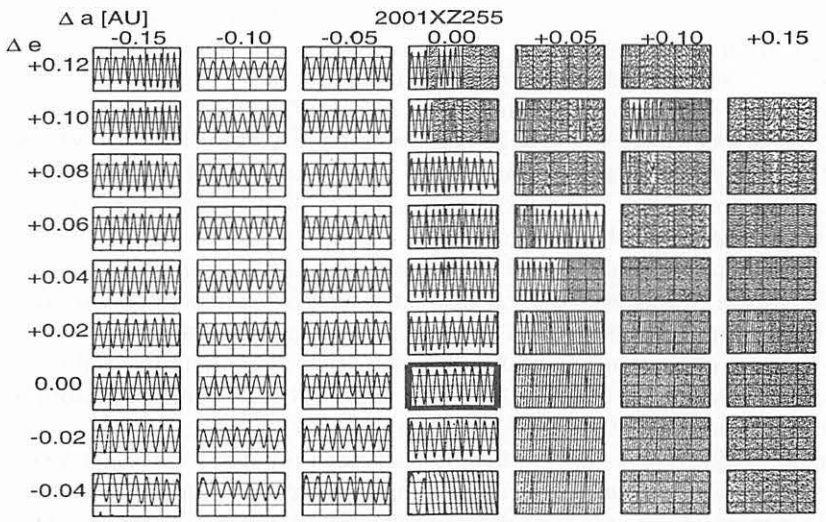

(b)2001XZ$_{255}$

Figure 5: Clone tests for (a)2000QC$_{243}$ and (b)2001XZ$_{255}$. Each panel corresponds to one clone particle. The initial orbital elements are shifted by small amounts designated as Δa AU and Δe at the top and the left of the figures. The time-evolution of the critical argument is plotted on a (t, σ) plane; the horizontal axis spans from 0 to 50,000 years (one division equals 10,000 years) and the vertical axis spans from -180 to 180 degrees (one division equals 90 degrees). The result of the original orbital data listed in Table 1 is plotted on a panel with a thick frame which is located at $\Delta a = 0.00$ AU and $\Delta e = 0.00$.

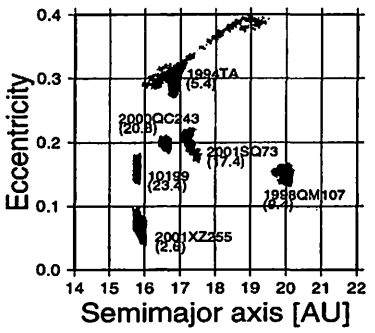

Figure 6: Orbital evolution of other Centaurs near the resonant candidates. We plot the evolutional tracks on an (a,e) plane for the next 50,000 years. These objects are not wandering around so much on the (a,e) plane, in contrast to other Centaurs which have eccentric and/or planet-crossing orbits. Large orbital changes in the elements of 1994TA occur after the resonance is unlocked. The present orbital inclinations (unit: degree) are also indicated in parentheses.

orbital evolution than a highly eccentric one, even if it has a relatively low orbital inclination. This region may temporarily harbour some Centaurs until long periodic or secular perturbations expel them.

Today, several Centaurs are seen in this region (Fig. 6). None of them (except for 1994TA) drastically change their semimajor axes for the next 50,000 years. These low-eccentricity Centaurs make a clear contrast with most other Centaurs; the latter group has a highly eccentric or planet-crossing orbit and changes its orbit within a shorter timescale.

We note that the orbital eccentricity is suppressed at a small value while a Centaur is trapped in a mean motion resonance. Similar phenomena are also reported in Levison & Duncan (1997) for some resonant EKBOs.

The existence of resonant Centaurs indicates that some long-lived objects may stay in the region of $a \sim 16$ AU. It is expected that the mean motion resonance with Uranus contributes to the temporary stability.

Resonant Centaurs may have different material property from other Centaurs. However, observation to clarify the surface physical property is not so easy, because these objects are faint due to their large distances. Moreover, they have small eccentricities, the distance from the Earth is almost constant, even if Centaurs are in the opposition.

Fig. 7 shows destribution of the abosolute magnitude H for 44 Centaurs on an (a,e)-plane. H magnitude is one of the easily obtained observable quantities, and depends on the physical property (albedo) of the surface material and the

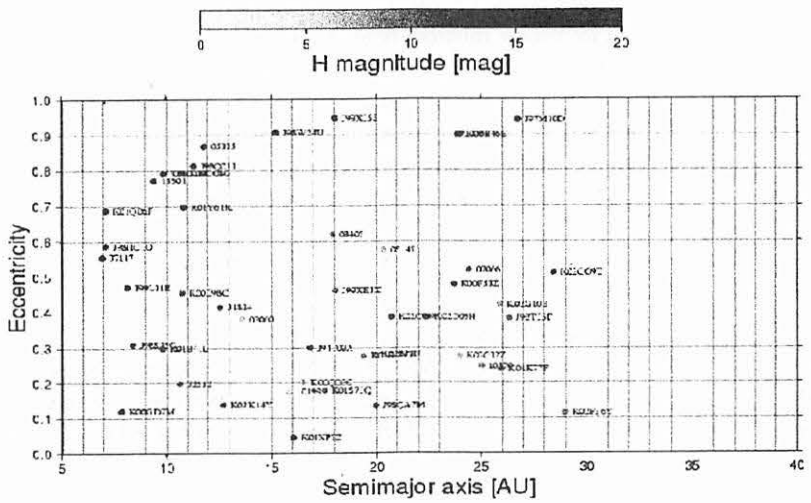

Figure 7: Absolute magnitude of Centaurs on an (a-e) plane. The gray scale shows the H magnitude.

diameter of the body.

We cannot find any differences in absolute magnitude between resonant Centaurs and other ones. However, we cannot conclude that resonant Centaurs have same physical character to common Centaurs.

7 Conclusion

We integrated the equations of motion of 44 Centaurs. Four giant planets are included in the calculation. We have found that Centaurs $2000QC_{243}$ and $2001XZ_{255}$ are likely to be temporarily locked in mean motion resonances with Uranus. Some other Centaurs also show a resonant character. These objects move in low eccentricity orbits, which contrast with the other Centaurs. They do not show significant changes in the orbital elements for at least some tens of thousands of years. They are protected from close approaches to the giant planets due to their small eccentricities and the resonant mechanism.

However, since the orbits of the resonant Centaurs are strongly perturbed by giant planets, their eccentricities are gradually pumped up to collapse the resonant state. Finally, their orbits evolve into Saturn/Uranus-crossing orbits.

We interpret this situation to mean that these Centaurs are temporarily harboured in this region. It is consistent with previous studies (Gladman &

Duncan (1990); Holman & Wisdom (1993); Grazier et al. (1999); see also Masaki & Kinoshita (2003)) on the stability of planetesimal distributed in the giant planets region. The mean motion resonance with Uranus contributes to the temporal stability in this region.

When we discuss the material evolution of Centaurs, it is also important to think about the timescale of their dynamical evolution because it is believed that the past environment (e.g. thermal history) and their ages are recorded on the surface material. The dynamical character may provide some hints about the nature of Centaurs.

ACKNOWLEDGEMENTS

We express our sincere thanks to Ms. Yolande McLean for improving our English. We are also grateful to Mr. Hiroshi Nakai, at National Astronomical Observatory, Japan, for giving us the information on the asteroidal database.

REFERENCES

Asher, D.J., Bailey, M.E., Hahn, G., & Steel, D.I. 1994, MNRAS, 267, 26

Dones, L., Levison, H.F., & Duncan M., 1996, in ASP Conf. Ser. 107, Completing the Inventory of the Solar System, eds. T.W. Rettig & J.M. Hahn, 233

Duncan, M., Quinn, T., & Tremaine, S. 1989, Icarus, 82, 402

Gladman, B., & Duncan, M. 1990, AJ, 100, 1680

Grazier, K.R., Newman, W.I., Varadi, F., Kaula, W.M., & Hyman J.M. 1999, Icarus, 140, 353

Holman, M.J. 1997, Nat, 387, 785

Holman, M.J., & Wisdom, J. 1993, AJ, 105, 1987

Kozai, Y., & Nakai, H. 2002, preprint

Levison, H.F., & Duncan, M.J. 1997, Icarus, 127, 13

Masaki, Y., & Kinoshita, H. 2003, A&A, 403, 769

Oikawa, S., & Everhart, E. 1979, AJ, 84, 134

Tholen, D.J., Hartmann, W.K., & Cruikshank, D.P. 1988, IAU Circ. 4554

日本中世の日月食データの吟味と地球自転

相馬　充，谷川清隆 (国立天文台)，
河鰭公昭 (名古屋大学名誉教授)，今江廣道 (元國学院大学教授)

Examination of the eclipse records of Japanese medieval times and the Earth's rotation

Mitsuru SÔMA[1], Kiyotaka TANIKAWA[1],
Kin-aki KAWABATA[2], Hiromichi IMAE[3]

[1] National Astronomical Observatory, somamt@cc.nao.ac.jp, tanikawa.ky@nao.ac.jp
[2] Nagoya University (Emeritus Prof.), kawabata-nagoya@jcom.home.ne.jp
[3] Kokugakuin University(Retired Prof.)

Abstract

Timed records of solar and lunar eclipses were written in many medieval Japanese books. The present article examines those in the 9–12 centuries for studying the earth's rotation. Recordings of timed data of solar and lunar eclipses started in the 9th century in Japan. Because the moon was in the penumbral area of the earth's shadow in many of lunar eclipses recorded in Japanese books, the definition of the time of the beginng and the end of eclipses is not clear cut and then we can't use them for studies of the earth's rotation. The time of the beginning of solar eclipses written by predictions was very early comparing with the true values in all the cases and then these are not suitable to use for our studies.

The predicted time of the maximum and the end for solar eclipses in the 10th century are confirmed to be those in Kyoto. The eclipses were actually observed at the predicted time in Kyoto as we can confirm from these books.

In the 11th – 12th centuries, the predicted time of the maximum and the end of solar eclipses were, curiously, those in China and then observed eclipses were different from the prediction in Kyoto. In cases of solar eclipses predicted to end before the sunrise in China, Japanese book sometimes recorded that the predictor did not report to the authorized office of the Government because the event was nighttime eclipse and that the solar eclipse was observed at the time of sunrise contradicting the prediction. In cases of solar eclipses predicted to occur just before the sunset in China, Japanese books sometimes recorded predicted time of the begining, the maximum, and the end in China as those in Kyoto and that the solar eclipse did not occur contraditing the prediction.

1　序

望遠鏡のない時代の日月食の観測や星食の観測記録は，個々に見ると精度は悪いが，現在との時間距離が長いので，地球自転変動や月軌道の永年変化に関して有用な情報を与えてくれる．古代のバビロニア・ギリシャ・アラ

図 1: 日食の計算誤差

ビアの日月食が時刻付きで記録されているのに対し, 中国の日月食記録では大部分に時刻が記載されていない. この事実の反映かヨーロッパに於ける日月食の研究は時刻を用いた研究が多い. これに対し, わが国に於ける日月食研究では時刻を問題にしたものが非常に少ない. 時刻を記録した日食が中国史書に始めて記録されたのは我々が知る限りでは隋書 (開皇六年十月晦丁丑, 586/12/16) であるが, 渡邊 (1979) や斉藤・小沢 (1992) からは脱落している.

神田 茂著「日本天文史料」には, 時刻の記載された日食や月食の記録が多数掲載されている. これらの時刻が観測に基づくものであれば, 過去の地球回転の研究に大きな寄与がある. 予測の記録から予測方法の検定が可能である. そこで, 本論文ではわが国の日月食史料の時刻記録利用の可能性を探る為のデータ検証を行った. 斉藤国治氏はその著書「国史国文に現れる天文記録の検証」並びに「中国古代天文記録の検証」(小沢賢二氏との共著) において,「日本天文史料」に取り上げられた月星接近や中国・日本の史書にある日月食を吟味し, 記録の信憑性, 現象に拘った惑星や星の同定を行っている. 残念なことに, 斉藤氏が 1952 年の国際天文学連合総会で採択された暦表時の地球自転永年減速率と比べて大分大きい地球自転減速率を用いていること・地球の慣性能率の変化を考慮していない事から氏の計算は誤差が非常に大きい.

図 1 は日食を例にした誤差要因の説明図である. 日食は太陽と地球の間に月が入った場合に起こることは今更説明を要しない. 日食の状況を計算により算出する場合には, 次の二つの誤差要因が挙げられる.

1. **地球の回転角** この誤差を表すのに現在では天体の運行の計算に使えるニュートンの力学第 3 法則により定義された力学時 TT と地球の回転角を表す世界時 UT の差 $\Delta T = \mathrm{TT} - \mathrm{UT}$ が使われている. この誤差は潮汐による地球の回転速度の減少と慣性能率の変動による地球の自転速度の変化の二つの原因に起因する.

2. **月の公転角** 潮汐効果による地球の自転速度の減少は, 角運動量保存の法則により月の公転角運動量の増加, 公転角運動量の増加に伴なった月の地球からの距離の増加, 地球からの距離の増加に伴なった月の公転速度の減少により生ずる. 月公転速度の増加率を潮汐項と呼び, 現在ではアポロ 11 号の月面着陸に際し月面に設置された反射鏡を用いた月距離のレーザー測距から導かれる.

従って日月食・星食の計算に考慮する必要のある物理量は潮汐効果と慣性能率の変化の二つである. 潮汐効果を表すパラメータは月黄経の潮汐項であるが, この量は過去 3000 年程度の範囲では有意な変化はしていないと考えられるから一つのパラメータを与えればすむ. 慣性能率も短期間の間に急激に変化する量では無いが, 100 – 200 年経過すると日月食や星食の見え方に大きな差を生ずる程変化することに留意しなければならない.

近世に於ける日月食の研究は Hansen (1857), Oppolzer (1887) に始まると言って良いであろう. 小倉伸吉 (1916) や渡邊敏夫 (1979) の解説もこれらの論文の紹介から始まっている. これらの初期の日月食の研究では地球回転の潮汐効果による減速を月黄経の永年加速から調べようとしていたので, 月の公転角と地球の自転角の差だけを問題にしていた. 従ってパラメータは地球回転の潮汐効果による減速一つだけである. 地球回転の潮汐効果による減速率は急激には変化しないと考えられるので, 歴史的年代を考える限り, パラメータ一つの値を決めれば良い筈であった.

この点に初めて疑問を投げかけたのは Cowell (1905, 1906a, 1906b, 1907) で, 図 1 には書かれていないバックの恒星に対する太陽や春分点の運行にも永年加速が有る事から, これらの数値の辻褄を合わせるには上記の二つの要素を考慮する必要性が有ることを示唆している.

表 1: 地球自転の永年減速率 q (sec/cy^2)

著者	q
Fotheringham	36.8
Schoch	33.7
Spencer Jones	29.9
暦表時	29.949
Stephenson	31

この研究に刺激されて Fotheringham (1920) は月及び太陽の対恒星永年加速として $10''.8/\mathrm{cy}^2$, $1''.5/\mathrm{cy}^2$ を得た. この太陽黄経の永年加速は地球の自転速度の減速によるものと考えられるから, 月黄経にはこの値に 1 恒星年と 1 恒星月の比 13.4 倍の $20''.1/\mathrm{cy}^2$ の永年加速が生じることになる. これに惑星の重力に起因する地球軌道の離心率の減少に伴なった月黄経の永年加速 $6''.0/\mathrm{cy}^2$ を加えた $26''.1/\mathrm{cy}^2$ が理論的な月黄経の対恒星永年加速となる. Fotheringham が得た月黄経の観測的永年加速は $10''.8/\mathrm{cy}^2$ だから, $\mathrm{O-C} = -15''.3/\mathrm{cy}^2$ が潮汐項になる. 以来地球回転の研究は ΔT と潮汐項を用いて研究される様に変わった.

更に 1939 年には Spencer Jones により太陽・月・金星の位置に関する不規則的変動が同期し, 且つその振幅が地球回転の不規則性として説明されることが定量的に確認された. こうして 1952 年の IAU 総会に於いて暦表時の採用が採択された. 暦表時では地球回転に一定レートの減速 29.950sec/cy^2 に不規則的変動を加えた ΔT を採用している.

参考の為に地球自転の永年減速率を表 1 に数値を得た研究者名と共に纏めた. 図 2 は ΔT の比較を図示したもので, 実線・点線・破線は Fotheringham, Schoch, 暦表時の地球自転の永年減速を示したものである. ○, ●, ⋆, ∗ はバビロニア, ギリシャ, アラブ, 中国の日月食の記録から Stephenson (1997) が求めた値であり, ◇, × は谷川・相馬 (1991), Kawabata, Tanikawa, and Sôma (2003) の日本・中国の日食観測から求めた値をプロットしたものである.

斉藤氏が使用した太陽や月などの位置の計算式は Neugebauer (1912, 1925, 1929) や Schoch (1927) による UT を引数としたもので, たとえば, 太陽の平均黄経については TT を引数とする Newcomb (1985) の理論式に比べて次のような違いがある.

斉藤: $L_{\mathrm{Sun}} = 279^\circ.6968 + 36000^\circ.769325T + 2''.600T^2$

Newcomb: $L_{\mathrm{Sun}} = 279^\circ.6967 + 36000^\circ.768925T + 1''.089T^2$

(T in centuries from J1900.0)

上記の Newcomb の太陽黄経の計算式は後に暦表時 ET の定義に採用されたもので, 現在の力学時 TT は ET に連続していると考えられるので, Newcomb の式の時刻引数は TT によるとみなすこともできる. したがって, 上記の 2 つの式の係数の違いは時刻引数の違い $\Delta T = \mathrm{TT} - \mathrm{UT}$ を反映していることになり, 斉藤氏は地球の自転速度が一定の割合で減速しているとしていることに対応する. 斉藤氏の採用した太陽黄経の永年加速は Fotheringham (1920) に等しく, 斉藤氏が Fotheringham (1920) の地球回転の減速率を採用したことが判る. しかし, Fotheringham の研究は太陽黄経の永年加速から地球の自転速度の減少率を求めた最初の研究で, 当時としては測定限界に近い小さな値の差に大きな数を掛けて答えを得ると言う微妙な演算を必要とし, 当然の事ながら誤差は大きい. この事実は表 1 並びに図 2 を見れば明らかであろう.

Fotheringham (1920) の論文ではこの地球回転減速の過大評価を打ち消す絶対値に於いて大きい潮汐項を採用して, 計算結果が観測記録と一致する様に辻褄を合わせている. この様な辻褄合わせは Fotheringham が使用した中近東の食に対してのみ可能な方法で, 他の地域の観測も合わせると破綻する.

Fotheringham (1920) により始められた太陽黄経の永年加速から地球回転の永年的減速を求める方法はその後地球回転の不規則的変動も含めて太陽・惑星・月の永年加速並びに不規則的変動から総合的に求める方向に発展し, Spencer Jones (1939) やその後の暦表時につながっている. 地球回転の変動が斉藤氏が仮定した様に規則的なものでないことは 1952 年のローマに於ける国際天文学総会の時点で既

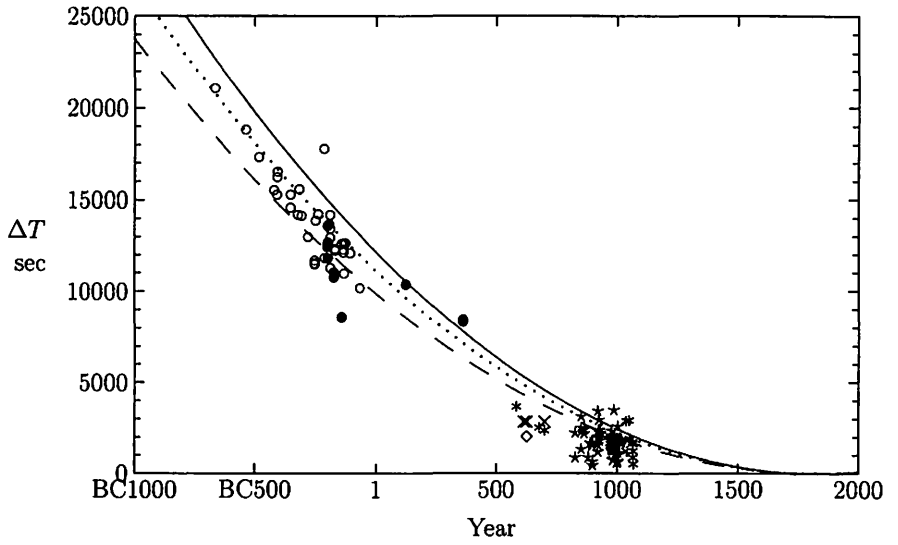

斉藤・小沢 (1992): 実線, ET (1952): 破線, Schoch (1926): 点線, Fotheringham (1920): 実線.
○: バビロニア, ●: ギリシャ, ⋆: アラブ ∗: 中国,
◇: 谷川・相馬 (2001). ×: Kawabata, Tanikawa and Soma (2003).

図 2: ΔT の比較

表 2: 六国史

書名	完成年	収載歴代
日本書紀	720	神代–持統
続日本紀	797	文武–桓武
日本後紀	840	桓武–淳和
続日本後紀	869	仁明
文徳実録	879	文徳
三代実録	901	清和・陽成・光孝

によく知られており，そのような仮定で，ある日食がどこで見られたかを判定するには無理がある．

2 天文記録

わが国の天文記録は六國史 (表 2) の他に扶桑略紀 (神武–堀川の編年史, 叡山の僧皇円著)・本朝世紀 (平安末期に六國史を継ぐ国史として編纂が始まったが未完, 935–1153 のものが断続的に残存)・朝野群載 (平安時代の詔勅・宣命・対策・公文などを類別に編集したもので元三十巻内九巻散逸)・個人の日記などに残されている．六国史は官製の史書なので解説も多数有り改めて紹介する必要は無かろう．日本書紀の最後の巻持統紀以降に予測による日月食の記載が多いことは既に多くの研究者により指摘されている．然しながら初期の記録では日月食が有ったことだけが記載されているに過ぎないので, 記録を見ただけでは実見か予測かの識別が不可能であるが, 平安時代になると予測か実見かが明瞭な記述も多いことは余り世に知られていない様である．

月食に関しては従来実現していない月食が多数記載されているとの説が有ったが, 長谷川一郎氏 (1995) が Liu and Fiela (1992) の月食表を用いて半影食であることを示している．

時刻付きの日月食記録には具注暦に記述された日記類が多い．具注暦と云うのは暦日の下に歳位・星宿・干支・吉凶・忌諱などが記述され, その下二〜三行の空白行を明け, 日記などを記載できる様にした日記帳の様なもので, 最初は毎年十一月に陰陽寮が作成し, 中務省から諸司に配布された．現存する最古のものは 746 (天平十八年), 749 (天平二十一年) の断簡で正倉院にある．具注暦の配布は最初は諸司らに限られていたが, 平安時代に入ると, 最初は公家の間で多用される様になり, 後に一般庶民も用いる様になった．具注暦が普及するに従って, 弊害も現れて来たので, 807 年 (大

同二年) に一旦廃止されたが, 公家の要請により 810 年 (弘仁二年) に再度配布される様になり, 以後の具注暦には吉凶・禁忌が必ず付けられるようになった. 藤原道長も, 曜日の記載で有名な日記「御堂関白記」を具注暦に記入している.

橋本万平氏の「日本の時刻制度」によると, 具注暦には日月食の初虧・食尽・復円の時刻, 各季節の日の出・日の入り時刻, 一日を百刻に分けた昼夜の刻数などが一定の規則に従って記されていると言う. 橋本氏によれば, 前年の八月一日迄に暦家が日月食の予測を陰陽寮に提出し, これらが十一月に陰陽寮から中務省に提出された具注暦に書き込まれていた. 従って具注暦に書かれている日月食の時刻は全て予測によることは明らかである. 具注暦の天文記録の使用には原資料の詳細な吟味が必要なので本論文では扱わない.

3 時刻制度

3.1 中国の時刻制度

中国では 1 日を十二支を用いて 12 分割する方法と 1 日を 100 刻に分割する方法を併用するのが通例だった. この分割法は既に前漢時代に確立している. 前漢末期の哀帝の BC 6 年に一旦一日を 120 刻とする制度が設けられたが, 2 ヶ月で元に戻った. 前漢が亡び新が建国されると再度一日 120 刻の制度に戻されたが, 新が亡び後漢が成立すると再度 1 日 100 刻制に戻っている. AD 507 年に 1 日 96 刻制になったが, 544 年には 1 日 108 刻に変わり, 563 年には再度 1 日 100 刻制に戻り, 1628 年迄続いている. 1628 年に 1 日 96 刻制に変わり, これが 20 世紀迄続いた.

100 刻は 12 で割れないので, 十二支の夫々の 2 時間を $8\frac{1}{3}$刻 に分割する方法と十二支の夫々を 1 時間ずつに分割し, 各々の 1 時間を夫々$4\frac{1}{6}$刻 に分割する方法が用いられている.

前者の方法では例えば一日の最初は子初刻から始まり、初刻・一刻・二刻・...八刻と続く. 八刻だけは他の刻の 1/3 の継続時間になる.

第二の方法では子初初刻から始まり, 一刻・二刻・三刻・四刻と続き, 子初四刻で最初の 1 時間が終わる. ここで子初四刻だけは他の刻の 1/6 の継続時間である. 次が子正初刻で, 一刻・二刻・三刻・四刻と続き, 子正四刻で終わる. 子正四刻も他の刻の 1/6 の継続時間である. こうして 1 日は $24 \times 4\frac{1}{6}$ 刻 $= 100$ 刻 となる.

3.2 延喜式の時刻制度

日本では 6 世紀の後半から 7 世紀の前半にかけて, 中国で隋・唐が中国の統一を達成し, 高句麗に対する侵攻による領土拡張政策を取り始めたことに対する警戒心から国力を高める為に中国の官僚制度を導入した. 中国の律令制では行政法の令と礼を基本とした刑法の律からなるが, 日本最初の律令制の飛鳥浄御原令の制定に際しても律は作られていない. 次の養老律令でも養老律は人々の関心を呼ばず散逸してしまった. 延喜式は律令を施行する時の細かい規則を集めたもので, 905 年 (延喜五年) に藤原時平を中心として編纂が, 927 年 (延長五年) 藤原忠平のもとで一応完成したが, その後も修訂を重ね, 967 年 (康保四年) から施行された. 延喜式は大宝–延喜の期間の式全てを包含する. 延喜式は当時の現行法とはなっていないが, 現在まで殆どそのまま残存しているので, 当時の習慣を知るには必要不可欠な文献とされている. 橋本万平 (2002) によると, 延喜式には陰陽寮に関する規程が細かく記され, 当時の宮城の門の開閉時刻・日の出日の入り時刻が記されている.

橋本万平 (2002) によると, 延喜式の時刻制度では 1 日を十二支により 12 分割し, これを辰刻と呼ぶ. 又 1 日を 48 分割した刻を用いる. 従って 1 辰刻は 4 刻に分割される. これを纏めると,

$$\begin{array}{rcrcrcr} 1\text{日} & = & 12\text{辰刻} & = & 48\text{刻} & = & 480\text{分} \\ & & 1\text{辰刻} & = & 4\text{刻} & = & 40\text{分} \\ & & & & 1\text{刻} & = & 10\text{分} \end{array}$$

と書ける. 従って現在の秒と対応させると 1 分 $= 180\,\mathrm{sec}$ となる.

刻は一刻から始まり四刻で終わる. 分は 0 分から始まり 9 分で終わる. 但し 0 分は書かず, 刻で終わる.

古代の時刻制度には日本に限らずエジプト等に於いても定時法と不定時法の二種類がある. 定時法は昼夜の長さとは無関係に一日を

表 3: 延喜式日出・日没時刻.

季節 始	季節 終	太陽黄経 始	日出	日没
		°	h	h
大雪 13 日	冬至 15 日	−93	7.10	16.80
小寒 1	小寒 12	−75	7.05	16.85
小寒 13	大寒 7	−63	6.95	17.05
大寒 8	大寒 15	−53	6.85	17.10
立春 1	立春 8	−45	6.75	17.25
立春 9	雨水 1	−37	6.60	17.35
雨水 2	雨水 9	−29	6.50	17.55
雨水 10	啓蟄 2	−21	6.35	17.60
啓蟄 3	啓蟄 10	−13	6.25	17.75
啓蟄 11	春分 2	−5	6.10	17.85
春分 3	春分 9	2	6.00	18.00
春分 10	清明 2	9	5.85	18.10
清明 3	清明 10	17	5.75	18.25
清明 11	穀雨 3	25	5.60	18.35
穀雨 4	穀雨 11	33	5.55	18.50
穀雨 12	立夏 4	41	5.35	18.60
立夏 5	立夏 12	49	5.25	18.75
立夏 13	小満 5	57	5.10	18.85
小満 6	小満 15	65	5.05	18.95
芒種 1	芒種 12	75	4.85	19.05
芒種 13	夏至 15	86	4.80	19.10
小暑 1	小暑 12	105	4.85	19.05
小暑 13	大暑 7	116	5.05	18.95
大暑 8	大暑 15	127	5.10	18.85
立秋 1	立秋 8	135	5.25	18.75
立秋 9	処暑 1	143	5.35	18.60
処暑 2	処暑 9	151	5.55	18.50
処暑 10	白露 2	159	5.60	18.35
白露 3	白露 10	167	5.75	18.25
白露 11	秋分 2	175	5.85	18.10
秋分 3	秋分 9	182	6.00	18.00
秋分 10	寒露 2	189	6.10	17.85
寒露 3	寒露 10	197	6.25	17.75
寒露 11	霜降 3	205	6.35	17.60
霜降 4	霜降 11	213	6.50	17.55
霜降 12	立冬 4	221	6.60	17.35
立冬 5	立冬 12	229	6.75	17.25
立冬 13	小雪 5	237	6.85	17.10
小雪 6	小雪 15	245	6.95	17.05
大雪 1	大雪 12	255	7.05	16.85

等分割する方法で, 現在の時法と同じである. 不定時法は昼と夜とを別々に分割する方法である. 中世日本の不定時法では日の出・日の入り時刻で昼夜を分け, 昼の何刻, 夜の何刻と云う呼び方がされている. 江戸時代には朝の薄明と夕の薄明を昼夜の分かれとしている.

延喜式では日の出・日の入りの時刻が季節と共に変化しているので定時法であることは明らかである. 又日の出時刻と日の入り時刻の平均値を取ると端数誤差を除いて正午になるので太陽の南中を正午に取る地方視太陽時が使われていたことが判る.

表 3 は橘本万平 (2002) に記載されている延喜式の日出・日没時刻を地方視太陽時に換算した値である. 延喜式の日出・日没, 門の開閉時刻などは日付として二十四節気が用いられているので, 該当する太陽黄経も合わせ掲載した. 図 3・4 の折線は延喜式で与えられている日出・日没時刻である. これらの図には 926 年の大雪 13 日から 928 年初めまでの現在の天文学に於ける地方視太陽時による日出・日没時刻も比較の為にスムーズな実線で書き入れてある. 現在の天文学に於ける日出・日没時刻は太陽の上端が地平線に達する時刻で, 大気による光の屈折も考慮されている. この点で延喜式の時代と日出・日没時刻の定義の差も考えられるが余り大きくはない.

延喜式の日出・日没時刻は年の後半では正しい日出・日没時刻と良く合っているが, 前半では合いが良くない. 宣明暦では冬至点と近日点を同じに取っており, 実際とは異なるが, 地球軌道の離心率は 0.0167 に過ぎないので, その影響は大きくない. 平均太陽時による日出・日没時刻をプロットすると宣明暦による計算と真の地球軌道を用いた計算結果に多少の差はあるが, 視太陽時でプロットした図 3・4 では完全に重なってしまうので宣明暦による誤差とは考えられない. 結局この差の原因は今のところ不明であるが, 時刻の差が有ると云っても最大 10 分程度なので, 実用上は余り気にしていなかったのかも知れない.

3.3 宣明暦の時刻制度

宣明暦は唐では 822 年から 71 年間使用された. 日本では貞観四年 (862) から貞享元年 (1684) 迄 823 年間使用された. 日本に於ける宣明暦の使用期間は世界史上ユリウス暦に次いで長い. 宣明暦では 1 年の長さが 365.2446 日で実際よりも 0.0024 日長い. 従って 800 年で 1.92 日の季節とのズレを生じている. この間に中国では何度も改暦が行われていることから, 「日本では中国で何度も改暦が行われていることも知らずに改暦を行わないまま 800 年も過ごした為に季節と二日ものズレを生じていることも知らずに日食を誤った予測で記録していた」との記述をしばしば見かける.

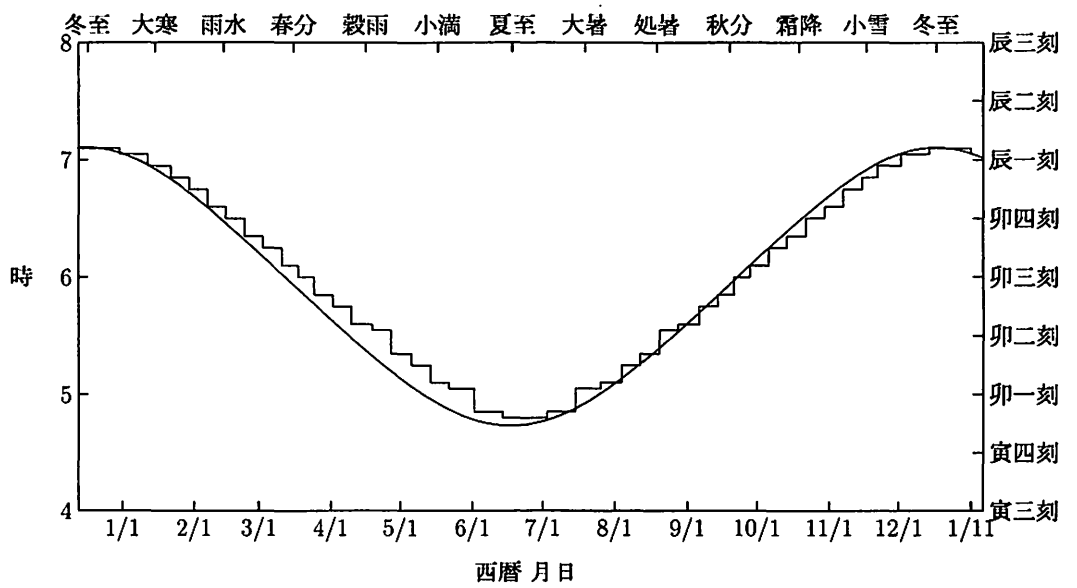

図 3: 延喜式日出時刻と視太陽時日出時刻の比較

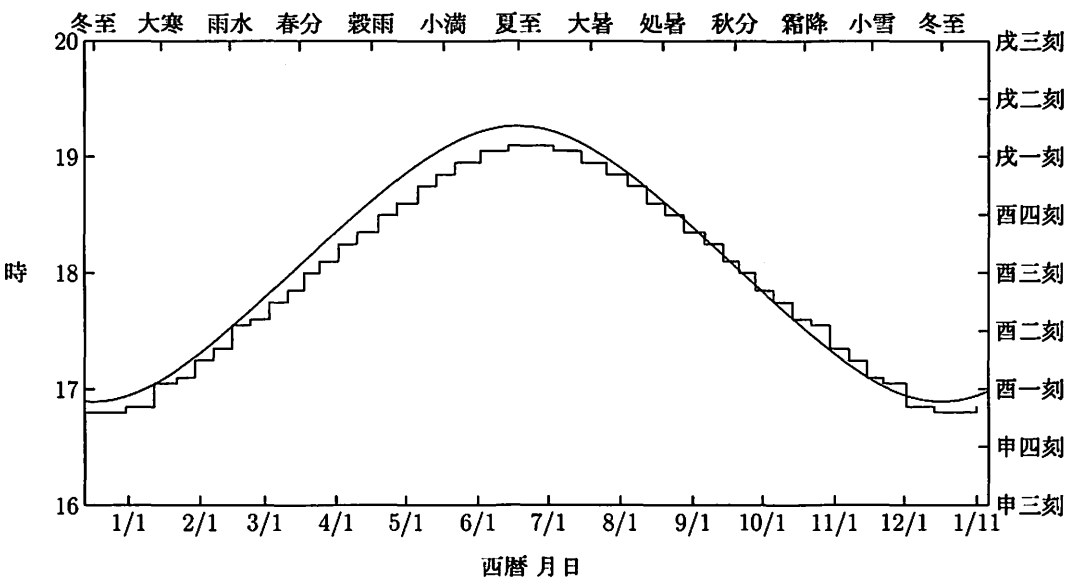

図 4: 延喜式日没時刻と視太陽時日没時刻の比較

然しながらこの種の記述は宣明暦の全くの誤解に基づくもので, 内田 (1975) によると, 宣明暦では近日点と冬至点を同一に取っているが, 宣明暦が用いられる様になった時点では近日点は冬至点よりも約 7° 前に在り, 800 年後には逆に約 7° 後ろになっている. 従ってこの近似は宣明暦が使われ始めてから約 400 年後に最も良くなり, その後次第の悪くなると云う関係がある. この事情の為に宣明暦による日食予測の精度は全く劣化していないと云う. 表 4 は宣明暦が採用されていた期間の日食予測の内田 (1975) の誤差評価を採録したものであるが, 事実予測精度の劣化の兆候は全くみられない.

宣明暦では

$$\begin{aligned} 1\text{日} &= 12\text{辰刻} = 100\text{刻} = 8400\text{分} \\ &\quad 1\text{辰刻} = 8\tfrac{1}{3}\text{刻} = 700\text{分} \\ &\quad\quad\quad 1\text{刻} = 84\text{分} \end{aligned}$$

と取る.

刻は初刻から始まり, 八刻で終わる. 但し八刻は他の刻の 1/3 の長さである.

橋本 (2002) では宣明暦による時刻を第 1 類

表 4: 宣明暦日食予報誤差

年代	日食数	平均誤差
年	回	分
562— 900	12	79
901—1000	31	89
1001—1100	33	109
1101—1200	30	98
1201—1300	27	82
1301—1400	32	61
1401—1500	33	72
1501—1600	33	69
1601—1684	23	55

と分類している.

3.4 橋本 (2002) による分類

橋本 (2002) は時刻付きの日月食記録を基に時刻制度の分類を行い, 以下の 4 分類を行っている.

第 1 類 宣明暦

1 日 = 12 辰刻 = 100 刻 = 8400 分
1 辰刻 = $8\frac{1}{3}$ 刻 = 700 分
1 刻 = 84 分

刻は初刻・一刻・...・八刻, 八刻は他の刻の 1/3.

1 刻 = 864 sec, 1 分 = 10.3 sec.

第 2 類 中国の第二の方法に近い.

1 日 = 12 辰刻 = 100 刻 = 4000 分
1 辰刻 = $2 \times 4\frac{1}{6}$ 刻 = $333\frac{1}{3}$ 分
1 刻 = 40 分

刻は初刻・一刻・...・四刻, 初刻は他の刻の 1/6. 例えば午初初刻・一刻・二刻・三刻・四刻と続き, 四刻は他の刻の 1/6 の継続時間. 次に午正初刻・一刻・二刻・三刻・四刻と続き, 初刻だけが他の 1/6. 中国では四刻が短いが, 橋本の分類では初刻が短い.

1 刻 = 14.4 min = 864 sec. 1 分 = 21.6 sec.

第 3 類 延喜式に近いが分が一分から始まる.

1 日 = 12 辰刻 = 48 刻 = 480 分
1 辰刻 = 4 刻 = 40 分
1 刻 = 10 分

刻は一刻・二刻・三刻・四刻. 分は一分・二分・...・十分. 1 刻 = 30 min, 1 分 = 3 min.

第 4 類 延喜式に近いが刻が初刻から始まり三刻で終わる. 分の単位が荒い.

1 日 = 12 辰刻 = 48 刻 = 192 分
1 辰刻 = 4 刻 = 16 分
1 刻 = 4 分

刻は初刻・一刻・二刻・三刻. 分は初分・一分・二分・三分. 1 刻 = 30 min, 1 分 = 7.5 min.

4 日食データ

今江は「日本歴史」1995 年 5 月号において, 陽明文庫所蔵の「兵範記」の断簡の中に日食記事を見出し, それが西暦 1169 年 8 月 24 日の日食 (オッポルツァー番号 5655) であることを確定した. この観測は神田茂著「日本天文史料」に掲載されておらず, 従来知られていない. 部分食であるが, 時刻と食分が書かれている.

天晴、日蝕、大分十五分之八、□初
巳一刻、廿七分、加時巳五□□

この日食は中国では雲に遮られて見えなかった. 高麗では日食記事はあるが, 詳しいことは記載されていない.

表 5 は橋本 (2002) の時刻付きの日月食表に記載されている 1148 年迄の日食に, 今江が見出した上記の日食と 1112/09/23, 1106/08/01 の日食を付加して纏めたものである. 日本で宣明暦が採用されたのは 862 年だから表の期間に使用されていたのは暦法は宣明暦である. 延喜式が採用されたのは 967 年からであるが, 延喜式には大宝令も含まれているので, 記載時刻に関しては表の期間については延喜式も否定出来ない.

この表を見ると, 橋本の表にある日食では 1118/05/22 の日食を除いて全て複数の記録

表 5: 橋本 (2002) による予測時刻記載の日食 (1148 迄) 及びその他の追加日食. * は今江 (1995) その他の追加日食. 主要記事欄は神田 茂 (1935) から抜載.

年月日	出典	主要記事
877/05/17	三代実録	夜丑一刻日有蝕之虧初子三刻三分復至寅二刻一分皇帝不視事...議日蝕在夜廃務以否
	他 2 文献	
975/08/10	朝野群載 十五 陰陽道	虧始卯一刻三分加時辰二刻一分復末巳初刻二分
	日本紀略	卯辰刻皆既如墨色無光群鳥飛乱衆星盡見
	扶桑略記	辰時日蝕
	和漢合符	自辰至未暗如夜
	他 10 文献	
982/03/28	小右記	虧始辰三刻加時巳一刻二分復末巳三刻 日蝕叶暦
	日本紀略	日蝕
1021/08/11	左經記	虧始巳四刻一分加時午二刻二分復末同刻三分
	日本紀略	日蝕符合
	扶桑略記	日食
1028/03/29	左經記	虧始寅初刻　　分加時卯一刻四拾七分復末辰二刻六十一分 虧始寅七刻八十三分加時卯一刻四十六分復末卯三刻三十七分、日出卯三刻二十六分、入酉四刻五十四分、日天在奎宿十四度八十七分、...両説雖不同、共立其道之人等也、仍共記之
	日本紀略	卯刻日蝕、十五分之八也、暦家不注、仍中務省不申、不廃務
1029/09/11	小右記	虧始卯一刻三分加時辰一刻一分復末巳一刻二分
	日本紀略	日蝕廃務
1080/12/14	水左記	虧始巳一刻　分加時巳四刻六分復末午三刻五分陰晴不定、蝕暫不現午刻雲
	他 2 文献	
1085/02/27	朝野群載 八 別奏	虧始寅一刻三分加時寅四刻九分復末卯三刻十分
	後二條師通記	日蝕雨降日脚不見
1100/05/11	朝野群載 八 日月蝕奏	申進大陽虧蝕事、虧初辰四刻二十四分加時巳二刻十二分復末午初刻一分
	他 3 文献	
1106/08/01*	永昌記	未一刻大陽初虧四点漸過末之聞
	中右記	及未刻日蝕正現
	他 2 文献	
1106/12/27	永昌記	天晴今日可有日蝕之由、...史定政一昨日持参、虧初未二刻三十二分加時未三刻三十六分復末四刻二十七分...雖入蝕限不可正見...
	中右記	天晴、...今日未刻可有少分日蝕之由、暦道所勘奏也、而宿曜家僧明算深算等、不可有之由進申文、彼此相論之間既無日蝕...
	他 2 文献	
1107/12/16	中右記	今日冬至、又可有日蝕之由、其日蝕十五分之十三半弱、虧初未一刻一九分、加時申□□十五分、復末酉一刻十分...相窺時刻之處、晩景片雲横漢、日光不現、就中天下不及暗計也、
	阿娑縛抄	至干當日卯辰刻、天晴無雲、日輪顕現、更無疑、干時有院宣云、晴天既晴、陰雲難掩、正現無疑、佛力似空、但猶至干蝕刻限、於仏前可令祈念、...而間...黒雲俄聳掩王城、終日不晴、
	他 5 文献	
1112/09/23*	中右記	日出之間少許帯蝕正現也
	他 1 文献	
1118/05/22	中右記	始申三刻二十四分加時酉一刻二九分復末酉三刻二十九分雨下不見日蝕
1147/10/26	本朝世紀	虧始申四刻十一分加時酉三刻五分復末戌二刻十四分
	台記	有食雖晴人不見食
	他 1 文献	
1148/04/20	本朝世紀	日蝕諸司廃務、本日陰雲合不正現矣 虧始午四刻七分加時未初刻二十七分復末未三刻十九分
	他 1 文献	
1169/08/24*	兵範記	虧初未一刻二十七分加時未五刻

が残されている．この例外の 1118/05/22 の日食は中右記に「雨下不見」と記載されたもので，計算によると日没直前に始まり，$\Delta T = 2000\,\mathrm{sec}$ とした時日没時の食分は 0.28 である．その他何れもどの様な日食であったかがある程度判る記録が残されている．

実見による記録と考えられるものは後に詳細に論ずることとし，ここではその他の日食に関し，どの様な日食かを簡単に纏める．日食の記録に屡「廃務」「不廃務」と記されたものがある．この他に「廃朝」がある．廃務は全ての役人が休む場合で，朝廷の仕事は全て止まる．廃朝は天皇だけが休む場合である．

1. 877/05/17 Oppolzer No. 4964 の日食であるが日本時間では夜間の日食の為廃務としなかった．
2. 1085/02/27 予測は食尽が 04:54 視太陽時であるが，計算値は 05:00 で日の出前の食になる．
3. 1106/12/27 Oppolzer No. 5498. 日本で食無し．
4. 1118/05/22 日没帯食．日没時食分 0.28.
5. 1147/10/26 Oppolzer No. 5600. 日本では夜間の食．

表 6 は表 5 の日食から，日本では見られない 877/05/17, 1085/02/27, 1147/10/26 の日食を除いた全ての日食に対する予測時刻と計算時刻の対照表である．但し，橋本氏が第 2 類と分類した 1100/05/11, 1107/12/16, 1118/05/22, 1148/04/20 に就いては，時刻の十二支の次に始又は正の字が記入されていないと現在の時刻への換算が一義的には出来ないので割愛した．1107/12/16 は橋本氏の分類では第 2 類であるが，金環食なので計算結果の節での議論には追加した．計算は仮の値として $\mathrm{TT} - \mathrm{UT} = 2000\,\mathrm{sec}$ と仮定し，京都 (135° 45', 35° 01') における食始，食尽，食終の時刻 (JST) と食尽のときの食分を求めた．記録は地方視太陽時と思われるが，計算は地方平均太陽時で与えられている．視太陽時から平均太陽時を引いた差を均時差と呼ぶが，最大約 15 min に達するのでこれ以上の精度を必要とする場合には均時差の補正を必要とする．

観測事実の記録から食の始め・食尽・食の終わりの時刻が判り，$\Delta T = 2000\,\mathrm{sec}$ とした時の $\mathrm{O} - \mathrm{C}$ が計算されれば，近似的には $\Delta T = 2000\,\mathrm{sec} - (\mathrm{O} - \mathrm{C})$ により ΔT が求まる．

表 6 の予測時刻と計算時刻の差を見ると，初虧の時刻が食尽の時刻に対し 1 時間位早くなっている．食尽と復円の時刻差は少数の例外があるが計算値に近い．この時刻差が極端に長い例や短い例 (番号 12, 10 番) は何かの間違いであろう．この点に留意して食尽時刻の予測値と計算値を比較すると，15 分程度の誤差を除くと良く合う例 (975/08/10, 982/03/28, 1029/09/11) と，予測値が 2 時間位早い例が有る事が判る．

良く一致している例は何れも橋本氏の分類で第 4 類に属し，予測値の文献は朝野群載 八巻 陰陽道並びに小右記である．内田 (1975) によると宣明暦では日食の予測地点が陽城とされていると云う．陽城とは洛陽の近くの町で，周の時代から周髀による測量の原点とされていた地点である (ニーダム 1991)．そこで次節で示す如く洛陽で計算してみると予測時刻が合わない．従ってこれらの記録の計算では宣明暦とは云っても計算場所は京都に修正されている．

他方合わない例は時刻が 2 時間近く早いことから陽城での計算値である可能性が高い．

5 計算結果

5.1 975/08/10

この日食に就いて，日本紀略に「日有蝕、十五分之十一或云皆既、卯辰刻、皆既如墨色無光、群鳥飛乱、衆星盡見」，扶桑略記に「辰時日蝕、皆既天下忽暗、己見衆星」，和漢合符に「自辰至未暗如夜」と記載されているので皆既でだった事は確かであろう．この日食が皆既食になる条件から

$$1167\,\mathrm{sec} < \Delta T < 4452\,\mathrm{sec}$$

が得られる．

$\Delta T = 1000\,\mathrm{sec}$ と取った時の京都に於ける太陽の南中時刻は 03:00:05 UT, ΔT が 1000 sec 変わった時の南中時刻の変化は 3 sec なので，京都に於ける太陽の南中時刻は 03:00 UT

表 6: 時刻付き日食の予測時刻と計算時刻の比較.
第 1 列の番号は橋本 (2002) 第十表に於ける日月食番号. * 印は本論文で追加したデータ. 第 3 列の類は太陽時への換算に使用した同じく橋本 (2002) による時刻制度の類別の番号.

番号	年月日	類	初虧	食甚	復円	食分
3	975/08/10		卯 1 刻 3 分	辰 2 刻 1 分	巳初刻 2 分	
		4	05:52:30	08:07:30	09:15	
	計算値		06:45	07:49	08:59	1.01
			(皆既 07:47 - 07:50)			
5	982/03/28		辰 3 刻 1 分	巳 1 刻 2 分	巳 3 刻 3 分	
		4	08:37:30	09:45	10:52:30	
	計算値		09:13	10:03	10:56	0.25
6	1021/08/11		巳 4 刻 1 分	午 2 刻 2 分	同刻 ? 3 分	
		1	08:58	11:29		
	計算値		12:40	14:04	15:20	0.81
9	1028/03/29		寅初	卯 1 刻 47 分	辰 2 刻 61 分	
		1		05:22	07:39	
			(これは No. 10 と同じ日食)			
10	1028/03/29		寅 7 刻 83 分	卯 1 刻 46 分	卯 3 刻 37 分	
		1	04:55	05:22	05:50	
	計算値		05:34	06:33	07:38	0.55
			(日出帯食, 日出 05:42 食分 0.11, 橋本には 1027 年とある)			
12	1029/09/11		卯 1 刻 3 分	辰 1 刻 1 分	巳 1 刻 2 分	
		4	05:52:30	07:37:30	09:45	
	計算値		06:25	07:23	08:28	0.72
15	1080/12/14		巳 1 刻	巳 4 刻 6 分	午 3 刻 5 分	
		3	09:00	10:45	12:12	
	計算値		10:07	12:00	13:50	0.93
			(金環 11:57 - 12:02)			
*	1106/08/01		未 1 刻			
		3	13:00			
	計算値		13:11	14:00	14:47	0.21
*	1112/09/23		日出帯食			
	計算値		04:11	05:09	06:13	0.72
			(日出帯食, 日出 05:36 食分 0.49)			
*	1169/08/24	日	巳 1 刻 27 分	巳 5 刻		
		1	09:19	10:14 分		
	計算値		11:04 分	12:14	13:21	0.55

と取って十分である. 京都の経度は 9 h 03 min だから, 京都に於ける太陽の太陽の南中時刻は 12:03 地方平均太陽時と取って良い. この日食が京都で視太陽時 07:00 に始まったとして, これを平均太陽時に直すと 07:03 にが得られる. $\Delta T = 2000\,\mathrm{sec}$ に取った時の京都に於ける食の始めは 06:45 平均太陽時なので, $\mathrm{O} - \mathrm{C} = 18\,\mathrm{min} = 1080\,\mathrm{sec}$ となる. 従って $\Delta T = 2000 - (\mathrm{O} - \mathrm{C}) = 920\,\mathrm{sec}$ が得られる. この日食が皆既の条件から $\Delta T > 1167\,\mathrm{sec}$ だから, この日食は 07:00 視太陽時より $1167 - 920 = 247\,\mathrm{sec}$ 以上前に始まらなければならない. 言い換えると 4 min 以上は卯の間であったことになる.

日本紀略の卯辰刻を採用すると 09:03 平均太陽時以前に食が終わらなければならないので, 復円を 09:03 平均太陽時とする. $\Delta T = 2000\,\mathrm{sec}$ の時の復円時刻は 08:59 平均太陽時だから, $\mathrm{O} - \mathrm{C} = 4\,\mathrm{min}$ が得られる. 従って $\Delta T = 2000 - (\mathrm{O} - \mathrm{C}) > 1760\mathrm{sec}$ が得られる.

この日食の継続時間は約 2h14m = 1 辰刻 2 分 足らずなので和漢合符の「自辰至未」は有り得ない. 日本紀略の「卯辰刻」をこの日食の始まりが卯の終わりから一分以上前を意味すると考えると, 終わりは巳に入って 1 分以下となる. 考えられるのは「未」が「巳」

の誤記又は誤写であるが, 日本紀略並びに扶桑略記が共に辰で終わっていることを考慮すると辰の終わり近くまで続いたと言うことであろう. これらを考慮すると $\Delta T = 1760\,\mathrm{sec}$ は数分程度の誤差で正しいと考えて良かろう.

この表に記載した全ての日食に就いて初虧は計算値に比べて約 1 時間以上早い. 従って初虧の予測値は全ての食に就いて信頼できないが, この日食の食尽時刻と復円時刻は計算値と 15 分程度で合致している. 内田 (1975) によると宣明暦では食の計算値が陽城とされていると云う. そこで洛陽でのこの日食の初虧・食尽・復円時刻を計算すると夫々 05:14, 06:07, 07:06 となり, 朝野群載の数値と異なる. 従って朝野群載に記載された食尽・復円時刻は京都の値となっていることが確かめられた.

5.2 982/03/28

この日食に関しては特に詳しい記述は無いが, 食尽・復円時刻は計算と良く合っている. 食尽・復円の予測時刻が記載されている小右記に「日蝕叶暦」は正しい. この日食の洛陽での食尽は 08:03:08 平均太陽時であるが, 食分は -0.06 で, 日食にはならない. 予測時刻が京都での時刻であることは間違いない.

5.3 1021/08/11

復円時刻が食尽時刻に近すぎて計算間違い以外は考えがたい. 食尽時刻も実際の値より 2 時間以上早い. 洛陽での食尽予測時刻は 11:56:49 なので, 中国に於ける予測時刻であろう. 日本に於ける予測時刻とは考えられない. 日本紀略に「日蝕叶暦」と記載されているが, これだけの時刻差が有っても「日蝕叶暦」と書いたのか, 他に正しい予測時刻が有って書いたのかは判断資料無し.

5.4 1028/03/29

予測時刻が 2 説書かれているが, 食尽時刻は殆ど差がない. 予測時刻が京都の日の出前だったので届け出なかったものであるが, 洛陽での食尽時刻を計算すると, 05:03:59 となるが, 高度は $-9°$ となるので, 食尽は日の出前

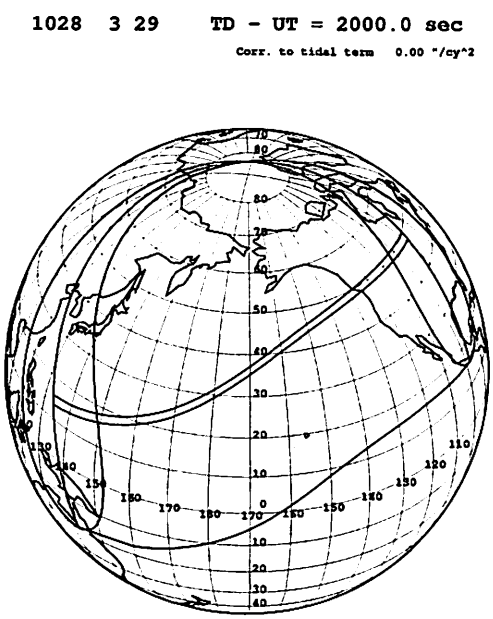

図 5: 1028/03/29 の日食帯.

である. 食尽は日の出前であるが, 復円の前に日の出となるので, 洛陽でも日食は日の出直後に見られる計算となったに違いない. 日の出前の予測が出るのは洛陽より西の地域の計算の場合. 図 5 はこの日食の日食帯の図で中国東部より東で朝日食が見られたことがしめされている. 日本紀略の記録から京都では日の出時に日食が観測されたことが判るが, 図 5 もこの事実を示している.

暦家が注記しなかった為に中務省が廃務にしなかったことが記されているが, この記録から, 982 年には正しい予測が実行されていたにも関わらず, 1028 年には暦家が洛陽より西の地点での予測を報告していたと判断される. この後 1029/09/11 の日食の食尽時刻は計算値と合っているが, 復円時刻が一見しただけで判る程遅くなっている. その他本論文で扱っている 1148 年の日食迄橋本論文で扱っている記録には正しい時刻を与えているものがない. この点が今後の課題である.

5.5 1029/09/11

洛陽に於ける食尽は 05:46:59 で日の出時が食の最大となる. 復円時刻が食尽時刻から大きく離れており, 誤記・誤写などの誤りと考えられる. 食尽時刻は計算と合致して居り, これ

が本論文で扱っている期間の中では最後の計算と一致する記録である.

5.6 1080/12/14

洛陽では食尽が 09:28:28 で, 食分は 0.95. 09:24:31–09:32:26 の間金環食となった. 京都では 11:57–12:02 の間金環食になったはずであるが, 食分が 0.93 なので, それ程は暗くならない. 記録によると金環食の時間帯は曇りで金環食は見られなかった.

5.7 1106/08/01

洛陽では食尽が 11:37:02 であるが, 食分は −0.04 で, 食にはならない. 宋史には「崇寧五年七月庚寅朔日當食不虧」と記されている. この日食に就いては観測記録のみが有り, 予測時刻が書かれていない. これは当時使われていた暦法では食にならない為ではなかろうか. これは日食予測に使われていた暦法が中国の値を与えていた為と思われる.

食の継続時間が 1h 36m 程なので, 未刻に日食と書かれているのを食尽が $14:00 \pm 15\,\mathrm{min}$ とすると, $\Delta T = 2000\,\mathrm{sec}$ の時の食尽が 14:00 だから, $\Delta T = 2000 \pm 900\,\mathrm{sec}$ となる. 翌年 1107/12/16 の日食が京都で金環食になる範囲が $1567\,\mathrm{sec} < \Delta T < 2648\,\mathrm{sec}$ だから, 記録通りに未刻の日食となる. 京都では食分が 0.21 程度になる.

5.8 1106/12/27

この日食は橋本論文では第 2 類に分類されている. 従ってこの日食に就いての永昌記に記載されている予測時刻は初虧未 2 刻 32 分, 食尽未 3 刻 36 分, 復円未 4 刻 27 分は夫々 13:40, 13:55, 14:07 視太陽時となる. 従ってこの日食は予測通りならば十分に観測されるはずだったが, 永昌記によれば, この時刻を過ぎても日食が無かったと記されている. この日食はモンゴルを中心とした地域で見られた部分食で, 日本では全く見られない. 予測時刻が日本の値で無いことは間違いが無い. 図 6 はこの日食の日食帯を示す.

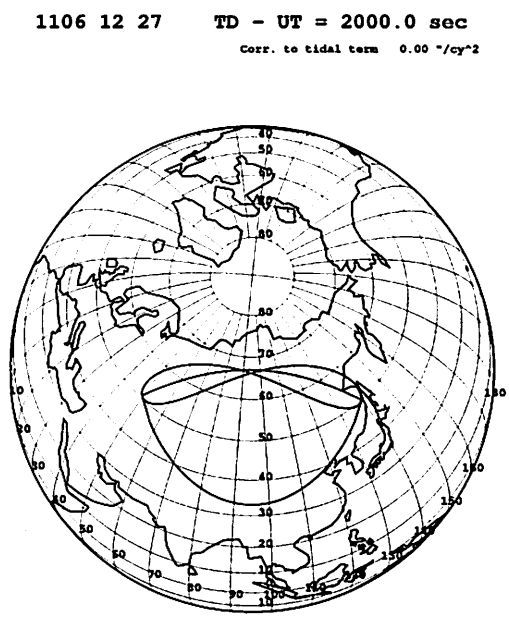

図 6: 1106/12/27 の日食帯

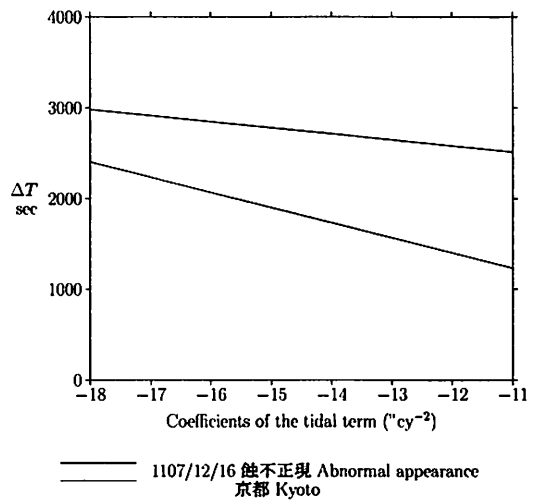

図 7: 1107/12/16 の日食が京都で金環食となるパラメータ領域.

5.9 1107/12/16

第 5 に掲載したこの日食に関する記録は, この日食が日没直前の金環食だった事を示していると思われる.

$\Delta T = 2000\,\mathrm{sec}$ に取った時, 16:36 - 16:41 の時間帯が食分 0.96 の金環食になる. 日没は 16:49 で, 食分は 0.83. 図 7 は 1107/12/16 の日食が京都で金環食となるパラメータ領域を示したもので, 横軸には潮汐項を, 縦軸には ΔT を取っている. この図の 2 本の実線の間が京都で金環食となるパラメータ領域である.

潮汐項は $-13''/\mathrm{cy}^2$ と知られているので, 潮汐項がこの値の ΔT の範囲, 即ち 1567 sec $< \Delta T <$ 2648 sec 京都で金環食となる ΔT の範囲を示す.

5.10 1112/09/23

洛陽では食尽 03:51:05, 高度は $-26°$ で日の出前, 食の終わりは 04:46:16, 日の出は 05:55 で食は日の出前となる. この日食に就いては予測時刻が残されていない. 京都では日の出は 05:36 で, $\Delta T = 2000$ sec の時, 日の出時の食分は 0.49, 食の終わりが 06:13. 中右記に日の出の時に少しばかり日食が見られたことが記録されている. この日食が日の出後に見られる為には食の終わりの時刻が日の出時刻より後でなければならない. そこで食の終わりを日の出時刻だったとすると, $\Delta T = 2000$ sec とした時の $\mathrm{O-C} = 05:36 - 06:13 = -37$ min $=$ 2220 sec となる. 従って, 食の終わりが日の出時刻と一致した場合の ΔT は 4220 sec となる. 従って, $\Delta T <$ 4220 sec ならばこの日食は日の出後に見られたこととなり記録と合う. この時代の ΔT は凡そ 2000 sec だから中右記の記録が正しいことがしめされる.

5.11 1169/08/24

この日食は今江 (1995) が見出した, 神田 (1935) に記載されていない日食で, 渡邊 (1979) も日本の日食としては取り上げていなかったが, 南宋・金・朝鮮の記録にあることが示されている. 図 8 はこの日食の日食帯を図示したものである. 洛陽での食尽は 10:01:57, 食分は 0.15. 記録の食尽予測時刻は洛陽の値に近い.

6 まとめ

本論文では, 橘本 (2002) の予測時刻付き日月食の表の内, 1148 年迄の日食に, 観測時刻が記載されている 1169/08/24 (今江 1995), 1106/08/01, 1112/09/23 の三つの日食を追加した総数 17 の日食に就いて, 記載されている時刻に関する吟味を行った.

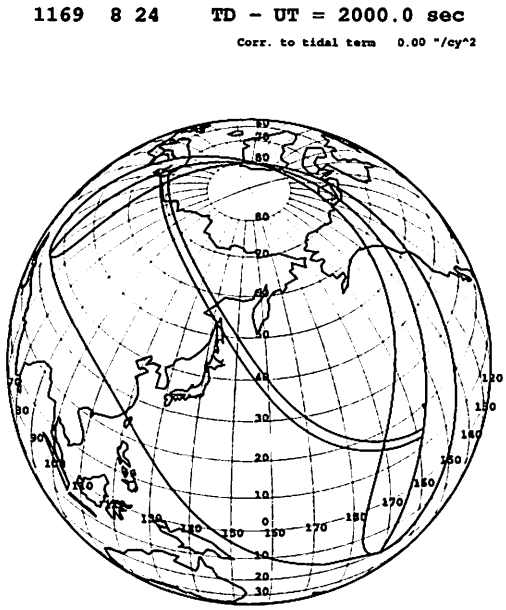

図 8: 1169/08/24 の日食の日食帯.

この吟味により 982 年迄の日食予測時刻は京都の値になっているが, 1021, 1028 年の日食は中国での日食時刻であり, その後は 1029/09/11 の日食の食尽時刻を除いて全て中国での予測値となっている. 中国で日の出前の食の場合には日本では日の出後となっても予測時刻の記録が見当たらず, 中国で日没前の場合には日本では日没後でも予測時刻が書かれ, これらの場合には予測と観測が異なったことが記載されている.

本論文で扱っている橘本論文の日食は 1148 迄で, これに 1169 の日食が一例追加してあるだけであるが, その後の日食予測がどの様になっているかは今後の問題として残されている.

謝辞

本研究は文部科学省科学研究費補助金 特定領域研究 14023233 により行われた.

杏林大学横尾広光氏には有益なご意見を頂いたことに感謝いたします.

参考文献

[1] Cowell, P. H., 1905, M.N., **66**, 3-5.

[2] Cowell, P. H., 1906a, M.N., **66**, 352–355.

[3] Cowell, P. H., 1906b, M.N., **66**, 523–541.

[4] Cowell, P. H., 1907, M.N., **68**, 18–19.

[5] Fotheringham, J. K., 1920, M.N. **81**, 104–126.

[6] Hansen, P. A., 1857, Tables de la Lune construites d'apres le Principe Mewtonien de la Gravitation Universelle. H. M. Statopmery Office, London.

[7] Liu, Bao-Lin, and Fiala, Alan D., Canon of Lunar Eclipses 1500 B.C. – A.D. 3000, Willmann-Bel, 1992.

[8] Jones, H. Spencer, 1939, M.N.,**99**, 541–558.

[9] Neugebauer, P.V., 1912, 1915, 1925, *Tafeln zur astronomischen Chronologie I, II, III*, J.C. Hinrichs'.

[10] Neugebauer, P.V., 1929, *Astronomische Chronologie I, II*, Walter de Gruyter & Co. (Berlin).

[11] Newcomb, S., 1895, Astron. Pap. Amer. Eph., **6**, Part 1.

[12] Oppolzer, Th. Ritter von, 1962, Canon of Eclipses, translated by O. Ringerich, Dover Publications Inc. New York. Originally published as vol. 52 of Memoirs, Mathematics Natural Sciences Class of the Imperal Academy of Sciences in Vienna (1887).

[13] Schoch, K., 1927, *Planeten-tafeln für Jedermann*, Linser-Verlag (Berlin).

[14] 今江廣道著, 1995, 陽明文庫所蔵「兵範記」断簡所見 – 日食記事とその年次, 「日本歴史」, 1995 年 5 月号, p. 86.

[15] 内田正男著, 1975, 「日本暦日原典」, 雄山閣.

[16] 小倉伸吉著, 1916, 天文月報, 第 9 号, 13–18, 25–29, 39–43, 52–55, 62–64.

[17] 神田 茂著, 1935, 「日本天文史料」, 恒星社.

[18] 斉藤国治著, 1986, 「国史国文に現われる星の記録の検証」, 雄山閣.

[19] 斉藤国治・小沢賢二著, 1992, 「中国古代天文記録の検証」, 雄山閣.

[20] ニーダム, ジョセフ著, , 東畑精一・藪内清監修 1991, 「中国の科学と文明 第 5 巻天の科学」, 思索社.

[21] 橋本万平著, 2002, 「日本の時刻制度」, 塙書房.

[22] 長谷川一郎著, 1995, 「『月食ナシ』と注記された日本天文史料について」, 大手前女子短期大学・大手前栄養文化学院・大手前ビジネス学院「研究集録」第 15 号, 290–297.

[23] 渡邊敏夫著, 1979, 「日本中国朝鮮–日食月食宝典, 雄山閣.

中国・日本の古代日食から推測される地球慣性能率の変動

河鰭公昭[1], 谷川清隆[2], 相馬 充[2]

[1]：名古屋大学 (名誉教授), [2]：国立天文台

Time variation of the moment of inertia of the Earth derived from Chinese and Japanese records of ancient solar eclipses

Kin-aki KAWABATA[1], Kiyotaka TANIKAWA[2] and Mitsuru SÔMA[2]
[1] : Nagoya University (Emeritus Prof.), [2] : National Astronomical Observatory
kawabata-nagoya@jcom.home.ne.jp

Abstract

Time variation of the Earth's rate of rotation from BC 709 through AD 975 is obtained from Chinese and Japanese records of solar eclipses. Chinese records employed in the present article are the Ch'un-ch'iu 春秋 focused on Lu 魯 affairs, the chronological tables of the Shih-chi 史記 六国表第三 (chap. 15), the Han-shu 漢書 (chap. 27), the Hou-han-shu 後漢書 (chap. 28), San-kuo-chih 三国志 (chap. 4), the Chin-shu 晋書 (chap. 12), the Song-shu 宋書 (chap. 34), Liang-shu 梁書 (chap. 3), Nan-shi 南史 (chap. 2, 6, 7), the Sui-shu 隋書 (chap. 4), the Chiu-t'ang-shu 旧唐書 (chap. 6), and the Hsin-t'ang-shu 新唐書 (chap. 32). Japanese records employed in the present article are the Nihongi 日本書紀 (chap. 22), the Sandai Jitsuroku 三代實録 (the Veritable Records of the Three Reigns 858–887), (chap. 24) and the Nihonkiryaku 日本紀略 (Outlines of the Annals of Japan, Chronicle up to 1036) (chap. 6).

We have selected 31 records of solar eclipses with descriptions of one of words of "total", "complete", or "stars were seen" in these Chinese books. Japanese records of candidates of total eclipses employed in the present article are from the list (3 of eclipses in the list appear to be total) by Ogura (1916).

Except a solar eclipse recorded in the Han-shu (chap. 27) as "Chien-chao reign period, 5th year, 6th month, day jen-shen, the last day of the month, a solar eclipse, not complete and like a hook 建昭五年六月壬申晦日有食之不盡如鉤 (BC 34/8/23)", 33 eclipses are identified with eclipses in the table of Canon of Eclipses by Th. Ritter Oppolzer (translated by Gingerich). The longitude of the moon measured from the ascending node of the lunar orbit at the time of conjunction in solar and lunar ecliptic longitude on BC 34/8/24 is 313.°68 and then the sun is not eclipsed in the conjucntion.

The sun on "Yuan-chia reign period, 30th year, 7th month, day hsin-ch'ou, the first day of the month 元嘉三十年七月辛丑朔" (453/8/20) was eclipsed in the region from South Atlantic Ocean through the Indian Ocean and then the eclipse recorded as "a total solar eclipse and stars were seen" in the Song-shu 宋書 (chap. 34) could not be observed in China. Therefore the eclipse was recorded in the book according to a prediction.

In two eclipses recorded in the Han-shu (BC 2/2/5) and the San-kuo-chih (243/6/5), the sun was totally eclipsed in an area far from the capital at that time but in the Chinese territory.

On tidal term versus ΔT plane (ΔT = TT − UT), we plot an area of parameters which gives total/annular eclipse in the capital of the dynasty. Since the tidal term and ΔT will not change significantly within short period, we expect substantially the same values of these paramaeters for two succsesive total/annular eclipses occurring within a period of 60 years. When we plot such belts for two successive eclipses occuring within a period shorter than 60 years, these two belts cross at the tidal term of $-13\,\mathrm{arcsec/cy^2}$. We can clearly see the feature in Figures 17, 21, and 22. The result agrees well with $(-12.94 \pm 0.25)\,\mathrm{arcsec/cy^2}$ obtained by Dickey *et al.* (1994) by LLR (lunar laser ranging). In other cases, two belts are more or less parallel and then we can not determine the tidal term.

In the next, we determine a range of ΔT for pairs of eclipses occuring within a period shorter than 60 years in such a way that ΔT in the range

gives eclipses with features described in these records, when data are available. We have determined ΔT's for 19 solar eclipses in this way and shown these in Figure 28 by thick vertical lines.

7 eclipses are separated from the others more than 60 years apart and then ΔT are determined from a single solar eclipse and these are shown by thin vertical lines in Figure 28.

Remaining 4 eclipses are recorded as "not complete". Our calculation for each eclipse indicates that the sun is not totally eclipsed at the latitude of the capital at that time but the magnitude of 3 eclipses among 4 is high. Therefore the descriptions in these books can be justified for these 3 eclipses.

These eclipses are, however, omitted from our analysis because our method can not be applied for these eclipses.

Figure 28 and 29 show ΔT versus year and O − C versus year plot of our results, respectively. Here C means the parabolic fitting by Stephenson (1997). The solid curve in Figure 28 shows the tidal components $\Delta T_{\rm tidal}$ of ΔT, for the tidal term of $-13.0\,{\rm arcsec/cy^2}$ obtained by Stephenson (1997). The long dashed curve in Figure 28 is the one obtained by a parabolic fiting by Stephenson (1997). For a convenience of comparison of our results with Stephenson's one, his spline fitting is also shown by a short dashed line. These figures show irregular variation of ΔT with a time scale of 600—1000 years is added to the parabolic line (long dashed curve).

Nontidal components of ΔT, $\Delta T_{\rm nontidal} = \Delta T - \Delta T_{\rm tidal}$, are due to variations of the moment of inertia of the earth. Suppose that glaciers in polar regions melt and then the sea level rises by 1 m. When we take into account that the total area of the sea is 2/3 of the earth surface, the total mass of melted ice becomes 3.5×10^{20} gr.

Putting the radius of the earth to R, we adopt an approximation that the mean square distance of the mass from the rotation axis of the earth is $\frac{2}{3}R^2$. We assume that the mean square distance of glaciers before melting is negligibly small comparing with $\frac{2}{3}R^2$. Then the increase of the moment of inertia of the earth is by a factor of 10^{-7} when the sea level rises 1 m due to melting of glaciers. The length of the day increases by 10 ms in this case. Supposing that the sealevel continues to rise over 1000 years in a constant rate, ΔT increases by 30 min. Therefore, the variation of the sea level due to the variation of atmospheric temperature in the polar region is a probable cause of the variation of the length of the day in hundreds of years or in a millenium.

1 はじめに

Stephenson (1997) によると地球の自転が潮汐の影響で減速するとの考えは Immanuel Kant により 1754 年に提出されている. Kant の推定した減速は現在の値の 2000 倍に相当するが, 考え方は基本的には同じである. 地球の自転周期が一定のレートで長くなると, 地球の自転周期で決めた時刻系による月黄経の表式に θ^2 (θ は任意のエポックから数えたユリウス世紀 36525 日) に比例する項が付け加わり, 月黄経の永年加速と呼ばれた. その値が約 $10\,{\rm arcsec/cy^2}$ であることは既に 18 世紀の中頃に知られ, 月黄経は 200 年で 10 arcsec の四倍の 40 arcsec だけ進み, 2000 年後には 400 倍の 4000 arcsec 進む計算になる.

Laplace は 1786 年に惑星の重力により地球軌道の離心率が減少することに伴い月黄経が $11.135\,{\rm arcsec/cy^2}$ の割合で減少することを示し, Adams は 1853 年に Laplace の計算の精度が不十分であることを指摘し, その値を $5.78\,{\rm arcsec/cy^2}$ に修正した. Chapront (1983) によるこの理論値は $6.0643\,{\rm arcsec/cy^2}$ となっている. 19 世紀の中頃になると春分点に永年加速が見つかり, Hansen (1857) は $1.1\,{\rm arcsec/cy^2}$ の数値を得ている. 月黄経の永年加速の観測値には春分点の移動によるものが加わっているので, これを差し引いたものが恒星系に対する月黄経の永年加速になる. 春分点の永年加速の最近の値 (Lasker 1986) は $1.112\,{\rm arcsec/cy^2}$ である.

Oppolzer (1887) は Hansen (1857) の月要素と Leverrier (1858) の太陽要素を使って, BC 1208 年 11 月 20 日から AD 2161 年 11 月 17 日までの 8,000 回の日食と 5,200 回の月食を記載した Canon der Finsternisse を発表した. この日食表では 1258 年 11 月 28 日で終わっている一つのサロス周期の後に続く数回の極を僅かにかすめるだけの日食と数回の月食が脱落していることが知られているが, これを除くと完全な日月食表になっていると云われている. この脱落は当時の月の運行式の不完全さに起因している.

その後, Ginzel, Cowell, Newcomb, Radau, Fotheringham, Schoch 等により中近東・地中海地域の日食の解析から月黄経の永年加速の研究が精力的に行われ, これらの研究は渡辺 (1979) に詳しく紹介されている. Fotheringham (1920) は歳差の加速以外に月黄経の永年加速として $10.8\,{\rm arcsec/cy^2}$ を, 太陽黄経の永年加速として $1.5\,{\rm arcsec/cy^2}$ を得た. 太陽黄経の永年加速が地球自転速度の減衰によるものと考えると, この地球回転の減速は月黄経に太陽黄経の永年加速の 13.4 倍 (恒星年と恒星月の比) の永年加速 $1.5\,{\rm arcsec/cy^2} \times 13.4 = 20.1\,{\rm arcsec/cy^2}$ を生じる. これに惑星の影響による $6.0\,{\rm arcsec/cy^2}$ を加えた $26.1\,{\rm arcsec/cy^2}$ が地球の自転速度の減衰と惑星の影響による月黄経の永年加速になる. Fotheringham が得た月黄経の永年加速は $10.8\,{\rm arcsec/cy^2}$ だから, Fotheringham の得た値には、理論的に得られた上記の $26.1\,{\rm arcsec/cy^2}$ との差 $-15.3\,{\rm arcsec/cy^2}$ だけ未知の加速が加算されていることになる. この差が今日月

黄経の潮汐項と呼ばれているもので, 地球・月系の角運動量の保存から潮汐による地球の自転の角運動量の減少に伴って起こる月の角運動量の増加によるものである. Spencer Jones (1939) は 1680—1939 の期間の月・太陽・水星・金星の平均黄経の不規則的変動が同期し且つこれらの天体の平均運動に比例していること, 太陽・水星・金星の永年加速が月の永年加速に比例することを示し, 上記の考えが正しいことを実証した.

月の平均距離を r, 公転運動の角速度を n と置くと, ケプラーの第三法則 $n^2r^3 = \text{const.}$ の時間微分により,

$$\frac{\dot{r}}{r} = -\frac{2}{3}\frac{\dot{n}}{n}$$

が得られる. この式に月の距離は $r = 3.84 \times 10^8$ m, 及び月の平均運動 $n = 1.732 \times 10^9$arcsec/cy を代入すると, $\dot{n}$ の単位を arcsec/cy^2, $\dot{r}$ の単位を m/cy とした時に, $\dot{r} = -0.148\dot{n}$ が得られる. 月黄経の加速 $\dot{n}$ は潮汐項の二倍だから, その今日の値 $-13\,\text{arcsec/cy}^2$ の 2 倍 $\dot{n} = -26\,\text{arcsec/cy}$ を代入すると, 月が 3.85 m/cy の割合で遠ざかっていることが判る. これは 1 恒星月の長さが, 0.038 sec/cy の割合で伸びることを示す. これは BC 700 から現在までの恒星月の伸びが 1.0 sec に過ぎないことを示す.

他方 20 世紀の中頃には, 水晶時計の時刻精度が天文観測から決める時刻精度を上回るようになった. こうして 1952 年の IAU 総会は世界時 (UT) に地球回転の永年減速の補正を行った暦表時の採用を決定し, 次いで 1967 年に原子時計により決まる SI 秒が時刻単位として用いられるようになった. 一般相対論によるとあらゆる座標系で共通して使える時刻系は存在しない. そこで SI 秒と合う地球中心の座標系で一般相対論の使える時刻系としての力学時 (TT) と太陽系中心で使える力学時が使われるようになった.

以来, 日月食・掩蔽の計算は潮汐項と $\Delta T = \text{TT} - \text{UT}$ をパラメータとして行われるようになった. ところで, ΔT のかなりの部分は潮汐効果による部分 ΔT_{tidal} なので, 潮汐項と無関係に独立に指定される量 (直交関係の量) は $\Delta T_{\text{nontidal}} = \Delta T - \Delta T_{\text{tidal}}$ となる. Stephenson (1997) は Christodoulidis *et al.* (1988) が月・地球系の角運動量の保存則を基にして得た月の潮汐加速 $\dot{n}$ と地球回転の加速 $\dot{\omega}_{\text{T}}$ の間の経験的関係式

$$\dot{\omega}_{\text{T}} = (+49 \pm 3)\dot{n}\,\text{arcsec/cy}^2$$

を採用し, 潮汐項を $-13\,\text{arcsec/cy}^2$ とした時に得られる

$$\Delta T_{\text{tidal}} = (44 \pm 2)t^2 - 20\,\text{sec} \qquad (1)$$

を用いている. ここで t は 1820 年をエポックとしたユリウス世紀を表す. $\Delta T_{\text{nontidal}} = \Delta T - \Delta T_{\text{tidal}}$ は地球の慣性能率の変化によると思われる.

1969 年のアポロ 11 号による月探査の際に宇宙飛行士アームストロングが月面にレーザー測距用の反射鏡を設置して以来, 潮汐項はレーザー測距により求められるようになった (Calame and Mulholland 1978). Calame and Mulholland が得た潮汐項は $(-12.3 \pm 2.5)\,\text{arcsec/cy}^2$ で Fotheringham, Spencer Jones の得た値と誤差範囲で一致している. Dickey *et al.* (1994) による潮汐項の値は $(-12.94 \pm 0.25)\,\text{arcsec/cy}^2$ で, 誤差範囲も大分小さくなった.

2 東洋の日食の解析

東洋の古代日食記録の解析は多分小倉 (1916) が最初であろう. 小倉は Opppolzer の月位置を採用し, 628 年—1183 年 の期間の日本の日食記録の検証を行い, 数多くの日食・月食について観測事実でなく予測により執筆されていることを指摘している. 又皆既日食と記されている 628/4/10, 873/7/29, 975/8/10 の三つの日食については, Hansen, Oppolzer, Ginzel, Cowell, Newcomb, Radau の月要素を使って, 採用月要素による食尽時刻・食分の差を論じている.

その後, 1940 年に東方文化京都研究所 (後の京都大学人文科学研究所) の暦算研究室長の能田忠亮氏の尽力で設けられた臨時東洋暦術調査会の事業として東洋の日食表の作成が企画され, 渡辺敏夫氏が委嘱されている. 渡辺 (1979) は Schoch の月要素を用いて, BC 801—AD 1900 の期間に 100°E—150°E, 10°N—50°N の地域で起った皆既食・金環食・皆既金環食 823 回総てを含む日食要素表・中心食帯表・中心食帯図を作成し, 更に中国・日本・朝鮮の歴史書に記載された日食の夫々の観測地点に於ける食尽・食分を計算した. この研究成果は戦時中の為出版されないままとなり, 一部がその後渡辺氏の所属した商船大学の研究報告として印刷された程度に留まっていた. 渡辺氏の研究成果はその後 1979 年に至り雄山閣から出版され, 1994 年にその復刻版が出版されている.

日本・中国・韓国の歴史資料に掲載された日食に関する食尽・食分の計算はこの他に鈴木 (1942), 内田 (1975), 斉藤・小沢 (1992) に掲載されているが, 何れも 20 世紀初頭の論文で採用された計算方法に従ったもので, その後の天文学の進展は考慮されていない.

最も大きな問題は地球の自転速度はこれらの論文で仮定されているように, 一定の比率で減速しているものでは無いと言うことである. 暦表時及び SI 秒 (原子時) の一日は 19 世紀中頃の一日に合わせられている. 従って暦表時や原子時が導入された頃の一日の長さは原子時の一日より大分長くなっている. そこで実用時刻系としては SI 秒で進むが「うるう秒」を必要に応じて挿入し地球の太陽に対する自転角を略表す協定世界時が使われるように変わった. 図 1 は 1920 年以来最近までの ΔT をプロットしたものである. この図を見れば実際の ΔT の変動が一定比率の日の長さの増大とは程遠いことが判ると思う.

地球回転の不規則的変動に関して最近の例を上げると 1985 年頃迄の約 20 年間は毎年の様に「うるう秒」が挿入されていた. これは 1965—1985 年の一日が 19 世紀中頃の一日より約 1/365 秒長くなっていたことを

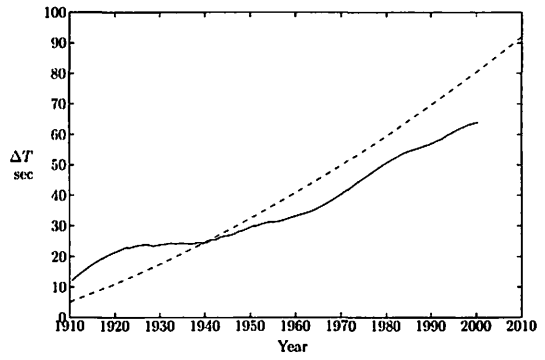

図 1: 1910 年以来の ΔT (理科年表による). 破線は Stephenson (1997) の得た parabola 近似.

示す. それが 1985 年を過ぎると「うるう秒」が挿入されることが少なくなった. これは最近の一日が 19 世紀の一日に逆戻りしつつあることを示している.

20 世紀初頭迄の論文は月黄経の永年加速 (年に比例する速度の増加) を求めることを眼目としたもので, 紀元前・西暦 1000 年前後・19 世紀の月平均黄経を世界時の二次式で表したものである. これらの研究は力学で定義されている時刻系 (力学時) を観測から探し出すと云う目的からは大変有意義だった. 然しながら, これらの計算式は永年加速に付け加わる地球自転の不規則的変動を含まず, 与えられた世界時での月の正しい位置は与えない. 従って本来, 計算と合うかどうかで古書を評価する議論とは馴染まないものである.

図 2 は Stephenson (1997) に掲載されているバビロニア・ギリシャ・アラブの時刻の記載された日月食の ΔT をプロットしたものである. これらのデータは 19 世紀中頃から 20 世紀初頭までの研究に使用されたものと同じではないが, これらの地域のデータには西暦元年頃からアラブの観測の始まる 9 世紀までのデータが欠落していることが判る. Fotheringham が扱った日食は BC 1063, BC 763, BC 648, BC 585, BC 463, BC 431, BC 310, BC 129, 29, 71, 364 である. 渡辺 (1979) によると, Oppolzer の共同研究者である Ginzel の研究では Oppolzer の使った紀元前のデータが除かれ, 採用されたのは 71, 590, 733, 840, 878, 891, 939, 968, 1030, 1093, 1133, 1147, 1178, 1185, 1187, 1191, 1207, 1239, 1241, 1267, 1330, 1386 の日食である. 19 世紀後半から 20 世紀初頭にかけて行われたヨーロッパ諸国の日月食の研究は図 2 の長破線から永年加速を求めたことと略等価である. Stephenson (1997) はこれらのデータに中国の記録によるものも加え, 図の短破線のスプラインを得ている.

谷川・相馬 (2001), Tanikawa and Sôma (2001) は渡辺 (1979) 及び斉藤・小沢 (1992) に与えられている食分が日本書紀の記述と合致しないのは, これらの著書が採用している計算法に問題があることを指摘し, 潮汐項を $-13\,\mathrm{arcsec/cy^2}$, $\Delta T = 2000\,\mathrm{sec}$ 或いは潮汐項を $-15\,\mathrm{arcsec/cy^2}$, $\Delta T = 3000\,\mathrm{sec}$ に取ると推古三十

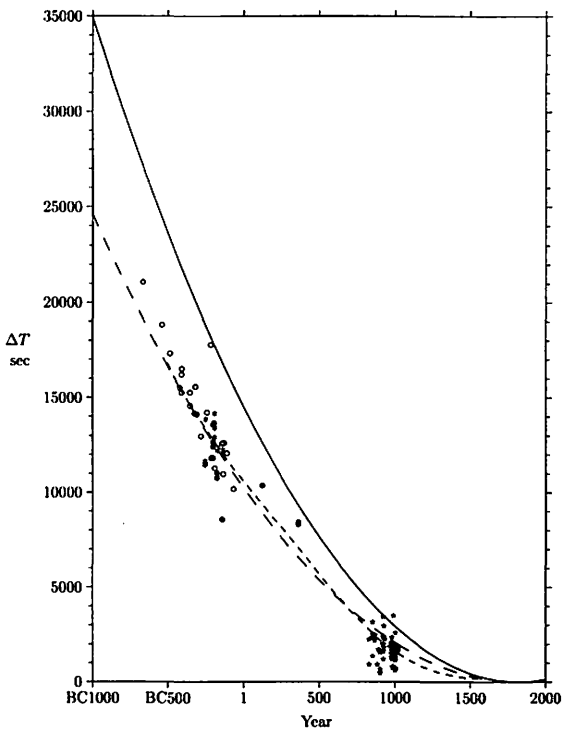

図 2: 時刻の記録されている日月食から求めた ΔT (Stephenson 1997). ○: Babylonia (solar and lunar < 25deg), ∗: Babylonia (solar > 25deg), •: Ancient Greek, ⋆: Arab. 実線: $\Delta T_{\mathrm{tidal}}$. 長破線: parabola 近似. 短破線: spline 近似

六年の日食が飛鳥で皆既に近くなることを示した. また, 河鰭・谷川・相馬 (2002) は隋書の煬帝紀に「既」と記載されている大業十二年 (616/5/21) の金環食 (中国の史書では金環食も「既」と記されている) が斉藤・小沢の著書と同じく長安で観測されたものと仮定し, 日本書紀の推古三十六年に皆既と推定される記述がある日食 (628/4/10) が飛鳥で観測されたものとして, 潮汐項を $-15\,\mathrm{arcsec/cy^2}$, ΔT を 3000 sec にと取ると, 夫々の食が金環食及び皆既食に近くなることを示した. 又潮汐項及び ΔT をこの様に取ると, 日本書紀の推古紀, 舒明紀, 天武紀に記載された日月食の記事が良く説明され又彗星の記事が中国の記録と合うこと, 持統紀に記されている日食は総て日本では観測出来ないことから総て予測によること, 日本書紀に天文関係の記録が始まる推古紀以降の巻でも皇極・孝徳・斉明・天智の各巻には天文関係の記録が殆ど無く有っても日本では観測出来ないものばかりであることを示した.

日本書紀には用字その他に巻による相違が多々有り, これらによる巻の分類が日本書紀研究者によりなされている. これらの分類と天文関係の記録の相違とを対比させると森 (2000) の分類と一対一の対応が付くことが判った. 森の分類によると, 推古, 舒明, 天武の各巻の特徴は引用歌謡を書くのに音標文字として使う漢字が和音により選択されていることで, 文章には漢文として文法上の誤りや慣用と異なるがもの多い. これ

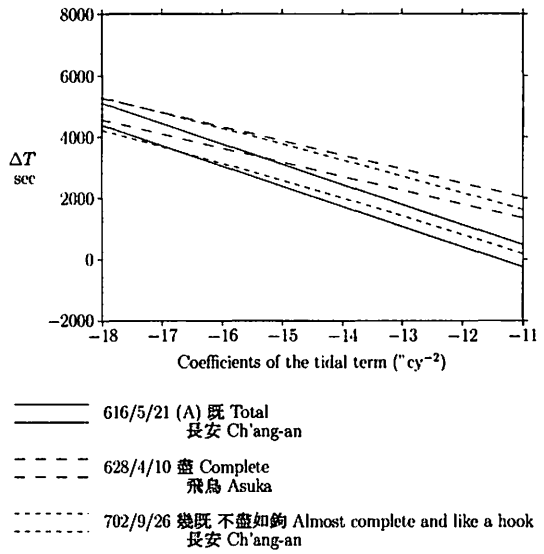

図 3: 図 22 の 616/5/21 の金環食が長安で金環食となるパラメータ領域.

に対して皇極・孝徳・斉明・天智の各巻では唐代の北方中国音により音標文字が選ばれている. 又これらの巻の筆者は日本の習慣に疎いところが多く, 文章は正格漢文であることから森は渡来中国人と推定している. 持統紀には歌謡その他の引用文が殆ど無く, 音標文字による分類は不可能であるが, 文章が正格漢文であることから, 森は筆者は中国人と推定している.

因みに日本書紀の持統紀には「日有蝕之」, 皇極紀には「月有蝕之」が有り, 漢書以降の中国史書と同じである. 他方推古紀・舒明紀・天武紀では「日蝕之」・「日有蝕尽之」・「日蝕」「月蝕」が使われている. 「日蝕」は史記で使われているが, 「日蝕之」・「日有蝕盡之」は中国史書に見当たらない. 中国史書では「日蝕之」の次には「変」や「咎」などが付き, 「日蝕之変」・「日蝕之咎」などの語句として使われ, 「日蝕之」が単独で使われている例は見当たらない. 中国史書で中心食又はそれに近い場合には「日有蝕之既」・「日有蝕之幾盡」・「日有蝕之不盡」・「日有蝕之幾既」が使われ, 「幾盡」・「不盡」はあるが「盡」が単独で使われている例は見当たらない.

河鰭・谷川・相馬 (2002) の問題点は採用した潮汐項がレーザー測距による値と一致しないことである. 日月食の計算には潮汐項と ΔT と二つのパラメータが有り, 一つの日食では一義的には決まらない. 推古三十六年の日食が皆既になるとの条件からは潮汐項と ΔT の面上で一つの帯状の領域が決まる. 例えば潮汐項を $-13\,\mathrm{arcsec/cy^2}$, $\Delta T = 2000\mathrm{sec}$ と取っても推古三十六年の日食は皆既に近くなり, 日本書紀に記載されている天文記事に関しては同じ結論が得られる. 然しながらこの場合大業十二年の日食は長安では金環食とは程遠い.

この事情の理解を助ける為に大業十二年の日食が大興 (長安) で金環食, 推古三十六年の日食が飛鳥で皆既食, 長安二年の日食が長安で皆既食となる潮汐項-ΔT 面上のパラメータ領域を図 3 に示す. この場合推古三十六年の日食が飛鳥で皆既になり, 大業十二年の日食が長安で金環食になる ΔT は潮汐項を $< -16\,\mathrm{arcsec/cy^2}$ に取らないと存在しない.

そこで我々は, Kawabata, Tanikawa, and Sôma (2003) に於いて, Stephenson (1997) に従って, 大業十二年の日食が洛陽で観測されたものとした. 図 22 は大業十二年 (洛陽)・推古三十六年 (飛鳥)・長安二年 (長安) の日食が中心食となるパラメータ領域を示したものである. この図を見れば大業十二年の日食と推古三十六年の日食が中心食となる帯域が潮汐項が $-13\,\mathrm{arcsec/cy^2}$ でクロスしていることが判る. この上記の論文では潮汐項 $= -13\,\mathrm{arcsec/cy^2}$, $2728\,\mathrm{sec} < \Delta T < 2959\,\mathrm{sec}$ にとると大業十二年・推古三十六年・長安二年の三つの日食の記述と潮汐項のレーザー測距の四つの条件が満足される事を示し, この ΔT の決定法が有力であることを示した.

3 日食記録

本論文では Kawabata, Tanikawa, and Sôma (2003) で採用された方法を BC 700 年から AD 1000 年までの中国の史書に既・盡・星見など皆既またはそれに近いことを示す語の記されている日食並びに小倉 (1916) に皆既食の候補として挙げられている三例に適用し, この間の ΔT の変動を論じる. 中国の日食記録の検索には上海人民出版社 迪志文化出版有限公司の文淵閣四庫全書の電子版を使用し, 一部の文字は中華書局出版の二十四史に従って修正した. 西暦との対応には渡辺 (1979) の復刻版 (1994) を使用した. なお, 本論文の日付は Oppolzer の日食表と合わせ, 合の時刻の世界時の日付を記した.

本論文では夫々の食の観測地はその王朝の都として解析を進めたので, これらの都の座標は表 1 に掲げる. 隋に関しては本論文で取り上げた大業十二年の日食を洛陽での観測結果としたので, 表 1 でも隋の都を洛陽と記した. 隋の建国以来 9 回の日食が隋書・北史に記録されているが, 内 6 回は中国で観測出来ないもので, 2 回は洛陽に都を造る前であるが皆既に近いものは無い.

史書に中心食の記録がありながら都で中心食が起こらない場合の中心食帯を図 5—11 に示す

次に上述の条件を満たす日食のリストを記す. ここで, Opp: に続く数字は Oppolzer の日食表で使用されている通し番号である. JD: に続く数字はユリウス日で, 日付の干支との対応のために付した. 中心食又はそれに近いことを示す記述と括弧で括って夫々の文の出典を記し, 又中心食となるパラメータ領域を示す図の図番号或いは中心食帯の図の図番号を記した. 又必要に応じて注を付した. 皆既にならないとのコメントを付した日食はその王朝の首都の緯度では中心食にならないと云う意味で, ΔT の値と無関係に中心食にならない. 同じ日食に就いて複数の史書・巻に記されて

表 1: 首都所在地.

国名	首都	経度	緯度
魯	曲阜	117° 3'E	35°39'N
秦	咸陽	108°40'E	34°20'N
西漢	長安	108°54'E	34°16'N
東漢	洛陽	112°26'E	34°46'N
魏	洛陽	112°26'E	34°46'N
西晋	洛陽	112°26'E	34°46'N
東晋	建康	118°48'E	32° 3'N
宋	建康	118°48'E	32° 3'N
梁	建康	118°48'E	32° 3'N
隋	洛陽	112°26'E	34°46'N
唐	長安	108°54'E	34°16'N
日本	飛鳥	135°49'E	34°28'N
日本	京都	135°45'E	35° 1'N

いる場合は必ずしも網羅はしていない.

1. BC 709/7/17 Opp: 1176 JD: 1,462,659
   桓三年秋七月壬辰朔日有食之既 (春秋左氏傳事類始末附録 災異)
   図 12
2. BC 601 9 20 Opp: 1449 JD: 1,502,171
   宣八年秋七月甲子日有食之既 (春秋左氏傳事類始末附録 災異)
   図 12
3. BC 549/6/19 Opp: 1582 JD: 1,521,071
   二十四年秋七月甲子朔日有食之既 (春秋左氏傳事類始末附録 災異)
   図 12
4. BC 444 10 24 Opp: 1842 JD: 1,559,549
   秦厲共公三十四年、日蝕昼晦星見 (史記卷十五 六國表第三)
   同定した日食の Oppolzer 番号は斉藤・小沢 (1992) による. 図 13
5. BC 198/8/7 Opp: 2402 JD: 1,649,322
   高帝、九年六月乙未晦日有食之既在張十三度 (前漢書卷二十七 下之下 五行志第七下之下)
   図 14
6. BC 188/7/17 Opp: 2425 JD: 1,652,954
   惠帝七年、五月丁卯先晦一日日有食之幾盡 (前漢書卷二十七 下之下 五行志第七下之下)
   図 14
7. BC 181/3/4 Opp: 2441 JD: 1,655,376
   高后、七年正月己丑晦日有食之既在營室九度 (前漢書卷二十七 下之下 五行志第七下之下)
   図 14
8. BC 147/11/10 Opp: 2523 JD: 1,668,045
   景帝、中三年九月戊戌晦日有食之幾盡在尾九度 (前漢書卷二十七 下之下 五行志第七下之下)
   皆既にならない.
   図 5
9. BC 89/9/29 Opp: 2661 JD: 1,689,188
   武帝、征和四年八月辛酉晦日有食之不盡如鉤在亢二度晡時食從西北日下晡時復 (前漢書卷二十七 下之下 五行志第七下之下)
   図 15
10. BC 80/9/20 Opp: 2684 JD: 1,692,466
    昭帝、元鳳元年七月己亥晦日有食之幾盡在張十二度劉向以為己亥而既其占重孟康曰己土亥水也純陰故食為最重也日食盡為既 (前漢書卷二十七 下之下 五行志第七下之下)
    図 15
11. BC 34/8/23
    元帝、建昭五年六月壬申晦日有食之不盡如鉤因入 (前漢書卷二十七 下之下 五行志第七下之下)
    合は BC 34/8/24. 合の時の月の黄緯引数は 313.°68 で日食は起こらない.
12. BC 28/6/19 Opp: 2813 JD: 1,711,366
    成帝、河平元年四月己亥晦日有食之不盡如鉤在東井六度 (前漢書卷二十七 下之下 五行志第七下之下)
    図 16
13. BC 2/2/5 Opp: 2879 JD: 1,720,728
    哀帝元寿元年正月辛丑朔日有食之不盡如鉤在營室十度與 (前漢書卷二十七 下之下 五行志第七下之下)
    皆既食帯は中国南部で観測地は首都と考えられないので本論文では採用しない.
    図 6, 16
14. 2/11/23 Opp: 2888 JD: 1,722,115
    平帝元始、二年九月戊申晦日有食之既 (前漢書卷二十七 下之下 五行志第七下之下)
    図 16
15. 65/12/16 Opp: 3050 JD: 1,745,149
    明帝、永平、八年十月古今注曰十二月壬寅晦日有蝕之既 (後漢書卷二十八 五行志第十八)
    図 17
16. 120/1/18 Opp: 3184 JD: 1.764,905
    安帝、元初、六年十二月戊午朔日有蝕之幾盡地如昏状古今注曰星盡見在須女十一度女主惡之後二歳三月鄧太后崩 (後漢書卷二十八 五行志第十八)
    図 17
17. 243/6/5 Opp: 3470 JD: 1,809,699
    正始、四年、五月朔日有蝕之既 (三国志 魏志卷四)
    皆既にならない. 観測地が西域と思われるので採用しない.
    図 7, 18,
18. 306/7/27 Opp: 3611 JD: 1,833,032
    晉惠帝光熙元年、七月乙酉朔又日有蝕之既 (宋書卷三十四 志第二十四 五行五)
    図 19
19. 360/8/28 Opp: 3730 JD: 1,852,788
    穆帝、升平四年八月辛丑朔日有蝕之幾既在角凡蝕淺者禍淺深者禍大角為天門人主惡之明年而帝崩 (晉書卷十二 志第二 天文中 七曜 雜星氣 客星 流星雲氣 十煇 雜氣 史傳事驗)
    晉穆帝、升平四年八月辛丑朔日有蝕之不盡如鉤 (宋

書巻三十四 志第二十四 五行五)
図 19

20. 429/12/12 Opp: 3888 JD: 1,878,096
文帝、元嘉六年、十一月己丑朔又日有蝕之不盡如鉤蝕時星見晡方沒河北地闇 (宋書巻三十四 志第二十四 五行五)
元嘉、六年、冬十一月己丑朔日有蝕之星晝見 (南史巻二 宋本紀中第二)
皆既にならないが食分は大きい. 中心食帯が河北を通るので記述は正しい.
図 8

21. 453/8/20 Opp: 3942 JD: 1,886,748
元嘉三十年七月辛丑朔日有蝕之既星辰畢見 (宋書巻三十四 志第二十四 五行五)
秋七月辛丑朔日有蝕之 (南史巻二 宋本紀中第二)
南大西洋・アフリカ・インド洋で見られ, アジアでは見られない日食.
図 9

22. 454/8/10 Opp: 3944 JD: 1,887,103
孝武帝孝建元年七月丙戌朔日有蝕之既列宿粲然 (宋書巻三十四 志第二十四 五行五), 日付誤記 [丙申]
孝武帝孝建元年, 秋七月丙申朔日有蝕之既 (南史巻二 宋本紀中第二)
図 20

23. 516/4/18 Opp: 4092 JD: 1,909,635
天監、十五年春三月戊辰朔日有蝕之既 (南史巻六 梁本紀上第六)
図 21

24. 522/6/10 Opp: 4107 JD: 1,911,879
普通、三年、五月壬辰朔日有蝕之既 (梁書巻三 本紀第三 武帝下)
普通、三年、五月壬辰朔日有蝕之既 (南史巻七 梁本紀中第七)
図 21

25. 523/11/23 Opp: 4110 JD: 1,912,410
普通、四年、十一月癸未朔日有蝕之太白晝見 (梁書巻三 本紀第三 武帝下)
図 21

26. 616/5/21 Opp: 4345 JD: 1,946,193
大業十二年、五月丙戌朔日有蝕之既 (隋書巻四 帝紀第四 煬帝下)
図 22

27. 628/4/10 Opp: 4374 JD: 1,950,535
推古三十六年 丁未朔戊申日有蝕尽之 (日本書紀 巻第二十二 推古天皇)
図 22

28. 702/9/26 Opp: 4561 JD: 1,977,732
長安二年、秋九月乙丑日有蝕之不盡如鉤京師及四方見之 (舊唐書巻六 本紀第六 則天皇后)
長安二年九月乙丑朔日有食之幾既在角初度 (唐書巻三十二 志第二十二 天文志)
図 22, 23

29. 729/10/27 Opp: 4626 JD: 1,987,625
開元、十七年、冬十月戊午朔日有蝕之不盡如鉤 (舊

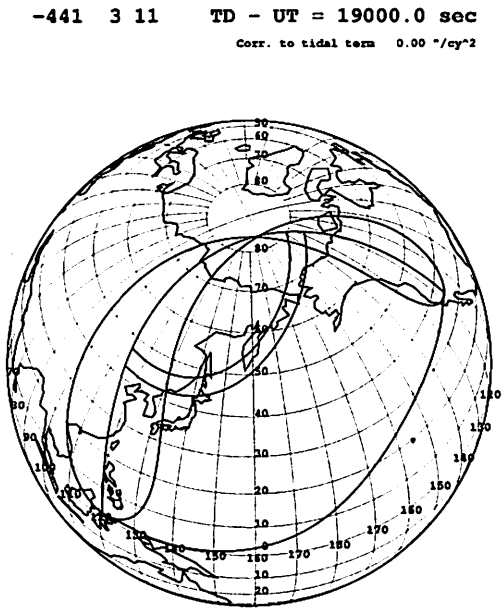

図 4: BC 442/3/11 の日食帯.

唐書巻八 本紀第八玄宗上)
開元、十七年十月戊午朔日有食之不盡如鉤在氐九度 (唐書巻三十二 志第二十二 天文志)
図 23

30. 754/6/25 Opp: 4685 JD: 1,996,632
天寶、十三載、六月乙丑朔日有蝕之不盡如鉤 (舊唐書巻九 本紀第九玄宗宗下)
皆既にならないが食分大.
図 10

31. 756/10/28 Opp: 4690 JD: 1,997,488
至德、元年、十月辛巳朔日有蝕之既 (舊唐書巻十 本紀第十 肅宗)
食尽は日没に近い. 長安では皆既にならないが, 北の万里の長城付近で皆既になる. 観測地点が都と考えられないので本論文では使用しない.
図 11

32. 761/8/5 Opp: 4701 JD: 1,999,230
上元、二年、秋七月癸未朔日有蝕之既大星皆見 (舊唐書巻十 本紀第十 肅宗)
上元、二年七月癸未朔日有蝕之大星皆見司天秋官正瞿曇譔奏曰 (舊唐書巻三十六 志第十六 天文下)
図 23

33. 873/7/28 Opp: 4955 JD: 2,040,130
貞觀十五年七月癸亥朔、日蝕無光、虧尽如月初生自午至未乃復 (三代実録 二十四 清和)
図 24

34. 975/8/10 Opp: 5184 JD: 2,077,398
天延三年七月一日辛未、日有蝕、十五分の十一、或云う皆既、卯辰刻皆虧、如墨色無光、群鳥飛乱、衆星盡見、詔書大赦天下、大辟以下常赦所不免者咸赦除、依日蝕之變也 (日本紀略 六 円融)
図 24

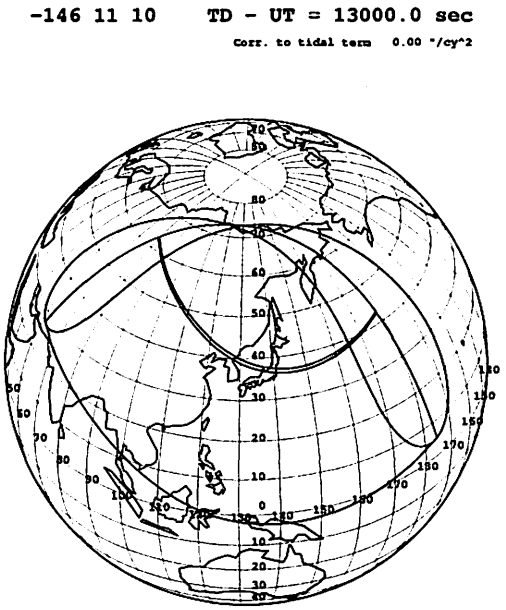

図 5: 漢 景帝 中三年九月戊戌晦 幾盡の日食帯.

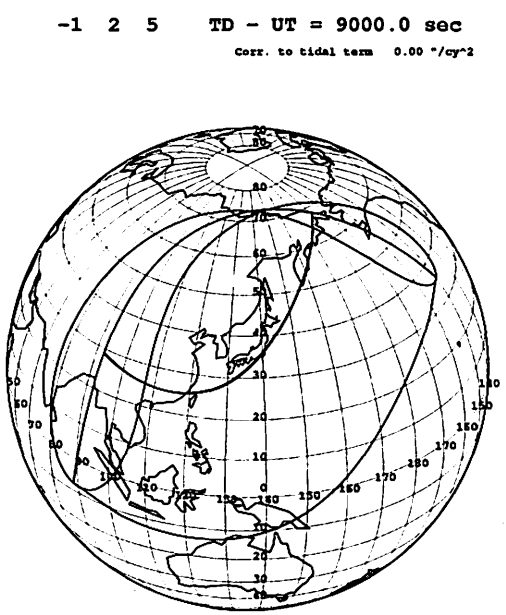

図 6: 漢 哀帝 元壽元年正月辛丑朔 不盡の日食帯.

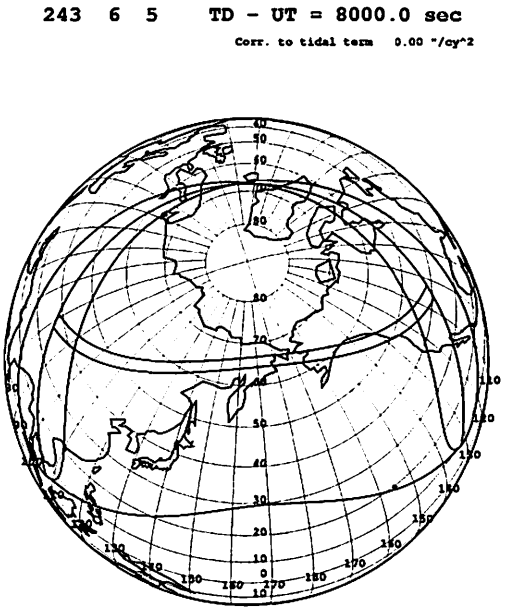

図 7: 魏 正始四年五月朔 既の日食帯.

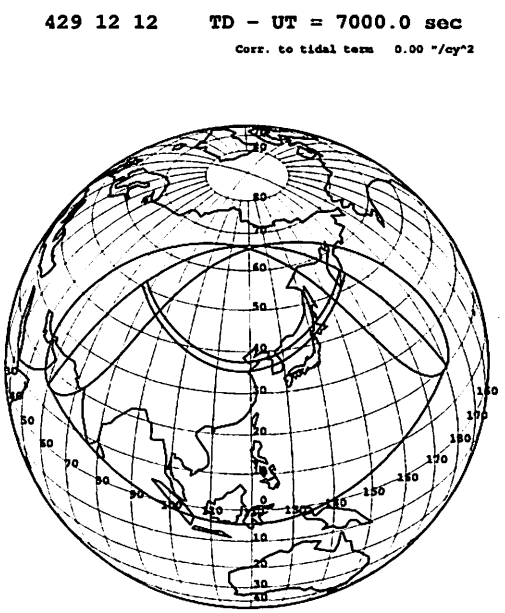

図 8: 宋 元嘉六年十一月己丑朔 不盡の日食帯.

史記には日食の日付が書いてない. 中華書局の史記「六国年表」では秦厲共公三十四年 (No. 4) を BC 443 に割り振っているが, BC 443 年には中国で見られる日食が無い. 前後では BC 444 と BC 442 に中国で見られる日食が有り, 斉藤・小沢 (1992) によると, 新城新蔵・朱文鑫・渡辺敏夫は BC 442 の日食と同定している. 図 4 は BC 442 の日食帯を図示したもので, 皆既食帯は中国東北地方で始まり沿海州・北海道・樺太・カムチャツカ半島を通り北極海で終わる日食で, 咸陽は通らない. そこで我々は, 斉藤・小沢に従って BC 444 の日食と同定した. 本論文では皆既食とし扱ったが, 史記には「星見」と有り, 皆既で無い可能性も否定できない. 従って図 28, 29, 30 の ΔT の範囲は実際より狭い可能性を否定出来ない.

これらの 34 の日食中 Oppolzer の日食表と対応が付かないのは前漢書巻二十七 下之下 五行志第七下之下に記載されている No. 11 の「元帝、建昭五年六月壬申晦 (BC 34/8/24) 日有食之不盡如鉤因入」のみである. 日月の合はこの翌日なので, 壬申晦と合致しているが, 合の時の月の黄緯引数は 313.°68 で黄道と白道の交点から 46° 以上離れて居り, 日食は起こらない. 当時の平均朔望月を使った暦法では晦に食になる可能性は高い. 日付の誤写又は誤記とすると, その日が偶

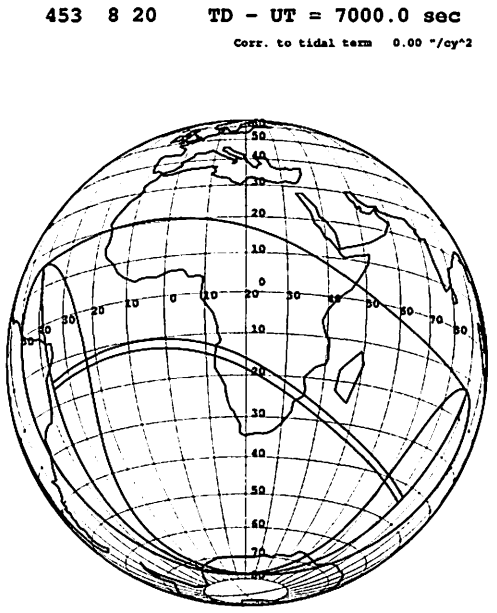

図 9: 宋 元嘉三十年七月辛丑朔 既星辰畢見の日食帯.

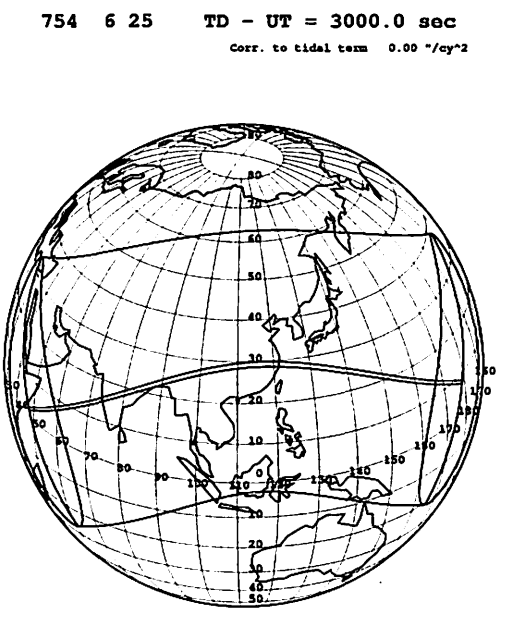

図 10: 唐 天寶十三載六月乙丑朔 不盡の日食帯.

然合の前日に当たる確率は小さい. 従って予測で書いたが, 当時の暦法の不完全さから皆既食として記録したと考えるのが穏当と考えられる. 古代中国では予測されていない日食が起こると天文官は斬首の刑に処される. 予測した日食が起こらなかった場合には祈りの成果で日食の咎を免れたと主張出来たので, 身の安全の為に日食は多めに予測されている.

残りの 33 例中, 中国で日食が見られないのは宋書に記載されている「元嘉三十年七月辛丑朔日有蝕之既星辰畢見」(No. 21) の一例である. この日食は南大西洋・アフリカ・インド洋で見られた日食 (図 9) で, 中

図 11: 唐 至徳元年十月辛巳朔 既の日食帯.

国では見られない. 従って予測で書かれたことは明白である.

「既」又は皆既と判断される記述のある食は 18 回である. 「既」と記されていて, 都では皆既にならないものは三国志に記載されている「正始、四年、五月朔日有蝕之既」(No. 17) と旧唐書に記載されている「至徳元年十月辛巳朔日有蝕之既」(No. 31) の 2 例である.

三国志の正始四年の金環食帯はタリム盆地から, 敦煌付近, ゴビ砂漠, バイカル湖の東を通ってヤクーツク付近からアラスカを経てアメリカで終わる. 中国の領域で云えば西域で皆既食が見られた日食である (図 7). 杉本・森 (1995) によると, 1965 年にウイグル自治区吐魯番(トルファン)の仏塔の下から仏典と共に, 西晋時代と推測される三国志 呉書 孫権伝の残巻が出土し, 晋が当時この地域と交流していたことは明らかである. 陳壽が三国志を執筆したのが西晋時代の 233–297 と推定され, 陳壽の手元に西域の観測記録が有ったことは十分推測される. 従って, 三国志の西始四年の日食は西域からの情報によって書かれたと思われる.

唐の至徳元年の日食 (図 11) は長安では $\Delta T < 3000\,\mathrm{sec}$ とすると食尽は日没後になる. $\Delta T = 3000\,\mathrm{sec}$ とすると日没 (09:51 UT) 時の食分は 0.87, $\Delta T = 3500\,\mathrm{sec}$ とすると食尽が 09:47 UT でこの時の食分が 0.92 高度が 0.3° で日没が 09:52 UT となる. 長安より北の万里の長城付近で皆既になる. この日食は出先からの報告による観測記録と考えられる.

残りの皆既にならなかったことが記述されている 15 例中次の四例は首都では皆既にならない. 漢書に記載されている「景帝、中三年九月戊戌晦日有食之幾盡在尾九度」(No. 8)・「哀帝元寿元年正月辛丑朔日有食之不盡如鉤在營室十度與」(No. 13), 宋書に記載されている「文帝、元嘉六年、十一月己丑朔又日有蝕之不盡如鉤蝕時星見晡方沒河北地闇」(No. 20), 旧唐書に記

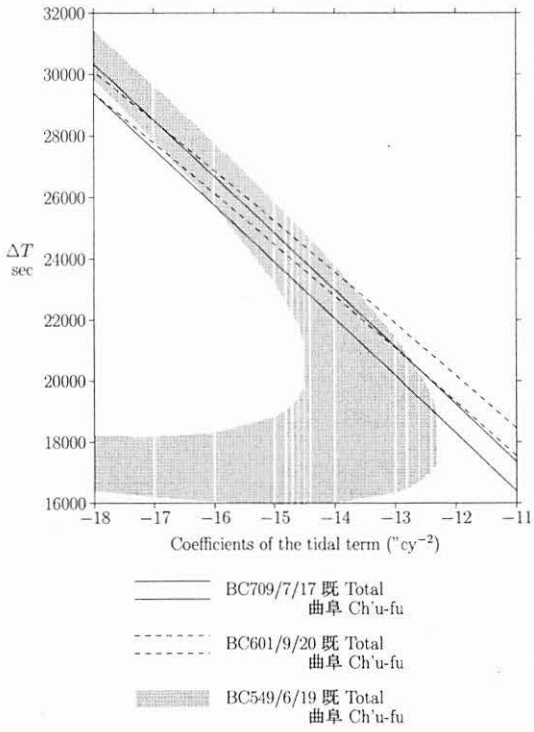

図 12: 春秋時代の日食が中心食となるパラメータ領域

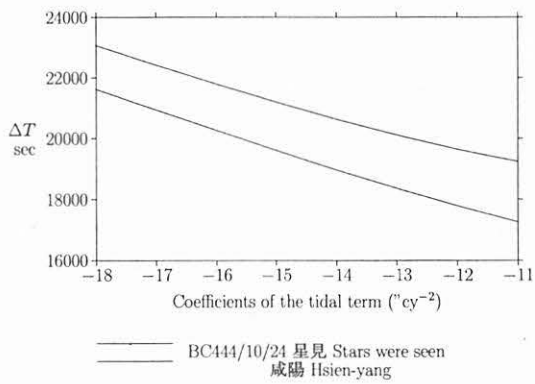

図 13: 史記の日食が中心食となるパラメータ領域

載されている「天寶、十三載、六月乙丑朔日有蝕之不盡如鉤」(No. 30). 内,「哀帝元寿元年正月辛丑朔日有食之不盡如鉤在營室十度與」を除いた三例は皆既にはなっていないが, 食分はかなり大きくなるので史書の記述と矛盾はしない.

漢書の「哀帝元寿元年正月辛丑朔日有食之不盡如鉤在營室十度與」は前後の日食と ΔT が大きく異なり, 皆既帯は中国南部を通る. 記録は首都以外の観測状況と思われるので本論文では取り上げない.

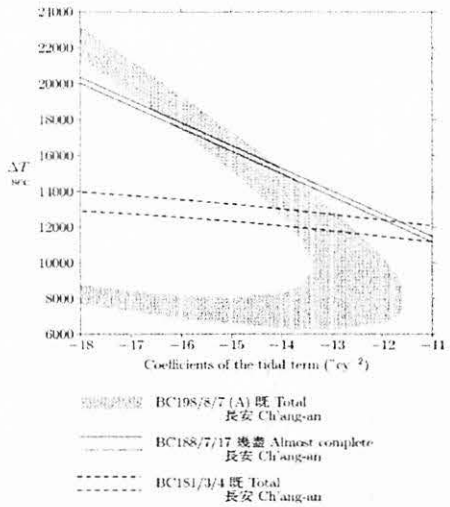

図 14: 漢代の日食が中心食となるパラメータ領域. 既と書かれている BC 198 及び BC 181 が共に皆既となるのは 11816 sec $< \Delta T <$ 12471 sec の場合. 幾既と記録されている BC 188 の ΔT をこの最大値 12471 sec に取った時のこの日食の食分は, 0.94 となり, BC 188 の実際の食分はこれよりやや小さくなる.

4 $\Delta T = \mathrm{TT} - \mathrm{UT}$ の決定

以上前節の結果を要約すると, 春秋から旧新唐書に至る中国史書に「既」・「盡」・「星見」の記述のある日食に小倉 (1916) に皆既の可能性のある日食として挙げられている三つの日食を加えた 34 回の日食の中で, 漢書に記載された「元帝、建昭五年六月壬申晦」には地球上どこにも日食が起こらない. 宋書に記載された「元嘉三十年七月辛丑朔」の日食は南大西洋からアフリカを経由してインド洋で終わる日食で, 予測で書かれたものである.

漢書の「哀帝元寿元年正月辛丑朔」の日食と三国志の「正始四年五月朔」の日食は首都では記述と異なった日食になるが, 夫々中国南部・西域で記述通りになる.

この四例を除いた 30 例で記録通りの日食が確認された. 本論文ではこれら 30 例中首都で皆既になり得ない 4 例を除いた 26 例の日食が首都で皆既となる ΔT を計算し, 解析を行った.

2 節の最後に日食の様子は潮汐項と ΔT の二つのパラメータにより決まることを述べた. 図 12—24 は横軸に潮汐項の大きさを縦軸に ΔT を取り, 図の下に記した日食が中心食となるパラメータ領域を示した図である。二つの日食が共に中心食となる場合に二つの日食の間隔が 50—60 年程度以下の場合には ΔT の値は

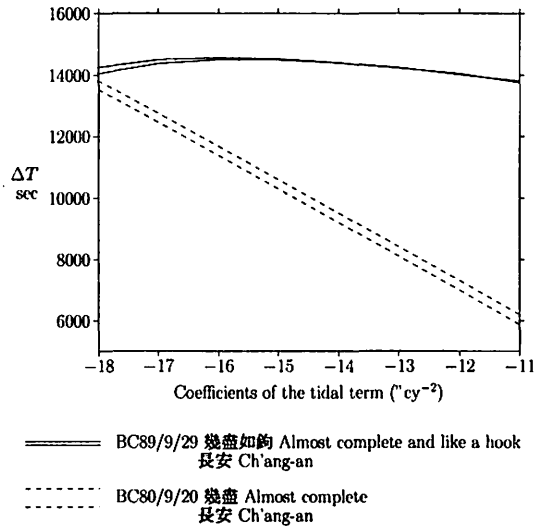

図 15: 漢代の日食が中心食となるパラメータ領域.

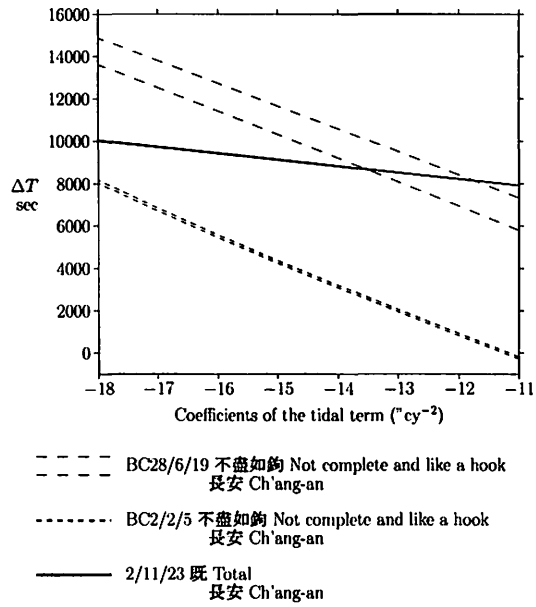

図 16: 漢代の日食が中心食となるパラメータ領域. AD 2 年の日食が皆既となる $\Delta T = 8510\,\mathrm{sec}$ に取ると, BC 2 年の不盡如鉤の日食の食分は 0.84 で, 時刻は 01:19 UT となる.

大きくは変わらないから, 二つの帯の重なった領域がこの二つの日食に共通したパラメータ範囲になる.

図 17, 21, 22 の三つの図に示す如く, 中心食又はそれに非常に近い場合には二つの帯状のパラメータ領域が潮汐項が $-13\,\mathrm{arcsec/cy^2}$ で交差し, 月のレーザー測距から得られた値と一致する. これは潮汐項が現代から後漢時代まで遡って同一の値を保っていることを示している. その他の例も殆どの場合, この帯状のパラメータ領域が平行に近い為に交差する潮汐項の値を決められないだけで, 潮汐項が $-13\,\mathrm{arcsec/cy^2}$ の時複数

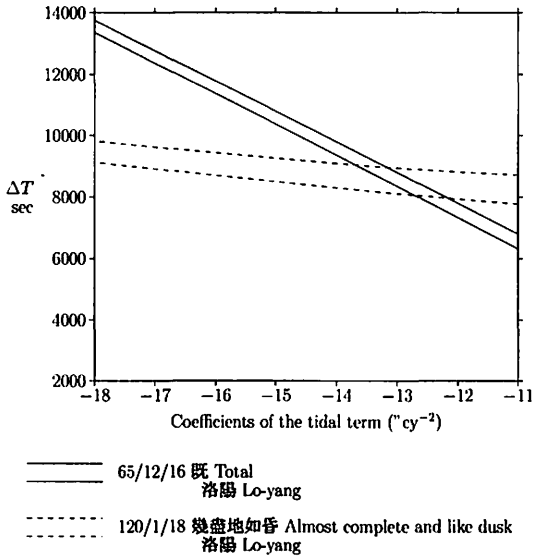

図 17: 後漢時代の日食が中心食となるパラメータ領域

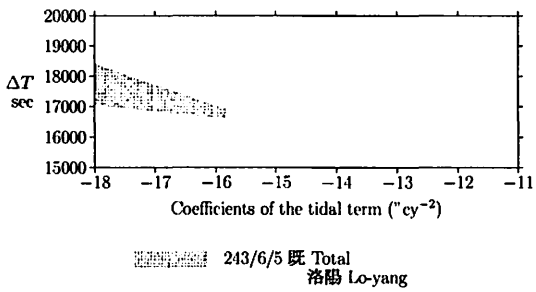

図 18: 三国時代の日食が中心食となるパラメータ領域

の食が成立する ΔT の領域が存在する. そこで, 潮汐項の値は以下の議論では $-13\,\mathrm{arcsec/cy^2}$ と取る.

図 15 では二つの日食が「幾盡如鉤」・「幾盡」で共に皆既でない. この例では, 潮汐項 $-13\,\mathrm{arcsec/cy^2}$ では ΔT の値が大きく異なっている. 表 2 はこれらの日食で ΔT を表の第一列に与えた値の時の食尽・食分を記したものである. この例では他の「幾盡」と記されている日食と比べて食分が小さくなるので, この程度の食分でも「幾盡」と書いたか, 何れかの観測地が首都でないかは微妙であるが, 本論文では一応 ΔT の範囲を図 28 にプロットした.

本論文の ΔT の決定法の例として, 702, 628 の日食

表 2: BC 89 年及び BC 80 年の日食の ΔT と食尽 (UT)・食分

ΔT	BC 89/9/29		BC 80/9/20	
s	食尽	食分	食尽	食分
10000	08:38	0.884	06:11	0.891
12000	07:56	0.929	05:26	0.739

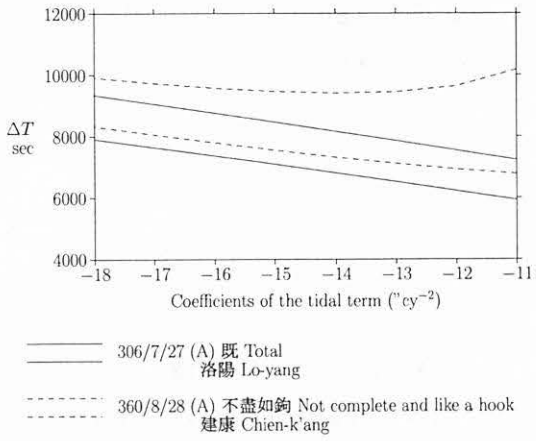

図 19: 晋代の日食が中心食となるパラメータ領域

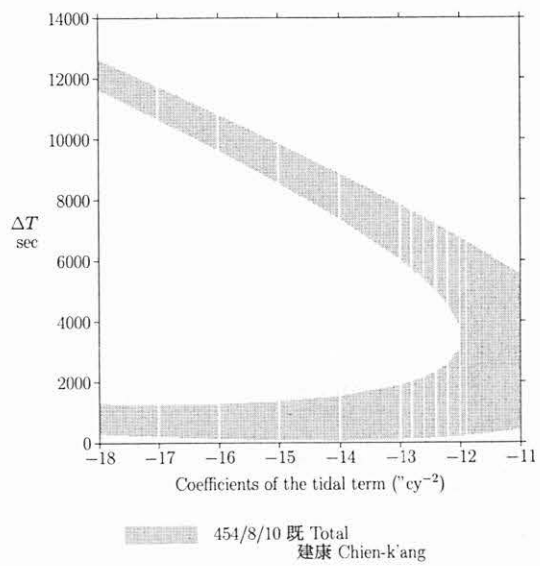

図 20: 宋代の日食が中心食となるパラメータ領域

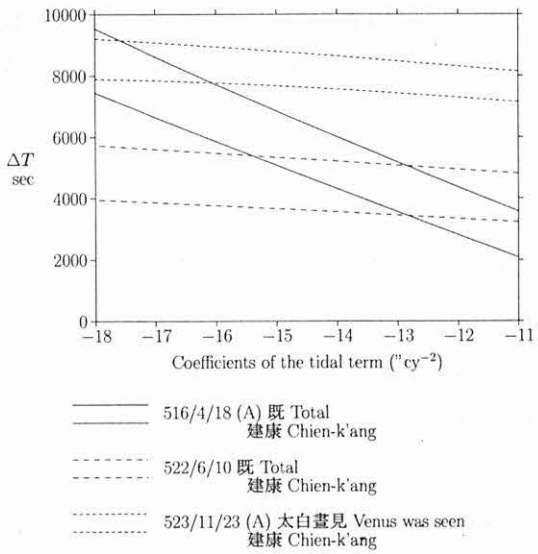

図 21: 梁代の日食が中心食となるパラメータ領域

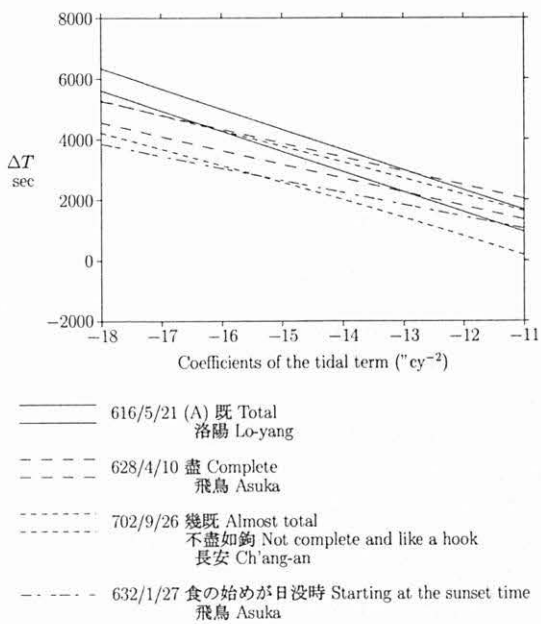

図 22: 飛鳥時代の日食が中心食となるパラメータ領域. $\Delta T = 2959$ sec に取ると, 702 年の日食の長安での食分は 0.99, 時刻は 08:12 UT.

の ΔT の決定法を記す. 図 23 で 761 年の日食が長安で皆既食になる条件は $1688 < \Delta T < 3254$ sec である. 702 年の日食が長安で皆既になる条件は $1429 < \Delta T < 2728$ sec だから, 702 年が如鉤となり, 761 年が皆既になる条件は $2728 < \Delta T < 3254$ sec となる. 次に図 22 で 628 年の日食が飛鳥で皆既になる条件は $2267 < \Delta T < 2959$ sec だから, 628 年の日食が飛鳥で皆既となり 702 年の日食が長安で如鉤となる条件は $2728 < \Delta T < 2959$ sec となる. これで 628 年の ΔT が $2728 < \Delta T_{628} < 2959$ sec と決まる.

等緯度で観測地点が西に移動すると中心食帯の ΔT が小さくなるので, 628 年の日食の場合飛鳥から 231 sec $\approx 1°$ 西に移動すると皆既食にならないので皆既帯の等緯度での西の限界は姫路付近になる. 皆既帯は東へは 692 sec $\approx 3°$ 付近まで広がっているので, 等緯度では伊豆半島付近が限界になる.

内田 (1975) は日本書紀の舒明八年一月朔の日食は舒明四年一月朔 (632/1/27, Opp: 4384) の誤記と主張している. この日食が飛鳥の日没時に始まるパラメータも図 22 に示してある. 内田の主張を採用し, 舒明四年一月朔の日蝕が日没前に始まる条件を求めると $\Delta T > 1851$ sec が得られる. 上記の 628 年の ΔT の範囲 $2728 < \Delta T_{628} < 2959$ sec は舒明四年の日蝕が日没前に始まる条件を満たしている. Kawabata, Tanikawa, and Sôma (2003) は $\Delta T = 2959$ sec と置いて, 舒明四年一月の日食の食分として 0.17 を, 斉藤・小沢 (1992) が大きな食分を算出している舒明九年の日食の食分と

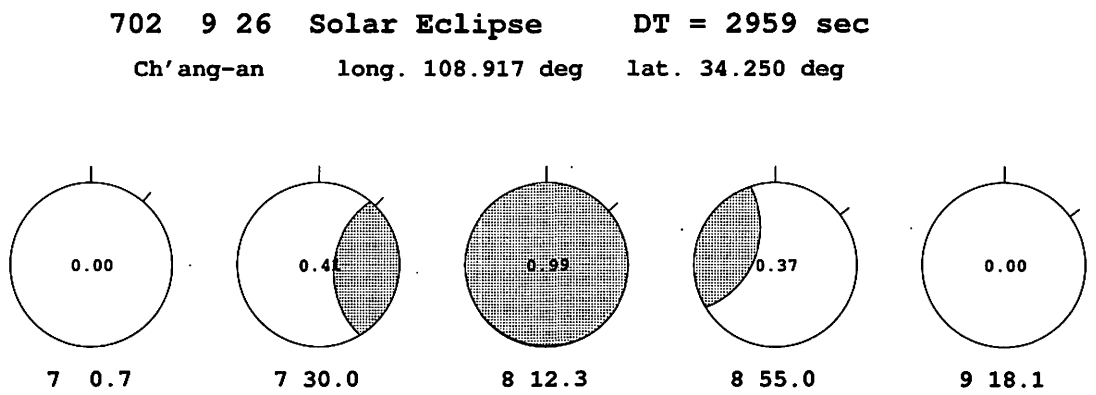

図 25: 長安二年の長安に於ける日食の時間経過. 上が天頂方向. 斜め右を指す斜線は北極の方向を示す.

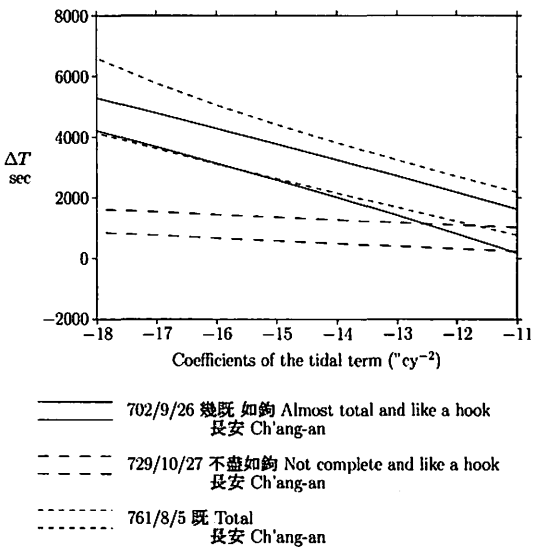

図 23: 唐代の日食が中心食となるパラメータ領域. 既と記されている 761 年の日食が皆既となり, 幾既と記されている 702 年の日食が皆既にならないパラメータ領域は実線で示されている 702 年の日食の皆既領域の上の限界線より上になる. これは図 22 とも一致する. ΔT をこのように取ると 729 の日食は皆既にならず不盡如鉤と一致する.

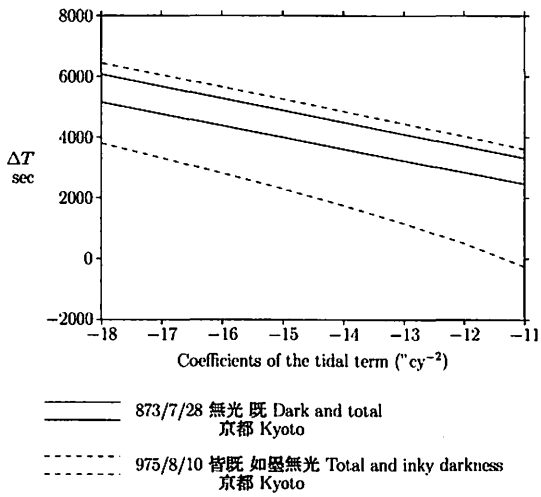

図 24: 平安時代の日食が中心食となるパラメータ領域

して 0.88 を得て日本書紀記載の通りに舒明九年の日食の方が推古三十六年の日食よりも有意に食分が小さいことを示している.

図 25, 26 は $\Delta T = 2959\,\mathrm{sec}$ とした時の長安二年の長安に於ける日食の様子を示したものである. 本論文の ΔT の決定法によると, 702 年の長安での食分は 0.99 となり, これらの図に見られる様にこの日食は長安では太陽の下が僅かに残っただけで旧唐書・新唐書に記載されている通りになる.

図 27 は天武十年 (681/11/3) の火星の飛鳥に於ける掩蔽の様子を示したものである. この時火星は月の縁から 34 arcsec 外を通過するが, 裸眼の分解能を考えると火星は日本書紀記載の通り月に入ったことになる.

以上に記した如く, 616 年の隋書に記されている洛陽の日食に始まり, 761 年の唐書にしるされている長安の日食に至る期間に 7 回の日食が中国・日本の史書に記録されている. その内, 616, 628, 702, 729, 761 の 5 回の日食は本論文で採用した方法による相互チェックが可能であり, 実際互いに良く一致する結果が得られた. 又残りの 2 回の日食もこれらと矛盾しないことが確かめられた. こうして得られた $\Delta T = 2840\,\mathrm{sec}$ を使って, 日本書紀の推古紀・舒明紀・天武紀に記載されている日食の食分・食尽時刻をまとめたのが表 3 である.

この表を見れば明らかな様に, 日本書紀に「日有蝕尽之」と記載されている推古三十六年の日食の食分が皆既になる. 又渡辺 (1979), 斉藤・小沢 (1992) では推古三十六年の日食より大きな食分が得られているが日本書紀には単に「日食之」と記されている舒明九年の日食の食分が 0.9 以下で, 同じく「日食之」と記されている天武九年の日食と略同じ食分であることが知られる.

既に河鰭・谷川・相馬 (2002) に記した如く, 舒明四年, 天武十年の日食の様に食分が小さな日食は何も予

表 3: 日本書紀 推古紀・舒明紀・天武紀の日食. $\Delta T = 2840$ sec

日付		食尽		食分	注
		UT	LT		
628/4/10	推古三十六年三月戊申	00:49	09:52	1.01	
632/1/27	舒明四年一月朔	08:24	17:27	0.16	日没時, 食尽は日没後 08:38 UT, 食分 0.18
637/3/31	舒明九年三月丙戌	23:44	08:47	0.87	LT では 637/4/1
680/11/27	天武九年十一月壬申	03:30	12:33	0.89	
681/11/16	天武十年十月丙寅	01:22	10:25	0.16	

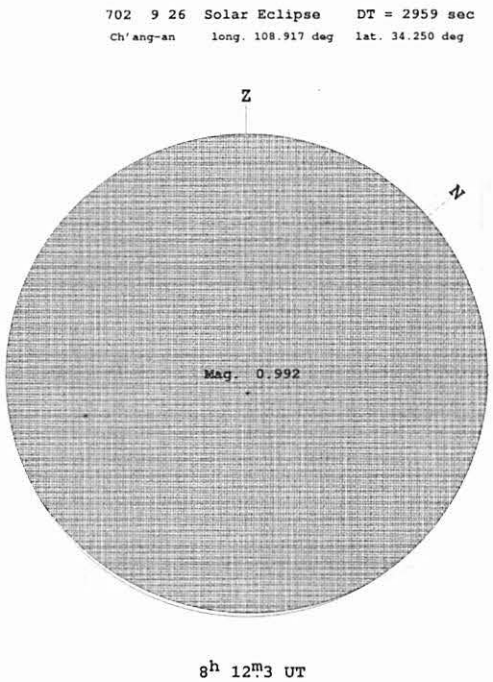

図 26: 長安二年の長安に於ける日食の様子. 食分の計算値は 0.99 で, 図に示されている如く, 太陽は下の部分を僅かに残して月に覆われた. 新唐書天文志の「幾既」, 旧唐書 則天皇后の不盡如鉤と合致する.

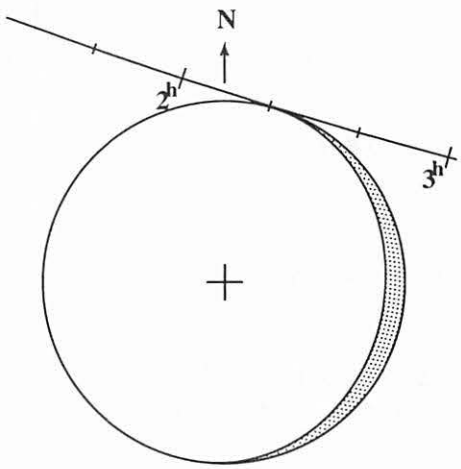

図 27: 日本書紀の天武十年に記載されている火星の掩蔽の際の火星の月に対する通過経路をしめす. 火星は月から 34 arcsec 外を通過するが, 裸眼の分解能以下なので, 火星は月に入った様に見える. この日は満月に近く, 黒く塗られた三日月型の領域が欠けた部分.

備知識の無い状態では気がつかない. 渡辺 (1979) によると, Ginzel は 563/10/2 — 1331/11/29 の期間の 50 回の日食の食分と太陽時を計算し, 予備知識が無い場合に日食に気がつくのは食分が 9 zoll を越えた時との結論を得ていると云う. 又太陽高度が高い程認知され難く, 日の出直後・日の入り直前の場合には 6 zoll でも認知されている場合があると云う. zoll は皆既の時を 12 zoll とした食分だから, 我々が現在使っている食分で云うと 9 zoll, 6 zoll は 0.75, 0.5 に当たる. 従って日本書紀に食分 0.16 の日食が記載されている事は, 当時の日本が既に日食の予報が可能だったと云えるであろう.

5 ΔT の経年変化

図 28 は前節で求めた夫々の日食の ΔT の範囲をプロットしたもので, 複数の日食から決めたものを太い縦線で, 一つの日食から求めたものは細い縦線で記してある. 又参考の為に, Stephenson (1997) に掲載されている Table A1 のバビロニアの日月食記録から求めた ΔT もプロットした. 斜めの実線は ΔT の潮汐成分 $\Delta T_{\rm tidal}$ を示したもので, 観測点の殆どが $\Delta T_{\rm tidal}$ より下になり, 既に知られていることであるが, 地球自転に潮汐効果以外の作用が働いていることを示している.

図の破線は Stephenson (1997) の放物線近似を示し, ΔT の永年変化を表している. 本論文で求めた値はその周りに分布している. この破線と今回求めた値を比べると, 6–7 世紀の値が破線から系統的に顕著に下がっている. 又 6–7 世紀程顕著では無いが, 1–2 世紀の ΔT も下がっている. 逆に 5 世紀, 7–8 世紀の ΔT はそれ程顕著では無いが破線の上に偏っている. Stephenson (1997) が得たバビロニアの記録による ΔT は我々が求めた値と良く合い, 紀元前 7 世紀から紀元前 5 世紀

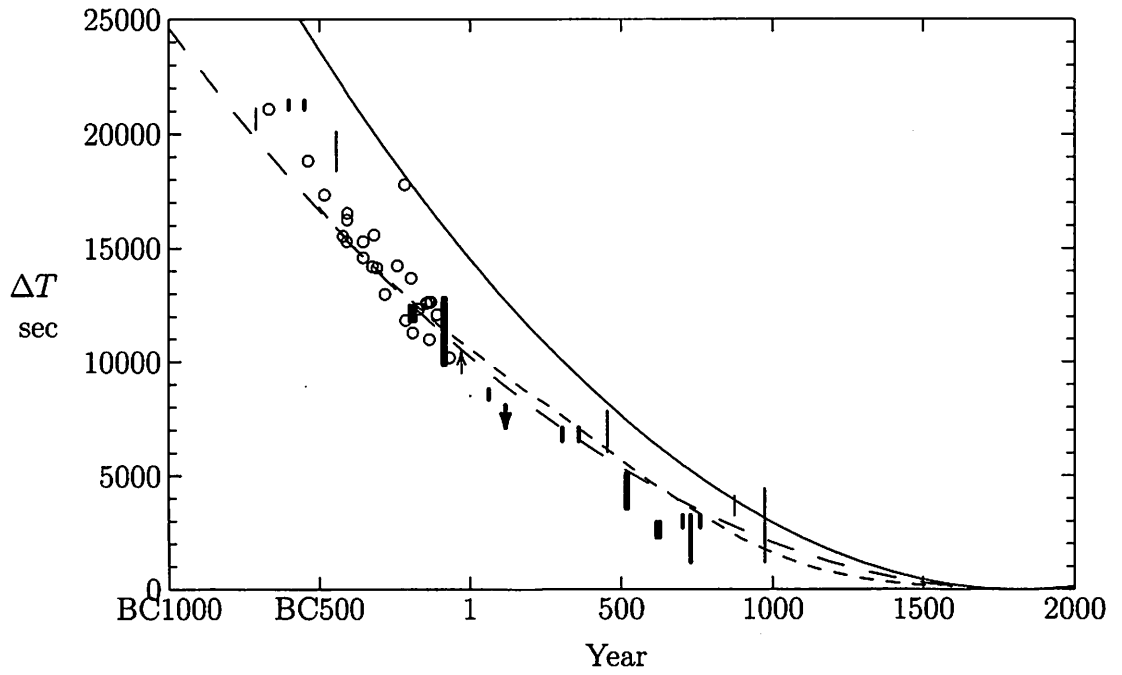

図 28: ΔT の経年変化. ○: Babylonia の日月食 (Stephenson 1997, Table A1.). 実線で書かれた放物線は Stephenson が得た ΔT の永年変化成分. 破線は同じく Stephenson のスプライン近似.

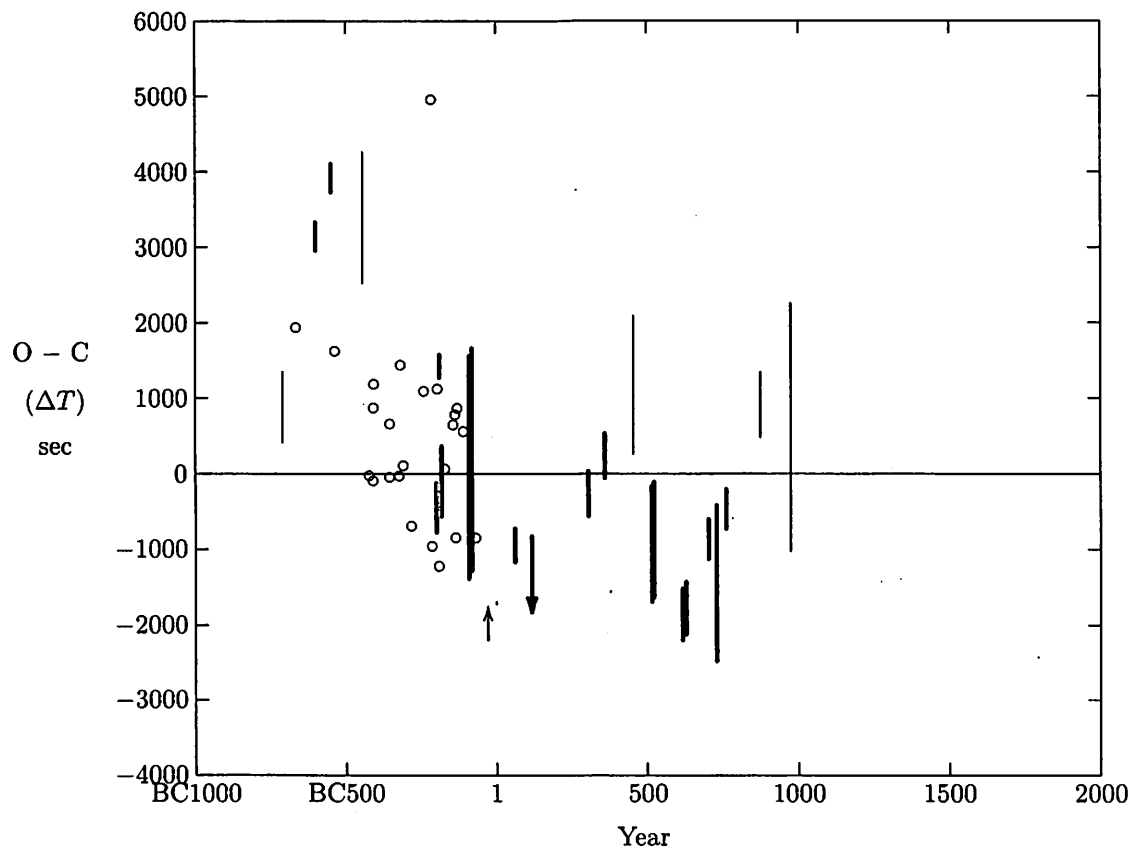

図 29: ΔT の図 28 の破線からの残差の経年変化. ○: Babylonia の日月食 (Stephenson 1997, Table A1).

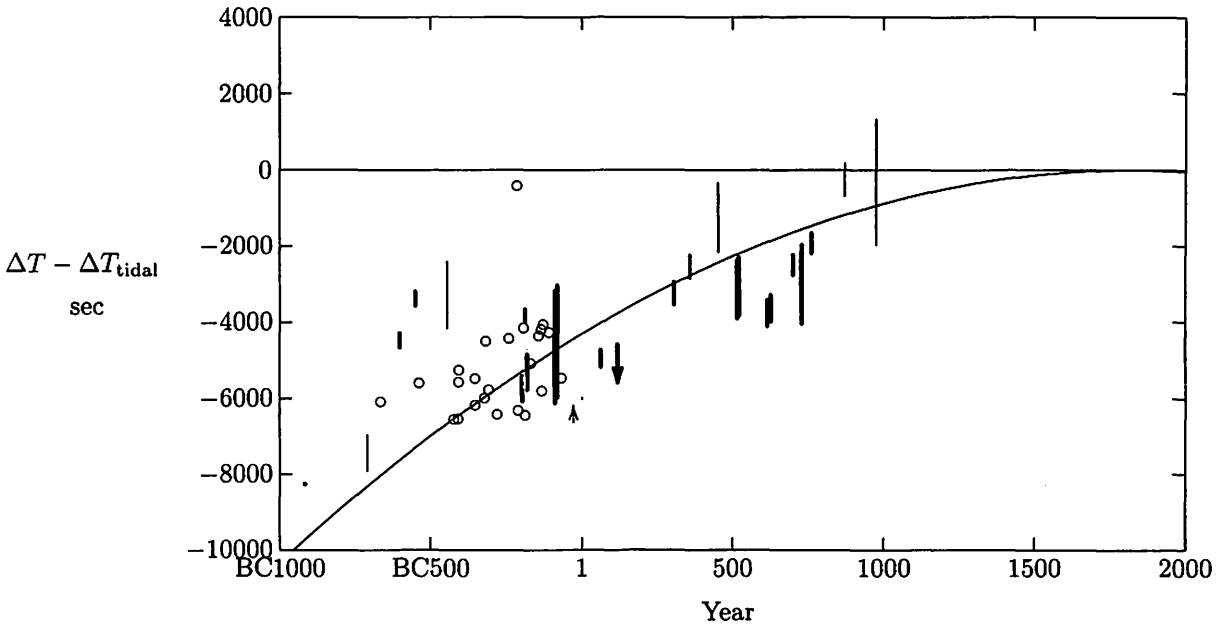

図 30: $\Delta T - \Delta T_{\rm tidal}$ の経年変化. ○: Babylonia の日月食 (Stephenson 1997, Table A1.). 図の実線で書かれた放物線は Stephenson が得た ΔT の永年変化から潮汐効果の成分を差し引いたもの.

にかけては中国の記録・バビロニアの記録共に破線より上の ΔT を与えている.

図 29 はこの ΔT の短期変動を明確にする為に, ΔT の O − C の経年変化を示したものである. ここで C としては Stephenson (1997) の $\Delta T_{\rm Cal} = 31t^2 - 20\,{\rm sec}$ を用いた. ここで t は AD 1820 からの経過年数をユリウス世紀 36525 日単位で表したものである. この図を見ると ΔT には 600—1000 年位の時間スケールの変動があることが読み取れる.

地球自転周期には潮汐以外の原因による成分が有る事は既に知られていることであるが, その起因として地球の慣性能率の変化が挙げられる. 図 30 は $\Delta T - \Delta T_{\rm tidal}$ をプロットしたもので, 地球の慣性能率の変化を反映した図になっている. この地球の慣性能率の変化の起因として, 気候変動に伴って氷河が解けると, それ迄氷河の重みで押さえられていた地盤が隆起し, 地球全体の地殻の質量分布が変化する為との説を Stephenson は唱えているが量的議論はされていない. 我々は地盤が隆起して地盤と氷河を合算した質量は変化しないこと, 地盤の隆起と地殻の変化には地質学的年代が必要で, 短期の変動は起こらないであろうとの推量から, 氷河が解けて海水として低緯度の海面が上昇することによるとの説を唱えた (Kawabata, Tanikawa, and Sôma 2003).

極地の気温が上昇して氷河が解けて海水面が 1 m 上昇したとしよう. 極地の氷河の氷は極軸に近いから地球の慣性能率には余り寄与しない. これが解けて海水になると, 海面の面積の大部分は低緯度になるので, 今まで地球の慣性能率に寄与していなかった水が低緯度に流れたことによって慣性能率を増加させる. 海面の面積は地球の表面積の約 2/3 を占める. この海面の面積を考慮すると 1 m の海面の上昇は海水の質量が 3.5×10^{20} gr 増加したことを意味する. 地球の半径を R と置き, 海水の地球の極軸からの平均二乗距離を $\frac{2}{3}R^2$ と近似し, 氷河は解ける前は地球の慣性能率に寄与していなかったとの近似をすると, 地球海水量の増加に伴った地球の慣性能率の増分は

$$10^{-7} \times \text{地球の慣性能率}$$

になる. 地球の慣性能率がこれだけ増加すると一日の長さは 10 ms だけ増加する. 氷河が徐々に解けて 1000 年かけて海面が 1 m 上昇したとすると, ΔT は 30 分増加する. 従って図 28 に見られる程度の ΔT の変動は海面の数 m の変動で起こり得ることになる.

この解釈に従うと, ΔT の永年変化は海面の上昇を意味し, 縄文海進以降の寒冷化の現れと定性的には解釈出来る. 今回の研究により見出された 600—1000 年スケールの ΔT の変動はこの寒冷化が一様でなく, 短期の変動を繰り返しながら進んでいることを意味しているのかもしれない.

6 まとめ

本論文では潮汐項と ΔT の二次元平面上に各日食が皆既となる領域をプロットし, 複数の日食の相互比較による較正によって, 記録の正確さをチェックする方法を採用した. この方法によると, 従来の方法に比べて ΔT の信頼性が著しく向上し, その値を狭い範囲に絞り込むことが出来る. この方法により, 後漢時代から飛鳥時代にわたって潮汐項が $-13\,{\rm arcsec/cy^2}$ と求まり, 月のレーザー測距から得られた値と一致することが確かめられた. この方法により, ΔT の変動を論ずるの

に必要な精度を得られ, 600—1000 年スケールの変動が見出された. この ΔT の変動成因として, 極地の氷河の解氷・成長に伴った海面の昇降による地球の慣性能率の変動を挙げた.

隋書に記載されている大業十二年の日食が長安の観測か洛陽の観測かの判定にこの方法を適用し, 洛陽の観測と確認が出来た. この事は, この解析方法が観測地の仮定が正しいか否かの判断の有力な手段であることも示している.

日本・中国の日食の食分などの計算は今迄にもわが国の天文学研究者によって多々為され, 計算結果が史書と合わないことから史書の記録を不当とする著作が出版されている. 然しながら, これらの著書では地球の慣性能率の変動が完全に無視されているので, その計算結果には経度にして 10° 程度の時代によって異なった誤差がある. 今回の論文の執筆に当たり調査した 34 の日食の中で日食が起こらないものは漢書に一例有るのみで, その他は総て日食が起こっている. この例外の一例は予測によって執筆されたものと思われるが, 日月の合の前日で日付は晦と書かれている. 当時の平均朔望月を用いた暦法では晦に日食が起こる事は多い. この時の合の時刻の黄道・白道の交点から計った月の黄経は約 46° で今日の知識からすれば日食とはならないが, 当時の知識からすれば日食と判断したのも無理はなかろう. 東アジアで見られない日食は宋書に大西洋からアフリカを経てインド洋で終わる日食が一例有るのみである. この例は明らかに予測によるものである. 首都の観測と考えられない例は中国史書に数例有り, 観測地不明の例は幾つか有るが記述は概ね正しい.

謝辞

本研究は文部科学省科学研究費補助金 特定領域研究 14023233 により行われた.

参考文献

Calame, O. and and D. Mullholand, 1978, *Science*, **199**, 977–978.

Chapront-Touze, M. and J. Chapront, 1983, *Astron. Astrophys.*, **124**, 50–62.

Christodoulidis, D. C. *et al.*, 1988, *J. Geophys. Res.*, **93**, 6216–6236.

Dickey, J. O. *et al.*, 1994, *Science*, **265**, 482–490.

Fotheringam, J. K., 1920, *Mon. Not. R. Ast. Soc.*, **81**, 104–126.

Hansen, P. A., 1857, *Tables de la Lune construites d'apres le Principe Newtonien de la Gravitation Universelle.* H. M. Stationery Office, London.

Kawabata, K., K. Tanikawa, and M. Sôma, 2003, *Proceedings of ICHA/IAU International Conference on Astronomical Instruments and Archives from the Asia-Pacific Region, Cheongju, Korea, 2-5 July 2002*, Yonsei Univ. Press (Korea), in press.

Lasker, J., 1986, *Astron. Astrophys.*, **157**, 59–70.

Leverrier, U. J. J., 1858, *Ann. de l'Obs. de Paris*, **4**.

Oppolzer, Th. Ritter von, 1962, Canon of Eclipses, translated by O. Gingerich, Dover Publications INC., New York. Originally published as vol. 52 of the Memoirs, Mathematics Natural Sciences Class of the Imperial Academy ofSciences in Vienna (1887).

Jones, H. S., 1939, *Mon. Not. R. Ast. Soc.*, **99**, 541–558.

Stephenson, F. R., 1997, *Historical Eclipses and Earth's Rotation*, Cambridge University Press.

Tanikawa, K., and M. Sôma, 2001, *Proceedings of International Conference on the 770th Birth Anniversary of Guo Shoujing and the History of Time Apparatus*, Xingtai, China, 18–22 October 2001 (in press).

河鰭公昭・谷川清隆・相馬 充 (Kawabata, Tanikawa, Sôma), 2002, 国立天文台報 (Report of the National Astronomical Observatory of Japan), **5**, 145—159.

森 博達 (Mori), 2000, 日本書紀の謎を解く 述作者は誰か, 中央新書.

小倉伸吉 (Ogura), 1916, 天文月報 (The Astronomical Herald published by the Astronomical Society of Japan), **9**, 13–18, 25—29, 39—43,52—55, 62—64.

斉藤国冶・小沢賢二 (Saito and Ozawa), 1992, 中国古代天文記録の検証, 雄山閣.

杉本憲司・森 博達 (Sugimoto and Mori), 1995, 『魏志』倭人伝を通読する, 日本の古代 1, 中公文庫.

鈴木敬信 (Suzuki), 1942, 日本天文学会要報, **6**, 143.

谷川清隆・相馬 充 (Tanikawa and Sôma), 2001, 天文月報, **95**, 27–37.

内田正男 (Uchida), 1975, 日本暦日原典, 雄山閣.

渡辺敏夫 (Watanabe), 1979, 日本・中国・朝鮮—日食月食宝典, 雄山閣.

火星探査機「のぞみ」の軌道決定における諸問題 2

Problems in the orbital determination for NOZOMI spacecraft 2

吉川真（宇宙科学研究所†）
宇宙研軌道決定グループ・「のぞみ」相対 VLBI グループ

Makoto Yoshikawa (ISAS†)
ISAS Orbit Determination group・NOZOMI Delta-VLBI group
3-1-1 Yoshinodai, Sagamihara,Kanagawa 229-8510, JAPAN
makoto@pub.isas.jaxa.jp

Abstract

The Japanese Mars explorer NOZOMI was launched in July 1998. It was planed to arrive at Mars in October 1999. But a problem occurred when it left from the earth to Mars and it will reach Mars at the end of 2003. Several troubles occurred up to now, and they made the orbit determination difficult. In this paper, the efforts and trials for the orbit determination of NOZOMI are summarized. We tried to use Delta-VLBI technique as well as the conventional range and range rate method. The Orbit determination of spacecraft in deep space by using the Delta-VLBI technique is a very promising method for the future mission

1．火星探査機「のぞみ」の状況

火星探査機「のぞみ」(Fig.1)は、1998 年 7 月に M-V ロケットによって鹿児島県の内之浦より打ち上げられた。すでに報告してあるように[1]、最初の予定では 1999 年秋には火星に到着するはずであったのだが(Fig.2)、1998 年 12 月に地球周回軌道から火星に向かう軌道に乗るときにトラブルがあり、軌道が 2004 年初めに火星に到着するものに変更された(Fig.3)。この新しい軌道では、2 回の地球スイングバイ(2002 年 12 月と 2003 年 6 月)が必要となるのだが、この時点では特に「のぞみ」の軌道決定に関連して問題はなかった。(Fig.4、Fig.5 に実際の軌道を示す。)

ところが、1999 年 7 月に「のぞみ」の S バンドにトラブルが生じ、「のぞみ」からの S バンドのダウンリンクが使用不能となってしまった。通常の運用は X バンドを使って行えばよいので問題はないのであるが、2 回の地球スイングバイの間においてレンジデータが取得できないという状況になることが分かったのである。これは、「のぞみ」の姿勢を太陽指向させるとハイゲインアンテナが地球を指向することができずに、レンジの計測が行えないためである。スイングバイ間では、レンジレートの計測はできるはずなのでレンジレートによる軌道決定がなされることになるが、軌道決定に高い精度が要求されるスイングバイを行うときだけに軌道決定には万全を期したい。そこで、相対 VLBI を使った軌道決定の検討が本格的に開始されることになった。

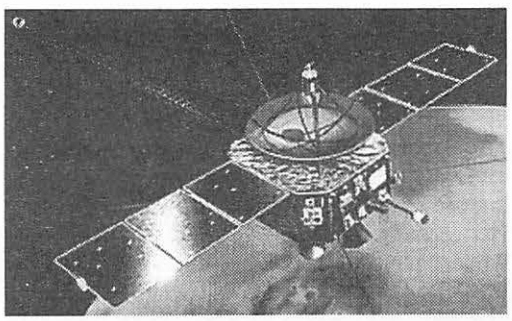

Fig.1 Mars Explorer NOZOMI.／「のぞみ」

†2003 年 10 月からは、それまでの宇宙科学研究所(ISAS)、航空宇宙技術研究所(NAL)、宇宙開発事業団(NASDA)が統合されて、宇宙航空研究開発機構(JAXA)となった。
JAXA：Japan Aerospace Exploration Agency

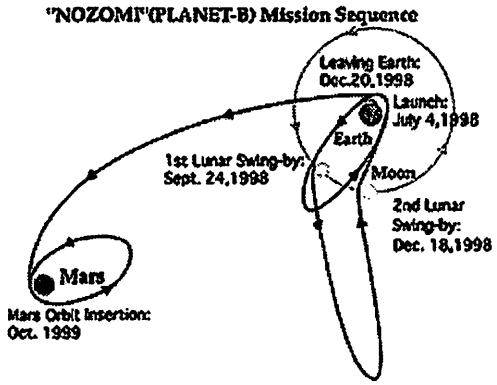

Fig.2 Original orbit plan of NOZOMI.
最初の「のぞみ」の軌道計画。
1998 年 7 月に打ち上げられた「のぞみ」は、2 回の月スイングバイを経て 1999 年 10 月には火星に到着する予定だった。

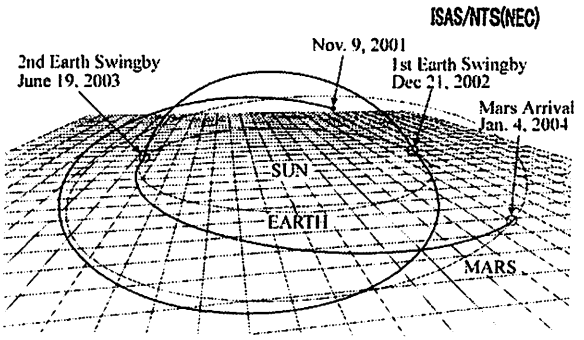

Fig.3 New orbit plan.
変更後の「のぞみ」の軌道計画。
2002 年 12 月と 2003 年 6 月に地球スイングバイを行い、2004 年初めに火星に到着する予定である（到着はその後、2003 年 12 月となる）。地球スイングバイ間は、黄道面に対して垂直方向に跳ね上げられるような軌道となる。

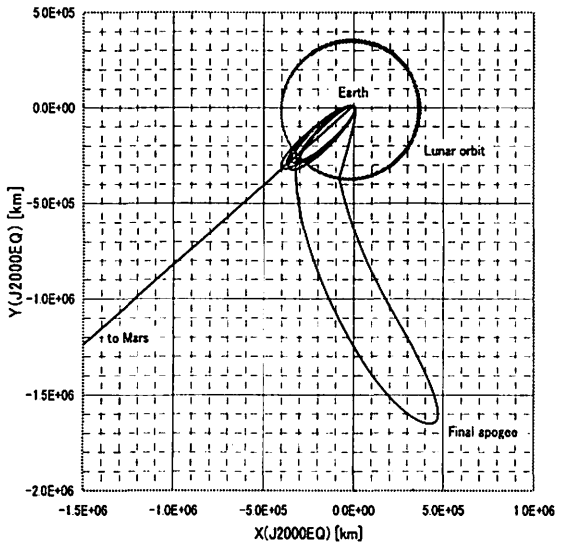

Fig.4 Trajectory of NOZOMI near Earth phase.
地球に近いフェーズでの「のぞみ」の実際の軌道。J2000 赤道座標系の xy 平面に投影した図。

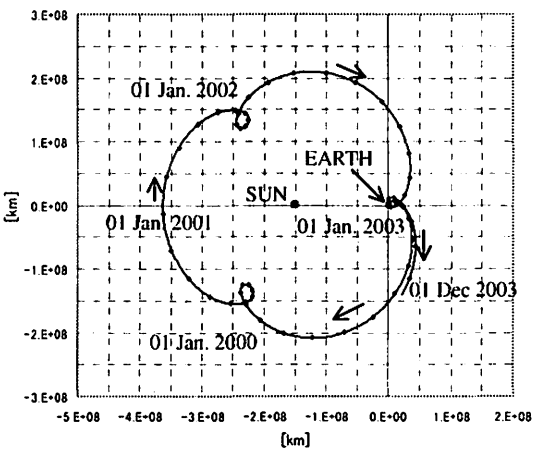

Fig.5 Trajectory of NOZOMI in the interplanetary phase.
惑星間空間での「のぞみ」の実際の軌道。太陽と地球を固定した回転座標系で描いてある。

その後、2000 年末から 2001 年初めにかけては、「のぞみ」が地球からみて太陽の反対側に位置する「合」となり一時通信ができなくなった。この合は無事に乗り切ることができて、その後も順調な運用が続いていたのであるが、2002 年の 4 月末に起こった強い太陽フレアのために電源系統の一部にトラブルが発生してしまったのである。このトラブルは非常に深刻なものである。これについては、次節以下で述べることにする。

2．2002 年 4 月の太陽フレアの影響

2002 年の 4 月末に、太陽で強いフレアが発生した。そのフレアによる太陽風が「のぞみ」に到達

したときに、電源のユニットの1つが停止してしまった。そのために、衛星からテレメトリーを得ることができなくなり、また、ヒーターも停止してしまった。テレメトリーが得られないことは、「のぞみ」からの情報が得られないことである。また、ヒーターの停止によって燃料が凍ってしまうために、姿勢制御や軌道制御が不能になってしまった。Fig.6 には、このトラブルが生じた前後でのドップラーデータ（レンジレートのデータ）を示す。

Fig.6 で分かるように、トラブルが起こる前までは、ドップラーデータの O-C の値は、ほぼ 0 近傍であった。これは、衛星の軌道決定が問題なくなされていたことによるが、トラブル後のドップラーデータの O-C は 0 近傍からずれてしまっている。ここの部分は、計算による予測値はトラブル前までに求められた軌道に基づいているのであるが、探査機が正常ならばこのようなずれは考えられない。ここで O-C が 0 近傍からずれている理由は、探査機の姿勢制御ができなくなったために、ハイゲインアンテナの指向方向が地球からずれていってしまったためと考えられる。つまり、サイドローブによる受信となってしまったため、ドップラー計測において異常なバイアスが生じているのである。この状況では、軌道決定は行うことができない。

その後、2002 年の 5 月半ばからは、約 2 ヶ月間にわたって、探査機からビーコン（情報は乗っていない電波）すら降りてこない状況になってしまったが、7 月半ばにはビーコンは復活した。しかし、テレメトリーは相変わらず降りてこないままであった。ただし、「のぞみ」は地上からのコマンドは受け付ける。そこで、データ・ハンドリング・ユニット（DHU）の自律化機能を用いて、ビーコンのオン・オフで探査機からの情報を知るという作業が始められた。これは、地上から打つコマンドで、探査機内の状態がある条件を満たせば、ビーコンをオフさせる（あるいはオンのまま保つ）というものである。つまり、いろいろな条件文をコマンドとして送って、ビーコンがオン・オフすることで少しずつ探査機の状況を知るのである。この一見原始的な方法がうまく動作し、探査機の主要な情報は把握できるようになった。

一方、太陽に対する探査機の姿勢が徐々に変化したことで、太陽熱によって燃料の一部が融けることが分かった。実際、一部の燃料が融けて、これによってスラスターを吹くことができ、姿勢制御および軌道制御もできるようになったのである。しかし、探査機の姿勢の条件として、太陽光によって燃料を融かすことができるということが新たに加わることになった。つまり、太陽電池のパドルに太陽光が当たるということに加えて、燃料が融けるような姿勢に保たなければいけないのである。そのことで、ハイゲインアンテナを地球方向に指向させることがいっそう難しくなってしまったのである。

Fig.6 に示されているように、ハイゲインアンテナが地球指向しないと正常なドップラーデータが取得できなくなる。その様子は、別の期間の O-C を示した fig.7 にも示されている。

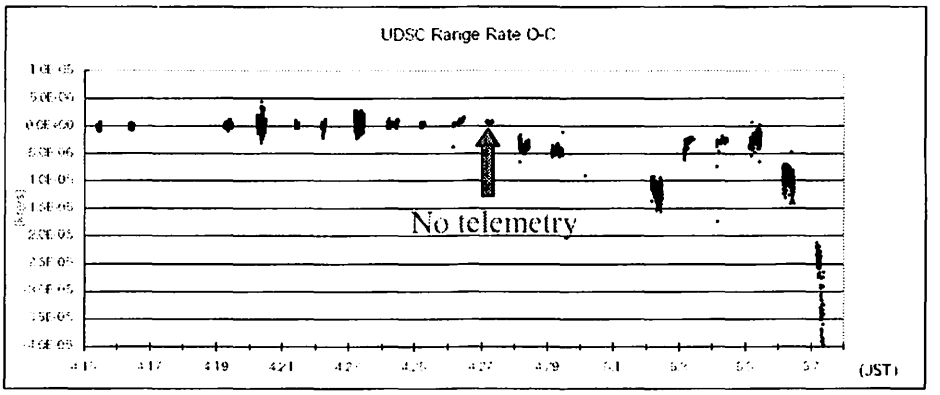

Fig.6 O-C of Doppler (renge rate) data around the severe trouble in April 2002.
2002 年 4 月に太陽フレアの影響で電源系にトラブルが生じた前後でのドップラーデータ。ここでは、ドップラーデータの O-C（O は観測、C は計算による予測値）を示すが、トラブルが生じた後は、姿勢制御が行えないために、O-C の値が 0 近傍からずれてしまっている。

Fig.7 では、2002 年の 10 月から 11 月にかけてのハイゲインアンテナの指向方向（θe）とドップラーデータの O-C が示されている。θe は、ハイゲインアンテナの指向方向と地球方向とがなす角度のことで、値が 0 度のときが、地球方向を向いていることに相当している。ただし、衛星の姿勢を正確に知ることができないため推定せざるを得ず、そのために複数の推定値（曲線）が示されている。この図より、まずθe が 0 度付近ならば、ドップラーデータの O-C は 0 近傍にあるが、θe が少し 0 からずれるとドップラーの O-C にバイアスが生じることが分かる。ただし、θe の角度がある角度になると、再び O-C が 0 付近にくる。そして、さらにθe が大きくなっていくと、ドップラーの O-C は大きく 0 からずれていくことになる。

ドップラーの O-C がこのような傾向を示すことは、ハイゲインアンテナからくる電波の特性によるものと考えられる。ハイゲインアンテナの指向方向に地球がある（受信機がある）場合には、ドップラー計測が正常に行われるのであるが、指向方向がずれるとサイドローブを受信することになり、正確なドップラーが計測できなくなるのである。この状態では、ドップラーデータを使って軌道決定を行うことはできない。

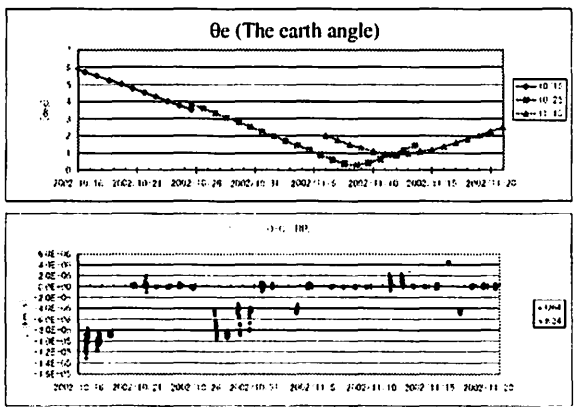

Fig.7 Bias in O-C of Doppler data, which is related to the earth angle (θe) of High gain antenna.
ドップラーデータに見られるバイアス。ハイゲインアンテナの指向方向（上）と、ドップラーデータの O-C（下）。

3．異常事態における軌道決定

このような異常な事態に直面して、軌道決定としては、2 つの方法をとることにした。1 つは、すでに述べた相対 VLBI による方法である。これについては、次節で述べることにする。

もう 1 つは、従来通りのレンジとレンジレートを使って軌道決定をする方法である。幸いなことに、このような異常な状態でも、レンジは計測さえできればそのデータは正常で軌道決定に使えることが分かった。また、ドップラーデータであるが、前節で述べたように、探査機の姿勢によっては、データの質が異常になってしまうのであるが、その場合、バイアスが加わる形となる。このときにドップラーデータの積分時間を探査機のスピンの周期と一致させると、バイアスが見られるパスについて、バイアスを含む計測点と含まない計測点とを分離できることが分かった。詳細は省略するが、バイアスを含まない計測点だけを分離して軌道決定に使うことで、レンジとドップラーによる軌道決定が可能になったのである。

なお、探査機の姿勢は、特に 2 回の地球スイングバイ間においては、そのハイゲインアンテナの指向方向が地球方向に対して直角付近（θe が 90 度付近）となることがほとんどであったが、ハイゲインアンテナの指向方向から 90 度の方向に漏れてくる電波を使って、レンジやドップラーデータを取得することができたのである。この場合、地球と探査機間の距離が 600 万 km くらいまでは、レンジやドップラーデータが取得できた。つまり、地球スイングバイ直前や直後については、レンジとドップラーデータによる軌道決定を行うことができたのである。

したがって、結果的には、相対 VLBI は使わずに、このレンジとドップラーを使った軌道決定によって、2 回の地球スイングバイを乗り切ることができた。しかし、相対 VLBI による軌道決定は、実用化できれば深宇宙ミッションにとって非常に有用なものになるので、「のぞみ」に関して行ったことを以下に簡単にまとめておく。

4．相対 VLBI による軌道決定

深宇宙探査機については、探査機までの距離であるレンジやその変化率であるレンジレートを計測し、それらのデータに基づいて軌道決定を行うのが通常のやり方である。探査機の見かけの位置（角度データ）が軌道決定に使われることもあるが、角度の計測精度がよくないため高精度の軌道決定には不向きであり、打ち上げ初期など限られたときに使われるのみである。

レンジ・レンジレート以外による軌道決定の可能性としては、相対 VLBI の技術を使う方法がある。VLBI とは、Very Long Baseline Interferometry の略であるが、複数の電波望遠鏡（アンテナ）で天体からの電波を観測しそれを干渉させることにより、電波源を高い角度分解能で調べたり、地球上の 2 点間の距離を高精度で求めたりするものである。さらに、近接する 2 天体を同時に観測し、共通する誤差要因を取り除いて精度の向上を図ろうとするのが相対 VLBI である(Fig.8)。

このような VLBI の技術を深宇宙探査機の軌道決定に応用しようという考えは以前からある。例えば、J.S.Border らの論文[2]に基本的なアイディアが記されているし、日本でも、西村敏充らの論文[3] [4] [5]に解析例が紹介されている。これらの理論的な研究では、従来のレンジ・レンジレートの観測データに加えて VLBI のデータが加わればより高精度の軌道決定が可能になることが報告されている。

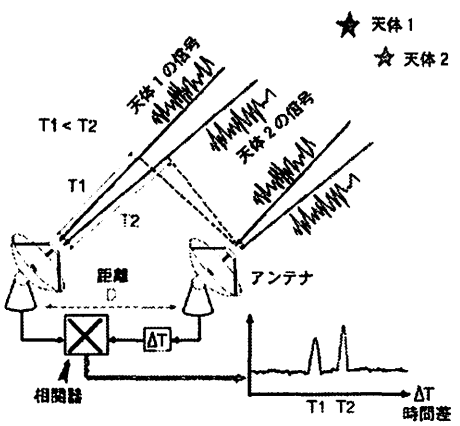

Fig.8 Delta-VLBI observation.
相対 VLBI の原理図。電波の到達時間の差(遅延時間)である τ_1, τ_2 を計測する。

VLBI の技術を実際の軌道決定運用に用いることに関しては、アメリカのジェット推進研究所(JPL)では実用として使われているが、日本ではまだ試験段階である。今まで日本で試みられた例としては、

・静止衛星（1984 年、電波研）
・「さきがけ」（1993 年、臼田－水沢）
・Lunar Prospector（1998 年、水沢－鹿島－筑波）

などがある。ここで、静止衛星については、電波研（現在の通信総合研究所）が JPL と共同で行った実験であり、静止衛星の軌道が高精度で求められた[6]。また、ハレー彗星に向かって打ち上げられた「さきがけ」を用いた実験であるが、これは宇宙研と天文台（水沢）の間で相対 VLBI の観測が試みられた。しかし、このときには、水沢で探査機の信号が受からず、相関処理を行うことができなかった。水沢では、最近、Lunar Prospector からの信号を受けて相対 VLBI 観測を行っているが、こちらは相関処理が成功している。このように、日本でも VLBI を用いた深宇宙探査機の軌道決定を実用化したいという機運は高まってきている。

以上のような状況の下で、火星探査機「のぞみ」についてすでに述べたような予想外の問題が発生し、急遽、「のぞみ」に対して VLBI を使った軌道決定を進めることになったのである。

5．相対 VLBI 観測実験

1 節で述べたように、新しい軌道計画に変更になったあと、S バンドのダウンリンクが使えなくなったため、特に 2 回の地球スイングバイ間の軌道決定に備えて、相対 VLBI による軌道決定の検討が開始された。しかし、2002 年 4 月末の太陽フレアによるトラブルにより、しばらくの間「のぞみ」からの電波を受信して相対 VLBI 観測が行えなかったため、まずは、GEOTAIL 衛星を用いて、相対 VLBI の観測実験を行った。GEOTAIL 衛星は、近地点距離約 5 万 km、遠地点距離約 19 万 km の楕円軌道を周回している。あまり地球からは離れないので深宇宙探査機とはいえないのであるが、相対 VLBI を試験するためには特に問題はない。GEOTAIL 衛星を使った観測実験は、2002 年 6 月 4 日に行われた。その後、「のぞみ」の運用がすでに述べたようにかなり厳しい状況の下ではあるが行えるようになったので、「のぞみ」を使った相対 VLBI の観測が 2002 年 10 月以降 2003 年の 6 月の地球スイングバイまで継続的に行われている。

観測には、通信総合研究所を中心としたグループと国立天文台を中心としたグループとが参加している。それぞれ独自の方法を用いているが、双方で協力しながら観測実験を行っている。この相対 VLBI の観測を行っているグループを「のぞみ」相対 VLBI グループと呼んでいる。観測に参加している局(アンテナ)は、宇宙研の臼田(64m)、通総研の鹿島・小金井(34m、11m)、天文台の水沢(10m)、

山口大学(32m：KDDIから天文台に譲渡されたアンテナ)である。また、観測によっては岐阜大学や北海道大学、国土地理院、そしてカナダのアルゴンキンのアンテナも使われている。

データの取得方法としては、通総研がIP-VPBIボードとK4(Fig.9)、天文台がRISEターミナル(Fig.10)を用いた。また、アップリンクのために、宇宙研の鹿児島局(20m)も使われた。観測のアンテナ配置を図にするとFig.11のようになる。

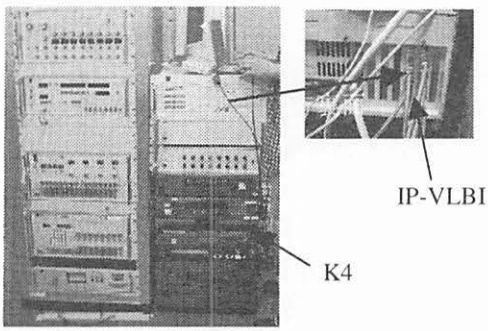

Fig.9 IP-VLBI and K4 systems of CRL.
臼田に設置された通総研のIP-VLBIとK4。

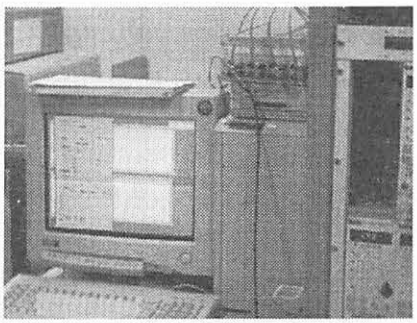

Fig.10 RISE system of NAO.
臼田に設置された天文台のRISEターミナル。

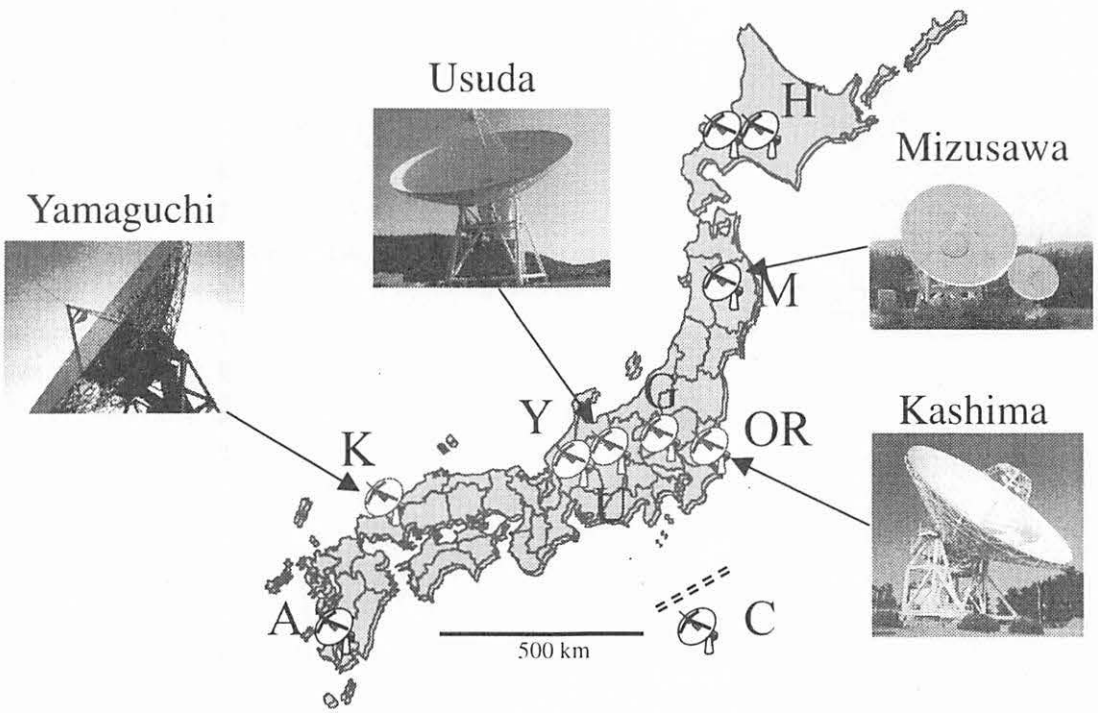

Fig.11 Locations of antennas for the Delta-VLBI observations of NOZOMI.
「のぞみ」の相対VLBI観測に参加したアンテナの位置。記号は以下の通り：H : Tomakomai (11m), M : Mizusawa (10m), O : Kashima (34m), R : Kashima (11m), G : Koganei (11m), U : Usuda (64m), Y : Gifu (11m), K : Yamaguchi (32m), A : Aira (11m), C : Chichi-jima (10m)

このような多くのアンテナを用いて観測を何度も行った。観測は、クエーサーから来る電波と「のぞみ」から来る電波とを交互に複数の局で同時に受信するものである。その結果、最終的には「のぞみ」から来る電波の相関処理に成功し、遅延時間としてのデータを取得することができるようになった。また、その取得したデータは、通常の電波航法による軌道決定（レンジとドップラーを用いたもの）と比較しても、矛盾はないものであることは確認された。しかし、相対 VLBI 観測から得られた遅延時間を元にして軌道決定を行うところには至っていない。これは、得られた遅延時間のばらつきが大きすぎることによる。現在、さらに解析を進めているところであり、結果については別の機会に報告したいと考えている。

6．軌道決定精度シミュレーション

前節で述べたように、まだ相対 VLBI の実データを用いた軌道決定には成功していないが、相対 VLBI のデータ処理がうまく行えた場合に軌道決定精度がどのくらい向上するのかを検討してみた。

宇宙科学研究所では、ISSOP と呼ばれるソフトウエアを開発し、深宇宙探査機（天文衛星も含む）の軌道決定を行っている。このソフトウエアでは、レンジとレンジレート（場合によると角度データも）を取り込んで軌道決定を行う。このソフトウエアに VLBI のデータ（ここでは遅延時間）を取り込んだ場合、軌道決定精度がどのように変化するかを解析した。なお、今回の解析は、VLBI データについては 1-way レンジ・ディファレンスモデルという簡易的なものを用いた。

ここでは、「のぞみ」が 2 回の地球スイングバイ間の中間地点(2003 年 3 月)にいる場合について、レンジレートと遅延時間データがあるとして軌道決定精度を調べた。パラメータとしては、レンジレートのノイズ(5 mm/s、1 mm/s)、遅延時間のノイズ(1 nsec、0.1 nsec)、そして VLBI データの取得日数を考慮した。

解析の結果を Table.1 に示す。また、位置誤差についてグラフにしたものを Fig.12 に示す。これらより、VLBI データが 1 日でも加われば位置誤差は半分くらいに減少することが分かる。また、VLBI データが 3 日間ほどあると、誤差は 1 桁程度小さくなる。従って、VLBI によるデータは軌道決定に非常に有効であるということが確認された。

Table.1 Accuracy analysis for Delta-VLBI

軌道決定精度解析(ΔR：位置誤差,ΔV：速度誤差)

case	A	VLBI obs. Date	B	ΔR (km)	ΔV (km/s)
R5	5			1.0E+2	1.7E-4
R1	1			2.0E+1	3.5E-5
R5-V10-P1	5	3/21	1	5.3E+1	1.0E-4
R5-V10-P3	5	3/21 23 25	1	2.2E+1	4.5E-5
R5-V10-P6	5	3/21-3/26	1	2.0E+1	3.9E-5
R5-V01-P1	5	3/21	0.1	5.0E+1	9.6E-5
R5-V01-P3	5	3/21 23 25	0.1	9.9E+0	8.9E-6
R5-V01-P6	5	3/21-3/26	0.1	9.6E+0	6.1E-6
R1-V10-P1	1	3/21	1	1.3E+1	2.4E-5
R1-V10-P3	1	3/21 23 25	1	1.0E+1	1.9E-5
R1-V10-P6	1	3/21-3/26	1	8.2E+0	1.5E-5
R1-V01-P1	1	3/21	0.1	1.0E+1	2.0E-5
R1-V01-P3	1	3/21 23 25	0.1	3.3E+0	6.6E-6
R1-V01-P6	1	3/21-3/26	0.1	2.9E+0	5.2E-6

A：レンジレートのノイズ mm/s、B：遅延時間のノイズ nsec. レンジレートは 3/21-3/26 の 6 日間取得したと仮定。

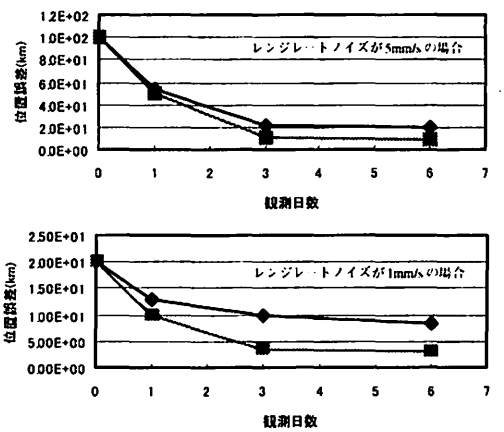

Fig.12 Accuracy of position when VLBI data is used.

VLBI データを併用した場合の軌道決定精度(位置)

◆印と■印はそれぞれ遅延時間のノイズが 1 nsec と 0.1 nsec の場合を示す。また、観測日数が 0 の場合の値は、VLBI データを使わずに軌道決定した場合である。

7．まとめ

火星探査機「のぞみ」は、日本としては初めての本格的な惑星探査機であるが、その運用には数々の困難があった。しかし、それぞれの困難に対しては様々な工夫を行い、最終的に火星に向かう軌道に乗せることができたのである。あとは、2002 年 4 月末からの電源系統の不具合が復旧してくれることを願うのみである。いずれにしても、

深宇宙探査機の軌道決定という観点から見ると、「のぞみ」は非常に多くの経験を我々に与えてくれたことは事実である。

日本の深宇宙ミッションとしては、「のぞみ」に続いて小惑星サンプルリターンミッションであるMUSES-Cが、「はやぶさ」として2003年5月9日に打ち上げられた。「はやぶさ」はイオンエンジンという特殊なエンジンによって微小加速度が継続的に働く探査機であり、軌道決定にとっては手強いものである。もちろん、高い軌道決定精度が要求されており、引き続き相対VLBIによる軌道決定を検討していきたいと考える。そして、さらに将来のミッションとしてソーラーセールや金星バルーンなどいろいろな構想があるが、これらのミッションが行われるときまでには、レンジ・レンジレートに加えて相対VLBIでの軌道決定も定常的に行えるというような状況になることを目指したい。

「のぞみ」相対VLBIグループのメンバー

宇宙研　軌道‡：加藤隆二, 市川勉, 川口淳一郎, 山川宏, 吉川真
（富士通）‡：大西隆史, 石橋史朗
宇宙研　VSOP：平林久, 村田泰宏, 朝木義晴, 澤田-佐藤聡子
通総研　鹿島：近藤哲朗, 市川隆一, 小山泰弘, 中島潤一
関戸衛, 川合栄治, 大崎裕生, 大久保寛
天文台　水沢：河野宣之, 花田英夫, 河野裕介, 菊池冬彦
平勁松, 亀谷収, 岩館健三郎, 鶴田誠逸
天文台　三鷹：川口則幸, 輪島清昭
山口大　：藤沢健太
宇宙開発事業団：岩田隆浩

‡宇宙研軌道決定グループ
※2003年3月現在

参考文献

[1]吉川真、加藤隆二、市川勉、山川宏、川口淳一郎、石橋史朗、佐藤耕一、大西隆史、野田明、篠崎憲次、黒須勝仁：火星探査機「のぞみ」の軌道決定における諸問題、草津天体力学N体力学研究会集録（Proceedings of the 33rd Symposium on Celestial Mechanics）、pp.277-283 (2001).

[2]J.S.Border, F.F.Donivan, S.G.Finley, C.E.Hildebrand, B.Moultrie, and L.J.Skjerve: Determining Spacecraft Angular Position with Delta VLBI: The Voyager Demonstration, AIAA/AAS Astrodynamics Conference, August 9-11, San Diego, Calif., AIAA-82-1471 (1982).

[3]西村敏充、金井喜美雄、村田正秋：航空宇宙における誘導と制御、計測自動制御学会 (1995).

[4]浅井義彦、西村敏充：差分VLBI技術を用いた高精度軌道決定、計測自動制御学会論文集、Vol.35、No.4、pp.467-472 (1999).

[5]吉川真、西村敏充：深宇宙機の軌道決定の現状と将来、計測自動制御学会論文集、Vol.39、No.9、pp.564-569 (2000).

[6]塩見正、河野宣之：VLBIによる静止衛星の高精度軌道決定、日本航空宇宙学会誌、第35巻 第404号 pp.425-432 (1987).

太陽輻射圧計算プログラムの開発

Development of solar radiation pressure computation software

久保岡 俊宏

Toshihiro Kubo-oka

通信総合研究所 鹿島宇宙通信研究センター

Kashima Space Research Center, Communications Research Laboratory

ABSTRACT

A new system to compute solar radiation pressure on a satellite with a complex shape has been developed. This software consists of three parts: Modeler, Polygon Maker, and Radiation Tracer. Numerical model of satellite shape is made by use of 3D CG software (LightWave 3D). The Polygon Maker converts the model data to the data set which contains several information of polygon, i.e. normal vector, area, coordinates of vertex, and so on. In the Radiation Tracer, the light source of the Sun is considered to be an array of pixels. Light from each pixel is traced and determined whether it intersects with polygons or not. The light from the pixel is considered to interact with the polygon that the light first intersects. The radiation pressure by each ray pixel is computed and vector summed to get the acceleration of the satellite. This method has an analogy with "ray tracing" in 3D CG. We found the system can be calculate solar radiation pressure with accuracy better than 0.5 [%]. The new system will be applied to high precision orbit determination of ETS-VIII and quasi-zenith satellites.

1. Introduction

これまでの静止衛星は、通信、放送、気象観測を主目的としている関係上、それほど高い軌道決定精度は求められていなかった。言い換えれば、所定の軌道位置をキープしているかどうかが分かればよく、軌道決定はkmオーダーの精度で十分であった。しかし、これから静止軌道高度に打ち上げられる衛星、例えば原子時計を搭載し測位実験を行うETS-VIII、日本向けの測位サービスを行う準天頂衛星は、「測位」というミッションを実現するために、これまでより1桁以上高い精度の軌道決定が要求されている。従って、静止衛星に関しても、低軌道（高度2万キロのGPS衛星より低いもの）と同様の高精度軌道決定が行えるシステムを構築することが急務とされている。

一般的に、人工衛星の軌道決定精度を向上するためには、トラッキングデータの質と量を向上させること、及び衛星に作用する摂動力の大きさを正確に見積もることが重要となる。本稿では、後者について考えることにする。静止衛星に作用する各種の摂動力の大きさをTable 1.1にまとめた。Table 1.1の中で地球重力場の影響及び、月・太陽による摂動は容易に計算出来る。これに対し、太陽輻射圧は衛星の形状、質量、表面の材質（反射率）、及び衛星姿勢（太陽電池パドルの様に可動部分のがある場合はその向き）に依存するため、高い精度で衛星に作用する力を見積もることが難しい。さらに、軌道制御の際の推進薬消費によって衛星の質量が減少したり、宇宙線の影響で表面の材質が劣化し反射率が変わることによって衛星に及ぼす力も変化するという厄介な性質を持っている。

静止軌道よりも低い高度を周回する衛星、たとえば、TOPEX/Poseidon (Antreasian and Rosborough, 1992)、GPS (Fliegel et al, 1992)、GLONASS (Ziebart

Cause	Acceleration [m/s^2]
Earth's monopole	$2.2*10^{-1}$
Earth's oblateness (J_{20})	$7.4*10^{-6}$
Low-order geopotential harmonics	
J_{22}	$4.3*10^{-8}$
J_{66}	$4.5*10^{-12}$
high-order geopotential harmonics	
$J_{18\ 18}$	$1.3*10^{-22}$
Perturbation due to the Moon	$7.3*10^{-6}$
Perturbation due to the Sun	$3.3*10^{-6}$
Perturbation due to other planets (Venus)	$4.3*10^{-10}$
Atomospheric Drag	0.0 (?)
Solar Radiation Pressure	$2.3*10^{-7}$
Earth's Albedo Radiation Pressure	$2.1*10^{-9}$

Table 1.1 Perturbations acting on geostationary satellites (after Milani et al, 1987).

et al, 2001) については、精密な太陽輻射圧モデルが作られており、高精度の軌道決定に活用されている。しかし、静止衛星に関しては、データ中継衛星 TDRS の太陽輻射圧モデルが成功しているものの (Luthcke et al, 1997)、INMARSAT に関しては詳細なモデルを入れたにもかかわらず、実際に軌道決定を行った後の測距値残差が、衛星形状を球形と仮定した簡易なモデルを用いた場合に比べて増大してしまうという結果に終わっている (Gambardella et al.)。

本研究では、Ziebart et al. (2001) と同様、計算機上で多数のポリゴンからなる衛星形状モデルをつくり、太陽光に相当する平行光線束を入射して衛星の加速度を計算するというアプローチを採用した。本稿では、現在開発を進めているソフトウェアの概要について述べると共に、来年度打ち上げ予定の ETS-VIII に適用した結果についても触れる。

2. システムの概要

現在開発中のシステムは大きく分けると Modeler、Polygon Maker、Radiation Tracer という 3 つのパートで構成される。最初の Modeler は、人工衛星の設計情報を元に数値モデルを作る部分である。ここは市販の 3D CG ソフトのモデラー部を利用する。現段階では、鹿島宇宙通信研究センターにあるワークステーション（SGI 社製 Indigo 2）に元々インストールされていた NewTek 社の Lightwave 3D ver. 5.6 を用いているが (Fig. 2.1)、基本的には頂点の座標を数値入力出来るものであれば何でも構わない。大抵の 3D CG ソフトには、異なるソフトウェア間で形状モデルを交換するために、共通フォーマットで出力する機能が備わっている。現在のシステムでは、各種ある共通フォーマットの中で Wavefront フォーマットと呼ばれるものを採用している。これは単なるテキストファイルで、最初のセクションに各頂点の座標が並び、その後の表面材質毎に分けられたセクションに 1 行毎にポリゴンを構成する頂点番号が並ぶという形式になっている。この様に、市販の 3D CG ソフトのモデラー部を利用することで、衛星の形状モデルの製作を効率良く行える。

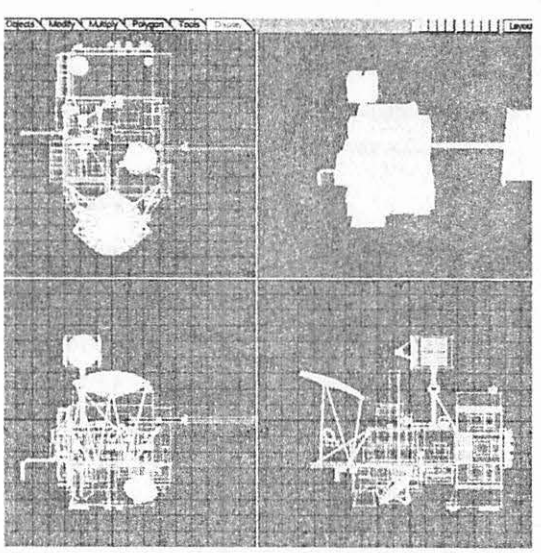

Fig. 2.1 Main window of LightWave3D Modeler.

これ以降のプログラムは新たに書いたものである。2 番目の Polygon Maker は、LightWave 3D が出力した Wavefront ファイルから、ポリゴンを構成する頂点の数（3 または 4）、頂点の座標、外向き法線ベクトル、ポリゴンの面積、表面の反射率（鏡面＆拡散）を各ポリゴン毎にまとめた新しいデータファイルを作るものである。言い換えれば、Wavefront ファイルから Radiation Tracer で使うフォーマットに変換するプログラムである。

最終段の Radiation Tracer は、本システムの根幹となる部分である。まず、Polygon Maker で作られたデータファイルを読み込み、座標原点にポリゴンで出来た衛星モデルを配置する。つぎに、仮想的なスクリーンから平行光線束を入射し、それぞれの光線毎にどのポリゴンと最初に交差するのかを判定する (Fig. 2.2)。どのポリゴンとも交差しない光線は輻射圧に寄与しないものとして、以後の計算では無視する。一方、ポリゴンと交差する光線は、最初に交差したポリゴンに力を作用させているものとして加速度を計算する。1 つのピクセルから出た光が及ぼす圧力は、

$$\mathbf{F}_i = -\frac{\Phi}{c}\left[(1-\rho_i)\mathbf{s} + 2\left(\frac{\delta_i}{3} + \rho_i \cos\beta_i\right)\mathbf{n}_i\right] dS_P \qquad (1)$$

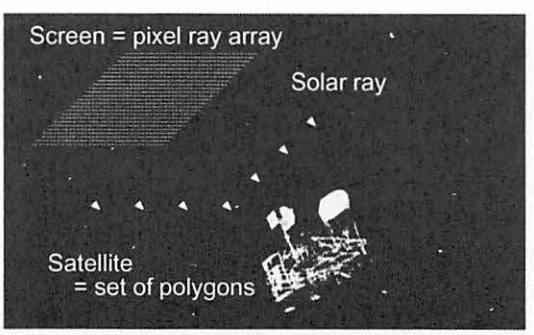

Fig. 2.2 Concept of Radiation Tracer.

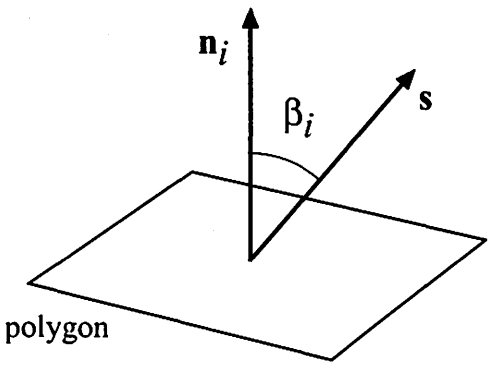

Fig. 2.3 Definition of angle β_i.

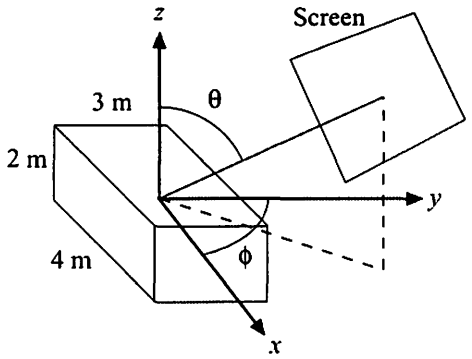

Fig 3.1 Arrangement of rectangular box and definition of coordinate system.

という式で表すことが出来る (Milani et al, 1987)。ここで、Φ は Solar Flux、c は光速度、ρ_i はポリゴンの鏡面反射率、s は太陽方向の単位ベクトル、δ_i はポリゴンの拡散反射率、$\mathbf{n}_i$ はポリゴンの法線ベクトル、dS_p は 1 つの "光線" ビクセルの面積を表している。また、β_i は Fig. 2.3 に示されている様に、s と $\mathbf{n}_i$ のなす角度である。ポリゴンによって反射あるいはポリゴンを透過した光を追跡することも可能である。この場合は、ポリゴンの反射率・透過率に応じて Flux が減少しているものとする。反射または透過した光が衛星の別の部分に当たる場合は、そこで再び加速度計算を行う。

上記の手法は、3D CG の作成で広く用いられているレイトレーシング法 (Lengyel, 2001) とよく似ている。ただし、レイトレーシング法は視点から光線を追跡していくのに対して、本手法は光源側から光線を追跡していく所が異なる。この方法の最大のメリットは、衛星のある部分で反射された光が衛星の別の部分に当たる「多重反射」や透過光、さらには衛星の一部が別の部分に影を落とす「Self shadowing」といった現象を考慮できるという点にある。逆にデメリットとしては、レイトレーシング法と同様に膨大な計算量を要するため、リアルタイムでの計算には向かないということが挙げられる。

現段階で、Polygon Maker と Radiation Tracer の両プログラムは一応完成しているが、モデラーとなる Lightwave 3D と Polygon Maker の間の連携に大きな問題を抱えている。前述の様に、LightWave 3D が出力する Wavefront ファイルは、2 番目以降のセクションの各行にポリゴンを構成する頂点番号が並ぶという構造になっている。ところが、この頂点番号の並びと、ポリゴンの外向き法線の向きとの間に一貫した関係が無いのである。頂点番号の若い順に並んでいる訳でもない。Radiation Tracer 内での処理の際に、ポリゴンの外向きの方向の情報が不可欠であるため、現段階では Wavefront ファイルを Polygon Maker にかけたものをそのまま Radiation Tracer で使うことが出来ない。形状モデルを構成するポリゴンが少数である場合は、手動で Wavefront ファイルを書き直すということも可能だが、後述する ETS-VIII のモデルの様にポリゴン数が千のオーダーに達する場合、この作業は現実的に不可能に近い。現在、Lightwave 3D 以外のソフトウェアに一旦形状ファイルを読み込ませ、改めて共通フォーマットで出力させる方法等を検討しているが、本稿執筆の段階ではまだ決定的な打開策を見いだせていない。

3. Radiation Tracer の精度評価

ポリゴン数が少ない場合は Wavefront フォーマットは手作業で容易に修正出来るので、衛星形状が簡単で、太陽輻射圧が解析的に計算できる場合について Radiation Tracer の精度評価を行ってみた。まず座標原点に 2 m × 3 m × 4 m の直方体を配する。全 6 面の材質は全て同一（鏡面反射率 $\rho = 0.2$、拡散反射率 $\delta = 0.8$）とする。スクリーンの大きさは 6 m × 6 m、1 ピクセルのサイズは 1 cm × 1 cm とする。座標系及び、スクリーンの方向を Fig. 3.1 の様に定義する。Radiation Tracer で計算した加速度値の理論値からの誤差を Fig 3.2 に示す。どの方向から太陽光を入射しても加速度の誤差は0.5 % 以下に押さえられている。

$\theta = 90$ deg の場合、及び $\theta = 45$、0 deg で ϕ が 0 と 90 deg の場合に誤差が増大しているのは、ポリゴンのエッジ部分の影響と考えられる。Radiation Tracer では、各ピクセルから出る光線の「中心」がポリゴンと交差するかどうかを判定し、交差する

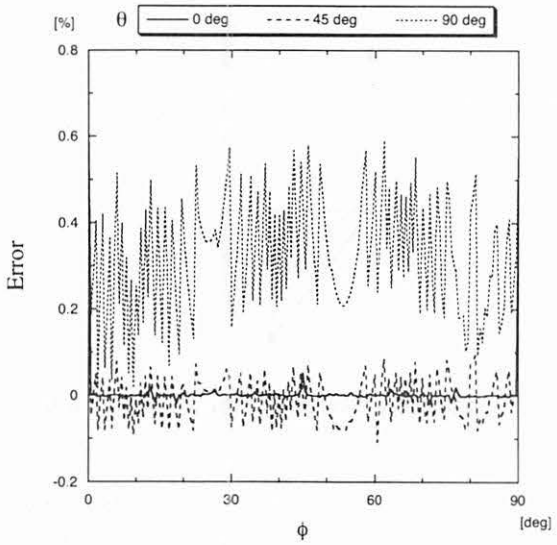

Fig 3.2 Relative error of accelerations computed by use of Radiation Tracer.

場合はそのピクセル全体の光束がポリゴンに入射するものと見なし、逆に光線の「中心」がポリゴンと交差しない場合、そのピクセル全体の光束は全くポリゴンに力を及ぼさないものとしている。このため、ポリゴンのエッジ付近に当たる光については、本来当たらないはずの光までカウントしたり、当たっているはずの光を数え落とすという事が起こりうる。上記の場合、特に θ = 90 deg の場合は、上下端（z = ± 1）付近に当たる光をオーバーカウントしているため、誤差がプラス方向に増大していると考えられる。この影響を除くには、ピクセルのサイズをさらに細かくするか、ＣＧでよく使われているアンチエイリアシング的な手法（エッジをなめらかにする）を採用する必要があるものと考えられる。

4. ETS-VIII に作用する太陽輻射圧

ETS-VIII（技術試験衛星 VIII 型）は３トンクラスの大型静止衛星で、2004 年度に打ち上げが予定されている。最大外形寸法が 19 m × 17 m という大型の展開アンテナ２基を持ち、移動体衛星通信の実験や、搭載原子時計から生成される正確な時刻信号を利用し、GPS 衛星からの信号と組み合わせた測位実験が計画されている。

Fig. 4.1 の写真からも分かるように、ETS-VIII は大別すると衛星構体、展開アンテナ、太陽電池パドルの３つの部分から構成される。衛星構体は、縦 2.45 m × 横 2.35 m × 高さ 3.7 m の本体バス部から地球側の面に高さ 1.98 m の給電部タワーが突

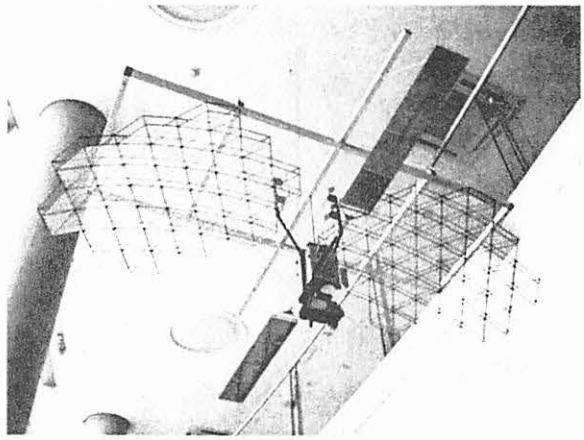

Fig 4.1 1/30 scale model of ETS-VIII (Engineering Test Satellite-VIII). The satellite has two large deployable refrector antennae and two large solar paddles.

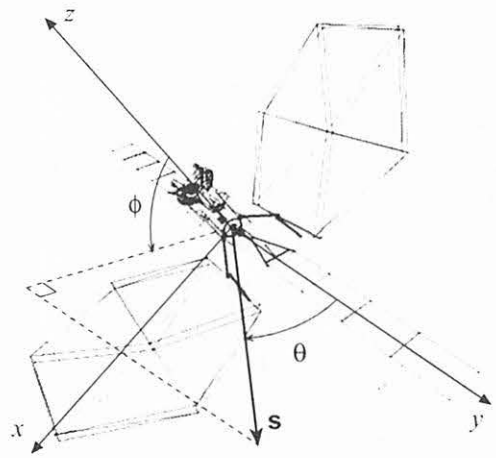

Fig 4.2 Polygon model of ETS-VIII and coordinate system adopted in this chapter.

きだした形状である。東西面にある２枚の展開アンテナは、金メッキを施したモリブデンメッシュからなる鏡面を骨組みで支える、いわばワンタッチ傘のような構造になっている。このメッシュ部の透過率及び反射率は、光の入射角によって変化する性質がある。太陽電池パドルは、横 2.46 × 縦 3.23 m のプレートを４枚連結したものをブームで支持している。これが南北面に１基ずつ配置されている。

ETS-VIII の設計データを元に、LightWave3D のモデラーで形状モデルを作ったところ、ポリゴンの数は合計で 1800 近くになってしまった (Fig. 4.2)。前述の理由から、これほど多数のポリゴンを含む形状データを Polygon Maker に入力することは出来ない。そこで、衛星構体に取り付けられて

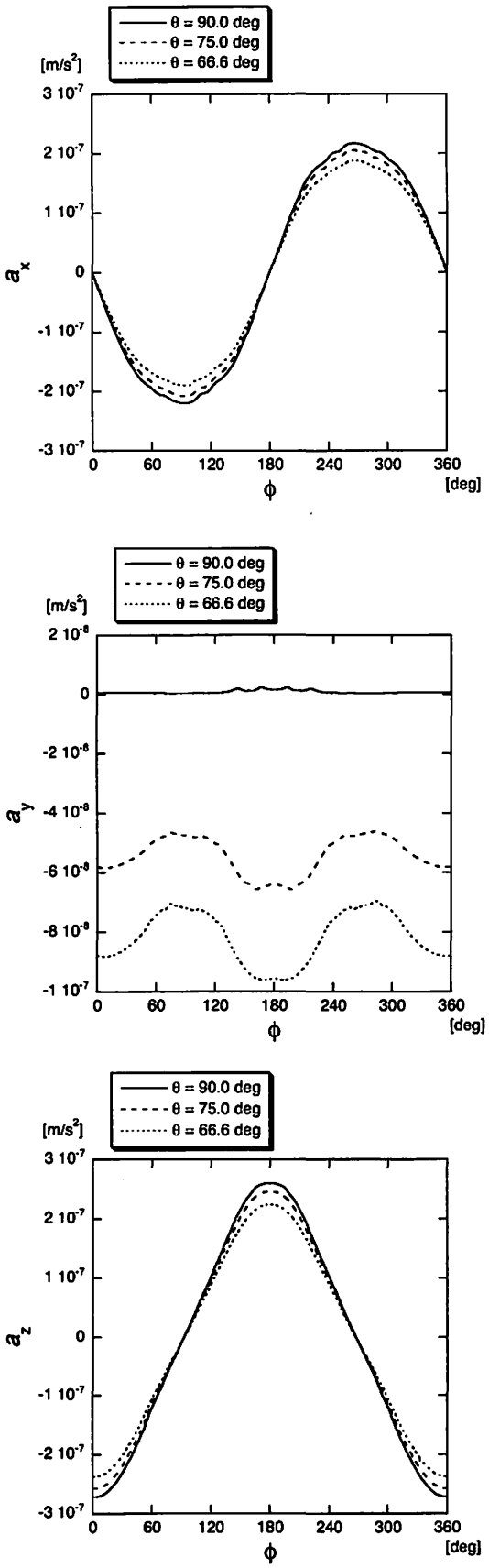

Fig 4.3 Acceleration of ETS-VIII due to the solar radiation pressure. It was computed by use of a simplified polygon model.

いる小型のアンテナや推進部等の微小な部分を省き、ポリゴン数を100程度まで減らした簡略なモデルを用いて、ETS-VIIIに作用する太陽輻射圧を計算してみた。Fig. 4.2に示す様に、座標系はz軸を地心方向とし、x軸を速度ベクトルの方向、y軸を右手系をなすようにとる。衛星の姿勢は、太陽電池パネル及び展開アンテナの軸が、それぞれy軸、x軸に沿う形になる。太陽電池パドルは発電効率を最大にするためy軸と太陽方向の単位ベクトル$\mathbf{s}$が張る平面内に、セル面の法線ベクトル$\mathbf{n}$が来るように、y軸周りにパドルを回転させる。太陽光の方向はFig. 4.2に示す様にθとφの2つの角度で表す。Fig. 3.1と定義が異なることに注意されたい。ETS-VIIIは静止衛星軌道上を運動するので、θの変域は66.6 deg ～ 113.4 degとなる。1ピクセルのサイズは前章と同じく1 cm × 1 cmとした。

θ = 90、75、66.6 degの3つの場合について、太陽輻射圧による加速度のx、y、z各成分のφによる変化をFig. 4.4に示す。加速度のz及びy成分については太陽電池パドルと展開アンテナに作用する輻射圧がほぼ同程度になる。衛星本体の寄与はこれより1桁小さくなる。展開アンテナについては、鏡面を構成するメッシュ部分よりも、メッシュを支えているステー部の影響が大きい。加速度のx成分については、太陽光が$\pm z$方向、つまり展開アンテナの正面から入射する様な場合を除いては、太陽電池パドルに作用する輻射圧が最も大きくなる。特に、φ = 90、270 deg（展開アンテナの横方向から光が入射）の場合、パドルの寄与が展開アンテナの2倍以上となる。

5. まとめ

複雑な形状をもつ人工衛星に作用する太陽輻射圧を計算するソフトウェアの開発について概説した。本ソフトウェアは、太陽輻射圧を誤差0.5%以下という精度で計算することができるが、実用に供するには、Modeler部とPolygon Maker部の連携の問題を解決しなければならない。今回のシステムは、静止衛星に限らずあらゆる種類の衛星（惑星探査機を含む）にも適用可能である。

現在、通信総合研究所を中心とするグループでは、独自の軌道解析ソフトウェアCONCERTO (e.g. Otsubo et al, 1996) の改良を進めている。その過程で、本研究で開発しているシステムから得られた結果を組み込み、ETS-VIIIや準天頂衛星の精密軌道決定に活用することを計画している。その際に

は、Topex/POSEIDON 衛星で行われた様に(Antreasian et al, 1992)、詳細な太陽輻射圧モデルを少数の平板の組み合わせで近似する" マクロ・モデル" 的なアプローチを取る必要があるが、ETS-VIII の大型展開アンテナの様に、反射率・透過率が太陽光の入射角度に依存する場合にそのまま適用できるのかについては、今後要検討である。

謝辞

ETS-VIII の形状及び反射率のデータを提供してくださった宇宙開発事業団 ETS-VIII プロジェクトチームの関係各位に深謝する。

References

Antreasian, P. G., and G. W. Rosborough, Prediction of radiant energy forces on the TOPEX/POSEIDON spacecraft, J. Spacecraft and Rockets, 29(1), pp. 81-90, 1992.

Fliegel, H., T. Gallini, and E. Swift, Global Positioning System radiation force model for geodetic applications, J. Geophys. Res. 97(B1), pp. 559-568, 1992.

Gambardella, E., J. P. Berthais, and F. Mercier, Geostationary Precise Orbit Determination Using Euridis Data, Colloque international, MÈcanique Spatiale, International Symposium Space Dynamics, Centre de Congrès, Biarritz (France), 26-30 June 2000.

Lengyel, E., Mathematics for 3D game programming & computer graphics, Charles River Media, 2001.
日本語訳：ゲームプログラミングのための３Ｄグラフィックス数学（訳：狩野智英、出版：ボーンデジタル）

Luthcke, S. B., J. A. Marshall, S. C. Rowton, K. E. Rachlin, C. M. Cox, and R. G. Williamson, Enhanced Radiative Force Modeling of the Tracking and Data Relay Satellite, Journal of Astronautical Sciences, vol. 45 No. 3, pp. 349-370, 1997.

Milani, A., A. M. Nobili, and P. Farinella, Non-gravitational perturbations and satellite Geodesy, Adam Hilger, Bristol, 1987.

Otsubo, T., H. Kunimori, B. Engelkemier, and F. Takahashi, Development of Space Geodetic Technology Analysis Software: CONCERTO, Journal of CRL, Vol. 43, No. 1, pp. 23-57, 1996.

Ziebart, M., and P. Dare, Analytical Radiation Pressure Modelling for GLONASS using a Pixel Array, Journal of Geodesy, 75, pp. 587-599, 2001.

Homoclinic Structure of a reduced Nonlinear Symplectic Map Chain

Shin-itiro GOTO[1], and Kazuhiro NOZAKI[2].
[1]Department of Applied Mathematics and Physics,
Kyoto University, 606-8501, Kyoto, JAPAN
[2]Department of Physics,
Nagoya University, 464-8602, Nagoya, JAPAN

abstract

We present a method to construct a symplecticity preserving rernormalization group map of an N-coupled periodic chain of weakly nonlinear symplectic maps, and obtain a general reduced map describing its long-time behavior. It is found that the modulationaly instability in the reduced map triggers random wandering of orbits around some homoclinic-like manifolds. We also mention that the possibility of having the connections between the waves which have various wave numbers due to their unstable manifolds and stable manifolds.

1 Introduction

多自由度ハミルトン力学系はカオスを示す場合がほとんどである. しかし, その相空間上の軌道族の振舞いを調べる研究はよく進んでいない. この問題の本質は, 相空間が高次元である事による軌道族の振るまいの可視化の困難さである. この種の高次元ハミルトン力学系における問題は, 多くの数学者や物理学者の数理的関心をひいてきた. また高次元ハミルトン力学系の相空間構造の理解は今述べた関心に留まらず, 化学反応系や天体力学方面などへ応用があるため重要で基礎的な課題である.

あるハミルトニアンフロー (即ち, 正準方程式のつくる相空間上の軌道族の流れ) をあるポアンカレ断面上で離散時間の力学系を構成すると自然にシンプレクティックマップ系を導く. そのためシンプレクティックマップ系は, ハミルトン力学系の問題を研究する際にしばしば用いられてきた. 典型例として, 全次元双曲型不動点を有するシンプレクティックマップ系のホモクリニック分岐の研究が挙げられる. これにより, 全次元双曲型の不動点を有する系のカオス化の理解が進んだ [HNK99].

では全次元楕円型不動点を有する場合のシンプレクティックマップの場合はどうであろうか？よく知られているように, ある仮定のもとに, その相空間中のあるトーラスは共鳴によって破壊される (ＫＡＭ理論). もし, そのトーラスが双曲型ならば, ウィスカーとして知られる不安定多様体や安定多様体がそのトーラスに付く事になる [AA89]. そのウィスカーが相空間大域的な輸送を起こす事が, あるクラスの近可積分高自由度ハミルトン力学系で起こることが言われている (アーノルド拡散)[LL91]. また, 共鳴と共鳴が交差した, 共鳴交差点近傍でのウィスカーの動的振舞いが調べられてきている [GN99],[HK03]. 一方, あるハミルトン系の結合振動子系のトーラスは変調不安定性と呼ばれる機構によりトーラス周りに安定多様体や不安定多様体を有する. その不安定多様体と安定多様体の交差でカオスが生じる可能性がある [MS92][GNY02].

今回, 我々はそのような機構によるカオスの性質にアプローチする. これは, 高自由度ハミルトン力学系における新たな機構によるカオスのオンセットを調べる事になると期待できる.

本研究ではこの種の問題を取り扱う. 2 節で上記の問題を一般的なモデルで調べるため, 楕円型不動点を有する 2 次元弱非線形シンプレクティックマップ系を最近接相互作用で結合したモデルを用意する [GNY02]. 次に特異摂動法として知られるくりこみ法を用い, 系の持つ共鳴項を拾いくりこみマップを導出する事を試みる. その際, くりこみ法のシンプレクティックマップ系への適用に対する問題点とその解決策の概要を述べる. 3 節では得られたくりこみ系を用いて一般的に波数 k の波の安定性を議論し, その近傍での相空間の様子を模式的に示す. 4 節では 3 節での線形安定性の結果を踏まえ, $k=0$ 周りの不安定多様体の様子を数値計算により示す. 5 節では 3 節で得られた安定性解析の結果と 4 節での $k=0$ の波の数値計算の結果を組み合わせ, 種々の不変多様体, 特に波数 k と k' の波達の間の不安定・安定多様体による相空間におけるネットワークの構造形成の可能性について議論する. 最後に 6 節において今回の報告と今後の展開についてまとめておく.

なお, 今回得られたくりこみマップは, ある離散非線形シュレーディンガー方程式として知られている.

2 Symplectic map chain and reduced map

考察するモデル系は以下の シンプレクティックマップ系とする.

$$x_j^{n+1} - x_j^n = \tau p_j^{n+1}, \tag{1}$$

$$p_j^{n+1} - p_j^n = \tau\left[-\Omega^2 x_j^n + \varepsilon\left\{ -\alpha (x_j^n)^3 + \nu \triangle_j^2 x_j^n \right\}\right], \tag{2}$$

ここで, x_j^n, p_j^n は 互いに正準共役な力学変数でサイト j, 時間 n での実数値をとる位置座標, 運動量座標とみなす事ができる. 従ってシンプレクティック性は以下のように表される

$$\sum_{j=1}^{N} dx_j^{n+1} \wedge dp_j^{n+1} = \sum_{j=1}^{N} dx_j^n \wedge dp_j^n.$$

また, ε はスモールパラメーター $(0 < \varepsilon \ll 1)$, τ は時間ステップ幅 $(\mathcal{O}(\varepsilon^0))$, Ω は各サイト上に配置された振動子の非摂動系の固有振動数 $(\mathcal{O}(\varepsilon^0))$, α は非線形性のパラメーター $(\mathcal{O}(\varepsilon^0))$, $\triangle_j^2 x_j^n := x_{j+1}^n - 2x_j^n + x_{j-1}^n$ は最近接相互作用項である. 従って ν は 振動子間の結合定数である $(\mathcal{O}(\varepsilon^0))$. また, この系は N 体の結合系で周期的であるとする $(x_{j+N}^n = x_j^n, p_{j+N}^n = p_j^n)$. つまり, 我々のモデルは離散時間の空間的に周期的な非線形格子モデルの一つである.

本研究では (1)-(2) を用いるが, 参考のため, 時間連続極限 $(\tau \to 0)$ をとったモデルは以下で与えられる.

$$\frac{dx_j}{dt} = p_j,$$

$$\frac{dp_j}{dt} = -\Omega^2 x_j + \varepsilon\left\{ -\alpha (x_j)^3 + \nu \triangle_j^2 x_j \right\},$$

すなわち, 弱非線形の調和振動子が線形結合で結ばれているモデルである. また, 今度は時間離散のまま無結合のモデルを考えると

$$x^{n+1} - x^n = \tau p^{n+1},$$

$$p^{n+1} - p^n \quad = \quad \tau\left\{ -\Omega^2 x^n - \varepsilon\alpha (x^n)^3 \right\},$$

であり, ダブルウェルマップとなる.

この様な特徴を持つシンプレクティックマップ系から, 簡約系を構成することを考える. ここでは, 特異摂動法として知られる "くりこみ法" を採用するものとする. この方法は近年研究がよく行われてきており [CGO96][GMN99][Kun95], ある一定の手続きにより, 与えられた弱非線形系の簡約系を構成する方法である. 簡約系もまた シンプレクティック性を有するという要請を課すと, 今までのくりこみ法ではその要請を自動的に満たさないという意味で不完全である. 著者らの提案するシンプレクティック性を有するくりこみマップの構成法は, 時間連続系のくりこみ方程式を構成し, そこからシンプレクティック積分法を経由することによりシンプレクティックマップを得るというものである. 詳しくは論文 [Got03],[GNY02] を参照されたい. 以下のダイアグラムはその手続きの計算手順を模式的に表したものである. ここで図中の RG とは Renomalization Group の略である.

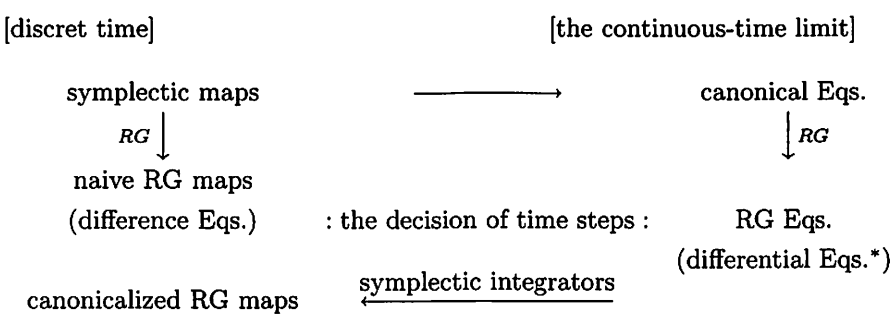

(*:If these Eqs. are of Hamiltonian systems, we can obtain symplecticity preserving RG maps.)

Fig. 1: The schematic diagram of the procedure to obtain symplecticity preserving rernormalization mappings.

ε の 1 次までの正準化くりこみの結果, 以下の離散非線形シュレーディンガー方程式を得る.

$$\left(1 - iT\,\triangle_j^2\right) A_j^{n+1} = \left(1 + iT\,\triangle_j^2\right) \exp\left(iQ|A_j^n|^2\right) A_j^n. \tag{3}$$

ここで, $T := \varepsilon\frac{\nu\tau^2}{4\sin\theta} \in \boldsymbol{R}$, $Q := \varepsilon\frac{-3\alpha\tau^2}{2\sin\theta} \in \boldsymbol{R}$, $\cos\theta := 1 - \Omega^2\tau^2/2$. であり, このくりこみ系は保存量を有し $\sum_{j=0}^{N-1} |A_j^{n+1}|^2 = \sum_{j=0}^{N-1} |A_j^n|^2$ が成立する. また, シンプレクティック性は以下のように表現される.

$$\sum_{j=0}^{N-1} dA_j^{n+1} \wedge dA_j^{*\,n+1} = \sum_{j=0}^{N-1} dA_j^n \wedge dA_j^{*\,n}.$$

ここで A_j^n, A_j^{*n} が正準共役な力学変数である. また, A_j^{*n} は A_j^n の複素共役を表し, 元もとの方程式 (1)- (2) とくりこみ変数の関係は $x_j^n \approx A_j^n \exp(-i\Omega n) + \text{c.c.}$, ここで $\approx$ の意味はくりこみ方程式を得る際, 非共鳴項と高次近似を無視したという意味である. また c.c. は前項までの複素共役項を表す. この表式をみるとわかるように, 非摂動項による固有振動数を元もとの変数 x_j^n, p_j^n から分離した形になっている事がわかる. すなわち, 解析的に遅い運動の従う方程式 (マップ) を抽出した事になる. これにより, 遅い運動に関する安定性解析が可能となる. 速い運動を含む元もとの系で

は, 遅い運動の安定性解析は困難である事が予想できるので, このくりこみ方程式は相空間の解析に役立つ. 以上を確かめるため, 数値計算による典型的な時系列を示す. 振動子の個数 N は 3, パラメーターの値は $\varepsilon = 0.01, \tau = 1.0, \Omega = 1.0, \nu = -0.25, \alpha = 1/3$ である.

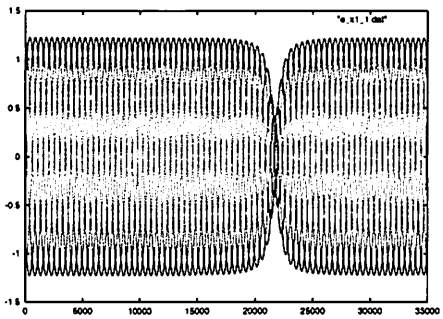

Fig. 2: The time evolution of x_1^n in the original mapping [Eqs. (1) - (2)] with $N = 3, \varepsilon = 0.01, \tau = 1.0, \Omega = 1.0, \nu = -0.25, \alpha = 1/3$. The number of initial phase points is 1.

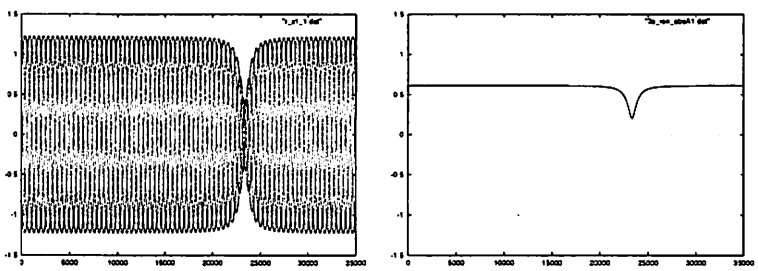

Fig. 3: The time evolution of x_1^n in the symplecticity preserving RG mapping [Eq. (3)] with $N = 3, \varepsilon = 0.01, \tau = 1.0, \Omega = 1.0, \nu = -0.25, \alpha = 1/3$. The number of initial phase points is 1. (The left figure): The time evolution of the reconstructed x_1^n by using the relation $x_j^n \approx A_j^n \exp(-i\theta n) + \text{c.c.}$. Here c.c. represents for the complex conjugate of the preceeding expression. (The right figure): The absolute value of the canonicalized reromalized variable $|A_1^n|$.

3 Stability analysis of some manifolds

次に相空間構造を調べておく. 以後非摂動系のもつ固有振動数が分離されたくりこみ系, すなわち (3) 式で議論を行う. 今から行う相空間構造に関する議論を元もとの系 (1)–(2) で考察したければ, くりこみ変数 A_j^n の定義に戻れば良い. この事を幾何学的に大まかに言うと, 固有振動数成分 (円周 : S^1) を相空間中の A_j^n 周りに付ければよい.

くりこみ系 (3) 式は次のような波数 k の波が特解として存在する :

$$A_j^n = A^0 \exp\left\{ i\left(\frac{2\pi k}{N} j + \omega(k) n \right) \right\}, \quad (k = 0, ..., N-1) \tag{4}$$

$$\omega(k) := \sigma(k) + Q|A^0|^2, \qquad \sigma(k) := \mathrm{Tan}^{-1}\left\{ \frac{-8T\sin^2(\pi k/N)}{1 - 16T^2\sin^4(\pi k/N)} \right\}.$$

ここで A^0 は初期値である. これは周期解なので相空間中で閉じた多様体になる. すなわち不変部

分空間である．我々はこれらをトーラス[1] と呼ぶことにする．またその絶対値 $|A_j^n|$ をトーラス半径と呼ぶことにする．またこのトーラスはそれ自身の周りの $2N$ 階の連立線形安定化方程式の $2N$ 個の固有値に実数が 1 つ以上あれば，その固有方向に不安定多様体と安定多様体がモジャモジャと生えているといえる．この時このトーラスを特に双曲型トーラスと呼ぶ．今考えている系はマップ系なので，固有値を正に限れば固有値が 1 以上の実数が不安定多様体を表し，1 以下の実数が安定多様体を表すことになることに注意されたい．また，トーラス周りの線形化固有値が純虚数に配位している空間はトーラス周りが楕円型相空間であることに相当する．

実際に波数 k 周りの線形安定性解析を行う．

$$A_j^n = A^0 \exp\left\{ i\left(\frac{2\pi k}{N} j + \omega(k) n\right)\right\}(1+\mu_j^n), \quad (k=0,...,N-1), \quad (|\mu_j^n| \ll 1)$$

をくりこみ系 (3) へ代入し μ_j^n の 1 次まで残し線形化方程式を構成する．更にフーリエ変換:

$$\mu_j^n := \frac{1}{\sqrt{N}} \sum_{m=0}^{N-1} \hat{\mu}_m^n \exp\left(\frac{i2\pi}{N} mj\right), \quad \hat{\mu}_m^n = \frac{1}{\sqrt{N}} \sum_{j=0}^{N-1} \mu_j^n \exp\left(-\frac{i2\pi}{N} mj\right),$$

により波数空間で線形化方程式を表すと

$$\begin{pmatrix} \hat{\mu}_{m-k}^{n+1} \\ \hat{\mu}_{-m+k}^{*\ n+1} \end{pmatrix} = \begin{pmatrix} \mathrm{e}^{i(\sigma(m)-\sigma(k))}\left(1+iQ|A^0|^2\right) & \mathrm{e}^{i(\sigma(m)-\sigma(k))} iQ \\ \mathrm{e}^{-i(\sigma(m)-\sigma(k))}(-iQ) & \mathrm{e}^{-i(\sigma(m)-\sigma(k))}\left(1-iQ|A^0|^2\right) \end{pmatrix} \begin{pmatrix} \hat{\mu}_{m-k}^{n} \\ \hat{\mu}_{-m+k}^{*\ n} \end{pmatrix} \tag{5}$$

この固有値は以下の様に表示される．

$$\begin{aligned} \lambda(m;k)_\pm &:= \beta(m;k) \pm \sqrt{\beta(m;k)^2 - 1}, \\ &\beta(m;k) := \cos(\sigma(m)-\sigma(k)) - Q|A^0|^2 \sin(\sigma(m)-\sigma(k)). \end{aligned}$$

なお，$\lambda(k;k) = 1$ (doublet) は中立安定で，$\lambda_+(m;k)\lambda_-(m;k) = 1$ はハミルトン力学系を反映し，不安定多様体と安定多様体が対になっている事に注意されたい．双曲化トーラスの生成条件，すなわち波数 k のトーラスの $\lambda(m;k) > 1$ という意味での双曲化は (i) $\beta(m;k) < -1$ と (ii) $\beta(m;k) > 1$ に起因する場合の 2 通りある．今回は (ii) の $\beta(m;k) > 1$ によるトーラスの双曲化分岐を考察するものとする．すると $\beta(m;k)$ の定義から，波数 k のトーラスの波数 m の空間が双曲型になる条件は，以下の様に波数 k のトーラスの初期値，特にトーラス半径の大小で表される．

$$|A^0|^2 > \frac{4T}{Q}\left\{ \sin^2\left(\frac{m\pi}{N}\right) - \sin^2\left(\frac{k\pi}{N}\right)\right\}. \tag{6}$$

言い換えれば，臨界トーラス半径 ($|A_c^0(m;k)|$) が存在し，その前後でトーラス周り様相が変化する．なお，$T/Q \propto \nu/\alpha$，すなわち最近接相互作用の大きさと個々の振動子の持つポテンシャルの非線形の比によってトーラスの性質が変化することを表している．トーラスの変化の様子を $k=0$ (一様振動解) の場合について図 4 に示す．

[1] 本来はこの不変多様体 (4) はトーラスと呼ぶよりも，S^1 と呼んだ方がよいのかもしれない．

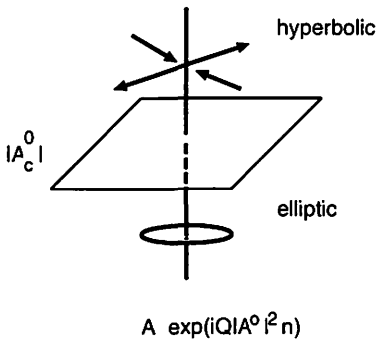

Fig. 4: The phase portrait of near the uniform oscillatory solution ($k = 0$ torus). The torus bifurcates at the critical radius $|A_c^0|$.

4 Homoclinic-like structure around the $k = 0$ wave

前節 3 において一般の波数を有する波の安定性の解析を行った. この節では $k = 0$ すなわち一様振動解, の双曲化の様子の具体的な様子について線形化方程式の固有値の分布と数値計算結果について言及する.

$k = 0$ トーラス周りの様子は (6) 式から臨界トーラス半径 $|A_c(1;0)| := \sqrt{4\frac{T}{Q}\sin^2(\frac{\pi}{N})}$ よりトーラスの半径が大きいと不安定・安定多様体を有することがわかる. $k = 0$ の場合の (6) 式 を用いて分岐パラメーターを $|A^0|$ にとり, 固有値の分布を複素平面上に表示してみる. 具体的に $N = 3$ の場合を図 5, $N = 4$ の場合を図 6 に示す.

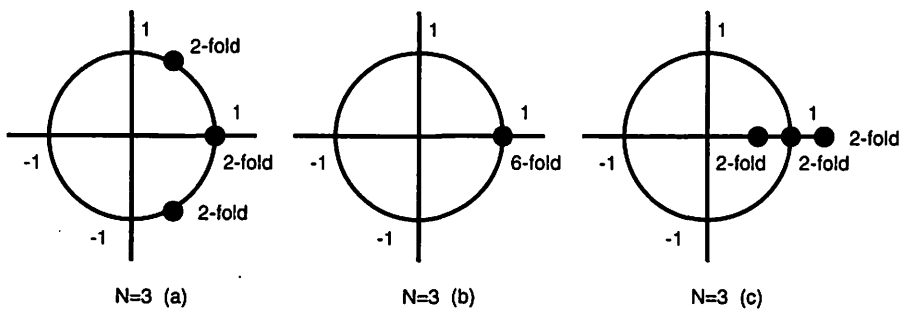

Fig. 5: The distribution of eigenvalues in the complex plane obtained by the Eq. (6) around ($k = 0$)-wave in the $N = 3$ system. (a): $k = 0$ tori are non-hyperbolic. (b): $k = 0$ torus is at the first bifurcation point. (c): $k = 0$ tori are hyperbolic.

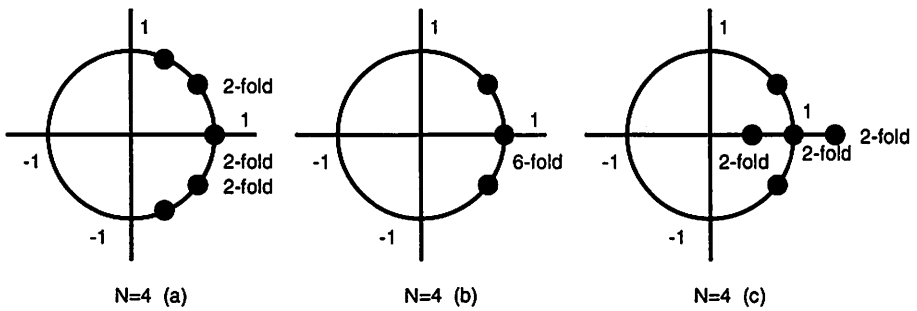

Fig. 6: The distribution of eigenvalues in the complex plane obtained by the Eq. (6) around ($k = 0$)-wave in the $N = 4$ system. (a): $k = 0$ tori are non-hyperbolic. (b): $k = 0$ torus is at the bifurcation point. (c): $k = 0$ tori are hyperbolic.

ここで我々は, 不安定・安定多様体が生成された直後の相空間の様子を数値計算により調べてみる. ハミルトン力学系の場合, 不安定多様体と安定多様体の交差がカオスの起源として知られているので, 不安定多様体と安定多様体の生成直後はある種のカオスのオンセットを捉える可能性が生じる. そのため我々はこの分岐に注目する.

その $k = 0$ トーラスの分岐直後の様子を観察するために, 初期値としてトーラスの半径を臨界トーラスよりわずかに大きな振幅に設定しておく. その数値計算結果を図 7 と図 8 に示す. 図 7 は $N = 5$ の場合で, 図 8 は $N = 20$ の場合である.

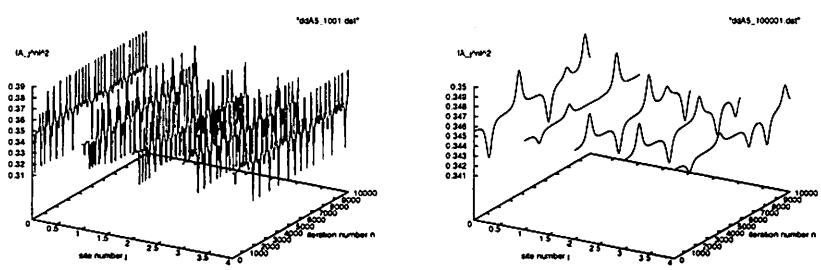

Fig. 7: The time evolution of the $|A_j^n|^2$ in the $N = 5$ system, which is calculated using numerical iterations with $T = 1/2, Q = 2.0$ $\mathrm{Re}(A_j^0) = \mathrm{Im}(A_j^0) = \sqrt{|A_c|/2}$ [Eq. (3)]. (The left fgure): $|A_j^0| = 1.001|A_c|$, (The right fgure): $|A_j^0| = 1.00001|A_c|$.

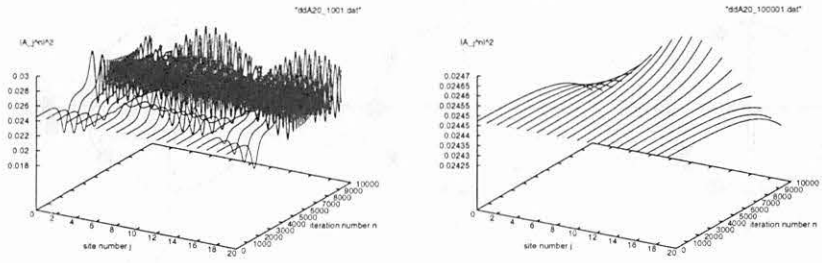

Fig. 8: The time evolution of the $|A_j^n|^2$ in the $N = 20$ system, which is calculated using numerical iterations with $T = 1/2, Q = 2.0$ $\mathrm{Re}(A_j^0) = \mathrm{Im}(A_j^0) = \sqrt{|A_c|/2}$ [Eq. (3)]. (The left fgure): $|A_j^0| = 1.001|A_c|$, (The right fgure): $|A_j^0| = 1.00001|A_c|$.

図 7 及び図 8 ともに臨界トーラスに近付くとホモクリニック的になってくる事が確認される. すなわち, 時間が進んでも $|A_j^n|^2$ が一様解に留まっている時間が長くなることが見てとれる. また, 軌道が $k = 0$ トーラスから離れている時は, あるサイト j^* に振幅が集中する. そのような時間は軌道がトーラス近傍にいる時間に比べて圧倒的に短い.

このような軌道のカオス化を見るために, 周期的境界条件であった系を開き, Z 上に配位空間を延長する. その配位空間上で $k = 0$ トーラスから最も離れた時刻に $|A_j^n|$ の最も大きな値をとる j の番号をプロットする. $N = 5$ の場合のその図が図 9 である.

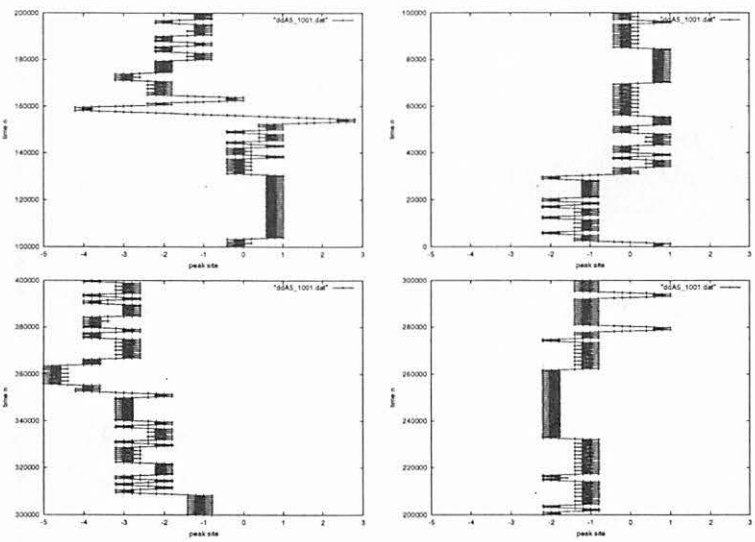

Fig. 9: The spatio-temporal diagram in the $N = 5$ system where the following three conditions are satisfied: (i) j satisfies $|A_j^n| = \max_j |A_j^n|$, (ii) n satisfies $(|A_j^n| > |A_j^{n-1}|) \cap (|A_j^n| > |A_j^{n+1}|)$, and (iii) $h^n < 0.999$ on an extended configuration space. This figure shows the peak of $|A_j^n|^2$ is wandering. In other words, this diagram implies the unstable manifold attached to the $k = 0$ wave manifold disturbs a orbit.

この際, $k = 0$ トーラスに軌道が近い相空間にいても, $|A_j^n|$ の最も大きな値をとる j は存在する

ので, 自由度数で規格化されたエントロピー的量 [LL91]:

$$h^n := \frac{-1}{\ln N} \sum_{j=0}^{N-1} \left(\frac{|A_j^n|^2}{\sum_{l=0}^{N-1} |A_l^n|^2} \right) \ln \left(\frac{|A_j^n|^2}{\sum_{m=0}^{N-1} |A_m^n|^2} \right),$$

の値が 0.999 より小さいときに j の値をプロットした. この h^n は $|A_0^n|^2 = |A_1^n|^2 = \cdots = |A_{N-1}^n|^2$(一様解) の時に 1 を与え, ある 1 サイトに集中した時に 0 を与える. すなわち, 時刻 n での相空間中の軌道のトーラスからの近さをはかる量となる (このくりこみ系 (3) の場合, $\sum_{j=0}^{N-1} |A_j^n|^2$ が力学系の保存量となることに注意されたい.).

図 9 の観察によるとホモクリニック的多様体の振る舞いは, その $|A_j^n|$ ピークがいろいろなサイトに現れている. これは $k = 0$ トーラス周りの不安定多様体の性質を反映しているものと考えられる. トーラス周りの不安定多様体はホモクリニック的であるが, カオス的要素を含むことを図 9 は意味している.

5 Paths connecting various hyperbolic tori

ここでは波数 k が 一般の場合のトーラスがなす多様体の線形解析の結果を用いて,

1. 波数 $k(= 0, ..., N-1)$ トーラスに付随する不安定多様体, 及び
2. 波数 $k'(= 0, ..., N-1)$ トーラスに付随する安定多様体

の両者の接続による軌道のヘテロ・ホモクリニック的遷移の可能性に言及しておく. アーノルドが示したウィスカードトーラスの不安定多様体と安定多様体の交差による拡散は, 同種の一様なトーラスの設定であった [Arn64]. 今のモデルでは相空間の場所によって注目するトーラス周りの様子が楕円的であったり, 双曲的であったりするのでアーノルド自身が示したモデルとは異なることに注意されたい. 線形解析の結果 (6) 式を用いて各トーラスの分岐の様子を例えば $N = 7$ の場合にまとめて書くと図 10 のようになる. これにより $N = 7$ の場合, 例えば $k = 1, 6$ のトーラスの $m = 2, 5$ の分岐による不安定多様体に注目すると $k = 0, 2, 5$ の安定多様体に乗り移れる可能性が生じる.

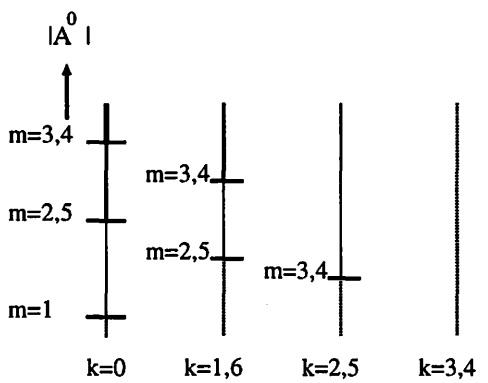

Fig. 10: The phase portrait of the various tori corresponding to oscillatory solutions in the $N = 7$ system. The k in the figure means wave number, m means a perturbation direction in the Fourier space. The tori are characterized by their radii. The dotted lines express that tori

are not hyperbolic, the thin solid lines express that ori have both elliptic and hyperbolic space, and the thick lines express that tori have not elliptic space.

しかし, これらのトーラス達を結ぶヘテロクリニク軌道の存在を数値的に示すのは難しい. それは $k=0$ のトーラスの双曲化分岐が終った後で $k\neq 0$ のトーラスの分岐が生じている. $k\neq 0$ のトーラスが双曲化するトーラス半径では $k=0$ のトーラスのすぐ近くでは良く発達したカオスになっているであろうことが 4 節, 特に図 7, 図 8 により示唆される. 従ってこの節で述べているようなヘテロクリニック的軌道の存在するであろうトーラス半径ではカオスの海の領域が広く広がっていると考えられるからである.

6 Conclusion

本研究は高次元ハミルトン系の相空間解析, 特に楕円型不動点を有する非線形シンプレクティックマップ結合系の結合による不安定性, 言い換えると, 楕円型トーラスからトーラスの双曲化を経ることによるカオス化へのルートを探索してみた. 2 節でくりこみ法をシンプレクティックマップ系にまで拡張する方法を与えることができた. これにより, シンプレクティックマップで定義される差分系に対して, 遅い変数の従うシンプレクティックマップを解析的に抽出することに成功した. この成果を踏まえ, 3 節では遅い運動の従う方程式の, 波数 k の振動解周りの安定性解析が行え, その相空間構造を捉える足掛かりを得ることができた. 特に 4 節では数値計算の結果も踏まえることにより $k=0$ トーラスの双曲化によるカオスの発生の断片を捉えられたが, それを今後特徴付けなければならない. 更に, 5 節で述べたようなヘテロクリニック的なトーラス間の遷移軌道の存在は, 相空間の幾何学を考える時, その骨組として重要であろう. これらの軌道の存在や, 非存在を示すのは今後の課題である.

Acknowlegement

One of the authors S.G. has been supported by supported by *JSPS Research Fellowships for Young Scientists.* S.G. would like to thank Dr. H. YAMADA for fruitful discussions.

参考文献

[AA89] V.I. Arnold and A. Avez, *Ergodic Problems in Classical Mechanics*, (Addison-Wesley Pub. Co.) (1989).

[Arn64] V.I. Arnold, "Instability of Dynamical Systems with Several Degrees of Freedom", *Sov. Math. Dokl.* **5**, (1964) 581 – 585.

[CGO96] L.Y. Chen, N. Goldenfeld and Y. Oono, "Renormalization Group and Singular Perturbations: Multiple Scales, Boundary Layers, and Reductive Perturbation Theory", *Phys. Rev.* **E54**, (1996) 376 – 394.

[GMN99] S. Goto, Y. Masutomi and K. Nozaki, "Lie-Group Approach to Perturbative Renormalization Group Method", *Prog. Theor. Phys.* **102**, (1999) 471 – 497.

[GN99] S. Goto, and K. Nozaki, "Dynamics near Resonance Junctions in Hamiltonian Systems", *Prog. Theor. Phys.* **102**, (1999) 937 – 946.

[GN01B] S. Goto and K. Nozaki, "Regularized Renormalization Group Reduction of Symplectic Maps", *J. Phys. Soc. Jpn.* **70**, (2001) 49 – 54.

[GNY02] S. Goto , K. Nozaki and H. Yamada, "Random Wandering around Homoclinic-Like Manifolds in a Symplectic Map Chain", *Prog. Theor. Phys.* **107**, (2002) 637 – 654.

[Got03] S. Goto, D-thesis, "Singular Perturbation Approach to Nearly Integrable Hamiltonian Systems", or "Rernormalization Group Method to Hamiltonian systems" in *SUKEN kokyuroku* **1282**, (2003) 121 – 141 (in Japanese).

[HK03] S. Honjo and K. Kaneko, to appear in this proceedings (2003).

[HNK99] Y. Hirata, K. Nozaki and T. Konishi, "The Intersection Angle between N-Dimensional Stable and Unstable Manifolds in 2N-Dimensional Symplectic Mappings", *Prog. Theor. Phys.* **102**, (1999) 701 – 706.

[Kun95] T. Kunihiro, "A Geometrical Formulation of the Renormalization Group Method for Global Analysis", *Prog. Theor. Phys.* **94**, (1995) 503 – 514.

[LL91] *For example*, A.J. Lichtenberg and M.A. Lieberman, *Regular and Chaotic Dynamics (second edition)*, (Springer, Berlin) (1991).

[MS92] D.W. McLaughlin and C.M. Schober, "Chaotic and Homoclinic Behavior for Numerical Discretizations of the Nonlinear Scröinger Equation", *Physica* **D57**, (1992) 447 – 465.

Collinear Three Body Problem with Non-equal Masses by Symbol Dynamics

Masaya Masayoshi Saito and Kiyotaka Tanikawa

National Astronomical Observatory/Department of Astronomical Science, SOKENDAI , Mitaka, Tokyo, JAPAN

Abstract

We study the collinear three body problem with the non-equal masses using symbol dynamics. In asymmetric cases, folds of triple collision curves, not observed in the equal mass case, appear.

1 Introduction

The collinear three body problem is one of the general three body problems whose degree of freedom is reduced by geometric symmetry. Hietarinta & Mikkola(1993) studied this problem for various masses with the help of a Poincaré map. They found that the initial value plane (equivalent to the Poincaré section) is divided into three regions: fast escape regions, the quasiperiodic region(the Schubart region) and the chaotic scattering region. The Poincaré map scarcely resolves the structure of the chaotic scattering region. Tanikawa & Mikkola(2000) found that this region is divided by an infinite number of triple collision curves by introducing symbol dynamics into this problem. They also found a rule of transitions among the regions separated by these curves.

The authors apply symbol dynamics to the case of non-equal masses, and study the structure of the Poincaré section for various masses. We pickup one sample each from symmetric and asymmetric cases in this report.

2 The Method of Calculation

2.1 Poincaré Section

We call three particles on a line m_1, m_0, and m_2 from the left, and take q_1(the distance between m_1 and m_0), q_2(the distance between m_0 and m_2) as coordinate variables. In this selection, the Hamiltonian of the system is

$$H = K - U; K = \frac{1}{2}\left(\frac{1}{m_1} + \frac{1}{m_0}\right) p_1^2 + \frac{1}{2}\left(\frac{1}{m_0} + \frac{1}{m_2}\right) p_2^2 - \frac{p_1 p_2}{m_0},$$
$$U = \frac{m_1 m_0}{q_1} + \frac{m_0 m_2}{q_2} + \frac{m_1 m_2}{q_1 + q_2}. \quad (1)$$

A Poincaré section (θ, R) for the isoenergetic surface, $H = E_0$, is introduced as follows. In the collinear three body problem, there is a special solution, the so-called homothetic solution, that repeats a triple collision retaining the relation,

$$q_1/q_2 = \dot{q}_1/\dot{q}_2 = \tau(m_i). \quad (2)$$

The constant τ depends on masses, and is unity in the symmetric case. For general initial conditions, there exist a time when $q_1/q_2 = \tau$. So we take the set of $(q, \dot{q})$ that satisfies relation(2) as a Poincaré section, and define R by

$$R = (q_1 + q_2)/2 \qquad \text{when } q_1/q_2 = \tau. \quad (3)$$

A freedom of distributing the kinetic energy among the particles still remains. The expression in $(\dot{q}_1, \dot{q}_2)$ of kinetic energy is

$$K = A\dot{q}_1^2 + B\dot{q}_2^2 + C\dot{q}_1\dot{q}_2$$
$$\text{with} A = \frac{m_1(m_0+m_2)}{2M}, B = \frac{m_2(m_0+m_1)}{2M}, C = \frac{m_2 m_0}{2M}, M \doteq \sum_i m_i \,. \quad (4)$$

The function K can be diagonalized by a linear transformation $\bar{v}_i = a_{ij}q_j$:

$$K = \bar{v}_1^2 + \bar{v}_2^2 \,. \quad (5)$$

A variable θ is introduced as

$$\sqrt{K}\sin\theta = \bar{v}_1, \sqrt{K}\cos\theta = \bar{v}_2 \,. \quad (6)$$

2.2 Symbol Dynamics

A *symbol sequence* is usually defined as the sequence of the identifier of regions that an orbit has visited, in the Poincaré section . However Tanikawa & Mikkola(2000) introduced symbol sequences using binary collisions. The symbol '1' is assigned to a collision between m_1 and m_0, '2' is to m_0 and m_2, and '0' is to a triple collision. In general, the symbol sequence is written in the form,

$$(\cdots n_{-2}n_{-1}.n_1n_2\cdots) \qquad ; n_i \in 0,1,2$$

This means that binary collisions occur in the order of n_1, n_2 , $\cdots$ to the future, and n_{-1}, n_{-2}, $\cdots$ to the past.

Suppose that orbits starting from (θ_1, R_1) and (θ_2, R_2), have the same symbols for first $n-1$ digits, but the former has '1' and the latter has '2' at the n-th digit. There must exist (θ, R) between (θ_1, R_1) and (θ_2, R_2), for which the center particle collides with both sides simultaneously at the n-th digit due to the continuity of orbits with respect to the initial condition. So, verifying two symbol sequences of neighboring points on the (θ, R) for all n, we obtain each point whose orbit ends in triple collision as one where the verification fails.

2.3 Specification of Calculations

We integrate orbits that begin at the lattice point of (θ, R)-plane for each masses, and obtain the symbol sequence. The specifications of mass, lattice and symbol sequence are shown in Table 1. Total energy E_0 is fixed to -1.

Masses	(1)Equal Masses (2)(Symmetric Case)$m_1 = 0.2$, $m_0 = 0.2$, $m_1 = 1.4$ (3)(Asymmetric Case)$m_1 = 0.9, m_0 = 1.0, m_1 = 1.1$
Cross Secion	$\{(\theta, R)\|0 \leq \theta \leq 180°, \Delta\theta = 180°/1800, \Delta R = R_{\max}/1000\}$
symbol sequence	To the future, until 64 digits

Table 1. The parameters determine the specification of calculation

3 The Result of Calculation

3.1 Triple Collision Curves on the (θ, R)-plane

According to the specification given in section 2.3, we calculate symbol sequences on the (θ, R)-plane. Fig. 1 shows triple collision curves(the set of (θ, R) whose orbit ends in a triple collision) on the (θ, R)-plane. The horizontal and vertical

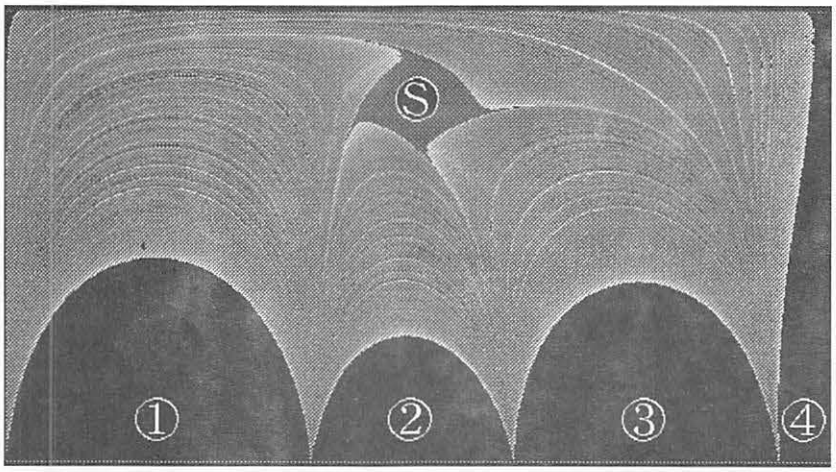

(1) Equal Masses

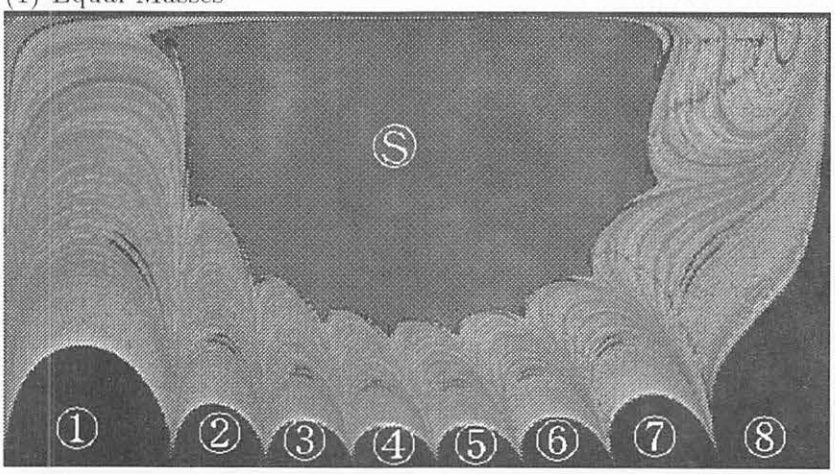

(2) $m_1 = 0.2,\ m_0 = 0.2,\ m_1 = 1.4$

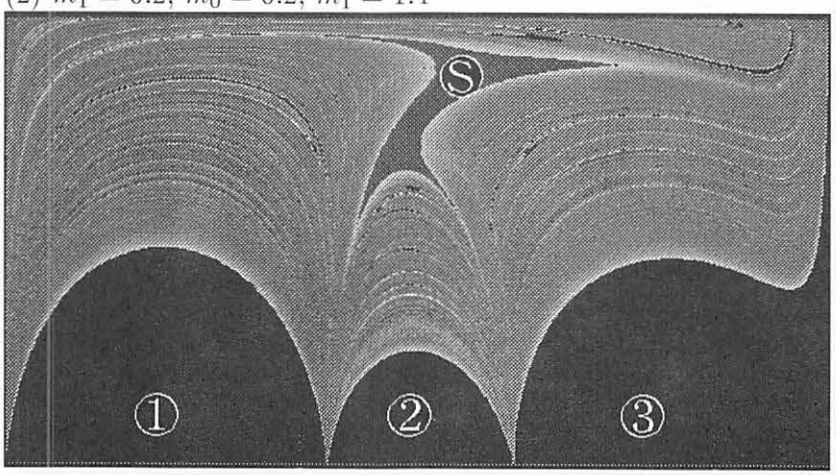

(3)$m_1 = 0.9, m_0 = 1.0, m_1 = 1.1$

Ⓢ	$1.(21)^{\infty}$	①	$1.(2)^{\infty}$	②	$1.2(1)^{\infty}$	③	$1.21(2)^{\infty}$	④	$1.212(1)^{\infty}$

FIG. 1. Triple collision curves on (θ, R)-plane

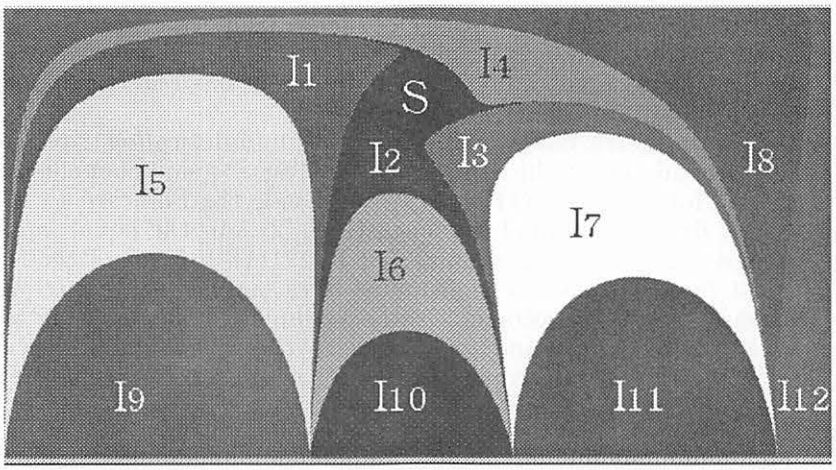

(1) Equal Masses

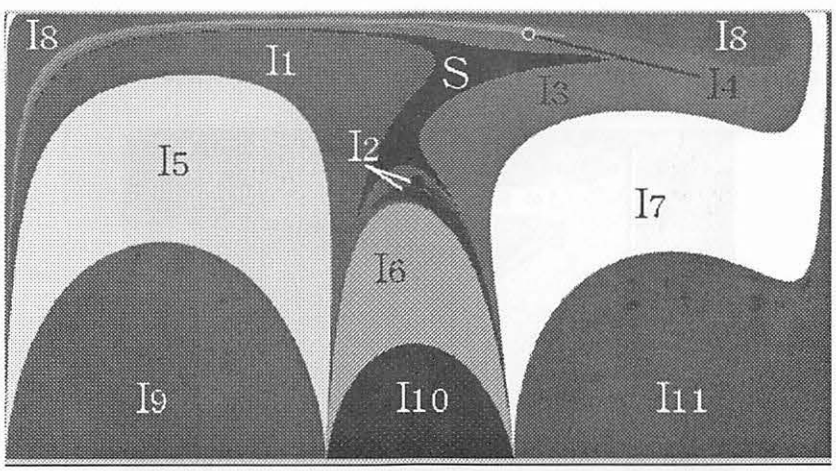

(3) $m_1 = 0.9$, $m_0 = 1.0$, $m_1 = 1.1$

S	$1.(21)^{\infty}$						
I_1	$1.(21)^{2k}22$	I_2	$1.(21)^{2k+1}1$	I_3	$1.(21)^{2k+1}22$	I_4	$1.(21)^{2k+2}1$
I_5	$1.(2)^{n}$	I_6	$1.2(1)^{n}$	I_7	$1.21(2)^{n}$	I_8	$1.212(1)^{n}2$
I_9	$1.(2)^{\infty}$	I_{10}	$1.2(1)^{\infty}$	I_{11}	$1.21(2)^{\infty}$	I_{12}	$1.212(1)^{\infty}$

FIG. 2. The partition of the Poincaré section by symbol sequence

axes represent θ and R, respectively. Three cases we consider are labeled as (1) – (3) in Table I. We use these labels throughout the paper. In any case, the Poincaré section is divided into fast escape regions(black, symbol sequence is $\cdots 1$ or $\cdots 2$), the Schubart region(gray, $(21)^{\infty}$) and the chaotic scattering region(between the above two)(Hietarinta & Mikkola 1993).

At first, let's look at the equal mass case. The chaotic scattering region is separated by an infinite number of triple collision curves. These curves and fast escape regions construct four *scallops* (Tanikawa and Mikkola 2000). Triple collision curves converge at four points on the θ-axis. Here we call each convergence point as a *root*, and the curves converging to the *root* as a *foot*. Note that all triple collision curves begin at one *root* and end at another *root*.

When the central mass becomes light in the symmetric case, the number of *scallops* increases, though overall features of triple collision curves seem unchanged. The lighter the central body, the more numerous *scallops* appear: this has been confirmed by additional integrations.

In a slightly asymmetric case, there exist in the middle *scallop* triple collision curves that begin and end at the same *root*. We describe this phenomenon as *a fold*. In addition, for the cases (1) and (3), we divide the Poincaré section into sub-regions with different symbol sequences(Fig. 2). In the equal mass case, there exist regions, I_{12} : $1.2121(1)^{\infty}$ and I_8 : $1.2121(1)^n$. *Roots* of their border are the leftmost ($\theta = 0°$) and the righthmost ones, and its symbol sequence is 1.21210. However if masses become slightly asymmetric, I_{12} vanishes and the right *foot* of 1.21210 rises up and folds back to the left root. The region I_8 becomes smaller, and is wrapped in the border. (However, this border is no longer the border between I_8 and I_{12}, but I_3 and I_8.)

4 Interpretation of Results

The phenomena observed in the preceding section are related to *roots*. So, we integrate limit orbits of triple close encounter in McGehee's variables to understand these observations. We enumerate minimal features of the variables necessary for later discussion.

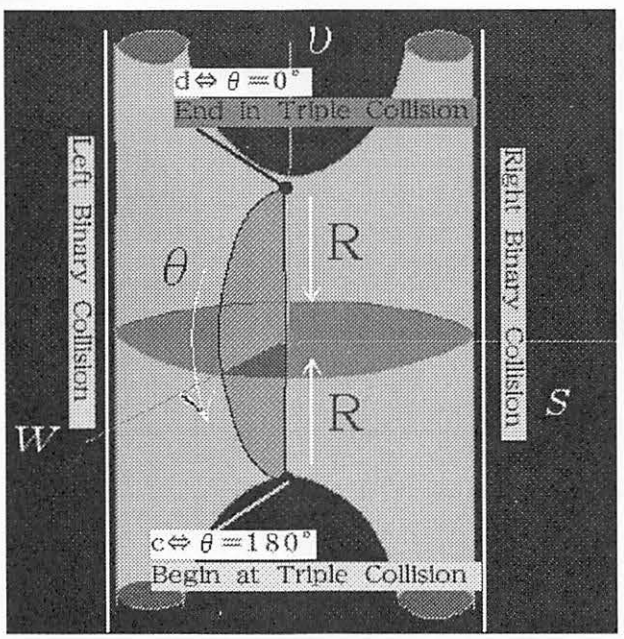

FIG. 3 The triple collision manifold(TCM)

- McGehee's variables are r, s, w, and v. r represents the scale of a system. s represents the relative configuration. The collision between the left and the center occurs at $s = -1$, and the center and the right at $s = +1$. w and v are variables for the velocity.
- For $r = 0$, the time evolution of (w, s, v) are well defined. The r=0 defines a manifold, which is called the *triple collision manifold* (hereafter TCM), and its shape is shown in Fig. 3. An orbit on TCM is called a *virtual orbit.*
- There exist two fixed points c and d in TCM.

- The flow on TCM is gradient-like with respect to $g(0, w, s, v) = -v$.

Fig. 3 shows also the Poincaré section embedded as the plane $s = 0$. The θ-axis is the intersection of TCM and $s = 0$. Two virtual orbits (light and dark lines) and the Poincaré section for each mass are shown in Fig. 4. We follow Simó's method for integration of virtual orbits(Simó 1980). In the symmetric cases, the virtual orbits for the lighter central mass wind around TCM more tightly, so intersect more frequently with the Poincaré section. Because these intersections correspond to *roots* in Fig. 1 or 2, the fact that the number of *scallops* increases with decrease of the central mass can be understood.

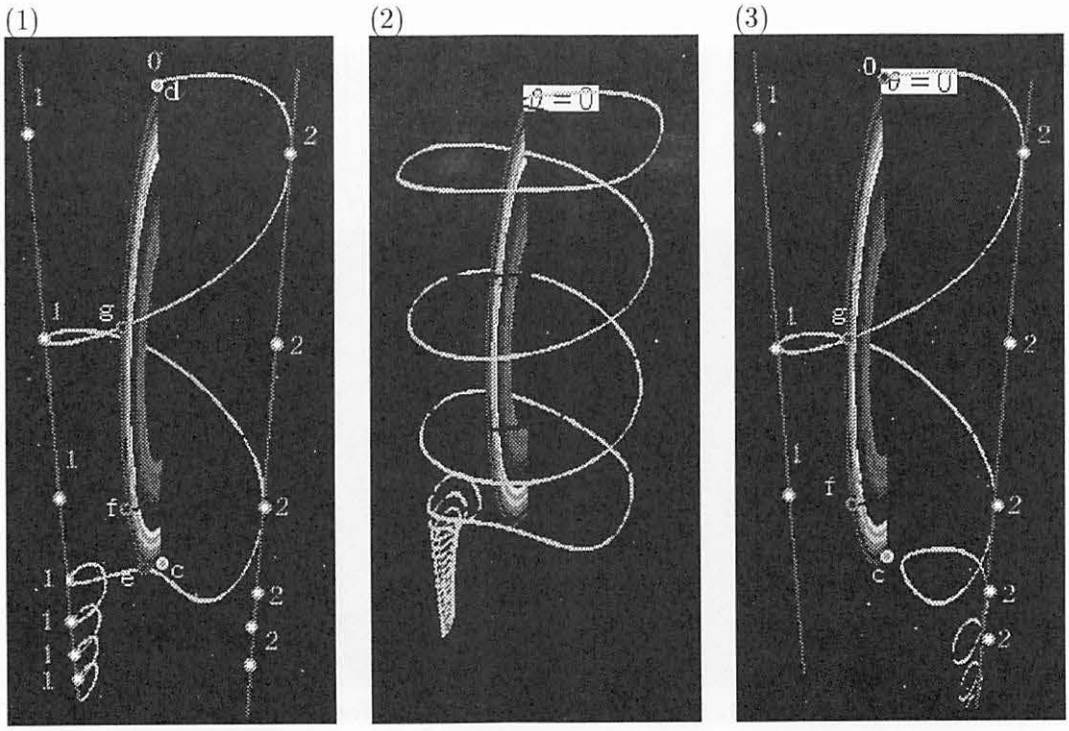

FIG. 4. Virtual orbits end in a triple collision
(1) Equal Masses, (2) $m_1 = 0.2$, $m_0 = 0.2$, $m_1 = 1.4$, (3)$m_1 = 0.9, m_0 = 1.0, m_1 = 1.1$

We assign symbol sequences to virtual orbits too, because the disappearance of the symbol sequence plays an important role in the asymmetric case. In (1), points e, f, and g are intersections of the orbit and the θ-axis, and corresponding symbols are shown where orbits intersect with $s = -1$('1') or $s = +1$('2'). Symbol sequences of these orbits are shown in Table 2. If orbits begin at the other points on the θ-axis, they shall wind up around one of the arms of TCM(They correspond to fast escape orbits). Symbol sequences for these cases are also shown in Table 2. Comparing Table 2 and $I_9 - I_{12}$ of Fig. 2, one can find that the symbol sequence of limiting point ($R \to 0$, θ_0) agrees with those of the neighboring points ($0 < R \ll R_{\max}$,θ_0).

Now we show how the form of virtual orbits changes continuously by increasing the asymmetry of masses from (1) to (3). The point e approaches and reaches fixed point c at $(m_2 - m_1)/2 \fallingdotseq 0.065$. As the asymmetry becomes larger, the point e vanishes, and the winding number of the bright-lined orbit decreases by 1. Then, we arrive at (3). Consequently symbol sequences of e and $e - c$ vanish, and all symbol sequences of orbits beginning between f and c become

$1.21(2)^{\infty}$. So the regions that touch the θ-axis at the lightmost root including I_8 etc., must part from it.

Finally region I_2, which has remarkable *folds* in Fig. 2-(3), can be obtained from the Poincaré map of I_8 to the past.

Table 2
Symbol sequences of virtual orbits

d		
	$1.(2)^{\infty}$	$\rightarrow I_9$
g	1.20	
	$1.2(1)^{\infty}$	$\rightarrow I_{10}$
f	1.210	
	$1.21(2)^{\infty}$	$\rightarrow I_{11}$
e	1.2120	
	$1.212(1)^{\infty}$	$\rightarrow I_{12}$
c		

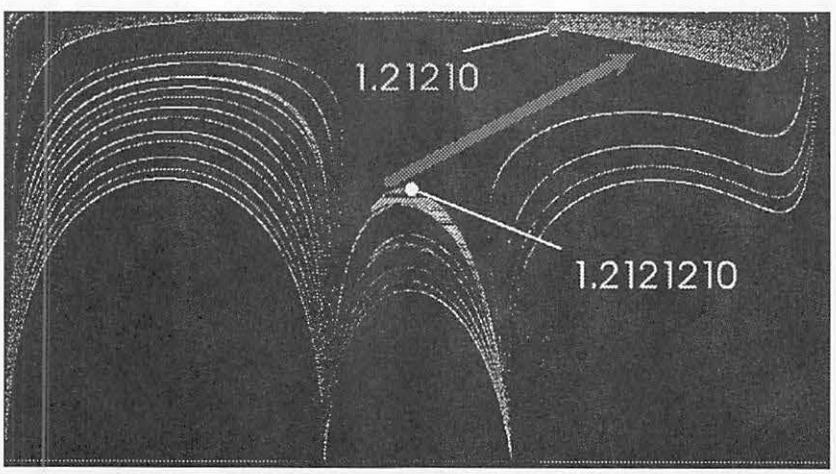

FIG. 5 The Poincaré map of I_2 for the past

5 Conclusion

We summarize the results of the present research :

1. **Symmetric case** - Systems with a lighter central mass have more *scallops*. This can be understood from the fact the virtual orbit winds around the triple collision manifold more tightly in this mass case.

2. **Asymmetric case** - The rightmost *foot* rises up from the θ-axis. Introducing the symbol sequence to the virtual orbit, one can understand these regions are detached from the θ-axis, due to the change of the winding number around TCM. As these regions are mapped to the past, the most significant *fold* appears.

Acknowledgement

We have used the code implemented by Dr. S. Mikkola for integration of orbits of collinear three body problem. We would like to thank him.

References

Hietarinta, J. & Mikkola, S. 1993, Chaos in the one-dimensional gravitational three-body problem, CHAOS, 3, 183

Tanikawa, K. & Mikkola, S. 2000, One-dimensional three-body problem via symbolic dynamics, CHAOS, 10, 649

McGehee, R. 1974, Triple collision in the collinear three body problem, Inventions Mathematicae, 27 , 191

Simó, C. 1980, Mass for which triple collision regularizable, Celestial Mechanics, 21 , 25

Low-Dimensional Subsystems in Anharmonic Lattices

Susumu SHINOHARA*
Department of Physical Sciences, Ritsumeikan University, Kusatsu 525-8577, Japan

Abstract

For anharmonic lattice systems, we study the low-dimensional subsystems described by sub-Hamiltonians containing only the variables of a subset of normal modes, called as the type I subsets. Analyzing the selection rules for mode interaction, we obtain the expressions for the type I subsets. For one- and two-mode subsystems, the sub-Hamiltonians are derived explicitly. In addition, integrability of the two-mode subsystem is discussed.

1 Introduction

An anharmonic lattice is one of the representative models of Hamiltonian systems with many degrees of freedom. Since the pioneering numerical simulation by Fermi, Pasta and Ulam (FPU)[1], classical dynamics of anharmonic lattices has been extensively studied[2]. A basic problem is to understand the energy redistribution process among the normal modes. Anharmonicity violates the dynamical independence of normal modes, but it does not always lead to the energy equipartition, which is deduced from the ergodicity. Indeed, there exists a set of initial conditions with which the energy equipartition would never be realized; for a certain type of initial excitation of modes, it is shown that the supplied energy does not spread over all the normal modes, but is retained by a subset of normal modes[3]. This phenomenon reflects the existence of invariant submanifolds in the phase space.

In this article, we present results that reveal which subsets of modes can retain the energy, and then explicitly derive one- and two-mode sub-Hamiltonians which describe the dynamics on invariant submanifolds. Details of these results have already been reported in ref.[4, 5]. In addition, we discuss the integrability of the two-mode sub-Hamiltonian for several important lattices.

2 The Hamiltonian for lattice vibrations

We consider a one-dimensional lattice of equimass particles coupled by anharmonic springs, whose Hamiltonian is given by

$$H = \sum_{j=1}^{N-1} \frac{p_j^2}{2} + \sum_{j=1}^{N} V(q_j - q_{j-1}), \tag{1}$$

*E-mail: susumu@ike-dyn.ritsumei.ac.jp

where q_j and p_j are the displacement of the j-th particle from its equilibrium position and its conjugate momentum, respectively. We impose the fixed-end boundary condition, i.e., $q_0 = q_N = 0$. As the potential, we consider a rather general form

$$V(r) = \sum_{n=2}^{\infty} \frac{\mu_n}{n} r^n, \tag{2}$$

where μ_n are real parameters. We assume μ_2 to be positive so that $V(r)$ becomes convex in the $r \to 0$ limit. For the lattice with fixed ends, the transformation to the normal mode coordinates is given by

$$Q_k = \sum_{j=1}^{N-1} S_{kj}\, q_j, \quad P_k = \sum_{j=1}^{N-1} S_{kj}\, p_j, \quad k = 1, \cdots, N-1, \tag{3a}$$

where

$$S_{kj} = \sqrt{\frac{2}{N}} \sin\left(\frac{\pi kj}{N}\right), \qquad k, j = 1, \cdots, N-1. \tag{3b}$$

By this transformation, the harmonic part of the Hamiltonian (1) is decomposed into a sum of independent normal modes

$$H_0 = \sum_{k=1}^{N-1} \frac{1}{2}\left(P_k^2 + \mu_2 \omega_k^2 Q_k^2\right), \tag{4}$$

where

$$\omega_k = 2\sin\left(\frac{\pi k}{2N}\right), \quad k = 1, \cdots, N-1. \tag{5}$$

The frequency of the k-th normal mode is given by $\sqrt{\mu_2}\omega_k$. By using the normal mode coordinates, the n-th order potential part, $V^{(n)} := \sum_{j=1}^{N}(q_j - q_{j-1})^n$, can be written as[5]

$$V^{(n)} = \frac{N}{2^{n/2}} \sum_{l_0=1}^{N-1} \cdots \sum_{l_{n-1}=1}^{N-1} \left(\prod_{s=0}^{n-1} \omega_{l_s} \frac{Q_{l_s}}{\sqrt{N}}\right) D^{(n)}(l_0, \cdots, l_{n-1}), \tag{6}$$

where

$$D^{(n)}(l_0, \cdots, l_{n-1}) = \sum_{i_0=0}^{1} \cdots \sum_{i_{n-1}=0}^{1} \Delta_{(-1)^{i_0} l_0 + \cdots + (-1)^{i_{n-1}} l_{n-1}}, \tag{7}$$

and Δ_r ($r \in \mathbf{Z}$) is defined by

$$\Delta_r = \frac{1}{N} \sum_{j=1}^{N} \cos\left(\frac{\pi(2j-1)r}{2N}\right) \tag{8}$$

$$= \begin{cases} (-1)^m & \text{for } r = 2mN \ (m \in \mathbf{Z}), \\ 0 & \text{otherwise.} \end{cases} \tag{9}$$

For $n = 2$, we have $D^{(2)}(k, l) = 2\delta_{k,l}$, which yields the harmonic Hamiltonian (4).

In the normal mode coordinates, the equations of motion are given by

$$\frac{d^2}{dt^2} Q_k = -\mu_2 \omega_k^2 Q_k + \sum_{n=3}^{\infty} \mu_n F_k^{(n)}, \qquad k = 1, \cdots, N-1 \tag{10a}$$

where

$$F_k^{(n)} = -\frac{\omega_k\sqrt{N}}{2^{n/2}} \sum_{l_1=1}^{N-1} \cdots \sum_{l_{n-1}=1}^{N-1} \left(\prod_{s=1}^{n-1} \omega_{l_s} \frac{Q_{l_s}}{\sqrt{N}} \right) D^{(n)}(k, l_1, \cdots, l_{n-1}) \tag{10b}$$

is the force due to the anharmonic part $V^{(n)}$ $(n \geq 3)$.

3 Subsystems for anharmonic lattices

3.1 Type I subsets of the mode number set

It is seen from the equations of motion (10) that the normal modes are not dynamically independent of each other in the presence of the anharmonicity. By the anharmonic terms $V^{(n)}$ $(n \geq 3)$, selection rules are imposed for the mode interaction; if the mode l_0 interacts with the $(n-1)$ modes $l_1, \cdots, l_{n-1}$, the relation

$$\sum_{s=0}^{n-1} \vec{l}_s = 0 \pmod{2N} \tag{11}$$

must be satisfied, where $\vec{l}_s \in \{-l_s, l_s\}$. This relation, known as the conservation law of crystal momentum[6], can be directly deduced from the equations of motion (10) taking into account the structure of the mode-coupling coefficients (7).

Because of the above constraints on the mode interaction, if one initially gives energy only to a subset of modes, $\mathcal{E}$, it turns out that the energy would not necessarily spread over all the modes, but can be shared only among the modes in a subset $\mathcal{I} \supset \mathcal{E}$. Following Poggi and Ruffo[3], we will call such a subset, $\mathcal{I}$, the type I subset. By denoting with $\mathcal{M}$ the set of mode indices, i.e., $\mathcal{M} := \{1, 2, \cdots, N-1\}$, a precise definition of the type I subset is given as follows: a subset $\mathcal{I} \subset \mathcal{M}$ is type I iff the following condition is met:

$$E_k(0) = \begin{cases} \text{nonzero} & \text{for } k \in \mathcal{I}, \\ 0 & \text{for } k \in \mathcal{M} \setminus \mathcal{I}. \end{cases} \tag{12a}$$

$$\Rightarrow \quad E_k(t) \equiv 0 \quad \text{for } k \in \mathcal{M} \setminus \mathcal{I}, \ \forall t > 0, \tag{12b}$$

where $E_k(t) := (P_k(t)^2 + \mu_2 \omega_k^2 Q_k(t)^2)/2$ is the k-th normal mode's energy.

For the initial condition (12a) with $\mathcal{I}$ being type I, we have $Q_k(t) \equiv 0$ for $\forall k \in \mathcal{M} \setminus \mathcal{I}$, $\forall t \geq 0$. Thus, the time evolution of the variables $\{Q_k\}_{k \in \mathcal{I}}$ can be completely described by a sub-Hamiltonian $H_{\mathcal{I}}$ obtained by eliminating all the terms containing the quiescent variables $\{Q_k\}_{k \in \mathcal{M} \setminus \mathcal{I}}$, i.e.,

$$H_{\mathcal{I}} = \frac{1}{2} \sum_{k \in \mathcal{I}} P_k^2 + N \sum_{n=2}^{\infty} \frac{\mu_n}{n 2^{n/2}} \sum_{l_0, \cdots, l_{n-1} \in \mathcal{I}} \cdots \sum \left(\prod_{s=0}^{n-1} \omega_{l_s} \frac{Q_{l_s}}{\sqrt{N}} \right) D^{(n)}(l_0, \cdots, l_{n-1}). \tag{13}$$

Note that the parameter N in the sub-Hamiltonian can be absorbed into the other parameter, the energy. Indeed, rescaling the variables as $\hat{Q}_k = Q_k/\sqrt{N}, \hat{P}_k = P_k/\sqrt{N}$ and $\hat{E} = E/\sqrt{N}$, one can vanish N in the sub-Hamiltonian.

The type I subsets consisting of r modes can be derived by analyzing the relation (11). For a potential of the form (27), it can be shown that the following two r-mode sets become type I[5][1].

$$\mathcal{X}_r^{(a)} = \left\{ \frac{m}{r+1} N \right\}_{m=1}^{r}, \tag{14}$$

$$\mathcal{X}_r^{(b)} = \left\{ \frac{2m}{2r+1} N \right\}_{m=1}^{r}. \tag{15}$$

For an even potential, in addition to the above two, the following two sets become type I.

$$\mathcal{Y}_r^{(a)} = \left\{ \frac{2m-1}{2r} N \right\}_{m=1}^{r}, \tag{16}$$

$$\mathcal{Y}_r^{(b)} = \left\{ \frac{2m-1}{2r+1} N \right\}_{m=1}^{r}, \tag{17}$$

For each of the above sets, we assume that N can be divided by the denominator (i.e. $r+1$, $2r+1$, or $2r$).

Now that the expressions for the type I subsets are obtained, one can calculate the mode coupling coefficients $D^{(n)}$ and the corresponding sub-Hamiltonians. In the next section, we present explicit expressions for the sub-Hamiltonians for one- and two-mode type I subsets.

3.2 One- and two-mode subsystems

From the expressions (14)-(17), we obtain three one-mode type I subsets:

$$\mathcal{X}_1^{(a)} = \mathcal{Y}_1^{(a)} = \left\{ \frac{N}{2} \right\}, \quad \mathcal{Y}_1^{(b)} = \left\{ \frac{N}{3} \right\}, \quad \mathcal{X}_1^{(b)} = \left\{ \frac{2N}{3} \right\}. \tag{18}$$

These coincide with the results previously obtained by Bivins et al.[8] for the FPU-β lattice (i.e. $V(r) = \frac{1}{2}r^2 + \frac{\beta}{4}r^4$). Note that the subset $\{N/3\}$ becomes type I only for even potentials.

For the one-mode type I subset $\{e\}$, the sub-Hamiltonian (13) can be written as

$$H_{\{e\}} = \frac{1}{2} P_e^2 + \sum_{n=2}^{\infty} \frac{\mu_n}{n} V_{\{e\}}^{(n)}(Q_e), \tag{19a}$$

with

$$V_{\{e\}}^{(n)}(Q_e) = \frac{N}{2^{n/2}} \left(\omega_e \frac{Q_e}{\sqrt{N}} \right)^n D^{(n)}(e), \tag{19b}$$

where we abbreviate to write $D^{(n)}(e)$ instead of $D^{(n)}(e, \cdots, e)$. Noting that $D^{(n)}(e)$ can be rewritten as

$$D^{(n)}(e) = \frac{2^n}{N} \sum_{j=1}^{N} \left\{ \cos\left(\frac{\pi(2j-1)e}{2N} \right) \right\}^n, \tag{20}$$

[1]Recently, similar expressions are derived for periodic lattices, directly using symmetry intrinsic to lattice systems, instead of analyzing the mode coupling coefficients[7]

one obtains for the one-mode type I subsets (18) the potential part of the sub-Hamiltonians as follows:

$$V^{(n)}_{\{N/2\}} = \begin{cases} 2\left(\frac{2}{N}\right)^{\frac{n}{2}-1} Q^n_{\frac{N}{2}} & \text{for even } n, \\ 0 \quad \text{for odd } n, \end{cases}$$

$$V^{(n)}_{\{N/3\}} = \begin{cases} \left(\frac{3}{2N}\right)^{\frac{n}{2}-1} Q^n_{\frac{N}{3}} & \text{for even } n, \\ 0 \quad \text{for odd } n, \end{cases}$$

$$V^{(n)}_{\{2N/3\}} = \begin{cases} \left(\frac{3}{2N}\right)^{\frac{n}{2}-1} (1+2^{n-1})\, Q^n_{\frac{2N}{3}} & \text{for even } n, \\ \left(\frac{3}{2N}\right)^{\frac{n}{2}-1} (1-2^{n-1})\, Q^n_{\frac{2N}{3}} & \text{for odd } n. \end{cases}$$

As mentioned, the subset $\{N/3\}$ becomes type I only for even potentials, which yields $V^{(n)}_{\{N/3\}}$ to be zero for odd n. Although $V^{(n)}_{\{N/2\}}$ also vanishes for odd n, $\{N/2\}$ is type I for the potentials containing both even- and odd-terms. Thus, it turns out, for instance, that $H_{\{N/2\}}$ becomes the harmonic Hamiltonian when the anharmonic part of the potential is odd, i.e., $\mu_{2m} = 0$ for $m \geq 2$. It is interesting to note that, using the above expressions, one can design an anharmonic lattice possessing a desired particular solution described by a one degree-of-freedom Hamiltonian. This can be implemented by suitably choosing the parameters μ_n so that the desired solution can be described, for example, by $H_{\{2N/3\}}$.

Let us next consider the two-mode subsystems. Two-mode type I subsets are given by

$$\begin{aligned} \mathcal{X}^{(a)}_2 &= \left\{\frac{N}{3}, \frac{2N}{3}\right\}, \quad \mathcal{X}^{(b)}_2 = \left\{\frac{2N}{5}, \frac{4N}{5}\right\}, \\ \mathcal{Y}^{(a)}_2 &= \left\{\frac{N}{4}, \frac{3N}{4}\right\}, \quad \mathcal{Y}^{(b)}_2 = \left\{\frac{N}{5}, \frac{3N}{5}\right\}, \end{aligned} \tag{21}$$

among which, only $\mathcal{X}^{(a)}_2$ is a direct sum of the one-mode type I subsets.

For the two-mode type I subset $\{e, f\}$, the sub-Hamiltonian (13) becomes

$$H_{\{e,f\}} = \frac{1}{2}\left(P_e^2 + P_f^2\right) + \sum_{n=2}^{\infty} \frac{\mu_n}{n} V^{(n)}_{\{e,f\}}(Q_e, Q_f), \tag{22a}$$

with

$$V^{(n)}_{\{e,f\}}(Q_e, Q_f) = \frac{N}{2^{n/2}} \sum_{s=0}^{n} {}_nC_s \left(\omega_e \frac{Q_e}{\sqrt{N}}\right)^s \left(\omega_f \frac{Q_f}{\sqrt{N}}\right)^{n-s} D^{(n)}_s(e, f), \tag{22b}$$

where we denoted

$$D^{(n)}_s(e, f) = D^{(n)}(\overbrace{e, \cdots, e}^{s}, \overbrace{f, \cdots, f}^{n-s}). \tag{23}$$

Rewriting this coefficient as

$$D^{(n)}_s(e, f) = \frac{2^n}{N} \sum_{j=1}^{N} \left\{\cos\left(\frac{\pi(2j-1)e}{2N}\right)\right\}^s \left\{\cos\left(\frac{\pi(2j-1)f}{2N}\right)\right\}^{n-s}, \tag{24}$$

we have for the two-mode type I subsets (21) the n-th order potential term (22b) as follows:

$$
\begin{aligned}
V^{(n)}_{\{\frac{N}{3},\frac{2N}{3}\}} &= \frac{3^{\frac{n}{2}-1}}{2^{\frac{n}{2}}} N \left\{ \left(\hat{Q}_{\frac{N}{3}} + \hat{Q}_{\frac{2N}{3}} \right)^n + \left(-\hat{Q}_{\frac{N}{3}} + \hat{Q}_{\frac{2N}{3}} \right)^n + \left(-2\hat{Q}_{\frac{2N}{3}} \right)^n \right\}, \\
V^{(n)}_{\{\frac{2N}{5},\frac{4N}{5}\}} &= \frac{2^{\frac{3n}{2}}}{5} N \left\{ \left(-\eta_{\frac{\pi}{5}} \hat{Q}_{\frac{2N}{5}} + \eta_{\frac{2\pi}{5}} \hat{Q}_{\frac{4N}{5}} \right)^n \right. \\
&+ \left. 2 \left(\eta_{\frac{\pi}{5}} \xi_{\frac{\pi}{5}} \hat{Q}_{\frac{2N}{5}} + \eta_{\frac{2\pi}{5}} \xi_{\frac{2\pi}{5}} \hat{Q}_{\frac{4N}{5}} \right)^n + 2 \left(-\eta_{\frac{\pi}{5}} \xi_{\frac{2\pi}{5}} \hat{Q}_{\frac{2N}{5}} - \eta_{\frac{2\pi}{5}} \xi_{\frac{\pi}{5}} \hat{Q}_{\frac{4N}{5}} \right)^n \right\}, \\
V^{(n)}_{\{\frac{N}{4},\frac{3N}{4}\}} &= \begin{cases} 2^{\frac{3n}{2}-1} N \left\{ \left(\eta_{\frac{\pi}{8}} \xi_{\frac{\pi}{8}} \hat{Q}_{\frac{N}{4}} + \eta_{\frac{3\pi}{8}} \xi_{\frac{3\pi}{8}} \hat{Q}_{\frac{3N}{4}} \right)^n \right. \\ \qquad \left. + \left(-\eta_{\frac{\pi}{8}} \xi_{\frac{3\pi}{8}} \hat{Q}_{\frac{N}{4}} + \eta_{\frac{3\pi}{8}} \xi_{\frac{\pi}{8}} \hat{Q}_{\frac{3N}{4}} \right)^n \right\} & \text{for even } n, \\ 0 \quad \text{for odd } n, \end{cases} \\
V^{(n)}_{\{\frac{N}{5},\frac{3N}{5}\}} &= \begin{cases} \frac{2^{\frac{3n}{2}+1}}{5} N \left\{ \left(\eta_{\frac{\pi}{10}} \xi_{\frac{\pi}{10}} \hat{Q}_{\frac{N}{5}} + \eta_{\frac{3\pi}{10}} \xi_{\frac{3\pi}{10}} \hat{Q}_{\frac{3N}{5}} \right)^n \right. \\ \qquad \left. + \left(-\eta_{\frac{\pi}{10}} \xi_{\frac{3\pi}{10}} \hat{Q}_{\frac{N}{5}} + \eta_{\frac{3\pi}{10}} \xi_{\frac{\pi}{10}} \hat{Q}_{\frac{3N}{5}} \right)^n \right\} & \text{for even } n, \\ 0 \quad \text{for odd } n, \end{cases}
\end{aligned}
$$

where we put $\hat{Q}_e = Q_e/\sqrt{N}$, $\xi_\theta = \cos(\theta)$ and $\eta_\theta = \sin(\theta)$.

3.3 Integrability of the two-mode subsystems

On the contrary to the one-mode cases, the two-mode subsystems are not necessarily integrable. It is obvious that if a full system is integrable, so are all of its subsystems. However, for a nonintegrable lattice such as FPU-β lattice, whose nonintegrability has been proved in ref.[9], the subsystems may not be integrable. Indeed, chaotic trajectories are numerically observed for some of the two-mode subsystems. Figures 1(a)-(d) show the numerical Poincaré sections for the two-mode subsystems of FPU-β lattice. For the sub-Hamiltonians $H_{\{N/4,3N/4\}}$ and $H_{\{N/5,3N/5\}}$, chaotic components are clearly observed. As for the other two sub-Hamiltonians, obvious chaotic components can not be seen even for extremely large anharmonicity (e.g. $\beta/N \approx 10^3$).

In order to study the integrability properties on a rigorous basis, we apply here to the subsystems a nonintegrability criterion by Morales-Ruiz and Simó for two degree-of-freedom systems[10]. The criterion is applicable to systems with a potential of the form

$$V(x,y) = \phi(x) - \frac{1}{2}\theta(x)y^2 + \mathcal{O}(y^3), \tag{25}$$

for which there exist integral curves written as

$$\Gamma_h : y = p_y = 0, \; x = x(t,h), \; p_x = p_x(t,h), \tag{26}$$

where h is the energy. Namely, $x(t,h)$ is a solution of $\frac{1}{2}\dot{x}^2 + \phi(x) = h$. The nonintegrability criterion is presented when the normal variational equation (NVE) along Γ_h

$$\frac{d^2}{dt^2}\delta y = \theta(x(t);h)\,\delta y \tag{27}$$

becomes Lamé type[10].

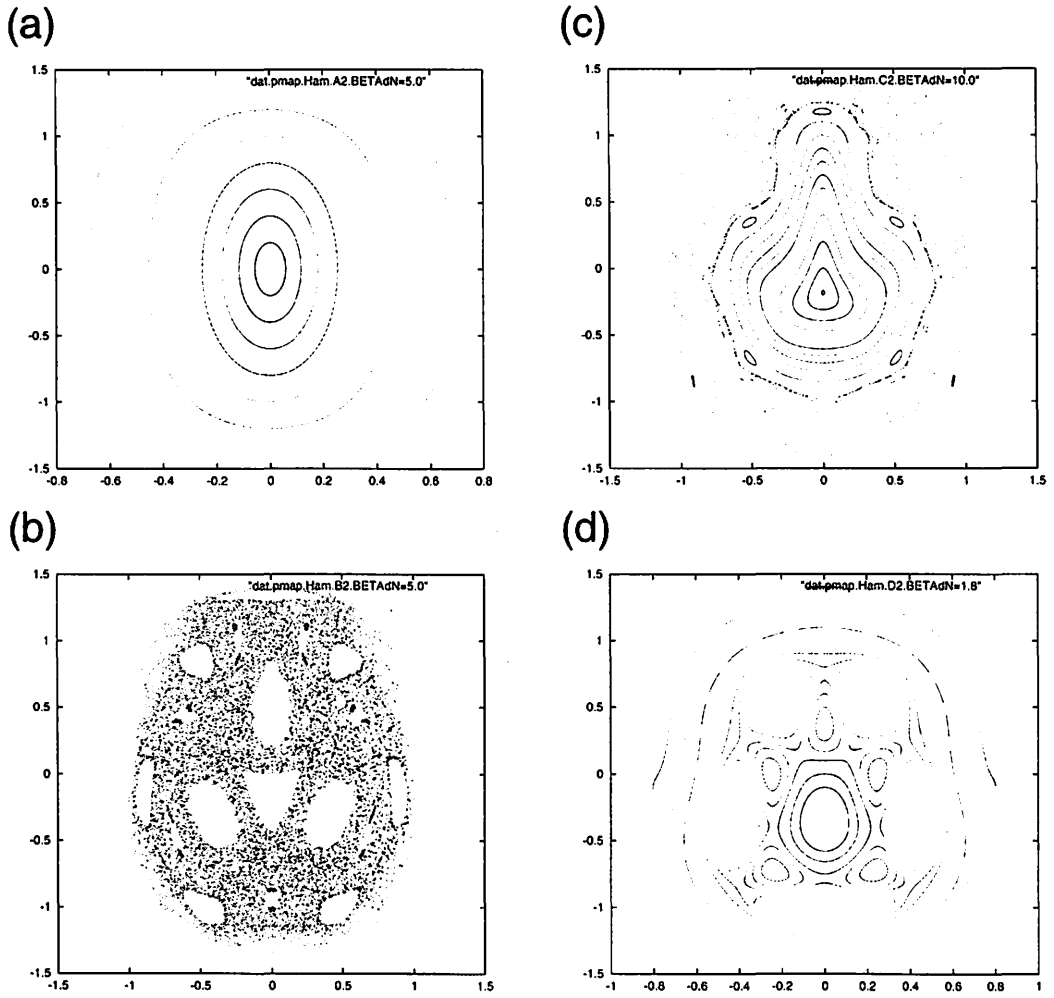

Figure 1: Poincaré sections of the two-mode subsystems (22) for the FPU-β lattice (i.e., $V(r) = \frac{1}{2}r^2 + \frac{\beta}{4}r^4$); (a) $\{e, f\} = \{N/3, 2N/3\}$, $\beta/N = 5.0$, (b) $\{e, f\} = \{N/4, 3N/4\}$, $\beta/N = 5.0$, (c) $\{e, f\} = \{N/5, 3N/5\}$, $\beta/N = 10.0$, (d) $\{e, f\} = \{2N/5, 4N/5\}$, $\beta/N = 1.8$.

Among the four two-mode sub-Hamiltonians derived above, the criterion is applicable to $H_{\{N/3,2N/3\}}$, for which $\theta(x)$ and $\phi(x)$ are respectively given by

$$\theta(x) = -\sum_{n=2}^{\infty}(n-1)\mu_n \left(\frac{3}{2N}\right)^{n/2-1} x^{n-2} \tag{28}$$

$$\phi(x) = \frac{N}{3}\sum_{n=2}^{\infty}\frac{\mu_n}{n}\left(\frac{3}{2N}\right)^{n/2}(2+(-2)^n)x^n, \tag{29}$$

where we rewrite $x = Q_{N/3}$ and $y = Q_{2N/3}$. After expressing x as a function of θ, we consider the following two functions of θ:

$$P_1(\theta) := -P_2(\theta)\cdot\phi(x(\theta)), \quad P_2(\theta) := 2\left(\frac{d}{dx}\theta(x)\right)^2$$

If the NVE is of Lamé type, P_1 and P_2 become cubic in θ, i.e., $P_j = a_j\theta^3 + b_j\theta^2 + c_j\theta + d_j$, $j = 1, 2$. Nonintegrability of a system with the potential (25) can be verified from the values of the

coefficients of the cubic polynomials P_1 and P_2 (see ref.[10] for details). For several lattice models, for which the NVE become Lamé type, $P_1(\theta)$ and $P_2(\theta)$ can be calculated as follows:

- FPU-α lattice ($V = \frac{1}{2}r^2 + \frac{\alpha}{3}r^3$): $P_1 = \frac{5}{3}\theta^3 + 2\theta^2 - \theta - \frac{4}{3}$, $P_2 = \frac{12\alpha^2}{N}$.
- FPU-β lattice ($V = \frac{1}{2}r^2 + \frac{\beta}{4}r^4$): $P_1 = 6\theta^3 + 6\theta^2 - 6\theta - 6$, $P_2 = -\frac{36\beta}{N}(\theta + 1)$.
- Toda lattice ($V = \frac{a}{b}\sum_{n\geq 2}\frac{(-b)^n}{n!}$ with $ab > 0$): $P_1 = 2\theta^3 + 3ab\theta^2 - a^3b^3$, $P_2 = \frac{3b^2}{N}\theta^2$.

Comparing these results with the necessary condition for integrability written in terms of the coefficients of P_1 and P_2 (Theorem 6.2 in ref.[10]), we can conclude that $\{N/3, 2N/3\}$-mode system is nonintegrable for both FPU-α and FPU-β lattice. While the necessary condition for integrability is satisfied for the case of Toda lattice (i.e., $\exists n \in \mathbf{N}\, s.t.\, a_1 = \frac{4}{n(n+1)}$), which is consistent with the integrability of Toda lattice.

Acknowledgement

The author would like to thank Prof. K. Yagasaki for discussions and informing him of the results on the application of the nonintegrability criterion.

References

[1] E. Fermi, J. Pasta and S. Ulam, Los Alamos Report LA1940 (1955), reproduced in Lecture Notes in Applied Mathematics, vol. 15 (AMS, 1974) 143.

[2] For review, see for example, J. Ford, Phys. Rep. **213** (1992) 272; G. Benettin, Prog. Theor. Phys. Suppl. **116** (1994) 207, and also ref.[3].

[3] P. Poggi and S. Ruffo, Physica **D103** (1997) 251.

[4] S. Shinohara, J. Soc. Phys. Jpn. **71** (2002) 1802.

[5] S. Shinohara, in the Proceedings of the 5th School/Conference "Let's Face Chaos through Nonlinear Dynamics", Maribor, Slovenia, June/July 2002, to be published in Prog. Theor. Phys. Suppl. (2003).

[6] J. M. Ziman, *Principles of the Theory of Solids* (Cambridge University Press, 1972).

[7] G. M. Chechin, N. V. Novikova and A. A. Abramenko, Physica **D166** (2002) 208; B. Rink, Physica **D175** (2003) 31.

[8] R. L. Bivins, N. Metropolis and J. R. Pasta, J. Comput. Phys. **12** (1973) 65.

[9] K. Umeno, Physica **D94** (1996) 116; in *Hamiltonian Systems with Three or More Degrees of Freedom*, ed. by C. Simó (Kluwer Academic, 1999).

[10] J. J. Morales-Ruiz, *Differential Galois Theory and Non-integrability of Hamiltonian Systems*, Progress of Mathematics, vol.179 (Birkhäuser, 1999).

A Classification of Subproblems in the Newtonian N-body Problem

Masayoshi SEKIGUCHI[1]
masa@kisarazu.ac.jp

Abstract

In this paper we consider subproblem of the Nwetoninan N-body problem, which describes motion of N particles in Euclidean space attracting with each other via inverse quadratic law. Subproblem is a restricted problem by limiting the phase space of the general N-body problem onto a certain subset of the phase space. Here we attempt to classify the set of subproblems whose configuration space X is a f-dimensional linear subset, then the phase space is $X \times T(X)$ with $T(X)$ being the tangent bundle over X and $0 < f < 3N$. We call such subproblems *linear f-subproblem.* The number f is called *degree of freedom.* First we point out that linear f-subproblem is an extension of homothetic solution to the Newtonian N-body problem. Homothetic solution is a homographic solution without rotation, and has much symmetry in some case. Thus f-subproblem has less symmetry and is far from the general problem. However, classifynig f-subproblem reduces the study of the original problem. Second we devide f-subproblem into composable subproblem and the other. In this class of composable subproblem, we can define two operations: *composition* and *decomposition.* Finally we present some examples although some of them are already known. This new point of view sheds light on a new aspect of the study on the Newtonian N-body problem: dynamically equivalent classification of subproblems. The study on an equivalent class is reduced to one on a representative element.

1 Introduction

Many linear f-subproblem have indivisually been studied: collinear three-body problem[7], isosceles three-body problem[1], collinear four-body problem[5], trapezoidal four-body problem[3], rhomboidal four-body problem[4], symmetric collinear four-body problem[14, 15, 21], rectangular four-body problem[15], and others[16, 20, 23, 24]. In some cases, these subproblems are utilized to study collision/non-collision singularity or such a special solution as oscillatory motion. They themselves have hardly been studied because they do not model a physical system due to its linear restriction.

On the other hand, relative equilibria which is a homographic solution with rotation have been studied as an independent problem, and have a long history. Especially in 1970's, Smale[17, 18, 19] raised a new problem after introducing a modern definition of relative equilibria. Many studies have been conducted according to the assertion of Smale. We believe that the first work on a classification of relative equilibria is ones by Palmore[8, 9, 10, 11, 12, 13].

Here linear f-subproblem is a purely mathematical subject, is not just a model of some physical systems.

2 Linear f-subproblem

As is usual, the Newtonian N-body problem is given in a form of Hamiltonian system:

$$\frac{dq}{dt} = \frac{\partial H}{\partial p}, \quad \frac{dq}{dt} = -\frac{\partial H}{\partial q},$$

with the hamiltonian function

$$H = \frac{1}{2} p^T M^{-1} p - U(q), \quad U(q) = \sum_{i<j} \frac{m_i m_j}{\|q_i - q_j\|},$$

where variables q and p are $3N$-vector, and $\|\cdot\|$ is euclidean norm.

Here we give a definition of linear f-subproblem.

[1]Kisarazu National College of Technology,
Kiyomidai-Higashi 2-11-1, Chiba 292-0041, JAPAN

Definition 1: Linear f-subproblem is a subproblem restricted on $X \times T(X)$ with a linear subset X which is the kernel space of a certain $(3N-f) \times 3N$ full-rank matrix A. Namely,

$$Aq = 0 \quad \text{and} \quad AM^{-1}\nabla_q U(q) = 0. \tag{1}$$

Since q is a vector of the kernel space of A, it is f-dimensional. In the case of $f = 1$, the equation (1) are reduced to the equation:

$$\nabla_q U(q) = \lambda M q, \tag{2},$$

which is the classical definition of central configuration[22]. Homographic solution is a class of special solutions where particles keep a central configuration with expanding, contracting and rotating. *Homothetic Solution* is a homographic solution without rotation. *Relative Equilibrium* is a homographic solution with rotation. In this sense, linear f-subproblem is an extension of homothetic solution. Although further extension of linear f-subproblem to a rotating system should be done, it is not treated here.

Obviously a matrix which defines an f-subproblem is not unique.

Definition 2: If two matrices A and A' define the same X where a linear f-subproblem is given, then we write $A' \sim A$ and we say A' and A are similar.

The following notes are trivial.

NOTE 1: For a regular $(3N-f) \times (3N-f)$ matrix R,

$$RA \sim A.$$

proof: The kernel spaces of A and RA are common. ■

NOTE 2: For a $3N \times 3N$ orthogonal matrix C,

$$AC \sim A.$$

proof: If we conduct a canonical transformation induced from a linear transformation $Q = Cq$, then we have the new kinetic energy $T = 1/2\dot{Q}^T\tilde{M}\dot{Q}$ with $\tilde{M} = C^{-T}MC^{-1}$ being CMC^T from the assumption. Then, we have

$$0 = ACM^{-1}\nabla_q U(q)) = A\tilde{M}^{-1}C\nabla_q U(q)) = A\tilde{M}^{-1}\nabla_Q \tilde{U}(Q)),$$

where $\tilde{U}(Q) = U(C^{-1}Q)$. ■

In general X for a set of arbitrary masses is the gravity-center integral: $\sum m_i q_i = 0$ or orbital plane/line segment where the system is restricted to. In the former case, $T(X)$ is the linear momentum integral.

2.1 Well-known examples of linear f-subproblem

Examples listed in the previous section are described according to Definition 1.

1. Collinear three-body problem ($f = 2$).

$$M = \mathrm{diag}(m_1, m_2, m_3), \quad A = (m_1 \; m_2 \; m_3)$$

2. Collinear four-body problem ($f = 3$).

$$M = \mathrm{diag}(m_1, m_2, m_3, m_4), \qquad A = (m_1 \; m_2 \; m_3 \; m_4)$$

3. Isosceles three-body problem ($f = 2$).
Two masses ($m_1/2$) move symmetrically about the vertical axis where the third mass (m_2) moves vertically.

$$M = \mathrm{diag}(\frac{m_1}{2}, \frac{m_1}{2}, \frac{m_1}{2}, \frac{m_1}{2}, m_2, m_2),$$

$$A = \begin{pmatrix} 0 & m_1/2 & 0 & m_1/2 & 0 & m_2 \\ 0 & 1 & 0 & -1 & 0 & 0 \\ 0 & 0 & 0 & 0 & 1 & 0 \\ 1 & 0 & 1 & 0 & 0 & 0 \end{pmatrix} \sim \mathrm{BlockDiagonal}\left(\begin{pmatrix} m_1 & 0 & m_2 \\ 1 & -1 & 0 \end{pmatrix}, \begin{pmatrix} 0 & 0 & 1 \\ 1 & 1 & 0 \end{pmatrix}\right)$$

Here we take

$$R = \text{BlockDiagonal}\left(\begin{pmatrix}1 & m_1/2\\ 0 & 1\end{pmatrix}, \begin{pmatrix}1 & 0\\ 0 & 1\end{pmatrix}\right), \quad C = \begin{pmatrix}0 & 0 & 0 & 1 & 0 & 0\\ 1 & 0 & 0 & 0 & 0 & 0\\ 0 & 0 & 0 & 0 & 1 & 0\\ 0 & 1 & 0 & 0 & 0 & 0\\ 0 & 0 & 0 & 0 & 0 & 1\\ 0 & 0 & 1 & 0 & 0 & 0\end{pmatrix}$$

It is very simple to determine these matrices R and C because the method is row/column elementary operation. Hereafter we omit to describe R and C.

4. Rectangular four-body problem ($f = 2$).
   All masses are equal. Then we have

$$M = mE_8,$$

$$A = \begin{pmatrix}1 & 0 & 1 & 0 & 0 & 0 & 0 & 0\\ 1 & 0 & 0 & 0 & 1 & 0 & 0 & 0\\ 1 & 0 & 0 & 0 & 0 & 0 & -1 & 0\\ 0 & 1 & 0 & -1 & 0 & 0 & 0 & 0\\ 0 & 1 & 0 & 0 & 0 & -1 & 0 & 0\\ 0 & 1 & 0 & 0 & 0 & 0 & 0 & 1\end{pmatrix} \sim \text{BlockDiagonal}\left(\begin{pmatrix}1 & 1 & 0 & 0\\ 1 & 0 & 1 & 0\\ 1 & 0 & 0 & -1\end{pmatrix}, \begin{pmatrix}1 & -1 & 0 & 0\\ 1 & 0 & -1 & 0\\ 1 & 0 & 0 & 1\end{pmatrix}\right)$$

5. Rhomboidal four-body problem ($f = 2$).
   Masses on the horizontal axis are equal to m_1, ones on the veratical axis are equal to m_2, so we have

$$M = \text{diag}(m_1,\ m_1,\ m_2,\ m_2,\ m_1,\ m_1,\ m_2,\ m_2),$$

$$A = \begin{pmatrix}1 & 0 & 0 & 0 & 1 & 0 & 0 & 0\\ 0 & 1 & 0 & 0 & 0 & 0 & 0 & 0\\ 0 & 0 & 1 & 0 & 0 & 0 & 0 & 0\\ 0 & 0 & 0 & 1 & 0 & 0 & 0 & 1\\ 0 & 0 & 0 & 0 & 0 & 1 & 0 & 0\\ 0 & 0 & 0 & 0 & 0 & 0 & 1 & 0\end{pmatrix} \sim \text{BlockDiagonal}\left(\begin{pmatrix}1 & 1 & 0 & 0\\ 0 & 0 & 1 & 0\\ 0 & 0 & 0 & 1\end{pmatrix}, \begin{pmatrix}1 & 0 & 0 & 0\\ 0 & 1 & 0 & 0\\ 0 & 0 & 1 & 1\end{pmatrix}\right)$$

6. Symmetric collinear four-body problem ($f = 2$).

$$M = \text{diag}(m_2,\ m_1,\ m_1,\ m_2),$$

$$A = \begin{pmatrix}1 & 0 & 0 & 1\\ 0 & 1 & 1 & 0\end{pmatrix} \sim \text{BlockDiagonal}((1\ 1), (1\ 1))$$

7. Other cases
   There are a lot of cases, which should be described similarly, but it takes a great amount of space in this paper, therefore we omit them.

2.2 Unknown examples of linear f-subproblem

Double n-gonal prisms problem

This system consists of two concentric n-gonal prism which masses stay at the vertices of. Masses of the outer prism are m_1, and ones of the inner m_2. The number of masses is $2n$ in total. Each prism expands/contracts about the center of masses which is the geometrical center of the prisms.

One might expect to find a new system by replacing "prism" by "polygon" or "polyhedron" in the above system. However, these are already known[2].

A few cases for $f = 3$ are known: examples given above and others[6]. Moreover, we have never seen the case for $f \geq 4$.

3 Subclassification

As is seen in the previous section, there are some cases where A is similar to a certain block diagonal matrix, and the other cases. So we give a name to them.

Definition 3: For $f \geq 2$, *f-graphic subproblem* is a linear f-subproblem which satisfies

$$A \sim \text{BlockDiagonal}(A_1, A_2, \cdots, A_f)$$

where each A_i defines a linear 1-subproblem.

Then, we say that f-graphic subproblem is **decomposed** into the linear 1-subproblems defined by A_i and is **decomposable**, or that the linear 1-subproblem defined by A_i is **composable**. According to the previous section, collinear three-body problem is **indecomposable** while isosceles three-body problem is decomposable. Also collinear four-body problem is indecomposable while symmetric collinear four-body problem is decomposable.

To an extent we investigate, one-dimensional two-body problem is generally *incomposable* if excluding the case of equal mass. Unfortunately we have no proof about this property. We would like to state this property as conjecture.

Conjecture: A homothetic solution with equal masses is composable while one with unequal masses is incomposable.

4 Discussion

The similarity between the collinear three-body problem and the symmetric collinear four-body problem is seen in the phase space[14, 21]. As mentioned above, these two subprblems are different in decomposability. This fact means that decmposability does not relate to the geometry in the phase space, but is clearly a kind of dynamical classifications.

We offer a new problem to clarify the structure of the set of subproblems of the gravitational N-body problem. There exit special elements which can be related to each other by operations of composition and decomposition. It is conjectured that the all elments of the set are confirmed by the multiple operations.

On the other hand, the remaining problems are

1. to collect the all subproblems which can be operated by composition and decomposition.
2. to complete the dynamical classification of subproblems.

It would be necessary to study the representative elements of each equivalent class as well as the collection of subproblems which are composable and/or decomposable. It might be an economical strategy to study the subproblems.

Acknowledgement

The author thanks to the suggestion of Carles Simó when the author had visited Universitat de Barcelona in 2001-02, the finacial support from National Astronomical Observatory of JAPAN for this research project, and grants for the reseach fellowship from the Ministry of Education, Culture, Sports, Science and Technology of JAPAN in 2002.

References

[1] Devaney, R.L.: 1980, 'Triple collision in the planar isosceles three-body problem', *Inventiones Mathematicae*, **60**, 249-267.

[2] Hagihara, Y.:1970, 'Celestial Mechanics', vol.1, The MIT Press.

[3] Lacomba, E.A.: 1981, 'Quadruple collision in the trapezoidal four-body problem', in *Classical Mechanics and Dynamical Systems*, 109-122, Marcel Dekker.

[4] Lacomba, E.A. and Pérez-Chavela, E.: 1992, 'A compact model for the rhomboidal 4-body problem', *Celestial Mechanics and Dynamical Astronomy*, **54**, 343-355.

[5] Mather, J. and McGehee, R.: 1975, 'Solutions of the collinear four-body problem which become unbounded in finite time', *Dynamical Systems Theory and its Applications*, 573-597, Lecture Notes in Physics, Springer-Verlag.

[6] Moeckel, R. and Simó, C.: 1998, 'Bifurcation of spatial central configurations from planar one', *SIAM Math. Anal.*, **26**, 978-998.

[7] McGehee, R.: 1974, 'Triple collision in the collinear three-body problem', *Inventiones Mathematicae*, **27**, 191-227.

[8] Palmore, .: 1973, 'Classifying relative equilibria I', *Bulletin of the American Mathematical Society*, **79**, 904-908.

[9] Palmore, .: 1975, 'Classifying relative equilibria II', *Bulletin of the American Mathematical Society*, **81**, 489-491.

[10] Palmore, .: 1975, 'Classifying relative equilibria III', *Letters in Mathematical Physics*, **1**, 71-73.

[11] Palmore, .: 1976, 'New relative equilibria of the N-body problem', *Letters in Mathematical Physics*, **1**, 119-123.

[12] Palmore, .: 1976, 'Measure of degenerate relative equilibria I', *Annals of Mathematics*, **104**, 421-429.

[13] Palmore, .: 1977, 'Minimally classifying relative equilibria', *Letters in Mathematical Physics*, **1**, 395-399.

[14] Sekiguchi, M. and Tanikawa, K.: 2003, 'On the symmetric collinear four-body problem', submitted to *PASJ*.

[15] Simó, C. and Lacomba, E.A.: 1982, 'Analysis of some degenerate quadruple collisions', *Celestial Mechanics*, **28**, 49-62.

[16] Sitnikov, K.A.: 1960, 'Existence of oscillatory motions for the three-body problem', *Dokl. Akad. Nauk. USSR*, **133**, 303-306.

[17] Smale, S.: 1970, 'Topology and mechanics I', *Inventiones Mathematicae*, **10**, 305-331.

[18] Smale, S.: 1970, 'Topology and mechanics II', *Inventiones Mathematicae*, **11**, 45-64.

[19] Smale, S.: 1971, 'Problems on the nature of relative equilibria in celestial mechanics', *Lecture Notes in Mathematics*, **197**, 194-198, Springer-Verlag.

[20] Steves, B.A. and Roy, A.E.: 1998, 'Some special restricted four-body problem — I. Modeling the Caledonian problem', *Planetary Space Science*, **46**(11/12), 1465-1474.

[21] Sweatman, W.: 2002, 'The symmetric one-dimensional newtonian four-body problem: numerical investigation', *Celestial Mechanics and Dynamical Astronomy*, **82**, 179-201.

[22] Wintner, A.: 1941, 'The analytical foundations of celestial mechanics', Princeton, N.J. University Press 1941.

[23] Vidal, C.: 1999, 'The tetrahedral 4-body problem problem with rotation', *Celestial Mechanics and Dynamical Astronomy*, **71**, 15-33.

[24] Xia, Z.: 1992, 'The existence of noncollision singularities in newtonian systems', *Annals of Mathematics*, **135**, 411-468.

A complete list of integrable two-dimensional homogeneous polynomial potentials with a polynomial first integral up to quartic in the momenta

Katsuya Nakagawa
Department of Astronomical Science, The Graduate University for Advanced Studies (SOKENDAI)
Mitaka, Tokyo 181-8588, JAPAN
e-mail: k.nakagawa@nao.ac.jp

Haruo Yoshida
National Astronomical Observatory of Japan, Mitaka, Tokyo 181-8588, JAPAN
e-mail: h.yoshida@nao.ac.jp

Abstract

We give a complete list of integrable Hamiltonian systems with a two-dimensional homogeneous polynomial potential that admit a polynomial first integral up to quartic in the momenta. In this paper, we simplify the derivation of our previous result with the help of Ziglin's fundamental lemma. In addition, we report the discovery of a new integrable system, which completes the classification of integrable systems in the range studied.

1 Introduction

A Hamiltonian system with n degrees of freedom is integrable, i.e., the equations of motion can be solved by quadratures, if there exist n independent first integrals in involution,

$$\Phi_1 = \text{constant}, \Phi_2 = \text{constant}, \ldots, \Phi_n = \text{constant}, \quad \{\Phi_i, \Phi_j\} = 0 \text{ for all } (i, j). \tag{1}$$

Here, $\{\cdot, \cdot\}$ represents the Poisson bracket, defined by

$$\{\Phi_i, \Phi_j\} = \sum_{l=1}^{n} \left(\frac{\partial \Phi_i}{\partial q_l} \frac{\partial \Phi_j}{\partial p_l} - \frac{\partial \Phi_i}{\partial p_l} \frac{\partial \Phi_j}{\partial q_l} \right). \tag{2}$$

The condition for a function Φ to be a first integral is that the Poisson bracket of Φ and the Hamiltonian vanishes, i.e.,

$$\{\Phi, H\} = \sum_{i=0}^{n} \left(\frac{\partial \Phi}{\partial q_i} \frac{\partial H}{\partial p_i} - \frac{\partial \Phi}{\partial p_i} \frac{\partial H}{\partial q_i} + \frac{\partial \Phi}{\partial q_i} \frac{\partial H}{\partial p_i} - \frac{\partial \Phi}{\partial p_i} \frac{\partial H}{\partial q_i} \right) = 0. \tag{3}$$

It is a fundamental problem in celestial or classical mechanics to know whether a given Hamiltonian system is integrable or not. To be more specific, the problem is

(a) to decide if a given Hamiltonian system is integrable, and if this is the case,

(b) to construct as many first integrals as the number of degrees of freedom.

Unfortunately, at present, we have no ultimate criterion for integrability that enables us to solve the problem (a). The best known result to date is due to Morales-Ruiz and Ramis [14, 15, 16], who obtained, from their own theorem based on the differential Galois theory, a strong necessary condition for the integrability of n-degree-of-freedom Hamiltonian systems defined by a natural Hamiltonian with a homogeneous potential of an integer degree,

$$H = \frac{1}{2}(p_1^2 + \cdots + p_n^2) + V(q_1, \ldots, q_n). \tag{4}$$

See also [11, 23]. Although this criterion has been applied to non-integrability proofs of many systems [1, 2, 8, 9, 20], it does not always meet our demand. There is indeed at least one non-integrable potential that satisfies the necessary condition [12, 13].

One of possible approaches to the fundamental problem would be

(c) to list all integrable potentials and the corresponding first integrals.

The list could solve not only the problem (a) but also the problem (b). We consider Hamiltonian systems with two degrees of freedom described by the Hamiltonian,

$$H = \frac{1}{2}(p_1^2 + p_2^2) + V(q_1, q_2). \tag{5}$$

The existence of an additional first integral which is independent of the Hamiltonian guarantees the integrability of the system. Let Φ be such a first integral. The partial differential equation (PDE) (3) becomes

$$\frac{\partial \Phi}{\partial q_1} p_1 - \frac{\partial \Phi}{\partial p_1}\frac{\partial V}{\partial q_1} + \frac{\partial \Phi}{\partial q_2} p_2 - \frac{\partial \Phi}{\partial p_2}\frac{\partial V}{\partial q_2} = 0. \tag{6}$$

In this paper, we search for the solutions of the PDE (6) under the following conditions.

- The potential $V(q_1, q_2)$ is a homogeneous polynomial.
- The first integral $\Phi(q_1, q_2, p_1, p_2)$ is a polynomial.

The motivations for putting such strong restrictions on functions considered are as follows.

1. The PDE (6) becomes an algebraic equation for the variables q_1, q_2, p_1, p_2, which reduces to simultaneous algebraic equations for the coefficients of V and Φ.
2. The homogeneity of potentials leads to the weighted-homogeneity of first integrals, which simplifies the form of first integrals. See Section 2.
3. If a non-homogeneous potential is integrable, then each of homogeneous parts of the highest degree and of the lowest degree must be integrable. That is, this study is a first step toward an understanding of the integrability of larger classes of systems.

In [17], the present authors obtained a list of integrable two-dimensional homogeneous polynomial potentials with an additional polynomial first integral up to quartic in the momenta. The main purpose of the present paper is to simplify the derivation of the same result by introducing a new process for determining what we call *integrable candidates*.

This paper is organized as follows. In Section 2, we formulate a method of searching for polynomial first integrals. In Section 3, we summarize the preceding works related to our study and then give a quick review of our previous result (Theorem 1). The derivation of Theorem 1 is simplified in Section 4, which is the main part of this paper. Finally, in Section 5, we present a complete list of integrable two-dimensional homogeneous polynomial potentials with a polynomial first integral up to quartic in the momenta (Theorem 3), adding a new integrable case.

2 The direct search for polynomial first integrals

In this section, we see a general method of the direct search for polynomial first integrals, which is based on [6].

Without loss of generality, a polynomial first integral Φ can be assumed to have the following two properties. See [17] for details.

1. Φ is either even or odd in the momenta.
2. Φ is weighted-homogeneous.

The first property here means that Φ satisfies

$$\Phi(q_1,q_2,-p_1,-p_2)=\Phi(q_1,q_2,p_1,p_2),\ \text{or}\ \Phi(q_1,q_2,-p_1,-p_2)=-\Phi(q_1,q_2,p_1,p_2), \tag{7}$$

which arises from the invariance of the system under the time-reflection,

$$t\to -t,\ q_1\to q_1,\ q_2\to q_2,\ p_1\to -p_1,\ p_2\to -p_2. \tag{8}$$

The second property is a consequence of the invariance of the system under the scale transformation,

$$t\to \sigma^{-1}t,\ q_1\to \sigma^{2/(k-2)}q_1,\ q_2\to \sigma^{2/(k-2)}q_2,\ p_1\to \sigma^{k/(k-2)}p_1,\ p_2\to \sigma^{2/(k-2)}p_2, \tag{9}$$

where σ is an arbitrary constant and k the degree of the homogeneous polynomial potential. It follows that Φ satisfies the following identity.

$$\Phi(\sigma^{2/(k-2)}q_1,\sigma^{2/(k-2)}q_2,\sigma^{k/(k-2)}p_1,\sigma^{k/(k-2)}p_2)=\sigma^M\Phi(q_1,q_2,p_1,p_2). \tag{10}$$

Here, M is a constant called the weighted-degree.

From the first property, we can put a polynomial first integral of order N in the momenta in the form

$$\begin{aligned}\Phi&=\sum_{n=0}^{[N/2]}\sum_{m=0}^{N-2n}A^{N-2n,m}(q_1,q_2)p_1^{N-2n-m}p_2^m\\&=A^{N,0}(q_1,q_2)p_1^N+A^{N,1}(q_1,q_2)p_1^{N-1}p_2+\cdots+A^{N,N}(q_1,q_2)p_2^N\\&\quad+A^{N-2,0}(q_1,q_2)p_1^{N-2}+A^{N-2,1}(q_1,q_2)p_1^{N-3}p_2+\cdots+A^{N-2,N-2}(q_1,q_2)p_2^{N-2}+\ldots,\end{aligned} \tag{11}$$

where $A^{N-2n,m}(q_1,q_2)$ are polynomials. Here, $[N/2]$ represents the greatest integer that is less than or equal to $N/2$. Then, the PDE (6) can be regarded as a polynomial for the momenta (p_1,p_2). By

arranging the left hand side of the PDE (6) in order of descending powers of p_1, p_2, we obtain

$$\sum_{n=0}^{[(N+1)/2]} \sum_{m=0}^{N-2n+1} \left[\frac{\partial A^{N-2n,m}}{\partial q_1} + \frac{\partial A^{N-2n,m-1}}{\partial q_2} \right.$$
$$\left. -(N-2n-m+2)A^{N-2n+2,m} \frac{\partial V}{\partial q_1} - (m+1)A^{N-2n+2,m+1} \frac{\partial V}{\partial q_2} \right] p_1^{N+1-2n-m} p_2^m = 0. \quad (12)$$

All the coefficients vanish to give

$$\frac{\partial A^{N-2n,m}}{\partial q_1} + \frac{\partial A^{N-2n,m-1}}{\partial q_2}$$
$$= (N-2n-m+2)A^{N-2n+2,m} \frac{\partial V}{\partial q_1} + (m+1)A^{N-2n+2,m+1} \frac{\partial V}{\partial q_2}, \quad (m = 0, 1, \ldots, N-2n+1). \quad (13)$$

Here, $n = 0, 1, \ldots, [(N+1)/2]$. For $n = 0$, the PDEs (13) become

$$\frac{\partial A^{N,m}}{\partial q_1} + \frac{\partial A^{N,m-1}}{\partial q_2} = 0, \quad (m = 0, 1, \ldots, N+1). \quad (14)$$

Let us here note that the second property, i.e., (10) requires that $A^{N-2n,m}$ with the same n should be homogeneous polynomials of the same degree. By integrating (14), we obtain

$$A^{N,m}(q_1, q_2) = \sum_{v=0}^{m} \sum_{u=0}^{N-m} (-1)^v \binom{u+v}{v} a_{N-(u+v),m-v} q_1^v q_2^u, \quad (m = 0, 1, \ldots, N) \quad (15)$$

with integration constants $a_{N-(u+v),m-v}$. Here, the sum $u + v \equiv d$ is fixed to be one of $\{0, 1, \ldots, N\}$, so that the solutions of the PDEs (14) are classified into $N+1$ cases labeled by the value of d, or the degree of $A^{N,m}$. For each case, the first integral is written as

$$\begin{aligned}
&\Phi = a_{0,0}(q_2 p_1 - q_1 p_2)^N + \ldots && (d = N) \\
&\Phi = (a_{1,0} p_1 + a_{1,1} p_2)(q_2 p_1 - q_1 p_2)^{N-1} + \ldots && (d = N-1) \\
&\ldots \\
&\Phi = a_{N,0} p_1^N + a_{N,1} p_1^{N-1} p_2 + \cdots + a_{N,N} p_2^N + \ldots && (d = 0)
\end{aligned} \quad (16)$$

or

$$\Phi = (q_2 p_1 - q_1 p_2)^d \sum_{m=0}^{N-d} a_{N-d,m} p_1^{N-d-m} p_2^m + \sum_{n=1}^{[N/2]} \sum_{m=0}^{N-2n} A^{N-2n,m}(q_1, q_2) p_1^{N-2n-m} p_2^m, \quad (17)$$

where $d = N, N-1, \ldots, 0$. Here, $A^{N-2n,m}(q_1, q_2)$ are homogeneous polynomials of degree $nk + d$. Check that the first integral (17) satisfies the second property ($M = (Nk + 2d)/(k - 2)$). We can obtain $A^{N-2n,m}$ by integrating (13) as

$$A^{N-2n,m} = \int \left\{ (N-2n-m+2)A^{N-2n+2,m} \frac{\partial V}{\partial q_1} + (m+1)A^{N-2n+2,m+1} \frac{\partial V}{\partial q_2} - \frac{\partial A^{N-2n,m-1}}{\partial q_2} \right\} dq_1$$
$$+ r_{N-2n,m} q_2^{nk+d} \quad (m = 0, 1, \ldots, N-2n). \quad (18)$$

where $n = 1, 2, \ldots, [N/2]$ and $r_{N-2n,m}$ are integration constants. For each $n \geq 1$, if we operate with $(-1)^m \partial^{N-2n+1} / \partial q_1^m \partial q_2^{N-2n+1-m}$ on the $(m+1)$-th equation of (13) and add them up, then we obtain $[(N+1)/2]$ linear PDEs for $V(q_1, q_2)$,

$$\sum_{m=0}^{N-2n+1} (-1)^m \frac{\partial^{N-2n+1}}{\partial q_1^{N-2n+1-m} \partial q_2^m} \left[(N-2n-m+2) A^{N-2n+2,m} \frac{\partial V}{\partial q_1} + (m+1) A^{N-2n+2,m+1} \frac{\partial V}{\partial q_2} \right] = 0, \tag{19}$$

where $n = 1, 2, \ldots, [(N+1)/2]$.

We put the potential V in the form of a homogeneous polynomial of degree k,

$$V = \sum_{j=0}^{k} \alpha_j q_1^{k-j} q_2^j = \alpha_0 q_1^k + \alpha_1 q_1^{k-1} q_2 + \cdots + \alpha_k q_2^k. \tag{20}$$

Substituting (20) in (19), we have polynomial identities for (q_1, q_2). Equating all the coefficients to zeros yields $[(N+1)/2]$ sets of simultaneous algebraic equations for the coefficients of the first integral and of the potential. There is no general method to find non-trivial solutions, so we have to deal with the problem on a case-by-case basis.

3 A review of the previous works

3.1 The known results before us

Let us summarize the known results which are related to our problem. For first integrals linear or quadratic in the momenta $(N = 1, 2)$, the general solutions of the PDEs (19) have been known [6]. We can obtain the polynomial solutions from them, which are displayed below.

$$\begin{cases} V_k = r^k = (q_1^2 + q_2^2)^{k/2}, \quad (k = \text{even}) \\ \Phi = q_2 p_1 - q_1 p_2 \end{cases} \tag{21}$$

$$\begin{cases} V_k = q_1^k \\ \Phi = p_2 \end{cases} \tag{22}$$

$$\begin{cases} V_k = \dfrac{1}{r} \left[\left(\dfrac{r+q_1}{2} \right)^{k+1} + (-1)^k \left(\dfrac{r-q_1}{2} \right)^{k+1} \right] \\ \Phi = p_2 (q_2 p_1 - q_1 p_2) + \dfrac{1}{2} q_2^2 V_{k-1} \end{cases} \tag{23}$$

$$\begin{cases} V_k = q_1^k + \alpha_k q_2^k \\ \Phi = p_2^2 + 2\alpha_k q_2^k \end{cases} \tag{24}$$

Note that the above four cases are all separable ones: (21) in polar coordinates, (23) in parabolic coordinates, (22) and (24) in Cartesian coordinates. As stated in the Bertrand-Darboux theorem [10], the existence of a quadratic integral is related with the separability of the system.

For first integrals cubic or higher orders in the momenta $(N \geq 3)$, we do not know the analytical solutions of the PDEs (19). In the range of our search, the following three cases have been known to be integrable. Grammaticos *et al* [3] and Hall [4] independently discovered

$$\begin{cases} V = q_1^3 + \dfrac{3}{16} q_1 q_2^2 \\ \Phi = p_2^4 - \dfrac{1}{4} q_2^3 p_1 p_2 + \dfrac{3}{4} q_1 q_2^2 p_2^2 - \dfrac{3}{64} q_1^2 q_2^4 - \dfrac{1}{128} q_2^6 \end{cases} \tag{25}$$

Ramani *et al* [19] discovered

$$\begin{cases} V = q_1^3 + \frac{1}{2}q_1q_2^2 \pm \frac{\sqrt{3}\,\mathrm{i}}{18}q_2^3 \\ \Phi = p_1p_2^3 \mp \frac{\sqrt{3}\,\mathrm{i}}{2}p_2^4 + \frac{1}{2}q_2^3p_1^2 - \left(\frac{3}{2}q_1q_2^2 \mp \frac{\sqrt{3}\,\mathrm{i}}{2}q_2^3\right)p_1p_2 + \left(3q_1^2q_2 \mp \sqrt{3}\,\mathrm{i}q_1q_2^2 + \frac{1}{2}q_2^3\right)p_2^2 \\ \quad + \frac{1}{2}q_1^3q_2^3 \mp \frac{\sqrt{3}\,\mathrm{i}}{8}q_1^2q_2^4 - \frac{1}{4}q_1q_2^5 \mp \frac{5\sqrt{3}\,\mathrm{i}}{72}q_2^6 \end{cases} \tag{26}$$

and

$$\begin{cases} V = q_1^4 + \frac{3}{4}q_1^2q_2^2 + \frac{1}{8}q_2^4 \\ \Phi = p_2^4 + \frac{1}{2}q_1^4p_1^2 - 2q_1q_2^3p_1p_2 + \left(3q_1^2q_2^2 + \frac{1}{2}q_2^4\right)p_2^2 + \frac{1}{4}q_1^4q_2^4 + \frac{1}{4}q_1^2q_2^6 + \frac{1}{16}q_2^8 \end{cases} \tag{27}$$

These three cases have a polynomial first integral which is genuinely quartic in the momenta. Here, we mean by "genuinely quartic" that the first integral cannot be expressed by any product of first integrals which are cubic or lower orders in the momenta. Note that two of the above three potentials are of degree three and the other is of degree four. Hietarinta [5] showed, by a direct computation, the non-existence of additional integrable cases in the range that the potential is of degree five or less ($k \leq 5$) and the first integral of order four or less in the momenta ($N \leq 4$).

3.2 Our previous result

We can make an infinite number of different-looking integrable potentials from a given integrable potential by rotating the coordinate system. Such potentials that are related to each other through rotations of the coordinate system should be categorized into the same family. In order to avoid this problem, we assume that we can rotate the coordinate system to eliminate the term of $q_1^{k-1}q_2$, which allows us to set $\alpha_1 = 0$ in the potential (20), i.e.,

$$V = \alpha_0q_1^k + \alpha_2q_1^{k-2}q_2^2 + \cdots + \alpha_kq_2^k. \tag{28}$$

Check that the integrable potentials in the previous section are all in the form of (28). For example, a rotation of coordinate system by an angle of the degree φ,

$$q_1 \to q_1\cos\varphi - q_2\sin\varphi, \quad q_2 \to q_1\sin\varphi + q_2\cos\varphi, \tag{29}$$

transforms the integrable potential in (25),

$$V = q_1^3 + \frac{3}{16}q_1q_2^2, \tag{30}$$

into a family of potentials of the form

$$\begin{aligned} V = \frac{1}{16}\big[&(16\cos^3\varphi + 3\cos\varphi\sin^2\varphi)q_1^3 - (42\cos^2\varphi\sin\varphi + 3\sin^3\varphi)q_1^2q_2 \\ &+ (3\cos^3\varphi + 42\cos\varphi\sin^2\varphi)q_1q_2^2 - (16\sin^3\varphi + 3\cos^2\varphi\sin\varphi)q_2^3\big], \end{aligned} \tag{31}$$

from which we obtain an infinite number of integrable potentials, varying the value of φ. If the term of $q_1^3 q_2$ is assumed to vanish, we have only to handle the finite number of potentials, which are explicitly given by

$$V = q_1^3 + \frac{3}{16} q_1 q_2^2, \quad V = q_1^3 + \frac{45}{2} q_1 q_2^2 \pm \frac{17\sqrt{14}\,\mathrm{i}}{2} q_2^3 \tag{32}$$

In [17], we solved simultaneous algebraic equations obtained from PDEs (19) to investigate the existence of polynomial first integrals up to quartic in the momenta ($1 \leq N \leq 4$) for potentials of the form (28). As a result, we proved the following theorem.

Theorem 1 ([17]) *There exists no polynomial first integral that is cubic or quartic in the momenta for the potential* (28) *of degree* $k \geq 5$.

In the next section, we introduce a new method for choosing candidates of the solutions to the simultaneous algebraic equations before solving them, which saves the labor of the computation.

4 An improvement of the method

We employ the following procedure to search for integrable potentials.

Step 1: With the help of Ziglin's fundamental lemma [24], we obtain necessary conditions for the existence of polynomial first integrals. We call the potentials satisfying the conditions *integrable candidates*.

Step 2: For each integrable candidate, we solve the simultaneous algebraic equations obtained from the PDEs (19) to examine the existence of a polynomial first integral.

4.1 Step 1: determine integrable candidates

Here, we deal with the case for $\alpha_0 \neq 0$ in the potential (28). After a proper scaling, the potential is transformed into the form of

$$V = q_1^k + \alpha_2 q_1^{k-2} q_2^2 + \cdots + \alpha_k q_2^k. \tag{33}$$

First, we linearize the equations of motion around a straight-line solution to derive the variational equations. The equations of motion for the potential (33) are given by

$$\frac{d}{dt}\begin{pmatrix} q_1 \\ q_2 \end{pmatrix} = \begin{pmatrix} p_1 \\ p_2 \end{pmatrix}, \quad \frac{d}{dt}\begin{pmatrix} p_1 \\ p_2 \end{pmatrix} = -\begin{pmatrix} kq_1^{k-1} + (k-2)\alpha_2 q_1^{k-3} q_2^2 + \cdots + \alpha_{k-1} q_2^{k-1} \\ 2\alpha_2 q_1^{k-2} q_2 + 3\alpha_3 q_1^{k-3} q_2^2 + \cdots + k\alpha_k q_2^{k-1} \end{pmatrix}, \tag{34}$$

which have a straight-line solution, $q_2 = p_2 = 0$. If we linearize the equations of motion around the straight-line solution, then we obtain the variational equations,

$$\frac{d}{dt}\begin{pmatrix} \xi_1 \\ \xi_2 \end{pmatrix} = \begin{pmatrix} \eta_1 \\ \eta_2 \end{pmatrix}, \quad \frac{d}{dt}\begin{pmatrix} \eta_1 \\ \eta_2 \end{pmatrix} = -q_1^{k-2}\begin{pmatrix} k(k-1)\xi_1 \\ 2\alpha_2 \xi_2 \end{pmatrix}, \tag{35}$$

where ξ_i, η_i are variations in the directions of q_i, p_i, respectively. The second component of (35),

$$\frac{d\xi_2}{dt} = \eta_2, \quad \frac{d\eta_2}{dt} = -2\alpha_2 q_1^{k-2}\xi_2, \tag{36a}$$

describe the variation normal to the straight-line solution. Here, $q_1 = q_1(t)$ satisfies the equations (34) evaluated on the straight-line solution $q_2 = p_2 = 0$,

$$\frac{dq_1}{dt} = p_1, \quad \frac{dp_1}{dt} = -kq_1^{k-1}. \tag{36b}$$

We call the equations (36) the *normal variational equations* (NVE).

Suppose that the equations of motion (34) have a polynomial first integral which is independent of the Hamiltonian,

$$\Phi(q_1, q_2, p_1, p_2) = \text{constant}. \tag{37}$$

Then, Ziglin's fundamental lemma in [24] guarantees the existence of a polynomial first integral for the NVE (36) (see also [7, 22]),

$$I_l(q_1, p_1, \xi_2, \eta_2) = \text{constant}, \tag{38}$$

and we can construct it as

$$I_l = D^l\Phi\big|_{q_2=p_2=\xi_1=\eta_1=0}; \quad D\Phi := \xi_1\frac{\partial\Phi}{\partial q_1} + \xi_2\frac{\partial\Phi}{\partial q_2} + \eta_1\frac{\partial\Phi}{\partial p_1} + \eta_2\frac{\partial\Phi}{\partial p_2}. \tag{39}$$

Here, l is the smallest positive integer for which I_l does not vanish identically.

We put a polynomial first integral in the form

$$\Phi = (q_2p_1 - q_1p_2)^d \sum_{m=0}^{N-d} a_{N-d,m}p_1^{N-d-m}p_2^m + \sum_{n=1}^{[N/2]}\sum_{m=0}^{N-2n} A^{N-2n,m}(q_1, q_2)p_1^{N-2n-m}p_2^m, \tag{40a}$$

where

$$A^{N-2n,m}(q_1, q_2) = \sum_{j=0}^{nk+d} a_j^{N-2n,m} q_1^{nk+d-j}q_2^j \tag{40b}$$

with constants $a_j^{N-2n,m}$ and parameters (N, d) $(d = N, N-1, \ldots, 0)$. By a straightforward calculation according to (39), we obtain

$$\begin{aligned} I_l &= \left(\xi_1\frac{\partial}{\partial q_1} + \xi_2\frac{\partial}{\partial q_2} + \eta_1\frac{\partial}{\partial p_1} + \eta_2\frac{\partial}{\partial p_2}\right)^l \Phi\Big|_{q_2=p_2=\xi_1=\eta_1=0} = \left(\xi_2\frac{\partial}{\partial q_2} + \eta_2\frac{\partial}{\partial p_2}\right)^l \Phi\Big|_{q_2=p_2=0} \\ &= \sum_{l_2=0}^{l}\binom{l}{l_2}\frac{\partial^l\Phi}{\partial q_2^{l-l_2}\partial p_2^{l_2}}\bigg|_{q_2=p_2=0} \xi_2^{l-l_2}\eta_2^{l_2} \\ &= l!\sum_{l_2=0}^{l}\left[\binom{d}{l-l_2}a_{N-d,l-d}(-q_1)^{l_2-l+d}p_1^{N-l_2} + \sum_{n=1}^{[N/2]} a_{l-l_2}^{N-2n,l_2}q_1^{nk+d-l+l_2}p_1^{N-2n-l_2}\right]\xi_2^{l-l_2}\eta_2^{l_2}. \end{aligned} \tag{41}$$

Here, $a_{N-d,l-d} = 0$ for $l < d$ and $a_{l-l_2}^{N-2n,l_2} = 0$ for $N - 2n < l_2$. The condition for $I_l(q_1, p_1, \xi_2, \eta_2)$ to be a first integral of the NVE (36) is that the following equation becomes an identity for $(q_1, p_1, \xi_2, \eta_2)$.

$$\begin{aligned}\frac{dI_l}{dt} &= \frac{\partial I_l}{\partial q_1}\frac{dq_1}{dt} + \frac{\partial I_l}{\partial p_1}\frac{dp_1}{dt} + \frac{\partial I_l}{\partial \xi_2}\frac{d\xi_2}{dt} + \frac{\partial I_l}{\partial \eta_2}\frac{d\eta_2}{dt} \\ &= p_1\frac{\partial I_l}{\partial q_1} - kq_1^{k-1}\frac{\partial I_l}{\partial p_1} + \eta_2\frac{\partial I_l}{\partial \xi_2} - 2\alpha_2 q_1^{k-2}\xi_2\frac{\partial I_l}{\partial \eta_2} = 0, \end{aligned} \tag{42}$$

which is computed to be

$$\begin{aligned}\frac{1}{l!}\frac{dI_l}{dt} &= \sum_{l_2=0}^{l}(-1)^{2k+d-l+l_2-1}\left\{k(N-l_2)\binom{d}{l-l_2} - 2(l_2+1)\binom{d}{l-l_2-1}\alpha_2\right\}a_{N-d,l-d}q_1^{k+d-l+l_2-1}\xi_2^{l-l_2}p_1^{N-1-l_2}\eta_2^{l_2} \\ &+ \sum_{l_2=0}^{l}\left\{(k+d-l+l_2)a_{l-l_2}^{N-2,l_2} + (l-l_2+1)a_{l-l_2+1}^{N-2,l_2-1}\right\}q_1^{k+d-l+l_2-1}\xi_2^{l-l_2}p_1^{N-1-l_2}\eta_2^{l_2} \\ &+ \sum_{l_2=0}^{l}\left[\sum_{n=1}^{[N/2]-1}\left(\{(n+1)k+d-l+l_2\}a_{l-l_2}^{N-2n-2,l_2} + (l-l_2+1)a_{l-l_2+1}^{N-2n-2,l_2-1}\right)\right. \\ &\left. - \sum_{n=1}^{[N/2]}\left\{k(N-2n-l_2)a_{l-l_2}^{N-2n,l_2} + 2\alpha_2(l_2+1)a_{l-l_2-1}^{N-2n,l_2+1}\right\}\right]q_1^{(n+1)k+d-l+l_2-1}\xi_2^{l-l_2}p_1^{N-2n-l_2-1}\eta_2^{l_2} = 0. \end{aligned} \tag{43}$$

The identity (43) determines the values of α_2 and $a_{N-d,m}$ which are consistent with the existence of a polynomial first integral of the form (40). The specific procedure is as follows.

1. Give specific values to (N, d) in (40),
2. solve the identity (43),
3. and we obtain such values of α_2 that I_l is a first integral of the NVE (36).

This procedure starts at $l = 1$ and stops at $l = N$. The potentials with α_2 obtained by the procedure are called integrable candidates. Let us take the case for $N = 4$, $d = 0$ as an example. The first integral is of the form

$$\begin{aligned}\Phi &= a_{4,0}p_1^4 + a_{4,1}p_1^3p_2 + a_{4,2}p_1^2p_2^2 + a_{4,3}p_1p_2^3 + a_{4,4}p_2^4 \\ &+ \sum_{j=0}^{k}a_j^{2,0}q_1^{k-j}q_2^jp_1^2 + \sum_{j=0}^{k}a_j^{2,1}q_1^{k-j}q_2^jp_1p_2 + \sum_{j=0}^{k}a_j^{2,2}q_1^{k-j}q_2^jp_2^2 + \sum_{j=0}^{2k}a_j^{0,0}q_1^{2k-j}q_2^j. \end{aligned} \tag{44}$$

Note that the three special integrable cases, (25), (26), (27), have a polynomial first integral of this form, so it is natural to expect that a new integrable potential, if any, would have a first integral of the form (44). The above procedure provides us with the values of α_2 and the corresponding values of the coefficients $a_{4,j}$ as follows (see Appendix A for other types of first integrals).

Table 1: The integrable candidates with a polynomial first integral (44).

l	The coefficients of the leading terms of Φ	The coefficient of V
1	$a_{4,0}=0,\ a_{4,1}\neq 0$	$\alpha_2=\dfrac{k(k-1)}{2},\ \dfrac{3k(2k-1)}{2}$
2	$a_{4,0}=0,\ a_{4,1}=0,\ a_{4,2}\neq 0$	$\alpha_2=0,\ \dfrac{k(k-1)}{2}$
3	$a_{4,0}=0,\ a_{4,1}=0,\ a_{4,2}=0,\ a_{4,3}\neq 0$	$\alpha_2=\dfrac{1}{2},\ 5\ (k=3)$
4	$a_{4,0}=0,\ a_{4,1}=0,\ a_{4,2}=0,\ a_{4,3}=0,\ a_{4,4}\neq 0$	$\alpha_2=0,\quad \alpha_2=\dfrac{3}{16}\ (k=3),\quad \alpha_2=\dfrac{3}{4}\ (k=4)$

Here, the degree of the potential is assumed to be greater than two, i.e., $k\geq 3$ (the potential (33) is always integrable when $k=1,2$). Table 1 shows that if we consider polynomial first integrals of the form (44), then we have only to check whether or not the following pairs of (V,Φ) give integrable systems.

- For general k ($k\geq 3$):

$$\begin{cases} V=q_1^k+\alpha_3 q_1^{k-3}q_2^3+\cdots+\alpha_k q_2^k \\ \Phi=p_1^2p_2^2+a_{4,3}p_1p_2^3+a_{4,4}p_2^4+\ldots,\ \text{or}\ \Phi=p_2^4+\ldots \end{cases} \tag{45}$$

$$\begin{cases} V=q_1^k+\dfrac{k(k-1)}{2}q_1^{k-2}q_2^2+\cdots+\alpha_k q_2^k \\ \Phi=p_1^3p_2+a_{4,2}p_1^2p_2^2+a_{4,3}p_1p_2^3+a_{4,4}p_2^4+\ldots,\ \text{or}\ \Phi=p_1^2p_2^2+a_{4,3}p_1p_2^3+a_{4,4}p_2^4+\ldots \end{cases} \tag{46}$$

$$\begin{cases} V=q_1^k+\dfrac{3k(2k-1)}{2}q_1^{k-2}q_2^2+\cdots+\alpha_k q_2^k \\ \Phi=p_1^3p_2+a_{4,2}p_1^2p_2^2+a_{4,3}p_1p_2^3+a_{4,4}p_2^4+\ldots \end{cases} \tag{47}$$

- When $k=3,4$, the following candidates are added to the above.

$$\begin{cases} V=q_1^3+\dfrac{1}{2}q_1q_2^2+\alpha_3 q_2^3 \\ \Phi=p_1p_2^3+a_{4,4}p_2^4+\ldots \end{cases} \tag{48}$$

$$\begin{cases} V=q_1^3+5q_1q_2^2+\alpha_3 q_2^3 \\ \Phi=p_1p_2^3+a_{4,4}p_2^4+\ldots \end{cases} \tag{49}$$

$$\begin{cases} V=q_1^3+\dfrac{3}{16}q_1q_2^2+\alpha_3 q_2^3 \\ \Phi=p_2^4+\ldots \end{cases} \tag{50}$$

$$\begin{cases} V=q_1^4+\dfrac{3}{4}q_1^2q_2^2+\alpha_3 q_1q_2^3+\alpha_4 q_2^4 \\ \Phi=p_2^4+\ldots \end{cases} \tag{51}$$

4.2 Step 2: check the integrability

We solve simultaneous algebraic equations obtained from the PDEs (19) for each integrable candidate. From the candidate (45), we obtain the Cartesian-separable case,

$$\begin{cases} V = q_1^k + \alpha_k q_2^k \\ \Phi = (p_1^2 + 2q_1^k)(p_2^2 + 2\alpha_k q_2^k) + a_{4,4}(p_2^2 + 2\alpha_k q_2^k)^2, \text{ or } \Phi = (p_2^2 + 2\alpha_k q_2^k)^2 \end{cases} \tag{52}$$

The candidate (46) yields

$$V = q_1^k + \frac{k(k-1)}{2} q_1^{k-2} q_2^2 + \alpha_3 q_1^{k-3} q_2^3 + \sum_{j=4}^{k} \alpha_j(k, \alpha_3) q_1^{k-j} q_2^j, \tag{53}$$

where $\alpha_j(k, \alpha_3)$ are polynomials of α_3 with rational functions of k as the coefficients. We find that this case reduces to a Cartesian-separable case, given by

$$\begin{cases} V = \dfrac{Q_1^k}{\cos^{k-2}\varphi} + \dfrac{Q_2^k}{\sin^{k-2}\varphi} \\ \Phi = \dfrac{1}{\sin^2 2\varphi}\left(P_2^2 + \dfrac{2Q_2^k}{\sin^{k-2}\varphi}\right)\left[\left(\dfrac{1}{\tan 2\varphi} - a_{4,2}\right)\left(P_1^2 + \dfrac{2Q_1^k}{\cos^{k-2}\varphi}\right) - 2\cos 2\varphi\left(\dfrac{2}{\tan 4\varphi} - a_{4,2}\right)H\right], \\ \text{or } \Phi = \dfrac{1}{4\cos^2\varphi \sin^2\varphi}\left(P_2^2 + \dfrac{2Q_2^k}{\sin^{k-2}\varphi}\right)^2 - \dfrac{1}{\cos^2\varphi}\left(P_2^2 + \dfrac{2Q_2^k}{\sin^{k-2}\varphi}\right)H \end{cases} \tag{54}$$

by the rotation

$$Q_1 = q_1 \cos\varphi - q_2 \sin\varphi, \quad Q_2 = q_1 \sin\varphi + q_2 \cos\varphi, \quad \tan 2\varphi = \frac{k(k-1)(k-2)}{3\alpha_3}. \tag{55}$$

The candidate (47) reduces to

$$\begin{cases} V = q_1^k + \dfrac{3k(2k-1)}{2} q_1^{k-2} q_2^2 + \alpha_3 q_1^{k-3} q_2^3 + \sum_{j=4}^{k} \alpha_j(k, \alpha_3) q_1^{k-j} q_2^j \\ \Phi = p_1^3 p_2 + a_{4,2}(k, \alpha_3) p_1^2 p_2^2 + a_{4,3}(k, \alpha_3) p_1 p_2^3 + a_{4,4}(k, \alpha_3) p_2^4 + \ldots \end{cases} \tag{56}$$

Here, α_3 must satisfy $2k-5$ algebraic equations, two of which are given by

$$-\frac{2(k+2)(5k-2)(7k-6)G_1(k)\alpha_3^4}{(k-2)^3(k-1)k^2(2k-1)^3(3k-2)^3 R(k)S(k)^2} - \frac{3(k+2)(5k-2)(7k-6)G_2(k)\alpha_3^2}{4(k-2)(k-1)(2k-1)(3k-2)R(k)S(k)^2} + \frac{9(k-2)k^2(k+2)(2k-1)(5k-2)G_3(k)}{4(k-1)S(k)^2} = 0 \tag{57}$$

and

$$-\frac{(k-3)(k+2)(5k-2)(7k-6)G_4(k)\alpha_3^5}{5(k-2)^4(k-1)k^3(2k-1)^4(3k-2)^4 R(k)S(k)^2} - \frac{3(k-3)(k+2)(5k-2)(7k-6)G_5(k)\alpha_3^3}{20(k-2)^2(k-1)k(2k-1)^2(3k-2)^2 R(k)S(k)} + \frac{9(k-3)k(k+2)(5k-2)G_6(k)\alpha_3}{20(k-1)(3k-2)R(k)S(k)^2} = 0, \tag{58}$$

where

$$
\begin{aligned}
G_1(k) &= 10736550k^{11} - 120201105k^{10} + 563283562k^9 - 1500811081k^8 + 2565200757k^7 \\
&\quad - 2978361002k^6 + 2408313485k^5 - 1360307178k^4 + 527295832k^3 - 133944304k^2 \\
&\quad + 20130192k - 1361952, \\
G_2(k) &= 7446900k^9 - 86588015k^8 + 371783811k^7 - 843129587k^6 + 1151765545k^5 \\
&\quad - 998755638k^4 + 553816792k^3 - 190561760k^2 + 37193808k - 3170144, \\
G_3(k) &= 16870k^7 + 118529k^6 - 810861k^5 + 1706012k^4 - 1727456k^3 + 932160k^2 \\
&\quad - 260400k + 29952, \\
G_4(k) &= 538285500k^{12} - 6761687100k^{11} + 35472298955k^{10} - 106294583086k^9 \\
&\quad + 206176050353k^8 - 275416174516k^7 + 261364852406k^6 - 178232080840k^5 \\
&\quad + 86929567784k^4 - 29645084416k^3 + 6725558432k^2 - 913712256k + 56393856, \\
G_5(k) &= 186064500k^{10} - 2562547775k^9 + 12720106145k^8 - 33457433369k^7 \\
&\quad + 53780522743k^6 - 56288554120k^5 + 39260441572k^4 - 18143124368k^3 \\
&\quad + 5346987920k^2 - 912699392k + 68988096, \\
G_6(k) &= 40055750k^{10} + 454376975k^9 - 4446138980k^8 + 15180036291k^7 \\
&\quad - 28351948208k^6 + 32872864764k^5 - 24787677856k^4 - 3817158400k^2 \\
&\quad + 687806528k + 12223132176k^3 - 54723072.
\end{aligned}
$$

We can make use of the quantity called the *resultant* to examine the existence of common solutions of the two algebraic equations (57) and (58).

Let us here digress for a moment to give a brief account of the resultant before investigating (57), (58). The resultant is an algebraic tool for eliminating a variable between two algebraic equations and gives the condition for the two algebraic equations to have a common solution. Let us consider the following two polynomials of x.

$$f(x) = a_n x^n + a_{n-1}x^{n-1} + \cdots + a_1 x + a_0, \quad a_n \neq 0, \tag{59}$$

$$g(x) = b_m x^m + b_{m-1}x^{m-1} + \cdots + b_1 x + b_0, \quad b_m \neq 0. \tag{60}$$

The following determinant of order $m + n$ is called the resultant of $f(x)$ and $g(x)$.

$$
R(f,g) = \begin{vmatrix}
a_n & a_{n-1} & \cdots & a_0 & 0 & \cdots & & 0 \\
0 & a_n & a_{n-1} & \cdots & a_0 & 0 & \cdots & 0 \\
 & & \ddots & & & \ddots & & \\
0 & \cdots & 0 & a_n & a_{n-1} & \cdots & & a_0 \\
b_m & b_{m-1} & \cdots & b_0 & 0 & \cdots & & 0 \\
0 & b_m & b_{m-1} & \cdots & b_0 & 0 & \cdots & 0 \\
 & & \ddots & & & \ddots & & \\
0 & \cdots & 0 & b_m & b_{m-1} & \cdots & & b_0
\end{vmatrix}
\begin{matrix}
\left.\vphantom{\begin{matrix}a\\a\\a\\a\end{matrix}}\right\} m \text{ rows} \\
\left.\vphantom{\begin{matrix}a\\a\\a\\a\end{matrix}}\right\} n \text{ rows}
\end{matrix}
\tag{61}
$$

Then, the following theorem holds. A proof is given in Appendix B.

Theorem 2 (e.g., [21]) *The two polynomials $f(x)$ and $g(x)$ has at least one common root if and only if the resultant $R(f,g)$ equals to zero.*

We are now back to the algebraic equations (57), (58). The resultant of them is computed to be

$$\frac{2893401(k-4)^2(k-3)^4(k+2)^9(2k-3)^4(3k-4)^4(3k-1)^4(5k-6)^2(5k-2)^{29}(7k-6)^4}{4096(k-2)^{11}(k-1)^9k^2(2k-1)^{11}(3k-2)^{16}R(k)^6S(k)^{10}}$$
$$\times(16870k^7+118529k^6-810861k^5+1706012k^4-1727456k^3+932160k^2-260400k+29952)$$
$$\times(450000k^9-5594600k^8+30037885k^7-91304549k^6+173025983k^5-211881739k^4$$
$$+167598204k^3-82567904k^2+23021920k-2787216)^2. \tag{62}$$

This cannot vanish for $k \geq 5$. Then, it is concluded from Theorem 2 that the algebraic equations (57) and (58) have no common solution. Therefore, the candidate $\alpha_2 = 3k(2k-1)/2$ for $k \geq 5$ is not integrable. When $k = 3, 4$, as deduced from the fact that the resultant (62) vanishes, the two algebraic equations have common solutions, which lead to integrable systems. The additional candidates, (48)–(51), also yield integrable systems. See Appendix A for details.

5 A complete list of integrable potentials

So far, we have set $\alpha_1 = 0$, which is based on the assumption that we can rotate the coordinate system so that the term of $q_1^{k-1}q_2$ in the potential will vanish. However, this is not always the case. We cannot eliminate the term $q_1^{k-1}q_2$ in the potential of the form

$$V = (q_1 + \mathrm{i}q_2)^{k-r}(q_1 - \mathrm{i}q_2)^r \tag{63}$$

by any rotation of the coordinate system. We searched for integrable cases for potentials of the form (63) and obtained the following ones.

$$\begin{cases} V = (q_1 \pm \mathrm{i}q_2)^k \\ \Phi = p_1 \pm \mathrm{i}p_2 \end{cases} \tag{64}$$

$$\begin{cases} V = (q_1 \pm \mathrm{i}q_2)^{k-1}(q_1 \mp \mathrm{i}q_2) \\ \Phi = (p_1 \pm \mathrm{i}p_2)^2 + \dfrac{4}{k}(q_1 \pm \mathrm{i}q_2)^k \end{cases} \tag{65}$$

$$\begin{cases} V = (q_1 \pm \mathrm{i}q_2)^k \\ \Phi = (p_1 \pm \mathrm{i}p_2)(q_2p_1 - q_1p_2) \mp \dfrac{k\,\mathrm{i}}{k+1}(q_1 \pm \mathrm{i}q_2)^{k+1} \end{cases} \tag{66}$$

$$\begin{cases} V = (q_1 \pm \mathrm{i}q_2)^5(q_1 \mp \mathrm{i}q_2)^2 \\ \Phi = (p_1 \pm \mathrm{i}p_2)^3(q_2p_1 - q_1p_2) \\ \quad \mp \dfrac{\mathrm{i}}{8}(q_1 \pm \mathrm{i}q_2)^6(3q_1^2 \pm 6\mathrm{i}q_1q_2 + 13q_2^2)p_1^2 - \dfrac{1}{4}(q_1 \pm \mathrm{i}q_2)^6(3q_1 \mp \mathrm{i}q_2)(q_1 \mp \mathrm{i}q_2)p_1p_2 \\ \quad \mp \dfrac{\mathrm{i}}{8}(q_1 \pm \mathrm{i}q_2)^6(13q_1^2 \mp 6\mathrm{i}q_1q_2 + 3q_2^2)p_2^2 \mp \dfrac{\mathrm{i}}{2}(q_1 \pm \mathrm{i}q_2)^{12}(q_1 \mp \mathrm{i}q_2)^3 \end{cases} \tag{67}$$

The first three, (64), (65), (66), are included in the general solutions of the PDEs (19) for first integrals linear or quadratic in the momenta [6]. The last one, (67), is a new integrable case, which admits a polynomial first integral genuinely quartic in the momenta. Adding these cases to the list in [17], we now obtain a complete list of integrable two-dimensional homogeneous polynomial potentials with a polynomial first integral up to quartic in the momenta.

Theorem 3 *If a homogeneous polynomial potential admits an additional polynomial first integral which is up to quartic in the momenta, then the potential must be one of the following or their rotational equivalents.*

- (21), (22), (64) *with a polynomial first integral linear in the momenta*:

$$V = (q_1^2 + q_2^2)^{k/2}, \qquad V = q_1^k, \qquad V = (q_1 \pm \mathrm{i} q_2)^k.$$

- (23), (24), (65), (66) *with a polynomial first integral quadratic in the momenta*:

$$V = \frac{1}{r}\left[\left(\frac{r+q_1}{2}\right)^{k+1} + (-1)^k\left(\frac{r-q_1}{2}\right)^{k+1}\right], \qquad V = q_1^k + \alpha_k q_2^k,$$
$$V = (q_1 \pm \mathrm{i} q_2)^{k-1}(q_1 \mp \mathrm{i} q_2), \qquad V = (q_1 \pm \mathrm{i} q_2)^k.$$

- *No potential with a polynomial first integral cubic in the momenta.*
- (25), (26), (27), (67) *with a polynomial first integral quartic in the momenta*:

$$V = q_1^3 + \frac{3}{16} q_1 q_2^2, \qquad V = q_1^3 + \frac{1}{2} q_1 q_2^2 \pm \frac{\sqrt{3}\,\mathrm{i}}{18} q_2^3, \qquad V = q_1^4 + \frac{3}{4} q_1^2 q_2^2 + \frac{1}{8} q_2^4,$$
$$V = (q_1 \pm \mathrm{i} q_2)^5 (q_1 \mp \mathrm{i} q_2)^2.$$

6 Summary

We introduced a two-step procedure to obtain integrable homogeneous polynomial potentials with a polynomial first integral. In the first step, we employed Ziglin's fundamental lemma to derive necessary conditions for integrability, which determined integrable candidates. After that, in the second step, we examined their integrability by solving the simultaneous algebraic equations to be satisfied. In this paper, we concentrated on a polynomial first integral of the particular form (44). A full version of the proof of Theorem 3 (including Theorem 1) is available in [18].

A The integrable candidates

A.1 The integrable candidates with a linear integral

Table 2 shows the integrable candidates with a linear integral of the form

$$\Phi = \begin{cases} a_{0,0}(q_2p_1 - q_1p_2) & \text{(Case 1)} \\ a_{1,0}p_1 + a_{1,1}p_2 & \text{(Case 2)} \end{cases}$$

Table 2: The integrable candidates with a linear integral.

Case	The coefficients of the leading terms of Φ	The coefficient of V (integrable candidates)
1	$a_{0,0} \neq 0$	$\alpha_2 = \dfrac{k}{2}$
2	$a_{1,0}$ = arbitrary, $a_{1,1} \neq 0$	$\alpha_2 = 0$

A.2 The integrable candidates with a quadratic integral

Table 3 shows the integrable candidates with a quadratic integral of the form

$$\Phi = \begin{cases} a_{0,0}(q_2p_1 - q_1p_2)^2 + \ldots & \text{(Case 1)} \\ (a_{1,0}p_1 + a_{1,1}p_2)(q_2p_1 - q_1p_2) + \ldots & \text{(Case 2)} \\ a_{2,0}p_1^2 + a_{2,1}p_1p_2 + a_{2,2}p_2^2 + \ldots & \text{(Case 3)} \end{cases}$$

Table 3: The integrable candidates with a quadratic integral.

Case	The coefficients of the leading terms of Φ	The coefficient of V (integrable candidates)
1	$a_{0,0} \neq 0$	$\alpha_2 = \dfrac{k}{2}$
2	$a_{1,0} \neq 0$	$\alpha_2 = \dfrac{k(k+2)}{2}$
	$a_{1,0} = 0, a_{1,1} \neq 0$	$\alpha_2 = \dfrac{k-1}{4}$
3	$a_{2,0} = 0, a_{2,1} \neq 0$	$\alpha_2 = \dfrac{k(k-1)}{2}$
	$a_{2,0} = 0, a_{2,1} = 0, a_{2,2} \neq 0$	$\alpha_2 = 0$

A.3 The integrable candidates with a cubic integral

Table 4 shows the integrable candidates with a cubic integral of the form

$$\Phi = \begin{cases} a_{0,0}(q_2p_1 - q_1p_2)^3 + \dots & \text{(Case 1)} \\ (a_{1,0}p_1 + a_{1,1}p_2)(q_2p_1 - q_1p_2)^2 + \dots & \text{(Case 2)} \\ (a_{2,0}p_1^2 + a_{2,1}p_1p_2 + a_{2,2}p_2^2)(q_2p_1 - q_1p_2) + \dots & \text{(Case 3)} \\ a_{3,0}p_1^3 + a_{3,1}p_1^2p_2 + a_{3,2}p_1p_2^2 + a_{3,3}p_2^3 + \dots & \text{(Case 4)} \end{cases}$$

Table 4: The integrable candidates with a cubic integral.

Case	The coefficients of the leading terms of Φ	The coefficient of V (integrable candidates)
1	$a_{0,0} \neq 0$	$\alpha_2 = \dfrac{k}{2}$
2	—	—
3	$a_{2,0} \neq 0$	$\alpha_2 = \dfrac{k}{2}, \dfrac{3k(k+1)}{2}$
4	$a_{3,0}$ = arbitrary, $a_{3,1} \neq 0$	$\alpha_2 = \mathbf{0}, \dfrac{k(3k-2)}{2}$
	$a_{3,0}$ = arbitrary, $a_{3,1} = 0$, $a_{3,2} = 0$, $a_{3,3} \neq 0$	$\alpha_2 = \mathbf{0}, \quad \alpha_2 = \dfrac{1}{2}$ $(k = 3)$

A.4 The integrable candidates with a quartic integral

Table 5 shows the integrable candidates with a cubic integral of the form

$$\Phi = \begin{cases} a_{0,0}(q_2p_1 - q_1p_2)^4 + \dots & \text{(Case 1)} \\ (a_{1,0}p_1 + a_{1,1}p_2)(q_2p_1 - q_1p_2)^3 + \dots & \text{(Case 2)} \\ (a_{2,0}p_1^2 + a_{2,1}p_1p_2 + a_{2,2}p_2^2)(q_2p_1 - q_1p_2)^2 + \dots & \text{(Case 3)} \\ (a_{3,0}p_1^3 + a_{3,1}p_1^2p_2 + a_{3,2}p_1p_2^2 + a_{3,3}p_2^3)(q_2p_1 - q_1p_2) + \dots & \text{(Case 4)} \\ a_{4,0}p_1^4 + a_{4,1}p_1^3p_2 + a_{4,2}p_1^2p_2^2 + a_{4,3}p_1p_2^3 + a_{4,4}p_2^4 + \dots & \text{(Case 5)} \end{cases}$$

Table 5: The integrable candidates with a quartic integral.

Case	The coefficients of the leading terms of Φ	The coefficient of V (integrable candidates)
1	$a_{0,0} \neq 0$	$\alpha_2 = \dfrac{k}{2}$
2	—	—
3	$a_{2,0} \neq 0$	$\alpha_2 = \dfrac{k(k+2)}{2}, \dfrac{k}{2}$
	$a_{2,0} = 0, a_{2,1} = 0, a_{2,2} \neq 0$	$\alpha_2 = \dfrac{k-1}{4}$
4	$a_{3,0} \neq 0$	$\alpha_2 = \dfrac{k(k+2)}{2}, k(3k+2)$
	$a_{3,0} = 0, a_{3,1} \neq 0$	$\alpha_2 = \dfrac{k-1}{4}, \dfrac{(k+1)(2k-1)}{4}$
	$a_{3,0} = 0, a_{3,1} = 0, a_{3,2} = 0, a_{3,3} \neq 0$	$\alpha_2 = \dfrac{3}{16}, \dfrac{15}{16}$ $(k = 3)$
5	$a_{4,0} = 0, a_{4,1} \neq 0$	$\alpha_2 = \dfrac{k(k-1)}{2}, \dfrac{3k(2k-1)}{2}$
	$a_{4,0} = 0, a_{4,1} = 0, a_{4,2} \neq 0$	$\alpha_2 = 0, \dfrac{k(k-1)}{2}$
	$a_{4,0} = 0, a_{4,1} = 0, a_{4,2} = 0, a_{4,3} \neq 0$	$\alpha_2 = \dfrac{1}{2}, 5$ $(k = 3)$
	$a_{4,0} = 0, a_{4,1} = 0, a_{4,2} = 0, a_{4,3} = 0, a_{4,4} \neq 0$	$\alpha_2 = 0,$ $\alpha_2 = \dfrac{3}{16}$ $(k = 3),$ $\alpha_2 = \dfrac{3}{4}$ $(k = 4)$

A.5 The successful candidates

Of the integrable candidates listed in Tables 2–5, we find the ones in boldface to be really integrable with an additional polynomial first integral. The other candidates are proved not to admit a polynomial first integral. See [18] for details.

For general k, we obtain the separable potentials and their rotational equivalents.

- The polar-separable case $\alpha_2 = k/2$

$$V = (q_1^2 + q_2^2)^{k/2}, \quad k = \text{even} \tag{68}$$

- The parabolic separable case

  - $\alpha_2 = (k-1)/4$

$$V = \frac{1}{r}\left[\left(\frac{r+q_1}{2}\right)^{k+1} + (-1)^k\left(\frac{r-q_1}{2}\right)^{k+1}\right] \tag{69}$$

  - $\alpha_2 = k(k+2)/2$

$$V = q_1^k + \frac{k(k+2)}{2}q_1^{k-2}q_2^2 + \alpha_3 q_1^{k-3}q_2^3 + \ldots, \tag{70}$$

    which reduces to (69) by the rotation

$$q_1 \to q_1\cos\varphi - q_2\sin\varphi,\ q_2 \to q_1\sin\varphi + q_2\cos\varphi,\ \tan\varphi = \frac{k(k+1)(2k+1)}{6\alpha_3} \tag{71}$$

- The Cartesian-separable case

  - $\alpha_2 = 0$

$$V = q_1^k + \alpha_k q_2^k \tag{72}$$

  - $\alpha_2 = k(k-1)/2$

$$V = q_1^k + \frac{k(k-1)}{2}q_1^{k-2}q_2^2 + \alpha_3 q_1^{k-3}q_2^3 + \ldots, \tag{73}$$

    which reduces to (72) by the rotation

$$q_1 \to q_1\cos\varphi - q_2\sin\varphi,\ q_2 \to q_1\sin\varphi + q_2\cos\varphi,\ \tan 2\varphi = \frac{k(k-1)(k-2)}{3\alpha_3} \tag{74}$$

For the extra candidates for $k = 3, 4$, we obtain some integrable systems. The candidates $\alpha_2 = 1/2, 5, 3/16, 3/4$ in Table 5, which correspond to (48), (49), (50), (51), respectively, yield integrable cases as follows:

$$\alpha_2 = \frac{1}{2} \to (26), \quad \alpha_2 = \frac{3}{16} \to (25), \quad \alpha_2 = \frac{3}{4} \to (27),$$

and

$$\alpha_2 = 5 \to \begin{cases} V = q_1^3 + 5q_1q_2^2 \pm \dfrac{22\sqrt{3}\,\mathrm{i}}{9}q_2^3 \\ \Phi = p_1p_2^3 \pm \dfrac{\sqrt{3}\,\mathrm{i}}{2}p_2^4 - 4q_2^3p_1^2 + (12q_1q_2^2 \pm 4\sqrt{3}\,\mathrm{i}\,q_2^3)p_1p_2 \\ \quad + (3q_1^2q_2 \pm 10\sqrt{3}\,\mathrm{i}\,q_1q_2^2 - 13q_2^3)p_2^2 \\ \quad + 32q_1^3q_2^3 \pm 64\sqrt{3}\,\mathrm{i}\,q_1^2q_2^4 - 128q_1q_2^5 \mp \dfrac{256\sqrt{3}\,\mathrm{i}}{9}q_2^6 \end{cases} \tag{75}$$

As mentioned at the end of Section 4, the candidate $\alpha_2 = 3k(2k-1)/2$ is found to be integrable when $k = 3, 4$ as shown below.

- The candidate $\alpha_2 = 3k(2k-1)/2$ for $k = 3$:

$$\begin{cases} V = q_1^3 + \dfrac{45}{2}q_1q_2^2 \pm \dfrac{17\sqrt{14}\,\mathrm{i}}{2}q_2^3 \\ \Phi = p_1^3p_2 \pm \dfrac{17\sqrt{14}\,\mathrm{i}}{28}p_1^2p_2^2 - \dfrac{1}{14}p_1p_2^3 \pm \dfrac{195\sqrt{14}\,\mathrm{i}}{784}p_2^4 \\ \quad + \left(\dfrac{45}{2}q_1^2q_2 \pm \dfrac{51\sqrt{14}\,\mathrm{i}}{2}q_1q_2^2 - \dfrac{3373}{28}q_2^3\right)p_1^2 \\ \quad + \left(-\dfrac{9}{2}q_1^3 \pm \dfrac{51\sqrt{14}\,\mathrm{i}}{28}q_1^2q_2 - \dfrac{129}{28}q_1q_2^2 \mp \dfrac{69\sqrt{14}\,\mathrm{i}}{392}q_2^3\right)p_1p_2 \\ \quad + \left(\pm\dfrac{17\sqrt{14}\,\mathrm{i}}{28}q_1^3 - \dfrac{3}{14}q_1^2q_2 \pm \dfrac{8775\sqrt{14}\,\mathrm{i}}{392}q_1q_2^2 - \dfrac{1665}{14}q_2^3\right)p_2^2 \\ \quad - \dfrac{27}{5}q_1^5q_2 \pm \dfrac{1683\sqrt{14}\,\mathrm{i}}{56}q_1^4q_2 - \dfrac{1325}{7}q_1^3q_2^3 \pm \dfrac{200331\sqrt{14}\,\mathrm{i}}{392}q_1^2q_2^4 \\ \quad - \dfrac{300051}{56}q_1q_2^5 \mp \dfrac{1586115\sqrt{14}\,\mathrm{i}}{1568}q_2^6 \end{cases} \tag{76}$$

$$\begin{cases} V = q_1^3 + \dfrac{45}{2}q_1q_2^2 \mp \dfrac{27\sqrt{3}\,\mathrm{i}}{2}q_2^3 \\ \Phi = p_1^3p_2 \mp \dfrac{27\sqrt{3}\,\mathrm{i}}{28}p_1^2p_2^2 - \dfrac{225}{784}p_1p_2^3 \mp \dfrac{351\sqrt{3}\,\mathrm{i}}{1568}p_2^4 \\ \quad + \left(\dfrac{45}{2}q_1^2q_2 \mp \dfrac{81\sqrt{3}\,\mathrm{i}}{2}q_1q_2^2 - \dfrac{77517}{1568}q_2^3\right)p_1^2 \\ \quad + \left(-\dfrac{9}{2}q_1^3 \mp \dfrac{81\sqrt{3}\,\mathrm{i}}{28}q_1^2q_2 - \dfrac{29025}{1568}q_1q_2^2 \pm \dfrac{6075\sqrt{3}\,\mathrm{i}}{1568}q_2^3\right)p_1p_2 \\ \quad + \left(\mp\dfrac{27\sqrt{3}\,\mathrm{i}}{28}q_1^3 - \dfrac{675}{784}q_1^2q_2 \mp \dfrac{15795\sqrt{3}\,\mathrm{i}}{784}q_1q_2^2 - \dfrac{60237}{1568}q_2^3\right)p_2^2 \\ \quad - \dfrac{27}{5}q_1^5q_2 \mp \dfrac{2673\sqrt{3}\,\mathrm{i}}{56}q_1^4q_2 - \dfrac{244917}{1568}q_1^3q_2^3 \mp \dfrac{2817585\sqrt{3}\,\mathrm{i}}{6272}q_1^2q_2^4 \\ \quad - \dfrac{5500305}{3136}q_1q_2^5 \pm \dfrac{3343923\sqrt{3}\,\mathrm{i}}{6272}q_2^6 \end{cases} \tag{77}$$

- The candidate $\alpha_2 = 3k(2k-1)/2$ for $k = 4$:

$$\begin{cases} V = q_1^4 + 42q_1^2q_2^2 \pm 28\sqrt{10}\,\mathrm{i}\,q_1q_2^3 - 48q_2^4 \\ \Phi = p_1^3p_2 \pm \dfrac{11\sqrt{10}\,\mathrm{i}}{20}p_1^2p_2^2 - \dfrac{2}{5}p_1p_2^3 \pm \dfrac{21\sqrt{10}\,\mathrm{i}}{200}p_2^4 \\ \quad + \left(28q_1^3q_2 \pm 42\sqrt{10}\,\mathrm{i}\,q_1^2q_2^2 - 192q_1q_2^3 \mp \dfrac{704\sqrt{10}\,\mathrm{i}}{25}q_2^4\right)p_1^2 \\ \quad + \left(-4q_1^4 \pm \dfrac{14\sqrt{10}\,\mathrm{i}}{5}q_1^3q_2 - 48q_1^2q_2^2 \mp \dfrac{364\sqrt{10}\,\mathrm{i}}{25}q_1q_2^3 + \dfrac{64}{5}q_2^4\right)p_1p_2 \\ \quad + \left(\pm\dfrac{2\sqrt{10}\,\mathrm{i}}{5}q_1^4 - \dfrac{8}{5}q_1^3q_2 \pm \dfrac{441\sqrt{10}\,\mathrm{i}}{25}q_1^2q_2^2 - \dfrac{644}{5}q_1q_2^3 \mp \dfrac{574\sqrt{10}\,\mathrm{i}}{25}q_2^4\right)p_2^2 \\ \quad -16q_1^7q_2 \pm \dfrac{196\sqrt{10}\,\mathrm{i}}{5}q_1^6q_2^2 - \dfrac{2448}{5}q_1^5q_2^3 \pm \dfrac{16288\sqrt{10}\,\mathrm{i}}{25}q_1^4q_2^4 - \dfrac{55424}{5}q_1^3q_2^5 \\ \quad \mp\dfrac{145152\sqrt{10}\,\mathrm{i}}{25}q_1^2q_2^6 + 13312q_1q_2^7 \pm \dfrac{28672\sqrt{10}\,\mathrm{i}}{25}q_2^8 \end{cases} \tag{78}$$

Finally, the candidate $\alpha_2 = k(k-1)/2$ yields the following integrable case when $k = 4$.

$$\begin{cases} V = q_1^4 + 6q_1^2q_2^2 + 8q_2^4 \\ \Phi = p_1^2p_2^2 + \dfrac{1}{2}p_2^4 + 16q_2^4p_1^2 + 8q_1^3q_2p_1p_2 + 4q_2^2(3q_1^2 + 4q_2^2)p_2^2 + 16q_2^2(q_1^2 + 2q_2^2)^3 \end{cases} \tag{79}$$

The classification by rotational equivalence is as follows:

$\{(25), (76)\}$, $\{(26), (75), (77)\}$, $\{(27), (78), (79)\}$.

Throughout this paper, we have taken (25), (26), (27) as the representative of each family.

B A proof of Theorem 2

Let us first prove the following lemma.

Lemma 1 (e.g., [21]) *The two polynomials $f(x)$ and $g(x)$ have a common factor if and only if there exist polynomials $h(x)$ and $k(x)$ with $\deg h < \deg g$, $\deg k < \deg f$ such that*

$$h(x)f(x) = k(x)g(x). \tag{80}$$

Proof. ($\Rightarrow$) Suppose that $f(x)$ and $g(x)$ have a common factor $\phi(x)$. Then, we can define $h(x)$ and $k(x)$ by

$$f(x) = \phi(x)k(x), \quad g(x) = \phi(x)h(x). \tag{81}$$

Therefore, the following identity holds.

$$h(x)f(x) - k(x)g(x) = h(x)\phi(x)k(x) - k(x)\phi(x)h(x) = 0. \tag{82}$$

($\Leftarrow$) Assume that there exist polynomials $h(x)$ and $k(x)$ such that (80) holds. Then, $f(x)$ must be a factor of $k(x)g(x)$. Since $\deg k < \deg f = n$, $f(x)$ cannot be a factor of $k(x)$. That is, some factor

of $f(x)$ is a factor of $g(x)$, which means $f(x)$ and $g(x)$ have a common factor. This completes the proof of Lemma 1.

Proof of Theorem 2. Let us put

$$h(x) = c_{m-1}x^{m-1} + c_{m-2}x^{m-2} + \cdots + c_1x + c_0, \tag{83}$$

$$k(x) = d_{n-1}x^{n-1} + d_{n-2}x^{n-2} + \cdots + d_1x + d_0. \tag{84}$$

Here, c_i, d_i are undetermined coefficients. Substituting (59), (60), (83), (84) in (80) and comparing the coefficients of the both sides, we obtain

$$\begin{cases} a_nc_{m-1} = b_md_{n-1} \\ a_{n-1}c_{m-1} + a_nc_{m-2} = b_{m-1}d_{n-1} + b_md_{n-2} \\ \quad\vdots \\ a_0c_1 + a_1c_0 = b_0d_1 + b_1d_0 \\ a_0c_0 = b_0d_0 \end{cases} \tag{85}$$

or

$$\begin{cases} a_nc_{m-1} + b_m(-d_{n-1}) = 0 \\ a_{n-1}c_{m-1} + a_nc_{m-2} + b_{m-1}(-d_{n-1}) + b_m(-d_{n-2}) = 0 \\ \quad\vdots \\ a_0c_1 + a_1c_0 + b_0(-d_1) + b_1(-d_0) = 0 \\ a_0c_0 + b_0(-d_0) = 0 \end{cases} \tag{86}$$

These can be regarded as simultaneous linear equations for the undetermined coefficients $(c_i, -d_i)$. The condition for the existence of non-trivial solutions, $(c_i, -d_i) \neq (0, 0)$, is that the determinant of the coefficient matrix vanishes, which is equivalent to $R(f, g) = 0$. This completes the proof of Theorem 2.

References

[1] M. A. Almeida, A. López-Castillo, and T. J. Stuchi, "Non-integrability proof of the frozen planetary atom configuration," *J. Phys. A: Math. Gen.* **36** (2003) 4805–4814.

[2] M. Arribas and A. Elipe, "Non-integrability of the motion of a particle around a massive straight segment," *Phys. Lett.* **281A** (2001) 142–148.

[3] B. Grammaticos, B. Dorizzi, and R. Padjen, "Painlevé property and integrals of motion for the Hénon-Heiles system," *Phys. Lett.* **89A** (1982) 111–113.

[4] L. S. Hall, "A theory of exact and approximate configurational invariants," *Physica* **8D** (1983) 90–116.

[5] J. Hietarinta, "A search for integrable two-dimensional Hamiltonian systems with polynomial potential," *Phys. Lett.* **96A** (1983) 273–278.

[6] J. Hietarinta, "Direct methods for the search of the second invariant," *Phys. Rep.* **147** (1987) 87–154.

[7] H. Ito, "Non-integrability of Hénon-Heiles system and a theorem of Ziglin," *Kodai Math. J.* **8** (1985) 120–138.

[8] A. J. Maciejewski and M. Przybylska, "Non-integrability of the Suslov problem," *Regular and Chaotic Dynamics* **7** (2002) 73–80.

[9] A. J. Maciejewski and M. Przybylska, "Non-integrability of ABC flow," *Phys. Lett.* **303A** (2002) 265–272.

[10] I. Marshall and S. Wojciechowski, "When is a Hamiltonian system separable?," *J. Math. Phys.* **29** (1988) 1338–1346.

[11] J. J. Morales-Ruiz, *Differential Galois Theory and Non-Integrability of Hamiltonian Systems*, *Progress in Mathematics* vol 179 (Birkhäuser Verlag, Basel, 1999)

[12] J. J. Morales-Ruiz, "Kovalevskaya, Liapounov, Painlevé, Ziglin and the differential Galois theory," *Regular and Chaotic Dynamics* **5** (2000) 251–272.

[13] J. J. Morales-Ruiz, "Meromorphic nonintegrability of Hamiltonian systems," *Reports on Mathematical Physics* **48** (2001) 183–194.

[14] J. J. Morales-Ruiz and J. P. Ramis, "Galoisian obstructions to integrability of Hamiltonian systems," *Methods and Applications of Analysis* **8** (2001) 33–96.

[15] J. J. Morales-Ruiz and J. P. Ramis, "Galoisian obstructions to integrability of Hamiltonian systems II," *Methods and Applications of Analysis* **8** (2001) 97–112.

[16] J. J. Morales-Ruiz and J. P. Ramis, "A note on the non-integrability of some Hamiltonian systems with a homogeneous potential," *Methods and Applications of Analysis* **8** (2001) 113-120.

[17] K. Nakagawa and H. Yoshida, "A list of all integrable two-dimensional homogeneous polynomial potentials with a polynomial integral of order at most four in the momenta," *J. Phys. A: Math. Gen.*, **34** (2001) 8611–8630.

[18] K. Nakagawa, "Direct construction of polynomial first integrals for Hamiltonian systems with a two-dimensional homogeneous polynomial potential," *Thesis* (2003) The Graduate University for Advanced Studies (SOKENDAI).

[19] A. Ramani, B. Dorizzi, and B. Grammaticos, "Painlevé conjecture revisited," *Phys. Rev. Lett.* **49** (1982) 1539–1541.

[20] A. W. Sáenz, "Nonintegrability of the Dragt-Finn model of magnetic confinement: a Galoisian-group approach," *Physica* **144D** (2000) 37–43.

[21] B. L. van der Waerden, *Algebra* vol 1 (Springer-Verlag, New York, NY, 1991)

[22] H. Yoshida, "A criterion for the non-existence of an additional integral in Hamiltonian systems with a homogeneous potential," *Physica* **29D** (1987) 128–142.

[23] H. Yoshida, "A new necessary condition for the integrability of Hamiltonian systems with a two dimensional homogeneous potential," *Physica* **128D** (1999) 53–69.

[24] S. L. Ziglin, "Branching of solutions and non-existence of first integrals in Hamiltonian mechanics. I," *Functional Analysis and Its Applications* **16** (1983) 181–189.

Is Arnold diffusion relevant to global diffusion?

Seiichiro Honjo* and Kunihiko Kaneko

Department of Basic Science, Graduate School of Arts and Science,
The University of Tokyo, 3-8-1 Komaba, Meguro, Tokyo 153-8902, Japan

Abstract

Global diffusion of Hamiltonian dynamical systems is investigated by using a 4-dimensional symplectic map. Structure of Arnold web and resonance overlaps are visualized in the frequency space, through long-term computation of local rotation numbers. It is shown that global diffusion in the phase space is mainly governed by diffusion across the overlapped higher-order resonances, rather than Arnold diffusion along the lower-order resonances.

1 Introduction

Hamilton 力学系において大域的な不安定性を導く機構としてよく知られているものに Arnold diffusion と resonance overlap の二つがある。相空間には共鳴条件 $\sum_i m_i\omega_i + M = 0$ (ω_i は各自由度の角周波数。m_i、M は任意の整数。) によって特徴づけられる resonance layer が存在し、それらの中では stochastic な運動が実現されている。Arnold diffusion は、resonance layer が網目状に交差して形成する Arnold web 上の運動であり、自由度が $N \geq 2$ (自励系では $N \geq 3$) の多自由度系で一般的に起きる現象である [Arn64, Chi79]。Resonance overlap は、非線形性の増大とともに厚みを増した resonance layer 同士が重なり合うことによって大域的な運動を可能とする機構であり、二次元写像 ($N = 1$) で集中的に調べられている [Chi79, LL92]。

自由度が大きい場合、相空間の次元も大きく、視覚的、直観的な理解は困難となる。このことは Arnold diffusion や多自由度系での resonance overlap の研究の障害となっており、一般の系において両者がどのように混在しているのかについては理解されているとは言いがたい。

そこで本研究では、共鳴の舞台であり、相空間の半分の次元しかもたない周波数空間の構造を観察することにより、多自由度系の不安定性や輸送の性質を調べる。

2 Methods and models

周波数空間で直接的に共鳴の構造を観察することは、Martens *et al.*[MDE87] や Laskar[Las90, Las93] によってもなされている。彼らは有限時間に区切った時系列をフーリエ変換し、大きなパワーをもつ周波数をその時刻での周波数として採用している。この方法は一般性をもつが、時系列の細かい揺らぎが優勢になることによって意図せぬ高周波にパワーをもってしまったり、秤動の周波数を拾ってしまったりすることのないように注意を払わなければならない。

そこで本研究ではそのような繁雑さを避けるため、カオスの研究で基本的な量である回転数が自然に定義できるモデルを選び、そこで求められる局所時間の回転数をフーリエ変換で求められる周波数の代わりに用いることにする。

*e-mail: honjo@complex.c.u-tokyo.ac.jp

Arnold diffusion が実現される自由度 $N \geq 2$ の系で、回転数が自然に定義できる系として Froeschlé map[Fro71, KB85]

$$\begin{cases} p_1(n+1) = p_1(n) + K_1 \sin(q_1(n)) + b\sin(q_1(n)+q_2(n)) \\ q_1(n+1) = q_1(n) + p_1(n+1) \pmod{2\pi} \\ p_2(n+1) = p_2(n) + K_2 \sin(q_2(n)) + b\sin(q_1(n)+q_2(n)) \\ q_2(n+1) = q_2(n) + p_2(n+1) \pmod{2\pi} \end{cases} \tag{1}$$

(K_1、K_2 は素子の非線形性を支配するパラメータ、b は素子間の結合強度。) を用いる。Froeschlé map は 2 個の回転子が結合した系と見なせるので、

$$\omega_i \equiv \lim_{T\to\infty} \frac{\tilde{q}_i(T) - q_i(0)}{2\pi T} = \lim_{T\to\infty} \sum_{n=1}^{T} \frac{p_i(n)}{2\pi T} \tag{2}$$

($\tilde{q}_i$ は 2π で剰余をとらない場合の q_i) で回転数が定義される。回転数は単位時間に回転子が平均で何回回転したかを測る量であり、周波数に対応する。

いま知りたいのは周波数空間での時間変化なので、有限の時間 T で求められた局所回転数

$$\omega_i(jT) \equiv \sum_{n=jT}^{jT+T-1} \frac{p_i(n)}{2\pi T} \tag{3}$$

を測定することになる。

考慮すべき Froeschlé map の共鳴条件は

$$m_1\omega_1 + m_2\omega_2 + M = 0 \tag{4}$$

(m_1、m_2、M : 任意の整数) である。

3 Visualization of Arnold web and overlapped resonances

求めた局所回転数から周波数空間の構造を観察するために以下の手続きをとる。まず、長時間の時間発展によって幅広いレンジの値を取る局所回転数を、決まった有限区間で表示するため、剰余をとって $[0,1)$ 区間に射影する。このことは運動量方向に 2π の周期をもつ Froeschlé map の性質を考慮すると自然である。次に、$[0,1)\otimes[0,1)$ の区間を 1024×1024 個のビンに切って局所回転数が滞在した数を数え、周波数空間での頻度分布を測定する。滞在頻度はグレイスケールで表示する。

図 1 は一本の軌道から周波数空間に構成した Arnold web である。パラメータは $K_1 = K_2 = 0.90$、$b = 0.002$ である。局所回転数は $T = 1\times10^3$ ステップ毎に求められており、写像自体は全部で 1×10^{10} ステップの時間発展がなされている。図 1 で特筆すべきは、$m_i\omega_i + M = 0$ という共鳴の他に、$\omega_1+\omega_2 = 0$ という coupling resonance が観察されることである。もう一つの最低次の coupling resonance、$\omega_1-\omega_2 = 0$ と比較すると Froeschlé map の結合の異方性が周波数空間の構造に反映していることがわかる。

図 2 はパラメータの値を $K_1 = K_2 = 0.50$、$b = 0.100$ とした以外は図 1 と同じ手続きによって得られている。このパラメータでは、図 1 のパラメータに比べて結合の効果が支配的になっており、周波数空間では様々な次数の coupling resonance とそれらを巻き込む resonance overlap が観察される。Resonance overlap が coupling resonance を含めて起きていることは、図 3 の、最大 Lyapunov 指数を有限の時間で計算することによって得られた相空間の断面からも確認される。つまり、局所回転数から求められる周波数空間から動力学的な構造がうまく捉えらることがわかる。

4 Lifetime distribution of resonances

Arnold diffusion と resonance overlap との違いを明確にするため、特定の resonance layer への滞在時間分布 $\rho(t)$ を求めることにする。

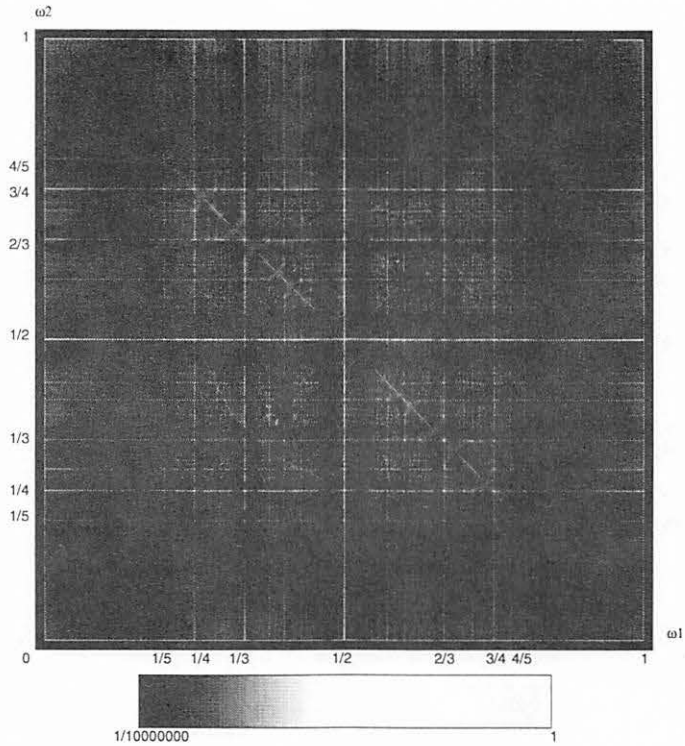

Figure 1: Arnold web in the 2-dimensional frequency space. The histogram of local rotation numbers, computed by the number of times visited at each local rotation number with 1024×1024 bins for 1×10^{10} iterations. $K_1 = K_2 = 0.90$, $b = 0.002$, $T = 1 \times 10^3$. $\omega_1 + \omega_2 = 0$ is one of the lowest-order coupling resonances.

局所回転数は有限の時間で求められているため、ゆらぎを消し去ることはできない。そこで、共鳴条件 $m_1\omega_1 + m_2\omega_2 + M = 0$ で決まる共鳴線からの距離が、ある閾値 W に入っているものを共鳴条件を満たしていると見なすことにする。閾値 W は、その値を変えても滞在時間分布が変化しないようにとる。

まず、同一パラメータの周波数空間で、滞在時間分布が共鳴線の次数に依存してどのように変わるかを調べる。結果は図 4 に見られるように、次数の低い共鳴線では $\rho(t) \sim t^{-3/2}$ であり、次数が高くなっていくと $\rho(t) \sim t^{-2}$ となっていくというものであった。

次に、注目する共鳴線を固定して、結合強度を変えたときに滞在時間分布がどのように変化するかを調べる。結果は図 5 に見られるように、結合力 b が小さい場合はは $\rho(t) \sim t^{-3/2}$ であり、結合力を増していくと $\rho(t) \sim t^{-2}$ となっていくというものであった。

有限区間へのブラウン運動の滞在時間分布は一次元では $t^{-3/2}$ に比例し、二次元では $\sim t^{-2}$ に比例する。

これらのことを統一的に解釈すると以下のようになる。低次の共鳴では共鳴線に沿った Arnold diffusion が実現されており、周波数空間では一次元運動がなされてる。高次の共鳴では resonance overlap が起きており、そこでは共鳴線に横断的な運動も許容されるため二次元運動が実現されている。また、低次の共鳴でも結合力が増していくと、resonance overlap が進み二次元運動が実現されるようになる。

5 Transition in the frequency space

次に、実際の軌道が共鳴の構造が見出された周波数空間でどのような運動をしているのかを、より詳しく調べることにする。

周波数空間は運動量空間から見れば時間的に平均化されたものである。しかし、それでも動力学の詳細はあまりに繁雑である。そこで、空間的な粗視化をした上で領域間の遷移を

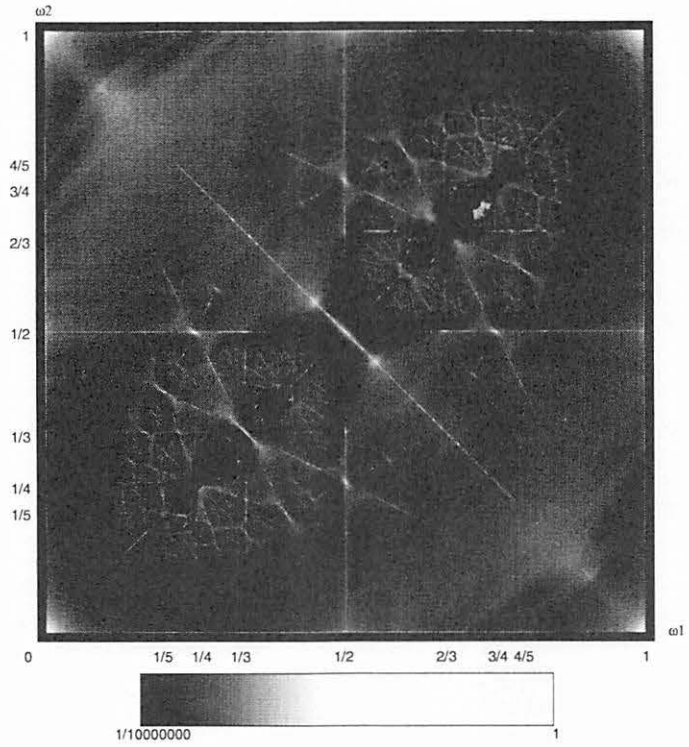

Figure 2: Same as Fig.1 except $K_1 = K_2 = 0.50$ and $b = 0.100$. Coupling resonances are overlapped in some part of the frequency space.

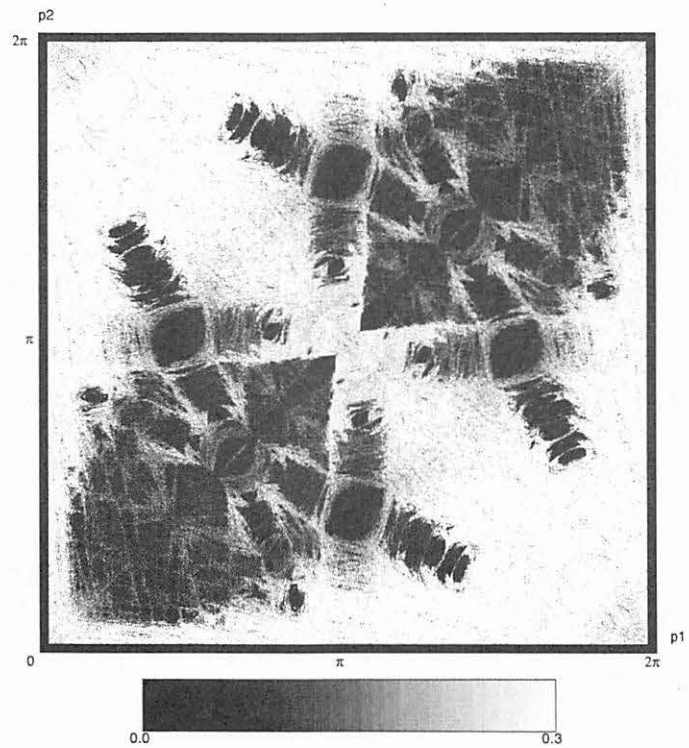

Figure 3: A 2-dimensional surface of section of phase space. The section is taken at $q_1 = q_2 = 0.00$. Maximal Lyapunov exponents averaged over only 256 steps are computed for each initial point in the phase space with increment of $2\pi/1024$ (i.e., 1024×1024 points). Parameters are same as Fig.2. Overlapped resonances are shown on the section.

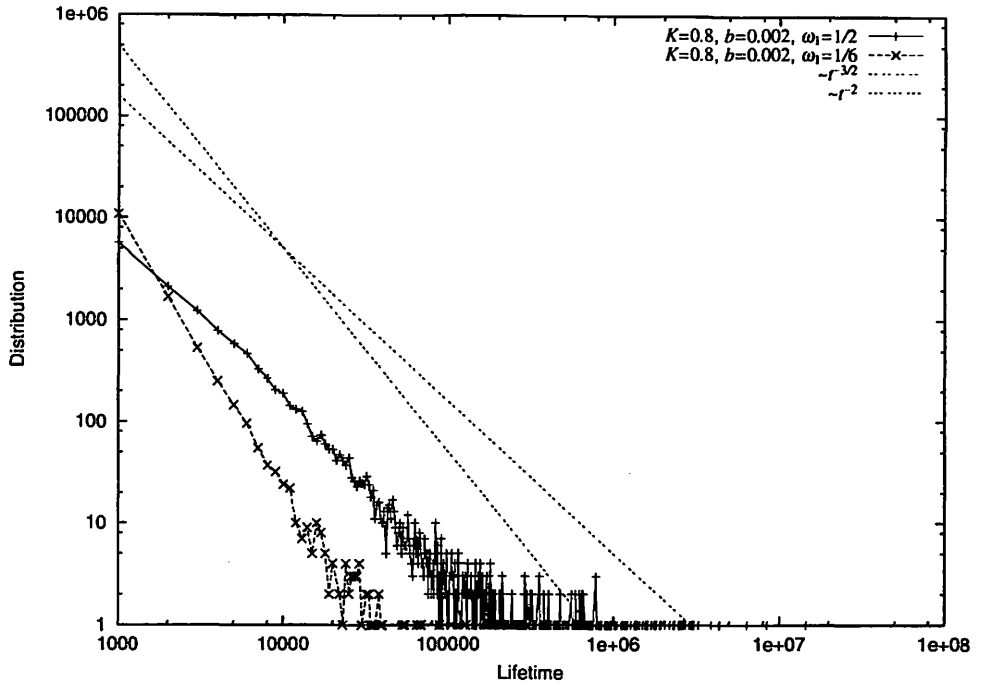

Figure 4: Lifetime distributions of certain resonances depending on the order of resonances. Distributions decay with a power law ($\sim t^{-3/2}$ for $\omega_1 = 1/2$ and $\sim t^{-2}$ for $\omega_1 = 1/6$, respectively) for $K_1 = K_2 = 0.80$ and $b = 0.002$.

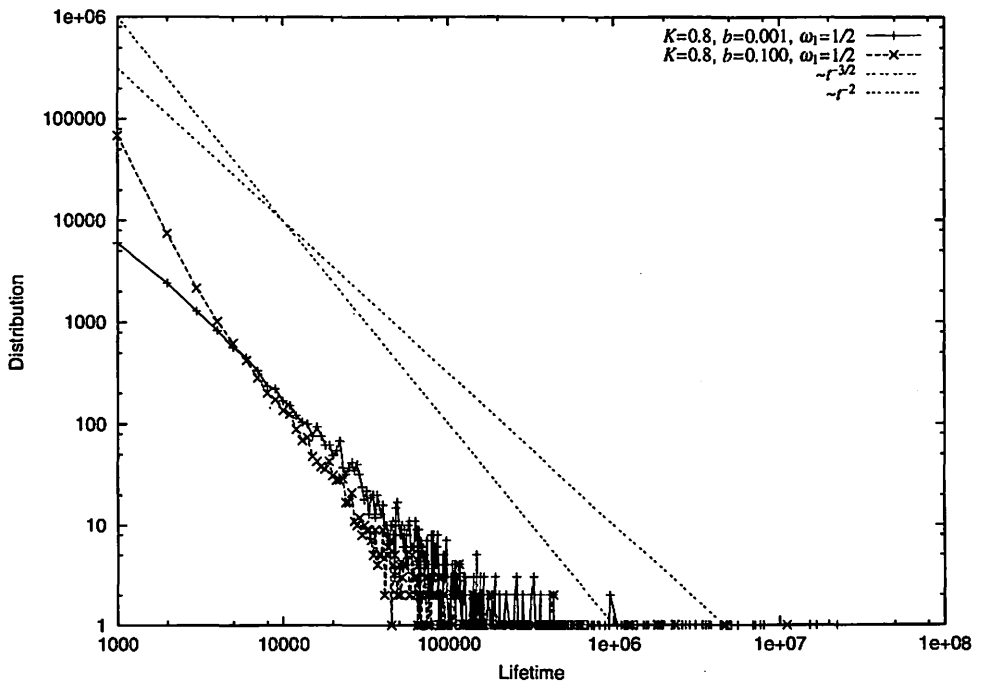

Figure 5: Lifetime distributions of $\omega_1 = 1/2$ resonance depending on coupling strength b. Distributions decay with a power law ($\sim t^{-3/2}$ for $b = 0.001$ and $\sim t^{-2}$ for $b = 0.100$, respectively) for $K_1 = K_2 = 0.80$.

考え、その上で動力学を観察する。

周波数空間の粗視化は、$\omega_i = 2/m_i$(あるいは $\omega_i = 1-(2/m_i)$) の共鳴線を各領域間の境界として用いて、周波数空間を分割することによって行う。このように領域分けをすると、$\omega_i = 1/m_i$(あるいは $\omega_i = 1-(1/m_i)$) の共鳴線同士によるジャンクションが各領域にそれぞれ一つずつ存在するようになる。周波数空間には ω_1、ω_2 ともに黄金数をとり、かつ coupling resonance $\omega_1+\omega_2=0$ 上にない点が、$S=(1-(\sqrt{5}-1)/2, 1-(\sqrt{5}-1)/2)$ と $G=((\sqrt{5}-1)/2, (\sqrt{5}-1)/2)$ の二つある。点 S を含む領域に始点を用意し、点 G を含む領域にたどりつくまでの遷移を観察する。

図 6 は、点 S を含む領域にランダムに用意した 64 サンプルの内、最も少ないステップ数で終領域にたどり着いたサンプルの遷移の様子を表したものである。少ないステップ数で終領域にたどり着く他のサンプルもほぼ同様のダイアグラムを与える。

周波数空間は図 2 で表される構造をもっている。遷移は resonance overlap した領域を coupling resonance に横断的に運動することよってなされており、共鳴線に横断的な運動が、共鳴に沿った Arnold diffusion に比べて速く、遷移に大きな寄与していることがわかる。

加えて、共鳴が coupling resonance も含めて交差して resonance overlap した領域では、必然的に横断的に移動できる方向が多くなっており、遷移に対してネットワークのハブと同様の振る舞いをしていることが観察される。

では、周波数空間が図 1 で表される構造をもっており、図 2 の場合のような一目でそれとわかるようなあからさまな resonance overlap 領域をもっていない場合は、どのような遷移ダイアグラムが書けるだろうか。図 7 がその場合の遷移ダイアグラムである。粗視化された遷移の向きだけに注目した場合は、いかなる運動がなされているのか判断がつかない。しかし、局所回転数自体を合わせて注目してみると、遷移は低次の共鳴線の間をぬって起きていることが観察される。つまり、運動は低次の共鳴線に沿った Arnold diffusion ではなく、高次の共鳴線が resonance overlap した領域を共鳴線に横断的に移動する、いわば裏道を通るものであることがわかる。

6 Global diffusion

これまで調べてきたのは、 Arnold diffusion と resonance overlap という微視的な機構である。そこで、次はこれらの機構が巨視的な量である拡散係数にはどのように反映するかを調べることにする。

拡散係数 D は

$$D \equiv \lim_{T\to\infty} \left\langle \frac{1}{2}\sum_{i=1}^{2} \frac{(p_i(T)-p_i(0))^2}{T} \right\rangle \tag{5}$$

で定義する。ここで、$\langle\cdot\rangle$ はサンプル平均を意味している。

Froeschlé map の周波数空間の構造に結合による異方性があることは、図 1 や図 2 に見られる通りである。この異方性が拡散係数に反映されるかどうかを調べるため、特定の方向に制限した拡散係数を測定してみる。このことは拡散係数の測定の際、運動量の変位を特定の軸方向にのみとれば可能である。

異方性を最も顕著に表しているのは最低次の coupling resonance の内の一方の $\omega_1+\omega_2=0$ である。また、$2\omega_1+\omega_2=0$ や $\omega_1+2\omega_2=0$ などの高次の coupling resonance に横断的な運動は、平均すると対称性によって $\omega_1+\omega_2=0$ に横断的な運動とみなせる。よって、$\omega_1+\omega_2=0$ を参照する軸として用いることにする。つまり、

p_2 = 0 に平行な拡散 (p_1 軸方向の拡散)
p_1 = 0 に平行な拡散 (p_2 軸方向の拡散)
p_2 = p_1に平行な拡散 (coupling resonance $\omega_1+\omega_2=0$ に横断的な方向の拡散)
p_2 = $-p_1$に平行な拡散 (coupling resonance $\omega_1+\omega_2=0$ に沿った方向の拡散)

をそれぞれ測定する。

図 8 はパラメータを $K=0.80$ としたときの拡散係数を、結合強度 b に対してプロットしたものである。$p_2=p_1$ に平行な拡散がもっとも速く、拡散には異方性があることがわか

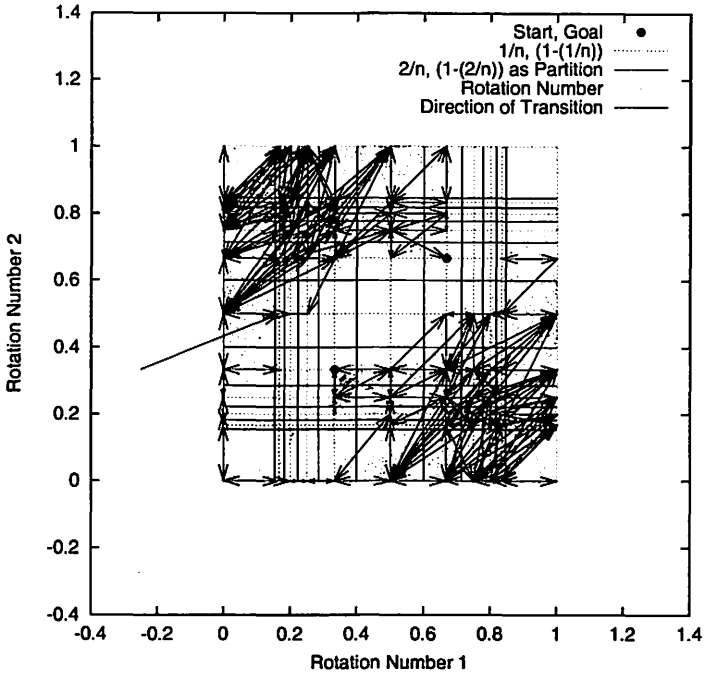

Figure 6: Transition diagram in the frequency space. Parameters are $K_1 = K_2 = 0.50$ and $b = 0.100$. It takes the shortest steps (1416×10^3 steps) to arrive at the final state in randomly chosen 64 samples. Remarkable transitions occur through the overlapped resonances across the coupling resonances.

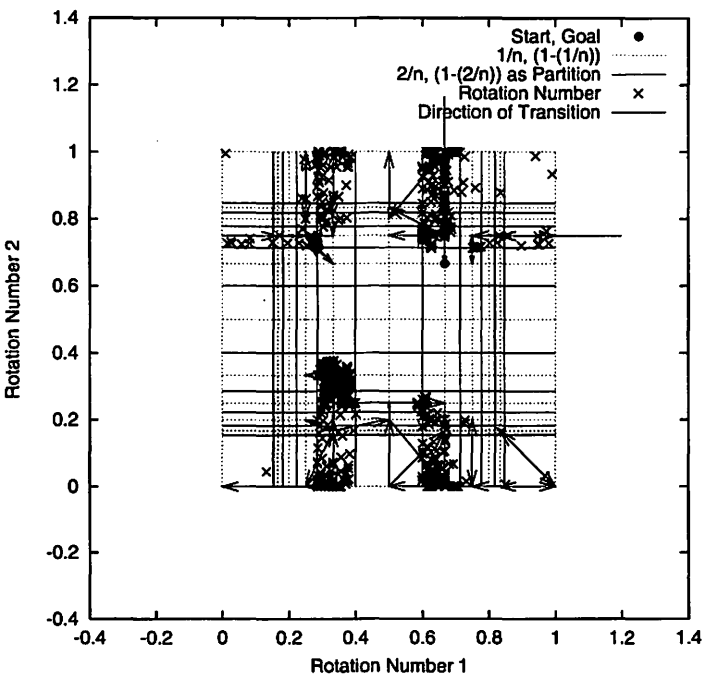

Figure 7: Transition diagram in the frequency space. Same as Fig.6 except $K_1 = K_2 = 0.90$ and $b = 0.002$. It takes 2187×10^3 steps to arrive at the final state. Transitions occur through the overlapped higher-order resonances.

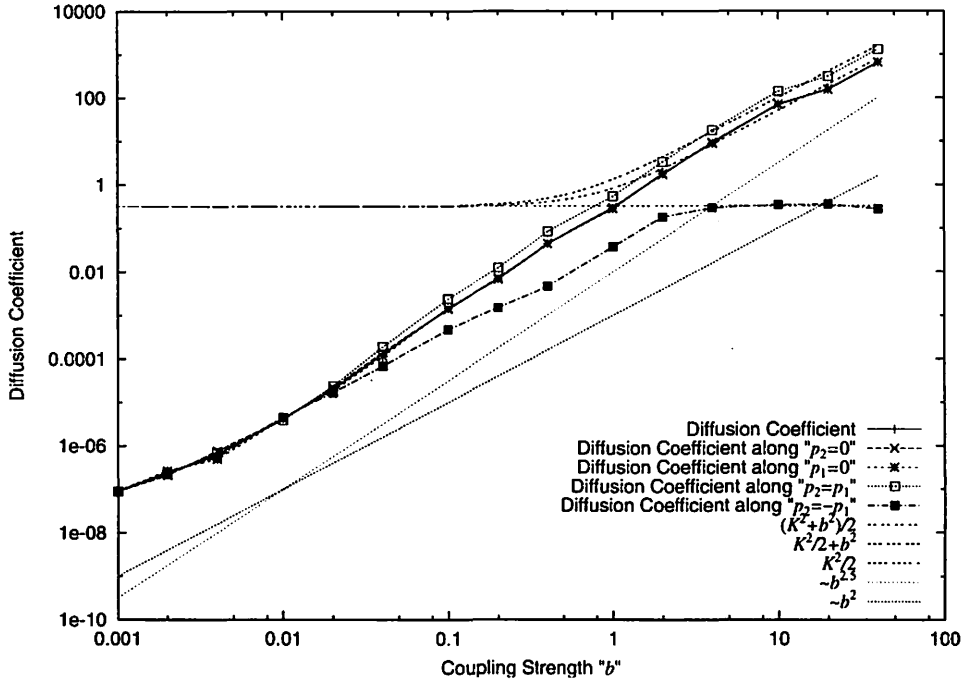

Figure 8: Diffusion coefficients depending on coupling strength b for $K(= K_1 = K_2) = 0.80$. Diffusion coefficients along certain directions are also calculated. Diffusion coefficients along $p_2 = 0$ and $p_1 = 0$ are the same as the ordinary diffusion coefficient. Diffusion across the resonances is faster than diffusion along the resonances.

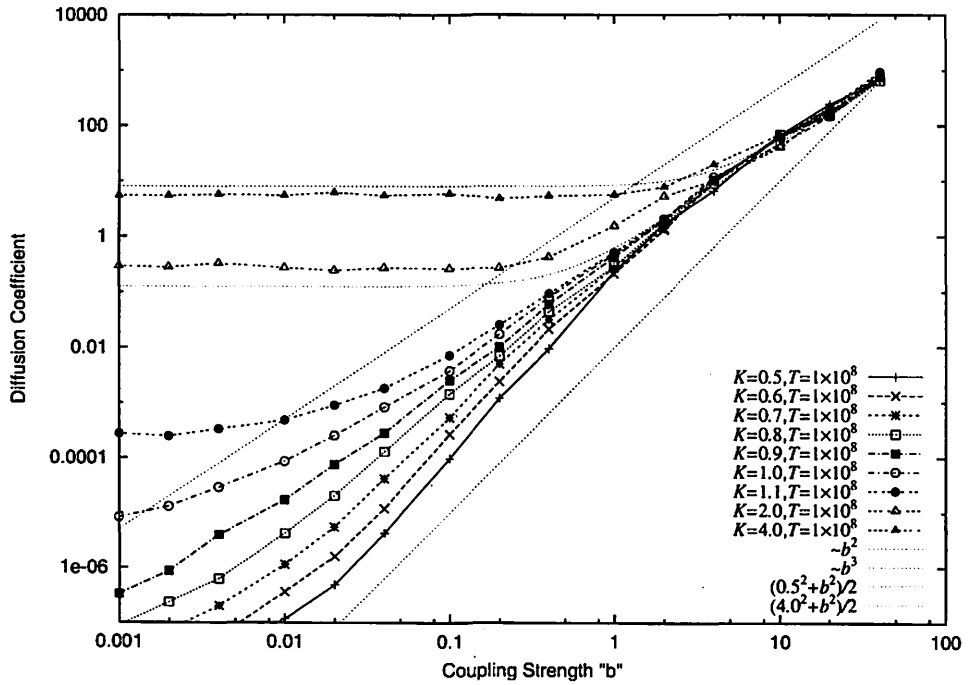

Figure 9: Diffusion coefficients depending on coupling strength b for several $K(= K_1 = K_2)$. Diffusion coefficients for $K \leq 0.97$ shows a power law dependence to b.

る。その異方性は resonance overlap 領域での、coupling resonance に横断的な運動が速いことと一致しており、微視的な共鳴構造が巨視的な拡散係数にも反映していることを表している。

結合強度 b を大きくすることは、大雑把にいうと coupling resonance の共鳴領域の大きさを増大させる。そのことによって resonance overlap が起こり、遷移のハブとして振る舞う領域が様々な位置に生じる。その過程が拡散係数の大きさの変化にどう反映するかを調べるため、様々な値のパラメータ $K(= K_1 = K_2)$ に対して拡散係数の結合力依存性を測定した結果が図 9 である。

Froeschlé map は $b = 0$ の時、独立な二つの standard map となる。Standard map は $K_i > K_c \simeq 0.97$ では resonance overlap により大域的な運動が可能となり、有限の拡散係数をもつ。図 9 で、$K_i \geq 1.00$ の時に $b \to 0$ で拡散係数が一定値をとるのは、そのような事情によるものである。

一方、standard map で $K_i \leq K_c \simeq 0.97$ の場合は、大域的な運動がトーラスによって妨げられるので、拡散係数が 0 となる。つまり、Froeschlé map も $b \to 0$ の極限で拡散係数が 0 となることが期待される。実際、$K_i \leq 0.90$ の場合、測定した図 9 の範囲では拡散係数は b の減少とともに 0 に向かっている。

このとき、拡散係数は結合力にべき依存している。このべき依存は resonance overlap 領域の形成のされ方を反映してのものと考えられる。

7 Summary and discussions

局所回転数から構成した周波数空間の構造を観察することによって Arnold diffusion と resonance overlap の混在した様子を観察することができた。その観察により resonance overlap によって実現される共鳴線に横断的な運動が、共鳴線に沿った運動よりも速いことが示され、大域的な拡散は主として共鳴線に横断的な運動に支配されていることがわかった。

多自由度 Hamilton 力学系の数値実験 [KK90] で求められた拡散係数や、その摂動項に対するべき依存を説明する場合、共鳴に沿った運動が仮定されることがしばしばある [WLL90, CV93, CV97]。これらの仮定は、拡散を支配するのが共鳴に横断的な運動であると知った今、根本的に再検討されなければならない。

系の自由度が大きくなっていくと Arnold web を形成する resonance layer はより多くの方向をとり得るようになる。このような、いわば Arnold spaghetti[Kan02] とも呼べるような状況が実現されたとき、resonance overlap はどのように起き巨視的な拡散に寄与するのであろうか。そのことを調べることこそ、熱平衡状態が実現される大自由度系とはいかなるものであるかを知るための一つの道筋となるのであろう。

References

[Arn64] V. I. Arnold. Instability of dynamical systems with several degrees of freedom. *Sov. Math. Dokl.*, Vol. 5, pp. 581–585, 1964.

[Chi79] B. V. Chirikov. A universal instability of many-dimensional oscillator systems. *Phys. Rep.*, Vol. 52, pp. 263–379, 1979.

[CV93] B. V. Chirikov and V. V. Vecheslavov. Theory of fast Arnold diffusion in many-frequency systems. *J. Stat. Phys.*, Vol. 71, pp. 243–258, 1993.

[CV97] B. V. Chirikov and V. V. Vecheslavov. Arnold diffusion in large systems. *JETP*, Vol. 85, pp. 616–624, 1997.

[Fro71] C. Froeshlé. On the number of isolating integrals in systems with three degree of freedom. *Astrophys. SpaceSci.*, Vol. 14, pp. 110–117, 1971.

[Kan02] K. Kaneko. Dominance of Milnor attractors in globally coupled dynamical systems with more than 7±2 degrees of freedom. *Phys. Rev. E*, Vol. 66, p. 05520(R), 2002.

[KB85] K. Kaneko and R. J. Bagley. Arnold diffusion, ergodicity and intermittency in a coupled standard mapping. *Phys. Lett. A*, Vol. 110, pp. 435–440, 1985.

[KK90] T. Konishi and K. Kaneko. Diffusion in Hamiltonian chaos and its size dependence. *J. Phys. A*, Vol. 23, pp. L715–L720, 1990.

[Las90] J. Laskar. The chaotic motion of the solar system: A numerical estimate of the size of the chaotic zones. *Icarus*, Vol. 88, pp. 266–291, 1990.

[Las93] J. Laskar. Frequency analysis for multi-dimensional systems. Global dynamics and diffusion. *Physica D*, Vol. 67, pp. 257–281, 1993.

[LL92] A. J. Lichtenberg and M. A. Lieberman. *Regular and Chaotic Dynamics.* Springer-Verlag, second edition, 1992.

[MDE87] C. C. Martens, M. J. Davis, and G. S. Ezra. Local frequency analysis of chaotic motion in multidimensional systems: Energy transport and bottlenecks in planar OCS. *Chem. Phys. Lett.*, Vol. 142, pp. 519–528, 1987.

[WLL90] B. P. Wood, A. J. Lichtenberg, and M. A. Lieberman. Arnold diffusion in weakly coupled standard maps. *Phys. Rev. A*, Vol. 42, pp. 5885–5893, 1990.

不安定ゾーン内の非バーコフ周期軌道
Non–Birkhoff Periodic Orbits in a Zone of Instability

Kiyotaka TANIKAWA[1] and Yoshihiro YAMAGUCHI[2]

[1] National Astronomical Observatory, Mitaka, Tokyo 181-8588, Japan.

[2] Teikyo Heisei University, Ichihara, Chiba 290-0193, Japan.

概 要

We consider a reversible (or Birkhoff-reversing) exact symplectic twist map which has a region of instability and prove that under an assumption on the number of Birkhoff periodic orbits of the same rotation number, there are, for any $\varepsilon > 0$, non-Birkhoff periodic orbits which have orbital points in the ε-neighborhoods of both boundaries of the region of instability.

§1. 序

1.1 結果の陳述

力学系が積分可能系から遠ざかれば遠ざかるほど, KAM (Kolmogorov-Arnold-Moser) 曲線 [1] の分布密度は減少する. ねじれ写像の場合, Aubry ら [2] と Mather[3] によって示されたとおり, KAM 曲線の残骸は Aubry–Mather 集合とよばれるカントール集合となる. これはカントーラスともよばれる [4]. カントーラスは完全な障壁ではないので, 相点は穴を通ってカントーラスをくぐり抜ける. 円筒で定義されたねじれ写像の場合, 円筒を巻く KAM 曲線が上下運動の障壁となる. このねじれ写像の外部パラメータを変化させ, 複雑化に向かうカオスのある時点に, ある二本の KAM 曲線の間に円筒を巻く他の KAM 曲線が存在しない場合があると期待される. この二本の KAM 曲線に挟まれた領域は Birkhoff[5] により不安定リングとよばれた. ここではそれを不安定ゾーンとよぶことにする. Birkhoff は面白い定理を証明した. 定理そのものは利用し尽くされていないように見える. その定理とは,

定理 A([5, Birkhoff, 1920, §47]). C^-, C^+ は不安定ゾーン C の境界を形成する二本のまったく異なる不変曲線であるとする. このとき任意の $\varepsilon > 0$ に対して, 整数 N を見つけることができ, C^- (または C^+) の任意の点 P から距離 ε 以内の点 P' で, C^+ (または C^-) の任意の点 Q から距離 ε 以内の点 Q' まで写像 f (または f^{-1}) の $n < N$ 回の繰り返しで到達するようにできる.

Herman[6] はこの定理を丁寧に調べた. LeCalvez[7] はこの定理を拡張した.

定理 B([7, LeCalvez, 2000, p.23, 定理 1.9]).

i) $x \in C$ があって次を満たす.

$$\lim_{n\to-\infty} d(f^n(x), C^-) = \lim_{n\to\infty} d(f^n(x), C^+) = 0.$$

ii) C^+ の任意の近傍 V に対して, $x \in V$ があって次を満たす.

$$\lim_{n\to\pm\infty} d(f^n(x), C^-) = 0.$$

上の定理の ii) は Birkhoff の元の定理を改善している. あらっぽく言えば, C^- の近傍から出発して C^+ の近傍に達し, ふたたび C^- の近傍に戻ってくる軌道があることを主張する.

本論文の目的は, 不安定ゾーンの上下の境界の任意に小さな近傍を無限回行き来する軌道があることを示すことである. これは LeCalvez の結果の拡張になっている. ただし, 証明のために,

ある前提をおく. その前提は成り立つと思われるが, いまのところ成り立つことは証明できていない.

前提 H. 不安定ゾーンの上下の境界のいくらでも近くに, バーコフ軌道が 2 つしかないような回転数がある.

定理 C. C は円環の, 完全シンプレクティック可逆ねじれ写像 f の不安定ゾーンであるとする. その上下の境界は C^+ と C^- であり, それらの回転数は, ρ^+ と ρ^- $(\rho^- < \rho^+)$ であるとする. ねじれ写像が前提 H を満たすなら, 任意 $\varepsilon > 0$ に対して, 有理数回転数 $p/q \in (\rho^-, \rho^+)$ を持つ f の非バーコフ周期軌道があって, その軌道点が, C^- の ε 近傍にも C^+ の ε 近傍にも存在する.

この定理 C を次のような段階を踏んで証明する. 不安定ゾーン内の回転数が与えられ, その回転数を持つバーコフ型周期軌道が 2 つしかないとき, サドル型バーコフ点がホモクリニックサドルであること, すなわち, その安定多様体と不安定多様体がすべて (必ずしも横断的ではなく) 交わることを証明する. すると, 筆者らの前の結果が使える.

定理 D([8]). f を円環 A の完全シンプレクティックねじれ写像とする. α_0 と α_1 $(\alpha_0 < \alpha_1)$ は境界 $S^1 \times \{0\}$ と $S^1 \times \{1\}$ の回転数であるとする. 不安定ゾーンがあるとする. その境界は C^- と C^+ であって, 回転数は ρ_1 および ρ_2 であるとする $(\alpha_0 < \rho_1 < \rho_2 < \alpha_1)$. W_s と W_u が任意の p/q-ホモクリニックサドルの安定および不安定多様体であるとする. ただし, $\rho_1 < p/q < \rho_2$. このとき, $W_s \supset C^- \cup C^+$ かつ $W_u \supset C^- \cup C^+$ である.

定理 D の系として次を得る.

Corollary E([8]). 定理 D の前提を仮定する. すると, 任意の p/q- および p'/q'-バーコフサドルの安定多様体と不安定多様体 $(p/q, p'/q' \in (\rho_1, \rho_2))$ は (必ずしも横断的とは言えないが) ヘテロクリニック点を持つ.

不安定ゾーンの上の境界近くの対称軸の弧であって, しかもバーコフサドル点の近傍にある弧の中には, 何回かの写像の後にバーコフサドルのホモクリニックロープに入り, 写像の繰り返しの後に, このホモクリニックロープの境界を構成する不安定多様体に連れられて, 不安定ゾーンの下の境界近くに到達するものがある. そこにおいて, 境界回転数近くの回転数を持つバーコフサドルのホモクリニックロープに入る. さらに写像を繰り返すと, このロープは対称軸と交わる. そのとき, 上の境界近くから来た対称軸の弧の像も対称軸と交わる. 対称軸と対称軸の像の交点は周期点である. このようにして, 上下の境界の任意の近傍内に点を持つ周期解の存在を示す.

必要な用語および定義は次の副節で導入する.

1.2 記法および定義

この副節では, 円筒の完全 (exact) シンプレクティック可逆ねじれ写像, 不安定ゾーン, 非バーコフ周期軌道, ホモクリニックバーコフサドルおよびその他の必要な概念を導入する.

円筒 $\mathbf{S}^1 \times \mathbf{R}^1$ $(x \in \mathbf{S}^1, y \in \mathbf{R}^1)$ からそれ自身へのねじれ写像 f で

$$y_{n+1} = \Phi(x_n, y_n) = y_n + \varphi(x_n), \tag{1}$$

$$x_{n+1} = \Psi(x_n, y_n) = x_n + \psi(y_{n+1}) \ (\mathrm{Mod}\ 2\pi) \tag{2}$$

なる形のものを考える. ここで, $\varphi(x)$ は周期 2π の奇関数であり, 2 つの関数 $\varphi(x)$ と $\psi(y)$ は可微分, 関数 $\psi(y)$ は次のねじれ条件を満たすとする [9].

$$\frac{\partial \psi(y_{n+1})}{\partial y_n} > 0. \tag{3}$$

鉛直線を右に傾けるので右ねじれ写像とよばれる. 写像 f は面積保存かつ方向保存である. 簡単に示せるように, 関数 $\varphi(x)$ は $\int_0^{2\pi}\varphi(x)\,dx=0$ を満たす. この関係と面積保存性より, f は完全 (exact) である. f が可逆であるのは, φ が奇関数だからである. こうして, f は可逆, 完全シンプレクティックねじれ写像である. $\varphi(x)$ が奇関数であってしかも周期的であるから, 関係 $\varphi(\pi)=0$ が成り立つ. 写像 f は2つの対合 G と H の積で表現できる [5,10].

$$f \;=\; H\circ G \tag{4}$$

ただし,

$$G\begin{pmatrix}x\\y\end{pmatrix}=\begin{pmatrix}-x\ (\mathrm{Mod}\ 2\pi)\\ y+\varphi(x)\end{pmatrix}\quad\text{and}\quad H\begin{pmatrix}x\\y\end{pmatrix}=\begin{pmatrix}-x+\psi(y)\ (\mathrm{Mod}\ 2\pi)\\ y\end{pmatrix} \tag{5}$$

ここで, $G^2=H^2=\mathrm{id}$ および $\det\nabla G=\det\nabla H=-1$ が対合 G と H の性質である. G や H の作用の下での不動点の集合は対称軸とよばれる. 以下では, G の対称軸のひとつである $x=0$ を出発する周期軌道を考える. 普遍被覆 $\mathbf{R}^2$ $(x\in\mathbf{R}^1, y\in\mathbf{R}^1)$ 上では, どの整数 n に対しても, 直線 $x=n\pi$ が対称軸である. これを $\mathcal{S}_G^n$ と書く. 記法の節約のため, 普遍被覆においても写像や座標に同じ記号を使うことにする. 一方 H の対称軸は $2x=\psi(y)$ およびそれを x 方向に $n\pi$ ずらした曲線である. $\psi(y)$ は y の増加関数であるから, H の対称軸は右上がりの曲線である. y の関数として1価である. $y=0$ のときに $\psi(y)=0$ となるように取れば写像の不動点は x 軸上 $(0,0)$ と $(0,\pi)$ の2点となり, 標準写像と同じになる. 普遍被覆面上で H の対称線は $(0,n\pi)$ を通る. これを S_H^n と書く. ただし, 本論文では不動点がどこにあるかは重要でない.

普遍被覆への持ち上げを考える. 点 $z\in\mathbf{R}^2$ の軌道を $o(z)=\{f^kz : k\in\mathbf{Z}\}$ と書く. z の拡張軌道 $eo(z)$ は $\{f^kz+(l,0) : k,l\in\mathbf{Z}\}$. z の回転数 $\nu(z)$ は

$$\nu(z)=\lim_{n\to\infty}\frac{\pi_1(f^nz)}{n} \tag{6}$$

と定義される. ここで $\pi_1(z)$ は z の x 座標への射影である. $z\in\mathbf{R}^2$ が

$$\widehat{f}^qz-(p,0)=z, \tag{7}$$

を満足するなら, z は p/q 周期点であり, その軌道は p/q 周期軌道とよばれる. p/q 周期軌道 $z\in\mathbf{R}^2$ が p/q-バーコフ軌道 [11] とよばれるのは, 任意の $r,s\in eo(z)$ に対して

$$\pi_1(r)<\pi_1(s)\ \Rightarrow\ \pi_1(fr)<\pi_1(fs). \tag{8}$$

が成り立つときである.

非バーコフ周期軌道の以下の定義は Yamaguchi&Tanikawa[12] による.

Definition. p/q 周期点 $z\in\mathbf{R}^2$ が与えられたとする.
(1) ある $r,s\in eo(z)$, $r\in o(s)$, に対して

$$\pi_1(r)<\pi_1(s)\ \Rightarrow\ \pi_1(fr)\geq\pi_1(fs), \tag{9}$$

なら, 点 z はI型非バーコフ周期点といわれる.
(2) 任意の $r,s\in eo(z)$, $r\in o(s)$, に対して

$$\pi_1(r)<\pi_1(s)\ \Rightarrow\ \pi_1(fr)<\pi_1(fs) \tag{10}$$

であり, かつある $r',s'\in eo(z)$, $r'\notin o(s')$, に対して

$$\pi_1(r')<\pi_1(s')\ \Rightarrow\ \pi_1(fr')\geq\pi_1(fs') \tag{11}$$

なら, 点 z はII型非バーコフ周期点といわれる.

Remark. 点 $r \in eo(z)$ が

$$\pi_1(f^{-1}r) < \pi_1(r), \pi_1(r) \geq \pi_1(fr), \text{ or} \tag{12}$$

$$\pi_1(f^{-1}r) > \pi_1(r),\ \pi_1(r) \leq \pi_1(fr), \tag{13}$$

を満たすとき, 前者は折り返し後退点, 後者は折り返し前進点とよばれ, どちらも折り返し点とよばれる. II型NBOには折り返し点がない. 軌道点は写像の下で単調に x 座標を進む.

無理数回転数 ρ_- および ρ_+ のKAM曲線が存在し, これらが $y = \phi_-(x)$ および $y = \phi_+(x)$ と表わされ, $y = \phi_\pm(x)$ に挟まれた領域に円筒を巻く普遍曲線がなければ、この領域 C はBirkhoffの導入した不安定ゾーンである。区間 (ρ_-, ρ_+) を不安定ゾーンの回転区間とよぶ.

サドル型の p/q バーコフ周期軌道の相隣り合う点の安定多様体と不安定多様体が滑らかにつながらず、交差しているとき、これを p/q ホモクリニックバーコフ周期軌道、その周期点をホモクリニックバーコフサドルとよぶ.

1.3. 対称軌道の一般的性質

本論文においては, 可逆性および可逆性の下での対称軌道が本質的な役割を果たす. 可逆性がなければ言えない, あるいは言うのが非常にむずかしいことを, 可逆性を使って主張してしまおう. これがこの論文の下心である. そこで, あとで必要となる可逆性および軌道の対称性をここで説明しておく. 1節では, 写像が2つの対合の積として表わされること, および対合の具体形を示しただけであった. 本節では, 可逆性および対称軌道の使い方について説明する. 詳しくは, DeVogelaere[10] あるいは筆者らの論文 [12] を参考にして欲しい. 対称線上, または対称線の写像による何回目かの像の上にある点は対称点と呼ばれる. 対称点が二重対称であるとは, 二本の対称線またはその像の交点上にあるときである.

Theorem 1.1(DeVogelaere[10]). 点が対称周期点であるための必要十分条件は, それが二重対称であることである.

DeVogelaere[10] にしたがって、作用素 $M_n = f^n G$ $(n \in \mathbf{Z})$ を定義し, 集合

$$\mathcal{M}_n = \{z |\ z = M_n z\}$$

導入する. 1.2節で導入した S_G^n 全体は $\mathcal{M}_0$ であり, S_H^n 全体は $\mathcal{M}_1$ である. すると,

Theorem 1.2(DeVogelaere[10]). 対称周期点は3種類ある.
i) r は $2k$ 周期であって, $r \in \mathcal{M}_0$ かつ $f^k r \in \mathcal{M}_0$.
ii) r は $2k$ 周期であって, $r \in \mathcal{M}_1$ かつ $f^k r \in \mathcal{M}_1$.
iii) r は $(2k-1)$ 周期であって, $r \in \mathcal{M}_0$ かつ $f^{k-1} r \in \mathcal{M}_{-1}$.

いま扱っているねじれ写像の場合, 対称軸に写像を作用させて簡単に確認できるように, 定理1.2に記述された対称周期点はバーコフ点である. [13] も見よ.

2. ホモクリニック バーコフ サドルの存在

この節で証明するのは次の補題である.

補題 2.1. 完全 (exact) シンプレクティック, 可逆ねじれ写像 f の不安定ゾーンの回転区間 (ρ_0, ρ_1) 内に p/q があって, この回転数 p/q のバーコフ周期軌道は2つしかないとする. このとき, $p/q-$ バーコフサドルは $p/q-$ ホモクリニックバーコフサドルである.

上の補題と前提Hからただちに次の結果を得る.

定理 2.2. 完全シンプレクティック, 可逆ねじれ写像 f が前提 **H** を満たすなら, C^+ の任意の近傍に p/q バーコフサドルがあって, 安定多様体と不安定多様体が (横断的に) 交わる. すなわち, p/q ホモクリニックバーコフサドルが存在する. また C^- の任意の近傍に p'/q' があって, p'/q' ホモクリニックバーコフサドルが存在する.

命題 2.3. 不安定ゾーンは, 対称軸およびその像 $\mathcal{M}_j, j = 0, 1, \ldots, n$ によって分割される. $n \to \infty$ のとき, 分割された区域の数は無限大に向かう.

証明. $\mathcal{M}_i$ と $\mathcal{M}_j$ $(i \neq j)$ は一致しない. すべて異なる曲線である. したがって, 必ず互いに交わるか, 不安定ゾーンの境界と交わる. $n \leq N$ までの分割された領域の数を k_N とする. $n = n + 1$ のとき, $\mathcal{M}_{n+1}$ はいままでの領域の境界と交わる. しかも, すでにある対称軸およびその像とは一致しないから, すでにある領域の辺を横切る. これにより, 少なくとも領域がひとつ増える. よって $k_{N+1} \geq k_N + 1$. □

補題 2.1 の証明. 円筒上で考える. 補題の回転数 p/q を取り, 対称 p/q-バーコフサドル軌道を取る. 問題を簡単にするため, このサドルの初期点は $S_G^0 \subset \mathcal{M}_0$ 上にあるとする. ほかの対称軸上にある場合も同様に扱えるので, ここでは $S_G^0 \subset \mathcal{M}_0$ の場合のみ考察する. 奇数周期なら初期点の $(q-1)/2$ 回目の像が $S_H^0 \subset \mathcal{M}_1$ または $S_H^1 \subset \mathcal{M}_1$ 上にあり, 偶数周期なら初期点の $q/2$ 回目の像が $S_G^1 \subset \mathcal{M}_0$ 上にある. 軌道点を $z_1, z_2, \ldots, z_q, z_{q+1}$ とし, $\pi_1(z_1) < \pi_1(z_2) < \ldots < \pi_1(z_q) < \pi(z_{q+1}) = \pi_1(z_1) + 2\pi$ とする. また, ポアンカレ–バーコフの定理より, 隣り合う z_i, z_{i+1} の間には楕円点または反転サドルのバーコフ軌道がある. それを w_i とする. ただし, $\pi_1(z_i) < \pi_1(w_i) < \pi_1(z_{i+1})$ とする. z_i と w_i は同一のリプシッツ曲線上に乗る.

f^q を取ると, z_i も w_i も不動点である. 以後, われわれは, z_1, w_1, z_2 のみを考える. z_1 は G の対称軸 $x = 0$ に乗っている. z_2 を対称軸の像が通る. また, w_1 を対称軸の像が通る. z_1, w, z_2 は対称線によって分割された領域の内部ではなく, その境界に位置する. 以後の便宜のため, 名前の付け換えを行なう. $z = z_1, w = w_1, z' = z_2$ とし, w を通る対称軸 (またはその像) は, ある k を用いて $\mathcal{M}_k$ と書ける. つまり, 軌道点 w_i の中には, 対称軸に乗るものがあり, その軌道点 w_i に何回写像を作用すれば, w に来るかも確定しており, したがって w が乗っている対称軸の像 $\mathcal{M}_k$ の添字 k が決まる.

z からは四方向に安定多様体, 不安定多様体の分枝が出る. z の不安定多様体の分枝のうち, z から右上方向に出るものを $W_u^r(z)$, 左下方向に出るものを $W_u^l(z)$ とし, z の安定多様体の分枝のうち, z から右下方向から入るものを $W_s^r(z)$, 左上方向に出るものを $W_s^l(z)$ と書く. 同様に z' に関しても $W_u^r(z')$, $W_u^l(z')$, $W_s^r(z')$, および $W_s^l(z')$ を導入する. われわれの目的は, $W_u^r(z)$ と $W_s^l(z')$ が交差し, $W_s^r(z)$ と $W_u^l(z')$ が交差することを示すことである. それを命題 2.5 と命題 2.6 で示す. □

補題 2.1 の証明中で導入した z, w, z' を通るリプシッツ曲線の弧を L と書く.

命題 2.5. ある回転数のバーコフ周期軌道が 1 組みしかないとする. サドル軌道を z_i, 楕円または反転サドル軌道を w_i とする. 隣り合う点 $z = z_i, w = w_i, z' = z_{i+1}$ を考える. z から右上に出る不安定多様体を W_u, z' から左上に出る安定多様体を W_s と書く. w を通る対称軸の像を $\mathcal{S} = \mathcal{M}_k$ とする. このとき W_u は $\mathcal{S}$ と交わる. W_s も $\mathcal{S}$ と交わる.

証明. z と w を結ぶリプシッツ曲線 L の弧を L_1, w と z' を結ぶ L の弧を L_2 とすると, w が時計回りの楕円点または 180 度反転のサドルであるから, $f^q L_1$ は w の近傍で右まわりに回転し, z の近傍では不安定多様体に全体として近づく. $f^q L_1$ は不動点からまっすぐ伸び, w のまわりで巻く. したがって, $k \geq 1$ があって $f^{kq} L_1$ は $\mathcal{S}_+$ (添字 $+$ は w より上の部分を表わす) と交わる. 同様に, $f^{-k'q} L_2$ $(k' \geq 1)$ も $\mathcal{S}_+$ と交わる.

一般に $f^{nq} L_1$ の一方の端点は z にあり, もう一方の端点は w にある. そして, 端点 w の近くで,

L_1 の像は回転する. したがって, ある $n \geq 1$ に対して $f^{nq}L_1$ は $\mathcal{S}_+$ と w 以外の点で交わる. L_1 上には2つの端点を除いて f^q の不動点はないから, $f^{nq}L_1$ と $f^{(n+1)q}L_1$ は端点以外に共通点を持たない. したがって, $f^{nq}L_1$ と $\mathcal{S}_+$ の交点は $f^{(n+1)q}L_1$ と $\mathcal{S}_+$ の交点は異なり, w の近傍における L_1 の像の回転を考慮すると, 後者の交点の方が, $\mathcal{S}_+$ に沿って w から遠い. もう少し正確に言うなら, $f^{nq}L_1$ と $\mathcal{S}_+$ の交点のうち $f^{nq}L_1$ に沿って z に一番近い点 s_n は $f^{mq}L_1$ と $\mathcal{S}_+$ の交点のうち $f^{mq}L_1$ に沿って z に一番近い点 s_m より, $\mathcal{S}_+$ に沿って外にある. このようにして, $\mathcal{S}_+$ 上, 単調に w から遠ざかる点列 $\{s_n\}_{n\in\mathbf{N}}$ が得られる.

この点列は必ず収束する. 実際, $\mathcal{M}_j$ $(j = 0, 1, \ldots, 2q)$ で不安定ゾーンを分割すると, L_1 を含む連結成分が一意に決まる. w から L_1 より上に出る対称軸像 S_+ はこの成分の境界の一部を構成し, S_+ 上に点 ξ があって, 別の対称軸像との交点となっている. ξ は周期点である. 点列が収束しないとすると, ある $k > 0$ があって, $f^{kq}L_1$ と $f^{(k+1)}L_1$ で囲まれる開領域に ξ は含まれる. すると ξ の像は $f^{(k-1)q}L_1$ と $f^{kq}L_1$ に囲まれる領域に含まれることになり, ξ が境界点であることに反する.

そこで点列の収束点を s とする. この s が W_u の点であることを示そう. 点列 $\{s_n\}_{n\in\mathbf{N}}$ に対応して, 点列 $\{\tilde{s}_n = f^{-nq}s_n\}$ は L_1 上にあり, n が大きいほど, z に近い. $\tilde{s} = \lim_{n\to\infty}\tilde{s}_n$ と置く. $\tilde{s}$ が z に一致することがわかれば, s は W_u の点である. 実際, 連続性により, $\lim_{n\to\infty} f^{-nq}s = \tilde{s} = z$ であるから, s は W_u 上の点である. そこで, $\tilde{s} = z$ を示す. 背理法を使う. $\tilde{s} \neq z$ とすると, $\tilde{s}$ は L_1 上, z の右にある. 上と同様, $\lim_{n\to\infty} f^{-nq}s = \tilde{s}$ である. これは L_1 上, 不動点が z と w のみであることに矛盾する. W_s に関しても f^{-q} を繰り返し L_2 に作用することによって同様な手続きにより, W_s が $\mathcal{S}$ と交わることが言える. □

命題 2.6. 命題2.5の前提の下で, W_u と W_s は同じ点で $\mathcal{S}$ と交わる.

証明. さて改めて, W_u が初めて $\mathcal{S}$ と交わる点を u と書く. W_s が初めて $\mathcal{S}$ と交わる点を $\tilde{u}$ とする. $u = \tilde{u}$ を言う. そのためには w を通る対称軸 $\mathcal{S}$ に関して $W_u^r(z)$ と $W_s^l(z')$ が対称であることが言えればいい.

そこで, 補題2.1の証明中で用いた対称 p/q バーコフ周期軌道 $z_0, z_1, \ldots, z_q$ と $w_0, w_1, \ldots, w_q$ を考える. $\pi_1(z_i) < \pi_1(w_i) < \pi_1(z_{i+1})$ であることも同様である. $w_0 \in \mathcal{M}_1$ の場合を考える. このとき, $z_0 = Hz_1$ であり, w_0 との x 座標差は等しい. そうでないとすると, $\pi_1(z_0) < \pi_1(z_0^*) < \pi_1(w_0)$ なる z_0^* が存在して $z_0^* = Hz_1$ であるか, $\pi_1(w_0) < \pi_1(z_1^*) < \pi_1(z_1)$ なる z_1^* が存在して $z_0 = Hz_1^*$ であるか, どちらかである. $O(z_0)$ が H に関して対称であるから, z_0^* も z_1^* も $O(z_0)$ に属する. すると z_0 と z_1 の間に $O(z_0)$ の別の点が入ることになり, 矛盾である. よって, z_0 と z_1 は H に関して対称な点である.

次に $w_0 \notin \mathcal{M}_1$ とする. 軌道 $O(w_0)$ は対称であるから, $1 \leq m < q-1$ があって, $f^m w_0 \in \mathcal{M}_1$ あるいは $1 \leq n < q-1$ があって, $f^n w_0 \in \mathcal{M}_0$ が成り立つ. 前者の場合を考える. $f^m w_0$ の左隣りは $f^m z_0$ であり, 右隣りは $f^m z_1$ である. 前段落と同様にして, $f^m z_0$ と $f^m z_1$ は H に関して対称な点である. このことから, z_0 と z_1 は w_0 を通る対合 $T^{-m}HT^m$ に関して対称な位置にあることがわかる. 後者の場合, やはり, $f^n z_0$ と $f^n z_1$ は $f^n w_0$ を挟んで x 座標で等距離にあることから, 上の段落の議論が使えて $f^n z_0$ と $f^n z_1$ は G に関して対称な位置にある. このことから, z_0 と z_1 は w_0 を通る対合 $T^{-n}GT^n$ に関して対称な位置にあることがわかる.

以上より, z_0 と z_1 は w_0 を通る対称軸の像 (補題2.1の証明中の $\mathcal{S}$) に関して対称の位置にあることがわかった. 次に z_0 の不安定多様体と z_1 の安定多様体, また z_0 の安定多様体と z_1 の不安定多様体がこの対称性により写り合うかどうか調べる. いま簡単のため, $\tilde{w} = f^n w_0$ が G または H の対称軸上にあるとする. $\tilde{z}_0 = f^n z_0$ と $\tilde{z}_1 = f^n z_1$ は G または H に関して対称である. $\tilde{z}_0$ から右上に出る不安定多様体の分枝を W^u, $\tilde{z}_1$ へ左上から入る安定多様体の分枝を W^s とする. W_u と W_s が対称性で写り合うことはほぼ自明である. 実際, G または H を R と書くことにして, W_u 上の点列を $\{u_i\}_i$ とし, $u_i = T^q u_{i-1}$ とおくと, 定義より, $\lim_{i\to-\infty} u_i = \tilde{z}_0$. そして,

$\tilde{u}_i = Ru_i = RT^q u_{i-1} = T^{-q}Ru_{i-1} = T^{-q}\tilde{u}_{i-1}$. つまり, $\tilde{u}_{i-1} = T^q\tilde{u}_i$, かつ $\lim_{i\to-\infty}\tilde{u}_i = \tilde{z}_1$. したがって $\{\tilde{u}_i\}_i$ は安定多様体上にある.

以上で, $\tilde{z}_0 = f^n z_0$ と $\tilde{z}_1 = f^n z_1$ の安定多様体と不安定多様体が $\tilde{w}_0$ を通る対称性で写り合うことが示された. このことから, z_0 と z_1 の安定多様体と不安定多様体が S に関して対称であることがいえる. ゆえに, z_0 と z_1 の安定多様体と不安定多様体は S と同じ点で交わる. □

§3. Proof of Theorem C

定理 C. C は円環の, 完全シンプレクティック可逆ねじれ写像 f の不安定ゾーンであるとする. その上下の境界は C^+ と C^- であり, それらの回転数は, ρ^+ と ρ^- $(\rho^- < \rho^+)$ であるとする. ねじれ写像が前提 **H** を満たすなら, 任意 $\varepsilon > 0$ に対して, 有理数回転数 $p/q \in (\rho^-, \rho^+)$ を持つ f の非バーコフ周期軌道があって, その軌道点が, C^- の ε 近傍にも C^+ の ε 近傍にも存在する.

証明. ねじれ写像 f が前提 **H** を満たすので, 2 節の定理 2.2 より, ρ^+ の十分近くに回転数 p/q があって, p/q ホモクリニック バーコフサドルが存在する. このサドルの軌道は対称周期軌道であり, S_G^0 上, C^+ の ε 近傍 $N^+(\varepsilon)$ 内に軌道点 z_0 を持つ. 軌道 $o(z_0)$ の点で, z_0 のすぐ右にある点を z_1 とする. 命題 2.6 より, z_0 から右に出る不安定多様体 $W_u^r(z_0)$ と z_1 から左に出る安定多様体 $W_s^l(z_1)$ は (横断的に) 交わる. z_0 と z_1 を結ぶリプシッツ弧があることはこれらの点がバーコフ軌道上にあることから言える. この弧の上に, 楕円, または反転サドルとなっているバーコフ周期点がひとつある. ひとつしかないことは前提 **H** の言うところである. この点を w とする. w は対称周期点である. $o(w)$ の点のうち, S_H^0 上にある点を w_0 とし, $w = f^k w_0$ であるとする. すると, w を通るのは $f^k S_H^0$ である.

さて, $W_u^r(z_0)$ と $f^k S_H^0$ との最初の交点を u とすると, $W_s^l(z_1)$ もこの点を通る. u はホモクリニック点である. $W_u^r(z_0)$ に沿って次のホモクリニック点を v とする. 標準写像における不動点のホモクリニック点の場合と同様, u と v を結ぶ $W_u^r(z_0)$ と $W_s^l(z_1)$ の弧が囲むホモクリニックロープ U が定義できる. U は、交差が横断的でない場合も定義できる。U は上記リプシッツ曲線より上にあることを注意しておく.

z_0, w, z_1 が f^q の不動点であることを考慮して, $F = f^q$ とおく. 上のホモクリニックロープ U に F^{-1} を何度か作用させると, u と v の逆像はどんどん z_0 に近づく. そしてホモクリニックロープの弧は引き延ばされて, どんどん $W_s^l(z_0)$ に近づく. このため, ホモクリニックロープの逆像は S_G^0 と交わる. その弧を I_i と書く. すなわち, $I_i = F^{-i}U \cap S_G^0$ なる弧である. 簡単にわかるように, $\lim_{i\to\infty} F^i I_i$ は弧 $[u, v] \subset W_u^r(z_0)$ に漸近する.

次に, 前提 **H** により, 回転数 p'/q' を十分 ρ^- に近く取ったとき, p'/q' ホモクリニック バーコフサドルが存在する. こんどは z_0' を $x = 0$ 上に取り, この点のすぐ右の軌道点を z_1' とし, この 2 点を結ぶリプシッツ弧上のバーコフ点を w' とする. あとは上とほぼ同様に z_0' から右に出る安定多様体を $W_s^r(z_0')$, z_1' から左に出る不安定多様体を $W_u^l(z_1')$ と記す. また $o(w')$ の点のうち, S_H^0 上にある点を w_0' とし, $w' = f^{k'} w_0'$ であるとする. すると, w' を通るのは $f^{k'} S_H^0$ である. $W_s^r(z_0')$ と $f^{k'} S_H^0$ の交点を u' とすると, $W_s^r(z_1')$ も u' を通る. u' はホモクリニック点である. $W_u^l(z_1')$ に沿って次のホモクリニック点を v' とする. u' と v' を結ぶ $W_s^r(z_0')$ と $W_u^l(z_1')$ の弧が囲むホモクリニックロープが定義できる. このホモクリニックロープ U' は上記リプシッツ曲線より下にある.

$F' = f^{q'}$ とおく. このホモクリニックロープ U' に F' を次々と作用させると, u' と v' の像はどんどん z_0' に近づく. そしてホモクリニックロープの弧は引き延ばされて, どんどん $W_u^l(z_0')$ に近づく. このため, ホモクリニックロープの像は S_G^0 と交わる. その弧を I_j' と書く. すなわち, $I_j' = (F')^j U' \cap S_G^0$ なる弧である. 簡単にわかるように, $\lim_{j\to\infty}(F')^{-j} I_j' = \lim_{j\to\infty} f^{-jq'} I_j'$ は弧 $[u', v'] \subset W_u^l(z_0')$ に漸近する.

1.1 節の系 E より, $W_u^r(z_0)$ と $W_s^l(z_1')$ は交わる. 横断的に交わるなら, $W_u^r(z_0)$ は $W_u^l(z_1')$ に漸近する弧列を持つ. したがって, $W_u^r(z_0)$ は I_j' と交わる弧を持つ.

これで準備が済んだ. I_i は i が十分大きければ弧 $[u,v] \subset W_u^r(z_0)$ に十分近い弧を持つ. この弧の f による前進像が $W_s^l(z_1')$ と交わる. したがって, I_i は i が十分大きければ I_j' と交わる. つまり, 対称軸 I_i の点で, 対称軸 I_j' に至るものがある. この軌道は対称軸に 2 点を持つから周期軌道である. これが求める周期点である.

この周期軌道が非バーコフであることは, $p'/q' < p^*/q^* < p/q$ なる p^*/q^* バーコフ軌道の Aubry グラフとこの周期軌道の Aubry グラフが何度でも交わることからただちに言える [14]. □

参考文献

[1] J. Moser 1962, *Nachr. Akad. Wiss., Gottingen, Math. Phys.* **KI**, 1.

[2] S. Aubry and P.Y. LeDaeron 1983, *Physica* **8D**, 381.

[3] J.N. Mather 1982, *Topology* **21**, 457.

[4] I.C. Percival 1980, Variational principles for invariant tori and cantori, in *Symp. on Nonlinear Dynamics and Beam-Beam Interactions*, (Eds. M.Month and J.C.Herrara), No.57, pp.310-320, Americal Institute of Physics, Conf. Proc.. または I.C. Percival 1979, *J. Phys. A: Math. Nucl. Gen.* **12**, L57.

[5] G. D. Birkhoff 1920, *Acta. Math.* **43**, 1; and Collected Math. papers, Vol. II, 111.

[6] M. R. Herman 1983, *Astérisques* **103-104**.

[7] P. LeCalvez 2000, SMF/AMS Texts and Monographs, Vol.4; the original French version has been published in 1991 by Societé Mathématiques de France.

[8] K. Tanikawa and Y. Yamaguchi 1994, *J. Math. Phys.* **35**, 2408; 1995, *ibid.* **36**, 3608.

[9] G. R. Hall 1984, *Ergod. Th. & Dynam. Sys.* **4**, 584.

[10] R. de Vogelaere 1958, in *Contributions to the Theory of Oscillations*, Fol. IV, Ann. Math. Studies No.41 (Princeton University Press).

[11] A. Katok 1982, *Ergod. Th. & Dynam. Sys.* **2**, 185.

[12] Y. Yamaguchi and K. Tanikawa 2002, *Prog. Theor. Phys.* **107**, 1117.

[13] R. S. Mackay and J. D. Meiss 1983, *Phys. Lett. A* **98**, 92.

[14] V. Bangert 1988, *Dynamics Reported* **1**, 1.

A Zone Void of Monotone Points in the Standard Map

Yoshihiro YAMAGUCHI[1] and Kiyotaka TANIKAWA[2]

[1] Teikyo Heisei University, Ichihara, Chiba 290-0193, Japan.

[2] National Astronomical Observatory, Mitaka, Tokyo 181-8588, Japan.

Abstract

Orbital points of monotone orbits are defined in twist maps. A zone Ω vertically connected and void of monotone points has been identified. Non-monotone periodic orbits have points in Ω. The destruction of the last Kolmogorov-Arnold-Moser curve and appearance of Ω are related. The expansion of the homoclinic lobes of the stable and unstable manifolds is a cause of the appearance of Ω.

1 Introduction

For near integrable twist maps of the cylinder, the Kolmogorov-Arnold-Moser(KAM) theory[1-3] says that a lot of rotationally invariant curves (KAM tori) still survive as long as the perturbations are small enough. Vertical motion is hampered by these curves. According to the Aubry-Mather theory,[4,5] monotone or rotationally ordered orbits with irrational rotation numbers are quasi-periodic. If these are not on the KAM tori, these form cantori or the Aubry-Mather sets. A cantorus has gaps. A gap is a pair of points such that there are no points of the cantorus between them in the sense of cyclic order of the horizontal coordinate. The orbit of a gap is called a hole. In around ten years ago, there have been extensive researches[6-9] of cantori, their gaps and holes, and bifurcations with reference to anti-integrable limits introduced by Aubry & Abramovici.[10] Vertical motions can be possible through gaps, though motions are slow when gaps are narrow.

It has been proved[6] that there is only one hole for the standard map near the anti-integrable limit. It has been also shown that there are as much holes as the number of potential wells near anti-integrable limit for the maps with multiharmonic potentials. Since the number of cantori are uncountable because there are at least one cantori for each irrational rotation number, the area of the phase space occupied by cantori might be of positive measure. It seems there is no proof or disproof for this. In any case, non-monotone points play a major role in the dynamics of the system far from the integrable situation.

Our interest here is the distribution of the areas occupied solely by non-monotone points. In the present paper, we propose a numerical procedure to identify non-monotone points, and then use this procedure to look for the behavior of the set of non-monotone points as the parameter changes. A priori, monotone points might be dispersed all over the phase space. We shall derive the existence of an infinite vertical strip void of monotone points which connects $y = -\infty$ and $y = +\infty$. This strip is a manifestation of chaotic motions along the vertical direction. As for the gap of cantori, our procedure bound the width of the gap from below, that is, the true width of the gaps is wider than our estimate. Meiss[11] noted that the largest gap of a cantorus for the standard map

appears around $x = \pi$ where the 'potential' is minimum. It has been shown that the points of long-periodic orbits are localized (see Fig. 1 of Ref. 7) for a large perturbation parameter. This indirectly shows that the width of the gaps of cantori increases with the perturbation parameter and accordingly the monotone points are localized. Monotone points are driven to a small region in the phase space if the perturbation parameter increases. We will see this in our figures.

We consider the standard map f defined in the cylinder $\mathbf{S}^1 \times \mathbf{R}$ ($\mathbf{S}^1$ is a circle and $\mathbf{R}$ is a real line):

$$\begin{aligned} y_{n+1} &= y_n + a\varphi(x_n), \\ x_{n+1} &= x_n + y_{n+1}, \end{aligned} \tag{1.1}$$

with $x \in \mathbf{S}^1$ and $y \in \mathbf{R}$ where a is a positive parameter and $\varphi(x) = \sin x$. There are two fixed points $P = (0, 0)$ and $Q = (\pi, 0)$, where P is a saddle and Q is an elliptic point($0 < a < 4$) or a saddle with reflection($a > 4$).

It is well known that the standard map f is expressed as a product of two involutions:[15]

$$f = H \circ G, \tag{1.2}$$

where

$$G\begin{pmatrix} x \\ y \end{pmatrix} = \begin{pmatrix} -x \\ y + a\varphi(x) \end{pmatrix} \quad \text{and} \quad H\begin{pmatrix} x \\ y \end{pmatrix} = \begin{pmatrix} -x + y \\ y \end{pmatrix} \tag{1.3}$$

with $G^2 = H^2 = \mathrm{Id}$ and $\det \nabla G = \det \nabla H = -1$.

The sets of fixed points of G and H are the symmetry axes. Two axes S_1 and S_2 are the symmetry axes of G and S_3 and S_4 are those of H.

$$\begin{aligned} &S_1 : x = 0 \quad \text{and} \quad S_2 : x = \pi \quad \text{for} \quad G, \\ &S_3 : y = 2x \quad \text{and} \quad S_4 : y = 2(x - \pi) \quad \text{for} \quad H. \end{aligned} \tag{1.4}$$

Let $\hat{f} : \mathbf{R}^2 \to \mathbf{R}^2$ be the unique lift of f which fixes the points P and Q. The lift of a point $z = (x, y) \in \mathbf{S}^1 \times \mathbf{R}$ will be denoted by $\hat{z} = (x, y)$ with $x \in \mathbf{R}$. We also denote this by $z = \mathrm{pr}(\hat{z})$ or $\hat{z} = \mathrm{pr}^{-1}(z)$. The projection to the first coordinate is denoted by $x = \pi_1(z)$ and $x = \pi_1(\hat{z})$. The orbit of $z = (x, y) \in \mathbf{S}^1 \times \mathbf{R}$ or its lift $\hat{z} = (x, y) \in \mathbf{R}^2$ is denoted by $o(z) = \{f^k z : k \in \mathbf{Z}\}$ or $o(\hat{z}) = \{\hat{f}^k \hat{z} : k \in \mathbf{Z}\}$. The extended orbit of $\hat{z}$ is $eo(\hat{z}) = \{\hat{f}^k \hat{z} + (l, 0) : k, l \in \mathbf{Z}\}$. A point z is said to be p/q–periodic if $\hat{f}^q \hat{z} - (p, 0) = \hat{z}$. The orbit of a p/q–periodic point is called a p/q–periodic orbit. If the orbit $o(z)$ of a point z has an orbital point on the symmetry axis, then the orbit is called symmetric. A symmetric orbit is periodic if and only if the orbit has exactly two points on the symmetry axes[12].

2 Monotone and non-monotone orbits

Here, we introduce a *monotone orbit* and a *non-monotone orbit* on the cylinder.

Definition 2.1(Meiss[11], LeCalvez[13]). A set $\Sigma \subset \mathbf{S}^1 \times \mathbf{R}$ is called a *monotone set* if it satisfies the following conditions:

i) Σ is invariant under f;

ii) the restriction of π_1 to Σ is injective;

iii) for each pair of $\hat{z}$ and $\hat{z}'$) in Σ,

$$\pi_1(\hat{z}) < \pi_1(\hat{z}') \implies \pi_1(\hat{f}\hat{z}) < \pi_1(\hat{f}\hat{z}'). \tag{2.1}$$

The orbit of a point of a monotone set is called a monotone orbit. Examples of monotone orbits are a monotone (or Birkhoff-type) periodic orbit, an orbit in a KAM (Kolmogorov–Arnold–Moser) curve and an orbit in a Aubry–Mather set.

Definition 2.1 characterizes a set of points which are the extension of the notion of monotone periodic points. The original definition of the Aubry-Mather set seems to coincide with that of a monotone set. In the present paper, we are interested in the orbits whose projection to the x-axis behave not like the rigid rotation. For this purpose, Definition 2.1 is not convenient because it does not characterize these orbits. In fact, a non-monotone set may contain a monotone subset.

Let us introduce a non-monotone orbit in a different manner. An orbit $o(z)$ is said to be non-monotone if there are $\hat{r}, \hat{s} \in eo(\hat{z})$ and an integer $k \neq 0$ such that

$$\pi_1(\hat{r}) < \pi_1(\hat{s}) \ \Rightarrow \ \pi_1(\hat{f}^k\hat{s}) \leq \pi_1(\hat{f}^k\hat{r}). \tag{2.2}$$

A point on the cylinder of a non-monotone orbit will be called a *non-monotone point.* An example of non-monotone orbits is an orbit on an invariant curve encircling a stable periodic point. In the case of periodic orbits, non-monotone orbits are also called non-monotone or non-Birkhoff periodic orbits.[15] There are two types of them:

Definition 2.2. Suppose a p/q-periodic point $z \in \mathbf{S}^1 \times \mathbf{R}$ is given.

(1) If there are $\hat{r}, \hat{s} \in eo(\hat{z})$ with $\hat{r} \in o(\hat{s})$ and an integer $k \neq 0$ such that

$$\pi_1(\hat{r}) < \pi_1(\hat{s}) \ \Rightarrow \ \pi_1(\hat{f}^k\hat{r}) \geq \pi_1(\hat{f}^k\hat{s}), \tag{2.3}$$

then, point z is called a non-Birkhoff periodic point of turning-back type and its orbits is called a non-Birkhoff periodic orbit of turning-back type.

(2) If for any $\hat{r}, \hat{s} \in eo(\hat{z})$ with $\hat{r} \in o(\hat{s})$,

$$\pi_1(\hat{r}) < \pi_1(\hat{s}) \ \Rightarrow \ \pi_1(\hat{f}\hat{r}) < \pi_1(\hat{f}\hat{s}) \tag{2.4}$$

holds and if there are $\hat{r}', \hat{s}' \in eo(\hat{z})$ with $\hat{r}' \notin o(\hat{s}')$ and an integer $k \neq 0$ such that

$$\pi_1(\hat{r}') < \pi_1(\hat{s}') \ \Rightarrow \ \pi_1(\hat{f}^k\hat{r}') \geq \pi_1(\hat{f}^k\hat{s}'), \tag{2.5}$$

then, point z is called a non-Birkhoff periodic point of passing-by type and its orbit is called a non-Birkhoff periodic orbit of passing-by type.

Remark 1. The orbits of turning-back type have turning points, whereas those of passing-by type do not. Here point p_k is called a turning point if

$$\begin{array}{l} \pi_1(\hat{p}_{k-1}) \leq \pi_1(\hat{p}_k), \pi_1(\hat{p}_k) > \pi_1(\hat{p}_{k+1}), \text{ or} \\ \pi_1(\hat{p}_{k-1}) \geq \pi_1(\hat{p}_k), \pi_1(\hat{p}_k) < \pi_1(\hat{p}_{k+1}) \end{array} \tag{2.6}$$

are satisfied, where $p_k = T^k p_0$ $(0 \leq k < q)$. As for the y coordinates, if $\pi_2(p_k) \geq 0$ (resp., $\pi_2(p_k) \leq 0$), then $\pi_2(p_{k+1}) < 0$ (resp., $\pi_2(p_{k+1}) > 0$). If the rotation number

is $1/q$ ($q \geq 2$), then all non-monotone orbits are of turning-back type. If the rotation number is p/q ($p \geq 2, q \geq 2$), then both types are available.

Remark 2. If a periodic point is in the homoclinic lobe bounded by stable and unstable manifolds of fix point Q, then it is a non-Birkhoff periodic point of turning-back type. If, on the other hand, a non-Birkhoff periodic point is sandwiched by two KAM curves of distinct rotation numbers of the same sign, then it is a non-Birkhoff periodic point of passing-by type.

3 A procedure to find non-monotone orbits

In this section, we propose a sufficient condition that an orbit be non-monotone and use this condition in the next section as a numerical procedure to obtain a region occupied by non-monotone points. In particular, we use this procedure to identify an infinite vertical strip which contains no monotone orbits. Here by 'infinite' we mean that the strip extends from $y = -\infty$ to $y = +\infty$.

Take a point $z = (x, y) \in \mathbf{S}^1 \times \mathbf{R}$, $\pi < x < 2\pi$. We have $Gz = (2\pi - x, y + a\varphi(x))$ and hence $\pi_1(Gz) < \pi_1(z)$. We summarize the properties of orbits of these points z and Gz. It is to be noted that when we consider a lifted point and its reflection with respect to symmetry G, the expression of G should be specified. In the present work, the line $x = \pi$ is taken to be the symmetry axis of G in the universal cover.

[1] If z is p/q–periodic, so is Gz. Their orbits have the same stability. If $eo(\hat{z}) = eo(G\hat{z})$, then $o(z)$ is symmetric periodic. If $eo(\hat{z}) \neq eo(G\hat{z})$, then both $o(z)$ and $o(Gz)$ are non–symmetric periodic.[16]
[2] If $o(z)$ is a Birkhoff-type periodic orbit, then so is $o(Gz)$. In this case, these orbits are located on the same graph of a Lipschitz function.[13,14]
[3] If $o(z)$ is on a KAM curve, then $o(Gz)$ is on the same curve. If $o(z)$ is on an Aubry–Mather set, then $o(Gz)$ is on the same set. The KAM curve is a graph of a Lipschitz function and the Aubry–Mather set is on a graph of a Lipschitz function.

Definition 3.1. A point $z = (x, y) \in \mathbf{S}^1 \times \mathbf{R}$ ($\pi < x < 2\pi$) is said to satisfy $\mathcal{G}_k$–non–monotone condition if for a given $k \geq 1$,

$$\mathcal{G}_k(x, y) \equiv \pi_1(\hat{f}^{-k}\hat{z}) - \pi_1(\hat{f}^{-k}G\hat{z}) \leq 0. \tag{3.1}$$

A point $z = (x, y) \in \mathbf{S}^1 \times \mathbf{R}$ ($\pi < x < 2\pi$) is said to satisfy $\mathcal{G}$–non–monotone condition if it satisfies $\mathcal{G}_k$-non-monotone condition for some $k \geq 1$.

Let us define sequences of sets for $k = 1, 2, 3, \ldots$ as follows:

$$\begin{aligned} U_k = \{z = (x, y) \in \mathbf{S}^1 \times \mathbf{R} \mid\ & z \text{ satisfies the } \mathcal{G}_k\text{–non – monotone condition but} \\ & z \text{ does not satisfy the } \mathcal{G}_j\text{–non – monotone} \\ & \text{condition for } 1 \leq j < k\} \end{aligned} \tag{3.2}$$

and

$$V_k = GU_k. \tag{3.3}$$

Let

$$U = \bigcup_{k\geq 1} U_k \quad V = \bigcup_{k\geq 1} V_k, \quad k = 1, 2, 3, \ldots \tag{3.4}$$

and

$$W = U \cup V. \tag{3.5}$$

By definition, U_i and U_j $(i \neq j)$ are disjoint.

Proposition 3.1. If $o(z)$ is a non-monotone orbit, so is $o(Gz)$.

Proof. In fact, this is trivially true if $eo(\hat{z}) = eo(G\hat{z})$. Let us consider the case $eo(\hat{z}) \neq eo(G\hat{z})$. Then there are $\hat{v}, \hat{w} \in eo(\hat{z})$ and $j \neq 0$ such that

$$\pi_1(\hat{v}) < \pi_1(\hat{w}) \quad \text{and} \quad \pi_1(\hat{f}^j\hat{w}) \leq \pi_1(\hat{f}^j\hat{v}) \tag{3.6}$$

On the other hand, we have $G\hat{v}, G\hat{w} \in eo(G\hat{z})$ and $\pi_1(G\hat{w}) < \pi_1(G\hat{v})$. In addition, we have $\hat{f}^j G\hat{w} = G(\hat{f}^{-j}\hat{w})$ and $\hat{f}^j G\hat{v} = G(\hat{f}^{-j}\hat{v})$. By the second inequality of Eq.(3.2), we have $\pi_1(\hat{f}^{-j}G\hat{v}) \leq \pi_1(\hat{f}^{-j}G\hat{w})$. Then

$$\pi_1(G\hat{w}) < \pi_1(G\hat{v}) \quad \text{and} \quad \pi_1(\hat{f}^{-j}G\hat{v}) \leq \pi_1(\hat{f}^{-j}G\hat{w}) \tag{3.7}$$

Thus $o(Gz)$ is a non-monotone orbit. Q.E.D.

Proposition 3.2. If z satisfies $\mathcal{G}$-non-monotone condition, then both $o(z)$ and $o(Gz)$ are non-monotone orbits.

Proof. If $eo(z) \neq eo(Gz)$, then at least one of $eo(z)$ and $eo(Gz)$ is a non-monotone orbit. This can be easily shown by introducing the Aubry graph. Let $\hat{z} = (x, y)$, and let $o(\hat{z}) = \{z_i = (\hat{x}_i, y_i)\}_{i\in\mathbf{Z}}$ be its orbit. For all i, the piecewise linear graph connecting $(i, \hat{x}_i)$ and $(i+1, \hat{x}_{i+1})$ is called the Aubry graph of $o(\hat{z})$. According to Bangert[17], Aubry graphs of two monotone orbits cross each other at most once. As is easily confirmed, Aubry graphs of $o(\hat{z})$ and $o(G\hat{z})$ which both satisfy $\mathcal{G}$-non-monotone condition cross each other at least twice. Therefore, either of $o(z)$ and $o(Gz)$ is a non-monotone orbit. By Property 3.1, both orbits are non-monotone orbits. Q.E.D.

Proposition 3.2 says that the set W is contained in the set of all non-monotone points. We here verify that W is strictly smaller than the set of all non-monotone points by showing examples.

Examples. (1) Consider a point z satisfying $\hat{z} = H\hat{z}$. Suppose the orbit of z is a periodic orbit of passing-by type. Then evidently, z does not satisfy $\mathcal{G}$-non-monotone condition.

(2) Let u be the first intersection point of the unstable manifold emanating from P to the right with $x = \pi$. Let $z = fu$.

Now we define a vertical strip void of monotone points.

Definition 3.2. Let Ω be the open region bounded by two vertical lines $x = c_1$ and $x = c_2$ with $0 \leq c_1 < c_2 \leq 2\pi$. If $\Omega \subset W$, then $\Omega = \Omega(c_1, c_2)$ is called a *vertical non-monotone strip* . If c_1 and c_2 are maximal in the sense that a wider vertical strip containing

$\Omega(c_1, c_2)$ is not a vertical non-monotone strip, then $\Omega(c_1, c_2)$ is called a *maximal vertical non-monotone strip.*

Proposition 3.3. A vertical non-monotone strip exists in the standard map for $a > 2$.

Proof. For $k = 1$, by directly using the lift map $\widehat{f}$

$$y_{n+1} = y_n + a\varphi(\widehat{x}_n), \quad \widehat{x}_{n+1} = \widehat{x}_n + y_{n+1}, \tag{3.8}$$

we find that the $\mathcal{G}_1$-non-monotone condition does not depend of y_0. This condition for point z is written as

$$\mathcal{G}_1(\widehat{x}) = 2(\widehat{x} - \pi) + a \sin \widehat{x} \leq 0. \tag{3.9}$$

It is easy to show that there exists x^* $(\pi < x^* < 2\pi)$ such that $x, \pi < x \leq x^*$ satisfies in Eq. . (3) at $a > 2$. This implies the existence of a vertical non-monotone strip. (Q.E.D.)

Remark. It is to be noted that the above condition (3.9) is the same as the Lipschitz criteria (Eq.(4.7) of Meiss, 1992) that the slope exceeds infinity. This is natural, since non-monotone condition is equivalent with the slope-infinity condition. However, the meaning we give is different from the Lipschitz criteria. Our condition is not for an orbit on rotationally invariant curve. We are consider general orbits and our condition requires that the cyclic order be violated. This requirement is in general stronger than the Lipschitz condition.

4 Numerical results

In this section, we will show the behavior of the set of non-monotone points as the parameter changes.

Before showing the main result, let us first examine the utility of our procedure using the familiar example of estimating the critical value for the destruction of the last KAM curve. Our procedure like others (e.g., Greene[18](1979), Chirikov[19] (1979, Fig.5.3), MacKay and Percival[20](1985), Yamaguchi & Tanikawa[21](1999) bounds the critical value from above. We make a smaller starting from $a = 2$. Our procedure is basically similar to that in MacKay and Percival if applied to the last KAM curve. They iterated the direction vector until its direction reverses, whereas we iterate a special pair of points, $\hat{z}$ and $G\hat{z}$, until the order of the x-coordinates reverses.

By Proposition 3.3, for a given $a > 2$, $\Omega(\pi, \hat{x}^*)$ with $\hat{x}^* = \pi + (2/a)\sin(\hat{x}^* - \pi)$ is a vertical non-monotone strip. This strip is not maximal because only $\mathcal{G}_1$-non-monotone condition is used. We can obtain a wider non-monotone strip. We are going to numerically confirm the existence of a vertical non-monotone strip in the vicinity of $x = \pi$ for a smaller than 2. We look at $\mathcal{G}_k(x, y)$ $(k \geq 2)$. These are functions of x and y. In Fig.1 as examples, functions $\mathcal{G}_2(x, y), \mathcal{G}_3(x, y), \mathcal{G}_4(x, y)$ and $\mathcal{G}_5(x, y)$ are displayed for different values of a. In order to obtain the value of a at which all vertical non-monotone strips disappear, we assume that the vertical non-monotone strip spreads from $x = \pi$ to $x = \pi + 0.001$ and take z on the line $x = \pi + 0.001$. We calculate $\mathcal{G}_k(y)$ up to $k = 3233$ and have the critical value $a_c = 0.9718$. This value is slightly larger than $0.9716\cdots$ evaluated by Greene at which the last KAM curves with $\nu = (\sqrt{5} - 1)/2$ and $(3 - \sqrt{5})/2$ $(0 < \nu < 1)$ are destroyed.

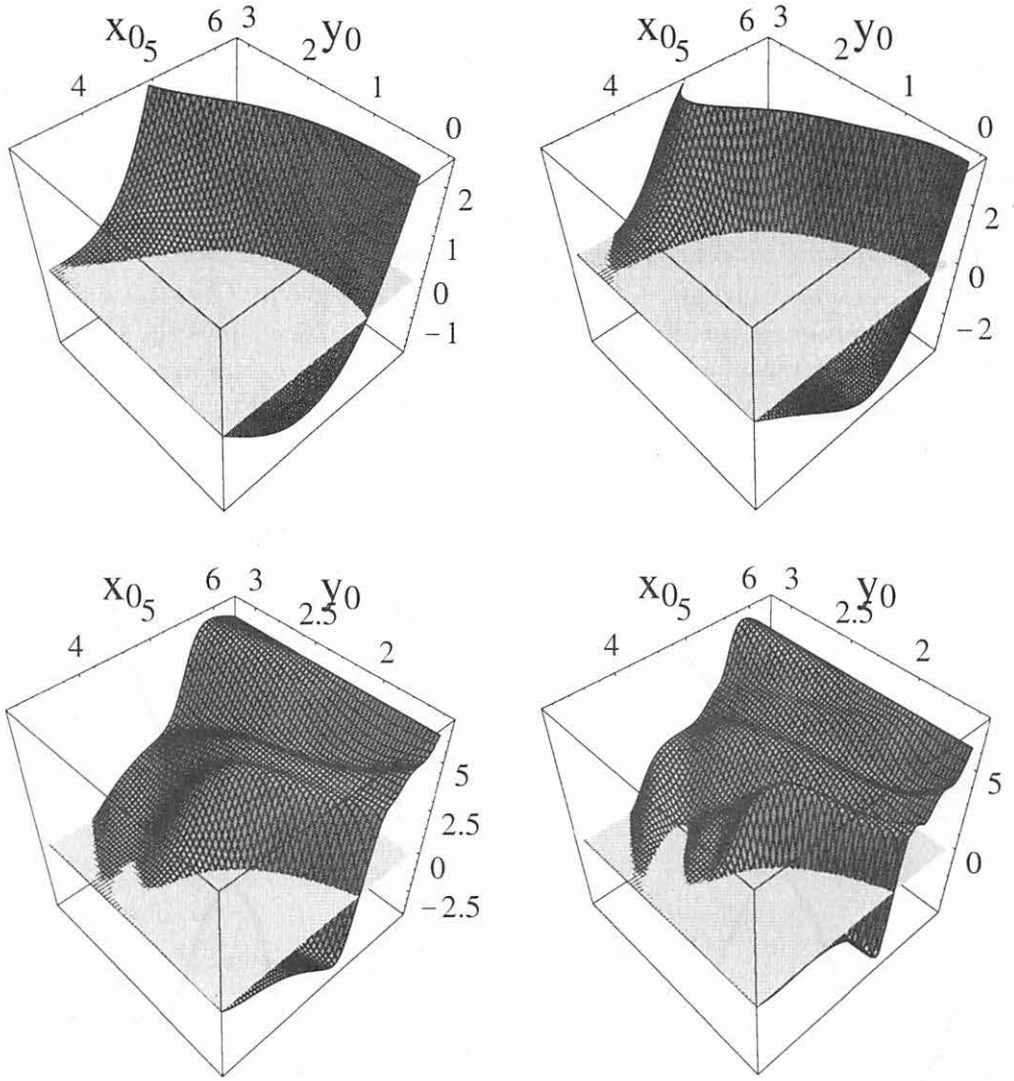

Figure 1: Three dimensional plots of $\mathcal{G}_2(x, y)$ at $a = 1.42$ (upper left), $\mathcal{G}_3(x, y)$ at $a = 1.24$ (upper right), $\mathcal{G}_4(x, y)$ at $a = 1.16$ (bottom left) and $\mathcal{G}_5(x, y)$ at $a = 1.13$ (bottom right). $\mathcal{G}_k(x, y)$ is positive at $x = \pi + 0.001$ in all figures if a is decreased by 0.01.

Let us show our main result. We increase parameter $a > 0$. The vertical line $x = \pi$ is obviously not contained in W, because it contains symmetric Birkhoff periodic points. On the other hand, Proposition 3.3 suggests that vertical non-monotone strips, starting as very thin strips at both sides of $x = \pi$, expand toward the right and left directions as a increases.

As we have pointed out in the Introduction, the standard map is considered to have a so-called 'one hole cantori', that is, all the gaps of cantori are obtained by iterating one largest gap. This has been proved near the anti-integrable limit(Baesens&MacKay, 1993). For smaller values of a, the proof seems not available. We have two evidence for the 'one-hole' nature.

First numerical evidence is the distribution function $\rho(x)$ of points in the last KAM

curves.[15] $\rho(x)$ is minimum at $x = \pi$ and $\rho(\pi)$ tends to zero as $a \to a_c$. This suggests that the gap of the last KAM curves open around $x = \pi$. The second evidence is that $x = \pi$ is the first gap obtained from $\mathcal{G}_k$–non–monotone conditions. The positions of the potential minimum moves starting from π to the right as a increases (see Fig.2 (a)). On the two-hole Aubry-Mather sets, Baesens and Mackay have studied the map having 'two holes Aubry–Mather set'. Using Eq. (3), it is easy to confirm that the map with $f(x) = a\sin x + b\sin(nx)$ $(n = 2, 3, \cdots)$ has 'n–hole Aubry–Mather set'. Fig. 2(a) shows the case of the standard map at which one hole exists around $x = \pi$. Fig. 2(b) is the case studied by Baesens–Mackay at which one hole exists around $x = 5.5$ and the other one exists at the symmetric position (not displayed). Fig. 2(c) shows the three hole case that one hole exists in the vicinity of $x = \pi$, the second one exists around $x = 5.7$ and the third one exists at the symmetric position (not displayed). Fig. 2(d) shows the case with the four holes.

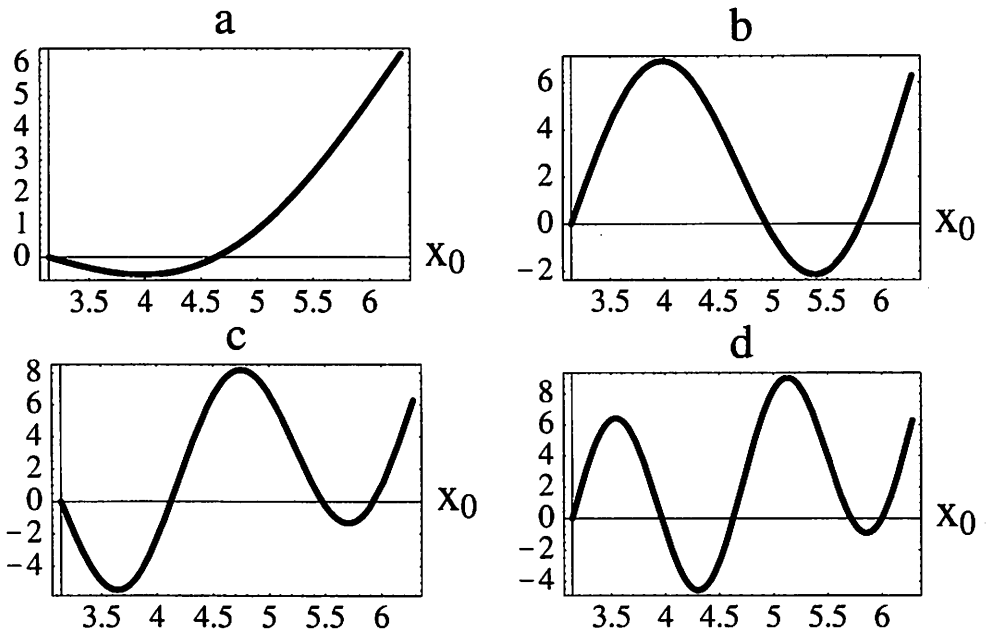

Figure 2: (a) $\mathcal{G}_1(x) = 2(x-\pi) + 2.5\sin x$, (b) $\mathcal{G}_1(x) = 2(x-\pi) + 6\sin 2x$, (c) $\mathcal{G}_1(x) = 2(x-\pi) + \sin x + 6\sin 3x$ and (d) $\mathcal{G}_1(x) = 2(x-\pi) + \sin x + 6\sin 4x$.

Now, the monotone points located in the vicinity of $x = \pi$ for small a are pushed away toward the right and left directions as a increases. Several orbits of Birkhoff saddles are displayed in Fig. 3 at $a = 1$. We can confirm the fact mentioned above. In Fig. 4, the stable and unstable manifolds and non-monotone orbits and elliptic monotone orbits with $q = 17$ are displayed at $a = 3$. It is easy to observe that the stable manifold of the saddle located at $(2\pi, 0)$ penetrates into the gap in the right side of $x = \pi$ and the stable manifold of the saddle located at $(0, 2\pi)$ penetrates into the gap in the left side of $x = \pi$. The regions at which the points of monotone periodic saddles and monotone periodic elliptic points are located are mainly shrunk in the vicinity of S_3 and S_4. It is difficult to plot periodic orbits with long periods at $a = 3$.

Next let us consider the distribution of monotone orbits along the x direction. We consider as a representative Birkhoff-type orbits located in the vicinity of the last KAM curve with $\nu = (3-\sqrt{5})/2$ and we measure the distance D between $x = \pi$ and the nearest neighbor point located in the right side of $x = \pi$. The distance D for Birkhoff-type orbits with $\nu = 44/377,\ 377/987,\ 610/1597$ are shown in Fig. 5. For these orbits, the nearest neighbor point is a saddle. Our results mean that the last KAM curve is isolated and the region containing the non-monotone orbits exists in the vicinity of it. This concept was proved by Boyland–Hall.[22)]

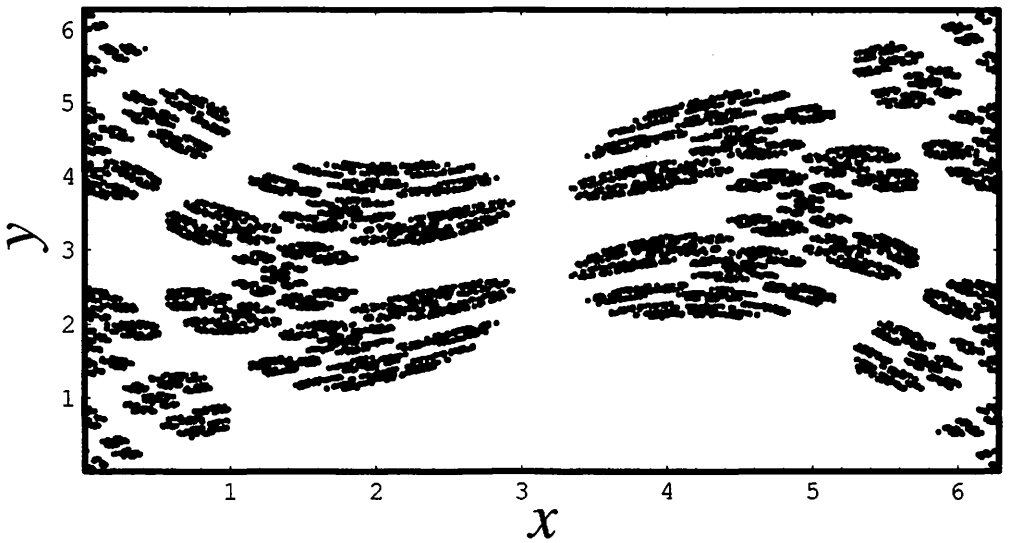

Figure 3: Monotone periodic saddles with $q = 31, 41, 53, 61$ and 73 are displayed at $a = 1$.

5 Discussions

If a vertical non-monotone strip exists, then evidently there exist no rotationally invariant curves. We have a question in a reverse direction. Does a vertical non-monotone strip exist if there are no rotationally invariant curves? Numerical evidence is given in this paper when we estimated the critical parameter value for the destruction of the last KAM curve. In the standard map, every Aubry-Mather set has a gap around $x = \pi$. Therefore as long as the last KAM curve disintegrates, a vertical non-monotone strip seems to appear around $x = \pi$.

The unstable manifold and the stable manifold of the saddles of Birkhoff type have the intersection points if Ω exists. In fact, since f is exact, there are two configurations of the stable and unstable manifolds of the saddle of Birkhoff type, that is, the saddle connection and the intersection of them. In the following, we show that the configuration of the saddle connection has a contradiction. The saddle connection is an invariant curve separating the cylinder and the universal cover. Therefore it is a graph for Lipschitz function. Here, we assume the existence of Ω. Thus the intersection interval L of the saddle connection and Ω exists. Take z in L. Then $Gz = Gz$ exists in GL located in the

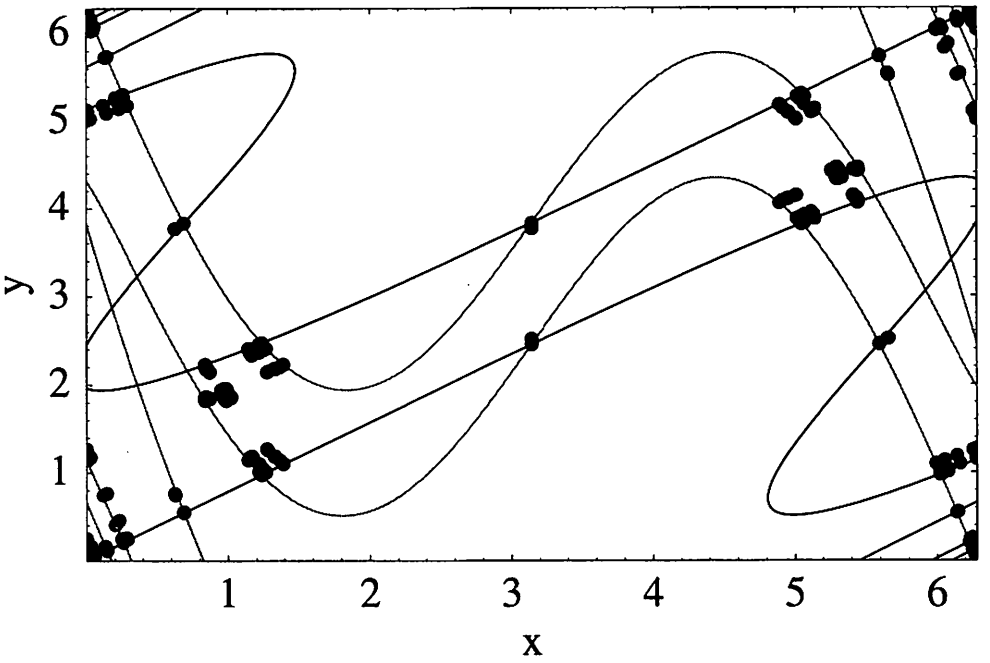

Figure 4: Points of monotone periodic saddles and ellipses with periods $q = 17$ starting from $x = 0$ (BSOs) and π (BEOs) at $a = 3$. The stable and unstable manifolds are also displayed.

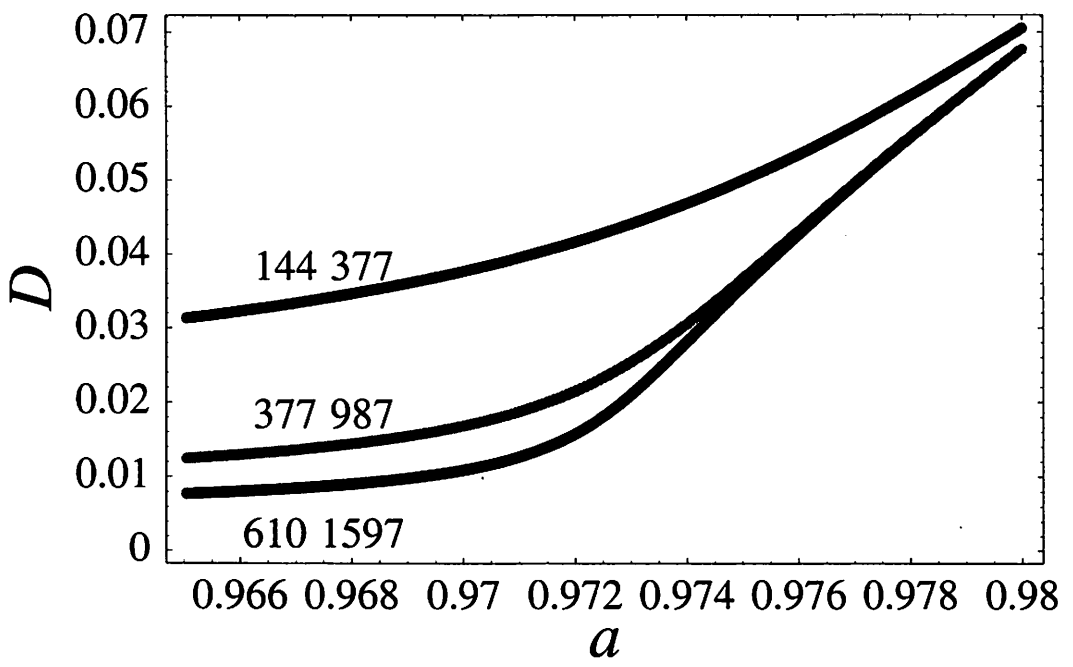

Figure 5: Distance $D(= x^* - \pi)$ as a function of a in the vicinity of a_c.

same saddle connection. The backward and the forward images of z and Gz located on the saddle connection accumulate toward the saddle and satisfy Birkhoff condition since the saddle connection is a graph. This is a contradiction.

In the present paper, we give results only for the standard map. Our procedure can be applied to a general reversible twist maps.

References

[1] A.N. Kolmogorov, *Dokl. Akad. Nauk. USSR* **98** (1954), 527.

[2] V.I. Arnold, *Russ. Math. Surveys* **16** (1963), 85.

[3] J. Moser, *Nachr. Akad. Wiss. Gottingen, II Math. Phys.* **1** (1962), 1.

[4] S. Aubry and P.Y. LeDaeron, *Physica* **D 8** (1983), 381.

[5] J. N. Mather, *Topology* **21** (1982), 457; *Comment. Math. Helv.* **60** (1985), 508.

[6] C. Baesens and R.S. MacKay, *Physica* **D69** (1993), 59.

[7] C. Baesens and R.S. MacKay, *Physica* **D71** (1994), 372.

[8] J.A. Ketoja and R.S. MacKay, *Physica* **D73** (1994), 388.

[9] J.A. Ketoja and R.S. MacKay, *Physica* **D35** (1989), 318.

[10] S. Aubry and G. Abramovici, *Physica* **D43** (1990), 199.

[11] J. D. Meiss, *Rev. Mod. Phys.* **64** (1992), 795.

[12] R. de Vogelaere, in *Contributions to the Theory of Oscillations*, Fol. IV, Ann. Math. Studies No.41 (Princeton University Press,1958).

[13] P. Le Calvez, *Dynamical properties of diffeomorphisms of the annulus and of the torus*, SMF/SMS Texts and Monographs Vol.4 (2000).

[14] G. D. Birkhoff, *Trans. Amer. Math. Soc.* **14** (1913), 14; and Collected Math. Papers, Vol.I, 673: *Acta Math.* **43** (1920), 1; and *Collected Math. Papers*, vol.II, 111.

[15] G. R. Hall, Ergod. Th. & Dynam. Sys. **4** (1984), 584.

[16] K. Tanikawa and Y. Yamaguchi, *Prog. Theor. Phys.* **108** (2002), 987.

[17] V. Bangert, *Dynamics Reported* **1** (1988), 1.

[18] J. M. Greene, *J. Math. Phys.* **20** (1979), 1183.

[19] B. V. Chirikov, *Phys. Repts.* **52** (1979), 263.

[20] R. Mackay and I. Percival, *Commum. Math. Phys.* **98** (1985), 469.

[21] Y. Yamaguchi and K. Tanikawa, *Prog. Theor. Phys.* **101** (1999), 1.

[22] P. Boyland and G. R. Hall, *Topology* **26** (1987), 21.

EFFICIENT ORBIT INTEGRATION BY SCALING FOR KEPLER ENERGY CONSISTENCY

TOSHIO FUKUSHIMA
National Astronomical Observatory, 2-21-1 Osawa, Mitaka, Tokyo 181-8588, Japan; Toshio.Fukushima@nao.ac.jp

ABSTRACT

Extending Nacozy's idea of manifold correction by using the concept of the integral invariant relation, we propose a new approach to numerically integrate quasi-Keplerian orbits. The method integrates the time evolution of the Kepler energy and the usual equation of motion simultaneously. Then it directly adjusts the integrated position and velocity by a spatial scale transformation in order to satisfy the Kepler energy relation rigorously at every integration step. The scale factor is determined by solving an associated cubic equation precisely with the help of Newton's method. In treating multiple bodies, the Kepler energies are integrated for each body and the scale factors are adjusted separately. The implementation of the new method is simple, the added cost of computation is low, and its applicability is wide. Numerical experiments show that the scaling reduces the integration error drastically. In the case of pure Keplerian orbits, the truncation error grows linearly with respect to time, and the round-off error grows more slowly than that. When perturbations exist, a component that grows with the second or a higher power of time appears in the truncation error, but its magnitude is reduced significantly as compared with the case without scaling. The rate of decrease varies roughly as the 5/4 to 5/2 power of the strength of the perturbing acceleration, where the power index depends on the type of perturbation. The method seems to suppress the accumulation of round-off errors in the perturbed cases, although the details remain to be investigated. The new approach provides a fast and high-precision device with which to simulate the orbital motions of major and minor planets, natural and artificial satellites, comets, and space vehicles at a negligible increase in computational cost.

Key words: celestial mechanics — methods: numerical

1. INTRODUCTION

Numerical integration has been the major tool for investigating complicated problems in celestial mechanics and dynamical astronomy. Thus, it is indispensable to know the accuracy of one's integrations in order to obtain reliable results. However, this is a difficult task. Aside from the direct methods of comparison, some of which we discuss below in § 3.1, a common tactic is to monitor the variation of the integrals of motion, such as the total energy or the total angular momentum.

Unfortunately, this has two main drawbacks. One is that the approach is useless in dissipative and other non-conservative systems, since no integrals of motion are available in these cases. Also, it is usually difficult[1] to find the integrals of motion in the restricted problems. The other drawback is that the constancy of the integrals of motion is merely a necessary condition for a correct integration. In fact, there are many cases in which the integrated position and velocity are erroneous while yielding the correct value of the total energy or other conserved quantities (see the discussion by Huang & Innanen 1983; see also example [4.4] of Hairer, Lubich, & Wanner 1999). A typical quantity easily conserved by numerical integrations is the direction of the total angular momentum vector.[2]

In order to overcome these demerits, Szebehely & Bettis (1971) considered checking an *integral invariant relation*, namely, following the time development of some analytical function (or functions) of position and velocity and comparing its integrated value with the value evaluated from the integrated position and velocity. They suggested using the first time derivative of the total moment of inertia, $\dot{I}$, as such a function in the case of a gravitational N-body system. For a subsystem of "binaries," a natural choice is the Kepler energy. It is the total specific energy in the case of pure Keplerian orbits and, therefore, is a conserved quantity in that case. Of course, it is no longer a constant of the motion when perturbations exist. Yet, its time evolution is easily integrated. Recently, by extending the idea in a more general form, Mikkola & Innanen (2002) adopted the individual Hamiltonians H_j as such functions to be integrated simultaneously and succeeded in establishing an effective way to monitor the accuracy of N-body symplectic integrations.

If this viewpoint is reversed, the monitoring of errors naturally leads to the correction of errors. A popular example of such corrections is the so-called *stabilization* of orbits (Baumgarte 1972). The basic idea is to add an artificial term in the equation of motion that enforces a reduction of the observed difference in the integral invariant relations. Usually some kind of energy is selected as the function to be monitored, such as the Kepler energy in the original work of Baumgarte (1972). In this case, the technique is referred to as *energy stabilization*. Note that this stabilization is implicitly used in the well-known Kustaanheimo-Stiefel (K-S) regularization, where the Kepler energy in the K-S equation of motion is replaced not by the value evaluated as a function of K-S variables but by the value integrated separately (Stiefel & Scheifele 1971). In any event, this type of stabilization technique has been widely used in N-body simulations (Aarseth 1985).

[1] Of course, a well-known exception is the Jacobi constant in the restricted three-body problem.

[2] Imagine integrating a planar restricted three-body problem on the x-y plane. Then the total angular momentum vector is ensured to be parallel to the z-axis by any integrator.

Another approach is the *manifold correction* of Nacozy (1971). When the integral relations are not satisfied by the integrated variables, this method modifies the latter so that the relations are satisfied. The modification is usually done by adding a linear correction vector computed from the gradient vectors of the integrals. By choosing the total energy as the integral to be satisfied, Nacozy integrated the motion of a 25-body system and obtained a significant gain in precision. Since this technique is equivalent to correcting the integrated variable back onto the correct manifold of constant energy, it is termed the manifold correction (Murison 1989) or the *projection method* (Hairer et al. 1999).

About two decades later, Murison (1989) applied the manifold correction to the restricted three-body problem and obtained a dramatic increase in the precision of the numerical integration. Of course, he combined it with other factors such as use of the extrapolation method and the introduction of K-S regularization. However, his Table 1 shows clearly that the manifold correction is the main cause of the improvement that was achieved. Note that this approach requires only a small amount of additional computation, as he demonstrated. Unfortunately, the applicability of the method is limited because " its implementation depends on the existence of at least one integral of the motion " (Murison 1989).

On the other hand, Hairer et al. (1999) reported that the projection method, enforcing the constancy of both the total energy and the total angular momentum, does not work in a five-body integration of the Sun and four outer planets (see their example [4.4] and Fig. 4.4). This illustrates that the conservation of constants of the motion does not always imply the correctness of the integration.

To resolve these difficulties, we borrow the idea of the integral invariant relation. Specifically, we conduct the manifold correction such that the Kepler energy, as the integral invariant, is to be maintained throughout the integration.

Before going into details, let us show an example indicating the effectiveness of the new approach. Figure 1 compares the results of an existing and the new approach to numerical integrations. Plotted are the relative position errors of Mercury in a simultaneous integration of the Sun and nine major planets for a few hundred thousand years. The error of the new method is drastically smaller than that of the existing one.

In this paper, we report that the new method significantly improves the quality of orbit integrations, as demonstrated in Figure 1, with a negligible cost of additional computation. In the following, § 2 describes the new method in detail, § 3 illustrates numerical examples, and § 4 concludes with some future prospects.

2. METHOD

In this section, we describe the new method and discuss some of its features. First, we define the Kepler energy in § 2.1. Next we present our idea to modify the integrated variables, the spatial scale transformation, in § 2.2. A method to solve for the scale factor is also detailed. In § 2.3, we examine the mechanism by which the new method, which we hereafter call the scaling method, reduces the integration error. As a by-product of the considerations in § 2.3, we extend the scaling method to the case of multiple bodies in § 2.4. Then we show how the scaling method can be

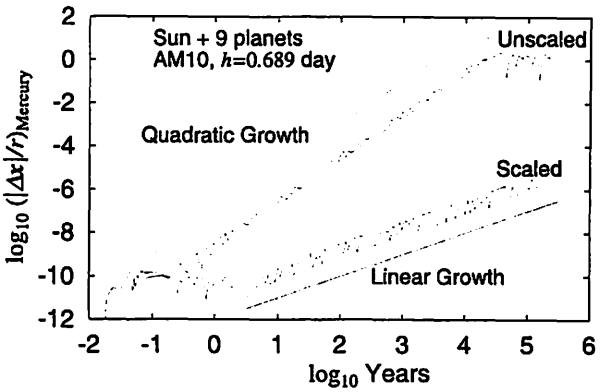

FIG. 1.—Relative position errors of Mercury obtained via the new and existing methods in a simultaneous numerical integration of the Sun and nine major planets for 2.4×10^5 yr. The new method is labeled "Scaled," while the existing one is denoted "Unscaled." The integrator used was the 10th-order implicit Adams method in PECE mode, and the step size was fixed at 0.689 days, 1/128 of Mercury's nominal orbital period. The initial conditions were those at J2000.0 in JPL's latest planetary ephemeris, DE405, and the starting tables were prepared via the extrapolation method using the same step size with a tiny relative error tolerance, 10^{-14}. The error of the unscaled integration increases in proportion to the square of time, while that of the scaled one seems to grow linearly over this period.

adapted to a change of coordinate systems in § 2.5. In § 2.6, we estimate the computational labor and time required in implementing the scaling method. Further, we discuss various aspects of the applicability of the scaling method in § 2.7. Finally, we compare the current method with Nacozy's approach in § 2.8.

2.1. *Kepler Energy*

Let us begin with a perturbed one-body problem. The usual equation of motion is written as

$$\frac{d\boldsymbol{v}}{dt} = \left(\frac{-\mu}{r^3}\right)\boldsymbol{x} + \boldsymbol{a}\,, \tag{1}$$

where $\boldsymbol{x}$ is the position, $\boldsymbol{v}$ is the velocity, $\mu \equiv GM$ is the gravitational constant, $r \equiv |\boldsymbol{x}|$ is the radius vector, and $\boldsymbol{a}$ is the perturbing acceleration.

Now we introduce a quantity K defined as

$$K \equiv T + U, \tag{2a}$$

where

$$T = v^2/2\,, \quad U = -\mu/r\,. \tag{2b}$$

We call K the Kepler energy, T the kinetic energy, and U the Keplerian potential energy. Note that K is the total specific energy for pure Keplerian orbits and, therefore, is a constant of the motion in that case. Under the perturbation, K is no longer a constant. Its time evolution is governed by the equation

$$\frac{dK}{dt} = \boldsymbol{v}\cdot\boldsymbol{a}\,. \tag{3}$$

Usually the variation of K is small compared with the value of K itself. As we have experienced in the generalization of Encke's method (Fukushima 1996), it is wise to integrate

not K but its difference from the initial value, $\Delta K \equiv K - K_0$:

$$\frac{d\Delta K}{dt} = \boldsymbol{v} \cdot \boldsymbol{a} , \tag{4}$$

where K_0 is the initial value of the Kepler energy. This change of integrated variable significantly reduces the accumulation of round-off errors.

In general, the integrated K, or the sum of K_0 and the integrated ΔK if speaking more specifically, is not the same as K analytically evaluated from the integrated $\boldsymbol{x}$ and $\boldsymbol{v}$ by using equation (2). In this case, there are three possibilities in principle: (1) the integrated K is correct and the integrated $\boldsymbol{x}$ and $\boldsymbol{v}$ are erroneous, (2) the integrated K is incorrect and the integrated $\boldsymbol{x}$ and $\boldsymbol{v}$ are valid, and (3) the integrated K, $\boldsymbol{x}$, and $\boldsymbol{v}$ are all wrong. Here we take the first standpoint and modify the integrated $\boldsymbol{x}$ and $\boldsymbol{v}$ such that the two K's are the same. The reason we choose this option will be explained in § 2.3.

2.2. *Scale Transformation*

Consider how to modify the position and velocity by using the difference in the Kepler energy. Since the additional information provides 1 degree of freedom, we may correct $\boldsymbol{x}$ and $\boldsymbol{v}$ using a one-parameter transformation at most. As such, we adopt a spatial scale transformation:

$$(\boldsymbol{x}, \boldsymbol{v}) \rightarrow (s\boldsymbol{x}, s\boldsymbol{v}) . \tag{5}$$

The unknown, s, called the scale factor, is determined such that the integrated K and the evaluated K coincide. Note that the kinetic and Keplerian potential energies are transformed as a result of the above scale transformation as

$$(T, U) \rightarrow (s^2 T, U/s) . \tag{6}$$

Then the condition of coincidence is written as

$$s^2 T + U/s = K , \tag{7}$$

where K refers to the integrated value, while T and U are those evaluated from the integrated $\boldsymbol{x}$ and $\boldsymbol{v}$ before the scaling. This condition can easily be rewritten as

$$f(s) \equiv Ts^3 - Ks + U = 0 . \tag{8}$$

We call this the equation of Kepler energy consistency. This is a simple cubic equation. We solve it numerically via Newton's method:[3]

$$s \rightarrow f^*(s) \equiv \frac{sf'(s) - f(s)}{f'(s)} = \frac{2Ts^3 - U}{3Ts^2 - K} , \tag{9}$$

with a starting value

$$s_1 = \frac{2T - U}{3T - K} , \tag{10}$$

which is actually the first iteration of the method started from a natural guess, $s_0 = 1$.

It can easily be shown that Newton's method with this starting point definitely converges (see the Appendix for details). Experience has shown us that the method converges rapidly, and usually *no* iterations are required, since the above starter is so precise.

2.3. *A Circular Orbit Integrated by Euler's Method*

Let us see how this scaling method works in the simplest case, a circular orbit integrated by the Euler method. The Euler method, namely, the first-order explicit Adams method, is written for a Keplerian orbit as

$$\boldsymbol{x}_{n+1} = \boldsymbol{x}_n + h\boldsymbol{v}_n , \quad \boldsymbol{v}_{n+1} = \boldsymbol{v}_n - h\Omega_n^2 \boldsymbol{x}_n , \tag{11}$$

where h is the step size of the integration and $\Omega_n^2 \equiv \mu / r_n^3$. For simplicity, we choose a system of units such that $\mu = 1$ throughout this subsection.

Consider integrating a circular orbit of unit radius on the x-y plane. We assume that the initial solution is given exactly as

$$\begin{pmatrix} x_0 \\ y_0 \end{pmatrix} = \begin{pmatrix} 1 \\ 0 \end{pmatrix} , \quad \begin{pmatrix} u_0 \\ v_0 \end{pmatrix} = \begin{pmatrix} 0 \\ 1 \end{pmatrix} , \tag{12}$$

where we used the fact that $\Omega_0 = 1$. Then the solution at the first step is integrated by Euler's method as

$$\begin{pmatrix} x_1 \\ y_1 \end{pmatrix} = \begin{pmatrix} 1 \\ H \end{pmatrix} , \quad \begin{pmatrix} u_1 \\ v_1 \end{pmatrix} = \begin{pmatrix} -H \\ 1 \end{pmatrix} , \tag{13}$$

where $H \equiv h\Omega_0 = h$ is the phase advance per step. Note that the radius vector at the first step is a little larger than its initial radius,

$$r_1 = \sqrt{1 + H^2} > r_0 = 1 . \tag{14}$$

Also, the magnitude of the velocity at the first step is larger than the initial value by the *same* factor[4] as the radius vector:

$$|\boldsymbol{v}_1| = \sqrt{1 + H^2} > |\boldsymbol{v}_0| = 1 . \tag{15}$$

The integrated Kepler energy is unchanged because there is no perturbation, and therefore it is an integration constant. Thus it retains its initial value,

$$K_1 = K_0 = T_0 + U_0 = -\tfrac{1}{2} . \tag{16}$$

On the other hand, the Kepler energy analytically evaluated by using the integrated position and velocity becomes at the first step

$$T_1 + U_1 = \frac{1 + H^2}{2} + \frac{-1}{\sqrt{1 + H^2}} . \tag{17}$$

Obviously this is different from the integrated K, which represents an integration error in some sense.

Now the scale transformation is to improve the position and velocity at the first step as

$$\begin{pmatrix} x_1' \\ y_1' \end{pmatrix} = s \begin{pmatrix} x_1 \\ y_1 \end{pmatrix} , \quad \begin{pmatrix} u_1' \\ v_1' \end{pmatrix} = s \begin{pmatrix} u_1 \\ v_1 \end{pmatrix} . \tag{18}$$

By rigorously solving the equation of Kepler energy

[3] Although the analytic formula for a general cubic equation is known as Cardano's formula, its direct application to this case is impractical because of its slowness when compared with the Newton method described here.

[4] This similarity of the magnification factors in the position and in the velocity was a trigger for us to consider the spatial scale transformation.

consistency,

$$T_1 s^3 - K_1 s + U_1 = 0 , \tag{19}$$

we determine[5] the scale factor to be

$$s = 1/\sqrt{1 + H^2} . \tag{20}$$

Then the corrected solution becomes

$$\begin{pmatrix} x_1' \\ y_1' \end{pmatrix} = \frac{1}{\sqrt{1+H^2}} \begin{pmatrix} 1 \\ H \end{pmatrix} , \quad \begin{pmatrix} u_1' \\ v_1' \end{pmatrix} = \frac{1}{\sqrt{1+H^2}} \begin{pmatrix} -H \\ 1 \end{pmatrix} . \tag{21}$$

When compared with the exact solution,

$$\begin{pmatrix} \hat{x}_1 \\ \hat{y}_1 \end{pmatrix} = \begin{pmatrix} \cos H \\ \sin H \end{pmatrix} , \quad \begin{pmatrix} \hat{u}_1 \\ \hat{v}_1 \end{pmatrix} = \begin{pmatrix} -\sin H \\ \cos H \end{pmatrix} , \tag{22}$$

the unscaled position (x_1, y_1) steps outside the unit circle, the solution curve, while the scaled solution (x_1', y_1') remains on it. The same is true for the velocity component.

On the other hand, the orbital longitude is calculated as

$$\lambda_1 = \tan^{-1}(y_1/x_1) = \tan^{-1} H . \tag{23}$$

Note that this quantity is unchanged by the scaling. Repeating the above procedure N times, we reach the conclusion that the radius and the magnitude of the velocity remain the same as their initial values, while the orbital longitude is smaller than the true angle by an amount that is linearly proportional to time,

$$\Delta\lambda = N(H - \tan^{-1} H) \approx \tfrac{1}{3}\Omega_0 H^2 t , \tag{24}$$

where we have replaced Nh with t.

Of course, it is still questionable whether the properties of the scaled integration observed in the above hold in non-circular cases or for other integrators. Also, the effect of perturbations is unclear. These issues will be addressed with numerical experiments in the next section. In any event, it is expected that the scaled integration will reduce the amount of integration error, especially in the radial sense.

2.4. *Multiple Bodies*

In the above simple analysis, we observed that the value of s that is determined depends on the magnitude of phase advance per step. In treating multiple bodies, it is usual to adopt a common step size for all bodies. In this case, the amount of phase advance per step differs from body to body. Thus, we deal with each celestial body separately. Namely, we integrate the time evolution of the Kepler energies for all bodies and adjust the scale factors one by one.

In other words, for each body ($j = 1, 2, \ldots$), we first simultaneously integrate the equations

$$\frac{d\boldsymbol{v}_j}{dt} = \left(\frac{-\mu_j}{r_j^3}\right)\boldsymbol{x}_j + \boldsymbol{a}_J , \quad \frac{d\,\Delta K_j}{dt} = \boldsymbol{v}_j \cdot \boldsymbol{a}_j , \tag{25}$$

then we determine the scale factors s_j separately by solving the associated cubic equations,

$$T_j s_j^3 - K_j s_j + U_j = 0 , \tag{26}$$

and, third, we adjust the integrated positions and velocities using the scale transformation at each integration step:

$$(\boldsymbol{x}_j, \boldsymbol{v}_j) \rightarrow (s_j \boldsymbol{x}_j, s_j \boldsymbol{v}_j) . \tag{27}$$

Here

$$T_j = \boldsymbol{v}_j^2/2 , \quad K_j = (K_j)_0 + \Delta K_j , \quad U_j = -\mu_j/r_j . \tag{28}$$

2.5. *Change of Coordinate System*

Sometimes, one faces the need to change the coordinate system to which the orbital motion is referred. This happens when a perturbation by a third body becomes so strong that it is more reasonable to change the coordinate origin from the primary to the third body, as we experience in close encounters of comets or asteroids with major planets or flyby orbits of space vehicles.

Fortunately, the scaling method is easily adapted to such a change of coordinates. Assume that the introduction of a coordinate transformation,

$$(\boldsymbol{x}, \boldsymbol{v}) \rightarrow (\tilde{\boldsymbol{x}}, \tilde{\boldsymbol{v}}) , \tag{29}$$

induces a new equation of motion as

$$\frac{d\tilde{\boldsymbol{v}}}{dt} = \left(\frac{-\tilde{\mu}}{\tilde{r}^3}\right)\tilde{\boldsymbol{x}} + \tilde{\boldsymbol{a}} , \tag{30}$$

where the quantities with tildes are the new ones. Then the equation for the time evolution of the new Kepler energy becomes

$$\frac{d\,\Delta\tilde{K}}{dt} = \tilde{\boldsymbol{v}} \cdot \tilde{\boldsymbol{a}} , \tag{31}$$

with the new initial condition $\Delta\tilde{K} = 0$. The initial value of the new Kepler energy, $\tilde{K}_0$, is simply reevaluated from the new Kepler energy relation as

$$\tilde{K} = \tilde{T} + \tilde{U} , \tag{32a}$$

where

$$\tilde{T} = \tilde{\boldsymbol{v}}^2/2 , \quad \tilde{U} = -\tilde{\mu}/\tilde{r} . \tag{32b}$$

Thus, there is no practical difficulty in a change of coordinate system, even if frequent.

2.6. *Computational Cost*

Let us estimate the increase in computational time due to the introduction of the scaling method. First, we note that the computational time to evaluate the right-hand side of the differential equations increases little. This is because the additional evaluation is of the form of an inner product of two vectors, $\boldsymbol{v} \cdot \boldsymbol{a}$, and both the velocity and the perturbing acceleration have already been evaluated in the right-hand side of the equation of motion.

Second, the relative increase in the number of components in the differential equations amounts to $\frac{1}{6}$. This sounds like a significant increase, but almost all the computational time used for integration is spent evaluating the right-hand side of the differential equations, which, as we saw above,

[5] The reader may easily check the correctness of the solution by substituting it into the equation.

does not increase much. Therefore, the effect of this portion of the increase is subtle.

Third, the analytical computation of the Kepler energy from the integrated position and velocity seems to require some additional time, especially in taking the square root of the squared position, $r = \sqrt{x^2}$. However, we note that the evaluated square root is used again in the next step to evaluate the Keplerian acceleration, $(-\mu/r^3)x$. This is true even after the scaling, $(x, v) \to (sx, sv)$, because the scaled radius vector is obtained simply by multiplying the scale factor as $r \to sr$. Therefore, the actual increase is only that incurred in the evaluation of v^2, which is negligible.

Finally, one may expect an increase in computational time due to our policy of determining the scale factor without approximation. However, note that the Newton's method iteration converges quadratically (see eq. [A20] in § A.5). This means that no more iterations are required in double-precision arithmetic when the relative inequality of the Kepler energy becomes less than 10^{-8}. This condition is almost always satisfied before the iteration begins, since we usually adopt a sufficiently high order integrator and/or a sufficiently small step size in practical integrations. Even if it is not satisfied, the Newton corrector (eq. [9]) is rapidly evaluated, for it is expressed in the form of a simple rational function. Therefore, this part costs little. In conclusion, we see no actual increase in computational time under the new method.

2.7. *Applicability*

Consider various factors in the applicability of the scaling method to orbit integrations. First, the line of logic developed in the previous subsections has no relation to the details of the perturbing acceleration. Therefore, it is to be expected that the method will be applicable to any kind of perturbation. Namely, the method should work (1) whether the problem is restricted or not, that is, whether the perturbation explicitly depends on time; (2) whether the perturbation depends on not only the position but also the velocity, such as one faces in post-Newtonian mechanics; (3) whether the perturbing acceleration is derived from a potential as usual or not; (4) whether the perturbation is dissipative, such as air drag, or not; and (5) whether the perturbing force is continuous or not,[6] as in the shadow effect of radiation pressure.

Second, it is easy to see that the method is universal because it assumes nothing about the type of unperturbed orbit—whether elliptical, parabolic, or hyperbolic.

Third, the formulation described so far does not depend on the coordinate system adopted. In other words, it will work both in an inertial frame and in a rotating or other noninertial frame. Also, the effectiveness of the new approach will remain unchanged by any choice of coordinate origin, such as barycentric, heliocentric, or Jacobi coordinates, so long as the resulting problem is properly posed as quasi-Keplerian. In fact, this method is easily adapted to changes of coordinate system, as shown in § 2.5.

Fourth, the new method is expected to work for any number of bodies as long as their orbital motions are regarded as quasi-Keplerian.

Fifth, the current formulation is independent of the integrator used so long as it is designed for general first-order ordinary differential equations (ODEs), as in $dy/dt = f(y, t)$, since not only the position but also the velocity is needed at every integration step. In other words, it is applicable to both (1) the one-step methods, such as the Runge-Kutta family, as well as the extrapolation methods, and (2) the linear multistep methods, such as the Adams methods.

It is also expected that the method should not depend on any parameters specific to these integrators, such as (1) the order; (2) the magnitude of the step size, as long as the integrator itself remains stable; (3) the implicitness, namely, whether the integrator is explicit or implicit or whether an implicit formula is approximated by a finite iteration not achieving perfect implicitness (4) the method of extrapolation or the number of extrapolation stages for the extrapolation methods; and (5) the variability of these parameters of integration, say, the order, the number of extrapolation stages, or the step size.

Among the latter, the method is expected to work under a policy of changing the integration order body-by-body, as is usually done when integrating multiple bodies that span a wide range of orbital periods, such as the Sun and nine major planets. It would also remain effective even for integrators that exploit variable step sizes, as are used in integrating highly eccentric orbits such as those of comets and some peculiar asteroids.

Unfortunately, the new approach is not compatible with integrators designed for special second-order ODEs of the form $d^2x/dt^2 = f(x, t)$. Examples are the Störmer-Cowell methods, the extrapolation method based on the modified midpoint rule, and the symmetric linear multistep methods of Lambert & Watson (1976) and Quinlan & Tremaine (1990).

One may imagine that this approach could be realized in a symplectic integrator, such as the symplectic Euler method. This is not easy, since the time evolution of the Kepler energy must be integrated by one of the integrators for first-order ODEs. Of course, this difficulty would be resolved by introducing a conjugate variable to be paired with the Kepler energy (Mikkola & Innanen 2002). However, we should admit that the total symplecticity would be violated in general, because the scale transformation is not symplectic.

On the other hand, the symmetric linear multistep methods seem to be applicable to the new method as long as they are capable with general first-order ODEs. Since only a few formulae of this kind are known (Evans & Tremaine 1999), we will leave this issue as future work to be tackled.

Finally, we must speak of the limitations of the new approach. Since the scaling method is based on the assumption that the orbits integrated remain close to Keplerian, the effectiveness of the method will decrease if the strength of the perturbation increases. In particular, the method would be useless for general N-body problems in which the departure from Keplerian motions is large. In any event, all these speculations must be checked with numerical experiments.

2.8. *Relation to Nacozy's Approach*

Let us clarify the relation between the scaling method and Nacozy's (1971) original method of manifold correction. There is a substantial difference in the nature of the quantity

[6] Of course, we must use an appropriate integrator such as a one-step method utilizing no higher derivatives, e.g., the Runge-Kutta method using variable step sizes.

to be monitored: it is a constant of the motion in Nacozy's approach, such as the total energy, while it is the Kepler energy—a function of time—in the new method. As for the availability of such quantities, the former are much more limited than the latter. Aside from round-off error a constant of the motion is error-free in its evaluation, while the Kepler energy suffers a sort of truncation error during its integration. Thus, we anticipate that the applicability of the scaling method is wider than that of the original manifold correction, at the cost of a possible degradation in precision.

As for the manner of correction, the two methods are more similar than it might seem from the difference in outlook. In Nacozy's case, the correction of the integrated x and v is determined by the steepest-descent method, in terms of minimization theory. That is, the correction vectors are set to be in proportion to the gradient vectors. If the base integral relation is the Kepler energy consistency, as in the scaling method, this becomes

$$\Delta x \propto \frac{\partial K}{\partial x} = \left(\frac{-\mu}{r^3}\right) x\,, \quad \Delta v \propto \frac{\partial K}{\partial v} = v\,. \tag{33}$$

Apart from the coefficients of proportionality, this method of correction is nothing other than the scaling transformation. In other words, the scaling method can be regarded as a variation of manifold correction in which the proportionality coefficient to be multiplied with the gradient vector is a diagonal matrix with time-varying components.

3. NUMERICAL EXPERIMENTS

Let us show the results of some numerical experiments on the scaled integration. In § 3.1, we specifically define the *error* of numerical integration, which will be used in the following subsections. Then in § 3.2 we present the case of pure Keplerian orbits. Next, in §§ 3.3 through 3.9, we will show that the observed properties of the scaled integration are independent of various factors: the eccentricity in § 3.3; the type of perturbation in § 3.4; the type of unperturbed orbit in § 3.5; the method of integration in § 3.6, as well as some parameters of the integration method, such as the order, in § 3.7; the number of extrapolation stages in § 3.8; and the variability of step size in § 3.9. Also, the body dependence of the scaled integrations is illustrated in § 3.10. The limitations of the scaling method are described in § 3.11 by discussing a strong-perturbation case. As an extension, we demonstrate the relation between the integration errors and the perturbation strength in § 3.12. Summarizing these experiments, we present two typical results in §§ 3.13 and 3.14: the features in cases where the dominant source of integration error is truncation or round-off, respectively. Finally, we report that the scaling enhances the stability of the integrators in § 3.15.

3.1. *Error Estimation*

First of all, we discuss how to measure the error of numerical integrations whose exact solutions are unknown. This is important because, as we will show later, the scaling method achieves such a significant reduction of integration error that it is difficult to confirm in the usual way,[7] by comparison with results obtained by standard integrators.

Of course, the local precision of an integration is easy to monitor, say, by comparing the explicit and implicit formulae in the linear multistep methods, by measuring a specially designed quantity in the Runge-Kutta-Fehlberg methods, or by watching the manner of convergence in the extrapolation methods. Rather more problematic is to estimate the global accuracy.

One way is to (1) do a forward integration for some amount of time, (2) do a backward one starting from the arrived-at solution for the same amount of time, and (3) compare the final state of the backward integration with the initial conditions. However, we did not adopt this approach, for a few reasons. First, it is not applicable to dissipative or similar problems, in which a backward integration is physically meaningless. Second, it is useless for the time-reversible integrators, such as the symplectic integrators and the symmetric linear multistep methods, although we do not test them in this paper. Finally, it is quite time-consuming if one wants to monitor the variation of the errors as a function of integration time.

Another remedy is to conduct two different integrations and take the difference. Typically the two integrations are designed to be different in (1) step size,[8] (2) some other parameter of integration such as the order, the mode, the number of extrapolation stages, or the error tolerance, (3) the type of integration, (4) the arithmetic precision, or (5) a combination of these factors.

Throughout this paper, we adopt the first case listed in the previous paragraph. More specifically, we perform two integrations simultaneously—one integration by a certain integrator with a certain step size, which we call the target integration, and another by the same integrator with half the step size, which we call the reference integration. When dealing with the variable step sizes, we change the step size of the reference integration so as to keep the ratio of step sizes at 2. Then we define the error as the difference between the target and the reference integrations at the same times.

By comparison with results from integrations of the reference solutions via the extrapolation method with a tiny error tolerance in quadruple-precision arithmetic,[9] we confirmed that this error estimate is accurate in double-precision arithmetic for various kinds of problems.

3.2. *Pure Keplerian Orbits*

Let us begin with the simplest case: numerical integration of a pure Keplerian orbit. When using an ordinary integrator, the integration errors of a Keplerian orbit grow as plotted in Figure 2. This is the result of numerically integrating a Keplerian orbit with $e = 0.05$ and $I = 23°$ using the 10th-order implicit Adams method in PECE (predict, evaluate, correct, evaluate) mode with a step size of 1/128 of the orbital period. In the figure, we show three components of the error in the position Δx, namely, that in the radius vector, Δx_r; that in orbital longitude, Δx_λ; and that in orbital latitude, Δx_β. They were evaluated as

$$\Delta x_r = e_r \cdot \Delta x\,, \quad \Delta x_\lambda = e_\lambda \cdot \Delta x\,, \quad \Delta x_\beta = e_\beta \cdot \Delta x\,. \tag{34}$$

[7] Diamond is cut by diamond.

[8] The ratio of the step sizes is usually chosen as a fixed integer to make the comparison easy. The typical ratio is 2.

[9] Typically, the reference integration was done by using around 20 extrapolation stages and an error tolerance of 10^{-33}.

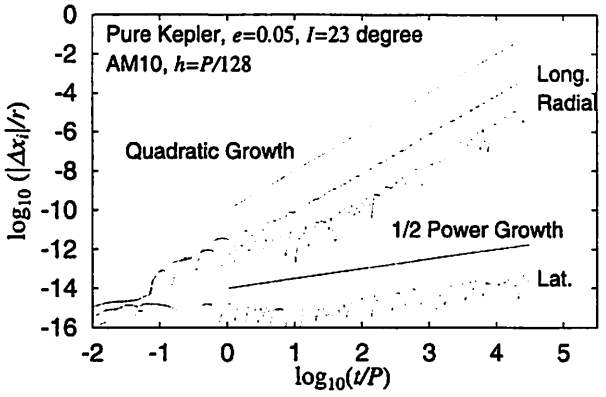

FIG. 2.—The three orthogonal components of the position errors for the unscaled integration. Integrated is a pure Keplerian orbit with $e = 0.05$ and $I = 23°$ for about 3×10^4 orbital periods. The longitude and radius components grow in proportion to the square of time, whereas the latitude one grows in proportion to the square root of time.

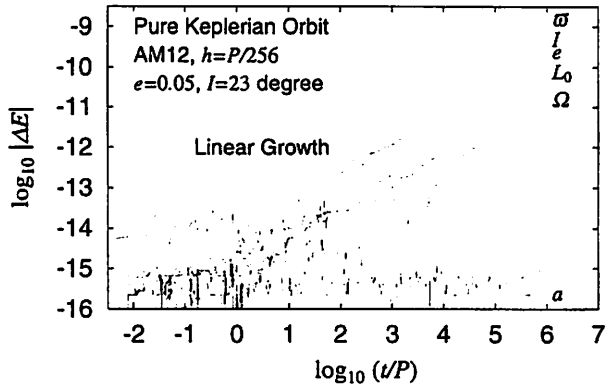

FIG. 4.—Errors in the Keplerian elements (a, e, I, Ω, $\varpi \equiv \Omega + \omega$, $L_0 \equiv M_0 + \varpi$) of the scaled integration. Growing linearly with respect to time are all the errors except that of the semimajor axis, a, which remains randomly on the order of the machine epsilon.

Here the three orthonormal base vectors are defined as

$$e_r = x/r\,, \quad e_\lambda = e_\beta \times e_r\,, \quad e_\beta = L/|L|\,, \tag{35}$$

where

$$L = x \times v \tag{36}$$

is the specific orbital angular momentum vector. Note that both the longitude and radius components grow in proportion to the square of time, while the latitude component does so in proportion to the square root of time. It is well known that the largest is the longitude component.

On the other hand, the manner of error growth is different in the scaled integration (Fig. 3). This time, all three components grow linearly with respect to time. As for the magnitude, the longitude and radius components are comparable, while the latitude one is smaller than the others.

In order to examine the reason for the linear error growth, we prepared Figure 4, showing the errors in the Keplerian elements for the scaled integration. Here the integrated problem is a pure Keplerian orbit with $e = 0.05$ and $I = 23°$, and the integration time was $2^{20} \approx 10^6$ periods. For the integrator, we used the 12th-order implicit Adams method in PECE mode, whose starting values were prepared by the extrapolation method. The step size was chosen as 1/128 of the orbital period. It is clear that the errors in all the elements except the semimajor axis increase linearly with respect to time. Therefore, the longitude error is not generally the largest error component in the scaled integration.

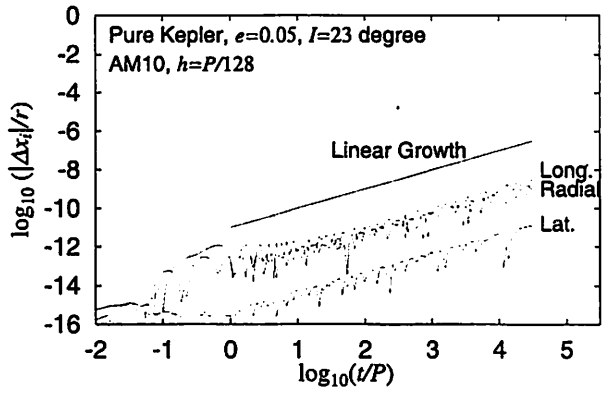

FIG. 3.—Same as Fig. 2, but for the scaled integration. All components grow linearly with respect to time.

On the other hand, the error in the semimajor axis, δa, remains on the order of the machine epsilon. This situation is achieved by virtue of the fact that the Kepler energy is a constant of the motion in this case. Note that δa seems to follow a random distribution of zero mean value. Then, applying the logic developed by Brouwer (1937), we would expect that its secular effect on the orbital longitude will grow in proportion to the square root of time.

Unfortunately, it is difficult to confirm this conjecture directly, since any component growing as the $\frac{1}{2}$ power of time would be embedded in a linearly growing component, which is the result of the secular effect of truncation error in the phase advance per step, as we observed in § 2.3, or other factors such as the errors in preparing the starting tables from the given initial conditions.

In any event, the effects of round-off are reduced to some degree by the scaling, as we now prove. Assume that the accumulation of round-off errors in the longitude grows in the usual manner: following the 3/2 power of time, as Brouwer (1937) predicted. Then the estimated magnitude of the round-off errors in the longitude roughly amounts to $\epsilon N^{3/2}$, where N is the number of steps and ϵ is the machine epsilon. At the end of the integration in Figure 4, the number of steps is $N = 2^{27}$. Thus the expected magnitude of round-off error in double-precision arithmetic becomes $\epsilon N^{3/2} = 2^{-53}(2^{27})^{3/2} \approx 1.7 \times 10^{-4}$, whereas the actual error in the longitude, δL_0, is around 10^{-10}, smaller than the expectation by six digits or so. Therefore, the figure implies that the accumulation of round-off errors is suppressed in some manner.

3.3. *Eccentricity Dependence*

In § 2.3, we proved that the scaling method works for a circular orbit integrated by the Euler method. However, it is questionable whether it would still be effective for eccentric orbits, especially highly eccentric ones such as the orbits of

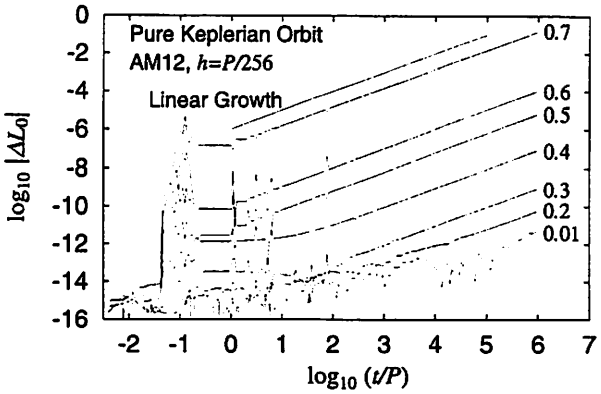

FIG. 5.—Errors in the mean longitude L_0 at the epoch for various eccentricities, as indicated. While the magnitude of the error increases with the eccentricity, the linear growth rate is unchanged.

asteroids and comets. In order to answer this question, we prepared Figure 5, which illustrates the longitude errors in pure Keplerian orbits of eccentricities from nearly zero up to 0.7. (For higher eccentricities, see § 3.5 below.) The total integration time was around 1 million periods, the integrator used was the 12th-order implicit Adams method in PECE mode, and the step size was 1/256 of the orbital period.

This figure tells us that the magnitude of the errors themselves increases as the eccentricity goes up. However, the rate of linear growth of the integration error does not depend on the eccentricity. Although this conclusion was derived from the results for unperturbed orbits, we report that we have confirmed the independence of eccentricity even for perturbed cases.

3.4. *Perturbation Type Dependence*

In § 2.7, we claimed that the scaled integration would not depend on the type of perturbing acceleration. In order to prove this, we provide Figure 6. The figure shows the relative position errors in the scaled integration of an artificial Earth satellite under various types of perturbation: (1) general relativistic effects, or the post-Newtonian acceleration in the one-body problem within the framework of Einstein's theory of general relativity, as a typical case of conservative but velocity-dependent accelerations; (2) third-body attraction, or the tidal force, roughly speaking, as a typical case of conservative and nonautonomous perturbations; (3) air drag in the form $a \propto -|v|v$, as a typical case of nonconservative accelerations; and (4) the J_2 perturbation, as a typical case of conservative and autonomous accelerations. Note that the errors in the figure have been multiplied by various factors in order to show the parallel nature of their growth curves clearly. Also, the integration time was sufficiently long, 160 years.

It is clear that the error initially grows linearly with respect to time. Then, for some perturbation types, a more rapidly increasing component appears after a certain amount of time. We observed that the growth rate of the more rapidly increasing component is 2 for J_2 and 3 for the air drag. Although not shown in the figure, we have confirmed that the growth rate of the more rapidly increasing component is 2 for the third-body attraction and the general relativistic effects.

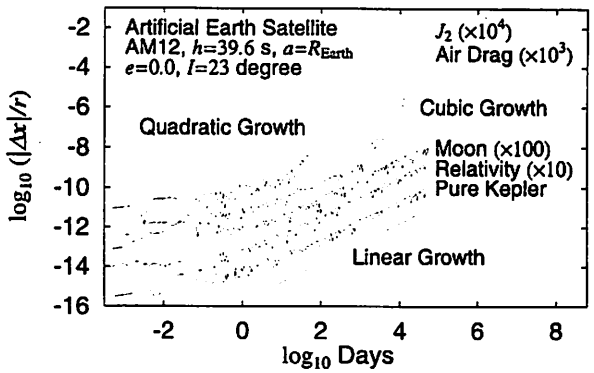

FIG. 6.—Relative position errors in the scaled integration of an artificial Earth satellite under various type of perturbations. The errors were multiplied by the factors indicated to show the parallel nature of their growth curves clearly. The initial conditions were fixed at $e = 0.0$, $a = 1\ R_{\oplus}$, and $I = 23°$. The integrated time spans up to 160 yr, 10^6 times the initial orbital period. Initially the error grows linearly with respect to time. For some perturbations, a more rapidly increasing component appears after a certain amount of time. The growth rate of the more rapidly increasing component is 2 for J_2 and 3 for the air drag. Although not presented here, we have confirmed that the growth rate of the more rapidly increasing component is 2 for third-body attraction (labeled "Moon") and general relativistic effects.

3.5. *Orbit Type Dependence*

In order to show that the scaled integration works independent of the type of unperturbed orbit, we prepared Figure 7. This graph presents the integration errors in terms of relative position for nearly parabolic orbits under post-Newtonian perturbations.

Note that the errors have been multiplied by the factors indicated to show the parallel nature of their growth curves clearly. The integrator used was the 12th-order implicit Adams method in PECE mode. The eccentricity dealt with ranges from $e = 0.90$ to $e = 1.10$, covering most practical values for periodic and nonperiodic comets. The starting time of the integration was pericenter passage. Since the concept of "orbital period" based on mean motion in the elliptical sense is not appropriate to describe times for such

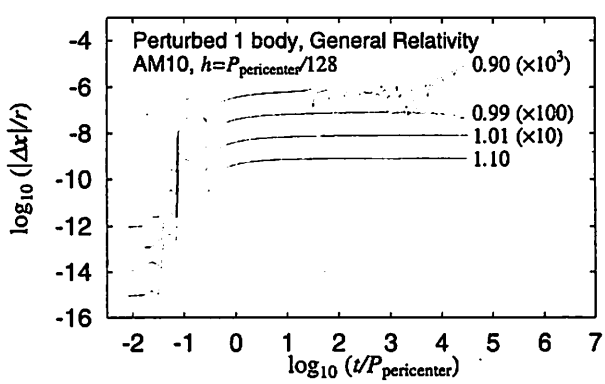

FIG. 7.—Errors in the relative position in the scaled integration of nearly parabolic orbits, ranging from $e = 0.90$ to $e = 1.10$, under general relativistic perturbations. The errors were multiplied by the factors indicated to show the parallel nature of their growth curves clearly. The initial location was at pericenter passage. The step size was fixed as 1/128 of P_{peri}, the orbital period of a circular orbit of the same pericenter distance.

nearly parabolic orbits, we measure the time using units of P_{peri}, the orbital period of a circular orbit with the same pericenter distance.

In the case of hyperbolic orbits, the final state is an escape with an almost linear motion. Thus, it is natural that the relative position error tends to be flat with respect to time, which implies a constant offset of the escape longitude. For elliptical cases, there was a sign of an error component that grew linearly in time after several hundred pericenter passages. Of course, the timing of the appearance of such linear error growth does depend on the eccentricity in the adopted time unit.

3.6. *Integrator Type Dependence*

Figure 8 illustrates the independence of the scaled integration with respect to the type of integrator used, as we predicted in § 2.7. The case examined is the three-body problem of the Sun, Jupiter, and Saturn, whose initial conditions were quoted from the DE405 ephemeris at epoch J2000.0. The errors indicated in the figure are those in the relative position of Jupiter, the largest error component in this case.

The integrators tested were (1) the fourth-order Runge-Kutta method (RK4), (2) the four-stage extrapolation method of Gragg (EX4), (3) the sixth-order explicit Adams method (AB6), and (4) the sixth-order implicit Adams method in PECE mode (AM6). The step size was fixed at 16.92 days, 1/256 of Jupiter's nominal orbital period; the integration time was around 10^4 yr. Note that the usual extrapolation method employs a *variable* number of extrapolation stages. Here we adopted a *fixed* number of extrapolation stages in order to separate the issue of its variability, which will be discussed below, from the issue of the nature of the integrator.

Apart from the similarity of the error growth, the magnitude of the errors varies by method, as can be seen. In addition, the computational cost, specifically, the number of acceleration evaluations per step, significantly differs with the type of integrator; 4 for RK4, 10 for EX4, 1 for AB6, and 2 for AM6. Here we adopted the harmonic sequence,

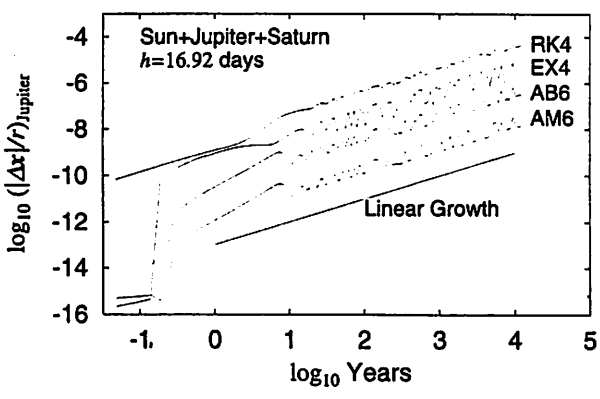

FIG. 8.—Relative position errors of Jupiter in the scaled integration of the three-body problem of the Sun, Jupiter, and Saturn for various methods of integration: the fourth-order Runge-Kutta method ("RK4"), the four-stage extrapolation method of Gragg ("EX4"), the sixth-order explicit Adams method ("AB6"), and the sixth-order implicit Adams method in PECE mode ("AM6"). The step size was fixed at 16.92 days, 1/256 of Jupiter's nominal orbital period. The growth of the integration error barely depends on the choice of integration method.

$n = 1, 2, 3, 4, 5, \ldots$, for the number of substeps in the extrapolation method, which is known to require the least number of evaluations. The superiority of linear multistep methods is obvious: smaller errors with smaller computational time.

3.7. *Integrator Order Dependence*

As a continuation of the discussion in the preceding subsection, we prepared Figure 9, showing the order dependence of the scaled integration for the implicit Adams method in PECE mode. In this case, the perturbation was fixed as the Moon's third-body attraction on an artificial Earth satellite. For the step size chosen, an 11th-order integrator is of the highest order among those that are stable. Easily observed are the facts that (1) the growth of the integration error hardly depends on the order, although (2) the magnitude of the integration error does so significantly. Thus, we anticipate that the introduction of order variability during an integration would not change the growth of the integration error in the scaled integration. If using linear multistep methods, we recommend that the method of highest available order be chosen, since the computational cost is the same for all orders if the mode is fixed.

3.8. *Extrapolation Stage Dependence*

Let us examine the dependence on another parameter of integration, the number of extrapolation stages in Gragg's extrapolation method with a *fixed* number of stages. Figure 10 is the same as Figure 3, but this time the number of extrapolation stages has been varied. Again the harmonic sequence was adopted.

Just as in the case of order dependence for linear multistep methods observed in the previous subsection, the growth of the integration error is independent of the number of extrapolation stages, although the magnitude of the integration error itself does depend. These facts support our expectation that variability in the number of extrapolation stages would not cause any significant change in the manner of error growth in the scaled integration. In fact, we have confirmed this conjecture through comparisons of the results obtained by the usual extrapolation method.

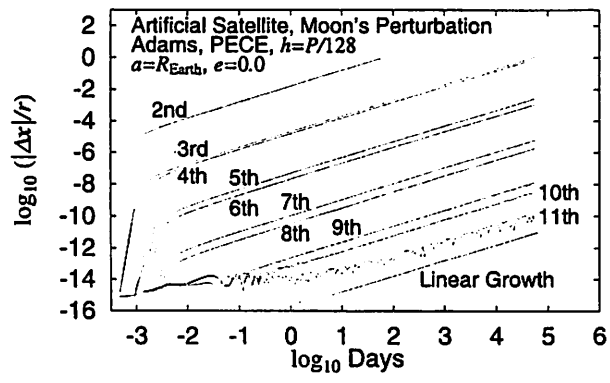

FIG. 9.—Same as Fig. 6, but for various orders of the implicit Adams method in PECE mode while the perturbation was set to be the Moon's third-body attraction. The growth of the integration error hardly depends on the order, although the magnitude of the integration error itself does.

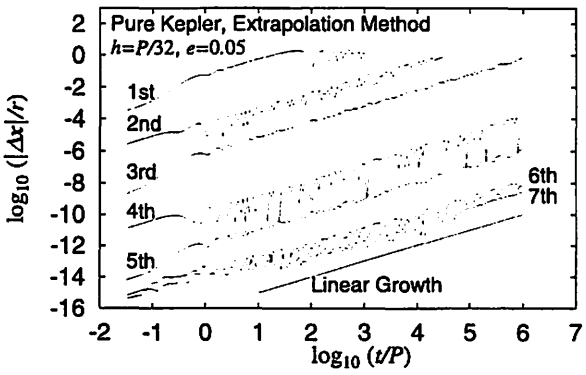

FIG. 10.—Same as Fig. 3, but for different numbers of extrapolation stages in Gragg's extrapolation method. The growth of integration error hardly depends on the number of extrapolation stages, although the magnitude of the integration error itself does.

3.9. *Step Size Variability Dependence*

Let us examine the effects of variability of the integration parameters in the scaled integration. Among them, the most important is that of variability of the step size, for it is directly connected to the possibility of reduced computational time.

Figure 11 illustrates the relative position errors of Icarus, whose eccentricity is as high as $e \approx 0.83$, under Jupiter's perturbation for around 10^5 yr. The curves shown were obtained with various combinations of the scaling and the variability of the step size: (1) an unscaled integration with fixed step size, (2) an unscaled integration with variable step size, (3) a scaled integration with fixed step size, and (4) a scaled integration with variable step size. Here we adopted the fourth-order Runge-Kutta method as the integrator and chose the step for the fixed-size integrations such that the total number of acceleration evaluations was the same as in the integrations with variable step size.

For the policy for changing the step size, we selected the rule[10]

$$h \propto r , \tag{37}$$

where r is the heliocentric distance. This closely resembles taking a fixed step size in the eccentric anomaly. It can easily be seen that the error growth depends on whether the scaling is applied or not, while the error magnitude depends on whether the step size is fixed or varied.

Although we do not present the details, we report that we have confirmed that similar results are obtained if variability is introduced for other integration parameters, such as the integration order or the number of extrapolation stages. This is what we expected as a basic property of the scaling method.

3.10. *Body Dependence*

In Figure 1, we showed that the scaled integration is effective in treating multiple bodies moving on quasi-Keplerian orbits. Here let us examine its details: the dependence on the bodies. Figure 12 shows the relative position errors of the planets in the same integration conducted to prepare Figure 1. The magnitudes of the relative position errors are smallest for Jupiter, increasing through Uranus, Neptune, Pluto, Saturn, Mars, Earth, and Venus, to Mercury. In order to make clear the similarity, we show some of them, including the smallest case, Jupiter, and the largest, that of Mercury. As can be seen, the observed growth rate is linear for Mercury but quadratic for the others. The reason is partially that, for the order adopted, the common step size selected was so close to the stable limit for Mercury as to be much smaller for the other planets.

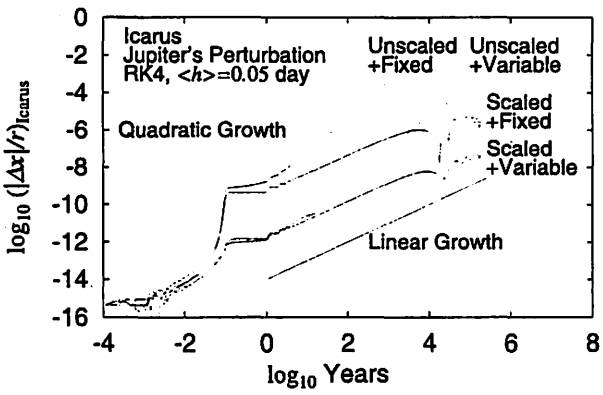

FIG. 11.—Position errors of Icarus under Jupiter's perturbation for around 10^5 yr. The four curves are the errors obtained in various combinations of scaling and variability of step size: (1) an unscaled integration with fixed step size, (2) an unscaled integration with variable step size, (3) a scaled integration with fixed step size, and (4) a scaled integration with variable step size. The variability was controlled by changing the step size in proportion to the heliocentric distance. The number of steps were arranged such that the average step size is the same for the fixed and variable cases, 0.05 days. The scaling governs the growth of the integration error, while the variability of the step size determines the magnitude of the integration error.

[10] We performed similar integrations using other power laws $h \propto r^{\nu}$, where $\nu = 1/2$, 3/2, and 2. The results were so similar to the $\nu = 1$ case that we omitted their presentation.

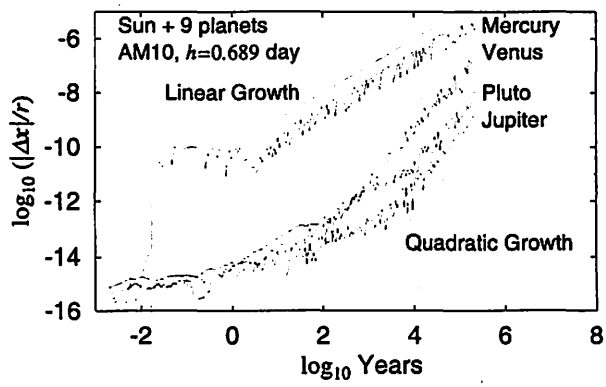

FIG. 12.—Same as Fig. 1, but showing the relative position errors of some of the planets in the scaled integration. The magnitudes of the relative position errors are smallest for Jupiter, increasing through Uranus, Neptune, Pluto, Saturn, Mars, Earth, Venus, and Mercury. Except for Mercury, the integration errors of all the planets grow quadratically after some amount of time, although they are much smaller than that of Mercury, which grows linearly for this period.

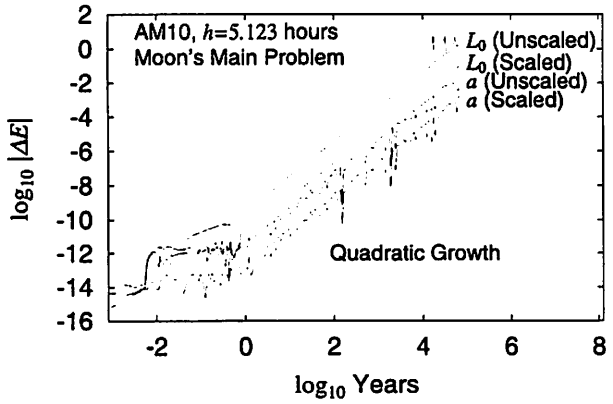

FIG. 13.—Errors in L_0 and a of the Moon in the so-called main lunar problem, namely, the restricted three-body problem of the Sun, Earth, and the Moon. The scaling reduces the error slightly, by a factor of about 30. Its growth rate is actually the same as that of unscaled integration, quadratic. This is because of the strong perturbation of the Sun.

3.11. *Strong Perturbations*

As we stated earlier, the scaling method fully relies on the assumption that the orbits to be integrated remain nearly Keplerian. Thus, we should examine how the effectiveness of the scaling method degrades in the case of strong perturbations. As such an example, we prepared Figure 13 for the so-called main lunar problem, namely, the restricted three-body problem of the Sun, Earth, and the Moon.

The scaling reduces the errors by around a factor of 30 with respect to the unscaled case. However, the growth rate is the same for both L_0 and a, being quadratic. This is because of the rapid appearance of the quadratically growing component, as we faced in the case of the J_2 perturbation in Figure 6, due to the strong perturbation of the Sun.

To confirm this estimate, we performed similar integrations by artificially changing the magnitude of the Sun's perturbation. The results are shown in Figure 14, where the strength of the Sun's perturbation was reduced by the factors indicated. It is noteworthy that the magnitude of the quadratically growing component is roughly proportional

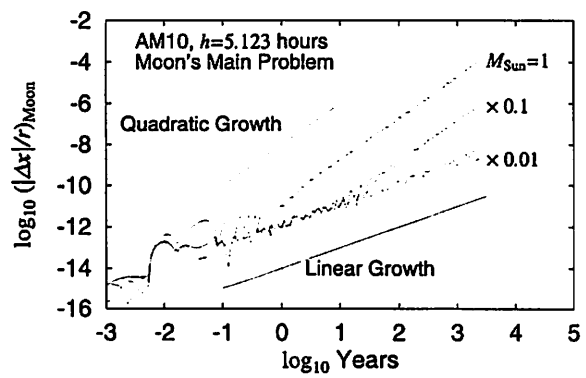

FIG. 14.—Same as Fig. 13, but for scaled integrations with the strength of the Sun's perturbation reduced by the factors indicated. The magnitude of the quadratically growing component is roughly in proportion to the square of the perturbation strength, while that of the linearly growing component remains unchanged.

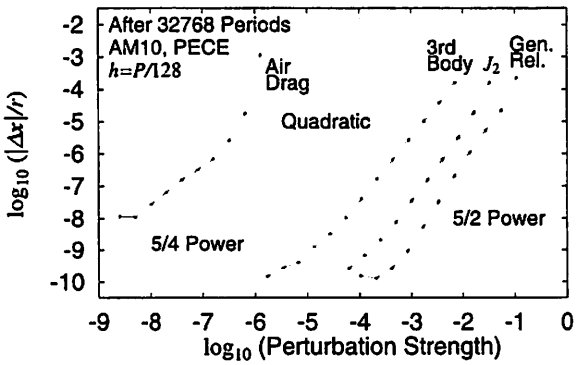

FIG. 15.—Relative position errors in the perturbed one-body problem as a function of the strength of the perturbing acceleration. The integration errors roughly follow power laws with respect to the perturbation strength: to the 5/4 power for air drag, quadratic for the third-body perturbation and the J_2 perturbation, and to the 5/2 power for the general relativistic corrections in acceleration.

to the square of the perturbation strength, while that of the linearly growing component remains unchanged.

3.12. *Perturbation Strength Dependence*

In response to the result we found in Figure 14, we investigated the dependence of the scaled integration with respect to the strength of the perturbing acceleration. Figure 15 shows the results obtained after sufficiently long integrations of 32,768 nominal orbital periods for the various types of perturbing accelerations we tried when preparing Figure 6. All the dependences seem to follow power laws of the perturbation strength. The index is 5/4 for the air drag, 2 for the third-body and J_2 perturbations, and 5/4 for the post-Newtonian acceleration.

3.13. *Truncation Error*

In order to examine the accumulated effects of round-off in the scaled integration, we first prepared Figure 16 as a

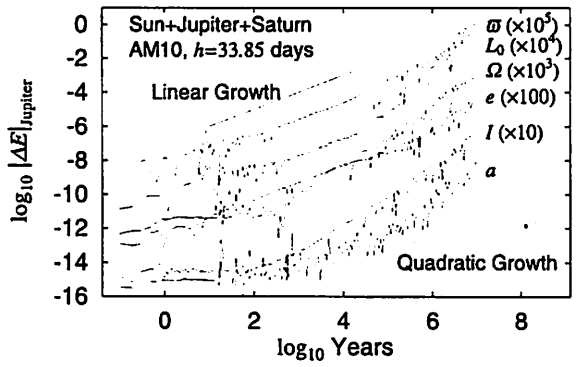

FIG. 16.—Same as Fig. 4, but for Jupiter in the scaled integration of the three-body problem of the Sun, Jupiter, and Saturn. The element errors were multiplied by the factors indicated to show the parallel nature of their growth curves clearly. In order to keep the truncation errors larger than the round-off errors, we selected a step size of 33.85 days, 1/128 of Jupiter's nominal orbital period. The element errors grow linearly with respect to time for the first 10^3 yr or so. After that, they increase in proportion to the square of time.

typical case in which truncation errors are dominant. The figure illustrates the element errors for Jupiter in the scaled integration of the three-body problem of the Sun, Jupiter, and Saturn for 10^7 yr. In order to keep the truncation errors sufficiently larger than the round-off errors, we chose a suitable step size for the given integrator: 33.85 days, 1/128 of Jupiter's nominal orbital period, for the 10th-order implicit Adams method in PECE mode. In this case, the element errors grow linearly with respect to time for the first 10^3 yr or so. After that, they increase in proportion to the square of time.

3.14. *Round-off Error*

On the other hand, we performed a similar integration to that in the preceding subsection while setting the step size much smaller, 8.462 days (1/512 of Jupiter's nominal orbital period), so that round-off errors are dominant. The result is Figure 17. This time, all the angle element errors grow in proportion to the 3/2 power of time, while the other element errors, especially that in a, seem to grow quadratically. Although the detailed mechanism is not known, we observed that the integration in the round-off–dominant region would reduce the long-term error growth to the 3/2 power, as we face in the unscaled integrations.

3.15. *Stability Region*

As we learned in § 2.3, the scaling enhances the stability of orbit integration. Thus it is natural to expect that it would also enlarge the stability region of high-order integrators such as Adams methods. Figure 18 shows the result of our investigation of H_{max}, the maximum stable phase for integrating perturbed Keplerian orbits. In preparing the figure, we judged the stability by whether the error increase with respect to time after the integration of 1024 orbital periods followed some power law with respect to time, as was observed in the previous subsections. We confirmed that this quantity is dependent on the order and the mode of the integration method but not on the eccentricity or the perturbation type.

The six curves are the scaled and unscaled cases for the explicit Adams method (PE) and the implicit Adams method in the PEC and PECE modes. It is clear that the PEC mode is the least stable, while the PECE mode is the most stable. The figure tells us that the scaling roughly doubles the stability region for the PE and PEC modes while enlarging it a little in the PECE case.

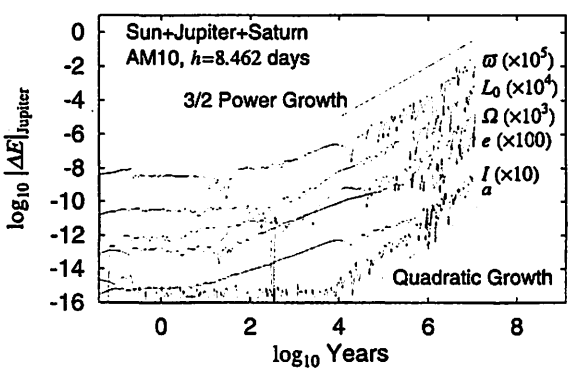

FIG. 17.—Same as Fig. 16, but the step size was changed to 8.462 days, 1/512 of Jupiter's nominal orbital period, so that round-off errors are dominant. This time, all the angle element errors grow in proportion to the 3/2 power of time.

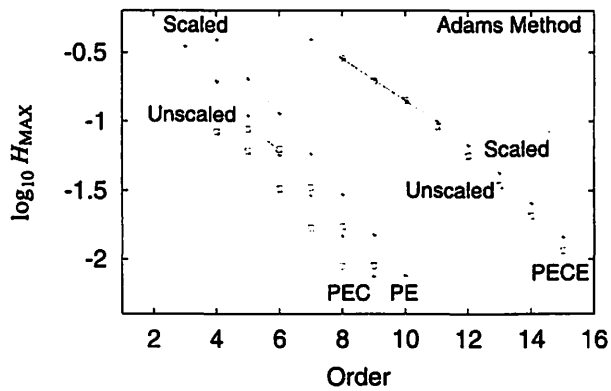

FIG. 18.—Maximum stable phase, H_{max}, for integrating perturbed Keplerian orbits. Stability was judged by whether the error growth with respect to time was normal after 1024 orbital periods. The maximum stable step size is obtained as H_{max} divided by the mean motion. We confirmed that H_{max} is dependent on the order and the mode of integration methods but independent of the eccentricity and the perturbation type. The curves are the scaled and unscaled cases for the explicit Adams method, labeled "PE," and the two modes of the implicit Adams methods, labeled "PEC" and "PECE." As usual, the PEC mode is the least stable, while the PECE mode is the most stable. The scaling roughly doubles the stability region for the PE and PEC modes, while it enlarges H_{max} a little in the PECE case.

4. CONCLUSION

As a new approach to integrating quasi-Keplerian orbits, we propose simultaneously integrating not only the usual equation of motion but also the time evolution of the Kepler energy, the total energy for pure Keplerian orbits. Then we correct at each integration step the integrated position and velocity by a spatial scale transformation such that the Kepler energy analytically evaluated by them coincides with the integrated Kepler energy.

The scale factor is determined by solving an associated cubic equation using Newton's method from a natural starting value, unity. We observed that the determined value of the scale factor depends on the magnitude of the phase advance per step and the order and other properties of the integrator adopted. Thus, in treating multiple bodies we integrate the Kepler energies for all bodies and adjust the scales separately.

Numerical experiments show that the scaling reduces the integration error significantly. In the case of pure Keplerian orbits, the truncation error grows only linearly with respect to time. The linearly growing component is due to discretization error along the track, which is not in principle compensated by the scaling. When perturbations exist, a more rapidly growing[11] component appears as usual; however, its magnitude is significantly decreased compared with the case without scaling. The nature of the decrease roughly follows power laws with respect to the strength of the perturbing acceleration, where the power index depends on the type of perturbation: 5/4 for air drag, 2 for J_2 and third-body

[11] Typically quadratic with time.

acceleration, and 5/2 for general relativistic effects. In addition, the scaling seems to suppress the accumulation of round-off errors, though the detailed mechanism is still to be studied.

As a result, when perturbations are weak, the position error of the scaled integration seems to grow linearly with respect to time for a considerable duration. For example, in the case of an integration of the Sun and nine major planets, the position error of Mercury, which grows most rapidly, is observed to increase almost linearly with respect to time for the first 1 million years.

The applicability of the new method is wide. In fact, it works for (1) any type of numerical integrator for general first-order ODEs, such as the Runge-Kutta methods, the extrapolation methods, and the linear multistep methods for first-order ODEs, including the well-known Adams methods; (2) any type of perturbations, whether velocity-dependent or not, conservative or not, or autonomous or not; (3) any number of integrated bodies; (4) any type of base orbit, that is, elliptical, parabolic, or hyperbolic; and (5) any choice of integration order, extrapolation stage, variability of step size, or other parameters of integration.

On the other hand, the implementation is simple, as shown in the foregoing. Also, the additional cost of computation is low. In fact, the evaluation of the time variation of the Kepler energy is straightforward because the perturbation acceleration is already evaluated in the equation of motion.

We must admit that the effect of rounding off in the scaled integration is not completely understood. However, from the observation of a linear error growth in integrating the pure Keplerian orbits, we report that the accumulation of round-off error is suppressed in the scaled integration regardless.

Another drawback of the current method is that it cannot be used with the Störmer-Cowell method and other integrators for special second-order ODEs, which are known to possess better properties than those for general first-order ODEs, such as larger stability regions or smaller error constants. To overcome this difficulty, we need another breakthrough in the methodology.

Note that the Kepler energy is not the only quantity conserved in unperturbed orbits. The other local quasi-conserved properties are the orbital angular momentum and the Laplace-Runge-Lenz vector. For example, Hairer et al. (1999) report in their example (4.3) and Figure 4.3 that a simultaneous manifold correction using the energy and the angular momentum leads to a better numerical integration in the case of a perturbed Keplerian orbit.

Also available would be the global quasi-conserved properties such as the total energy and the total angular momentum. Of course, it is not easy to find an appropriate way to modify the integrated position and velocity from the integrated values of these quantities. These issues are challenging but worthwhile to investigate.

The current approach is not limited within the framework of orbital dynamics. The key point of the new method is to modify the integrated variables by using the information obtained by simultaneously tracking the time development of quasi-conserved quantities. This concept is applicable to other types of motion, rotational motion being an example. This would be an interesting line of pursuit.

In conclusion, the new approach provides a fast and high-precision device to simulate the orbital motions of major and minor planets, natural and artificial satellites, comets, and space vehicles at a negligible increase in computational time and involving little labor for its implementation.

APPENDIX

SOLUTION OF THE EQUATION OF KEPLER ENERGY CONSISTENCY

Consider how to solve the equation of Kepler energy consistency, equation (8). It is obvious that a physically meaningful value of the scale factor must be positive. Thus we limit the solution domain to $s > 0$.

A1. DEGENERATE CASE

First of all, consider a trivial case, $T = 0$. In this case the equation reduces to a linear equation:

$$Ks - U = 0 . \tag{A1}$$

Since $U < 0$, this equation has a positive solution,

$$s = U/K , \tag{A2}$$

only when $K < 0$. We do not have to worry about the other case, $T = 0$ and $K \geq 0$, since it corresponds to the artifact of zero velocity at finite distance in a parabolic or hyperbolic orbit.

A2. EXISTENCE OF A MEANINGFUL SOLUTION

Let us prove the existence of a meaningful solution when $T \neq 0$. Note that T is positive definite in this case, as

$$T = v^2/2 > 0 . \tag{A3}$$

Then

$$f(0) = U = -\mu/r < 0 ,$$
$$f(+\infty) = \lim_{s \to \infty} f(s) = \lim_{s \to \infty} Ts^3 = +\infty > 0 . \tag{A4}$$

Thus, at least one meaningful solution always exists, since $f(s)$ is continuous.

A3. UNIQUENESS OF THE MEANINGFUL SOLUTION

Next we will show that the meaningful solution is unique. In the domain $s > 0$,

$$f''(s) = 6Ts > 0 . \tag{A5}$$

Thus $f'(s)$ is monotonically increasing in this domain. Now we will discuss the issue in the following three cases depending on the sign of K.

1. *Case* $K < 0$: Assume that $K < 0$. This corresponds to elliptical orbits in the osculating sense. Note that $f'(s)$ is positive definite, as

$$f'(s) = 3Ts^2 - K > 0 . \tag{A6}$$

This indicates that $f(s)$ is monotonically increasing, and therefore the meaningful solution is unique.

2. *Case* $K = 0$: In the case that $K = 0$, the original equation reduces to a simpler form,

$$f(s) = Ts^3 + U = 0 . \tag{A7}$$

Since $U < 0$ and $T > 0$, this has a unique positive solution.

$$s = \sqrt[3]{-U/T} . \tag{A8}$$

3. *Case* $K > 0$: Consider the case $K > 0$, which implies hyperbolic orbits. The equation $f'(s) = 0$ then has two real solutions,

$$s_{\pm} = \pm\sqrt{\tfrac{1}{3}K/T} . \tag{A9}$$

It is easy to see that $f'(s) > 0$ when $s < s_-$ and $s > s_+$, while $f'(s) < 0$ when $s_- < s < s_+$. For the positive solution,

$$f(s_+) = U - (2K/3)s_+ < 0 , \tag{A10}$$

since $U < 0$, $K > 0$, and $s_+ > 0$. We separate the $s > 0$ solution domain into two subdomains, $0 < s \leq s_+$ and $s_+ < s$.

a) Subdomain $0 < s \leq s_+$: In this region, $f(s)$ is monotonically decreasing because $f'(s) < 0$. Since $f(0) < 0$, we have $f(s) < 0$ in the subdomain. This means that the equation $f(s) = 0$ has no solution in this subdomain.

b) Subdomain $s_+ < s$: Here $f(s)$ is monotonically increasing because $f'(s) > 0$. Since $f(s_+) < 0$ and $f(+\infty) > 0$, the equation $f(s) = 0$ has a unique solution in this subdomain.

Combining these two results, we have proved that the equation $f(s) = 0$ has a unique solution in the meaningful domain $s > 0$.

In conclusion, except for the physically meaningless case in which $T = 0$ and $K \geq 0$, the equation of Kepler energy consistency has a unique solution in the meaningful domain $s > 0$.

A4. DEFINITE CONVERGENCE OF NEWTON'S METHOD

We have shown the uniqueness of the solution in the domain $s > 0$. Therefore, once we find a solution satisfying the cubic equation, it is ensured to be the true solution.

As for the technique to solve the equation, we adopt Newton's method because of its fast convergence. However, the method has the possibility of diverging for inappropriate choices of the starting value. Thus, let us consider sufficient conditions for the definite convergence of Newton's method for the cubic equation.

Denote the true solution by s_∞. The discussion in the previous subsection leads to the conclusion that $f(s)$ and $f'(s)$ are always positive if $s > s_\infty$. For such s,

$$f^*(s) - s = -f(s)/f'(s) < 0 . \tag{A11}$$

On the other hand, from the definition of $f^*(s)$, it is easy to show that

$$f^*(s_\infty) = \frac{s_\infty f'(s_\infty) - f(s_\infty)}{f'(s_\infty)} = s_\infty , \tag{A12}$$

since $f(s_\infty) = 0$. Thus, there exists a value s' satisfying the condition $s_\infty < s' < s$ such that

$$f^*(s) - s_\infty = f^*(s) - f^*(s_\infty) = \frac{df^*}{ds}(s')(s - s_\infty) > 0 . \tag{A13}$$

Thus we have shown that the Newton corrector gets closer to the solution than the previous guess, as

$$s_\infty < f^*(s) < s \tag{A14}$$

if approaching from upper bounds of the solution. Aside from the speed of convergence, this means that a sufficient condition for convergence is to start from an upper bound of the solution.

A5. STABLE STARTING POINT FOR NEWTON'S METHOD

Let us seek suitable upper bounds of the solution as starting points. To do this, we study the properties of the Newton corrector, $f^*(s)$. By using its differential expression,

$$\frac{df^*}{ds} = \frac{f(s)f''(s)}{[f'(s)]^2} , \tag{A15}$$

we rewrite equation (A13) as

$$f^*(s_0) - s_\infty = \frac{f(s_1)f''(s_1)}{[f'(s_1)]^2}(s_0 - s_\infty) , \tag{A16}$$

where we have renamed s and s' in equation (A13) s_0 and s_1, respectively. Note that this relation holds even when $s_0 < s_\infty$, although the range of s_1 changes to $s_0 < s_1 < s_\infty$ in that case.

On the other hand, there exists another value, s_2, satisfying the condition $s_\infty < s_2 < s_1$ or $s_1 < s_2 < s_\infty$, such that

$$f(s_1) = f(s_1) - f(s_\infty) = f'(s_2)(s_1 - s_\infty) , \tag{A17}$$

since $f(s_\infty) = 0$. Using this, we rewrite the above relation as

$$f^*(s_0) - s_\infty = \frac{f''(s_1)f'(s_2)\theta}{[f'(s_1)]^2}(s_0 - s_\infty)^2 , \tag{A18}$$

where

$$0 < \theta \equiv \frac{s_1 - s_\infty}{s_0 - s_\infty} < 1 . \tag{A19}$$

If the guess s_0 is sufficiently close to the solution s_∞, we may approximate the factor in the right-hand side of equation (A18) as

$$f^*(s_0) - s_\infty \approx A(s_0 - s_\infty)^2 , \tag{A20}$$

where the proportionality coefficient A is bounded by

$$0 < A < f''(s_\infty)/f'(s_\infty) . \tag{A21}$$

This means that if the method converges, it converges quadratically.

Now, equation (A18) indicates that since $f''(s) > 0$ for $s > 0$, $f^*(s_0)$ becomes an upper bound of the solution if

$f'(s) > 0$ holds for all s such that $|s - s_\infty| < |s_0 - s_\infty|$. Next let us find such an s_0.

A6. CHOICE OF STABLE STARTING POINT

Note that $s = 1$ is a natural approximation of the solution; it means that the integrated Kepler energy coincides with the analytically evaluated one. Thus it is a candidate for s_0 in the previous subsection. Since $K \approx T + U < T$, we know that $f'(1) = 3T - K > 0$. Note that $f''(s) > 0$ when $s > 0$ and $f'(s_\infty) > 0$, as we have seen in the previous subsections. Then, $f'(s) > 0$ so long as $s_\infty \le s \le 1$ or $1 \le s \le s_\infty$. Therefore,

$$f^*(1) = \frac{2T - U}{3T - K} \tag{A22}$$

is an upper bound of the solution, and we adopt it as the starting point.

This starting point includes the solution in the degenerate case, equation (A2), as a special case obtained by substituting $T = 0$. Also, in the case that $K = 0$, Newton's method using this starting point obtains a solution faster than evaluating the cube root as in equation (A8).

REFERENCES

Aarseth, S. J. 1985, Multiple Time Scales (New York: Academic)
Baumgarte, J. 1972, Celest. Mech., 5, 490
Brouwer, D. 1937, AJ, 46, 149 (erratum 47, 84 [1938])
Evans, N. W., & Tremaine, S. 1999, AJ, 118, 1888
Fukushima, T. 1996, AJ, 112, 1263
Hairer, E., Lubich, C., & Wanner, G. 1999, Geometric Numerical Integration (Berlin: Springer)
Huang, T.-Y., & Innanen, K. A. 1983, AJ, 88, 870
Lambert, J. D., & Watson, I. A. 1976, J. Inst. Math. Applications, 18, 189
Mikkola, S., & Innanen, K. 2002, AJ, 124, 3445
Murison, M. A. 1989, AJ, 97, 1496
Nacozy, P. E. 1971, Ap&SS, 14, 40
Quinlan, G. D., & Tremaine, S. 1990, AJ, 100, 1694
Stiefel, E. L., & Scheifele, G. 1971, Linear and Regular Celestial Mechanics (New York: McGraw-Hill)
Szebehely, V., & Bettis, D. G. 1971, Ap&SS, 13 365

Explicit Symmetric Multistep Methods for First-Order Differential Equations

Tadato YAMAMOTO
tadato.yamamoto@nao.ac.jp
Department of Astronomical Science,
Graduate University for Advanced Studies(SOKENDAI),
2-21-1, Osawa, Mitaka, Tokyo 181-8588 JAPAN

Toshio FUKUSHIMA
Toshio.Fukushima@nao.ac.jp
National Astronomical Observatory of Japan,
2-21-1, Osawa, Mitaka, Tokyo 181-8588 JAPAN

ABSTRACT

We show the comprehensive evaluations of symmetric linear multistep methods for first-order ordinary differential equations (ODEs). First, paying attention to the maximum value of stable stepsize and the error constants, we investigate widely. Because the symmetric formulas contain multiple free parameters in each order, the property of formula is greatly different depending on the values of free parameters. Thus, changing values of free parameters every time, we calculate the maximum value of stable stepsize and the error constant, and find the formulas which have good properties. Next, in order to investigate the time dependence and the stepsize dependence, we carry out numerical experiments using *pure* first-order ODEs, the elliptic function corresponding to torque-free rotational motion.

1 Introduction

線形多段法は自由度が高く、さまざまな形の公式を作ることができるが、優れた公式となると限られてくる。その優れた公式の一つが係数に対称性を持つ対称線形多段法である。対称線形多段法の最大の特徴はエネルギーなどの保存量の誤差が時間に対して増大せず、その結果、経度方向の誤差が時間の一次でしか成長しないことである。非対称型の多段法やルンゲ・クッタ法などでは、エネルギーは時間の一次、経度は二次で誤差が成長していく。

対称型公式が注目されるようになったのは比較的最近で、主な先行研究としては、加速度が位置のみの関数である場合に相当する特殊な二階の微分方程式系 $\frac{d^2x}{dt^2} = f(x,t)$ についてはLambert & Watson (1976) が最初の論文で、Quinlan & Tremaine (1990)、Fukushima (1998)、Quinlan (1999)、Arakida & Fukushima (2000) などごくわずかである。一階の微分方程式系についてはEvans & Tremaine (1999) しかないが、彼らは特殊な二階の微分方程式である、軌道運動への応用しか議論していない。

このようなことから、従来、まったく研究されていない一般の一階の微分方程式系用の対称線形多段法に注目した。一階の微分方程式用の公式というのは適用範囲が広く、特殊な二階の微分方程式に対しても当然使用できる。逆に特殊な二階の微分方程式系用の公式では、一般相対論的効果など加速度が速度にも依存するような微分方程式系には使用できない。もちろん、

オイラーの自転運動方程式のように純粋な一階の微分方程式系は、一階用の公式でなければ計算できない。

一般に対称型公式は係数に自由パラメータを含む形で表現でき、高次の公式になるほどパラメータの数が増えていく。本研究では、自由パラメータを値を変化させることによって変動する安定領域の最大値と誤差定数の値に注目し、10次までの公式の広範な調査を行ない、最適な公式群を導出した。最後に得られた公式で実際に数値実験を行ない、総合的に公式を評価した。

2 Symmetric Multistep Methods

線形多段法の一般型は以下のように書ける。

$$\sum_{j=0}^{k} \alpha_j y_{n-j} = h \sum_{j=0}^{k} \beta_j f_{n-j} \tag{1}$$

とくに一階の対称型公式の場合、係数 α と β は

$$\alpha_j = -\alpha_{k-j} \quad , \quad \beta_j = \beta_{k-j} \tag{2}$$

をみたす。

線形多段法の公式の構築および評価を行なう際には特性多項式を使い、以下のように書く。

$$\rho(z) = \sum_{j=0}^{k} \alpha_j z^{k-j} \quad , \quad \sigma(z) = \sum_{j=0}^{k} \beta_j z^{k-j} \tag{3}$$

$\rho(z)$ を第一特性多項式、$\sigma(z)$ を第二特性多項式と呼ぶ。

• 公式の作り方

演算子法を用いることにより、任意次数に対する最も一般的な線形多段法の公式は、数式処理ソフトなどを使えば、以下の手順で簡単に作ることができる。

1. $\rho(z) = 0$ のすべての根が複素単位円の内側、つまり $|z| \leqq 1$ となるように係数 α を決定
2. 係数 β は陽型公式 ($\beta_0 \equiv 0$) の場合、

$$B(z) = \frac{\rho(z)}{z \log z} \tag{4}$$

を $z = 1$ のまわりでテーラー展開したときの各 z の係数

Adams 型の4次の公式を作る場合はテーラー展開を3次まで行なえば係数が得られる

$$\frac{z-1}{z \log z} \quad \Longrightarrow \quad \frac{55}{24} - \frac{59}{24} z + \frac{37}{24} z^2 - \frac{9}{24} z^3 + \cdots \tag{5}$$

$$y_{n+1} = y_n + \frac{1}{24} h \Big(55 f_n - 59 f_{n-1} + 37 f_{n-2} - 9 f_{n-3} \Big) \tag{6}$$

とくに、対称型公式の場合は $\rho(z)=0$ の根はすべて複素単位円周上になるので、対称型公式の係数 α は

$$\rho(z)=(z-1)\prod(z^2-2\cos\theta_i z+1) \tag{7}$$

係数 β は

$$B(z)=\frac{(z-1)\prod(z^2-2\cos\theta_i z+1)}{z\log z}\quad,\quad 0<\theta_i<\pi \tag{8}$$

から得られる。

また、一階の対称型公式の場合、$z=-1$ に根を置くことも可能であり、このようにすると最も少ない段数で最大の次数が得られることから、「最良型」と呼ばれている (Henrici , 1962)。以後、最良型でない公式を「標準型」と呼ぶ。具体的に 4 次の公式を書くと

- **最良型 4 次** (4th-order optimal type)

$$y_{n+1}=2a(y_n-y_{n-2})+y_{n-3}+\frac{1}{3}h\Big\{(8-2a)(f_n+f_{n-2})-(4+8a)f_{n-1}\Big\} \tag{9}$$

- **標準型 4 次** (4th-order normal type)

$$y_{n+1}=(2b+2c+1)(y_n-y_{n-3})-2\Big((2b+1)c+b+1\Big)(y_{n-1}-y_{n-2})+y_{n-4}+ \tag{10}$$

$$+\frac{1}{6}h\Big\{\Big((-b-5)c-5b+11\Big)(f_n+f_{n-3})+\Big((13b-7)c-7b+1\Big)(f_{n-1}+f_{n-2})\Big\}$$

$$(-1<a,b,c<1)$$

4 次の最良型はフリーパラメータは 1 つ、普通型は 2 つになる。

● 安定領域の最大値と誤差定数

我々が公式の評価をするにあたって注目するのは 1) 数値不安定を起こさない刻み幅の最大値がどれだけ大きくできるか、2) 差分方程式が微分方程式に対する良い近似であるかの指標となる誤差定数の値が、どれだけ小さくできるかである。

◇ 誤差定数の計算

誤差定数の計算は簡単で一階の公式の場合は以下のようになる。

$$C_0=\sum_{m=0}^{k}\alpha_m\quad,\quad C_q=\frac{1}{q!}\sum_{m=0}^{k}\alpha_m m^q-\frac{1}{(q-1)!}\sum_{m=0}^{k}\beta_m m^{q-1}\qquad(q\geqq 1) \tag{11}$$

で $C_0=\cdots=C_p=0$, $C_{p+1}\neq 0$ となったとき、誤差定数 C は

$$C=\frac{C_{p+1}}{\sum_{m=0}^{k}\beta_m}=\frac{C_{p+1}}{\sigma(1)} \tag{12}$$

で与えられ、このときの p の値が公式の次数になる。したがって、誤差の成長は次のように表現できる。

$$\delta=C\times h^p\times t^n \tag{13}$$

このとき、h は刻み幅、t は積分時間である。t^n の n の値は使う公式や対象とする要素（位置、速度、エネルギー、角運動量など）に依存する。

◇安定領域の最大値（すべての根を求める方法）

安定領域の最大値を理論的に求めるには調和振動子を用いる。今回は一階の微分方程式系を対象にしているので、調和振動子を純粋な一階の運動方程式に書き換えて考える。

$$\text{微分系} \qquad \frac{dy}{dt} = f(\,y\,,\,t\,) = -i\omega_0 y \tag{14}$$

$$\text{差分系} \qquad \sum_{j=0}^{k} \alpha_j y_{n-j} = h\sum_{j=0}^{k} \beta_j f_{n-j} = -i\omega_0 h \sum_{j=0}^{k} \beta_j y_{n-j} \tag{15}$$

ここで安定性多項式を導入し、以下のようにする。

$$\Omega(\,z\,;\,H\,) \equiv \rho(z) + iH\sigma(z) = 0 \quad , \quad H = \omega_0 h \tag{16}$$

安定領域の最大値 H_{MAX} は安定性多項式 Ω の H の値を少しずつ増やしていきながら $\Omega = 0$ の根を求めていき、根の一つが以下の条件に達したときの値である。

$$H_{\mathrm{MAX}} = \lim_{\epsilon \to 0} \left[\min_{\exists j\,,\,|z_j|=1+\epsilon} H \right] \tag{17}$$

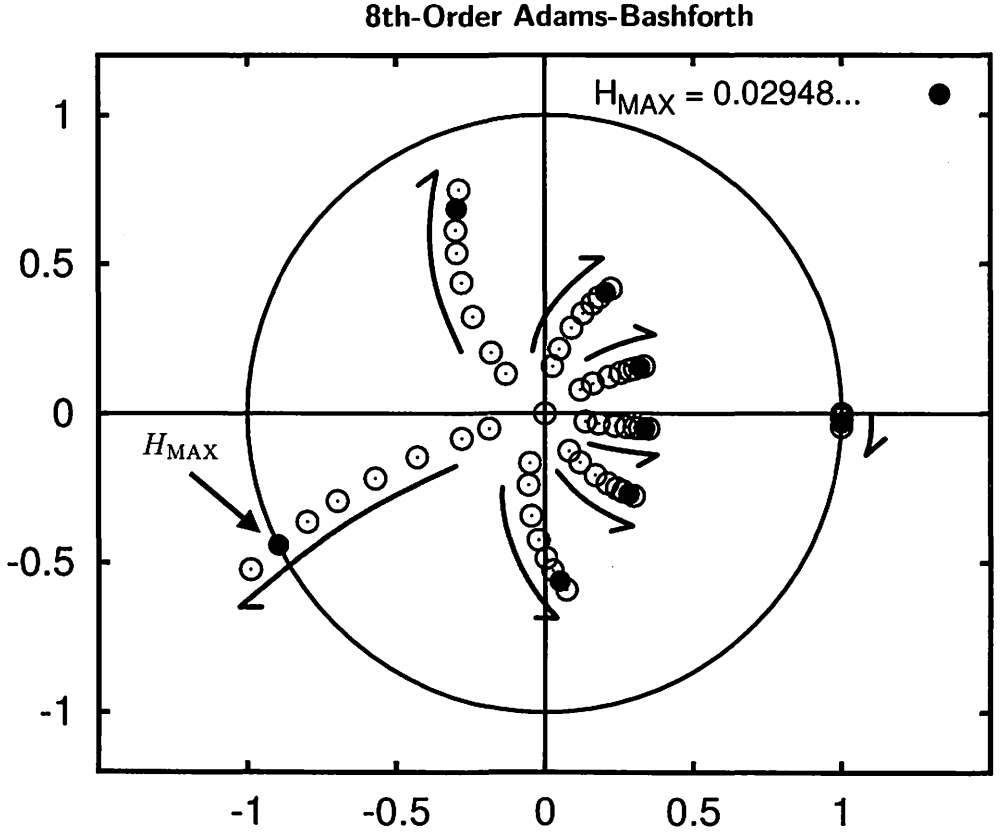

Fig. 1 — Roots in the complex plane of the characteristic polynomial for the 8th-order Adams-Bashforth. Filled circle: $H_{\mathrm{MAX}} = 0.0294855\ldots$. Arrows indicate the direction of movement of roots.

Fig. 1 はアダムス型の 8 次の公式の例である。$H = 0$ のとき根は $z = 1$ に一つと $z = 0$ に 7 重根であるが、H を増やしていくと根が移動していき、矢印のところで複素単位円の外へ出る。

この方法は「安定性多項式の根をすべて求める」という煩雑かつ低速の手法であるため効率は悪いが、根の移動の様子を知るには適している。次に紹介する方法は Lambert (1991) で述べられている周期性関数を使った手法である。

★安定領域の最大値（周期性関数を使った方法）

1. (16) 式の安定性多項式を H について解く

$$H = i\frac{\rho(e^{i\theta})}{\sigma(e^{i\theta})} \equiv F(\theta) \quad , \quad e^{i\theta} = z \tag{18}$$

$z = e^{i\theta}$ とするのは、根を複素単位円周上に限定するため

2. 刻み幅 H は実数でなければならないので、最大値 H_{MAX} は

$$H_{\mathrm{MAX}} = \min_{\substack{0<\theta\leq 2\pi \\ \mathrm{Im}[F(\theta)]=0}} \left|\mathrm{Re}[F(\theta)]\right| \tag{19}$$

虚数部分がゼロであるときの実数部分の最小値が H_{MAX} となる

この手法は、具体的に根を求めることなく、問題を周期性関数の実最大値を求めることに還元し、効率的に最大値を得る方法である。

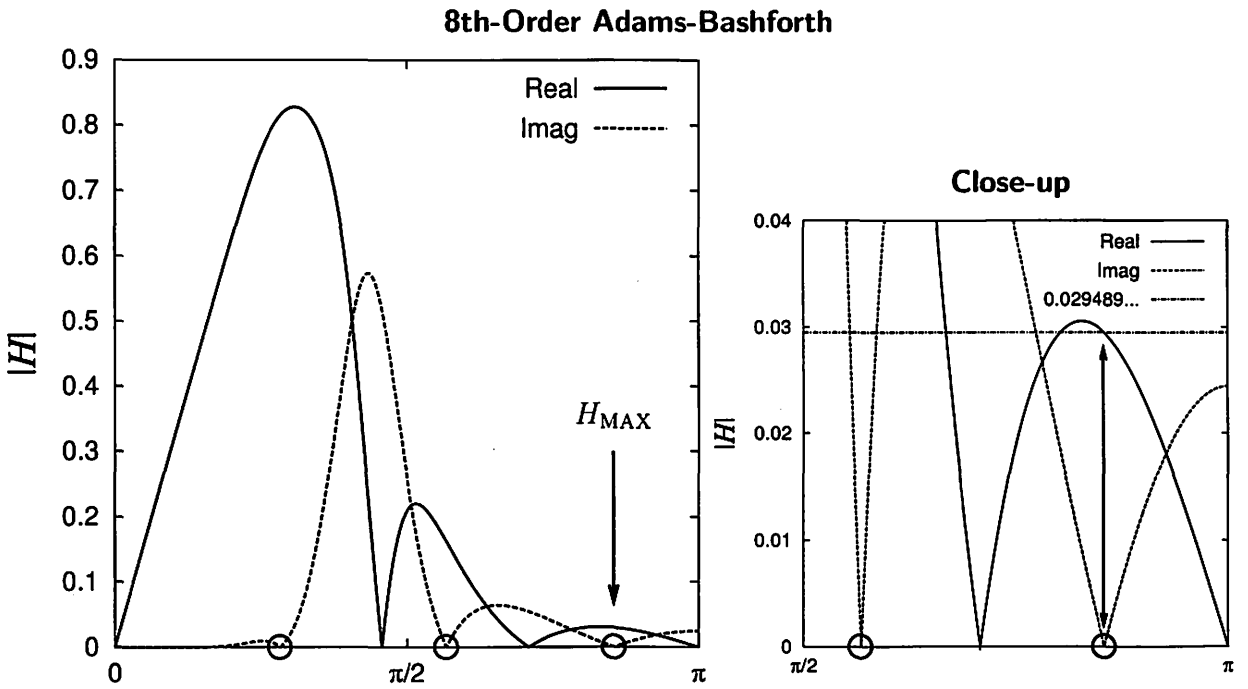

Fig. 2 — Periodicity curve for the 8th-order Adams-Bashforth method; solid lines: real part, dashed lines: imaginary part, dot-dashed lines: $H_{\mathrm{MAX}} = 0.0294855\ldots$.

Fig. 2 のようにグラフを描いてみれば虚数部分がゼロとなる場所（黒円部分）の中で一番小さい値が、すべての根を求める方法で得られた安定領域の最大値に一致していることがわかる。Lambert (1991) では、関数 $F(\theta)$ を複素平面上で図示しているが、容易に理解をするためには我々のように表現することを奨める。また、Lambert では、安定性多項式に指数関数を使っているため、安定領域の最大値が我々と異なることに注意が必要である。

我々の研究対象となっている対称型公式は (9) 式や (10) 式のように自由変数を含む形で表現でき、高次の公式になるほど変数の数が増えていく。この変数の値により安定領域の最大値と誤差定数が変化するため、変数の値を少しずつ変えていきながら広範な調査を行ない、安定領域の最大値と誤差定数を計算するための高速なアルゴリズムを確立した。今回は 2、4、6、8、10 次の公式について詳細な調査を行ない以下のような結果を得た。また、ここでは重根となる場合は考えないこととする。

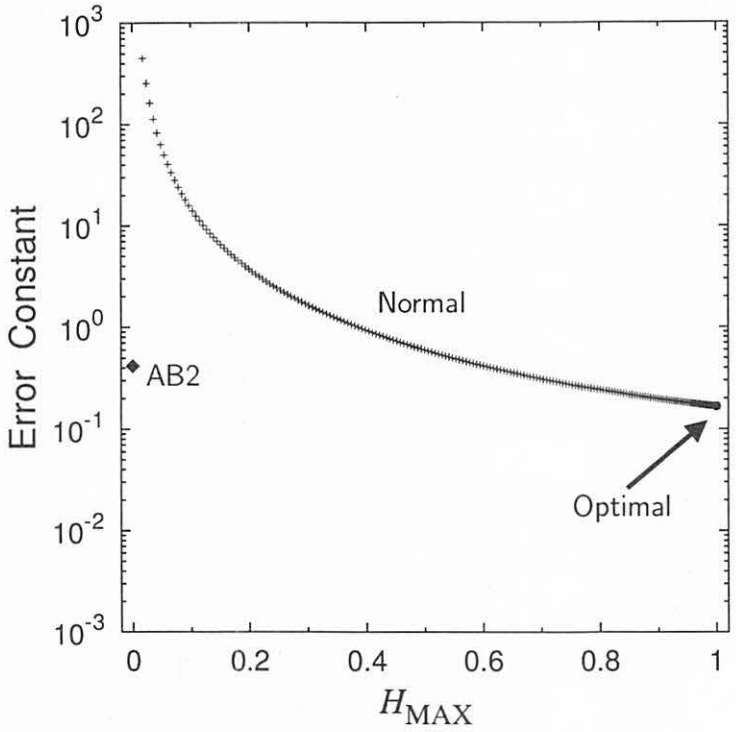

Fig. 3 — 2nd-order explicit formulas: Black circle is the optimal type, the number of free parameters is zero. $H_{\mathrm{MAX}} = 1$ and $C = 1/6$. Crosses are the standard type, the number of free parameters is one and $\Delta\theta = \pi/200$. Black diamond is the 2nd-order Adams-Bashforth method, $H_{\mathrm{MAX}} = 0$ and $C = 5/12$.

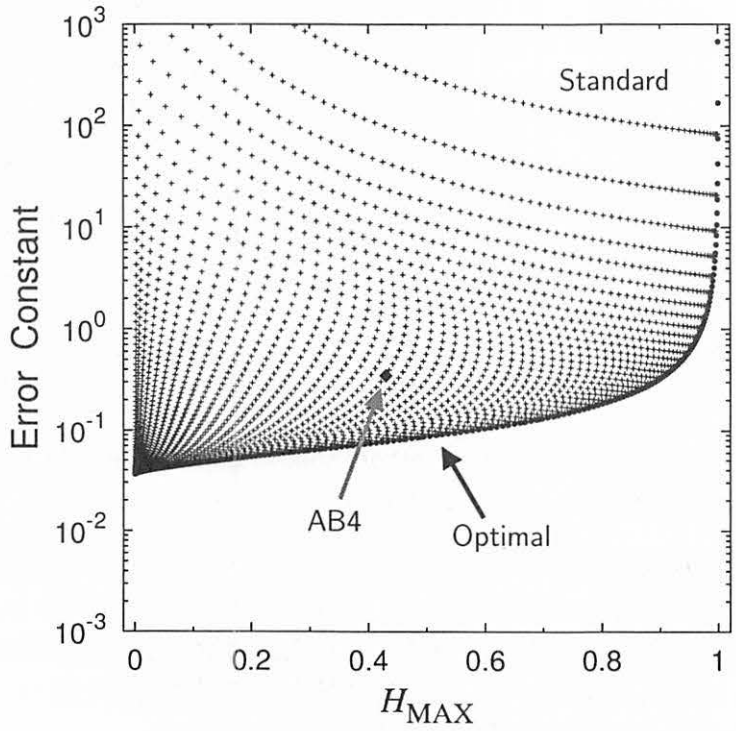

Fig. 4 — 4th-order explicit formulas: Black circles are the optimal type, the number of free parameters is one and $\Delta\theta = \pi/200$. Crosses are the standard type, the number of free parameters is two and $\Delta\theta = \pi/70$. Black diamond is the 4th-order Adams-Bashforth method, $H_{\mathrm{MAX}} = 0.429987...$ and $C = 251/720$.

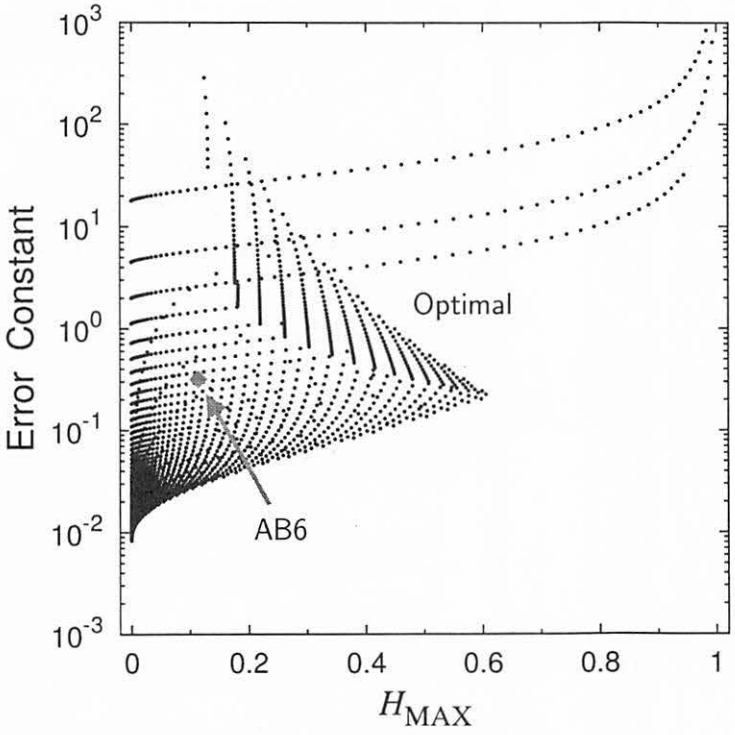

Fig. 5 — 6th-order explicit formulas: Black circles are the optimal type, the number of free parameters is two and $\Delta\theta = \pi/70$.
Gray diamond is the 6th-order Adams-Bashforth method,
$H_{\mathrm{MAX}} = 0.114314...$ and
$C = 19087/60480$.

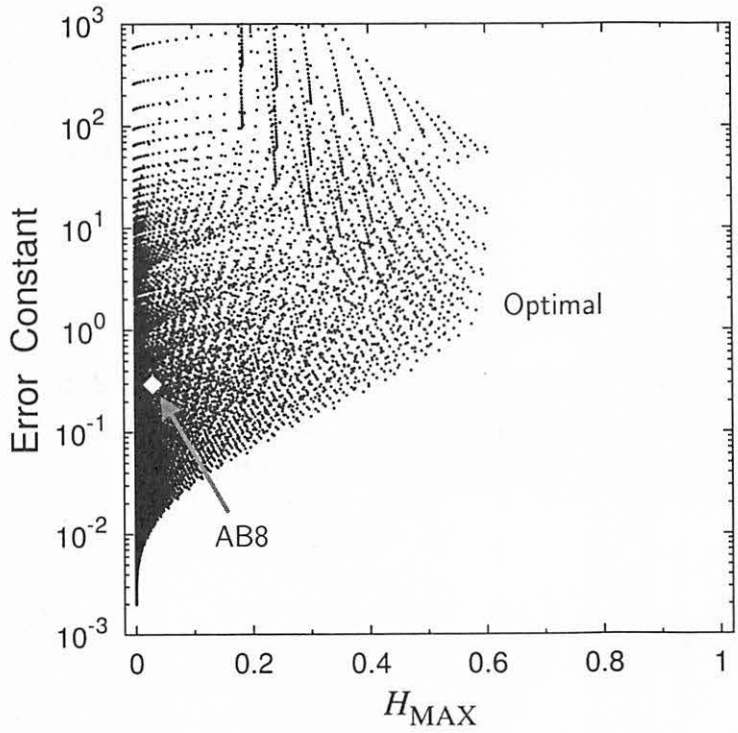

Fig. 6 — 8th-order explicit formulas: Black circles are the optimal type, the number of free parameters is three and $\Delta\theta = \pi/50$.
Gray diamond is the 8th-order Adams-Bashforth method,
$H_{\mathrm{MAX}} = 0.0294895...$ and
$C = 1070017/3628800$.

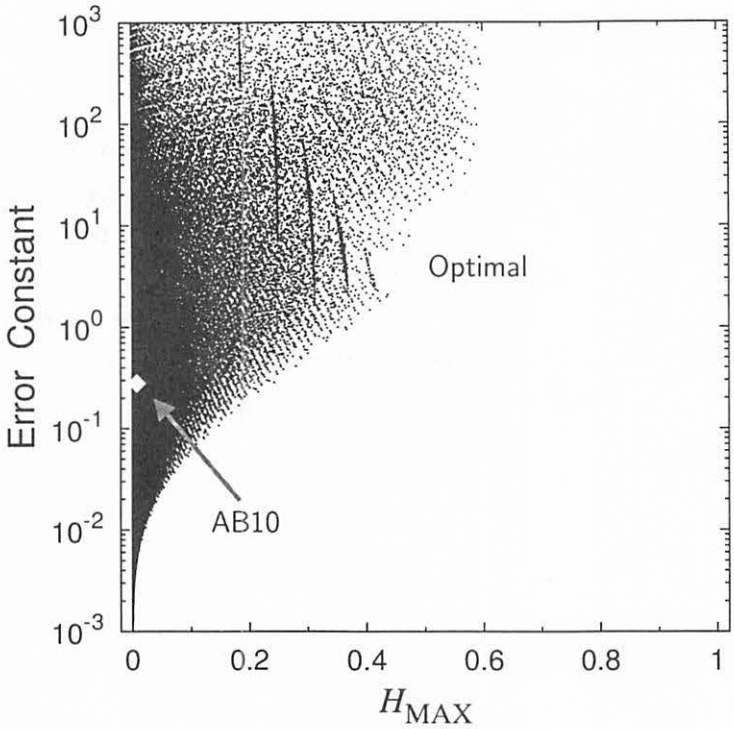

Fig. 7 — 10th-order explicit formulas: Black circles are the optimal type, the number of free parameters is four and $\Delta\theta = \pi/50$.
Gray diamond is the 10th-order Adams-Bashforth method, $H_{\mathrm{MAX}} = 0.00758750...$ and $C = 26842253/95800320$.

各図の $\Delta\theta$ はフリーパラメータを変化させるときの増分である。Fig. 3 と Fig. 4 の 2、4 次の公式からわかることは、最良型公式が標準型公式の最も良い性質を持った公式群になっていることである。Fig. 5〜Fig. 7 の 6〜10 次の公式は最良型のみであるが、この性質は高次の公式でも同様である。したがって、一階用の対称型公式を用いて数値計算する場合、最良型を使えば標準型より変数の数が一つ少なくてすみ、使用する段数も減ることから誤差の削減と計算速度の向上が多少は望める。

3 Numerical experiments

前章で得られた結果を用いて各次数毎に実際に数値計算を行なった。計算に使用する微分方程式は純粋な一階の微分方程式であるオイラーの自転運動方程式のトルクがない場合に相当する楕円関数を用いて数値実験を行なった。微分方程式と解は以下で与えられる。

$$\begin{aligned} \frac{dx}{du} &= yz & & & x &= \mathrm{sn}\, u \\ \frac{dy}{du} &= -zx & & (0 < k < 1) & y &= \mathrm{cn}\, u \\ \frac{dz}{du} &= -k^2 xy & & & z &= \mathrm{dn}\, u \end{aligned} \tag{20}$$

楕円関数における保存量は

$$\begin{aligned} x^2 + y^2 &= 1 \\ k^2 x^2 + z^2 &= 1 \end{aligned} \tag{21}$$

である。出発値は $x = 0$, $y = 1$, $z = 1$ である。

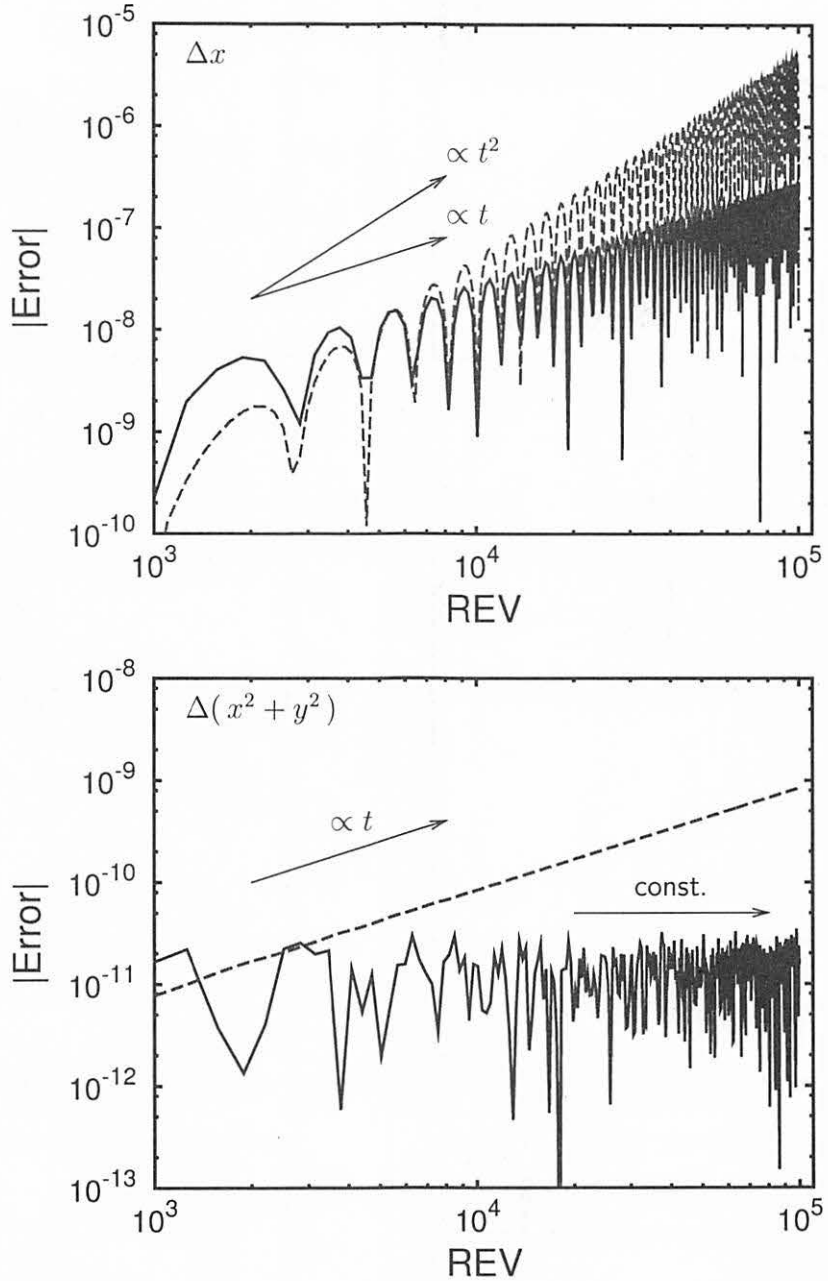

Fig. 8 — The error growth (x and x^2+y^2) in the numerical integration for the elliptic function with $k=0.2$. The solid line denotes the 8th-order symmetric formula with $h=0.04$ and the dashed line does the 8th-order Adams-Bashforth method with $h=0.02$.

Fig. 8 は楕円関数を数値積分した際の時間に対して誤差成長が非対称型と対称型によってどう変わるかを示した例である。対称型公式は保存量の誤差が時間に対して増大せず、経度方向の誤差が時間の一次でしか成長しないことがわかる。

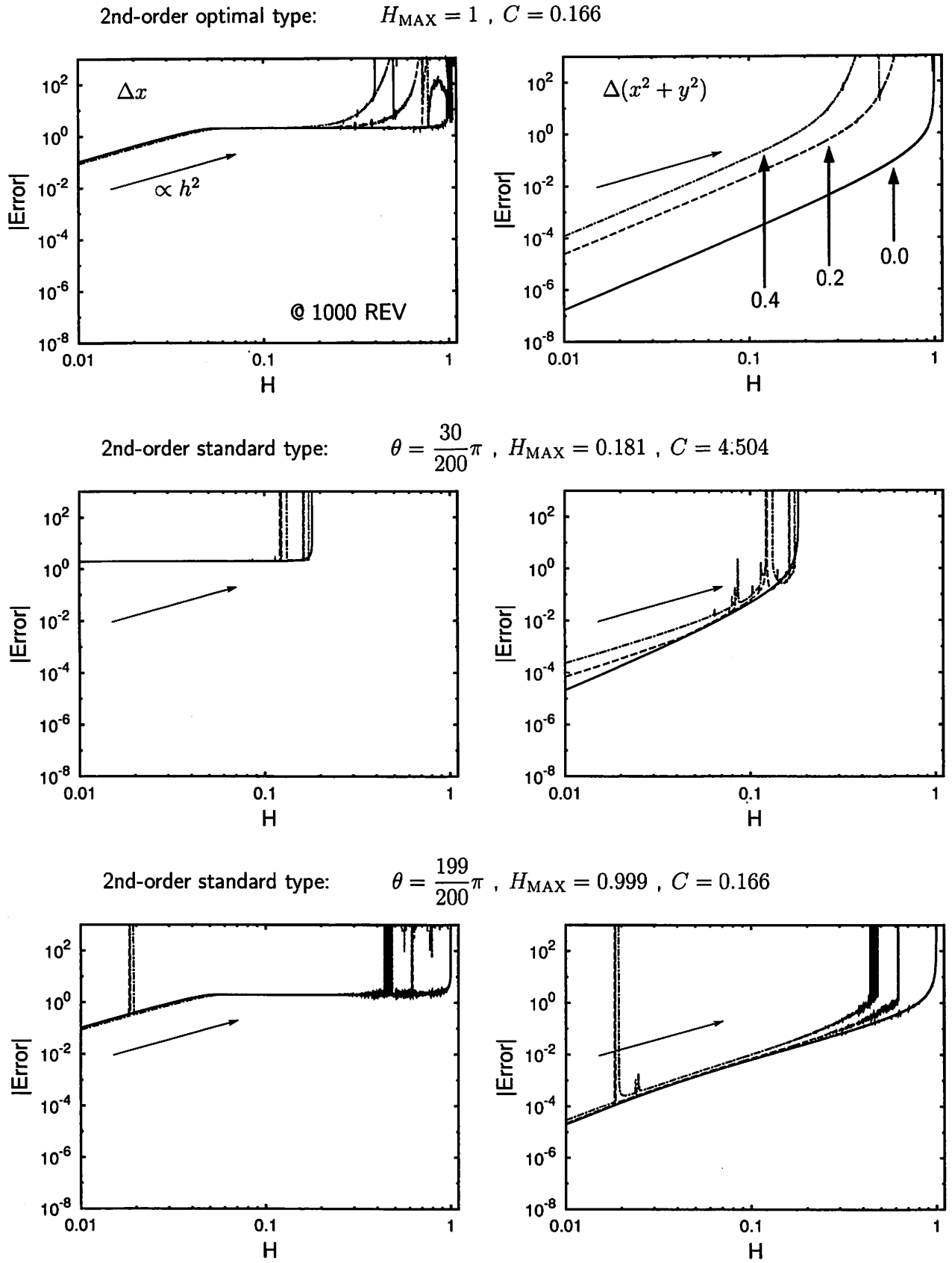

Fig. 9 — 2nd-order symmetric formulas: Stepsize dependence of the error of x (left) and the conserved quantity $x^2 + y^2 = 1$ (right) for the elliptic function after 1000 revolutions with $k = 0.0$ (solid line), 0.2 (dashed line), 0.4 (dot-dashed line). Stepsize H is incremented by $\Delta H = 0.0002$.

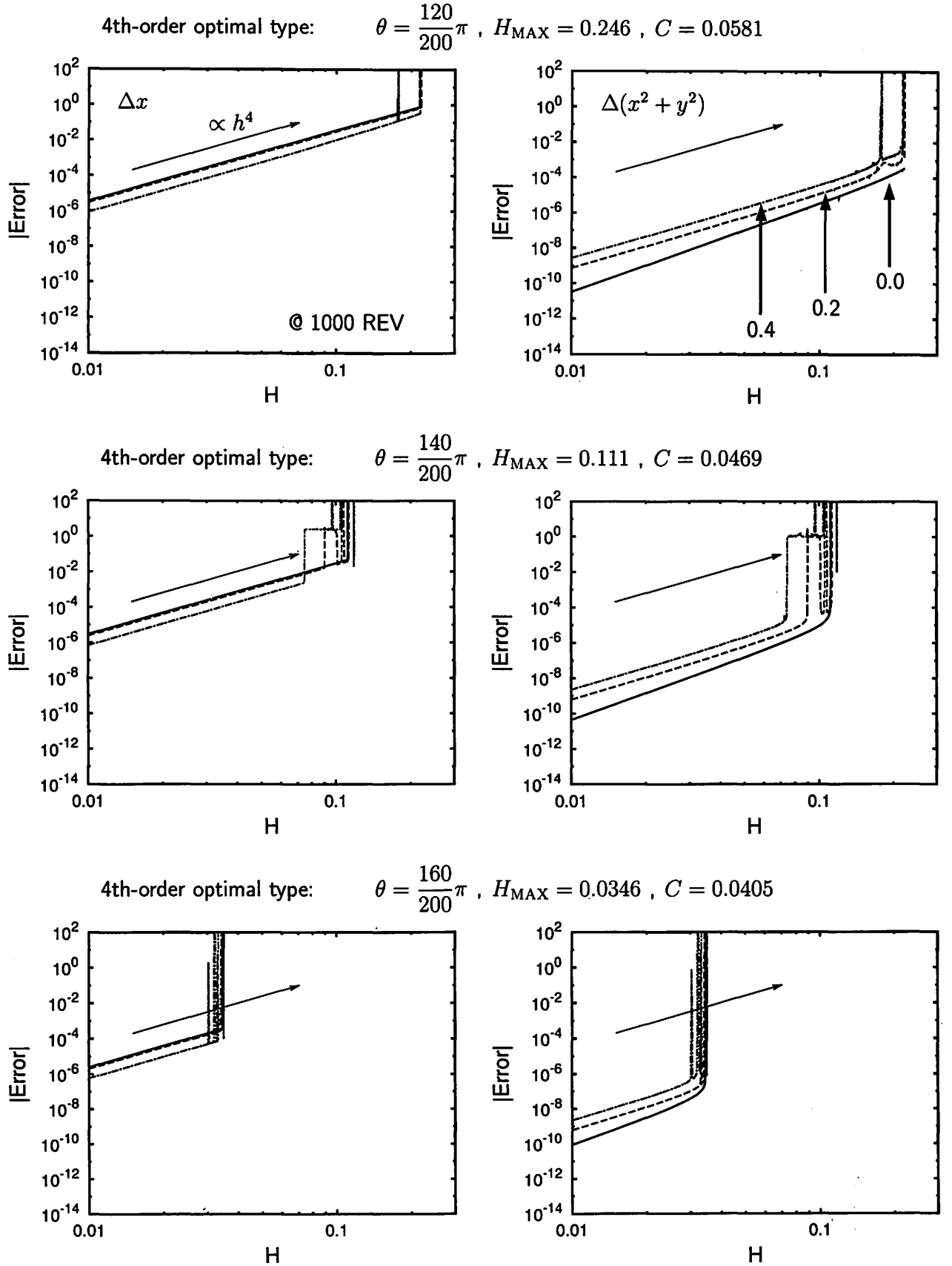

Fig. 10 — 4th-order symmetric formulas: Same as Fig. 9.

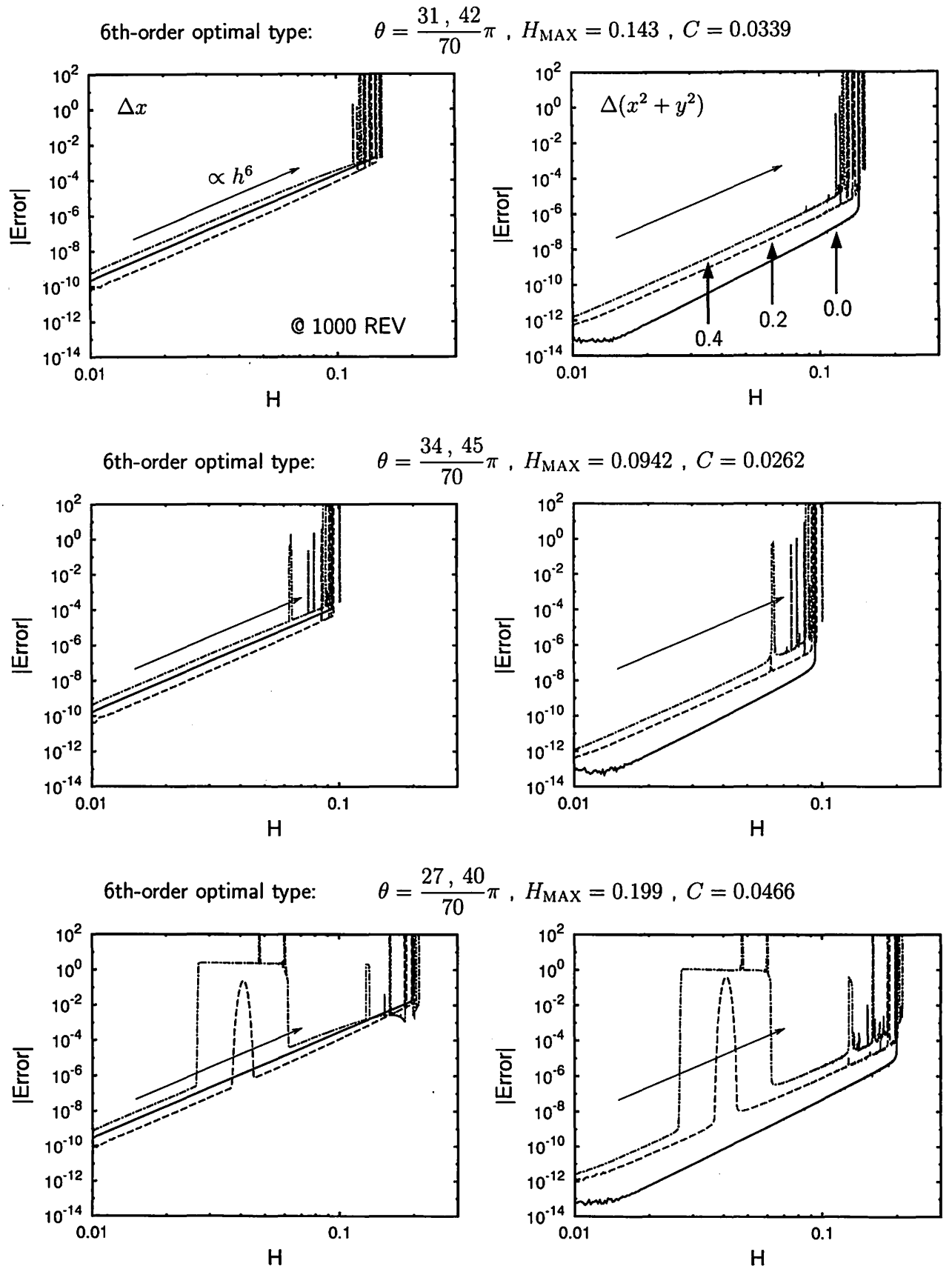

Fig. 11 — 6th-order symmetric formulas: Same as Fig. 9 .

8th-order optimal type: $\theta = \frac{16\,,\,21\,,\,31}{50}\pi$, $H_{\rm MAX} = 0.103$, $C = 0.0374$

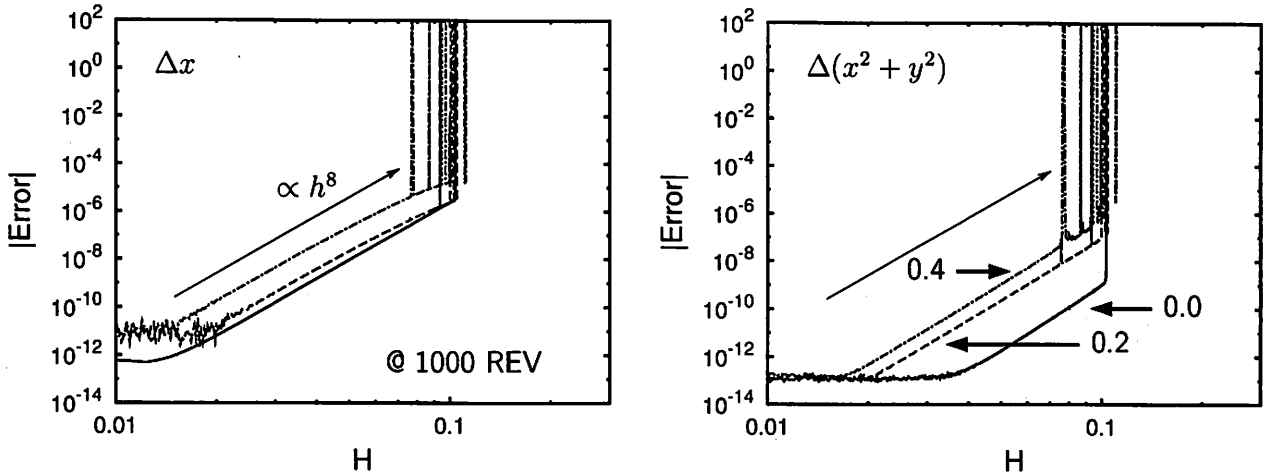

8th-order optimal type: $\theta = \frac{18\,,\,21\,,\,31}{50}\pi$, $H_{\rm MAX} = 0.0935$, $C = 0.0301$

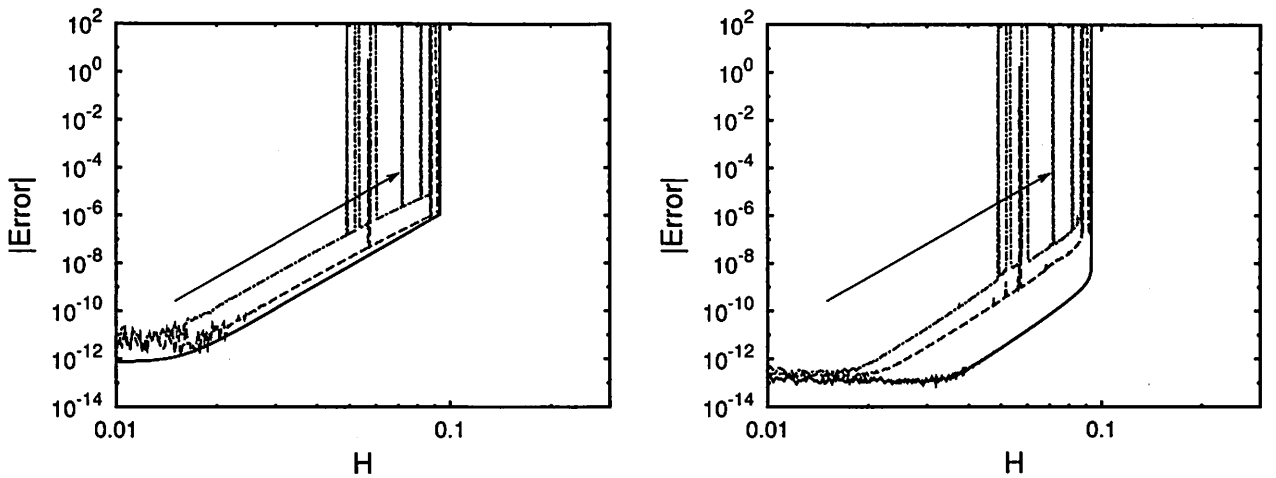

8th-order optimal type: $\theta = \frac{13\,,\,17\,,\,28}{50}\pi$, $H_{\rm MAX} = 0.197$, $C = 0.0947$

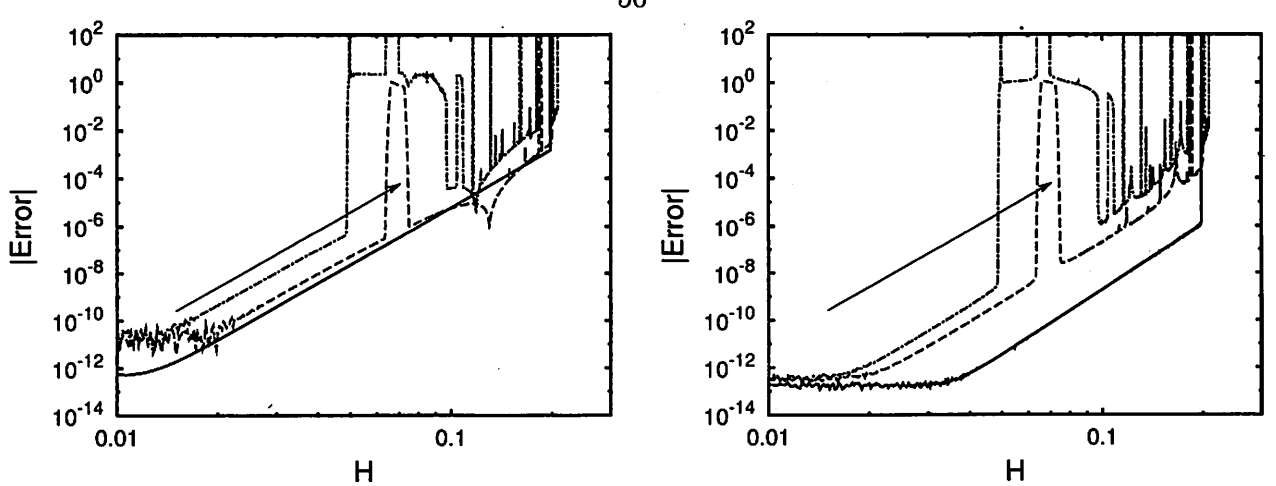

Fig. 12 — 8th-order symmetric formulas: Same as Fig. 9 .

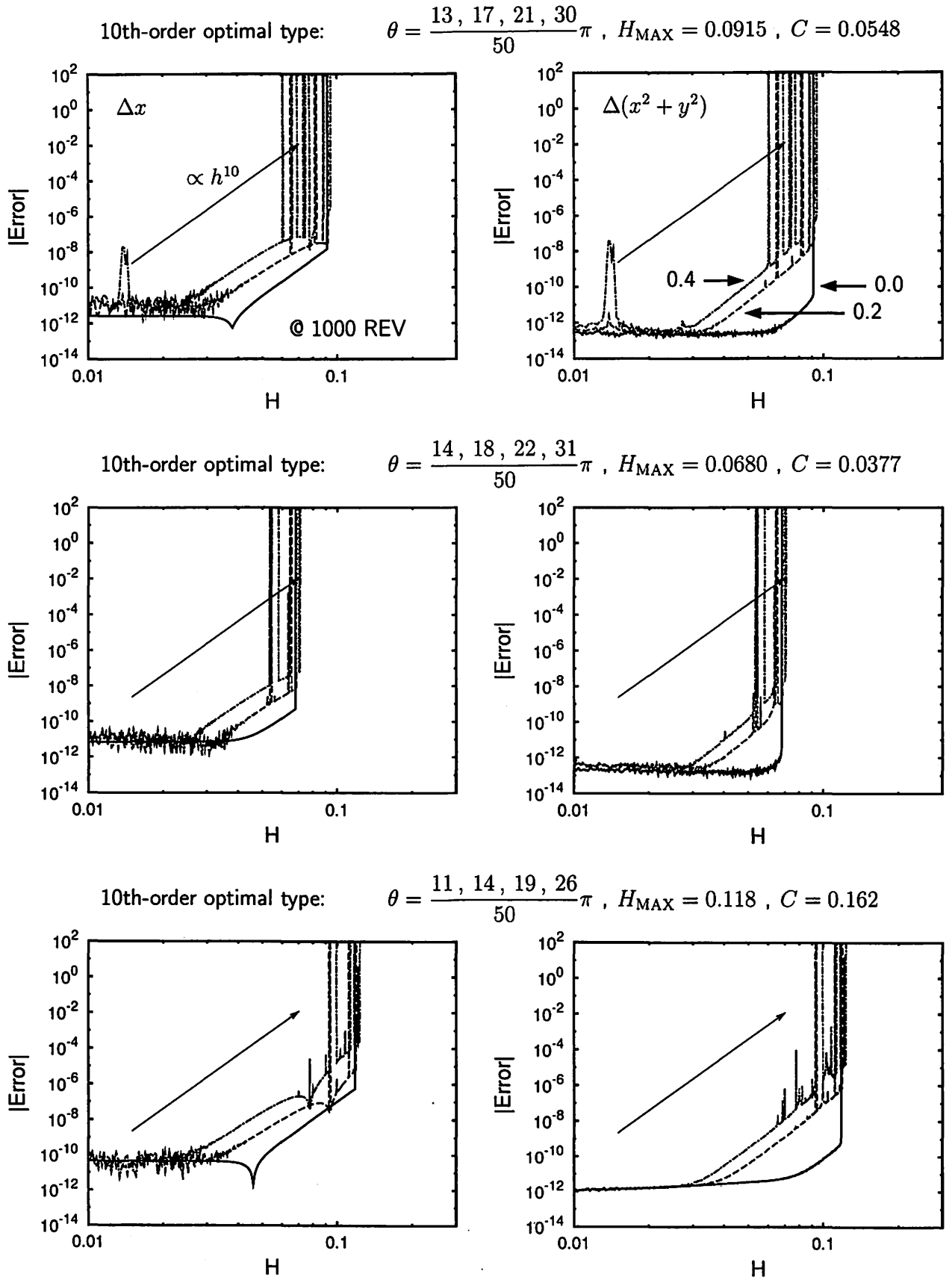

Fig. 13 — 10th-order symmetric formulas: Same as Fig. 9 .

対称型公式には重大な問題がある。それは Quinlan & Tremaine (1990) 発表直後の 1991 年に Toomre が発見した「刻み幅共鳴問題」である。刻み幅共鳴とは非線形な微分方程式系に対称型公式を使用すると、特定の刻み幅の場合、計算誤差が増加する現象である。Fig.10〜Fig.14 で、ところどころで誤差が増大している部分が刻み幅共鳴を起こしている部分である。この現象のメカニズムとしては刻み幅に対応する公式の内在周波数と方程式系が本来含む固有周波数とが共鳴を起こすことに起因すると考えられている。この問題に対する唯一の先行研究が Quinlan (1999、プレプリのみで論文としては発表されていない) であり、原因についてはある程度わかったが、未だ問題の解決には至っていない。彼の議論は特殊な二階の微分方程式系のみなので、我々のように純粋な一階の微分方程式系の場合とは共鳴現象の性質が少し異なっいるようである。楕円関数の場合は k の値によって周期が変化することも共鳴現象の出現場所の特定を困難にする原因の一つと考えられる。ただ、数値実験からわかるように、同じ次数の公式で変数の値がそれほど変わらなくても、共鳴の現れ方には随分違いが生じることがわかった。また、Cano & Sanz-Serna (1998) で証明されている二階の微分方程式系を一階の連立系に変換して一階の対称型公式を使用すると不安定を起こす問題は、今回のように純粋な一階の微分方程式系に対しては当てはまらない問題であることもわかった。

4 Conclusions

今回、我々は一階の微分方程式系に対する対称線形多段法の公式の評価を総合的に行なった。まず、公式の性質を調べるために安定領域の最大値と誤差定数に注目し、対称型公式に含まれるフリーパラメータを変化させていきながら広範な調査を行う手法の確立と計算を行なった。その結果、組合せによって安定領域と誤差定数が幅広く分布することがわかった。また、同次数なら最良型を使用するのが効率が良いこともわかった。次に、実際に純粋な一階の微分方程式で解析解が存在する楕円関数を使用して数値実験を行ない、刻み幅共鳴がどのように現れるのか調べた。結果として、k の値がそれほど大きくなければ、十分実用可能なものであるといえる。また、共鳴が現れにくい組合せと、現れやすい組合せがあるのではないかと思われる。

今後の方針として、実際にトルクがある場合の自転運動問題に適用し、実用可能かどうかを議論し、刻み幅共鳴問題の解決についても行なっていく予定である。

REFERENCES

- Arakida, H. and Fukushima, T. , (2000) , "Long-Term Integration Error of Kustaanheimo-Stiefel Regularized Orbital Motion" , *Astron. J.* , **120** , 3333-3339
- Cano, B. and Sanz-Serna, J.M. , (1998) , "Error growth in the numerical integration of periodic orbits by multistep methods, with application to reversible systems" , *IMA Journal of Numerical Analysis* , **18** , 57-75
- Evans, N.W. and Tremaine, S. , (1999) , "Linear Multistep Methods for Integrating Reversible Differential Equations" , *Astron.J.* , **118** , 1888-1899
- Fukushima, T. , (1998) , "Symmetric multistep methods revisited" , *Proc. 30th Symp. Celest. Mech.* , 229-247
- Fukushima, T. , (1999) , "Symmetric multistep methods revisited : II. Numerical Experiments" , *IAU Colloq.* , **173** , 309-314
- Goldstein, D. , (1996) , Ph. D. Dissertation , "The Near-Optimality of Störmer Methods for Long Time Integrations of $y'' = g(y)$ " , Department of Mathematics , University of California , Los Angeles
- Hairer, H. , Nørsett, S.P. and Wanner, G. , (1987) , *Solving Ordinary Differential Equations I : Nonstiff Problems* , Springer-Verlag , Berlin
- Henrici, P. , (1962) , *Discrete Variavle Methods in Ordinary Differential Equations* , Jhon Wiley & Sons , New York
- Lambert, J.D. , (1973) , *Computational Methods in Ordinary Differential Equations* , Jhon Wiley & Sons , New York
- Lambert, J.D. , (1991) , *Numerical Methods for Ordinary Differential Systems* , Jhon Wiley & Sons , New York
- Lambert, J.D. and Watson, I.A. , (1976) , "Symmetric Multistep Methods for Periodic Initial Value Problems" , *J. Inst. Maths. Applics.* , **18** , 189-202
- Quinlan, G.D. , (1999) , "Resonances and instabilities in symmetric multistep methods" , *astro-ph/9901136*
- Quinlan, G.D. and Tremaine, S. , (1990) , "Symmetric multistep methods for the numerical integration of planetary orbits" , *Astron. J.* , **100** , 1694-1700

Comment on Cowell's Method

Watanabe, Noriaki (Chiba University of Commerce)
Konodai 1-3-1, Ichikawa, 272-8512 Japan

Abstract

Interpolation formulas have been used to obtain the integration formulas, and thus obtained integration formulas have been applied to solve numerically the equations of motion of heavenly bodies.

In the present paper I show that coefficients of integration formulas can easily be derived from the coefficients of Adams-Moulton's formula by employing operators to express interpolation formulas.

1 Introduction

Interpolation methods have long been used to integrate numerically the equations of motion of celestial bodies ([4], [6], [9]). In [5], Oesterwinter and Cohen sketched Cowell's method. They listed there two kinds of coefficients a_i and c_i and therefrom constructed other coefficients necessary to proceed integration. These coefficients can we obtain by generating functions, if we find them ([1], [10]). But we can also find such coefficients by employing operators to express interpolation formulas ([2], [3], [7], [8]).

In the present paper I will show that we can easily find interpolation formulas and integration formulas by employing operators, and all the coefficients of integral formulas can be derived from the coefficients of Adams-Moulton's formula.

2 Differnce Formulas Derived by Using Operators

We introduce an operator τ which shifts an argument of a function $f(t)$ by h :

$$\tau f(t_0) = f(t_0 + h), \quad \tau^{-1} f(t_0) = f(t_0 - h), \quad \tau^0 f(t_0) = f(t_0) \tag{1}$$

Applying τ to $f(t)$ by k times, we get

$$\tau^k f(t_0) = f(t_0 + kh). \quad (k : \text{integer}) \tag{2}$$

Hereafter we write for any integer k

$$f_k = f(t_0 + kh), \quad (k : \text{integer}) \tag{3}$$

We generalize (2) so that it holds for any real u

$$\tau^u f(t_0) = f(t_0 + uh), \quad (u : \text{real}) \tag{4}$$

For any real u, w the following relations hold :

$$\tau^u \tau^w = \tau^{u+w} = \tau^w \tau^u. \quad (u, w : \text{real}) \tag{5}$$

We define a forward difference operator Δ as follows :

$$\Delta f_k = f_{k+1} - f_k \tag{6}$$

From this definition and (1), it follows that

$$\Delta f_k = f_{k+1} - f_k = \tau f_k - f_k = (\tau - 1) f_k$$

$$\therefore \quad \Delta = \tau - 1, \quad \tau = 1 + \Delta \tag{7}$$

The n-th difference is defined by

$$\Delta^n f_k = \Delta^{n-1} f_{k+1} - \Delta^{n-1} f_k, \quad (n : \text{integer}) \tag{8}$$

We get from (7)

$$\begin{aligned}
\Delta^n f_k =& (\tau - 1)^n f_k \\
=& \left\{ \tau^n + (-1)\binom{n}{1}\tau^{n-1} + (-1)^2\binom{n}{2}\tau^{n-2} + (-1)^3\binom{n}{3}\tau^{n-3} \right. \\
& \left. + \cdots + (-1)^{n-1}\binom{n}{n-1}\tau + (-1)^n \right\} f_k \\
=& \tau^n f_k - \binom{n}{1}\tau^{n-1} f_k + \binom{n}{2}\tau^{n-2} f_k - \binom{n}{3}\tau^{n-3} f_k + \cdots + (-1)^n f_k \\
=& f_{k+n} - \binom{n}{1} f_{k+n-1} + \binom{n}{2} f_{k+n-2} + \binom{n}{3} f_{k+n-3} + \cdots + (-1)^n f_k
\end{aligned}$$

$$\therefore \Delta^n f_k = \sum_{i=0}^{n} (-1)^i \binom{n}{i} f_{k+n-i} \tag{9}$$

From (4) and (7), it follows for any real u that

$$\begin{aligned}
f((t_0 + kh) + uh) =& \tau^u f(t_0 + kh) = \tau^u f_k \\
=& (1 + \Delta)^u f_k \\
=& \left\{ 1 + \binom{u}{1}\Delta + \binom{u}{2}\Delta^2 + \binom{u}{3}\Delta^3 + \ldots \right\} f_k
\end{aligned}$$

$$\begin{aligned}
\therefore f((t_0 + kh) + uh) =& f_k + \binom{u}{1}\Delta f_k + \binom{u}{2}\Delta^2 f_k + \binom{u}{3}\Delta^3 f_k + \ldots \\
=& \sum_{i=0}^{\infty} \binom{u}{i} \Delta^i f_k
\end{aligned} \tag{10}$$

This is Newton's forward difference formula.

Next we introduce a backward difference operator ∇ :

$$\nabla f_k = f_k - f_{k-1}, \qquad \nabla^n f_k = \nabla^{n-1} f_k - \nabla^{n-1} f_{k-1} \tag{11}$$

From (1) and (6), it follows that

$$\nabla f_k = f_k - f_{k-1} = \Delta f_{k-1} = \Delta \tau^{-1} f_k$$

$$\therefore \quad \nabla = \Delta\tau^{-1} = \tau^{-1}\Delta, \qquad \Delta = \nabla\tau = \tau\nabla \tag{12}$$

From (12) and (7), it follows that

$$\nabla = (\tau - 1)\tau^{-1} = 1 - \tau^{-1}, \qquad \therefore \quad \tau^{-1} = 1 - \nabla, \qquad \tau = (1 - \nabla)^{-1} \tag{13}$$

τ, Δ, ∇ are commutative each other :

$$\tau\Delta = \Delta\tau, \quad \tau\nabla = \nabla\tau, \quad \Delta\nabla = \nabla\Delta \tag{14}$$

$$\therefore \quad \Delta^n = \nabla^n\tau^n = \tau^n\nabla^n, \qquad \nabla^n = \Delta^n\tau^{-n} = \tau^{-n}\Delta^n \tag{15}$$

Applying (15) to f_k, we get

$$\Delta^n f_k = \nabla^n\tau^n f_k = \nabla^n f_{k+n} \tag{16}$$

Multiply both sides by τ^{-n} :

$$\tau^{-n}\Delta^n f_k = \tau^{-n}\nabla^n f_{k+n}$$

$$lhs = \Delta^n\tau^{-n} f_k = \Delta^n f_{k-n}, \quad rhs = \nabla^n\tau^{-n} f_{k+n} = \nabla^n f_k$$

$$\therefore \quad \nabla^n f_k = \Delta^n f_{k-n} \tag{17}$$

Therefore we get from (9) and (17)

$$\nabla^n f_k = \Delta^n f_{k-n} = \sum_{i=0}^{n} (-1)^i \binom{n}{i} f_{k-i} \tag{18}$$

From (4) and (13), it follows for any real u that

$$f((t_0 + kh) + uh) = \tau^u f(t_0 + kh) = \tau^u f_k = (1 - \nabla)^{-u} f_k$$

$$= \left\{1 + \binom{-u}{1}(-\nabla) + \binom{-u}{2}(-\nabla)^2 + \binom{-u}{3}(-\nabla)^3 + \dots\right\} f_k$$

$$\therefore \quad f((t_0 + kh) + uh) = f_k - \binom{-u}{1}\nabla f_k + \binom{-u}{2}\nabla^2 f_k - \binom{-u}{3}\nabla^3 f_k + \dots$$

$$= \sum_{i=0}^{\infty} \binom{u + i - 1}{i} \nabla^i f_k \tag{19}$$

This is Newton's backward difference formula.

3 Integration by Difference Formulas

We put throughout this section

$$t = (t_0 + kh) + uh, \tag{20}$$

$$\varphi(t) = \int f(t)\, dt, \tag{21}$$

$$\psi(t) = \int \varphi(t)\, dt = \iint f(t)\, dt^2 \tag{22}$$

3.1 The case where $f(t)$ is expressed with a forward difference formula

In this case

$$f(t) = f((t_0 + kh) + uh) = (1 + \Delta)^u f(t_0 + kh) = (1 + \Delta)^u f_k \tag{23}$$

Therefore we get as an integral of $f(t)$

$$\begin{aligned}\varphi(t) &= \int f(t)\,dt = \int (1 + \Delta)^u f_k\,dt = h\int (1 + \Delta)^u f_k\,du \\ &= \frac{h}{\log(1 + \Delta)}(1 + \Delta)^u f_k + C = \frac{h}{\log(1 + \Delta)} f(t) + C\end{aligned} \tag{24}$$

and as a twice-integral

$$\begin{aligned}\psi(t) &= \int \varphi(t)\,dt = \int \left\{\frac{h}{\log(1 + \Delta)} f(t) + C\right\} dt = \frac{h}{\log(1 + \Delta)}\int f(t)\,dt + Ct + C' \\ &= \frac{h^2}{\{\log(1 + \Delta)\}^2}(1 + \Delta)^u f_k + Ct + C' = \frac{h^2}{\{\log(1 + \Delta)\}^2} f(t) + Ct + C'\end{aligned} \tag{25}$$

If we put

$$I_k = \int_{t_0 + kh}^{t_0 + (k+1)h} f(t)dt$$

we get from (24)

$$\begin{aligned}I_k &= \varphi(t_0 + (k + 1)h) - \varphi(t_0 + kh) = \frac{h}{\log(1 + \Delta)}\{f(t_0 + (k + 1)h) - f(t_0 + kh)\} \\ &= \frac{h}{\log(1 + \Delta)}\Delta f_k\end{aligned} \tag{26}$$

and

$$\begin{aligned}I_{k-1} &= \varphi(a + kh) - \varphi(t_0 + (k - 1)h) = \frac{h}{\log(1 + \Delta)}\Delta f_{k-1} = \frac{h}{\log(1 + \Delta)}\Delta\tau^{-1} f_k \\ &= \frac{h}{\log(1 + \Delta)}\Delta(1 + \Delta)^{-1} f_k\end{aligned} \tag{27}$$

Next we put

$$J_k = \iint_{t_0 + kh}^{t_0 + (k+1)h} f(t)dt^2$$

then we get from (25)

$$\begin{aligned}J_k &= \psi(t_0 + (k + 1)h) - \psi(t_0 + kh) \\ &= \frac{h^2}{[\log(1 + \Delta)]^2}\{f(t_0 + (k + 1)h) - f(t_0 + kh)\} + Ch \\ &= \frac{h^2}{[\log(1 + \Delta)]^2}\Delta f_k + Ch\end{aligned} \tag{28}$$

and

$$\begin{aligned}J_{k-1} &= \psi(a + kh) - \psi(t_0 + (k - 1)h) = \frac{h^2}{[\log(1 + \Delta)]^2}\Delta f_{k-1} + Ch \\ &= \frac{h^2}{[\log(1 + \Delta)]^2}\Delta\tau^{-1} f_k + Ch = \frac{h^2}{[\log(1 + \Delta)]^2}\Delta(1 + \Delta)^{-1} f_k + Ch\end{aligned} \tag{29}$$

3.2 The case where $f(t)$ is expressed with a backward difference formula

In this case

$$f(t) = f((t_0 + kh) + uh) = (1 - \nabla)^{-u} f(t_0 + kh) = (1 - \nabla)^{-u} f_k \tag{30}$$

Therefore we get as an integral of $f(t)$

$$\begin{aligned} \varphi(t) &= \int f(t)\,dt = \int (1 - \nabla)^{-u} f_k\,dt = h \int (1 - \nabla)^{-u} f_k f_k\,du \\ &= -\frac{h}{\log(1 - \nabla)} (1 - \nabla)^{-u} f_k + C = -\frac{h}{\log(1 - \nabla)} f(t) + C \end{aligned} \tag{31}$$

and as a twice-integral

$$\begin{aligned} \psi(t) &= \int \varphi(t)\,dt = -\int \left\{ \frac{h}{\log(1 - \nabla)} f(t) + C \right\} dt \\ &= -\frac{h}{\log(1 - \nabla)} \int f(t)\,dt + Ct + C' \\ &= \frac{h^2}{\{\log(1 - \nabla)\}^2} (1 - \nabla)^u f_k + Ct + C' \\ &= \frac{h^2}{\{\log(1 - \nabla)\}^2} f(t) + Ct + C' \end{aligned} \tag{32}$$

Similarly as before, we get

$$\begin{aligned} I_{k-1} &= \varphi(t_0 + kh) - \varphi(t_0 + (k - 1)h) \\ &= -\frac{h}{\log(1 - \nabla)} \{ f(t_0 + kh) - f(t_0 + (k - 1)h) \} \\ &= -\frac{h}{\log(1 - \nabla)} \nabla f_k \end{aligned} \tag{33}$$

$$\begin{aligned} I_k &= \varphi(t_0 + (k + 1)h) - \varphi(t_0 + kh) = -\frac{h}{\log(1 - \nabla)} \nabla f_{k+1} \\ &= -\frac{h}{\log(1 - \nabla)} \nabla \tau f_k = -\frac{h}{\log(1 - \nabla)} \nabla (1 - \nabla)^{-1} f_k \end{aligned} \tag{34}$$

Also

$$\begin{aligned} J_{k-1} &= \psi(t_0 + kh) - \psi(t_0 + (k - 1)h) \\ &= \frac{h^2}{[\log(1 - \nabla)]^2} \{ f(t_0 + kh) - f(t_0 + (k - 1)h) \} + Ch \\ &= \frac{h^2}{[\log(1 - \nabla)]^2} \nabla f_k + Ch \end{aligned} \tag{35}$$

$$\begin{aligned} J_k &= \psi(t_0 + (k + 1)h) - \psi(t_0 + kh) = \frac{h^2}{[\log(1 - \nabla)]^2} \nabla f_{k+1} + Ch \\ &= \frac{h^2}{[\log(1 - \nabla)]^2} \nabla \tau f_k + Ch = \frac{h^2}{[\log(1 - \nabla)]^2} \nabla (1 - \nabla)^{-1} f_k + Ch \end{aligned} \tag{36}$$

4 Solving Differential Equation by Difference Formulas

4.1 Differential equation of the first order

Let the differential equation be of the form

$$\frac{dx}{dt} = \tilde{f}(x,t) = f(t) \tag{37}$$

4.1.1 The case where $f(t)$ is expressed with a forward difference formula

In this case we get from (24) as a solution of (37)

$$x = \varphi(t) = \frac{h}{\log(1+\Delta)} f(t) + C \tag{38}$$

We now write $x_k = \varphi(t_0 + kh)$ then we get from (26)

$$\Delta x_k = x_{k+1} - x_k = \varphi(a + (k+1)h) - \varphi(a + kh) = I_k = \frac{h}{\log(1+\Delta)} \Delta f_k$$

Developing the right hand side into a power series of Δ, we get

$$\frac{h}{\log(1+\Delta)} \Delta f_k = h \sum_{i=0}^{n} \bar{a}_i \Delta^i f_k + \bar{R}_{n+1}, \tag{39}$$

where $\bar{R}_{n+1}$ is the remainder term, and we neglect it hereafter. Then we get

$$\Delta x_k = h \sum_{i=0}^{n} \bar{a}_i \Delta^i f_k \tag{40}$$

If we take note of $\Delta x_k = x_{k+1} - x_k$, we get

$$x_{k+1} = x_k + h \sum_{i=0}^{n} \bar{a}_i \Delta^i f_k, \quad \text{or} \quad x_k = x_{k+1} - h \sum_{i=0}^{n} \bar{a}_i \Delta^i f_k \tag{41}$$

Likewise from (27) we get

$$\begin{aligned} \Delta x_{k-1} &= x_k - x_{k-1} = \varphi(t_0 + kh) - \varphi(t_0 + (k-1)h) = I_{k-1} \\ &= \frac{h}{\log(1+\Delta)} \Delta (1+\Delta)^{-1} f_k \end{aligned}$$

Developing the right hand side into a power series of Δ, we get

$$\frac{h}{\log(1+\Delta)} \Delta (1+\Delta)^{-1} f_k = h \sum_{i=0}^{n} \bar{b}_i \Delta^i f_k + \bar{R}'_{n+1}, \tag{42}$$

where $\bar{R}'_{n+1}$ is the remainder term, and we neglect it hereafter. Then we get

$$\Delta x_{k-1} = h \sum_{i=0}^{n} \bar{b}_i \Delta^i f_k \tag{43}$$

If we take note of $\Delta x_{k-1} = x_k - x_{k-1}$, we get

$$x_k = x_{k-1} + h \sum_{i=0}^{n} \bar{b}_i \Delta^i f_k, \quad \text{or} \quad x_{k-1} = x_k - h \sum_{i=0}^{n} \bar{b}_i \Delta^i f_k \tag{44}$$

4.1.2 The case where $f(t)$ is expressed with a backward difference formula

In this case we get from (31)

$$x = \varphi(t) = -\frac{h}{\log(1-\nabla)} f(t) + C \tag{45}$$

It results from (34) that

$$\begin{aligned} \nabla x_{k+1} &= x_{k+1} - x_k = \varphi(t_0 + (k+1)h) - \varphi(t_0 + kh) = I_k \\ &= -\frac{h}{\log(1-\nabla)} \nabla(1-\nabla)^{-1} f_k \end{aligned}$$

Developing the right hand side into a power series of ∇, we get

$$-\frac{h}{\log(1-\nabla)} \nabla(1-\nabla)^{-1} f_k = h \sum_{i=0}^{n} b_i \nabla^i f_k + R_{n+1}, \tag{46}$$

where R_{n+1} is the remainder term, and we neglect it hereafter. Then we get

$$\nabla x_{k+1} = h \sum_{i=0}^{n} b_i \nabla^i f_k \tag{47}$$

If we take note of $\nabla x_{k+1} = x_{k+1} - x_k$, we get

$$x_{k+1} = x_k + h \sum_{i=0}^{n} b_i \nabla^i f_k \tag{48}$$

Likewise from (33) we get

$$\begin{aligned} \nabla x_k &= x_k - x_{k-1} = \varphi(t_0 + kh) - \varphi(t_0 + (k-1)h) = I_{k-1} \\ &= -\frac{h}{\log(1-\nabla)} \nabla f_k \end{aligned}$$

Developing the right hand side into a power series of ∇, we get

$$-\frac{h}{\log(1-\nabla)} \nabla f_k = h \sum_{i=0}^{n} a_i \nabla^i f_k + R'_{n+1}, \tag{49}$$

where $R'_{n+1}$is the remainder term, and we neglect it hereafter. Then we get

$$\nabla x_{k-1} = h \sum_{i=0}^{n} a_i \nabla^i f_k \tag{50}$$

If we take note of $\Delta x_{k-1} = x_k - x_{k-1}$, we get

$$x_k = x_{k-1} + h \sum_{i=0}^{n} a_i \nabla^i f_k \tag{51}$$

(51) is Adams' interpolation formula (*or* Adams-Moulton's formula), and (48) is Adams' extrapolation formula (*or* Adams-Bashforth's formula).

4.2 Differential equation of the second order

Let the differential equation be of the form

$$\frac{d^2x}{dt^2} = \tilde{f}(x,t) = f(t) \tag{52}$$

4.2.1 The case where $f(t)$ is expressed with a forward difference formula

In this case we get from (25) as a solution of (52)

$$x = \psi(t) = \frac{h^2}{\{\log(1+\Delta)\}^2} f(t) + Ct + C' \tag{53}$$

Introducing the notation $x_k = \psi(t_0 + kh)$, we can write

$$\Delta^2 x_k = \Delta x_{k+1} - \Delta x_k \tag{54}$$

The first term of the right hand site can be written as

$$\Delta x_{k+1} = x_{k+2} - x_{k+1} = \psi(t_0 + (k+2)h) - \psi(t_0 + (k+1)h)$$

It follows from (53) that

$$\Delta x_{k+1} = \frac{h^2}{[\log(1+\Delta)]^2} \Delta f_{k+1} + Ch \tag{55}$$

Replacing k by $k-1$ in this expression, it becomes

$$\Delta x_k = \frac{h^2}{[\log(1+\Delta)]^2} \Delta f_k + Ch \tag{56}$$

Subtracting the latter equation from the former, we get

$$\Delta^2 x_k = \Delta x_{k+1} - \Delta x_k = \frac{h^2}{[\log(1+\Delta)]^2} \{\Delta f_{k+1} - \Delta f_k\} = \frac{h^2}{[\log(1+\Delta)]^2} \Delta^2 f_k \tag{57}$$

Here we note that

$$\Delta^2 x_k = \Delta x_{k+1} - \Delta x_k = x_{k+2} - 2x_{k+1} + x_k$$

then we get

$$x_k = 2x_{k+1} - x_{k+2} + \frac{h^2}{[\log(1+\Delta)]^2} \Delta^2 f_k \tag{58}$$

Developing the right hand side into a power series of Δ, we get

$$\frac{h^2}{[\log(1+\Delta)]^2} \Delta^2 f_k = h^2 \sum_{i=0}^{n} \bar{c}_i \Delta^i f_k + \bar{R}_{n+1}, \tag{59}$$

where $\bar{R}_{n+1}$ is a remainder term, and we neglect it hereafter. Then (58) can be written

$$x_k = 2x_{k+1} - x_{k+2} + h^2 \sum_{i=0}^{n} \bar{c}_i \Delta^i f_k \tag{60}$$

In this equation we replace k by $k-1$ and we get

$$\begin{aligned} x_{k-1} &= 2x_k - x_{k+1} + \frac{h^2}{[\log(1+\Delta)]^2}\Delta^2 f_{k-1} \\ &= 2x_k - x_{k+1} + \frac{h^2}{[\log(1+\Delta)]^2}\Delta^2 \tau^{-1} f_k \\ &= 2x_k - x_{k+1} + \frac{h^2}{[\log(1+\Delta)]^2}\Delta^2 (1+\Delta)^{-1} f_k \end{aligned} \tag{61}$$

Developing the right hand side into a power series of Δ, we get

$$\frac{h^2}{[\log(1+\Delta)]^2}\Delta^2(1+\Delta)^{-1} f_k = h^2 \sum_{i=0}^{n} \bar{d}_i \Delta^i f_k + \bar{R}'_{n+1}, \tag{62}$$

where $\bar{R}'_{n+1}$ is a remainder term, and we neglect it hereafter. Then (61) can be written

$$x_{k-1} = 2x_k - x_{k+1} + h^2 \sum_{i=0}^{n} \bar{d}_i \Delta^i f_k \tag{63}$$

4.2.2 The case where $f(t)$ is expressed with a backward difference formula

In this case we get from (32) as a solution of (52)

$$x = \psi(t) = \frac{h^2}{\{\log(1-\nabla)\}^2} f(t) + Ct + C' \tag{64}$$

Here we note that

$$\nabla^2 x_k = \nabla x_k - \Delta x_{k-1} \tag{65}$$

The first term of the right hand site can be written as

$$\nabla x_k = x_k - x_{k-1} = \psi(t_0 + kh) - \psi(t_0 + (k-1)h)$$

It follows from (64) that

$$\Delta x_k = \frac{h^2}{[\log(1-\nabla)]^2} \nabla f_k + Ch \tag{66}$$

Replacing k by $k-1$ in this equation, it becomes

$$\nabla x_{k-1} = \frac{h^2}{[\log(1-\nabla)]^2} \nabla f_{k-1} + Ch \tag{67}$$

Subtracting the latter equation from the former, we get

$$\nabla^2 x_k = \nabla x_k - \Delta x_{k-1} = \frac{h^2}{[\log(1-\nabla)]^2} \{\nabla f_k - \nabla f_{k-1}\} = \frac{h^2}{[\log(1-\nabla)]^2} \nabla^2 f_k \tag{68}$$

here we note that

$$\nabla^2 x_k = \nabla x_k - \nabla x_{k-1} = x_k - 2x_{k-1} + x_{k-2}$$

we get

$$x_k = 2x_{k-1} - x_{k-2} + \frac{h^2}{[\log(1-\nabla)]^2} \nabla^2 f_k \tag{69}$$

Developing the right hand side into a power series of ∇, we get

$$\frac{h^2}{[\log(1-\nabla)]^2}\nabla^2 f_k = h^2\sum_{i=0}^{n} c_i\nabla^i f_k + R_{n+1}, \tag{70}$$

where R_{n+1} is a remainder term, and we neglect it hereafter. Then (69) can be written

$$x_k = 2x_{k-1} - x_{k-2} + h^2\sum_{i=0}^{n} c_i\nabla^i f_k \tag{71}$$

Replacing k by $k+1$ in this equation, it becomes

$$\begin{aligned} x_{k+1} &= 2x_k - x_{k-1} + \frac{h^2}{[\log(1-\nabla)]^2}\nabla^2 f_{k+1} \\ &= 2x_k - x_{k-1} + \frac{h^2}{[\log(1-\nabla)]^2}\nabla^2\tau f_k \\ &= 2x_k - x_{k-1} + \frac{h^2}{[\log(1-\nabla)]^2}\nabla^2(1-\nabla)^{-1} f_k \end{aligned} \tag{72}$$

Developing the right hand side into a power series of ∇, we get

$$\frac{h^2}{[\log(1-\nabla)]^2}\nabla^2(1-\nabla)^{-1} f_k = h^2\sum_{i=0}^{n} d_i\nabla^i f_k + R'_{n+1}, \tag{73}$$

where R'_{n+1} is a remainder term, and we neglect it hereafter. Then (72) can be written

$$x_{k+1} = 2x_k - x_{k-1} + h^2\sum_{i=0}^{n} d_i\nabla^i f_k \tag{74}$$

(71) is Störmer's interpolation formula (*or* Cowell's formula), and (74) is Störmer's extrapolation formula.

5 Relations between Coefficients of Integration Formulas

I here collect series expansions :

$$\frac{x}{\log(1+x)} = \sum \bar{a}_i x^i, \tag{75}$$

$$\frac{x(1+x)^{-1}}{\log(1+x)} = \sum \bar{b}_i x^i, \tag{76}$$

$$-\frac{x}{\log(1-x)} = \sum a_i a^i, \tag{77}$$

$$-\frac{x(1-x)^{-1}}{\log(1-x)} = \sum b_i x^i, \tag{78}$$

$$\frac{x^2}{[\log(1+x)]^2} = \sum \bar{c}_i x^i, \tag{79}$$

$$\frac{x^2(1+x)^{-1}}{[\log(1+x)]^2} = \sum \bar{d}_i x^i, \tag{80}$$

$$\frac{x^2}{[\log(1-x)]^2} = \sum c_i x^i, \tag{81}$$

$$\frac{x^2(1-x)^{-1}}{[\log(1-x)]^2} = \sum d_i x^i \tag{82}$$

Replacing x by $-x$ in (75)

$$\frac{x}{\log(1+x)} = \sum \bar{a}_i x^i,$$

it becomes, by taking note of (77),

$$-\frac{x}{\log(1-x)} = \sum \bar{a}_i (-x)^i = \sum a_i x^i$$

Therefore we get a relation between $\bar{a}_i$ and a_i

$$\bar{a}_i = (-1)^i a_i \tag{83}$$

By the same way we get relations between $\bar{b}_i$ and b_i, between $\bar{c}_i$ and c_i, and between $\bar{d}_i$ and d_i :

$$\bar{b}_i = (-1)^i b_i, \tag{84}$$

$$\bar{c}_i = (-1)^i c_i, \tag{85}$$

$$\bar{d}_i = (-1)^i d_i \tag{86}$$

Next if we compare two equations (75) and (76), we get a relation

$$\sum \bar{a}_i x^i = (1+x) \sum \bar{b}_i x^i$$

$$\therefore \quad \bar{b}_0 = \bar{a}_0, \quad \bar{b}_i + \bar{b}_{i-1} = \bar{a}_i, \quad \text{or} \quad \bar{b}_i = \bar{a}_i - \bar{b}_{i-1} = \sum_{j=0}^{i} (-1)^j \bar{a}_{i-j} \tag{87}$$

Taking note of (83), (87) becomes

$$\bar{b}_0 = a_0, \qquad \bar{b}_i = (-1)^i \sum_{j=0}^{i} a_{i-j} = (-1)^i \sum_{j=0}^{i} a_j \tag{88}$$

From (84) and (87) we get

$$b_0 = a_0, \qquad b_i = \sum_{j=0}^{i} a_j \tag{89}$$

Likewise if we compare (75) and (79), we get

$$\sum \bar{c}_i x^i = \frac{x^2}{\{log(1-x)\}^2} = \left[\sum \bar{a}_i x^i\right]^2$$

$$\therefore \quad \bar{c}_i = \sum_{j=0}^{i} \bar{a}_{i-j} \bar{a}_j \tag{90}$$

From (85) and (90) we get

$$\bar{c}_i = (-1)^i \sum_{j=0}^{i} a_{i-j} a_j \tag{91}$$

And from (83) and (91) we get

$$c_i = \sum_{j=0}^{i} a_{i-j} a_j \tag{92}$$

Next comparing (79) and (80), we get

$$\sum \bar{c}_i x^i = \frac{x^2}{\{log(1-x)\}^2} = (1-x) \sum \bar{d}_i x^i$$

$$\therefore \quad \bar{d}_0 = \bar{c}_0, \quad \bar{d}_i - \bar{d}_{i-1} = \bar{c}_i, \quad \text{or} \quad \bar{d}_i = \bar{c}_i + \bar{d}_{i-1} = \sum_{j=0}^{i} (-1)^j \bar{c}_{i-j} \tag{93}$$

From (85) and (93) we get

$$\bar{d}_0 = c_0, \quad \bar{d}_i = (-1)^i \sum_{j=0}^{i} c_{i-j} = (-1)^i \sum_{j=0}^{i} c_j \tag{94}$$

And from (86) and (94) we get

$$d_0 = c_0, \quad d_i = \sum_{j=0}^{i} c_j \tag{95}$$

We see from this equation that we can get d_i from a_i through c_i. But we can also derive d_i directly from a_i.(*cf* [7] p.352) As it holds that

$$\frac{d}{dx} \frac{1}{log(1-x)} = \frac{(1-x)^{-1}}{[log(1-x)]^2}$$

we get

$$\sum d_i x^i = \frac{x^2(1-x)^{-1}}{[log(1-x)]^2} = x^2 \frac{d}{dx} \frac{1}{log(1-x)}$$

The result of differentiation of the right hand side is

$$\begin{aligned} \frac{d}{dx} \frac{1}{log(1-x)} &= \frac{d}{dx} \left\{ \frac{1}{x} \frac{1}{log(1-x)} \right\} = \frac{d}{dx} \left\{ -\frac{1}{x} \sum a_i x^i \right\} \\ &= -\frac{d}{dx} \left\{ \frac{a_0}{x} + a_1 + a_2 x + a_3 x^2 + \dots \right\} \\ &= -\left\{ -\frac{a_0}{x^2} + a_2 + 2a_3 x + a_4 x^2 + \dots \right\} \end{aligned}$$

Therefore it follows that

$$\begin{aligned} \sum d_i x^i &= -x^2 \left\{ -\frac{a_0}{x^2} + a_2 + 2a_3 x + a_4 x^2 + \dots \right\} \\ &= -\left\{ -a_0 + a_2 x^2 + 2a_3 x^3 + a_4 x^4 + \dots \right\} \\ &= \sum -(i-1) a_i x^i \end{aligned}$$

Finally we get

$$d_i = -(i-1) a_i \tag{96}$$

Thus we see that all the coefficients of integration formulas obtained above can be derived from the coefficients a_i of Adams-Moulton's formula (*or* Adams' interpolation formula).

6 Integration Formulas Expressed with f_k's

6.1 The case of forward interpolation

I collect here integration formulas for this case :

$$x_k = x_{k+1} - h\sum_{i=0}^{n} \bar{a}_i \Delta^i f_k, \tag{97}$$

$$x_{k-1} = x_k - h\sum_{i=0}^{n} \bar{b}_i \Delta^i f_k, \tag{98}$$

$$x_k = 2x_{k+1} + x_{k+2} + h^2\sum_{i=0}^{n} \bar{c}_i \Delta^i f_k, \tag{99}$$

$$x_{k-1} = 2x_k + x_{k+1} + h^2\sum_{i=0}^{n} \bar{d}_i \Delta^i f_k; \tag{100}$$

$$\Delta^i f_k = \sum_{j=0}^{i} (-1)^j \binom{i}{j} f_{k+i-j} \tag{101}$$

We can use these integration formulas for retrograde integration by replacing k by $-k$.

Applying (101) to the sum of the right hand side of (97), we can rewrite the sum as follows :

$$\begin{aligned}
\sum_{i=0}^{n} \bar{a}_i \Delta^i f_k &= \sum_{i=0}^{n}\sum_{j=0}^{i} (-1)^i \bar{a}_i \binom{i}{j} f_{k+i-j} \\
&= a_0 f_k \\
&\quad + \bar{a}_1 f_{k+1} - \bar{a}_1 \binom{1}{1} f_k \\
&\quad + \bar{a}_2 f_{k+2} - \bar{a}_2 \binom{2}{1} f_{k+1} + \bar{a}_2 \binom{2}{2} f_k \\
&\quad + \bar{a}_3 f_{k+3} - \bar{a}_3 \binom{3}{1} f_{k+2} + \bar{a}_3 \binom{3}{2} f_{k+1} - \bar{a}_3 \binom{3}{3} f_k + \cdots \\
&= \sum_{j=0}^{n} (-1)^j \bar{a}_j \binom{j}{j} f_k + \sum_{j=1}^{n} (-1)^{j+1} \bar{a}_j \binom{j}{j-1} f_{k+1} \\
&\qquad + \sum_{j=2}^{n} (-1)^{j+2} \bar{a}_j \binom{j}{j-2} f_{k+2} + \sum_{j=3}^{n} (-1)^{j+3} \bar{a}_j \binom{j}{j-3} f_{k+3} + \cdots \\
&= \sum_{i=0}^{n}\sum_{j=i}^{n} (-1)^{j+i} \bar{a}_j \binom{j}{i} f_{k+i} \\
&= \sum_{i=0}^{n} (-1)^i \sum_{j=i}^{n} a_j \binom{j}{i} f_{k+i}
\end{aligned}$$

Finally we get as the sum of the right hand side of (97)

$$\sum_{i=0}^{n} \bar{a}_i \Delta^i f_k = \sum_{j=0}^{n} a_i^* f_{k+i}, \qquad a_i^* = (-1)^i \sum_{j=i}^{n} a_j \binom{j}{i} \tag{102}$$

By the same way we get as the sum of the right hand side of (98), (99) and (100)

$$\sum_{i=0}^{n} \bar{b}_i \Delta^i f_k = \sum_{j=0}^{n} b_i^* f_{k+i}, \qquad b_i^* = (-1)^i \sum_{j=i}^{n} b_j \binom{j}{i}, \tag{103}$$

$$\sum_{i=0}^{n} \bar{c}_i \Delta^i f_k = \sum_{j=0}^{n} c_i^* f_{k+i}, \qquad c_i^* = (-1)^i \sum_{j=i}^{n} c_j \binom{j}{i}, \tag{104}$$

$$\sum_{i=0}^{n} \bar{d}_i \Delta^i f_k = \sum_{j=0}^{n} d_i^* f_{k+i}, \qquad d_i^* = (-1)^i \sum_{j=i}^{n} d_j \binom{j}{i} \tag{105}$$

6.2 The case of backward interpolation

Like before I collect here integration formulas for this case :

$$x_k = x_{k-1} + h \sum_{i=0}^{n} a_i \nabla^i f_k, \tag{106}$$

$$x_{k+1} = x_k + h \sum_{i=0}^{n} b_i \nabla^i f_k, \tag{107}$$

$$x_k = 2x_{k-1} + x_{k-2} + h^2 \sum_{i=0}^{n} c_i \nabla^i f_k, \tag{108}$$

$$x_{k+1} = 2x_k + x_{k-1} + h^2 \sum_{i=0}^{n} d_i \nabla^i f_k; \tag{109}$$

$$\nabla^i f_k = \sum_{j=0}^{i} (-1)^j \binom{i}{j} f_{k-j} \tag{110}$$

Applying (110) to the sum of the right hand side of (106), we can rewrite it as follows :

$$\begin{aligned}
\sum_{i=0}^{n} a_i \nabla^i f_k &= \sum_{i=0}^{n} \sum_{j=0}^{i} (-1)^i a_i \binom{i}{j} f_{k-j} \\
&= a_0 f_k \\
&\quad + a_1 f_k - a_1 \binom{1}{1} f_{k-1} \\
&\quad + a_2 f_k - a_2 \binom{2}{1} f_{k-1} + a_2 \binom{2}{2} f_{k-2} \\
&\quad + a_3 f_k - a_3 \binom{3}{1} f_{k-1} + a_3 \binom{3}{2} f_{k-2} - a_3 \binom{3}{3} f_{k-3} + \cdots \\
&= \sum_{j=0}^{n} a_j f_k - \sum_{j=1}^{n} a_j \binom{j}{1} f_{k-1} + \sum_{j=2}^{n} a_j \binom{j}{2} f_{k-2} + \sum_{j=3}^{n} a_j \binom{j}{3} f_{k-3} + \cdots \\
&= \sum_{i=0}^{n} \sum_{j=i}^{n} (-1)^i a_j \binom{j}{i} f_{k-i}
\end{aligned}$$

Therefore we get the following expression as the sum of the right hand side of (106) :

$$\sum_{i=0}^{n} a_i \nabla^i f_k = \sum_{i=0}^{n} a_i^* f_{k-i}, \qquad a_i^* = (-1)^i \sum_{j=i}^{n} a_j \binom{j}{i} \tag{111}$$

By the same way we get as the sum of the right hand side of (107), (108) and (109)

$$\sum_{i=0}^{n} b_i \nabla^i f_k = \sum_{i=0}^{n} b_i^* f_{k-i}, \qquad b_i^* = (-1)^i \sum_{j=i}^{n} b_j \binom{j}{i}, \tag{112}$$

$$\sum_{i=0}^{n} c_i \nabla^i f_k = \sum_{i=0}^{n} c_i^* f_{k-i}, \qquad c_i^* = (-1)^i \sum_{j=i}^{n} c_j \binom{j}{i}, \tag{113}$$

$$\sum_{i=0}^{n} d_i \nabla^i f_k = \sum_{i=0}^{n} d_i^* f_{k-i}, \qquad d_i^* = (-1)^i \sum_{j=i}^{n} d_j \binom{j}{i} \tag{114}$$

Coefficients $a_i^*, b_i^*, c_i^*, d_i^*$ obtained above are respectively identical with $\beta_j^*, \beta_j', \alpha_j^*, \alpha_j'$ in [5], $p.300$. And d_i is identical with c_j'.

References

[1] **Bordries,N.** *Time Regulation of an Adams-Moulton-Cowell Algolithm*, Celes.Mech., **16**, pp.291 ~ 308 (pp.300 ~ 304), 1977

[2] **Brower,D and Clemence,G.** *Methods of Celestial Mechanics*, pp.163 ~ 166, Academic Press, 1961

[3] **Jeffreys,H. & Jeffreys,B.** *Method of Mathemtical Physics*, pp.261 ~ 300, Cambridge, 1972

[4] **Kinoshita,H. and Nakai,H.** *Numerical Integration Methods in Dynamical Astronomy*, Celes.Mech., **45**, pp.231~ 244 (p.233), 1989

[5] **Oesterwinter,C. and Cohen,C.** *New Orbital Motion for Moon and Planets*, Celes.Mech., **5**, pp.317 ~ 395 (pp.328 ~ 332), 1972

[6] **Schubart,J & Stumpff,K** *On an N-Body Program of Computation of Ephemerides of Minor Planets and Comets*, Veröffentlichungen des Astronomischen Rechen-Instituts, Nr.18, 1966

[7] **Stumpff,K.** *Himmelsmechanik*, Bd2, pp.336 ~ 352, VEB Deutscher Verlag der Wissenschaften, 1965

[8] 篠原能材 「数値解析の基礎」pp.211 ~ 222, 日新出版, 1978

[9] 長谷川一郎 「天体軌道論」pp.241 ~ 280, 恒星社厚生閣, 1983

[10] ヘンリッチ,P 著, 一松・平本・本田 訳 「数値解析の基礎」pp.255 ~ 258, 培風館, 1973

Symbols and Names often used in Celestial Mechanics

a	:	semi-major axis	n	:	mean motion
b	:	semi-minor axis	l	:	mean anomaly
e	:	eccentricity	τ	:	time of pericenter passage
I	:	inclination	σ	:	mean anomaly at epoch
Ω	:	longitude of ascending node	λ	:	mean longitude
ω	:	argument of pericenter	ϵ	:	mean longitude at epoch
ϖ	:	longitude of pericenter			
u	:	eccentric anomaly	f	:	true anomaly

r : radius ϕ : longitude θ : latitude

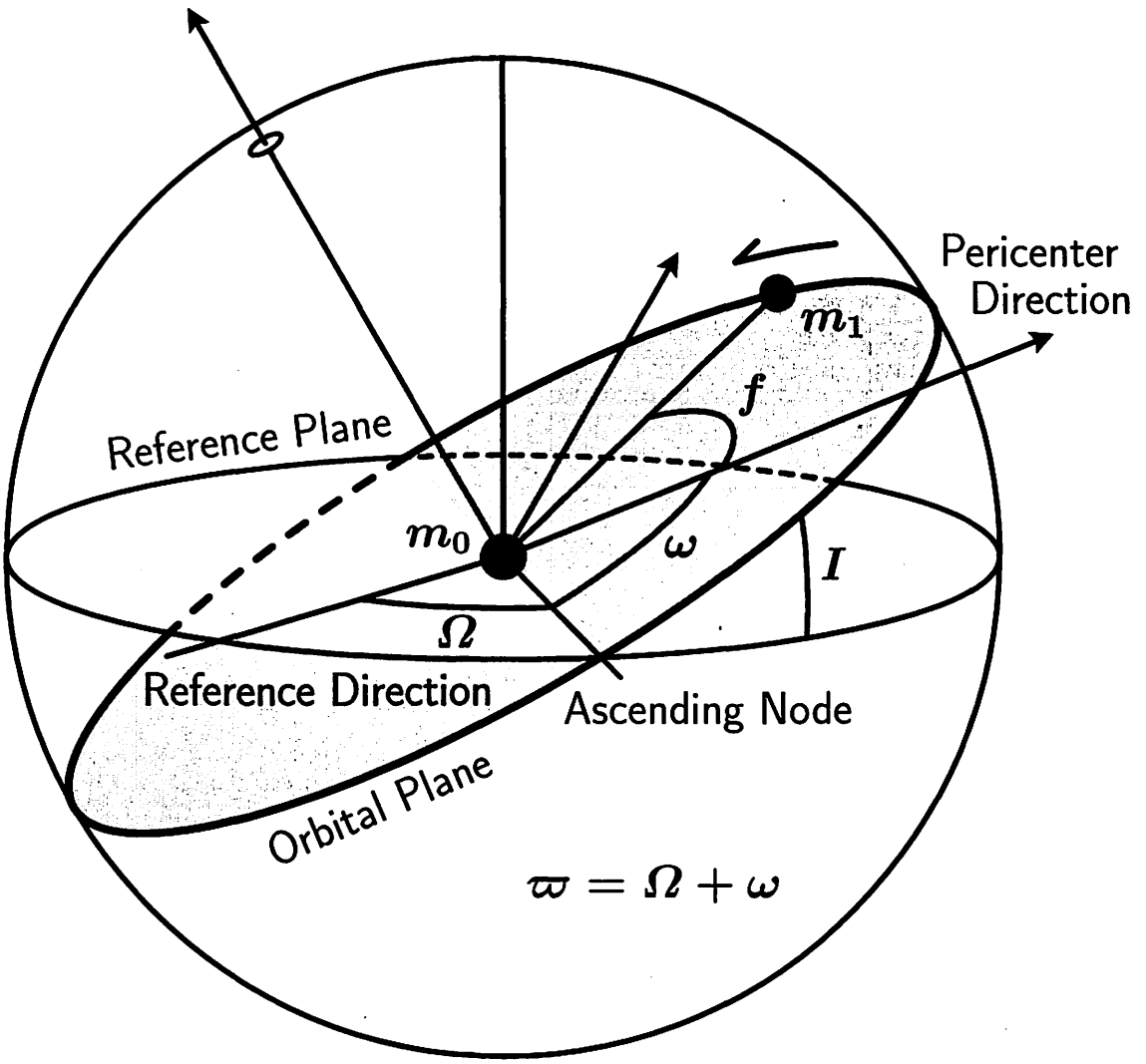

Reference Plane & Orbital Plane

Relation of r, ϕ and θ

$$r = \frac{a(1-e^2)}{1+e\cos f} = a(1-e\cos u)$$

$$\tan(\phi - \Omega) = \cos i \tan(\omega + f)$$

$$\sin\theta = \sin I \sin(\omega + f)$$

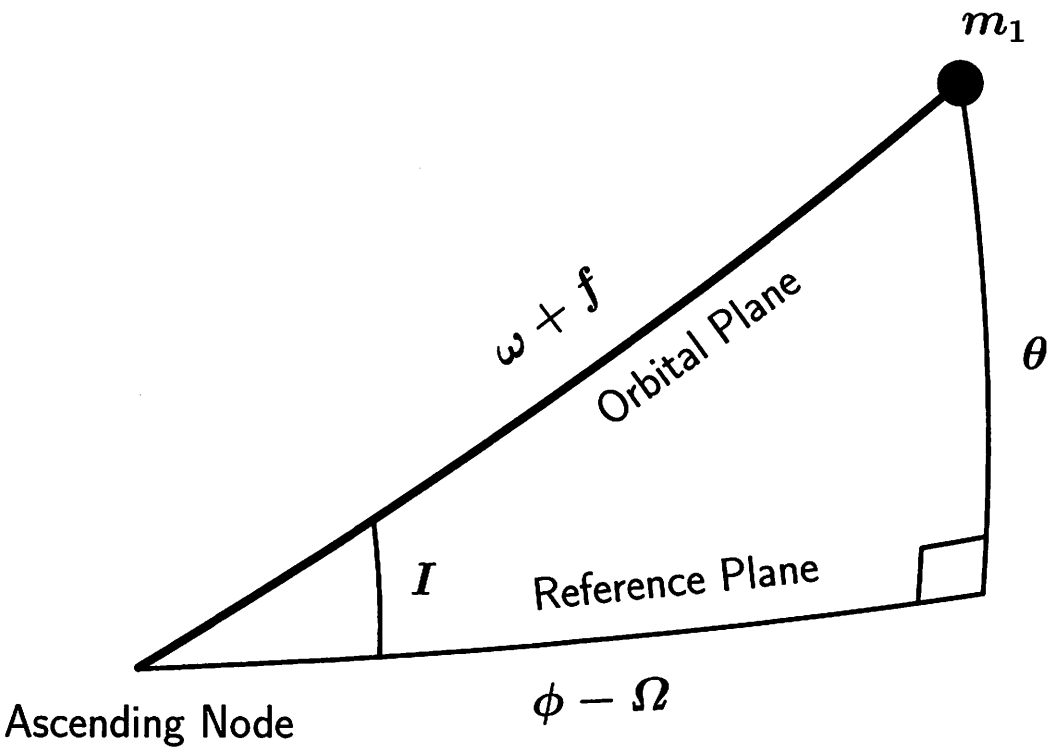

longitude & latitude

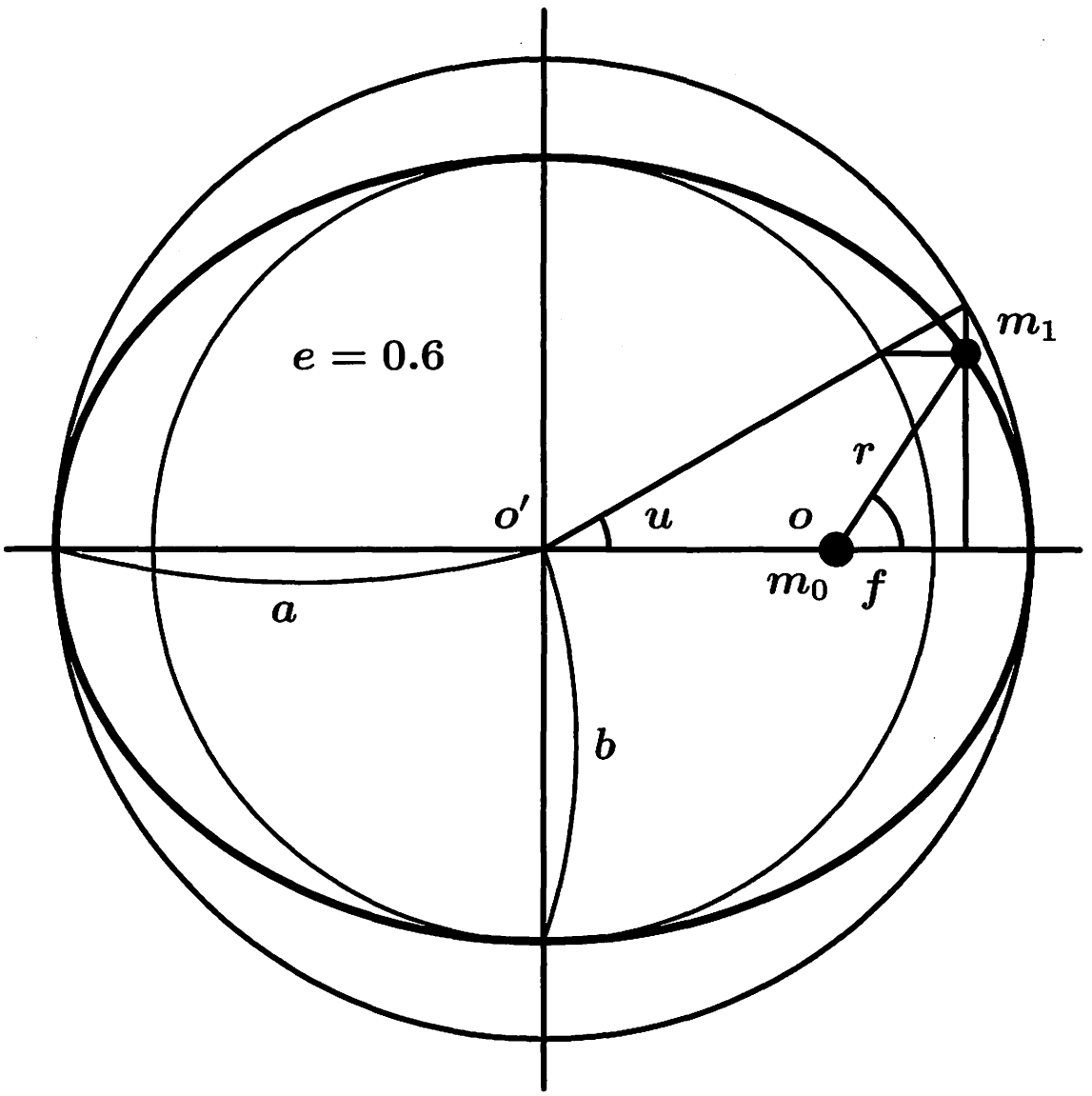

Orbital Plane

$$e = \frac{\sqrt{a^2 - b^2}}{a} \quad , \quad n = \sqrt{\frac{G(m_0 + m_1)}{a^3}}$$

$$\tan\frac{f}{2} = \sqrt{\frac{1+e}{1-e}}\tan\frac{u}{2}$$

$$u - e\sin u = l = n(t - \tau) = nt + \sigma$$

$$\lambda = nt + \epsilon \quad , \quad \epsilon = \sigma + \varpi$$

Symposium Program/プログラム

第1日 – 6日 (木)

13:30-14:20	受け付け
14:20-14:30	小久保 英一郎 (国立天文台) はじめに
14:30-14:40	山本 一登 (総合研究大学院大学) 軌道要素の説明
【力学系】	**座長: 小南 淳子**
14:40-15:00	井上 猛 (京都産業大学) Kepler 要素に対する Poisson 括弧の直接計算法
【地球回転】	**座長: 小南 淳子**
15:00-15:20	相馬 充 (国立天文台) 日本中世の日月食データの吟味と地球回転
15:20-15:40	河鰭 公昭 (名古屋大学) 古代日食から推測される地球慣性能率の変動
★テーマ公演★	**座長: 小久保 英一郎**
15:50-16:00	井田 茂 (東京工業大学) メインテーマについて - 共鳴と構造形成 -
16:00-16:30	跡部 恵子 (東京工業大学) 自転-軌道共鳴
【ポスター発表】	**座長: 樋口 有理可**
16:30-17:40	ポスター 3 分発表
18:30-19:30	夕食兼懇親会 (2 階宴会場)
19:30-	ポスターセッション兼ウェルカムパーティ (ポスター会場に飲み物を用意します)

第2日 – 7日 (金)

08:00-09:00	朝食 (2 階食堂)
09:00-10:00	ポスターセッション
★テーマ公演★	**座長: 井田 茂**
10:15-11:30	吉川 真 (宇宙科学研究所) 太陽系内の平均運動共鳴
11:30-12:00	武田 隆顕 (国立天文台) 見て分かる Lindblad 共鳴
12:00-13:00	昼食 (2 階食堂)
13:00-13:45	ポスターセッション

★テーマ公演★ 座長: 荒木田 英禎

13:45-15:00 木下 宙 (国立天文台)
永年共鳴について

15:00-15:30 小久保 英一郎 (国立天文台)
古在共鳴

【惑星系形成】 座長: 酒井 圭

15:40-16:00 今枝 佑輔 (国立天文台)
連星周りの Circumbinary Disk の構造

16:00-16:20 小南 淳子 (東京工業大学)
地球型惑星形成における原始惑星系円盤及び
巨大ガス惑星の重力の影響

16:30-16:50 高橋 啓介 (名古屋大学)
原始海王星移動メカニズムについて

16:50-17:19 小林 浩 (東京工業大学)
The Evidence of a Stellar Encounter and the Gas Drag on the Orbital Distribution of Edgeworth-Kuiper Belt Objects

17:10-17:30 船渡 陽子 (東京大学)
Three-Body Affairs in the Outer Solar System

18:00-20:00 夕食兼懇親会 (2 階宴会場)

第3日 – 8日 (土)

08:00-09:00 朝食 (2 階食堂)

09:00-10:00 ポスターセッション

【銀河・恒星系力学】 座長: 水谷 有宏

10:00-10:20 樽家 篤史 (東京大学)
Long-term Evolution of Stellar Self-Gravitating System away from the Thermal Equilibrium : Connection with Non-Exntensive Statistics

10:20-10:40 牧野 淳一郎 (東京大学)
巨大ブラックホールの「恒星系力学的証拠」について

【太陽系】 座長: 水谷 有宏

10:40-11:00 台坂 博 (東京大学)
羊飼い衛星の逆襲

【人工天体】 座長: 斎藤 正也

11:10-11:30 吉川 真 (宇宙科学研究所)
火星探査機「のぞみ」の軌道決定における諸問題 2

【数値計算法】 座長: 斎藤 正也

11:30-11:50 福島 登志夫 (国立天文台)
スケール変換による効率的な軌道シミュレーション

11:50-12:00 荒木田 英禎 (国立天文台)
おわりに

ポスター発表 (50 音順)

伊東 真史 (東京工業大学)	輻射効果を入れた系における原始惑星系円盤と惑星の重力相互作用
井上 猛 (京都産業大学)	水星近日点黄経に於ける余剰永年変化問題への最終解答
金枝 直子 (お茶の水女子大学)	自己重力系の崩壊過程における非ガウス的速度分布の形成とその起源
久保岡 俊宏 (通信総合研究所)	太陽輻射圧計算ソフトウェアの開発
後藤 振一郎 (名古屋大学)	離散非線形シュレーディンガー方程式におけるホモクリニック構造の自由度依存性について
斎藤 正也 (総合研究大学院大学)	1 次元 3 体問題の記号列による探索
酒井 圭 (東京工業大学)	Disc-Planet Gravitational Interaction
坂本 強 (総合研究大学院大学)	球状星団系の形成と進化
篠原 晋 (立命館大学)	非線形格子における低次元部分系
住谷 秀夫 (大阪音楽大学)	Kreutz 群のサブグループ
関口 昌由 (木更津高専)	N体問題における部分系の分類
立川 崇之 (早稲田大学)	一次元シート系におけるフラクタル構造と膨脹則
中井 宏 (国立天文台)	カイパーベルト帯における共鳴構造
中川 克也 (総合研究大学院大学)	運動量について 4 次の多項式第一積分を持つ 2 次元同次多項式ポテンシャル系，Part 2
本條 晴一郎 (東京大学)	Arnold Web の崩壊と大域的拡散
眞崎 良光 (国土地理院)	巨大惑星と平均運動共鳴にあるケンタウルス天体とその軌道進化
水谷 有宏 (総合研究大学院大学)	球状星団 ω Centauri の起源となる矮小銀河の動力学進化
山口 喜博 (帝京平成大学)	(1) 不安定領域におけるノンバーコフ型周期軌道の存在 (2) 順序を保存する軌道の点が存在しない領域の存在
山本 一登 (総合研究大学院大学)	一階の陽型対称線形多段法
吉田 春夫 (国立天文台)	岩波数学辞典・第 4 版の項目「天体力学」と「3 体問題」について
渡辺 憲昭 (千葉商科大学)	Cowell の方法のコメント

Author Index and Participant List/参加者リスト

ATOBE, Keiko（跡部 恵子）, *Tokyo Institute of Technology* 2
ARAKIDA, Hideyoshi（荒木田 英禎）, *National Astronomical Observatory of Japan*
CHIBA, Masashi（千葉 柾司）, *National Astronomical Observatory of Japan*
DAISAKA, Hiroshi（台坂 博）, *University of Tokyo* 216
FUKUSHIMA, Toshio（福島 登志夫）, *National Astronomical Observatory of Japan* ... 396
FUNATO, Yoko（船渡 陽子）, *University of Tokyo* 190
GOTO, Shin-itiro（後藤 振一郎）, *Nagoya University* 313
HATANAKA, Yoshizumi（畑中 至純）,
HIGUCHI, Arika（樋口 有理可）, *Kobe University*
HONJO, Seiichiro（本條 晴一郎）, *University of Tokyo* 367
IDA, Shigeru（井田 茂）, *Tokyo Institute of Technology* 1
IGUCHI, Osamu（井口 修）, *Ochanomizu University*
IMAEDA, Yusuke（今枝 佑輔）, *National Astronomical Observatory of Japan*
INOUE, Takeshi（井上 猛）, *Kyoto Sangyo University* 208, 230
ISHIBASHI, Nobuo（石橋 延夫）, *Kanagawa University*
ITO, Masafumi（伊東 真史）, *Tokyo Institute of Technology* 198
KANAEDA, Naoko（金枝 直子）, *Ochanomizu University* 77
KAWABATA, Kin-aki（河鰭 公昭）, *Nagoya University* 282
KINOSHITA, Hiroshi（木下 宙）, *National Astronomical Observatory of Japan* 39
KOBAYASHI, Hiroshi（小林 浩）, *Tokyo Institute of Technology* 149
KOKUBO, Eiichiro（小久保 英一郎）, *National Astronomical Observatory of Japan* 52
KOMINAMI, Junko（小南 淳子 ）, *Tokyo Institute of Technology* 128
KONISHI, Tetsuro（小西 哲郎）, *Nagoya University*
KUBO-OKA, Toshihiro（久保岡 俊宏）, *Communications Research Laboratory* 307
MAKINO, Junichiro（牧野 淳一郎）, *University of Tokyo* 70
MASAKI, Yoshimitsu（眞崎 良光）, *Geographical Survey Institute* 255
MIZUTANI, Arihiro（水谷 有宏）, *Graduate University for Advanced Studies* 115
NAKAGAWA, Katsuya（中川 克也）, *Graduate University for Advanced Studies* 345
NAKAI, Hiroshi（中井 宏）, *National Astronomical Observatory of Japan* 243
SAITO, Masaya（斎藤 正也）, *Graduate University for Advanced Studies* 324
SAITO, Nobuaki（斎藤 信明）, *Kyoto Sangyo University*
SAKAGAMI, Masaaki（阪上 雅昭）, *Kyoto University*
SAKAI, Kei（酒井 圭）, *Tokyo Institute of Technology* 205
SAKAMOTO, Tsuyoshi（坂本 強）, *Graduate University for Advanced Studies* 95
SEKIGUCHI, Masayoshi（関口 昌由）, *Kisarazu National College of Techonology* 340
SHINOHARA, Susumu（篠原 晋）, *Ritsumeikan University* 332
SÔMA, Mitsuru（相馬 充）, *National Astronomical Observatory of Japan* 267

SOTA, Yasuhide（曽田 康秀）, *Ochanomizu University*
SUMITANI, Hideo（住谷 秀夫）, *Osaka College of Music* 235
SUTO, Yasushi（須藤 靖）, *University of Tokyo*
SUZUKI, Masaru（鈴木 将）, *University of Tokyo*
TAKAHASHI, Keisuke（高橋 啓介）, *Nagoya University* 144
TAKEDA, Takaaki（武田 隆顕）, *National Astronomical Observatory of Japan* 33
TAMURA, Ryoko（田村 涼子）, *Ochanomizu University*
TANIKAWA, Kiyotaka（谷川 清隆）, *National Astronomical Observatory of Japan* 377
TARUYA, Atsushi（樽家 篤史）, *University of Tokyo* . 60 TATEKAWA, Takayuki（立川 崇之）, *Waseda University* 88
TSURIBE, Toru（釣部 通）, *Osaka University*
URAYAMA, Fuminobu（浦山 文伸）, *Japan Air Self-Defense Force*
WADA, Keiichi（和田 桂一）, *National Astronomical Observatory of Japan*
WATANABE, Noriaki（渡辺 憲昭）, *Chiba University of Commerce* 427
YAMAGUCHI, Yoshihiro（山口 喜博）, *Teikyo Heisei University* 385
YAMAMOTO, Tadato（山本 一登）, *Graduate University for Advanced Studies* 411
YOSHIDA, Haruo（吉田 春夫）, *National Astronomical Observatory of Japan*
YOSHIKAWA, Makoto（吉川 真）, *Institute of Space and Astronautical Science* 21, 299

(所属は 2003 年 3 月現在の所属)

天体力学N体力学研究会

平成15年3月6日－8日 伊豆長岡 千歳荘